The effect of intense electromagnetic fields with complex configuration on nuclear betadecay

V. N. Rodionov

Moscow State Academy for Geological Exploration 101000 Moscow, Russia
(Submitted 20 June 1996; resubmitted 30 August 1996)
Zh. Éksp. Teor. Fiz. **111**, 3–24 (January 1997)

This paper discusses how an electromagnetic field consisting of a superposition of a constant magnetic field and a field of laser type can affect nuclear beta decay. In general it is not assumed that the intensities of the two types of fields are small compared to the characteristic field $H_{cr}^{*}=\beta_1 H_{cr}$, where $H_{cr}=m^2c^3/e\hbar$ and the quantity β_1 depends on the energy liberated in the decay and the configuration of the electromagnetic field. For nonrelativistic decays the quantity β_1 is found to be of the same order as the maximum kinetic energy of an electron referenced to its rest energy $\beta_1 \sim I \ll 1$. It is assumed that the frequency of the wave field satisfies $\hbar\omega/mc^2 \leqslant I$. The behavior of the probability for the process is studied over a wide range of the fundamental parameters that characterize the fields. Corresponding asymptotic expressions are derived in the ''weak''- and ''strong''-field regimes. Also discussed are so-called interference corrections to the unperturbed decay probability, which cannot in principle be studied by the methods of perturbation theory. It is shown that the times and distances that are important in generating these contributions exceed the parameters of the unperturbed processes, just as in the case of a plane-wave field previously investigated in detail by Nikishov and Ritus. However, in contrast to the case of a pure wave field, when a system is simultaneously subjected to a constant magnetic field and a wave field, the degree to which these characteristic regions are enlarged can depend not only on the intensities of the electromagnetic fields but also on their rates of change, even in the limit in which the wave field is slowly varying.
[S1063-7761(97)00101-7]

1. INTRODUCTION

Considerable attention has been focused on the study of the excitation and decay of nuclei under the action of intense electromagnetic fields. A large number of papers (see the review article Ref. 1) have been written about the possibility of using both constant magnetic fields and focused laser radiation to affect nuclear beta decay. In another group of papers, the authors discuss how intense plane-wave electromagnetic fields affect such decays (see Refs. 2, 3 and the papers cited therein).

Interest in this problem dates back to the 1920's, when Einstein first discussed the possibility that radioactivity could be induced by the action of optical quanta.[4] Recently, renewed interest in this possibility has arisen, reinforced both by new data from studies of processes observed in the vicinity of pulsars, where magnetic fields with gigantic intensities are well known to exist, and by the development of new experimental techniques.

The first studies of the beta decay of a neutron in an intense electromagnetic field were carried out by Korovina *et al.*[5] and Ternov *et al.*[6] In these studies the effect of a static magnetic field on the process was included. A comprehensive investigation of weak-interaction decays in a plane-wave field can be found in Ref. 7, which also contains a detailed analysis of the analytic properties of the probability with respect to charge. A description of the important characteristics of neutron decay under the combined action of a magnetic field and a wave field was presented in Ref. 8.

In essentially all of the papers devoted to this topic, the authors have noted that the external fields can give rise to fundamentally new physical effects when the intensities of the electric and magnetic components are comparable to the quantity $H_{cr}^{*}=\beta_1 H_{cr}$, where $H_{cr}=m^2/e$ is a characteristic field magnitude that measures the importance of fundamental quantum electrodynamic phenomena (here e, m are the charge and mass of an electron; the value of the characteristic field is written in a system of units where $\hbar=c=1$, which is also used in what follows). In this case the coefficient β_1 depends both on the energy liberated in the decay,

$$\varepsilon_0=\frac{M_x-M_y}{m}, \tag{1}$$

where M_x, M_y are the masses of the mother and daughter nuclei respectively, and on the specific type of electromagnetic field configuration acting on the nuclei. Thus, e.g., for nonrelativistic decay ($\varepsilon_0-1=I\ll 1$) in a constant magnetic field[8,9]

$$\beta_1=2I, \tag{2}$$

while for a wave field that varies sufficiently slowly, or in the case of the so-called constant crossed field[2,3,7–14] ($E=H$, $\mathbf{E}\perp\mathbf{H}$),

$$\beta_1=(2I)^{3/2}. \tag{3}$$

It is noteworthy that results analogous to (2), (3) apply to a variety of situations in which processes that occur in the

absence of an electromagnetic field are subject to such fields, both static magnetic fields and fields of laser type, when the wave frequency is sufficiently low.[1,5,16]

Although the presence of electromagnetic fields with intensities $H \ll H_{cr}^{*}$ can be felt only through corrections to the total decay probability in the absence of the field, it turns out that even in this range, nontrivial behavior of field dependences can be observed. In particular, a few papers have noted that there are external fields of a special type for which the decay probability contains nonanalytic terms when the fields are turned off, which cannot in principle be reproduced by the methods of perturbation theory. It must be pointed out that the basis for studying such effects was laid by V. I. Ritus in Ref. 7, who concluded that at the time the external field is turned off, the probability has an essential singularity as a function of the external field. The emergence of this type of behavior in the decay probability when a static magnetic field is present was discussed in Refs. 1, 15.

Although each of these examples has been studied in considerable detail in isolation, it is fair to say that we are still far from constructing any sort of definitive theory of beta decay in external fields. Among other things, this conclusion follows from the limitations that characterize essentially all studies in this area, namely those connected with having to treat the interaction in the nonrelativistic limit. However, there is also a lack of studies of interference effects arising from the simultaneous application of different kinds of electromagnetic fields. Although predicting such effects is usually difficult even at the qualitative level, we can distinguish, for example, the possibility that the total field might act resonantly on the charged particles of a reaction.

It is this latter situation, i.e., nuclear beta decay in the presence of a superposition of electromagnetic fields that admit the possibility of resonant behavior, that excites interest. It should be noted that although a general approach based on the use of exact solutions of relativistic quantum equations of motion of charged particles in an external field (the Furry representation) has been known for a relatively long time, inclusion of external fields of a specific type requires formulation and development of special methods of investigation (see, e.g., Refs. 1–3, 9, 16).

The fundamental difficulty in studying how fields with compound structure affect the course of a decay is the complexity of the equations involved and their analysis, which is typical of multiparameter processes. This difficulty can to some extent be avoided if the superposition of fields under study consists of a static magnetic field and the field of a plane electromagnetic wave propagating along it.

This combination of electromagnetic fields is well known to have the property that the relativistic quantum equations of motion of a charged particle interacting with it can be solved exactly. This enables us to develop and generalize methods based on exact inclusion of the characteristics of the external field to the case of electromagnetic fields with compound structure. We note that these solutions were first obtained by Redmond;[17] hence, in what follows we will refer to this superposition of electromagnetic fields as the Redmond configuration, with the understanding that it consists of the following components: a constant uniform magnetic field and the field of a plane electromagnetic wave with circular polarization and with frequency and amplitude ω and E, respectively.

In this paper we discuss the effect of an intense electromagnetic field with the Redmond configuration on the nuclear beta decay process $\mathrm{X} \to \mathrm{Y} + \mathrm{e} + \overline{\nu}$. We assume that the masses M_x and M_y of the initial and final nuclei are so large compared to the electron mass m and the energy yield in the decay $m\varepsilon_0$ that we can neglect effects of order m/M and $m\varepsilon_0/M$. In this case, however, we assume that the intensities of both the constant and time-varying fields can be comparable to $\beta_1 H_{cr}$ or even exceed that value.

The fundamental result of this paper is the derivation of a relatively compact analytic expression for the total probability of beta decay in an external field with the Redmond configuration and its detailed analysis in both the nonrelativistic and relativistic limits. Let me emphasize that the integral representations given here, to my knowledge, have not been presented anywhere in the literature before, even for those special cases where one of the components of the Redmond configuration is missing. The nonrelativistic limit of the decay probability in a field with the Redmond configuration is investigated here using an expression in the form of a single integral, which in special cases agrees with the results of Refs. 1–3, 5–15. Another topic we will investigate in detail is interference effects for a field with the Redmond configuration over a wide range of the fundamental parameters, including the region of cyclotron resonance. The results obtained here generalize well-known studies of analogous effects in a plane-wave field[7,11–13] to the case in which a constant magnetic field affects the decay at the same time.

2. PROBABILITY OF NUCLEAR BETA-DECAY IN AN ELECTROMAGNETIC FIELD WITH THE REDMOND CONFIGURATION

In Ref. 8, Ternov *et al.* investigated effects related to the polarization of particles that participate in the beta- decay of a neutron in an intense electromagnetic field with the Redmond configuration. In obtaining expressions for the beta decay probability that took into account the influence of an external field, they used exact solutions of the Dirac equation that describe the motion of an electron. If we repeat all the fundamental steps of their calculation, which is described in detail in Ref. 8, but generalize their results to the case in which the energy ε_0 released in the decay is arbitrary, we can write the final expression for the total decay probability of nucleus X within the allowed-transition approximation in the form (analogous to Eq. (6) of Ref. 8)

$$W_i = G_0 \mu \sum_{n,n'}^{\infty} \int_0^{\infty} d\alpha \int_0^{\infty} d\tau \; \tau^2 \Phi_i \delta(f_i), \tag{4}$$

where $i = 1, 2$, $W = W_1 + W_2$, $G_0 = G_v^2 m^5 (1 + 3\alpha_0^2)/4\pi^3$, G_v is the weak interaction constant, α_0 is the ratio of the axial vector and the vector contributions, and

$$\Phi_1 = \alpha I_{n',n-1}^2(z), \tag{5}$$

$$\Phi_2 = \alpha_+ I_{n'-1,n}^2(z) + \xi_1^2 \alpha I_{n'-1,n-1}^2(z)$$

$$+2\xi_1\sqrt{2\mu n}I_{n'-1,n}(z)I_{n'-1,n-1}(z). \quad (6)$$

Here we also introduce the notation:

$$\alpha=\frac{p_0-p_3}{m}, \quad \alpha_+=\frac{p_0+p_3}{m}, \quad \xi=\frac{eE}{m\omega}, \quad \xi_1=\frac{\xi\omega}{\delta_1},$$

$$\mu=\frac{H}{H_{cr}}, \quad \omega_H=m\mu, \quad \delta_1=\alpha\omega-\omega_H,$$

p_0 and p_3 are the energy and longitudinal component (with respect to the direction of the magnetic field) of the electron momentum, τ is the neutrino energy, and $I_{n',n}(z)$ is the Laguerre function, which is related to the degenerate Gauss hypergeometric function:

$$I_{n',n}(z)=\frac{\sqrt{n!/n'!}}{(n-n')!}\exp\left(-\frac{z}{2}\right)z^{(n-n')/2} \times F(-n',n-n'+1,z),$$

where $z=\xi_1^2\mu/(2\lambda^2)$, $\lambda=\omega/m$.

In Eq. (4) we have averaged over the polarization states of the nucleus X and summed over the states of Y. The contributions Φ_i essentially correspond to the different orientations of the electron spin. The special property of an electron in the quantum state $n=0$ (where n is a Landau level), i.e., that its spin can only be oriented opposite to the magnetic field, leads to two different conservation laws, which are determined by the different δ-function arguments that correspond to orientations of the electron spin along and opposite to the direction of the magnetic field:

$$f_{1,2}=-S_0+2\beta\mu\eta(n-n'\mp1)-2\mu n + \xi^2\beta\eta/(1-\beta\eta), \quad (7)$$

where $S_0=1-2\alpha(\varepsilon_0-\tau)+\alpha^2$, $\eta=\gamma\omega/\omega_H$, $\gamma=M_x/m$, $\gamma\beta=\alpha$.

Note in comparing with Eq. (6) of Ref. 8 that in (4) the variable of integration has been changed:

$$\frac{dq_3}{q_0^*}=-\frac{d\alpha}{\alpha},$$

the expression has been integrated over the angle of flight of the neutrino, and a new summation index $n'=n+l\mp1$ has been introduced. Here q_0^* is the average energy of an electron in a field with the Redmond configuration, and q_3 is the longitudinal component of its quasimomentum (see Ref. 8).

By exchanging the orders of integration and summation in (4) and using the properties of the Laguerre functions, we can obtain a representation for the total probability of nuclear beta decay in the form

$$W_k=-\frac{iG_0}{2\pi}\int_{-\infty}^{\infty}dx\int_0^{\infty}d\alpha\int_0^{\infty}d\tau\tau^2\exp(iS\mp ix)F_k, \quad (8)$$

where $k=1,2$, $W=W_1+W_2$,

$$F_1=\frac{\alpha}{2\sin x},$$

$$F_2=\frac{\varepsilon_0-\tau-\alpha/2}{\sin x}-\frac{iU}{\gamma},$$

$$U=\left(\frac{\xi\eta}{\sin x}\right)^2\left[\frac{\beta\sin^2(x\Delta)}{\Delta^2}\exp(-ix) - \frac{\sin(x\beta\eta)\sin(x\Delta)}{\eta\Delta}\right],$$

$$S=-\frac{xS_0}{\mu}+\frac{x\xi^2\eta\beta}{\Delta\mu}-\frac{\xi^2}{\mu\Delta^2}\frac{\sin(x\beta\eta)\sin(x\Delta)}{\sin x},$$

$$\Delta=1-\beta\eta.$$

The procedure for obtaining this result will be demonstrated for the example of contribution (5). For this we can use the integral representation of the δ-function and the explicit form of the dependence of its arguments on summation index:

$$f_1=An+Bn'+C, \quad (9)$$

where

$$A=-2\mu+2\mu\eta\beta, \quad B=-2\mu\eta\beta,$$

$$C=\xi^2\eta\beta\Delta^{-1}-S_0-2\mu\eta\beta,$$

and apply the formula for summation of bilinear combinations of Laguerre functions (see Ref. 16)

$$\sum_{n'=0}^{\infty}I_{n,n'}^2(z)\exp(-in'\varphi) = \exp[-i(n\varphi+z\sin\varphi)]I_{n,n}(u).$$

After summation over the index n', the expression

$$\Phi_1^*=\alpha\sum_{n,n'=0}^{\infty}I_{n,n'}^2(z)\,\delta(f_1)$$

takes the form

$$\Phi_1^*=\frac{\alpha}{2\pi}\int_{-\infty}^{\infty}dt\,\exp(iCt)\sum_{n=0}^{\infty}\exp[-i(n\varphi+z\sin\varphi - tAn)]I_{n,n}(u), \quad (10)$$

where $u=4z\sin^2(\varphi/2)$, and $\varphi=-tB$, $z=\xi^2/(2\mu\Delta^2)$ is the argument of the Laguerre function in Eqs. (5), (6).

The remaining sum over n can be expressed in terms of elementary functions. For this it is necessary to use yet another formula for the summation of $I_{n,n}(z)$, which can also be obtained from the properties of the Laguerre function:

$$\sum_{n=0}^{\infty}\exp(in\varphi_1)I_{n,n}(u)=\frac{i\exp(-i\varphi_1/2)}{2\sin(\varphi_1/2)} \times\exp\left(-\frac{iu}{2}\cot\frac{\varphi_1}{2}\right), \quad (11)$$

where $\varphi_1=t(A+B)=-2\mu t$.

After these transformations we can obtain

$$\Phi_1^*=-\frac{i\alpha}{4\pi}\int_{-\infty}^{\infty}dt\,\frac{\exp[i(S_1-\varphi_1/2)]}{\sin(\varphi_1/2)}, \quad (12)$$

where

$$S_1 = Ct - 2z\,\frac{\sin(\varphi/2)\sin(\varphi_2/2)}{\sin(\varphi_1/2)},$$

$$\varphi_2 = \varphi + \varphi_1.$$

Introducing the new variable of integration $x=\mu t$ and shifting the index of summation n by unity, we finally obtain for the contribution Φ_1

$$\sum_{n,n'=0}^{\infty} \Phi_1 \delta(f_1) = -\frac{i\alpha}{4\pi\mu}\int_{-\infty}^{\infty}\frac{dx}{\sin x}\exp[i(S-x)]. \tag{13}$$

By making analogous transformations for Φ_2, we obtain the result (4) given above. Note that in these expressions we must pass the contours under the real-axis singularities of the function being integrated. Before integrating over the neutrino factor τ, we may regard expression (4) as the differential probability distribution with respect to the neutrino energy.

The integration over the neutrino spectrum is easily carried out using the expression

$$\int_0^{\infty} t^{\lambda}\exp(-ixt)dt = -i\,\exp\left(i\,\frac{\pi}{2}\lambda\right)\frac{\Gamma(1+\lambda)}{(x-i0)^{1+\lambda}}, \tag{14}$$

$$\lambda \neq -1,-2,\ldots,$$

which we must regard as an integral transformation of generalized functions. After this the total probability for nuclear beta decay in an electromagnetic field with the Redmond configuration reduces to the form

$$W = \frac{G_0\mu}{2\pi}\int_0^{\infty}\frac{d\alpha}{\alpha}\int_{-\infty}^{\infty}\frac{d\rho}{\rho^3}\left[\left(\varepsilon_0+\frac{3i}{\rho}\right)(\cot x + i) - i\left(\alpha + \frac{U\exp(ix)}{\gamma}\right)\right]\exp(iS^*), \tag{15}$$

where $x=\mu\rho/(2\alpha)$, $S^*(\rho,\alpha)=S(\rho,\alpha,\tau)+\rho\tau$ no longer depends on τ.

Equation (15) enables us to obtain rather easily a number of new representations for the probability of nuclear beta decay when the Redmond configuration is lacking one or the other of its components.

Thus, for example, if we reduce the parameter that characterizes the wave intensity ξ to zero, we have from Eq. (15)

$$W = \frac{G_0\mu}{2\pi}\int_0^{\infty}\frac{du}{u}\int_{-\infty}^{\infty}\frac{d\rho}{\rho^3}\cot\left(\frac{\mu u\rho}{2}\right) \times\left(\varepsilon_0+\frac{3i}{\rho}\right)\exp\left[i\rho\varepsilon_0 - \frac{i\rho}{2}\left(u+\frac{1}{u}\right)\right], \tag{16}$$

where $u=1/\alpha$.

Equation (16) defines an integral representation that has not been presented previously in the literature. It corresponds to the total probability for nuclear beta decay with arbitrary energy release in the presence of a constant uniform magnetic field H. If we assume that the energy released in the decay is small, i.e.,

$$\varepsilon_0 - 1 = I \ll 1,$$

then it is easy to obtain from (16)

$$W = \frac{G_0\mu}{\sqrt{2\pi}}\exp\left(-i\,\frac{\pi}{4}\right)\cdot\int_{-\infty}^{\infty}\frac{\cot(\mu\rho/2)}{\rho^{7/2}}\exp(i\rho I)d\rho. \tag{17}$$

In the weak-field limit ($\mu \ll I$) it follows that

$$W = W_0\left\{1+\sum_{n=1}^{\infty}\frac{\Gamma(9/2)2^{2n}B_{2n}}{(2n)!\Gamma(9/2-2n)}\left(\frac{\mu}{2I}\right)^{2n} + \frac{7}{2}\left(\frac{\mu}{I}\right)^{7/2}\zeta\left(-\frac{5}{2},v\right)\right\}, \tag{18}$$

where $v=a-[a]$, $a=I/\mu$, $0<v<1$, $[a]$ is the integer part of the number a, and

$$W_0 = \frac{4}{105}\,G_0(2I)^{7/2} \tag{19}$$

is the decay probability in the absence of a field in the nonrelativistic limit.

Note that the asymptotic expansion (18) can be obtained by expanding $\cot x$ in (17) about zero

$$\cot x = \sum_{n=0}^{\infty}\frac{(-1)^n 2^{2n}}{(2n)!}B_{2n}x^{2n-1},$$

where B_{2n} are the Bernoulli numbers. If we integrate this series term by term, also taking into account the contributions to the integral (17) from nonvanishing poles of the cotangent $\rho=2n\pi/\mu$, where $n=\pm 1, \pm 2,\ldots$, we find that the generalized Riemann zeta function $\zeta(a,v)$ appears.

Substituting in the values of the Bernoulli numbers $B_2=1/6$, $B_4=-1/30$, $B_6=1/42$ and using the Hurwitz representation for $\zeta(-5/2,v)$, we can write Eq. (18) in the form

$$W = W_0\left\{1+\frac{35}{12}\left(\frac{\mu}{2I}\right)^2 - \frac{7}{48}\left(\frac{\mu}{2I}\right)^4 + \frac{1}{96}\left(\frac{\mu}{2I}\right)^6 - \frac{105}{8\pi^3}\left(\frac{\mu}{2I}\right)^{7/2}\left[\sin\left(\frac{2\pi I}{\mu}-\frac{\pi}{4}\right)+\frac{1}{2^{7/2}}\sin\left(\frac{4\pi I}{\mu} - \frac{\pi}{4}\right)\right]+\ldots\right\}. \tag{20}$$

The appearance in the field dependence (20) of ''monotonic'' and ''oscillating'' components is unremarkable for processes in an external field (see Refs. 1–3, 7, 11–15). Both of these contributions disappear when the field is turned off. However, in contrast to the monotonic term, which owes its appearance to our expanding the expression under the integration sign in (17) about zero, the oscillatory contribution is determined by a broader range of the variable of integration. Since this integral (17) is essentially a so-called proper-time representation of the probability of the process,[18] we can argue physically that the time for creation of the oscillatory corrections can considerably exceed the characteristic time for creation of the monotonic terms. Thus, from Eqs. (17)–(20) it follows that whereas the time for generation of the monotonic corrections is determined only by the energy released in the decay, $\rho\sim I^{-1}$, as in a free process, for the oscillatory corrections we have $\rho\sim\mu^{-1}$. Inasmuch as

$\mu \ll I$, this indicates that the characteristic time and region of formation of the decay in a field exceed the time and region of the unperturbed process by a factor of I/μ. The specific form of the dependence of the oscillatory contributions on field is determined by the characteristics of the process itself and the field configuration (see Refs. 7, 11–13, 15); however, a common feature for both is nonanalyticity when the field is turned off. The need to include a broader region of generation of the oscillatory terms than the region around zero implies that the form of these terms cannot be reproduced by the methods of perturbation theory, but rather requires the use of other, more powerful, methods of investigation.

In the strong-field limit ($\mu > I$) in (17), taking into account the rule for avoiding poles and approximating the cotangent in the upper half-plane of the complex variable $x=\mu\rho/2$ (for $|x| \gg 1$, $\cot x \sim -i$), we have

$$W = \frac{7\mu}{4I}\, W_0. \tag{21}$$

From (21) it follows directly that in this strong-field limit, the beta decay probability increases linearly with field H, which first noted in Ref. 5.

Also of no small interest is the fact that if we use the representation of the function $\zeta(s,a)$ for large values of the argument $a=I/\mu>1$, in place of (18) we can obtain a more general result:

$$W = W_0\left\{\frac{7}{4}\, a^{-1} + \frac{7}{2}\, a^{-7/2}\left[\zeta\left(-\frac{5}{2},v\right) - \zeta\left(-\frac{5}{2},a\right)\right]\right\}. \tag{22}$$

In a strong field where $\mu > I$, it follows in particular from (22) that $[a]=0$, and hence that $a=v$, which again leads to Eq. (21). Equation (22) clearly demonstrates that the total probability for beta decay ceases to oscillate when the parameter μ reaches values at least equal to I. Note that Nikishov *et al.* predicted similar behavior for the total probabilities of certain processes in the field of an electromagnetic wave in Ref. 13.

In the other limiting case, where there is no constant magnetic field in the Redmond configuration ($\mu \to 0$), we obtain from (15) another new representation for the nuclear beta decay probability in the field of an electromagnetic wave with arbitrary release of energy:

$$W = \frac{G_0}{\pi}\int_0^\infty \frac{du}{u^2}\int_{-\infty}^\infty \frac{d\rho}{\rho^4}\exp(iS_2^*) \times\left\{\varepsilon_0 - \xi^2 u\,\sin^2\left(\frac{\lambda\rho}{2}\right) + \frac{3i}{\rho}\right\}, \tag{23}$$

where

$$S_2^* = \rho\varepsilon_0 - \frac{\rho}{2u} - \frac{\rho u}{2}\left\{1 + \xi^2\left(1 - \frac{\sin^2(\lambda\rho/2)}{(\lambda\rho/2)^2}\right)\right\},$$

$$\lambda = \frac{\omega}{m}. \tag{24}$$

Note that Eqs. (23), (24) follow from (15) after we expand the cotangent about zero, and evaluate the function in the exponent S^* and the function U under the integral sign in the limits $\mu \to 0$ and $\eta \to \infty$. Note also that in obtaining (23), (24) we have discarded terms due to wave polarization. However, this contribution is easy to recover if we include terms of higher order in $1/\eta$ in these processes, assuming in this case that $x\beta\eta \sim 1$. In particular, in this approximation

$$\frac{Ue^{ix}dx}{\gamma} = \frac{\xi^2}{\alpha}\left(-i\,\frac{\sin^2 f}{f} - \frac{\sin f\,\cos f}{f} + \frac{\sin^2 f}{f^2}\right)df, \tag{25}$$

where $f=\beta\eta x$; the exponent in the same variables reduces to the expression

$$S_2 = -Af + B\,\frac{\sin^2 f}{f},$$

where

$$A = -\frac{2}{\lambda}\left[\varepsilon_0 - \frac{1}{2}\left(u + \frac{1}{u}\right) - \frac{\xi^2 u}{2} - \tau\right], \quad B = \frac{\xi^2 u}{\lambda}$$

and the dependence on neutrino energy is recovered.

From (24), (25) we obtain the well-known representation for the probability of beta decay in a wave field in the form of a sum of bilinear combinations of Bessel functions. Note that to do this, we transform the integrals

$$I(A,B) = \int_{-\infty}^\infty \frac{df}{f}\exp(-iAf)\exp\left\{iB\,\frac{\sin^2 f}{f}\right\},$$

by representing the second exponential factor in series and trigonometric functions in the numerator by exponentials, to the form

$$I^{l,k}(A) = \int_{-\infty}^\infty \frac{dx}{x^{l+1}}\exp[ix(2l-2k-A)]. \tag{26}$$

Recalling that in (26), as before, the singularity at ''zero'' is shifted into the upper half-plane, after integration over x we have

$$I^{l,k}(A) = 2\pi\,\frac{i^{l+1}}{l!}\,(2l-2k-A)^l,$$

where $2l-2k-A \geqslant 0$, whereupon

$$k \leqslant k_{\max} = \left[l - \frac{A}{2}\right], \quad l \geqslant l_{\min} = \left[\frac{A}{2}\right].$$

Thus, $I(A,B)$ represented in the form of a sum,

$$I(A,B) = 2\pi i\sum_{l=l_{\min}}^\infty \sum_{k=0}^{k_{\max}} \frac{B^l(2l)!(-1)^k}{(l!)^2 2^{2l}(2l-k)!k!} \times(2l-2k-A)^l.$$

Changing the order of summation and introducing a new summation index $n=l-k$, we obtain

$$\sum_{l=l_{\min}}^\infty \sum_{k=0}^{k=l-l_{\min}} \ldots = \sum_{k=0}^\infty \sum_{l=k+l_{\min}}^\infty \ldots = \sum_{k=0}^\infty \sum_{n=n_{\min}}^\infty \ldots$$

while for $I(A,B)$ we have

$$I(A,B) = 2\pi i\sum_{n=n_{\min}}^\infty \sum_{k=0}^\infty \frac{(-1)^k (z/2)^{2n+2k}\Gamma(2n+2k+1)}{k!\Gamma^2(n+k+1)\Gamma(2n+k+1)},$$

where $z=\sqrt{B(2n-A)}$, $n_{\min}=[A/2]$.

It is easy to see that the sum over k reduces to the well-known representation for the square of Bessel functions:

$$I(A,B)=2\pi i\sum_{n=n_{\min}}^{\infty} J_n^2(z).$$

The contribution

$$I_1(A,B)=\int_{-\infty}^{\infty}\frac{df}{f}\sin^2 f\,\exp(-iAf)\exp\left\{iB\,\frac{\sin^2 f}{f}\right\}$$

can be reduced to the form

$$I_1(A,B)=-\frac{1}{4z}\frac{d}{dz}\left[z\,\frac{d}{dz}I(A,B)\right],$$

which in turn gives

$$I_1(A,B)=-\frac{\pi i}{2}\sum_{n=n_{\min}}^{\infty}(J_{n+1}^2+J_{n-1}^2-2J_n^2).$$

In a completely analogous way, we obtain for the remaining terms in (25)

$$I_2(A,B)=-\frac{i}{2}\int_{-\infty}^{\infty}\frac{df}{f}\sin(2f)\times\exp(-iAf)\exp\left\{\frac{iB\,\sin^2 f}{f}\right\}$$

$$=-2\pi i\sum_{n=n_{\min}}^{\infty}\frac{n}{z}J_n(z)J_n'(z),$$

$$I_3(A,B)=i\int_{-\infty}^{\infty}\frac{df}{f^2}\sin^2 f\,\exp(-iAf)\exp\left\{\frac{iB\,\sin^2 f}{f}\right\}$$

$$=2\pi i\,\frac{z}{B}\sum_{n=n_{\min}}^{\infty}J_n(z)J_n'(z).$$

Substituting these expressions into the original integral, we obtain an expression for the probability in the field of an electromagnetic wave which agrees with the results obtained previously in investigations of beta decay in a laser field.[1,3,8,10,12]

The integral representation (23) makes it possible to write the probability in an electromagnetic wave field in the form of a single integral, while including the relativistic character of the interaction. For this, note that the integral over the energy variable u can be written in the form

$$\int_0^{\infty}\frac{du}{u^2}\exp\left\{-i\,\frac{\rho}{2}\left(uA_1+\frac{1}{u}\right)\right\}=-\pi\sqrt{A_1}H_1^{(2)}(\rho\sqrt{A_1}),$$

where $H_1^{(2)}(z)$ is a Hankel function, and

$$A_1=1+\xi^2\left(1-\frac{\sin^2 f}{f}\right).$$

In a completely analogous way, we also calculate the remaining integrals entering into (23). Substituting these expressions, we have

$$W=-G_0\int_{-\infty}^{\infty}\frac{d\rho}{\rho^4}\exp(i\rho\varepsilon_0)\sqrt{A_1}\left\{\left(\varepsilon_0+\frac{3i}{\rho}\right)H_1^{(2)}-\xi^2\sin^2\left(\frac{\lambda\rho}{2}\right)H_0^{(2)}\right\}. \tag{27}$$

These results, which are single integrals over $H_0^{(2)}$ and $H_1^{(2)}$, correspond as before to a proper-time representation of the distribution function for a light, charged particle in the field of an electromagnetic wave. This assertion becomes obvious if we note that the total probability of the process can be calculated by starting with the optical theorem and identifying this probability as the imaginary part of the elastic scattering amplitude integrated over all final states, leaving the integration with respect to time to the final stage of the calculation. Note that an analogous result was used in Refs. 13, 14, and 19 in investigating processes in an external field. As the wave field turns off ($\xi\to 0$) it is easy to obtain an analogous representation from (27), expressed in terms of the free-particle distribution function.[20] For this, using the integral

$$W_0=\frac{G_0}{\pi}\int_0^{\infty}\frac{du}{u^2}\int_{-\infty}^{\infty}d\rho\left(\frac{\varepsilon_0}{\rho^4}+\frac{3i}{\rho^5}\right)\exp(iS_0\rho)$$

and the replacement described above, we have

$$W_0=-G_0\int_{-\infty}^{\infty}d\rho H_1^{(2)}(\rho)\left(\frac{\varepsilon_0}{\rho^4}+\frac{3i}{\rho^5}\right)\exp(i\varepsilon_0\rho).$$

This last expression furnishes an explicit form for the dependence of the decay probability on the energy release ε_0 if we take into account that

$$\int_{-\infty}^{\infty}\frac{\exp(i\rho\varepsilon_0)}{\rho}H_1^{(2)}(\rho)=-4i\sqrt{\varepsilon_0^2-1},$$

and use the analytic dependence of the right-hand side on the parameter ε_0. In the special case of a nonrelativistic decay ($I\ll 1$), which provides the main contribution to the integral coming from values $|\rho|\gg 1$, after approximating the Hankel functions for large values of the argument

$$H_1^{(2)}(\rho)=\sqrt{\frac{2}{\pi\rho}}\exp\left(i\,\frac{3}{4}\,\pi\right)\exp(-i\rho),$$

it follows that

$$W_0=\frac{4}{105}G_0(2I)^{7/2},$$

which is found to be in agreement with Eq. (19).

3. ASYMPTOTIC EXPRESSION FOR THE BETA DECAY PROBABILITY IN A FIELD WITH THE REDMOND CONFIGURATION

We now discuss in more detail the case in which both the influence of the constant magnetic field and that of the electromagnetic wave field in the Redmond configuration are not assumed to be small. Let us assume that $\mu\ll 1$. In this approximation the dominant term in the integral (15) comes from the region $x\ll 1$. Let us expand the integrand about zero. Then the exponent reduces to the form

$$S=-yz-y^3/3,$$

where

$$y=\left(\frac{\xi\lambda}{u}\right)^{2/3}\rho,\quad z=\left(\frac{u}{\chi}\right)^{2/3}S_0,\quad f=\left(\frac{u}{\chi}\right)^{2/3}\frac{y\lambda}{u},$$

$$\xi\lambda=\chi,$$

and the preexponential factor is given by

$$\frac{iUe^{ix}}{\gamma}\,dx=\xi^2 uf\,df=\left(\frac{\chi}{u}\right)^{2/3}uy dy.$$

Thus, in this limit, the beta decay probability can be written in the form

$$W=\frac{G_0}{8\pi}\chi^2\int_{-\infty}^{\infty}\frac{dy}{y^5}\int_0^{\infty}\frac{du}{u}\exp\left(-iyz-i\frac{y^3}{3}\right)\times\left\{\varepsilon_0 y-u\left(\frac{\chi}{u}\right)^{2/3}\left(y^3-\frac{3}{2}i\right)\right\}. \tag{28}$$

This expression coincides with the analogous expression for the probability in a constant crossed field taking into account the relativistic character of the interaction, written in terms of Airy functions.[8] It generalizes previous results for a nonrelativistic integral representation,[13,14] and also allows us to analyze this process without appealing to the properties of the Airy functions, which were widely used previously.

In particular, in the nonrelativistic limit ($I\ll 1$), we can obtain from (28) an expression in the form of a Mellin–Barnes-type integral:

$$W=\frac{G_0}{\sqrt{\pi}}\chi^{7/3}R(\chi), \tag{29}$$

where

$$R(\chi)=\frac{3^{-5/6}}{105}\frac{1}{2\pi i}\int_{\gamma-i\infty}^{\gamma+i\infty}\Gamma\left(\frac{s}{3}+\frac{1}{6}\right)\Gamma(-s)\times\left(\frac{1}{3}\right)^{-s/3}u^s F(u,s)\cos\frac{\pi}{3}(2s+1)ds, \tag{30}$$

$$-1/2<\gamma<0,$$

$$F(u,s)=4u^4+u\{18+2s+4s(s-1)\}+\frac{15}{u^2}s(s-1),$$

$$u=2I/\chi^{2/3}.$$

The singularities of the integrand in (30) are determined by the poles of the gamma function; The integration contour contains the vertical straight line Re $s=\gamma$, which separates a left-hand and a right-hand series of poles. Hence, by closing the contour of integration respectively ''on the right'' or ''on the left,'' we can obtain asymptotic expansions from (30) for different values of the field parameter χ. It should be noted that in the present case, i.e., the nonrelativistic limit with respect to energy released in the decay, the actual expansion parameter is

$$\chi_*=\frac{\chi}{(2I)^{3/2}}.$$

Therefore, setting $\chi_*\gg 1$, we must close the integration contour on the right. Then from (30) we obtain a series in inverse powers of χ_*:

$$W=W_0(3\chi_*)^{7/3}\frac{5\Gamma^2(2/3)}{12\cdot 6^{2/3}\pi\Gamma(5/6)}\sum_{n=0}^{\infty}\frac{u^{n-2}}{n!}\times\Gamma\left(\frac{n}{3}+\frac{1}{6}\right)3^{n/3}\cos\frac{\pi}{3}(2n+1)\times\left\{n(n-1)+\frac{4}{15}u^6+\frac{2}{15}u^3(9-n+2n^2)\right\}.$$

Here $u=\chi_*^{-2/3}$.

Using the latter relation, we obtain

$$W=W_0(3\chi_*)^{7/3}\frac{5\Gamma^2(2/3)}{24\pi 2^{2/3}}\left\{1+\frac{6}{5}\frac{\Gamma(1/6)}{\Gamma(5/6)}(3\chi_*)^{-2/3}-\frac{8\Gamma(1/2)}{\Gamma(5/6)}(3\chi_*)^{-4/3}+\ldots\right\}. \tag{31}$$

Note that the first term of our expansion was derived previously (see Refs. 3, 11, 13) in a discussion of the analogous process in a constant crossed field in the low energy release limit.

In the opposite limiting case, where the parameter $\chi_*\ll 1$, the asymptotic series is obtained by closing the integration contour on the left, because the singularities of the gamma function for $s<0$ lie there:

$$W=W_0(R_1+R_2),$$

where

$$R_1=\sum_{n=0}^{\infty}\frac{\Gamma(3n+1/2)}{n!\Gamma(1/2)}\left(-\frac{\chi_*^2}{3}\right)^n\left\{1+\frac{\chi_*^2}{2}(18n^2+9n+10)+\frac{15}{16}\chi_*^4(36n^2+24n+3)\right\}, \tag{32}$$

$$R_2=\frac{1}{2}\sum_{n=0}^{\infty}\left(-\frac{4}{9}\right)^n\left\{g^{-2n}\sin g\left[-\frac{d_n}{g^2}\left(1+\frac{5}{3g^2}\right)+\frac{2}{3g^2}(a_{2n}+b_n)\right]+g^{-2n-1}\cos g\left[-\frac{14}{9}a_{2n}+\left(f_n-\frac{h_n}{g^2}\right)\left(1+\frac{5}{3g^2}\right)+\frac{2}{3}\frac{c_n}{g^2}\right]\right\}. \tag{33}$$

Here

$$g=\frac{2}{3\chi_*},\quad b_n=\frac{2}{3}a_{2n+1}-\left(2n+\frac{1}{3}\right)a_{2n},$$

$$c_n=\frac{4}{3}a_{2n+1}\left(n+\frac{2}{3}\right),$$

$$d_n=2c_n+2b_n(2n+1),$$

$$f_n=2b_n-4na_{2n}-\frac{2}{3}a_{2n+1},$$

$$h_n=4c_n(n+1),$$

and the coefficients are given by

$$a_m=\sum_{k=0}^{2m}\frac{(2k-1)!!}{3^{2m-k}(2m-k)!(2k)!!}\frac{\Gamma(3m-k+1/2)}{\Gamma(1/2)}.$$

Expressions (32), (33) determine the monotonic (R_1) and oscillating (R_2) contributions in this weak-field approximation $\chi_*\ll 1$. Calculation of the coefficients that determine the oscillatory field corrections in general leads to somewhat more complicated expressions than for the case of a constant magnetic field (see (18), (20)); however, the first of these can be easily calculated by using the values

$$a_0=1,\quad a_1=\frac{5}{12},\quad a_2=\frac{205}{2^5 3^2},\quad a_3=\frac{5\cdot 7\cdot 11\cdot 59}{2^7\cdot 3^4},$$

which finally yields

$$W=W_0\left\{1+\frac{35}{8}\chi_*^2+\frac{35}{128}\chi_*^4-\left(\frac{35}{32}\right)^2\chi_*^6+\frac{105}{16}\chi_*^4\sin\left(\frac{2}{3\chi_*}\right)+\ldots\right\}. \tag{34}$$

The first corrections (up to χ_*^4) coincide with analogous results of calculations given previously (see Refs. 1, 7, 10–14). It is also quite noteworthy that despite the formal presence in the expansion (33) of terms of all orders in g, the oscillatory part vanishes as $\chi\to 0$ like χ_*^4.

Finally, it is also of interest to obtain the asymptotic dependence of the probability when the parameter χ turns out to be large, while at the same time taking the relativistic character of the interaction into account. In this limit we use Eq. (28) and discuss the situation in which the parameter χ takes on values $\chi\gg\varepsilon_0>1$. Introducing a new variable of integration

$$u=\frac{u_1}{\sqrt{1+a^2\rho_1^2}},$$

where

$$a=\frac{\chi}{\sqrt{12}},\quad \rho_1=\frac{2}{u}\left(\frac{u}{\chi}\right)^{2/3}y,\quad \chi=\xi\lambda=\frac{E}{H_{cr}},$$

the expression for the probability can be written in the form

$$W=\frac{G_0}{\pi}\int_{-\infty}^{\infty}\frac{d\rho_1}{\rho_1^4}\int_0^{\infty}\frac{du_1}{u_1^2}\sqrt{1+a^2\rho_1^2}\times\left\{\varepsilon_0+\frac{3i}{\rho_1}-\frac{\chi^2\rho_1^2}{4}\frac{u_1}{\sqrt{1+a^2\rho_1^2}}\right\}\times\exp\left[i\rho_1\varepsilon_0-i\frac{\rho_1}{2}\sqrt{1+a^2\rho_1^2}\left(u_1+\frac{1}{u_1}\right)\right]. \tag{35}$$

Using Hankel functions, from here it is not difficult to obtain once again a representation for the beta decay probability in the form of a single integration:

$$W=-\frac{G_0\chi}{\sqrt{12\pi}}\left\{\int_0^{\infty}\frac{d\varrho}{\varrho^3}\left[\exp(i\varrho\varepsilon_0)\left[\left(\varepsilon_0+\frac{3i}{\varrho}\right)H_1^{(2)}(z)-i\sqrt{\frac{3}{4}}\chi\varrho H_0^{(2)}(z)\right]+\exp(-i\varrho\varepsilon_0)\left[\left(\varepsilon_0-\frac{3i}{\varrho}\right)\times H_1^{(1)}(z)-i\sqrt{\frac{3}{4}}\chi\varrho H_0^{(1)}(z)\right]\right]\right\}, \tag{36}$$

where $z=\varrho\sqrt{1+\chi^2\varrho^2/12}$.

In this approximation χ can be regarded as the largest parameter; hence, it is not difficult to see that the dominant contribution to the integral (36) in this case will come from the region $z\gg 1$. Using the asymptotic form of the functions $H^{(1,2)}(z)$ for large values of the argument, we have from (36)

$$W=\frac{2G_0A_1}{\pi}\left\{\int_0^{\infty}\frac{d\varrho}{\varrho^5}\sin\left(a\varrho^2+\frac{\pi}{4}\right)-\frac{\chi}{\sqrt{12}}\int_0^{\infty}\frac{d\varrho}{\varrho^3}\cos\left(a\varrho^2+\frac{\pi}{4}\right)\right\}, \tag{37}$$

$$A_1=\frac{3\sqrt{2\pi}}{12^{1/4}}\chi^{1/2}.$$

Recall that we avoid the singularities in the integral (37) by detouring below them, as before. In this case the calculation can make use of tabulated integrals:[21]

$$\int_0^{\infty}\frac{\sin t}{t^{n+1}}dt=\frac{(-1)^n}{n!}\left\{\frac{\pi}{2}\cos\left(n\frac{\pi}{2}\right)-\Psi(n+1)\sin\left(n\frac{\pi}{2}\right)\right\},$$

$$\int_0^{\infty}\frac{\cos t}{t^{n+1}}dt=\frac{(-1)^n}{n!}\left\{\Psi(n+1)\cos\left(n\frac{\pi}{2}\right)+\frac{\pi}{2}\sin\left(n\frac{\pi}{2}\right)\right\},$$

where

$$\Psi(n+1)=1+\frac{1}{2}+\frac{1}{3}+\ldots+\frac{1}{n}$$

is the γ-logarithmic derivative of the gamma function. Substituting these values into (37), we finally obtain

$$W=\frac{3}{4\sqrt{\pi}}G_0\left(\frac{\chi}{2\sqrt{3}}\right)^{5/2}(1+\pi-2\gamma), \tag{38}$$

from which it follows that in this approximation the probability is independent of the energy released in the decay and increases with increasing field as $\chi^{5/2}$. Note that in the nonrelativistic limit, the leading term of the asymptotic expansion of the decay probability as $\chi_*\gg 1$ is also independent of I,[3,11,13] which is clearly indicated by Eq. (32) in particular. The explanation is that in these limits, the region of formation of the decay is determined exclusively by the field; however, the field dependence turns out to be different when we take the relativistic structure of the interaction into account.

4. NONRELATIVISTIC LIMIT OF THE BETA DECAY PROBABILITY IN A FIELD WITH THE REDMOND CONFIGURATION

The least-studied situation is the one in which both the magnetic field and a wave field are retained in the Redmond configuration; that is, neither of these is regarded as small. Expression (15) can give a complete picture in this case, if we take the relativistic character of the interaction into account. However, the double integration eliminates the possibility of a thorough analysis. In the nonrelativistic limit ($I \ll 1$), one of the integrations in (15) can be carried out, after which the total probability for nuclear beta decay becomes

$$W = \frac{\mu G_0}{\sqrt{2\pi}} \exp\left(-i\,\frac{\pi}{4}\right) \int_{-\infty}^{\infty} \frac{\cot(\mu\rho/2)}{\rho^{7/2}} \exp(iS)\,d\rho, \quad (39)$$

where

$$S = \xi^2 \frac{2I}{\lambda\delta}\left\{x\left(\frac{\delta}{\xi^2}-1\right) + \frac{1-\delta}{\delta}\frac{\sin x\,\sin(x\delta)}{\sin[x(1-\delta)]}\right\},$$

$$x = \frac{\rho\lambda}{2}, \quad \delta = 1-\frac{\mu}{\lambda}, \quad \lambda = \frac{\omega}{m}, \quad \mu = \frac{H}{H_{cr}}, \quad (40)$$

and the characteristic parameter for the wave intensity in the nonrelativistic limit has the form

$$\xi = \frac{eE}{m\omega\sqrt{2I}}.$$

Expressions (39), (40) provide information about the process over a wide range of the fundamental parameters of the problem. Representing the exponent in the form

$$S = Q\Psi(x), \quad Q = \frac{2I}{\lambda}\frac{\xi^2}{\delta},$$

$$\Psi(x) = \left(\frac{\delta}{\xi^2}-1\right)x + \frac{1-\delta}{\delta}\frac{\sin x\,\sin(x\delta)}{\sin[(1-\delta)x]}$$

and finding the derivatives of the function $\Psi(x)$,

$$\Psi' = \frac{\delta}{\xi^2} - 1 - \frac{1-\delta}{\delta}\frac{\sin^2(x\delta) - \delta\sin^2 x}{\sin^2[x(1-\delta)]},$$

$$\Psi'' = \frac{1-\delta}{\delta}\left\{\frac{2\cos[(1+\delta)x]}{\sin[(1-\delta)x]} - 2(1-\delta)\frac{\sin(2x)}{\sin^2[(1-\delta)x]} + 2(1-\delta)^2\frac{\sin^2 x\,\cos[(1-\delta)x]}{\sin^3[(1-\delta)x]}\right\}, \quad (41)$$

we can use the condition $\Psi'(x)=0$ to find the stationary points in the integral (39), which leads to the equation

$$\delta\left(\frac{\delta}{\xi^2}-1\right) = (1-\delta)\left\{(1-\delta)\frac{\sin^2 x}{\sin^2[(1-\delta)x]} - \frac{\sin[(1+\delta)x]}{\sin[(1-\delta)x]}\right\}. \quad (42)$$

Note that δ can take on values $-\infty < \delta \leqslant 1$. Depending on where the value of field intensity ξ lies within the range of δ, the left side of Eq. (42) reduces to zero either at a single point or at two points. (A plot of the left-hand side of (42) is shown in Fig. 1.) Thus, when $\xi<1$, this occurs at $\delta=0$ and $\delta=\xi^2$. When $\xi>1$, the left-hand side of the equation can vanish only at $\delta=0$. At $\xi=1$, the root for the left-hand side merges with the endpoint value of the parameter $\delta=1$. It is easy to see that $\delta=1$ corresponds to eliminating the constant magnetic field from the Redmond configuration ($\mu\to 0$). In this limit the left- and right-hand sides of Eq. (42) reduce to

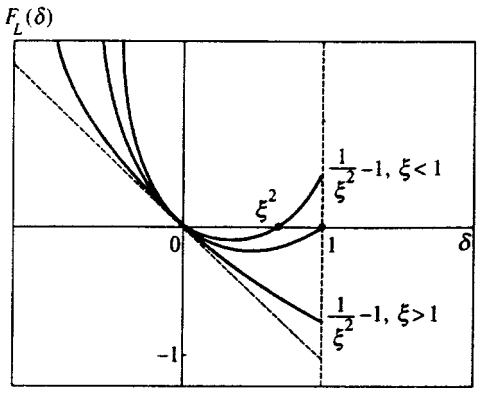

FIG. 1.

$$F_L = \frac{1}{\xi^2} - 1,$$

$$F_R(x) = -\frac{\sin(2x)}{x} + \frac{\sin^2 x}{x^2},$$

and the stationary points are determined in the same manner as for an electromagnetic wave field, which was discussed in detail in Ref. 13. In particular, it was shown in Ref. 13 that only as ξ approaches unity does the series of saddle points become infinite.

In an electromagnetic field with the Redmond configuration this situation is much more complex. Thus, e.g., when $\delta=1/2$, which corresponds to $\omega = 2\omega_H$, we have from (41) that

$$\Psi(x) = \left(\frac{1}{2\xi^2}-1\right)x + \sin x, \quad (43)$$

$$\Psi'(x) = \frac{1}{2\xi^2} - 1 + \cos x, \quad (44)$$

$$\Psi''(x) = -\sin x. \quad (45)$$

The stationary points in this case are roots of the equation

$$1 - \frac{1}{2\xi^2} = \cos x, \quad (46)$$

from which it follows that for $1/2 \leqslant \xi < \infty$ the series of saddle points is unbounded. For $\xi \gg 1$ the roots of Eq. (46) reduce to the form

$$x_n = 2\pi n \pm 1/\xi, \quad n = 0, \pm 1, \pm 2, \ldots .$$

By virtue of the evenness of the function $\Psi'(x)$, the saddle points appear in pairs; the first pair is $\pm x_1 = \pm 1/\xi$, which yields

$$\Psi(x_1)=\frac{1}{3\xi^3},\quad \Psi''(x_1)=-\frac{1}{\xi}.$$

Substituting these values into the original integral

$$W=\frac{G_0}{\sqrt{2\pi}}\exp\left(-i\,\frac{\pi}{4}\right)\times\left(\frac{\lambda}{2}\right)^{7/2}\int_{-\infty}^{\infty}\frac{\cot(x/2)}{x^{7/2}}\exp\left\{i\,\frac{4I}{\lambda}\,\xi^2\Psi(x)\right\}dx,$$

which is determined by the saddle-point method, leads to the probability in a slowly varying field (see (32), (33)), but with a frequency dependence that differs from the dependence of a pure wave field (see Refs. 3, 13):

$$W=W_0\left\{1+\frac{35}{8}\,\chi_*^2-\frac{7}{128}\,\frac{\chi_*^4}{\xi^2}+\frac{7}{64}\,\frac{\chi_*^3}{\xi^2}\left[\cos\left(\frac{2}{3\chi_*}\right)-\frac{\chi_*}{12}\sin\left(\frac{2}{3\chi_*}\right)\right]+\ldots\right\}.$$

By taking the limit $\delta\to 0$ in (39), which physically corresponds to equating the frequency of the wave ω and the cyclotron frequency ω_H, we can reduce the integral (39) to the form

$$W=\frac{G_0\lambda^{7/2}}{8\sqrt{\pi}}\exp\left(-i\,\frac{\pi}{4}\right)\int_{-\infty}^{\infty}\frac{\cot x}{x^{7/2}}\exp\left\{i\,\frac{2I}{\lambda}\,\xi^2\times\left[\left(\frac{1}{\xi^2}-1\right)x+x^2\cot x\right]\right\}dx,\tag{47}$$

from which it once again follows that for $\xi\gg 1$, the probability (39) will have a form characteristic of that of the constant crossed field case, preserving the overall structure of (32), (33), but with modified frequency dependences of both the monotonic and oscillatory contributions:

$$W=W_0\left\{1+\frac{35}{8}\,\chi_*^2+\frac{7}{96}\,\frac{\chi_*^4}{\xi^2}-\frac{7}{48}\,\frac{\chi_*^3}{\xi^2}\left[\cos\left(\frac{2}{3\chi_*}\right)-\frac{\chi}{12}\sin\left(\frac{2}{3\chi_*}\right)\right]+\ldots\right\}.$$

In order to estimate the integral (47) by the saddle-point method, we must determine the stationary points from the equation

$$1-\frac{1}{\xi^2}=2x\cot x-\frac{x^2}{\sin^2 x}.\tag{48}$$

A plot of the right-hand side of Eq. (48), $F_R(x)$, is shown in Fig. 2. Depending on the value of ξ, Eq. (48) can have different numbers of roots. Maxima of the even function $F_R(x)$ for $x\geqslant 0$ occur at $x=0$, 4.29, 7.60,.... Values of the function at these points are respectively 1, -18.3, -57.7,... The left-hand side of Eq. (48) reaches these same values at $\xi=\infty$, 0.23, 0.13,...

Thus, for $0.23<\xi<\infty$ there is only one pair of stationary points. As ξ decreases, the number of saddle points grows

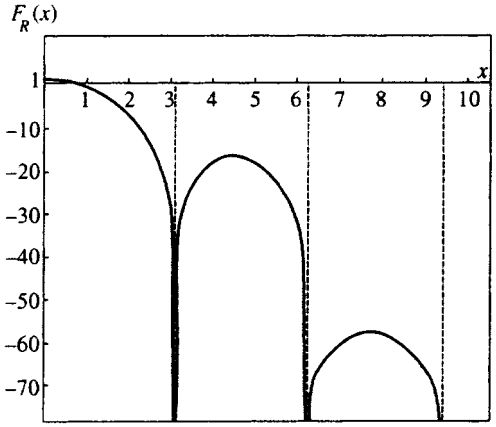

FIG. 2.

without bound. In the region $\xi\gg 1$, as we have already verified, the probability (47) becomes the probability of a slowly varying field.

Let us estimate the probability for $\xi\ll 1$. It is easy to show that the first pair of roots of Eq. (48) then takes the form

$$\pm x_1=\pm\pi(1-\xi).$$

Moreover, by estimating the quantities $Q\Psi(x_1)=2I\pi/\lambda$ and $\Psi''(x_1)=2/\pi\xi^3$, we obtain for the decay probability

$$W=W_0\left\{1+\frac{35}{8}\,\chi_*^2-\frac{105}{8\pi^4}\left(\frac{\lambda}{2I}\right)^4\times\frac{1}{\sqrt{2\xi}}\sin\left(\frac{2\pi I}{\lambda}-\frac{\pi}{4}\right)\right\}.\tag{49}$$

Note that in Eq. (49) the dependence of the oscillatory contribution on the field parameters is appreciably changed. In this case the oscillation frequency is determined not by the wave field intensity, but by its frequency. Note also that the formal presence of the small parameter ξ in the denominator of this expression increases the importance of the oscillatory contributions in the resonance case; however, it can be shown that as $\xi\to 0$ its inclusion requires special consideration, due to overlap of the regions of influence of the saddle points (which in this case become larger and larger).

Equation (39) can also be greatly simplified by discussing the limit $|\delta|\gg 1$. Physically this situation implies an increase in the importance of the constant magnetic field, although here we must still formally take the relationship between $|\delta|$ and ξ into account. In this case the characteristic integral in (39) reduces to the form

$$R(\xi,\lambda,\mu,I)=\int_{-\infty}^{\infty}\frac{\cot(|\delta|x)}{x^{7/2}}\exp\left\{i\,\frac{2I\xi^2}{\lambda|\delta|}\times\left[\left(\frac{|\delta|}{\xi^2}+1\right)x-\sin x\right]\right\}dx.\tag{50}$$

When $\xi^2\ll|\delta|$, (39), (50) lead to a result that coincides with the constant magnetic field case (see (17)–(19)). In the other

limit $\xi^2 \gg |\delta| \gg 1$ we once again find that the probability is the same as for slowly varying field; however, the expansion parameter then turns out to be different:

$$\chi_1 = \frac{\chi_*}{\sqrt{2|\delta|}}. \tag{51}$$

Note that in the region $|\delta| \gg 1$ the effect of the field, as measured by the quantum parameter χ_*, is thus weakened by the increase in the classical parameter $|\delta|$.

5. CONCLUSION

An electromagnetic field with complex configuration can affect nuclear beta decay by giving rise to corrections to the total probability for an unperturbed decay. The identification of so-called monotonic and oscillatory contributions to these corrections makes it plausible that their origins are significantly different. Whereas the monotonic contribution comes from the work that the field does over distances of the order of the de Broglie wavelength of an electron, i.e., in regions where the free particle is created, for the oscillatory contribution considerably larger scales are involved. The superposition of two electromagnetic fields, one a constant magnetic field and the other the field of an electromagnetic plane wave, possesses a number of special features.

In particular, our investigation of the influence of the magnetic field leads us to conclude that in a weak field $\mu \ll 1$, the time and spatial region over which oscillatory contributions form increase by a factor of $2I\mu^{-1}$ as compared to the unperturbed process. An analogous study of processes in the wave field, which was carried out in Refs. 3 and 13, shows that the increase is proportional to $(2I)^{3/2}H_{cr}/E$.

However, when the magnetic field and the wave field act simultaneously, a situation can arise ($\omega = \omega_H$) in which the coefficient that determines the scale of enhancement of the role of the electromagnetic field is determined not only by the field intensity but also by its rate of change $2Im\omega^{-1}$, which for $\omega \ll mI$ also leads to a considerable increase of the time within which the field acts on the process, even under conditions in which its intensity is bounded.

Thus, whereas for an electromagnetic wave field or a purely magnetic field we deal only with effects caused by interference of waves generated by the electron at different points within the region where the decay takes place, when these are superimposed we must include interference by the electromagnetic fields themselves, which changes the parameter that determines the scale of increase of the characteristic regions.

When the frequency difference is considerable, the way the compound field influences the decay is also determined by the relationship between the parameters $|\delta|$ and ξ. When $|\delta| \gg 1$ and $\xi^2 \ll |\delta|$, the magnetic field is decisive. Otherwise, if

$$\xi^2 \gg |\delta| \gg 1,$$

the effect of the field on the decay process reduces to the case of a slowly varying plane wave field; the characteristic parameter becomes $\chi_1 = \chi_*/\sqrt{2|\delta|}$, which effectively implies a weaker role for the quantum field effects due to the increase in the classical parameter $|\delta| \gg 1$.

Finally, in the region where $|\delta| \to 1$, the problem of finding the decay transition probability reduces to the case of a plane wave field with expansion parameter χ_*.[3,7–14]

Intermediate ranges of the parameter δ require a separate investigation of the decay probability; however, we can assert in this case that when $\xi \gg 1$, we are dealing with a slowly varying plane wave, although the frequency dependence of both the monotonic and oscillatory contributions may change.

The asymptotic forms we have found for the probability in strong fields also suggest that in these cases the external field can completely determine the course of the decay, in both the nonrelativistic and in the relativistic limits. Note, however, that inclusion of the relativistic structure of the interaction leads to an appreciable change in the character of the field dependence.

To summarize, we can say that the approach developed here, which is based on a generalization of well-known methods that exactly solve for the motion of an electron in electromagnetic fields of complex structure, enables us to study interference effects that arise when a beta decay process is simultaneously subjected to a static magnetic field and a wave field. Remarkably, there are a number of situations in which the decay probability in the combined fields reduces to the probability in a plane wave field,[3,7,13] with a relabeling of the effective parameters. However, there are also conditions in which the magnetic field and the wave field act together to produce behavior that differs significantly from the plane wave limit, in particular for resonant fields.

The author is grateful to V. R. Khalilov for his interest in this work and for valuable comments. The author is grateful to the Competitive Center for Higher Education in the Fundamental Natural Sciences, Goskomitet, of the Russian Federation at St. Petersburg State University for their support (grant 95-0-5.3-58).

[1] I. M. Ternov, V. N. Rodionov, Fiz. Elem. Chastits At. Yadra **20**, 51 (1989) [Particles and Nuclei **20**, 22 (1989)].
[2] V. I. Ritus, Proc. FIAN **111**, 84 (1979).
[3] A. I. Nikishov and V. I. Ritus, Proc. FIAN **168**, 232 (1986).
[4] A. Einstein, *Collected Scientific Works*, Vol. 4 [in Russian], (Nauka, Moscow (1967), p. 114.
[5] L. I. Korovina, Izv. Vyssh. Uchelon. Zaved., Fiz. **6**, 86 (1964).
[6] I. M. Ternov, B. A. Lysov, and L. I. Korovina, Bull. Moscow State Univ. Physics and Astronomy **5**, 58 (1965).
[7] V. I. Ritus, Zh. Éksp. Teor. Fiz. **56**, 986 (1969) [Sov. Phys. JETP **29**, 532 (1969)].
[8] I. M. Ternov, V. N. Rodionov, V. G. Zhulego, and A. I. Studentkin, Yad. Fiz. **28**, 1454 (1978) [Sov. J. Nucl. Phys. **28**, 747 (1978)].
[9] V. N. Rodionov, in *Electrons in Strong Electromagnetic Fields: An Advanced Classical and Quantum Treatment*, V. R. Khalilov (Ed.), Gordon and Breach, Amsterdam (1996).
[10] I. M. Ternov, V. N. Rodionov, and O. F. Dorofeev, Zh. Éksp. Teor. Fiz. **84**, 1225 (1983) [Sov. Phys. JETP **57**, 710 (1983)].
[11] I. M. Ternov, V. N. Rodionov, O. F. Dorofeev, V. G. Zhulego, A. E. Lobanov, and V. K. Perez-Fernandez, Bull. Moscow State Univ., Physics and Astronomy **4**, 79 (1983).

[12] A. I. Nikishov and V. I. Ritus, Zh. Éksp. Teor. Fiz. **85**, 24 (1983) [Sov. Phys. JETP **58**, 14 (1985)].
[13] A. I. Nikishov and V. I. Ritus, Zh. Éksp. Teor. Fiz. **85**, 1544 (1983) [Sov. Phys. JETP **58**, 898 (1985)].
[14] E. Kh. Akhmedov, Zh. Éksp. Teor. Fiz. **85**, 1521 (1983) [Sov. Phys. JETP **58**, 883 (1985)].
[15] V. N. Rodionov, S. G. Starchus, M. A. Tasev, and I. M. Ternov, Zh. Éksp. Teor. Fiz. **94**(1), 56 (1988) [Sov. Phys. JETP **67**(1), 30 (1988)].
[16] I. M. Ternov, V. R. Khalilov, and V. N. Rodionov, *Interaction of Charged Particles with a Strong Electromagnetic Field* [in Russian], (Moscow State Univ. Press, Moscow (1982).
[17] R. Redmond, J. Math Phys. **6**, 1163 (1965).
[18] J. Schwinger, *Particles, Sources, and Fields*, Addison-Wesley, Reading, Mass. (1970).
[19] V. N. Baier, A. I. Mil'shtein, and V. M. Strakhovenko, Zh. Éksp. Teor. Fiz. **69**, 1983 (1975) [Sov. Phys. JETP **42**, 1006 (1975)].
[20] N. N. Bogolyubov and D. V. Shirkov, *An Introduction to the Theory of Quantized Fields*, Nauka, Moscow (1976) [English translation: Wiley, New York (1975)].
[21] Yu. A. Brychkov and A. P. Prudnikov, *Integral Transforms of Generalized Functions*, Nauka, Moscow, (1976) [English translation: Gordon and Breach, Amsterdam (1977)].

Translated by Frank J. Crowne

Parametric excitation of spin waves in ferromagnets by longitudinal pumping localized in space

Yu. V. Gulyaev, P. E. Zil'berman, and A. V. Lugovskoĭ

Institute of Radio engineering and Electronics, Russian Academy of Sciences, 141120 Fryazino, Moscow Region, Russia
(Submitted 31 May 1996)
Zh. Éksp. Teor. Fiz. **111**, 199–219 (January 1997)

The equations of motion for the slowly varying complex amplitudes of spin waves parametrically excited by a localized pumping magnetic field have been derived. A solution of these equations satisfying given boundary and initial conditions has been obtained. The energy dissipated by spin waves decreases with the pumping intensity beyond a certain pumping power, which can be termed the regeneration threshold. The losses vanish and change sign at the instability threshold. Both thresholds depend heavily on the linear dimension L of the pumping zone, increasing with decreasing L. Owing to the regeneration process, the dissipation length of spin waves increases without bound as the pumping power approaches the instability threshold. Consequently, perturbations of a uniform state due to the boundary penetrate throughout the pumping zone, regardless of the dimension L. As a result, the full pattern of parametric instability is strongly affected by the zone boundary: 1) the spatial distribution of wave amplitudes becomes nonuniform everywhere inside the zone; 2) the amplitude growth rate in the unstable regime decreases at all points when perturbations due to the boundary reach these points; 3) the instability threshold is independent of the spin-wave frequency offset from the parametric resonance frequency. The calculated minimum instability threshold as a function of the bias magnetic field (the ''butterfly'' curve) changes shape with L, in agreement with the available experimental data. [S1063-7761(97)01301-2]

1. INTRODUCTION

The parametric instability of spin waves which was initially discovered and investigated in ferromagnets in the 1950s and 60s,[1–8] has remained a subject of research to this day. In a recent review article,[9] it was noted that this research can be divided into two stages. In the first, the theoretical description did not take into consideration the boundaries of a sample or pumping zone.[4,8] This approach was probably based on the seemingly obvious assumption that inside a large enough system with uniform parameters, the amplitudes of parametrically generated waves should be independent of the coordinates. In our discussion we will term this approach the uniform model. Theoretical results of the uniform model are in good agreement with experiments of those times.

The second stage of research,[9] was stimulated by progress in technology that led to fabrication of high-quality spherical samples of yttrium–iron garnets (YIG). Jantz and Schneider[10] were the first to record the fine structure of the subsidiary absorption spectrum due to the effect of the spherical boundary, i.e., the reflection of parametrically excited spin waves from this boundary and standing waves established in the sample. The boundary effect on the spectrum of parametric absorption was also detected in experiments with antiferromagnets.[11] A similar effect in ferrite films was later investigated both theoretically and experimentally.[12–14]

If, following Patton,[9] we classify the experiments on parametric instability and take recent research into account, the onset of the third stage becomes apparent. This latest stage is related to progress in the growth of YIG single-crystal films by liquid-phase epitaxy. Owing to this progress, experimenters' attention was switched, starting with the 1970s, to traveling spin waves generated in YIG films by local sources—conductors carrying microwave currents, dielectric resonant cavities, etc.

A typical experimental configuration is shown in Fig. 1. It has the following features: 1) a magnetic microwave field generating spin waves is localized near the source in a region of linear size L, and 2) the resulting spin waves can propagate beyond this localization region. At high enough amplitude of the pumping magnetic field, parametric instability can occur in the localization region. Thus we have a new situation in which the sample size in some direction can be infinite, but the size of the pumping field localization zone in this direction is limited.[1)]

Parametric instability was studied experimentally in this new configuration by Melkov and Sholom[19] and Zilberman *et al.*,[20] who used slightly different techniques for generating the localized pumping field and detecting parametric instability. Their basic conclusions, however, were identical: the instability threshold depended on the dimension L of the field localization zone and, as a rule, the threshold increased with decreasing L. This effect was interpreted[19,20] in terms of the theory developed earlier.[21] According to that theory, the instability threshold increases because the propagating wave can carry the energy away from the pumping zone.

Some fundamental problems of the theory, however, have yet to be discussed. For example, 1) how the amplitudes of parametrically excited spin waves depend on position and time; 2) how these amplitudes behave as $L \to \infty$; 3)

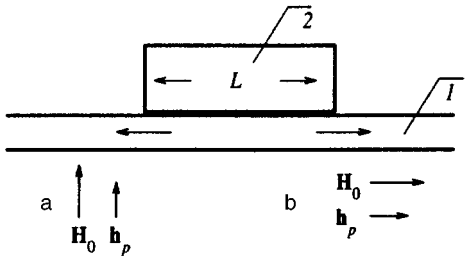

FIG. 1. Typical experimental setup for excitation of traveling spin waves by pumping localized in space: *1*) YIG film; *2*) localized source of spin waves; L) approximate size of the pumping zone. Arrows in film *1* show the direction of spin wave propagation. The lower part of the figure shows two orientations of the bias field $\mathbf{H}_0$ and longitudinal pumping field $\mathbf{h}_p$ with respect to the pumping zone: (a) transversely localized pumping; (b) longitudinally localized pumping.

how the instability threshold depends on the difference between the spin-wave frequency and the parametric-resonance frequency $\omega_p/2$; 4) the behavior of the minimal instability threshold as a function of the bias magnetic field (''butterfly'' curve) at finite L. The aim of our work was to get answers to these questions.

In addition, there is a general problem which we wish to discuss. This problem emerged in the theory of parametric instability of plasma waves,[22] but has not been solved. The point is that the theory[22] indicates that the parametric instability threshold, is a complicated function of L, that may not converge to a unique value as $L\to\infty$. What is the physical reason for it? In this paper we will try to demonstrate that this effect is a direct consequence of parametric instability. In an unstable system, perturbations due to the boundary cannot be confined near the boundary, but instead efficiently penetrate the entire system. For this reason, the boundary should affect the entire pattern of parametric instability, regardless of the size L.

2. SYSTEM UNDER STUDY, BASIC EQUATIONS AND APPROXIMATIONS

In this paper, the typical experimental configuration (Fig. 1) is somewhat simplified. Instead of a ferrite film with large dimensions, we consider a ferromagnet infinite in all directions. We expect that this model should yield the most faithful description of the experiment when the boundary conditions on the film surface lead to either total absorption of incident waves or diffuse scattering.

We assume, in addition, that the ferromagnet is in a uniform saturating bias field $\mathbf{H}_0$ and in the pumping field $\mathbf{h}_p(\mathbf{r},t)$, which is a function of both time t and radius vector $\mathbf{r}$. Let the pumping field be confined in a layer whose boundaries are perpendicular to a vector $\mathbf{L}$ (''localization vector'' with $|\mathbf{L}|=L$).

The mutual orientation of the vectors $\mathbf{H}_0$, $\mathbf{h}_p$, and $\mathbf{L}$ is quite important. The following configurations were implemented in experiments[19,20]: 1) $\mathbf{H}_0 \parallel \mathbf{h}_p \perp \mathbf{L}$ and 2) $\mathbf{H}_0 \parallel \mathbf{h}_p \parallel \mathbf{L}$. Thus the pumping was always longitudinal, but the region of the pumping field could be either longitudinal or transverse with respect to the bias field. The basic features of the configuration with a longitudinal confinement region will be discussed at the end of the paper.

We now proceed to the equations of motion and note that we are essentially dealing with spin-wave turbulence in an inhomogeneous medium. The equations of motion were derived in general form from the Hamiltonian by Zakharov and L'vov,[23] and L'voc and Rubenchik.[24] According to their calculations, if the inhomogeneities are sufficiently smooth and the lengths of excited waves are short,[2)] the dynamical equations for statistical averages of wave amplitudes, which can be derived from the Landau and Lifshitz standard equations for precession and the magnetostatics equations, are valid. Therefore our calculation will be based on the latter equations.

Let us neglect for simplicity the effect of ferromagnetic anisotropy and express the total magnetic field $\mathbf{H}(\mathbf{r},t)$ and magnetization $\mathbf{M}(\mathbf{r},t)$ as sums, i.e.,

$$\mathbf{H}(\mathbf{r},t)=\mathbf{H}_0+\mathbf{h}_p(\mathbf{r},t)+\delta\mathbf{H}(\mathbf{r},t),$$
$$\mathbf{M}(\mathbf{r},t)=\mathbf{M}_0+\delta\mathbf{M}(\mathbf{r},t), \tag{1}$$

where the static values are $\mathbf{H}_0=-H_0\mathbf{e}_z$ and $\mathbf{M}_0=-M_0\mathbf{e}_z$, $H_0>0$ and $M_0>0$, $\mathbf{e}_z$ is the unit vector aligned with the z-axis, and $\delta\mathbf{H}(\mathbf{r},t)$ and $\delta\mathbf{M}(\mathbf{r},t)$ are variable components due to the pumping field. Assuming that the deviations from the equilibrium values and the pumping field are small, so that

$$|\delta\mathbf{H}|,|\delta\mathbf{M}|\ll|\mathbf{h}_p|\ll M_0, \tag{2}$$

we write the linearized system of equations of motion (precession and magnetostatics) in the form

$$\frac{1}{\gamma}\frac{\partial\delta\mathbf{M}}{\partial t}+[\mathbf{M}_0,\delta\mathbf{H}_{\text{eff}}]+[\delta\mathbf{M},(\mathbf{H}_0+\mathbf{h}_p)]=0,$$
$$\delta\mathbf{H}_{\text{eff}}=\delta\mathbf{H}+A\Delta\delta\mathbf{M}-\frac{\omega_d}{(\gamma M_0)^2}\frac{\partial\delta\mathbf{M}}{\partial t},$$
$$[\nabla,\delta\mathbf{H}]=0,\quad \nabla(\delta\mathbf{H}+4\pi\delta\mathbf{M})=0, \tag{3}$$

where $\gamma>0$ is the gyromagnetic ratio, A is the nonuniform exchange constant, and ω_d is the relaxation frequency.[25] The latter is assumed to be small:

$$\varepsilon_d\equiv\frac{\omega_d}{\gamma M_0}\ll 1. \tag{4}$$

The pumping field, which oscillates with frequency ω_p, can be expressed as

$$\mathbf{h}_p(\mathbf{r},t)=\frac{1}{2}[h(\mathbf{r})e^{-i\omega_p t}+h^*(\mathbf{r})e^{i\omega_p t}]\mathbf{e}_z, \tag{5}$$

and we seek a solution of Eq. (3) in Bloch functions,

$$\delta\mathbf{M}(\mathbf{r},t)=e^{i(\mathbf{qr}-\omega t)}\sum_{n=0}^{\infty}\delta\mathbf{M}_n(\mathbf{r},t)e^{-in\omega_p t},$$
$$\delta\mathbf{H}(\mathbf{r},t)=e^{i(\mathbf{qr}-\omega t)}\sum_{n=0}^{\infty}\delta\mathbf{H}_n(\mathbf{r},t)e^{-in\omega_p t}, \tag{6}$$

where the frequency ω and wave vector $\mathbf{q}$ satisfy the dispersion relation for spin waves. We assume that the pumping amplitude $h(\mathbf{r})$ is a sufficiently smooth function of coordinates that

$$\varepsilon_L \equiv \frac{|\nabla h|}{q|h|} \ll 1. \tag{7}$$

Then, since the interaction with the pumping field is relatively weak [see Eq. (2)],

$$\varepsilon_h \equiv \frac{|h|}{M_0} \ll 1, \tag{8}$$

the complex amplitudes of the harmonics of $\delta\mathbf{M}_n(\mathbf{r},t)$ and $\delta\mathbf{H}_n(\mathbf{r},\mathbf{t})$ must also be slowly-varying functions of $\mathbf{r}$ and t.

Without loss of generality, we can assume that the complex amplitude of the pumping field $h(y)$ is a function only of the coordinate y, and that the vector $\mathbf{q}$ is in the yz-plane, i.e., $\mathbf{q}=q_y\mathbf{e}_y+q_z\mathbf{e}_z$ and $q_y/q_z=\tan\theta$ (the localization vector $\mathbf{L}\parallel\mathbf{e}_y$). Given these conditions, by substituting Eqs. (5) and (6) into Eq. (3) and equating coefficients of identical powers to zero, we obtain the following equations for $\delta\mathbf{M}_n$ and $\delta\mathbf{H}_n$:

$$\begin{aligned}
a_n\delta M_{nx}+b\,\delta M_{ny}-\delta H_{ny}&=\frac{1}{\gamma M_0}\frac{\partial\delta M_{nx}}{\partial t}+2iAq_y\frac{\partial\delta M_{ny}}{\partial y}\\
&\quad+i\varepsilon_n\delta M_{ny}+\frac{h(y)}{2M_0}\,\delta M_{n-1,y}\\
&\quad+\frac{h^*(y)}{2M_0}\,\delta M_{n+1,y},\\
b\,\delta M_{nx}-a_n\delta M_{ny}&=\frac{1}{\gamma M_0}\frac{\partial\delta M_{ny}}{\partial t}+2iAq_y\frac{\partial\delta M_{nx}}{\partial y}\\
&\quad+i\varepsilon_n\delta M_{nx}+\frac{h(y)}{2M_0}\,\delta M_{n-1,x}\\
&\quad+\frac{h^*(y)}{2M_0}\,\delta M_{n+1,x},\\
iq_y\delta H_{nz}-iq_z\delta H_{ny}&=\frac{\partial\delta H_{nz}}{\partial y},\quad \delta M_{nz}=0,\quad \delta H_{nx}=0,\\
iq_y(\delta H_{ny}+4\pi\delta M_{ny})+iq_z\delta H_{nz}&=-\frac{\partial(\delta H_{ny}+4\pi\delta M_{ny})}{\partial y},
\end{aligned} \tag{9}$$

where we have introduced the notations

$$a_n=\frac{i(\omega+n\omega_p)}{\gamma M_0},\quad b=\frac{H_0}{M_0}+Aq^2,$$

$$\varepsilon_{dn}=\frac{\omega_d(\omega+n\omega_d)}{(\gamma M_0)^2}\ll 1. \tag{10}$$

In (9), the harmonics with index n are coupled, owing to the pumping field, to harmonics with indices $n+1$ and $n-1$. Therefore all harmonics are in principle coupled to each other, but this coupling is weak because the parameter ε_h [Eq. (8)] is small.

On the right-hand side of Eq. (9) the terms of first order in ε_h [Eq. (8)], ε_L [Eq. (7)], and ε_d [Eq. (4)] are collected. If we ignore these terms in zeroth-order perturbation theory, we obtain a set of noninteracting harmonics. The parameter q at fixed ω is derived by requiring that the determinant of (9) vanish when $n=0$. This harmonic can then always be treated as an eigenstate, and q and ω as parameters coupled by the dispersion relation for this wave:

$$\omega^2=(\omega_H+\widetilde{A}q^2\omega_m)(\omega_H+\widetilde{A}q^2\omega_m+\omega_m\sin^2\theta), \tag{11}$$

where $\omega_H=\gamma H_0$, $\omega_m=4\pi\gamma M_0$, and $\widetilde{A}=A/4\pi$. We next find ω by requiring that another determinant for a harmonic with $n\neq 0$ vanish. Thus, harmonic number n also becomes an eigenstate. This condition is satisfied at the frequency of parametric resonance $\omega=-n\omega_p/2$. Only two harmonics of those in Eq. (6) can describe eigenstates at the same time.

The two characteristic harmonics (numbers 0 and n) are coupled by the pumping field, generally speaking, via a set of driven harmonics with intermediate numbers ranging between ± 1 and $\pm(|n|-1)$. This coupling is of the order of the parameters $\varepsilon_h^{|n|}$, $\varepsilon_L^{|n|}$, and $\varepsilon_d^{|n|}$. The coupling is the strongest at $n=\pm 1$. In what follows, we limit our study to the case of strong coupling between the characteristic harmonics with numbers 0 and -1 at frequencies close to $\omega_p/2$.

To first order in ε_h, ε_L, and ε_d, terms with amplitudes δM_{1x} and δM_{1y} of the $(+1)$st harmonic in the equations for the zeroth harmonic can be omitted, and in the equations for the (-1)st harmonic, terms with amplitudes δM_{-2x} and δM_{-2y} of the (-2)nd harmonic can be dropped. We then have a closed system of eight partial differential equations with eight unknown functions.

3. DERIVATION OF EQUATIONS FOR THE AMPLITUDES OF PARAMETRICALLY COUPLED SPIN WAVES

Even after these simplifications, the system (9) is too cumbersome. This is not surprising, since these equations contain nearly all information about spectra of spin waves, whereas in zeroth-order perturbation theory in ε_h, ε_L, and ε_d, the structure of spin waves is known.[26] Two questions must be answered, namely how the amplitudes of spin waves change in space and time owing to the pumping field, and what the small corrections are to the spin wave structure caused by the pumping field. In order to answer in the context of second quantization, it suffices to obtain only equations for the amplitudes.

The standard technique for deriving such equations is based on introducing amplitudes through the Holstein–Primakoff transforms.[23,24] There is, in principle, a different and simpler approach, which can be reduced to direct transformations of Eq. (9). We will use the latter for subsequent analysis.

Let us write the equations for the amplitudes of the zeroth and (-1)st harmonics derived from Eq. (9) as

$$\hat{\Omega}\frac{\partial\vec{e}}{\partial t}+\hat{Q}\frac{\partial\vec{e}}{\partial y}+\hat{R}\vec{e}+\hat{E}\vec{e}=\hat{P}\vec{f},$$
$$\hat{\Omega}\frac{\partial\vec{f}}{\partial t}+\hat{Q}\frac{\partial\vec{f}}{\partial y}-\hat{R}\vec{f}+\hat{F}\vec{f}=\hat{P}^{*}\vec{e}, \tag{12}$$

where the unknown functions $\vec{e}$ and $\vec{f}$ are column vectors with four components:

$$\vec{e}=\begin{Vmatrix}\delta M_{0x}\\ \delta M_{0y}\\ \delta H_{0y}\\ \delta H_{0z}\end{Vmatrix},\quad \vec{f}=\begin{Vmatrix}\delta M_{-1x}\\ \delta M_{-1y}\\ \delta H_{-1y}\\ \delta H_{-1z}\end{Vmatrix}, \tag{13}$$

and the coefficients in Eq. (12) are 4×4 matrices:

$$\hat{E}=\begin{Vmatrix}a_0 & b & -1 & 0\\ b & a_0 & 0 & 0\\ 0 & 0 & -iq_z & iq_y\\ 0 & 4\pi iq_y & iq_y & iq_z\end{Vmatrix},$$

$$\hat{F}=\begin{Vmatrix}a_{-1} & b & -1 & 0\\ b & -a_{-1} & 0 & 0\\ 0 & 0 & -iq_z & iq_y\\ 0 & 4\pi iq_y & iq_y & iq_z\end{Vmatrix},$$

$$\hat{\Omega}=\frac{1}{\gamma M_0}\hat{A},\quad \hat{Q}=-2iAq_y\hat{B},\quad \hat{R}=-i\varepsilon_{d0}\hat{B},$$

$$\hat{P}=\frac{h}{2M_0}\hat{B}, \tag{14}$$

$$\hat{A}=\begin{Vmatrix}-1 & 0 & 0 & 0\\ 0 & 1 & 0 & 0\\ 0 & 0 & 0 & 0\\ 0 & 0 & 0 & 0\end{Vmatrix},\quad \hat{B}=\begin{Vmatrix}0 & 1 & 0 & 0\\ 1 & 0 & 0 & 0\\ 0 & 0 & 0 & 0\\ 0 & 0 & 0 & 0\end{Vmatrix}.$$

The frequency ω can be offset from parametric resonance, i.e., $\omega=[\omega_p/2+\Delta\omega]$, where $\Delta\omega/\omega_p\sim\varepsilon_h,\varepsilon_L,\varepsilon_d$. In this case, $\hat{F}=\hat{F}_0+\delta\hat{F}$, where

$$\hat{F}_0\equiv\hat{F}(\omega)\big|_{\omega=\omega_p/2},\quad \delta\hat{F}=-\frac{i\Delta\omega}{\gamma M_0}\hat{A}. \tag{15}$$

We now seek a solution of Eq. (12) in the form

$$\vec{e}=C\vec{e}_0+\delta\vec{e},\quad \vec{f}=D\vec{f}_0+\delta\vec{f}, \tag{16}$$

where $\vec{e}_0$ and $\vec{f}_0$ are solutions of the unperturbed problem

$$\hat{E}\vec{e}_0=0,\quad \hat{F}_0\vec{f}_0=0, \tag{17}$$

C and D are the amplitudes of spin waves described by slow functions of **r** and t, which are, generally speaking, not small, and $\delta\vec{e}$ and $\delta\vec{f}$ are small and slowly-varying corrections to the solution describing the changes in spin-wave ''structure'' due to the pumping field. Since the determinants of the matrices $\hat{E}$ and $\hat{F}_0$ vanish, we set one component of each of the vectors $\vec{e}_0$ and $\vec{f}_0$ to unity for definiteness. Moreover, we set one of the components of $\delta\vec{e}$ and $\delta\vec{f}$ to zero in order to maintain a fixed number of unknown functions. After substituting Eq. (16) into (12), terms of zeroth order vanish by virtue of Eq. (17). If only terms of first order in ε_h, ε_L, and ε_d are retained, the derivatives of small and slow functions $\delta\vec{e}$ and $\delta\vec{f}$ can be omitted. Eliminating these functions from Eq. (12), we obtain two equations for the amplitudes C and D,

$$\frac{\partial C}{\partial t}+V_1\frac{\partial C}{\partial y}+\gamma_1 C=g_1(y)D+\gamma_1 C_0,$$
$$\frac{\partial D}{\partial t}+V_2\frac{\partial D}{\partial y}+\gamma_2 D=g_2(y)C+\gamma_2 D_0, \tag{18}$$

where the parameters $V_{1,2}$, $\gamma_{1,2}$, and $g_{1,2}$ connote the y-components of the group velocity, dissipation, and parametric coupling of waves, respectively. For these coefficients, we obtain

$$V_1=-V_2\equiv V,$$
$$V=2k\frac{\omega_m\sin\theta}{q}\left[\tilde{A}q^2+\frac{\cos^2\theta}{2k\left(k+\dfrac{\omega_m}{\omega_p}\sin^2\theta\right)}\right],$$
$$\gamma_1=\gamma\Delta Hk,\quad y_2=\gamma\Delta Hk-2i\Delta\omega, \tag{19}$$
$$g_1(y)=-i\gamma h(y)\frac{\sin^2\theta}{2}\frac{\omega_m}{\omega_p},$$
$$g_2(y)=g_1^{*}(y),\quad k=\sqrt{1+\left(\frac{\omega_m}{\omega_p}\sin^2\theta\right)^2},$$
$$\Delta H=\frac{\omega_d\omega_p}{2\gamma^2 M_0}.$$

In order to take into account an initial (noise) amplitude of spin waves at zero pumping field, additional summands $\gamma_1 C_0$ and $\gamma_2 D_0$ describing ''sources'' of noise are added to the right-hand side of Eq. (18). Then at zero pumping field the wave amplitudes are $C=C_0$ and $D=D_0$. We demand that the following condition be satisfied at $t=0$, when the pump is turned on:

$$C(y,t=0)=C_0,\quad D(y,t=0)=D_0. \tag{20}$$

The pumping field $h(y)$ is confined to the region $0<y<L$ (Fig. 2). At the edges of this interval it drops to zero over a distance $\Delta L\ll L$ defined by

$$\Delta L\left|\frac{\partial C}{\partial y}\right|\ll|C|,\quad \Delta L\left|\frac{\partial D}{\partial y}\right|\ll|D|. \tag{21}$$

Within this interval the pumping field is constant at h_0. Note that the condition (7) introduced previously is equivalent to $q\Delta L\gg 1$. Thus the length ΔL is bounded in our model both above and below. We next take into account that the waves enter the region of the pumping field from opposite directions, since $V_1=-V_2$ [Eq. (19)]. Therefore the amplitude of

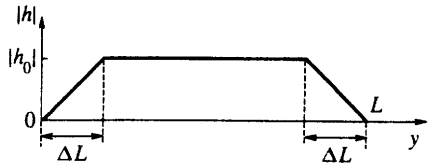

FIG. 2. Profile of the pumping-field amplitude.

the incident wave at the region boundary is determined by the noise, since boundary conditions similar to those discussed in Ref. 22 must be satisfied:

$$C(y=0,t)=C_0, \quad D(y=L,y)=D_0. \tag{22}$$

If we limit our discussion to the uniform model, we should substitute into Eq. (18) $\partial C/\partial y \equiv \partial D/\partial y \equiv 0$. Then the solution of Eq. (18) would be a linear combination of the functions $\exp(p_1 t)$ and $\exp(p_2 t)$, where the arguments of the exponentials are

$$p_{1,2}=-\frac{\gamma_1+\gamma_2}{2}\pm\sqrt{\left(\frac{\gamma_1-\gamma_2}{2}\right)^2+g_1g_2}, \tag{23}$$

and the coupling parameters g_1 and g_2 are taken within the pumping region. The instability condition for such a solution, $\mathrm{Re}\, p_1>0$, can be written with due account of Eq. (19) as

$$\sqrt{g_1g_2}>\sqrt{(\mathrm{Re}\ \gamma_1)^2+(\Delta\omega)^2}. \tag{24}$$

Now let us assume that $\mathrm{Re}\ \gamma_1 \neq \mathrm{Re}\ \gamma_2$. According to Eq. (19), this condition cannot be satisfied. But in more complex systems it can be satisfied. For example, it holds in parametric generation of plasma waves or in generation of a pair of waves of different natures (spin and acoustic) in a ferromagnet. By assuming this condition formally, we obtain the following instability condition at $\Delta\omega=0$:

$$\sqrt{g_1g_2}>\sqrt{\mathrm{Re}\ \gamma_1\ \mathrm{Re}\ \gamma_2}. \tag{25}$$

It will be useful to compare Eq. (24) and (25) to instability conditions described below and derived from the nonuniform model, i.e., for solutions of Eq. (18) with boundary conditions (22).

4. SOLUTIONS OF WAVE-AMPLITUDE EQUATIONS. INSTABILITY CONDITIONS

Using the Laplace transform with respect to t and with due account of Eq. (20), let us rewrite Eq. (18) in the form of ordinary differential equations for the transformed functions $C(y,p)$ and $D(y,p)$. The solution of these equations with the boundary conditions (22) is

$$C(y,p)=\frac{U(y,p)}{p(p-p_1)(p-p_2)\Delta(p)}, \tag{26}$$

where

$$\Delta(p)=\cosh\frac{\beta L}{V}+\frac{\alpha}{\beta}\sinh\frac{\beta L}{V}, \tag{27}$$

where $\alpha=p+(\gamma_1+\gamma_2)/2$, $\beta=\sqrt{\alpha^2-g_1g_2}$, and

$$U(y,p)=[g_1D_0+(p+\gamma_1)C_0]\left\{(p+\gamma_2)\Delta(p)-\frac{g_1g_2}{\beta}\sinh\frac{\beta y}{V}\exp\left[\frac{\gamma_1-\gamma_2}{2}\frac{L-y}{V}\right]\right\}$$
$$-g_1[g_2C_0+(p+\gamma_2)D_0]\left[\cosh\frac{\beta(L-y)}{V}+\frac{\alpha}{\beta}\sinh\frac{\beta(L-y)}{V}\right]\exp\left[-\frac{\gamma_1-\gamma_2}{2}\frac{y}{V}\right]. \tag{28}$$

The expression for $D(y,p)$ can be derived from Eqs. (26)–(28) by substituting $\gamma_1\to\gamma_2$, $C_0\to D_0$, $g_1\to g_2$, and $y\to L-y$.

In order to calculate the inverse transforms, one must investigate the analytic properties of the functions $C(y,p)$ and $D(y,p)$ in the complex plane of the Laplacian variable p. This topic has been discussed in the literature.[22,27] Some details, however, call for further investigation. Above all, note that at the points $p=p_{1,2}$ [Eq. (23)] the transformed functions $C(y,p)$ and $D(y,p)$ have no singularities at all, even at arbitrarily large lengths L. This can be tested by performing a straightforward, albeit cumbersome, transformation of Eq. (28) with a view to proving that the function $U(y,p)$ is regular in the complex plane p and can be expressed near the points $p=p_{1,2}$ as $U(y,p)=(p-p_{1,2})U'(y,p)$, where $|U'(y,p_{1,2})|<\infty$ at all L. Thus the transformed functions $C(y,p)$ and $D(y,p)$ can have singularities only at $p=0$ and at the roots of the equation

$$\Delta(p)=0. \tag{29}$$

In order to calculate solutions of Eq. (29), let us introduce, following Gorbunov,[22] a new variable φ instead of p:

$$\cosh\varphi=\frac{\alpha}{\sqrt{g_1g_2}}, \quad \sinh\varphi=\frac{\beta}{\sqrt{g_1g_2}}, \tag{30}$$

where $\varphi=u+i(v+\pi\nu)$, u and v are real, and ν is an integer. Then we obtain the following equations for deriving u and v from Eq. (30):

$$\begin{aligned} &u+\lambda(-1)^\nu\sinh u\cos v=0,\\ &v+\lambda(-1)^\nu\cosh u\sin v=0, \end{aligned} \tag{31}$$

where the parameter λ is defined as $\sqrt{g_1g_2}L/V$. It will suffice to find only solutions (u,v) with $u\geq 0$ and $v\geq 0$. Then the rest of the solutions can be expressed as $(-u,v)$, $(u,-v)$, and $(-u,-v)$. The nonnegative solutions of Eq. (31) as functions of λ are shown in Fig. 3. It is convenient to number branches of the solutions by the index ν: $u_\nu(\lambda)$ and $v_\nu(\lambda)$. Then the desired roots $p=p_\nu(\lambda)$ of Eq. (29) are

$$p_\nu(\lambda)=-\frac{\gamma_1+\gamma_2}{2}+(-1)^\nu\sqrt{g_1g_2}\cosh[u_\nu(\lambda)+iv_\nu(\lambda)], \quad \nu=3,4,5,\ldots \tag{32}$$

Let us proceed to analyzing the roots of Eq. (32). Suppose that $u\neq 0$. Then Eq. (32) can be transformed using Eq. (31) to the equivalent form

$$p_\nu(\lambda)=-\frac{\gamma_1+\gamma_2}{2}-\frac{1}{\lambda}\sqrt{g_1g_2}\left(\frac{u}{\tanh u}+iv\tanh u\right),$$

which clearly indicates that always $\mathrm{Re}\, p_\nu<0$. Thus all the roots with $u\neq 0$ describe stable, i.e., decaying with time, contributions to $C(y,t)$ and $D(y,t)$. This conclusion is in agreement with Ref. 22. Now let us consider the roots with $u=0$.

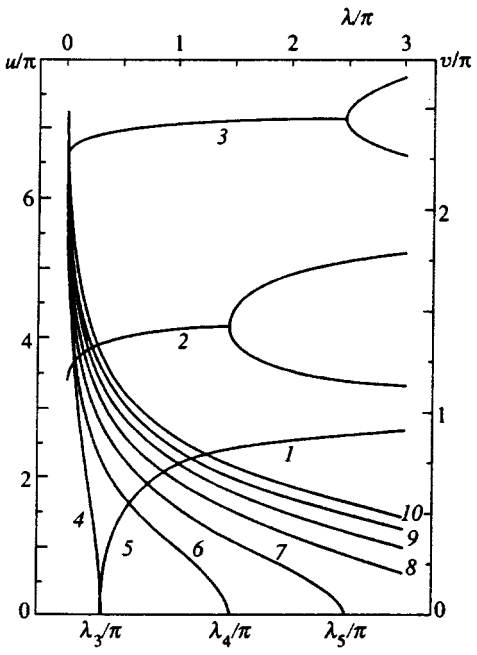

FIG. 3. Numerical solutions of Eq. (31). Curves *1*, *2*, and *3* show the function $v_\nu(\lambda)$ at $\nu=3$, 4 and 5, respectively, where $v_3(\lambda)\equiv 0$ at $\lambda<\lambda_3$, and the function $v_\nu(\lambda)$ bifurcates at the points $\lambda=\lambda_\nu$ with $\nu\geqslant 4$. Curves *4*,*5*,...,*10* show the function $u_\nu(\lambda)$ at $\nu=3,4,...,9$, respectively, where $u_\nu(\lambda)\equiv 0$ at $\lambda>\lambda_\nu$.

The first line of Eq. (31) is an identity in this case. By eliminating v from the second line of Eq. (31) and from Eq. (32), we obtain

$$\begin{aligned}\mathrm{Im}\ p_\nu(\lambda)&=-\frac{1}{2}\,(\mathrm{Im}\ \gamma_1+\mathrm{Im}\ \gamma_2),\\ \mathrm{Re}\ p_\nu(\lambda)&=\frac{1}{2}\,(\mathrm{Re}\ \gamma_1+\mathrm{Re}\ \gamma_2)\Gamma_\nu(\lambda),\end{aligned}\tag{33}$$

with the dimensionless increment

$$\Gamma_\nu(\lambda)=-1+\frac{\zeta_\nu(\lambda)}{|\zeta_\nu(\lambda)|}\,\frac{\eta}{\sqrt{1+\zeta_\nu^2(\lambda)}},\tag{34}$$

where $\zeta_\nu(\lambda)$ are real roots of the equation

$$\lambda=\frac{\sqrt{1+\zeta_\nu^2(\lambda)}}{|\zeta_\nu(\lambda)|}\,[\pi(\nu-3)-\arctan\,\zeta_\nu(\lambda)],\tag{35}$$

$\nu=3,\ 4,\ 5...$, $|\arctan\,\zeta_\nu(\lambda)|\leqslant\pi/2$, and the dimensionless pumping power $\eta=2\sqrt{g_1g_2}(\mathrm{Re}\ \gamma_1+\mathrm{Re}\ \gamma_2)^{-1}$. It is also convenient to introduce a dimensionless pumping field range $\xi=L(\mathrm{Re}\ \gamma_1+\mathrm{Re}\ \gamma_2)/2V$, hence the parameter $\lambda=\xi\eta$.

It follows from Eq. (34) that instability can occur only if there are roots for which $\zeta_\nu(\lambda)>0$. For such roots a set of curves separating the regions of stability and instability can be drawn in the plane of the system parameters (ξ,η). If $\Gamma_\nu(\lambda)=0$ in Eq. (34), which should occur on the boundary of instability, we obtain $\zeta_\nu(\lambda)=\sqrt{\eta^2-1}>0$. By substituting this expression into Eq. (35), we obtain the following equations for the above-mentioned set of curves:

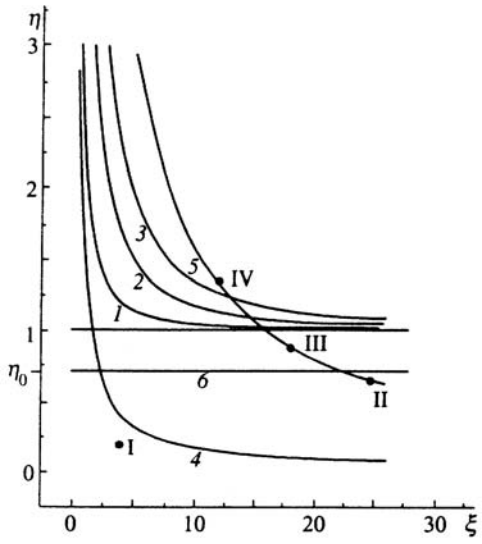

FIG. 4. Plane of pumping power η and localization length ξ: curves *1*, *2*, and *3* are plots of Eq. (36) at $\nu=4$, 5, and 6, respectively; curve *4* is the hyperbola $\xi\eta=\pi/2$; curve *5* is the hyperboal $\xi\eta=\lambda$ at $\lambda=5\pi$; curve *6* is a plot of $\eta=\eta_0\equiv 2\sqrt{\mathrm{Re}\ \gamma_1\mathrm{Re}\ \gamma_2}/(\mathrm{Re}\ \gamma_1+\mathrm{Re}\ \gamma_2)$ at arbitrary ratio $\mathrm{Re}\ \gamma_1/\mathrm{Re}\ \gamma_2$.

$$\xi=\frac{\pi(\nu-3)-\arctan\sqrt{\eta^2-1}}{\sqrt{\eta^2-1}},\quad \nu=4,\,5,\ldots\tag{36}$$

Shapes of the curves defined by Eq. (36) are shown in Fig. 4. Since the curve with $\nu=4$ is below all other curves, it presents a special case and defines the instability threshold. At $\nu=4$, Eq. (36) yields a quantitative relation between the threshold pumping power and its degree of localization. According to Eq. (36) and Fig. 4, the threshold pumping increases with localization (with decreasing ξ). This conclusion is in agreement with earlier publications.[19–21] At the same time, it is noteworthy that as $\xi\to\infty$, the threshold pumping power $\eta\to 1$, so that the instability condition at all admissible offsets $\Delta\omega$ and decrements $\mathrm{Re}\ \gamma_1$ and $\mathrm{Re}\ \gamma_2$ takes the form

$$\sqrt{g_1g_2}>\frac{1}{2}\,(\mathrm{Re}\ \gamma_1+\mathrm{Re}\ \gamma_2).\tag{37}$$

This condition is different from Eqs. (24) and (25) in two respects: 1) the threshold is independent of the offset, which contradicts Eq. (24), and 2) at $\mathrm{Re}\ \gamma_1\neq\mathrm{Re}\ \gamma_2$ and $\Delta\omega=0$, the threshold equals the arithmetic mean of the dissipation factors, but not the geometric mean, as in Eq. (25). In Fig. 4 the threshold defined by Eq. (37) is shown by the horizontal line $\eta=1$, and the threshold defined by Eq. (25) by the line $\eta=\eta_0\leqslant 1$. Thus, even in the limit $L\to\infty$, the expression for the threshold pumping may be different from that derived from the uniform model. The reason for this discrepancy has not been discussed in literature, and we will try to explain it in the next section.

To conclude this section, let us discuss in detail the increment as a function of the pumping power, $\Gamma_4(\eta)$, working from Eqs. (34) and (35). A set of such curves at different localization lengths is given in Fig. 5. It is remarkable that parametric regeneration of the system, i.e., partial compen-

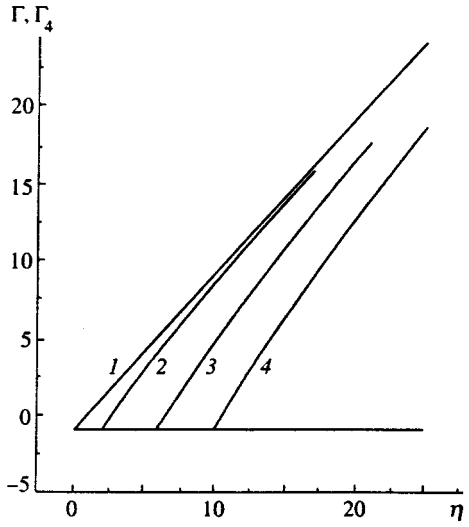

FIG. 5. Increments as functions of the pumping power: *1*) increment calculated by the uniform model using Eq. (23) at Re γ_1=Re γ_2 and $\Delta\omega$=0, i.e., $\Gamma(\eta)$=Re p_1/Re $\gamma_1=-1+\eta$; *2*, *3* and *4*) increments $\Gamma_4(\eta)$ calculated for systems with boundaries using Eqs. (34) and (35) at $\xi=\pi/4$, $\pi/12$, and $\pi/20$, respectively.

sation for the dissipative loss due to pumping, has a threshold if ξ is finite. $\Gamma_4=-1$, at the regeneration threshold and it grows with η. According to Eq. (34), this corresponds to the parameter $\lambda=\pi/2$, for which there is a positive root $\zeta_4=\infty$. Let us plot the curve $\xi\eta=\pi/2$ (Fig. 4). This curve essentially shows the regeneration threshold as a function of the localization length. Note that at the regeneration threshold, the increment grows with pumping faster than in the uniform model illustrated by curve *1* in Fig. 5, which has a derivative $d\Gamma/dy=1$ at $\Gamma=-1$, whereas the other curves *2*, *3*, and *4* have equal derivatives $d\Gamma_4/dy=\lambda=\pi/2>1$ at $\Gamma_4=-1$. Thus, although the initial slopes of $\Gamma_4(\eta)$ are independent of the localization, they are obviously different from that calculated by the uniform model. Only at high pumping powers does the function $\Gamma_4(\eta)$ asymptotically approach that calculated in the uniform model. The smaller the localization length (the smaller ξ), the higher the pumping power η required to bring the curve $\Gamma_4(\eta)$ closer to $\Gamma(\eta)$.

5. WAVE AMPLITUDES AS FUNCTIONS OF COORDINATES AND TIME. DISCUSSION

The transformed functions $C(y,p)$ and $D(y,p)$ [Eqs. (26)–(28)] have no singularities in the p-plane except the poles at the points $p=0$ and $p=p_\nu(\lambda)$ [Eq. (32)]. Therefore we could use the residue theorem in calculating the inverse Laplace transforms of $C(y,t)$ and $D(y,t)$. In this calculation we took into account that second-order poles occur at (1) $p=0$ if $\Delta\omega=0$ and one of the roots $p_\nu(\lambda)$ is at the instability threshold, and (2) $p=p_\nu(\lambda)$ if the parameter λ corresponds to a bifurcation point in Fig. 3. Otherwise the poles are simple. At small t too many poles should be included in the sum of residues. Then it is more convenient to calculate numerically the integrals expressing the amplitudes.

Figure 6 shows such calculations of amplitudes. Calculations for four points of types I, II, III, and IV shown in Fig. 4 are plotted. In the first stage of the calculations we assumed for simplicity that Re γ_1=Re γ_2, and the offset was assumed to be zero, i.e., $\Delta\omega=0$.

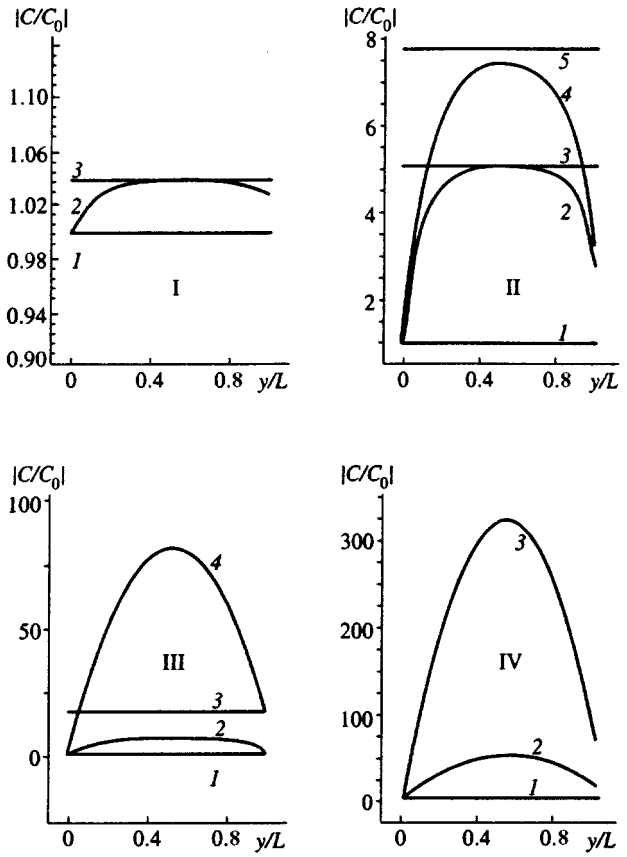

FIG. 6. Modulus of the relative amplitude $|C/C_0|$ as a function of the dimensionless coordinate y/L at different moments of time for characteristic points I, II, III, and IV in Fig. 4. The following values of the parameters were taken for different points: I) $\xi=3\pi$, $\eta=0.16$, $Vt/L=0$ (curve *1*), and $Vt/L=\infty$ (curves *2* and *3*); II) $\xi=5.5\pi$, $\eta=0.9091$, $Vt/L=0$ (curve *1*), $Vt/L=0.6$ (curves *2* and *3*), and $Vt/L=\infty$ (curves *4* and *5*); III) $\xi=4.95\pi$, $\eta=1.0101$, $Vt/L=0$ (curve *1*), $Vt/L=1.4$ (curves *2* and *3*), and $Vt/L=\infty$ (curve *4*); IV) $\xi=4.75\pi$, $\eta=1.0526$, $Vt/L=0$ (curve *1*), $Vt/L=2$ (curve *2*), and $Vt/L=5$ (curve *3*). In all the graphs $\Delta\omega=0$, $\gamma_1=\gamma_2$, $g_{1,2}=g^*_{1,2}$, and $C_0=D_0$. The horizontal lines show for comparison absolute values of relative amplitudes calculated by the uniform model.

The feature of type I is that the point is below both the instability and regeneration thresholds, i.e., below the curves *1* and *4* in Fig. 4, respectively. The curves for points of type I in Fig. 6 indicate that a steady-state distribution of amplitude in space is achieved at times $t>L/V$. This distribution is identical to that obtained in the uniform model throughout almost the entire pumping range except the boundary sections, whose length is of the order of the ''dissipation length'' $L_d=2V/(\text{Re }\gamma_1+\text{Re }\gamma_2)$. Thus we can see that the uniform model yields a faithful description at the points of type I if $L\gg L_d$.

The points of type II are above the regeneration threshold (curve *4* in Fig. 4), but below the instability threshold in both the real system with boundaries (curve *1* in Fig. 4) and the uniform model (curve *6* in Fig. 4). The curves for points of type II in Fig. 6 indicate that the effect of boundaries penetrates into the excitation zone through a much larger distance than for points of type I. This is naturally accounted

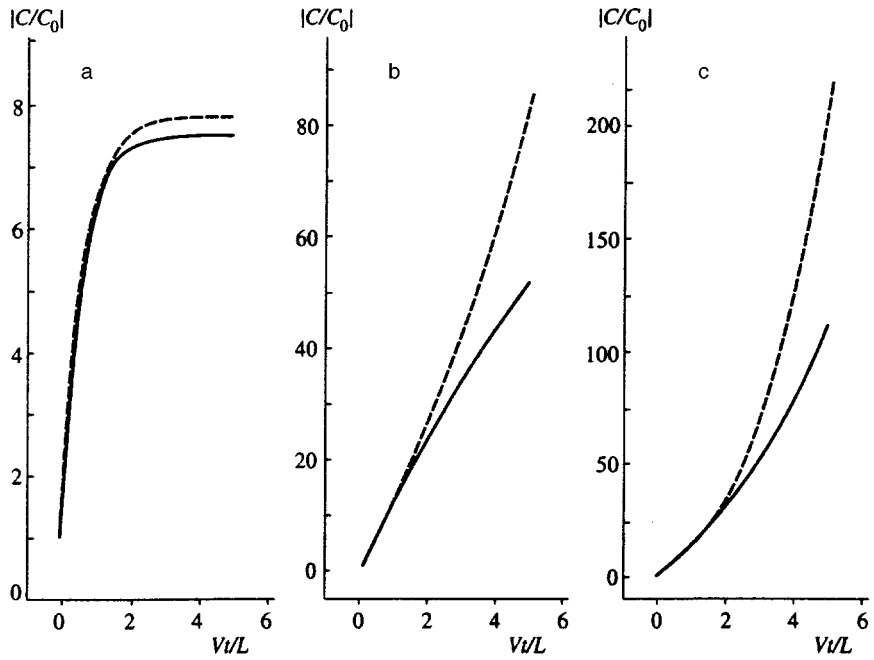

FIG. 7. Modulus of the relative amplitude $|C/C_0|$ as a function of dimensionless time Vt/L at the center of the pumping zone, $y=L/2$, for a point (a) of type II, $\xi=5.5\pi$, $\eta=0.9091$; (b) of type III, $\xi=4.95\pi$, $\eta=1.0101$; (c) of type IV, $\xi=4.75\pi$, $\eta=1.0526$. For all the curves $\Delta\omega=0$, $\gamma_1=\gamma_2$, $g_{1,2}=g_{1,2}^*$ and $C_0=D_0$. Solid lines show calculations by the model of a bounded pumping zone, dashed lines correspond to the uniform model.

for in terms of the partial compensation for loss and the respective increase in the effective dissipation length. It is remarkable that in this case the steady-state distribution is markedly nonuniform throughout the excitation zone and deviates at all points from that of the uniform model.

The difference between points of type III and type II is that they are above curve *6* in Fig. 4. At these points a steady-state distribution is not achieved in the uniform model, but it is achieved in the model with boundaries (curve *3*).

Finally, the point of type IV is above the instability threshold. According to Fig. 6, the amplitude distribution at the point of type IV is nonuniform, and no steady-state distribution is achieved. Note that for all points under discussion, the maximum of $|C/C_0|$ is shifted to the right of the excitation zone center. The maximum of the amplitude $|D/D_0|$ is shifted to the left.

Now let us discuss the wave amplitude as a function of time at a fixed point in space. It is convenient to consider the excitation zone center, i.e., the point $y=L/2$. Figure 7 shows calculations for points of types II, III, and IV in the plane of parameters of Fig. 4. There is a time interval $0\leqslant t\leqslant L/2V$ in which the amplitude versus time is identical to that calculated in the uniform model, since the dashed and solid lines in Fig. 7 coincide. This takes place because of the finite velocity V at which perturbations propagate in the system. As a result, there is a section around the central point $y=L/2$ within which the boundary is irrelevant, and which narrows with time. At $t>L/2V$ and with a sufficient degree of regeneration in the system for propagating waves not to be attenuated in the zone, the boundaries affect the entire zone, regardless of its length L. In Fig. 7, this shows up as a separation between the dashed and solid curves. At a point of type II, both curves tend to different steady-state levels. At a point of type III, a steady-state level is achieved owing to the effect of the boundaries. At a point of type IV, there is no steady-state level, and parametric instability develops.

Thus, the boundaries of the pumping zone have a considerable effect on the development of parametric instability at all L, even $L\to\infty$. But the instability threshold for spin waves at $L\to\infty$ coincides with that calculated in the uniform model only if $\Delta\omega=0$. In fact, according to Eq. (18), Re $\gamma_1=$Re γ_2 for spin waves, so the lines $\eta=1$ and $\eta=\eta_0$ coincide in Fig. 4. Since the threshold level is the parameter most often measured in experiments, it is clear that many features of the underlying phenomena are not detected. It would be interesting to understand why the threshold levels can coincide despite radical differences in the patterns of instability development in space and time. The reason for their coincidence is illustrated by Fig. 8.

If the pumping localization length is not too large, as in Figs. 8a and 8c, the distributions of the moduli and phases of the amplitudes C and D are different, but they are symmetric about the central point $y=L/2$. At any point inside the pumping zone, at least one of the two inequalities, $\partial C/\partial y\neq 0$ or $\partial D/\partial y\neq 0$, holds. As the length L increases, the amplitude distributions are deformed in the directions shown by arrows in Figs. 8a and 8c. As a result, at sufficiently large L (Figs. 8b and 8d), the distributions of the amplitudes C and D coincide, and a flat section, where $\partial C/\partial y=0$ and $\partial D/\partial y=0$ simultaneously, is formed about the center of the zone. This flat section is due to the symmetry of wave parameters and the fact that the amplitude distribution becomes independent of the direction of wave propagation as $L\to\infty$. The coordinate derivatives in Eq. (18) can be omitted inside the flat section, and the resulting equations directly yield the instability threshold equal to that obtained in the uniform model.

We must stress once again that the above conclusion holds only in the symmetric configuration, for which Re $\gamma_1=$Re γ_2 and $\Delta\omega=0$. If $\Delta\omega\neq 0$, the symmetry of the wave parameters is broken, since $\gamma_1\neq\gamma_2$ [Eq. (19)]. Our cal-

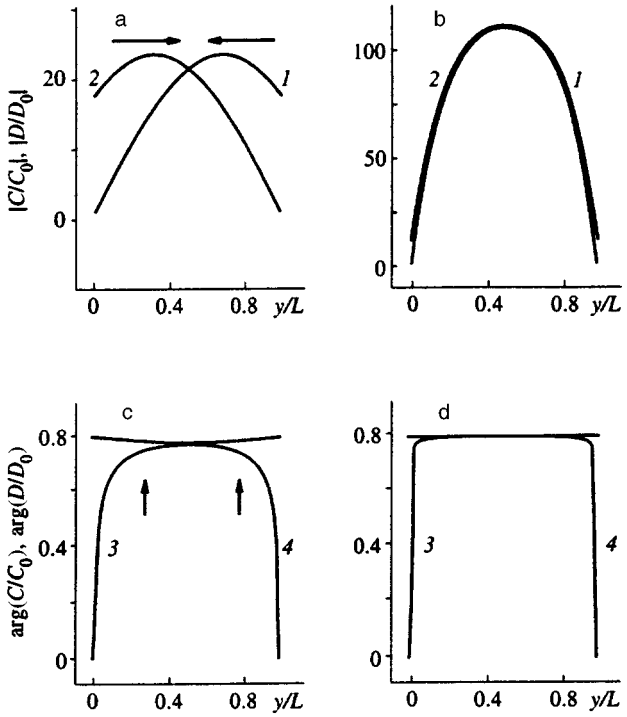

FIG. 8. Steady-state curves of complex wave amplitudes versus coordinate at $\Delta\omega=0$, $\gamma_1=\gamma_2$, $g_{1,2}=g_{1,2}^*$, and $C_0=D_0$. Curves *1* and *2* show $|C/C_0|$ and $|D/D_0|$, respectively, at (a) $\xi=0.7\pi$, $\eta=1.43$ and (b) $\xi=14.98\pi$, $\eta=1.001$. Curves *3* and *4* are plots of $\arg(C/C_0)$ and $\arg(D/D_0)$, respectively, at (c) $\xi=0.7\pi$, $\eta=1.43$ and (d) $\xi=14.98\pi$, $\eta=1.001$.

culations indicate that in this case the amplitude distribution is also asymmetric, even when $L\to\infty$, and the derivatives $\partial C/\partial y$ and $\partial D/\partial y$ in Eq. (18) cannot be neglected at any point. As a result, the instability condition can be derived from Eq. (37), assuming Re $\gamma_1=$Re γ_2. Thus, in contrast to the uniform model, the threshold is independent of $\Delta\omega$ in a system with boundaries,—this, of course, within plausible constraints on $\Delta\omega$ (recall that $\Delta\omega/\omega\sim\varepsilon_h,\varepsilon_L,\varepsilon_d\ll 1$).

6. FEATURES OF LONGITUDINAL LOCALIZATION

As was noted in Sec. 2, in experiments with localized pumping[19,20] two configurations were studied, namely transverse localization with $\mathbf{L}\perp\mathbf{H}_0$, and longitudinal localization with $\mathbf{L}\|\mathbf{H}_0$. To this point, we have limited our discussion to transverse localization. Now let us consider some features of longitudinal localization.

The procedure of constructing the theory described in the previous sections is almost the same. By following this procedure, we obtain equations for the wave amplitudes like Eq. (18) with the following substitutions:

$$V_1\frac{\partial C}{\partial y}\to V_1'\frac{\partial C}{\partial z},\quad V_2\frac{\partial D}{\partial y}\to V_2'\frac{\partial D}{\partial z},$$

where V_1' and V_2' are z-projections of the group velocities, and the field $\mathbf{H}_0$ is still aligned with the z-axis. Equations (19) defining the coefficients are still valid, but the newly introduced velocities satisfy the relation $V_1'=-V_2'\equiv V'$, where

$$V'=2k\,\frac{\omega_m\cos\theta}{q}\left[\tilde{A}q^2-\frac{\sin^2\theta}{2k(k+\omega_m\sin^2\theta/\omega_p)}\right]. \tag{38}$$

Equation (38) demonstrates that $V'=0$ at $\theta=\pi/2$. According to the dispersion relation (11), waves with $\theta=\pi/2$ propagating in the direction normal to the field $\mathbf{H}_0$ really exist at sufficiently small H_0—specifically, when

$$H_0<H_{0c}=\frac{\omega_p}{2\gamma}(k-\sqrt{k^2-1}). \tag{39}$$

At these fields, the wave vectors q of such waves are nonzero and may be fairly large.[3)] Therefore the instability threshold for these waves can be estimated using the relations of the previous sections. The dimensionless localization parameter ξ introduced in Sec. 4 is in this case $\xi\equiv L\gamma_1/2V'=\infty$, since $V_1'=0$. According to Eq. (36) and Fig. 4, the instability threshold is a minimum ($\eta=\eta_0=1$) at $\xi=\infty$, and coincides with the result of the uniform model.

Our conclusion is based on Eq. (38), which determines the velocity, and applies only to longitudinal localization. In fact, in the case of transverse localization, the velocity is zero only at $\theta=0$ [Eq. (19)]. Waves with $\theta=0$ propagate along the field vector $\mathbf{H}_0$, so they do not interact with the pumping field.[8] This statement also follows from Eq. (19): at $\theta=0$ the parametric coupling factor $g_1=0$. Therefore the pumping field cannot generate waves that do not transport energy outside the pumping zone in the case of strictly transversely localized pumping. In the case of strictly longitudinal localization, such waves can be generated, and they determine the minimum instability threshold.

The proposed interpretation of the minimum threshold is in good agreement with experimental data[20] obtained under the condition of almost longitudinal localization. The measured threshold was an oscillating function of the field H_0,[20] and the minima corresponded to zero projection of the group velocity onto the film plane. Such waves did not leave the pumping zone and therefore did not carry off any energy.

7. "BUTTERFLY" CURVE

In this section we discuss the curve of the minimum parametric instability threshold versus the field H_0 (the ''butterfly'' curve[28]). It is interesting to determine how the boundaries of the pumping zone affect this curve. As was noted in Sec. 6, the boundaries exert an influence over a wider range of fields H_0 in the case of transverse localization. Therefore we will discuss this type of localization.

Our calculation is based on Eq. (36), which determines the instability threshold at $\nu=4$. In this equation the parameters ξ and η can be expressed, with due account of Eq. (19), as

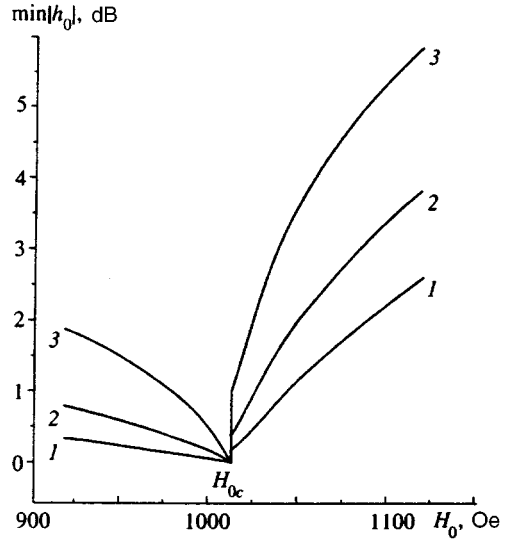

FIG. 9. Calculations of minimum instability threshold, $\min|h_0|$, versus applied field H_0 expressed in decibels with respect to the threshold at the bias field $H_0=H_{0c}$. The pumping field $\mathbf{h}_p$ is localized longitudinally ($\mathbf{h}_p\|\mathbf{H}_0$) and transversely ($\mathbf{L}\|\mathbf{H}_0$). The calculations were performed at different dimensions of the pumping zone L: (*1*) 3.5 mm; (*2*) 2 mm; (*3*) 1 mm. The system parameters are $4\pi M_0=1750$ Oe, $\omega_p=2\pi\times 9.37\times 10^9$ s^{-1}, $2\Delta H=0.4$ Oe.

$$\xi=\frac{\gamma\Delta H}{\omega_p}\,\frac{qL}{\sqrt{k^2-1}\left[2\tilde{A}q^2+\dfrac{\cos^2\theta}{k(k+\sqrt{k^2-1})}\right]},$$

$$\eta=\frac{|h_0|}{2\Delta H}\,\frac{\sqrt{k^2-1}}{k}. \tag{40}$$

The parameters can thus be expressed as functions of q and θ. The wave number q can be expressed in terms of θ using Eq. (11), with $\omega=\omega_p/2$. It turns out that the basic equation (36) determines the modulus of the threshold field $|h_0|$ as a function of angle θ at given M_0, ΔH, ω_p, L, and H_0. The following values correspond to actual experimental conditions[19]: $4\pi M_0=1750$ G, $\omega_p=2\pi\times 9.37\times 10^9$ s^{-1}. The values of θ corresponding to the minimum of the threshold field $|h_0|$ at given H_0 can be numerically derived from Eq. (36). It turns out that if H_{0c} is determined by Eq. (39), there is only one optimum value of θ at $H_0<H_{0c}$, namely $\theta_{\rm opt}=\pi/2$. At $H_0>H_{0c}$ the angle $\theta_{\rm opt}$ tends to zero at large H_0. The value $\theta=\theta_{\rm opt}$ is substituted into Eq. (36), and the minimal threshold field, $\min|h_0|$, as a function of H_0 is calculated.

The family of resulting curves calculated at various L is given in Fig. 9. These demonstrate that the threshold increases with decreasing L at all H_0. Absolute variations in the threshold at $H_0<H_{0c}$, however, are slightly smaller than at $H_0>H_{0c}$.

It is interesting to compare the curves of Fig. 9 to measurements of a normally magnetized YIG film.[19] The experimental geometry[19] was identical to that shown in Fig. 1, and the field alignment was close to that of Fig. 1a. Thus the localization was almost transverse. One can see that at $L=0.25$–0.87 mm, the theoretical and experimental curves for $H_0>H_{0c}$ are in fair agreement. At $H_0<H_{0c}$ the minimum threshold measured in the experiment was independent of L, whereas Fig. 9 demonstrates such a dependence.

We assume that this discrepancy is partly due to the difference between the theoretical model and real experimental conditions,[19] since the film surface was smooth, rather than rough with diffuse reflection of spin waves. Another reason for the discrepancy may be the dependence between the line width $2\Delta H$ and the wave number q, which is not reflected in the theoretical model. The importance of this dependence has been pointed out in the literature.[8,25] At the smallest L, comparable to the dissipation length L_d or even smaller, the threshold is almost independent of ΔH, and is determined only by the outflow of spin-wave energy from the pumping zone. Under these conditions, the increase in ΔH with q cannot have a notable effect on the shape of the ''butterfly'' curve at $H_0<H_{0c}$. At larger L this effect is stronger. As a result, the ''butterfly'' curve moves upwards owing to an increase in ΔH with q. Hence the lower curves of Fig. 9 should approach the upper curve at $H_0<H_{0c}$, and the agreement with the experimental data should improve.

8. CONCLUSIONS

The parametric instability of spin waves generated by localized pumping field is interesting from the viewpoints of both fundamental and applied research. It is interesting, in principle, to determine the effect of boundaries on system instability, which was done in our work, but only in the linearized model, the interaction among spin waves being ignored. The role of boundaries in the nonlinear stage of the instability is an interesting line of further theoretical research.

From the viewpoint of applications, the instability under the conditions of localized pumping is interesting because it controls the admissible power fed to linear devices. From this point of view, the effects of the following factors should be investigated: 1) boundaries of ferrite films, which often reflect, but do not absorb or scatter incident spin waves; 2) parametric generation of not only purely exchange, but also dipole spin waves, if the frequency $\omega_p/2$ is within the dipole spectrum; 3) the actual configuration of the localized pumping field.

This work was supported by the International Science Foundation (Grant MSZ000) and the Russian Fund for Fundamental Research (Grant No. 94-0204928a). We are grateful to S. A. Nikitov, A. G. Temiryazev, and M. P. Tikhomirova for helpful discussions.

[1)]In this connection, the following comment is relevant. A conductor with a microwave-frequency current pressed to a film surface can generate, in principle, dipole or dipole-exchange spin waves of fairly large wavelengths in the linear mode at the current frequency ω_p. These waves propagate fast along the surface and can go far beyond the generator near-field zone; they can then act as a driving force, generating a parametric instability at frequencies close to $\omega_p/2$. Such processes have been investigated both experimentally[15] and theoretically.[16–18] But in this paper, we only mean the near-field instability when considering the parametric instability in the zone of localized pumping field. This instability is in some cases the only one possible—for example, if the pumping magnetic field $\mathbf{h}_p$ is parallel to the bias magnetic field $\mathbf{H}_0$ (longitudinal pumping), or if the frequency ω_p is far beyond the boundary of the dipole spectrum of the film.

[2)]The applicability condition is formally equivalent to Eq. (7).

[3)]Recall that the theory, in accordance with Eq. (7) and the condition $L \gg \Delta L$, applies at $qL \gg q\Delta L \gg 1$.

[1] R. W. Damon, Rev. Mod. Phys. **25**, 239 (1953).
[2] N. Bloembergen and S. Wang, Phys. Rev. **93**, 72 (1954).
[3] H. J. Suhl, J. Phys. Chem. Sol. **1**, 209 (1957).
[4] H. J. Suhl, J. Appl. Phys. **29**, 416 (1958).
[5] E. R. Morgenthaler, J. Appl. Phys. **31**, 95S (1960).
[6] E. Schloemann, J. J. Green, and U. Milano, J. Appl. Phys. **31**, 386 (1960).
[7] E. Schloemann, J. Appl. Phys. **31**, 1647 (1960).
[8] E. Schloemann and R. J. Joseph, J. Appl. Phys. **32**, 1006 (1961).
[9] Carl E. Patton, Phys. Rep. **103**, 251 (1984).
[10] W. Jantz and J. Schneider, Sol. St. Commun. **9**, 69 (1971).
[11] V. Ya. Kotyuzhanskii and L. A. Prozorova, Zh. Éksp. Teor. Fiz. **81**, 1913 (1981) [Sov. Phys. JETP **54**, 1013 (1981)].
[12] I. L. Berezin, B. A. Kalinikos, N. G. Kovshikov *et al.*, Fiz. Tverd. Tela (Leningrad) **20**, 2101 (1978) [Sov. Phys. Solid State **20**, 1214 (1978)].
[13] G. Wiese, Z. Phys. B **91**, 57 (1993).
[14] G. Wiese, P. Kabos, and C. E. Patton, Phys. Rev. B **51**, 15085 (1995).
[15] O. A. Chivileva, A. G. Gurevich, A. N. Anisimov *et al.*, Fiz. Tverd. Tela (Leningrad) **29**, 1774 (1987) [Sov. Phys. Solid State **29**, 1020 (1987)].
[16] B. A. Kalinikos, Pis'ma Zh. Tekh. Fiz. **9**, 811 (1983) [Sov. Tech. Phys. Lett. **9**, 349 (1983)].
[17] B. A. Kalinikos and A. N. Slavin, IEEE Trans. Magn. **27**, 5444 (1991).
[18] G. A. Melkov, Fiz. Tverd. Tela (Leningrad) **30**, 2533 (1988) [Sov. Phys. Solid State **30**, 1458 (1988)].
[19] G. A. Melkov and S. V. Sholom, Fiz. Tverd. Tela (Leningrad) **29**, 3257 (1987) [Sov. Phys. Solid State **29**, 1870 (1987)].
[20] P. E. Zil'berman, N. S. Golubev, and A. G. Temiryazev, Zh. Éksp. Teor. Fiz. **97**, 634 (1990) [Sov. Phys. JETP **70**, 353 (1990)].
[21] V. S. L'vov and A. M. Rubenchik, Preprint IAÉ SO AN SSSR No. 31 [in Russian], Moscow (1976).
[22] L. M. Gorbunov, Zh. Éksp. Teor. Fiz. **67**, 1386 (1974) [Sov. Phys. JETP **40**, 689 (1975)].
[23] V. E. Zakharov and V. S. L'vov, Fiz. Tverd. Tela (Leningrad) **14**, 2913 (1972) [Sov. Phys. Solid State **14**, 2513 (1972)].
[24] V. S. L'vov and A. M. Rubenchik, Zh. Éksp. Teor. Fiz. **72**, 127 (1977) [Sov. Phys. JETP **45**, 67 (1977)].
[25] A. G. Gurevich, *Magnetic Resonance in Ferrite and Antiferromagnetics* [in Russian], Nauka, Moscow (1973).
[26] A. I. Akhiezer, B. G. Bar'yakhtar, and S. V. Peletminskii, *Spin Waves* [in Russian], Nauka, Moscow (1967).
[27] D. L. Bobroff and H. A. Haus, J. Appl. Phys. **38**, 390 (1967).
[28] Ya. A. Monosov, *Nonlinear Ferromagnetic Resonance* [in Russian], Nauka, Moscow (1971).

Translation was provided by the Russian Editorial office.

Density of states near an Anderson transition in a four-dimensional space. Renormalizable models

I. M. Suslov

P. L. Kapitsa Institute of Physical Problems, Russian Academy of Sciences, 117334 Moscow, Russia
(Submitted 6 June 1996)
Zh. Éksp. Teor. Fiz. **111**, 220–249 (January 1997)

Asymptotically accurate results are obtained for the average Green function and density of states of a disordered system for a renormalizable class of models (as opposed to the lattice model examined previously [I. M. Suslov, Zh. Éksp. Teor. Fiz. **106**, 560 (1994)]. For $N\sim 1$ (where N is the order of perturbation theory), only the parquet terms corresponding to the higher powers of large logarithms are taken into account. For large N, this approximation is inadequate because of the higher rate of increase with respect to N of the coefficients for the lower powers of the logarithms. The latter coefficients are determined from the renormalization condition for the theory expressed in the form of a Callan–Symanzik equation using the Lipatov asymptote as boundary conditions. For calculating the self-energy at finite momentum, a modification of the parquet approximation, is used that allows the calculations to be done in an arbitrary finite logarithmic approximation, including the principal asymptote in N of the expansion coefficients. It is shown that the phase transition point moves in the complex plane, thereby ensuring regularity of the density of states for all energies and avoiding the ''false'' pole in such a way that the effective interaction remains logarithmically weak. © *1997 American Institute of Physics.* [S1063-7761(97)01401-7]

1. INTRODUCTION

The problem of calculating the average Green function that determines the density of states for the Schrödinger equation with a gaussian random potential is mathematically equivalent to the problem of a second-order phase transition with an n-component order parameter $\varphi=(\varphi_1,\varphi_2,\ldots,\varphi_n)$ in the limit $n\to 0$;[1,2] the coefficients in the Ginzburg–Landau Hamiltonian

$$H\{\varphi\}=\int d^dx\left\{\frac{1}{2}\,c|\nabla\varphi|^2+\frac{1}{2}\,\kappa_0^2|\varphi|^2+\frac{1}{4}\,g_0|\varphi|^4\right\} \tag{1}$$

are related to the parameters of a disordered system by the equations

$$c=1/2m,\quad \kappa_0^2=-E,\quad g_0=-W^2a_0^d/2, \tag{2}$$

where d is the dimensionality of the space, m is the particle mass, E is the energy relative to the lower boundary of the seed spectrum, W is the amplitude of the random potential, and a_0 is the lattice constant. (In the following $c=1$ and $a_0=1$.) The ''wrong'' sign on the coefficient of $|\varphi|^4$ leads to the ''false'' pole problem[3] and for a long time it was doubted that an ε-expansion could be constructed near a spatial dimensionality of $d=4$.[4] Encouraging results in this area have been obtained recently by the author.[5,6]

It has been shown[6] that there are two fundamentally different classes of models which show up in estimates based on the optimal fluctuation method.[7,8] The probability $P(E,R)$ of the appearance of an energy level $E<0$ owing to a fluctuation in a potential with characteristic size R has the form

$$P(E,R)\sim\exp\{-S(E,R)\}, \tag{3}$$

where $S(E,R)\sim W^{-2}\gg 1$. The total probability $P(E)$ of the resulting level E, which determines the density of states $\nu(E)$, is obtained by integrating Eq. (3) with respect to R, which in the approximation of the saddle-point method reduces to replacing R by R_0, the minimum point for $S(E,R)$. For $d<4$ and $d>4$ we have $R_0\sim|E|^{-1/2}$ and $R_0\sim a_0$, respectively.[5,6] For $d=4$ (Fig. 1), the function $S(E,R)=\text{const}=S_0$, and the situation is close to degeneracy: for large R the degeneracy is removed owing to the finiteness of E and $S(E,R)-S_0\sim E^2R^d$, while for small R the deviation of the spectrum $\varepsilon(k)$ from quadratic is large. If $\varepsilon(k)=k^2+\beta k^4$, then for $\beta>0$ the function $S(E,R)$ lies above S_0, ensuring the appearance of a minimum at $R_0\sim|E|^{-1/4}$, while for $\beta<0$ it lies below and the minimum is attained at $R_0\sim a_0$;[6] thus, models with $\beta>0$ and $\beta<0$ yield a different asymptote for the fluctuation tail as $E\to-\infty$. For small negative E the boundary between the two types of models shifts and is no longer sharp, so that integrating Eq. (3) with respect to R results in a competition between the contributions from the minimum S_1 and the higher lying plateau $S(E,R)=S_0$, whose width increases without bound as $|E|$ is reduced:

$$P(E)\sim\nu(E)\sim e^{-S_1}+\left(\frac{J}{|E|}\right)^{\alpha}e^{-S_0}, \tag{4}$$

where $J\sim 1/ma_0^2\sim 1$. As S_1 is increased the second term (the contribution of the plateau) becomes dominant before S_1 approaches S_0. Direct integration of Eq. (3) with respect to R yields an exponent $\alpha=1/2$,[6] which cannot be taken seriously, since the accuracy of the method does not allow for an estimate of the coefficient of the second exponential. The exact value of α is 1/3 (see below).

In the domain of applicability of the optimal fluctuation method, the damping Γ, defined by the imaginary part of the self-energy $\Sigma(p,\kappa)$ for $p=0$ (κ is the renormalized value of κ_0), is proportional to the density of states $\nu(E)$ and, when the dimensionality is taken into account, can be estimated as

$$\Gamma \sim J\left\{ e^{-S_1} + \left(\frac{J}{|E|} \right)^{1/3} e^{-S_0} \right\}. \tag{5}$$

The energy always enters in the combination $E+i\Gamma$, and in the neighborhood of an Anderson transition $|E|$ can be replaced by Γ. It is easily verified that the first term in brackets is dominant when $S_1<3S_0/4$, and the second when the inequality is reversed. Since $S(E,R)\sim W^{-2}$,[6] in the limit of weak disorder a sharp boundary $S_c=3s_0/4$ appears between the two types of models: for $S_1<S_c$ the optimum fluctuation is determined by the atomic scale length and the discreteness of the lattice is of fundamental importance, by analogy with the case $d>4$. For $S_1>S_c$ fluctuations with a large radius are important and the analysis can be carried out in a continuum model with a quadratic spectrum; the situation is analogous to that for the lowest dimensionalities.

The above classification of models is directly related to the renormalizability of the theory. The Nth-order graph for the self-energy Σ has momentum dimensionality k^r, where $r=2+(d-4)N$. For $d>4$ the degree of divergence at high momenta increases with the graph order, and the theory is unrenormalizable;[9] a cutoff parameter Λ must be introduced explicitly as an indication of the significance of the structure of the Hamiltonian on an atomic scale. For $d<4$ we have $r<2$ at all N: when its value is deducted from each graph for $p=\kappa=0$ the index r is reduced by 2 and the difference $\Sigma(p,\kappa)-\Sigma(0,0)$ contains no divergences, which are absorbed by $\Sigma(0,0)$, and leads only to a shift in the energy origin. For $d=4$ the difference $\Sigma(p,\kappa)-\Sigma(0,0)$ contains logarithmic divergences which are removed by renormalizing the charge and Green function;[9,10] however, it is necessary to keep in mind that in the standard proofs of renormalizability only distances greater than Λ^{-1} are considered. Of course, scale lengths shorter than Λ^{-1} do not make the δ-function contributions that are so important for $\Lambda\to\infty$. The above estimate shows that this is not always so: the renormalizable contribution from large distances (the contribution of the plateau) is dominant only for $S_1>S_c$; otherwise, it is small compared to the unrenormalizable contribution from small distances.

Therefore, there are four fundamentally different types of theory: (1) an unrenormalizable theory for $d>4$; (b) unrenormalizable theories under logarithmic conditions ($d=4$, $S_1<S_c$); (c) renormalizable theories under logarithmic conditions ($d=4$, $S_1>S_c$); and (d) theories that are renormalizable with a single subtraction (superrenormalizable) for $d<4$. Cases (a) and (b) have been examined in Refs. 5 and 6, respectively. In this paper we examine case (c), the zeroth approximation for the $4-\varepsilon$ theory, which belongs to type (d).

The exponent α in Eq. (4) can be determined from the renormalization condition for the plateau contribution. The contribution of the latter to the damping Γ, which depends on Λ and the bare values for κ_0 and g_0, becomes a function of κ and g alone upon transforming to the renormalized quantities. From dimensional considerations $\Gamma=\kappa^2 f(g)$, where the function $f(g)$ is determined mainly by the exponential $\exp(-1/ag)$ owing to the need to agree with the result from the optimal fluctuation method as $E\to-\infty$, in which $g\approx g_0$. Given the relationship between the renormalized and bare charges,[11]

$$g=\frac{g_0}{1+W_2 g_0 \ln(\Lambda/\kappa)}, \quad W_2=K_4(n+8) \tag{6}$$

($K_4=(8\pi^2)^{-1}$ is the area of a unit sphere in four-dimensional space, divided by $(2\pi)^4$), we have

$$\Gamma \sim \kappa^2 \exp\left\{ -\frac{1}{ag_0} - \frac{W_2}{a} \ln\frac{\Lambda}{\kappa} \right\}$$
$$\sim \Lambda^2 \left(\frac{\Lambda^2}{\kappa^2} \right)^{-W_2/2a-1} \exp\left(-\frac{1}{ag_0} \right), \tag{7}$$

which, given that $J\sim\Lambda^2$, $\kappa^2=|E|$,[1)] and $a=-3/8\pi^2$, reproduces the second term of Eq. (5). This value of a is obtained by a method[3,12,13] employing the standard instanton solution for $d=4$.[14]

The need to correctly account for the factorial divergence of a number of perturbation theories examined via Lipatov's method,[14] according to which subsequent coefficients in the expansion in g_0 are determined by saddle-point configurations, i.e., instantons, of the corresponding functional integrals, has been clarified previously.[5,6] An instanton in the Lipatov method satisfies the same equation as a typical wave function in the field of an optimal fluctuation (see Chapter IV of Ref. 8). In this way, the model classification given above shows up in yet another fundamental guise–the divergence of a number of perturbation theories. Unlike the lattice models for $d\geqslant 4$,[6] the continuum models for $d<4$,[15] and the renormalizable massless theories,[14,16] applying the Lipatov method to studies of four-dimensional models (1) with $\kappa\neq 0$ requires that certain difficulties associated with the absence of ''true'' instantons (Sec. 7) be overcome.

In order to obtain asymptotically accurate (in the limit of weak disorder) results in four-dimensional lattice models,[6] in the expansion

$$\Sigma(0,\kappa)-\Sigma(0,0)=\kappa^2 \sum_{N=1}^{\infty} g_0^N \sum_{K=0}^{N} A_N^K \left(\ln\frac{\Lambda}{\kappa} \right)^K \tag{8}$$

it is necessary to include: (a) the parquet coefficients A_N^N corresponding to the principal logarithmic approximation, and (b) for $N\geqslant N_0\gg 1$, the coefficients A_N^0 and A_N^1, which have the maximum growth rate with respect to N and dominate the higher orders of perturbation theory. They yield a nonperturbative contribution, which is related to the divergence of the series and does not depend on the choice of N_0. The qualitative result consists of a shift in the transition point from the real axis into the complex plane, which leads to regularity of $\nu(E)$ in the neighborhood of an Anderson transition and elimination of the false pole. This approximation ''deteriorates'' as S_1 approaches S_c:[6] (a) the equation for $\Gamma(E)$ has physically meaningless solutions when $S_1>S_c$; (b) the contribution from the approximations fol-

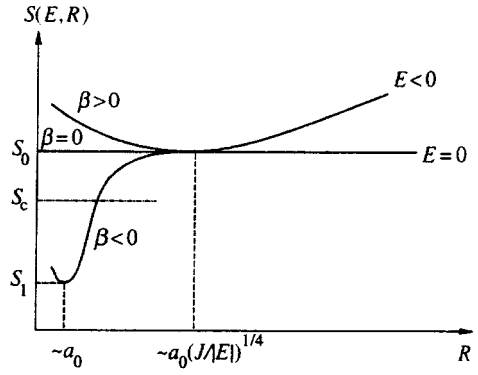

FIG. 1. The dependence of $S(E,R)$ on R for $E=\text{const}$ when $d=4$.

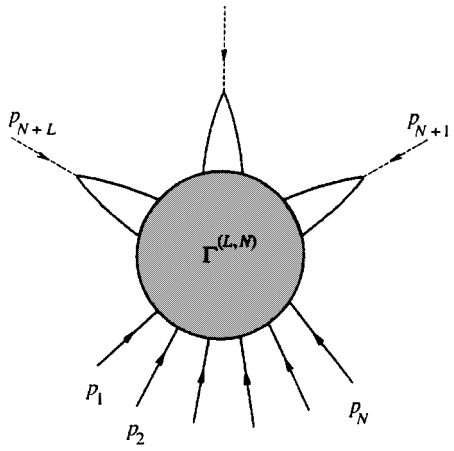

FIG. 2. The vertex $\Gamma^{(L,N)}$ with N free ends and L closed two-line loops studied in the renormalization theory of Ref. 10.

lowing the principal logarithmic approximation, which are determined by coefficients A_N^{N-K} with $K\sim 1$, increases rapidly as $S_1\to S_c$; and, (c) the plateau (Fig. 1) makes a contribution whose strong energy dependence indicates a growing role for the coefficients A_N^K with $K\neq 0$ (in the lattice models the weak dependence of S_1 on E makes the zero-logarithmic contribution predominate) that becomes important for $S_1\approx S_c$. Thus, if the ''highest'' and ''lowest''-order logarithms are dominant in the lattice models, then, in general, on going to the renormalizable models the contributions from all K become important in the sum (8).

In the latter case we arrive at the following statement of the problem: let us choose an integer N_0 that is large compared to 1, but small compared to the large parameters of the theory. For $N<N_0$ we retain only the parquet coefficients A_N^N, which are distinguished by large logarithms, in Eq. (8). For $N\geqslant N_0$, in general, all the terms are important in the sum over K, but the condition $N\gg 1$ allows us to calculate the coefficients A_N^K in the principal asymptotic dependence on N. The latter problem is solved in the following way: the renormalizability of the theory, expressed in the form of the Callan–Symanzik equation (Sec. 2), leads to a system of equations for the A_N^K that determines the coefficients with $K\neq 0$ in terms of specified A_N^0 On the other hand, the Lipatov method reproduces the coefficients A_N^K with small K well, so that they can be used as boundary conditions for this system of equations. In this way it is possible to determine all A_N^K with $N\gg 1$ (Sec. 3), which for small g_0 enables us to find the sum in Eq. (8) and determine the energy dependence of the damping Γ (Sec. 4).

For calculating the density of states (Sec. 6) it is necessary to find the self-energy $\Sigma(p,\kappa)$ for finite momenta, which requires solving of the parquet equations in the principal logarithmic approximation.[6] In the present theory $\Sigma(p,\kappa)$ is the sum of a nonperturbative contribution, mainly determined by the Lipatov asymptote, and a quasi-parquet contribution corresponding to a logarithmic approximation of arbitrary finite order, which allows only for the principal asymptote behavior in N. The calculations in the next order can be carried out with the aid of a curious modification of the parquet approximation (Sec. 5).

2. SYSTEM OF EQUATIONS FOR THE COEFFICIENTS A_N^K

In the following we shall only be interested in logarithmic divergences, assuming the quadratic to be eliminated by the renormalization κ. The Callan–Symanzik equations can be derived in the usual way,[10] but we need them in a somewhat nontraditional form. Dimensional considerations imply that a vertex $\Gamma^{(L,N)}$ with N free ends and L two-line loops (Fig. 2) can be written in the form[10]

$$\Gamma^{(L,N)}(p_i;\kappa,g_0,\Lambda)=\kappa^{d-N(d-2)/2-2L}\times\tilde{\Gamma}^{(L,N)}(p_i/\kappa;g_0,\Lambda/\kappa), \tag{9}$$

which allows us to proceed to examining $\tilde{\Gamma}^{L,N}$ (we omit the tilde in the following). Assuming that the bare charge g_0 is a function of Λ and introducing the renormalized charge g_μ applicable to a scale $\mu\gg\kappa$, in view of the multiplicative renormalizability of $\Gamma^{L,N}$,[10] we have

$$\Gamma_R^{(L,N)}\left(\frac{p_i}{\kappa};g_\mu,\frac{\mu}{\kappa}\right)=Z^{N/2}\left(\frac{Z_2}{Z}\right)^L\Gamma^{(L,N)}\left(\frac{p_i}{\kappa};g_0,\frac{\Lambda}{\kappa}\right), \tag{10}$$

where Z and Z_2 are functions of g_0 and Λ/μ. Since $\Gamma_R^{(L,N)}$ is independent of Λ, we have

$$d\Gamma_R^{(L,N)}/d\ \ln\Lambda=0,$$

which after substitution of Eq. (10) gives the Callan–Symanzik equation:

$$\left[\frac{\partial}{\partial\ \ln\Lambda}+W(g_0)\frac{\partial}{\partial g_0}+\left(L-\frac{N}{2}\right)\eta(g_0)-L\,\eta_2(g_0)\right]\Gamma^{(L,N)}\left(\frac{p_i}{\kappa};g_0,\frac{\Lambda}{\kappa}\right)=0. \tag{11}$$

The Gell-Mann–Low function $W(g_0)$ and the scaling functions[10] $\eta(g_0)$ and $\eta_2(g_0)$ are defined by the equations

$$W(g_0)=\frac{dg_0}{d\ \ln\Lambda},\quad \eta(g_0)=-\frac{d\ \ln Z}{d\ \ln\Lambda},$$

$$\eta_2(g_0)=-\frac{d\ \ln Z_2}{d\ \ln\Lambda} \tag{12}$$

and depend *a priori* on Λ/μ; however, by writing the three Eqs. (11) for different L and N, expressing W, η, and η_2 in terms of $\Gamma^{(L,N)}$, and noting that the latter functions are independent of the arbitrary parameter μ, it is easy to confirm that the first of them are independent of Λ/μ.

In order to find the renormalization law for the self-energy we use the Ward identity for the Green function $G(p,\kappa)$:

$$\frac{\partial G^{-1}(0,\kappa)}{\partial \kappa_0^2}=\frac{\partial \kappa^2}{\partial \kappa_0^2}=\Gamma^{(1,2)}(\kappa), \tag{13}$$

which, when integrated, yields

$$\kappa_0^2-\kappa_c^2=\kappa^2 Y\left(g_0,\frac{\Lambda}{\kappa}\right)\equiv\int_0^{\kappa^2} d\kappa^2[\Gamma^{(1,2)}(\kappa)]^{-1}, \tag{14}$$

where $\Gamma^{(1,2)}(\kappa)\equiv\Gamma^{(1,2)}(p_i=0,\ g_0,\ \Lambda/\kappa)$ and $\kappa_c^2=\Sigma(0,0)$. The function Y satisfies the equation

$$\left[\frac{\partial}{\partial\ \ln\Lambda}+W(g_0)\ \frac{\partial}{\partial g_0}+V(g_0)\right]Y\left(g_0,\frac{\Lambda}{\kappa}\right)=0 \tag{15}$$

with $V(g_0)\equiv\eta_2(g_0)$, which is easily confirmed by applying the operator in square brackets to Eq. (14) and using Eq. (11). Given that $\kappa_0^2=\kappa^2+\Sigma(0,\kappa)$, Eq. (14) can be rewritten in the form

$$\kappa^2+\Sigma(\kappa,0)-\Sigma(0,0)=\kappa^2 Y(g_0,\Lambda/\kappa) \tag{16}$$

and a comparison with Eq. (8) yields the following logarithmic expansion for Y:

$$Y\left(g_0,\frac{\Lambda}{\kappa}\right)=\sum_{N=0}^{\infty} g_0^N\sum_{K=0}^{N} A_N^K\left(\ln\frac{\Lambda}{\kappa}\right)^K, \tag{17}$$

with $A_0^0=1$. Expanding the functions W and V in the series

$$W(g_0)=\sum_{N=2}^{\infty} W_N g_0^N,\quad V(g_0)=\sum_{N=1}^{\infty} V_N g_0^N, \tag{18}$$

whose leading coefficients[10] are[2)]

$$W_2=K_4(n+8),\quad W_3=-K_4^2(9n+42),$$
$$V_1=-K_4(n+2),\quad V_2=3K_4^2(n+2), \tag{19}$$

substituting Eqs. (17) and (18) into Eq. (15), and collecting terms with the same powers of g_0 and the logarithms, we obtain a system of equations for the coefficients A_N^K:

$$-KA_N^K=\sum_{M=1}^{N-K+1}[W_{M+1}(N-M)+V_M]A_{N-M}^{K-1},$$
$$K=1,2,\ldots,N. \tag{20}$$

3. A STUDY OF THE COEFFICIENTS A_N^K

Equation (20) is a recurrence relation that determines the A_N^K in terms of specified A_{N-1}^{K-1}, A_{N-2}^{K-1}, ..., A_{K-1}^{K-1} and can be used to express all the A_N^K in terms of a single sequence A_N^0. The coefficients W_N and V_N can be determined from Eq. (20) if we specify two sequences A_N^1 and A_N^2 in addition to A_N^0. Thus, the renormalizability of the theory sharply reduces the arbitrariness in the choice of coefficients in Eq. (8).

Information on the coefficients A_N^K with $N\gg 1$ can be obtained by the Lipatov method. According to Sec. 7, the Nth order contribution to $\Sigma(0,\kappa)$ has the form

$$\kappa^2 g_0^N c_2\Gamma(N+b)a^N(\ln N)^{-\gamma}\exp\left(\sigma\ \ln\frac{\Lambda}{\kappa}\right), \tag{21}$$

where

$$b=\frac{n+8}{3},\quad a=-3K_4,\quad \gamma=\frac{n+2}{6},\quad \sigma=\frac{n+8}{3}. \tag{22}$$

Comparing this with the expansion (8), we obtain

$$A_N^K=\frac{\sigma^K}{K!}\,A_N^0,\quad A_N^0=c_2\Gamma(N+b)a^N(\ln N)^{-\gamma}. \tag{23}$$

Whereas in the lattice models[6] the Lipatov asymptote only reproduces the zero-logarithmic and first-logarithmic contributions, here it yields some ''extra'' logarithms. Formally, in Eq. (23) $K=0,1,\ldots,\infty$, while in Eq. (8) $K\leqslant N$. The reason for this is the rapid drop in A_N^K with increasing K and the limited accuracy ($\sim 1/N$) of the leading asymptote. The result (23) can be believed only for small K, but this is enough to use it as a boundary condition for the system of Eqs. (20).

Writing out Eq. (20) for small K,

$$\begin{aligned}
-1\cdot A_N^1&=[W_2(N-1)+V_1]A_{N-1}^0+[W_3(N-2)\\
&\quad+V_2]A_{N-2}^0+\ldots+[W_N\cdot 1+V_{N-1}]A_1^0+V_N A_0^0,\\
-2\cdot A_N^2&=[W_2(N-1)+V_1]A_{N-1}^1+[W_3(N-2)\\
&\quad+V_2]A_{N-2}^1+\ldots+[W_N\cdot 1+V_{N-1}]A_1^1\\
&\quad\ldots\ldots\ldots
\end{aligned} \tag{24}$$

and assuming that Eq. (23) is valid for A_N^0, it is easy to confirm the factorial growth in N for all A_N^K with $K\sim 1$. Retaining only the first terms in leading order in N on the right-hand sides of Eqs. (24), we obtain

$$A_N^K=\frac{N!}{K!(N-K)!}\,(-W_2)^K A_{N-K}^0\xrightarrow{K\ll N}\frac{1}{K!}\times\left(-\frac{W_2}{a}\right)^K A_N^0, \tag{25}$$

which, given that $\sigma=-W_2/a$ (see Eqs. (19) and (22)), reproduces the result (23) for $K\neq 0$ and establishes its domain of applicability, $K\ll N$. Retaining only the first terms on the right of Eqs. (24) is justified when W_N and V_N increase more slowly than A_N^0,[3)] which may regarded as a consequence of the validity of Eq. (23) for $K=0$, 1, 2.

For K close to N and assuming that $x_N=A_N^N$ and $y_N=A_N^{N-1}$, ..., we obtain a system of difference equations from Eq. (20),

$$\begin{aligned}
-Nx_N&=[W_2(N-1)+V_1]x_{N-1},\\
-(N-1)y_N&=[W_2(N-1)+V_1]y_{N-1}+[W_3(N-2)\\
&\quad+V_2]x_{N-2},\\
&\quad\ldots\ldots\ldots
\end{aligned} \tag{26}$$

which can be solved by the method of variation of constants and used to successively determine $A_N^N, A_N^{N-1}, \ldots$. For the parquet coefficients we have

$$A_N^N=(-W_2)^N\frac{\Gamma(N-\beta)}{\Gamma(N+1)\Gamma(-\beta)},\quad \beta=-\frac{V_1}{W_2}=\frac{n+2}{n+8} \tag{27}$$

in agreement with Ginzburg[11] (see Ref. 6). For A_N^{N-K} with $K\sim 1$ it is easy to identify the leading asymptote in N and prove the following result by induction:

$$A_N^{N-K}=\frac{1}{K!}\left(-\frac{W_3}{W_2^2}N\ln N\right)^K A_N^N. \tag{28}$$

In order to study the A_N^K with arbitrary K we use the estimate $A_{N-1}^K/A_N^K\lesssim 1/N$, which is valid for Eqs. (23) and (28) and is confirmed by the result for all K. Retaining the two leading terms in N on the right of Eq. (20), we have

$$-KA_N^K=[W_2(N-1)+V_1]A_{N-1}^{K-1}+W_3NA_{N-2}^{K-1},$$
$$K=1,2,\ldots,N. \tag{29}$$

The principal term in N is not sufficient, since the calculation of arbitrary A_N^K from known A_N^0 requires $\sim N$ iterations, which for an accuracy $\sim 1/N$ in each iteration leads to a buildup of errors. The last terms in Eq. (24), which contain W_N and V_N, generally give corrections $\sim 1/N$, but are present only in the equations with $K=1$, 2 and do not lead to an accumulation of errors. We assume by definition that $A_N^{N+1}=0$, which accounts for the absence of the latter term in the equation with $K=N$. Making the substitution

$$A_N^K=(-W_2)^K\frac{\Gamma(N-\beta)}{\Gamma(K+1)\Gamma(N-K-\beta)}A_{N-K}^0X_{N,N-K} \tag{30}$$

and noting that $X_{N+1,M}$-$X_{N,M}\sim 1/N$, we arrive at the equation

$$X_{N,M}=X_{N-1,M}+\frac{f(M)}{N}X_{N-1,M-1} \tag{31}$$

with the boundary conditions

$$X_{NN}=1,\quad X_{N0}=1, \tag{32}$$

where the function $f(M)$ is defined by

$$f(M)=\frac{W_3}{W_2}(M-1-\beta)\frac{A_{M-1}^0}{A_M^0}. \tag{33}$$

Equation (31) is convenient for studying a problem with initial conditions

$$X_{0,M}=\phi_M,\quad \text{where}\quad \phi_M=0\quad \text{for}\quad M=-1,-2,\ldots, \tag{34}$$

where ϕ_M can be chosen so as to satisfy the boundary conditions (32). Iteration of Eq. (31) yields

$$X_{NM}=\phi_M+B_N^1f(M)\phi_{M-1}+B_N^2f(M)f(M-1)\phi_{M-2}$$
$$+\ldots+B_N^Nf(M)f(M-1)\ldots f(M-N+1)\phi_{M-N}, \tag{35}$$

where the coefficients B_N^K are given by the sum of the C_N^K terms,

$$B_N^K=\sum_{\{p_i\}}\frac{1}{(1+p_1)(1+p_2)\ldots(1+p_K)}, \tag{36}$$

while $p_1,p_2,\ldots,p_K$ is a selection without replacement from the sequence 0,1, . . . , $N-1$. For $K\ll N$, sampling with and without replacement are essentiallly equivalent, and we obtain

$$B_N^K\approx\frac{(\ln N)^K}{K!},\quad K\leqslant N. \tag{37}$$

In fact, for large N, the sum in (35) is always dominated by $K\ll N$, and noting that $\phi_M=0$ for $M<0$, we obtain

$$X_{NM}=\sum_{K=0}^{M}\frac{(\ln N)^K}{K!}$$
$$\times f(M)f(M-1)\ldots f(M-K+1)\phi_{M-K}. \tag{38}$$

For the product in (38) we have

$$f(M)f(M-1)\ldots f(M-K+1)$$
$$=\left(\frac{W_3}{W_2}\right)^K\frac{A_{M-K}^0}{A_M^0}\frac{\Gamma(M-\beta)}{\Gamma(M-K-\beta)}\xrightarrow{M\gg K}(f_\infty)^K, \tag{39}$$

where

$$f_\infty=\lim_{M\to\infty}f(M)=\frac{W_3}{aW_2}=\frac{3n+14}{n+8}. \tag{40}$$

For $M=0$ the boundary condition (32) gives $\phi_0=1$ and for $M=N\gg 1$ the sum in Eq. (38) is replaced by an integral which is calculated by the saddle-point method and, on comparison with the boundary conditions (32), determines ϕ_M for $M\gg 1$:

$$\phi_M=\begin{cases}1, & M=0\\ M^{-f_\infty}, & M\gg 1\end{cases}. \tag{41}$$

Substituting Eq. (41) in Eq. (38) leads to the results ($M_0=f_\infty\ln N$)

$$X_{NM}=\frac{(\ln N)^M}{M!}\left(\frac{W_3}{W_2}\right)^M\frac{\Gamma(M-\beta)}{\Gamma(-\beta)A_M^0}\quad \text{for}\quad M\ll\ln N, \tag{42}$$

$$X_{NM}=\frac{(\ln M)^\gamma}{M^{b+\beta}}\frac{e^{M_0}}{\sqrt{2\pi M_0}}\int_0^\infty dx\,\exp\left(-\frac{(M-M_0-x)^2}{2M_0}\right)$$
$$\times(\ln x)^{-\gamma}x^{b+\beta-f_\infty}$$
$$\text{for}\quad M_0-M\ll M_0\quad \text{or}\quad M>M_0 \tag{43}$$

for $M_0-M\ll M_0$ or $M>M_0$. (In the first case the sum in Eq. (38) is determined by the term with $K=M$ and in the second, it is replaced by an integral.) Substituting Eq. (42) in Eq. (30) reproduces the result (28) and establishes its domain of applicability, $K\ll\ln N$. In the region $M\sim(M_0-M)$, which is not described by Eqs. (42) and (43), the magnitude of $X_{N,M}$ is determined by the values of ϕ_M for $M\sim 1$, which, in turn, are determined by the coefficients A_N^0 with $N\sim 1$.

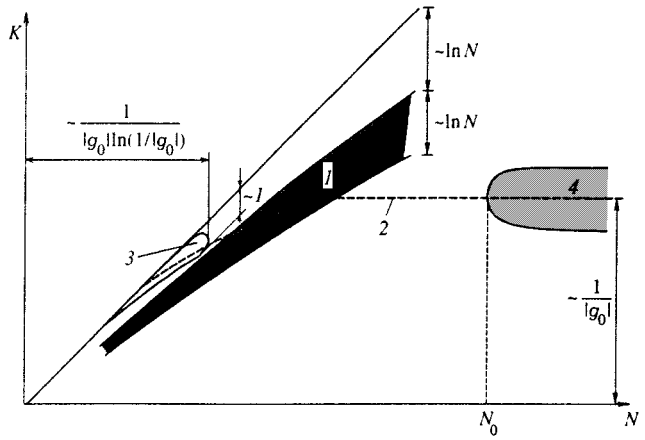

FIG. 3. Regions in the (N,K) plane that are of importance in studying the sum (8): (1) the nonuniversality region in which information of the coefficients A_N^0 with $N\sim 1$ is important; the universal asymptotes (42) and (43) are valid above and below this region; (2) the saddle-point values of K for $N=\text{const}$; for small N the parquet coefficients lying on the principal diagonal are dominant; (3) the region which makes a quasiparquet contribution to the sum (8); and (4) the region which makes a nonperturbative contribution to the sum (8) (N_0 may be chosen arbitrarily large).

The latter can be determined to within a few percent by matching the first orders of perturbation theory with the Lipatov asymptote (see the examples in Refs. 14 and 15).

4. SUMMING THE SERIES FOR $\Sigma(0,\kappa)$

The above information on the coefficients A_N^K can be used to identify the regions in the (N,K) plane which make significant contributions to the sum (8). Region *1* of Fig. 3 is a nonuniversality region in which the behavior of the A_N^K depends substantially on the specific values of A_N^0 with $N\sim 1$. Above and below region 1, the universal asymptotes (42) and (43), determined by the trivial coefficient $A_0^0=1$ and the Lipatov asymptote for A_N^0, respectively, are valid. The dashed line *2* denotes the saddle-point values of K for $N=\text{const}$ assuming $|g_0|\ll 1$ and $g_0\ln(\Lambda/\kappa)\sim 1$. When N is reduced the saddle point vanishes and the parquet coefficients A_N^N on the principal diagonal become dominant. An important contribution to the sum (8) comes from regions *3* and *4* which are adjacent to the dotted saddle-point line.

Region *3* gives a quasiparquet contribution, determined by coefficients A_N^{N-K} with $K\sim 1$, for which Eq. (28) is valid:

$$\left[Y\left(g_0,\frac{\Lambda}{\kappa}\right)\right]_{\text{quasiparq}}=\left[\Delta+\frac{W_3}{W_2}\,g_0\,\ln\Delta\right]^{\beta},$$

$$\Delta=1+W_2 g_0\,\ln\frac{\Lambda}{\kappa}. \tag{44}$$

To within logarithmic accuracy the quantity Δ in the logarithm can be replaced by its minimum value $\tilde{\Delta}\sim|g_0|\ln|g_0|$ (see below), since for $\Delta\gg\tilde{\Delta}$ the logarithmic term is unimportant and Eq. (44) can be rewritten in the form

$$\left[Y\left(g_0,\frac{\Lambda}{\kappa}\right)\right]_{\text{quasiparq}}\approx\left[1+W_2 g_1\,\ln\frac{\Lambda}{\kappa}\right]^{\beta}, \tag{45}$$

$$g_1=g_0\Big/\left(1+\frac{W_3}{W_2}\,g_0\,\ln\tilde{\Delta}\right)$$

$$\approx g_0\Big/\left(1+\frac{W_3}{W_2}\,g_0\,\ln|g_0|\right),$$

which differs from the parquet form[6] only in replacing g_0 by g_1.

Region *4* makes a nonperturbative contribution that has been discussed in detail in Refs. 5 and 6. It is obtained by substituting Eqs. (30) and (43) in Eq. (8), summing over K by the saddle-point method, and summing over N with the aid of the formula

$$\operatorname{Im}\sum_{N=N_0}^{\infty}\Gamma(N+b)a^N(g_0-i0)^N f(N)=\frac{\pi}{(ag_0)^b}$$

$$\times\exp\left(-\frac{1}{ag_0}\right)f\left(\frac{1}{ag_0}\right), \tag{46}$$

$$ag_0>0,\quad N_0\gg 1,$$

which is valid for slowly varying functions $f(N)$. It is obtained by expanding $f(N)$ in a Fourier integral, using Eq. (90) of Ref. 6, and including only the long wavelength Fourier components. The arbitrariness in determining $f(N)$ for $N<N_0$ makes it possible to satisfy the condition of slow variation for any function $f(N)$ which does not vary more rapidly exponentially. The unusual phenomenon associated with the divergence of the series is that the sum in Eq. (46) is determined by arbitrarily large N (so the result is independent of N_0), but the value of $f(N)$ for a finite $N=1/ag_0$ appears in the result. Thus, the correction factor which distinguishes the exact A_N^K from the Lipatov asymptote (23), is determined by Eqs. (30) and (43), and is negligible for $N\to\infty$, will lead to a substantial difference between the complete nonperturbative contribution and that calculated from the Lipatov asymptote (see Eq. (133) of Sec. 7.7 for $M=1$ below):

$$[\Sigma(0,\kappa)]_{\text{nonpert}}\equiv i\Gamma_0(\kappa^2)=[\Sigma(0,\kappa)]_{\text{nonpert}}^{\text{Lipatov}}\,\frac{1}{\sqrt{\pi}}\left(\ln\frac{1}{|g_0|}\right)^{\gamma}$$

$$\times\left(\frac{abg_0x_0}{2}\right)^{b+\beta-f_\infty}I\left(\frac{1+W_2g_1\,\ln(\Lambda/\kappa)}{abg_1x_0/2}\right),$$

$$[\Sigma(0,\kappa)]_{\text{nonpert}}^{\text{Lipatov}}=i\pi c_2\,\frac{1}{(ag_0)^b}\left(\ln\frac{1}{|g_0|}\right)^{-\gamma}$$

$$\times\exp\left(-\frac{1}{ag_0}\right)\kappa^2\,\exp\left(\sigma\,\ln\frac{\Lambda}{\kappa}\right),$$

$$x_0=\left(\frac{8f_\infty}{b^2}\ln\frac{1}{ag_0}\right)^{1/2},$$

$$I(y)=\int_0^\infty dz\left(\ln\frac{bx_0}{2}\,z\right)^{-\gamma}z^{b+\beta-f_\infty}\exp\{-(y-z)^2\}, \tag{47}$$

where $c_2\approx 3.44\cdot 10^{-2}$ for $n=0$. The condition $M>M_0$ in Eq. (43) corresponds to positive values of the argument $I(y)$, which happens in this range of parameters.

Approximating the series (17) by the sum of the contributions (45) and (47) and substituting in Eq. (14), we have

$$\kappa_0^2-\kappa_c^2=\kappa^2\left[1+W_2g_1\ln\frac{\Lambda}{\kappa}\right]^{1/4}+i\Gamma_0(\kappa^2),$$
$$\kappa^2=-E-i\Gamma, \tag{48}$$

which is solved similarly to Eq. (93) of Ref. 6 and determines the relationship between the damping Γ and the renormalized energy E with bare energy $E_B=-\kappa_0^2$ in the parametric form:

$$\Gamma=\Gamma_ce^x\sin\varphi,\quad E=-\Gamma_ce^x\cos\varphi,$$
$$-E_B+E_c=\Gamma_ce^x(4K_4|g_1|x)^{1/4}\{\cos(\varphi+\varphi/4x)$$
$$-\tan(\varphi/3)\sin(\varphi+\varphi/4x)\}, \tag{49}$$

where E_c is given by Eq. (108) of Ref. 6,

$$\Gamma_c=\Lambda^2\exp\left\{-\frac{1}{4K_4|g_1|}\right\}, \tag{50}$$

and $x(\varphi)$ is a unique function in the interval $0<\varphi\pi$ analogous to that shown in Fig. 2 of Ref. 6 and given by (cf. Eq. (100) of Ref. 6)

$$\sin\left(\varphi+\frac{\varphi}{4x}\right)=B\cos\left(\frac{\varphi}{3}\right)\frac{e^{-4x/3}}{x^{1/4}}I\left(\frac{x}{x_0}\right), \tag{51}$$

in which the constant B is equal to

$$B=\sqrt{\pi}c_2\left(\frac{3}{4}\right)^{1/4}\left(\frac{\tilde{\Delta}}{3K_4|g_0|}\right)^{7/4}\left(\frac{4}{3}x_0\right)^{7/6}\sim\left(\ln\frac{1}{|g_0|}\right)^{7/3}. \tag{52}$$

The minimum values of Δ and x are attained simultaneously and, to logarithmic accuracy, are

$$\Delta_{\min}\equiv\tilde{\Delta}\approx\frac{21}{4}K_4|g_0|\ln\frac{1}{|g_0|},\quad x_{\min}\approx\frac{7}{4}\ln\ln\frac{1}{|g_0|}. \tag{53}$$

The minimum distance to the false pole[3] is of order $|g_0|\ln\ln(1/|g_0|)$ and the ''effective interaction'' turns out to be logarithmically weak for small κ.

5. THE QUASIPARQUET APPROXIMATION

Calculating the density of states requires knowledge of the self energy $\Sigma(p,\kappa)$ for finite momenta.[6] As when $p=0$, this quantity consists of nonperturbative and quasiparquet contributions. The nonperturbative contribution will be important only at large negative E, where it is determined directly by the Lipatov asymptote and is given by Eq. (132) of Sec. 7.7 with $M=1$, $n=0$, and $p_1=-p_2=p$. For p below some p_0, $[\Sigma(p,\kappa)]_{nonpert}$ is independent of p, while for $p\gtrsim p_0$ it falls off rapidly with increasing p. Given the logarithmic accuracy of the subsequent calculations (Sec. 8, Ref. 6), the following result is adequate:

$$[\Sigma(p,\kappa)]_{\text{nonpert}}\approx[\Sigma(0,\kappa)]_{\text{nonpert}}\Theta(p_0-p),$$
$$p_0\sim\kappa\left(\frac{1}{|g_0|}\ln\frac{1}{|g_0|}\right)^{1/2}. \tag{54}$$

Major difficulties arise in calculating the quasiparquet contribution to $\Sigma(p,\kappa)$, which corresponds to a logarithmic approximation of arbitrary finite order including the principal asymptote in N of the expansion coefficients. The principal logarithmic approximation for calculating $\Sigma(p,\kappa)$ requires knowledge of the four-tail vertex $\Gamma^{(0,4)}(p,k,q)$, which depends on three substantially different momenta, $p\gg k\gg q\gg\kappa$.[6] The method used above allows us to find the quasiparquet contribution to $\Gamma^{(0,4)}$ for $p\sim k\sim q\gg\kappa$. Writing an expansion of the type (8),

$$\Gamma^{(0,4)}(p,p,p)=\sum_{N=1}^{\infty}g_0^N\sum_{K=0}^{N-1}A_N^K\left(\ln\frac{\Lambda}{p}\right)^K \tag{55}$$

(with different coefficients A_N^K) and noting that $\Gamma^{(0,4)}$ satisfies an equation like (15) with $V(g_0)\equiv-2\eta(g_0)$, in place of Eq. (20) we obtain

$$-KA_N^K=\sum_{M=1}^{N-K}[W_{M+1}(N-M)+V_M]A_{N-M}^{K-1},$$
$$K=1,\ldots,N-1, \tag{56}$$

which, given that $V_1=0$,[10] gives the following instead of Eqs. (27) and (28):

$$A_N^{N-K}=-2(-W_2)^N\frac{1}{(K-1)!}$$
$$\times\frac{(-W_3)^{K-1}}{(-W_2)^{2K-1}}(N\ln N)^{K-1},\quad K\sim1. \tag{57}$$

The quasiparquet contribution to the sum (55), which is determined by the coefficients (57), has the form

$$[\Gamma^{(0,4)}(p,p,p)]_{\text{quasiparq}}$$
$$=-2g_0\Big/\left(\Delta+\frac{W_3}{W_2}g_0\ln\Delta\right)\Big|_{\Delta=1+W_2g_0\ln(\Lambda/p)}$$
$$\approx\frac{-2g_1}{1+W_2g_1\ln(\Lambda/p)}. \tag{58}$$

In the principal logarithmic approximation, calculating $\Gamma^{(0,4)}(p,k,q)$ requires summation of the parquet graphs (Fig. 4a) obtained by successive splitting of simple vertices into two parts joined by two lines. When the order of the graph is increased by unity, the smallness $\sim g_0$ associated with the additional vertex is compensated by the large logarithm associated with the additional pair of lines.[18] It is possible to approach the parquet approximation from the standpoint of a general structural analysis of the graphs:[18,19] the complete vertex $\Gamma^{(0,4)}$ is represented in the form of three ''bricks'' $F_{ij,kl}$ and an irreducible four-tail vertex R^0 (Fig. 4b). Each brick is the sum of the graphs introduced along the pair of lines in the corresponding channel and obtained by repeating a ''crossed out'' vertex R (Fig. 4c), which in turn is the sum

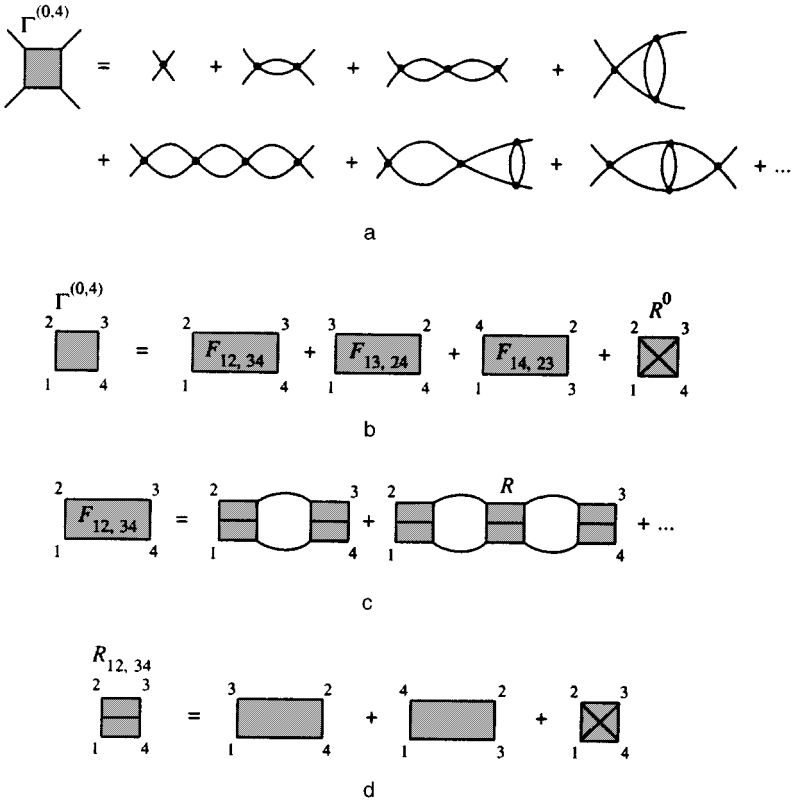

FIG. 4. (a) A parquet sequence of graphs for $\Gamma^{(0,4)}$ (obtained by successive splitting of simple vertices into two parts joined by a pair of lines); (b–d) the system of equations for the complete vertex $\Gamma^{(0,4)}$, three ''bricks'' $F_{ij,kl}$, three ''crossed out'' vertices $R_{ij,kl}$, and an irreducible vertex R^0. The approximation $R^0=-2g_0$ corresponds to summing the sequence of diagrams *a*.

of two bricks and an irreducible four-tailed vertex (Fig. 4d). Setting up the equations of type *c* and *d* for the two other bricks, we obtain a system of 7 equations for 8 variables.[19] All the variables are uniquely determined by specifying the vertex R^0, so that

$$\Gamma^{(0,4)}(p,k,q)=F\{R^0(p,k,q)\}, \tag{59}$$

where $F\{\dots\}$ is a functional. The parquet approximation corresponds to replacing the irreducible four-tail vertex with a simple vertex $R^0(p,k,q)=-2g_0$, so that the system *b-d* then corresponds to the sum of the graphs *a*.

In Appendix 2 it is shown that the vertex R^0 depends only on the maximum momentum and Eq. (59) takes the form

$$\Gamma^{(0,4)}(p,k,q)=F\{R^0(p,p,p)\}. \tag{60}$$

Taking $k=q=p$ and reverting Eq. (60), we can obtain an approximation for R^0 that corresponds to the result (58), after which Eq. (60) solves the problem in principle.

The function $F\{\dots\}$ is determined by the system of equations *b-d* (Fig. 4), which is very complicated and has never been solved. Usually the approximation technique of Sudakov[20] as refined by Polyakov[21] is used. This method does not assume any specific approximation for R^0, but is based on logarithmic calculations of the type

$$\int_0^\Lambda \frac{k^3dk}{(k^2+\kappa^2)^2}=\int_{\sim\kappa}^\Lambda \frac{k^3dk}{k^4}=\ln\frac{\Lambda}{\kappa}+O(1). \tag{61}$$

The lower limit in the second integral is determined only to order of magnitude, but this uncertainty does not affect the larger logarithm and shows up only as a quantity of $O(1)$. At first glance, this method of calculation is justified only in the principal logarithmic approximation; in fact, the substitution $\kappa\to c\kappa$ in the principal logarithms (8) yields

$$A_N^N\left(\ln\frac{\Lambda}{\kappa}\right)^N\to A_N^N\left(\ln\frac{\Lambda}{\kappa}-\ln c\right)^N, \tag{62}$$

which leads to a change in the coefficients for the lower-order logarithms,

$$A_N^{N-K}\to A_N^{N-K}+\frac{(-\ln c)^K}{K!}N^KA_N^N,\quad K\sim 1. \tag{63}$$

According to Eq. (28), however, $A_N^{N-K}\sim A_N^N(N\ln N)^K$ and the principal asymptote in N is ''insensitive'' to the substitution $\kappa\to c\kappa$. Thus, in the principal order in N, logarithmic calculations are permissible in an arbitrary finite logarithmic approximation. This makes it possible fully to employ the parquet scheme for calculating the quasiparquet contribution to $\Gamma^{(0,4)}$.

Substituting Eq.(58) in the parquet equation[19,21,11]

$$\Gamma^{(0,4)}(x,x,x)=R^0(x,x,x)+\frac{1}{2}K_4(n+8)\times\int_0^x dt[\Gamma^{(0,4)}(t,t,t)]^2, \tag{64}$$

where $x=\ln(\Lambda/p)$, we obtain $R^0(x,x,x)=-2g_1$ and $[\Sigma(p,\kappa)]_{\text{quasiparq}}$ is determined by the parquet formulas[6,11] with g_0 replaced by g_1. The final result for $\Sigma(p,\kappa)$ has the form

$$\Sigma(p,\kappa)-\Sigma(0,\kappa)=\kappa^2\left\{1-\frac{3}{2}\left[\frac{t(x)}{t(x_\infty)}\right]^{-1/4}+\frac{1}{2}\left[\frac{t(x)}{t(x_\infty)}\right]^{-3/4}\right\}-i\Gamma_0(\kappa^2)\Theta(p-p_0) \tag{65}$$

(cf. Eq. (116) of Ref. 6), where

$$t(x)=1+8K_4g_1x, \quad x=\ln(\Lambda/p), \quad x_\infty=\ln(\Lambda/\kappa). \tag{66}$$

6. THE DENSITY OF STATES

Calculations analogous to Sec. 8 of Ref. 6 yield the result

$$\nu(E)=\frac{\Gamma_c e^x}{4\pi|g_1|}(4K_4|g_1|x)^{1/4}\left\{\frac{1}{2}\sin\left(\varphi+\frac{\varphi}{4x}\right)[1+4K_4|g_1|x-4K_4|g_1|\ln|g_1|]-(4K_4|g_1|x)^{1/2}\sin\left(\varphi+\frac{3\varphi}{4x}\right)\right\}, \tag{67}$$

which, together with Eqs. (49) and (51), determine $\nu(E)$ in parametric form. For $|E|\gg\Gamma$ we have the asymptote

$$\nu(E)=\frac{1}{2}K_4E\left(1-4K_4|g_1|\ln\frac{\Lambda^2}{E}\right)^{-1/4}, \quad E\gg\Gamma,$$

$$\nu(E)=\frac{\Gamma_0(E)}{4\pi|g_1|}\left\{1-2K_4|g_1|\ln\frac{\Lambda^2}{|E|}-2K_4|g_1|\ln|g_1|-\left(1-4K_4|g_1|\ln\frac{\Lambda^2}{|E|}\right)^{1/2}\right\}, \quad -E\gg\Gamma, \tag{68}$$

where $\Gamma_0(E)\equiv\Gamma_0(|\kappa|^2)$. For large positive E the function $\nu(E)$ becomes the density of state of an ideal lattice, and for large negative E we have the result

$$\nu(E)=\frac{K_4}{2\pi}\Gamma_0(E)\ln\frac{1}{|g_0|}=\frac{K_4}{2}c_2\left(\frac{1}{3K_4|g_0|}\right)^{8/3}\left(\ln\frac{1}{|g_0|}\right)^{2/3}\times\exp\left(-\frac{1}{3K_4|g_0|}\right)\Lambda^2\left(\frac{\Lambda^2}{|E|}\right)^{1/3}, \tag{69}$$

which corresponds to the asymptotic behavior of a fluctuation tail obtained in the traditional forms of the instanton method.[3,12,13] It can be obtained by summing the outlying terms of the series for $G(p,\kappa)$ (see Eq. (113)). For a quadratic spectrum, Eq. (69) is only valid in the region $|E|\lesssim\Lambda^2$. In fact, deviations from a quadratic spectrum show up much earlier and lead to an exponential decrease in $\nu(E)$.[6]

7. CALCULATING THE LIPATOV ASYMPTOTE

The plateau contribution (Sec. 1) plays a fundamental role in the renormalizable models and an analysis can be carried out in the continuum limit, assuming the spectrum $\varepsilon(k)$ to be quadratic. On the whole, the calculations follow the scheme described in Ref. 6, with $\varepsilon(k)\to k^2$ and $\Sigma_x\to\int d^4x$. The differences are connected with the higher symmetry of the four-dimensional continuum model, which makes it possible to reduce the calculations ''to a number'' but lead to a number of technical difficulties along the way.

7.1. Four-dimensional continuum model

The standard procedure[6] reduces to the following conditions on the saddle point in the functional integral:

$$Ng_c^{-1}=-\frac{1}{4}\int d^4x\,\varphi_c(x)^4, \tag{70}$$

$$-\Delta\varphi_c(x)+g_c\varphi_c(x)^3+\kappa^2\varphi_c(x)=0. \tag{71}$$

In the ''massless'' theory ($\kappa=0$) the solution of Eq. (71), an instanton, has the form

$$\varphi_c(x)=(-g_c)^{-1/2}\phi_c(x), \quad \phi_c(x)=\frac{2\sqrt{2}R}{x^2+R^2}, \tag{72}$$

where the parameter R, the radius of the instanton, is arbitrary, consistent with the presence of a plateau in the optimal fluctuation method (Sec. 1). The deviations from the saddle point are expanded in terms of the eigenfunctions e_s^T and e_s^T, which obey the equations

$$\hat{M}_Le_s^L(x)=\lambda_s^Le_s^L(x), \quad \hat{M}_Te_s^T(x)=\lambda_s^Te_s^T(x) \tag{73}$$

for the operators

$$\hat{M}_L=-\Delta+3g_c\varphi_c^2(x), \quad \hat{M}_T=-\Delta+g_c\varphi_c^2(x), \tag{74}$$

which, as usual, have zero modes:[3] the operator $\hat{M}_L$ the translation modes

$$\lambda_\mu^L=0, \quad e_\mu^L(x)=\left[\int d^4x\left(\frac{\partial\phi_c}{\partial x_\mu}\right)^2\right]^{-1/2}\frac{\partial\phi_c(x)}{\partial x_\mu}, \quad \mu=1,\,2,\,3,\,4, \tag{75}$$

and the operator $\hat{M}_T$ the rotational mode

$$\lambda_0^T=0, \quad e_0^T(x)=\left[\int d^4x\,\phi_c(x)^2\right]^{-1/2}\phi_c(x). \tag{76}$$

The arbitrariness of the parameter R in Eq. (72) leads to the existence of yet another zero mode for $\hat{M}_L$, the dilatation mode[14,16]

$$\lambda_0^L=0, \quad e_0^L(x)=\left[\int d^4x\left(\frac{\partial\phi_c}{\partial R}\right)^2\right]^{-1/2}\frac{\partial\phi_c(x)}{\partial R}. \tag{77}$$

Its existence makes Eq. (71) insoluble for finite κ (a rigorous proof is given elsewhere[22]). Taking κ^2 into account through perturbation theory leads to the equation $\hat{M}_L\delta\phi=-\kappa^2\phi_c(x)$, whose right-hand side is nonorthogonal to $e_0^L(x)$. The significance of this insolubility is made clearer by the optimal fluctuation method (Sec. 1): for $E<0$, $d=4$, and $\varepsilon(k)=k^2$ the function $S(E,R)$ increases monotonically

with increasing R, so that the derivative of $S(E,R)$ with respect to R does not go to zero; thus, in the instanton method the variation of the Hamiltonian (1) with respect to φ, which leads to Eq. (71), does not vanish.

This difficulty can be overcome by minimizing $H\{\varphi\}$ for a fixed instanton radius R followed by an essentially non-Gaussian integration with respect to R.

7.2. Expansion near an ''anomalous'' instanton

For the $(N-1)$th coefficient of the expansion of the M-point Green function (see Eqs. (29) and (58) of Ref. 6) we have

$$[G_M(x_1,\alpha_1,\ldots,x_M,\alpha_M)]_{N-1}$$
$$=Z_0(\kappa)^{-1}\int\frac{dg}{2\pi i}\int D\varphi\varphi_{\alpha_1}(x_1)\ldots\varphi_{\alpha_M}(x_M)$$
$$\times\exp\{-H\{\kappa,g,\varphi\}-N\ln g\}, \tag{78}$$

where the Hamiltonian $H\{\kappa,g,\varphi\}$ is given by Eq. (1) and

$$Z_0(\kappa)=\int D\varphi\ \exp[-H\{\kappa,0,\varphi\}]=\left(\prod_s\frac{2\pi}{\lambda_s^0+\kappa^2}\right)^{n/2} \tag{79}$$

(the λ_s^0 are the eigenvalues of the operator $\hat{p}^2$). Let us introduce three expansions of unity under the integral of Eq. (78),

$$1=\left(\int d^4x|\varphi(x)|^4\right)^4\int d^4x_0$$
$$\times\prod_{\mu=1}^4\delta\left(-\int d^4x|\varphi(x)|^4(x-x_0)_\mu\right),$$
$$1=\int d^4x|\varphi(x)|^4\int_0^\infty d\ln R^2$$
$$\times\delta\left(-\int d^4x|\varphi(x)|^4\ln\left(\frac{x-x_0}{R}\right)^2\right). \tag{80}$$
$$1=\int d^nu\,\delta(\mathbf{u}-\mathbf{v}\{\varphi\}),$$

where the unit vector $\mathbf{v}$ is fixed by the condition

$$\mathbf{v}\{\varphi\}\|\int d^4x|\varphi(x)|^l\varphi(x),\quad l>1. \tag{81}$$

Making the change of variables

$$x-x_0=R\tilde{x},\quad \varphi_\alpha(x_0+R\tilde{x})=R^{-1}\tilde{\varphi}_\alpha(\tilde{x}) \tag{82}$$

and changing the order of integration, we have, on dropping the tildes,

$$[G_M]_{N-1}=\int_0^\infty d\ln R^2Z_0(\kappa_R)^{-1}\int d^4x_0\int d^nuR^{-M-4}$$
$$\times\int\frac{dg}{2\pi i}\int D\varphi\prod_{\mu=1}^4\delta\left(-\int d^4x|\varphi(x)|^4x_\mu\right)$$
$$\times\delta\left(-\int d^4x|\varphi(x)|^4\ln x^2\right)\delta(\mathbf{u}-\mathbf{v})$$
$$\times\left(\int d^4x|\varphi(x)|^4\right)^5\varphi_{\alpha_1}\left(\frac{x_1-x_0}{R}\right)\ldots\varphi_{\alpha_M}$$
$$\times\left(\frac{x_M-x_0}{R}\right)\exp\{-H\{\kappa_R,g,\varphi\}-N\ln g\}, \tag{83}$$

where

$$\kappa_R\equiv\kappa R. \tag{84}$$

The substitution (82) was made as in Eq. (79) and cancels the factor arising from the transformation $D\varphi$. The transformations (80)–(83) introduce integrations with respect to arbitrary parameters of the instanton: the location x_0 of its center, its ''orientation'' $\mathbf{u}$, and radius $\mathbf{r}$. In the integral of Eq. (83) the choice of these parameters is already fixed by the δ-functions: the center is at the point $x=0$, the orientation is along the vector $\mathbf{u}$, and the radius is determined by the condition

$$\int d^4x\varphi_c(x)^4\ln x^2=0, \tag{85}$$

or $R=1$ in the function (72).

Let us make the expansion in Eq. (83) near g_c determined by Eq. (70) and an arbitrary spherically symmetric function $\varphi_c(x)$ which falls off at infinity, assuming that

$$g=g_c+\delta g,\quad \varphi_\alpha(x)=[\varphi_c(x)+\delta\varphi_L(x)]u_\alpha+\delta\varphi_\alpha^T(x),$$
$$\delta\varphi^T\perp\mathbf{u} \tag{86}$$

and limiting ourselves to second order terms in the increments. Introducing the coefficients C_s^L and $C_s^{T,\alpha}$ of the expansions in terms of the eigenfunctions of the operators (74),

$$\delta\varphi_L(x)=\sum_s C_s^Le_s^L(x),\quad \delta\varphi_\alpha^T(x)=\sum_s C_s^{T,\alpha}e_s^T(x), \tag{87}$$

we obtain

$$[G_M]_{N-1}=\left(\int d^4x\varphi_c(x)^4\right)^5\int_0^\infty d\ln R^2Z_0(\kappa_R)^{-1}\int d^4x_0$$
$$\times\int d^nu\,\delta(|\mathbf{u}|-1)u_{\alpha_1}\ldots u_{\alpha_M}R^{-4-M}$$
$$\times\left(\int d^4x\varphi_c(x)^{l+1}\right)^{n-1}\varphi_c\left(\frac{x_1-x_0}{R}\right)$$
$$\ldots\varphi_c\left(\frac{x_M-x_0}{R}\right)\exp\{-N\ln g_c$$
$$-H\{x_R,g_c,\varphi_c\}\}\int\frac{dg}{2\pi i}\int DC^L\int DC^T$$
$$\times\prod_{\mu=0}^4\delta\left(\sum_s\gamma_s^\mu C_s^L\right)\prod_{\alpha=0}^{n-1}\delta\left(\sum_s C_s^{T\alpha}\beta_s\right)$$
$$\times\exp\left\{\frac{1}{2}N\left(\frac{\delta g}{g_c}\right)^2-\frac{\delta g}{g_c}\sum_s C_s^L\omega_s-\sum_s C_s^L\sigma_s\right.$$

$$-\frac{1}{2}\sum_s(\lambda_s^L+\kappa_R^2)(C_s^L)^2-\frac{1}{2}\sum_s\sum_\alpha(\lambda_s^T+\kappa_R^2)(C_s^{T,\alpha})^2\Bigg\},$$

where

$$\omega_s=g_c\int d^4x\varphi_c^3(x)e_s^L(x),$$

$$\sigma_s=\int d^4xe_s^L(x)[-\Delta\varphi_c(x)+\kappa_R^2\varphi_c(x)+g_c\varphi_c(x)^3],$$

$$\gamma_s^0=4\int d^4x\varphi_c^3(x)e_s^L(x)\ln x^2,$$

$$\gamma_s^\mu=4\int d^4x\varphi_c^3(x)e_s^L(x)x_\mu,\quad \mu=1,\ 2,\ 3,\ 4,$$

$$\beta_s=\int d^4x\varphi_c^l(x)e_s^T(x). \tag{89}$$

Transforming the δ-functions in the exponent using the formula

$$\delta(x)=\frac{1}{2\pi}\int_{-\infty}^{\infty}d\tau e^{i\tau x} \tag{90}$$

and reducing the expression in the exponent to a sum of squares, for the integral with respect to g, C^L, and C^T in Eq. (88) we obtain the result

$$\frac{g_c}{(2\pi)^{(n+5)/2}}\left(\prod_s\frac{2\pi}{\lambda_s^L+\kappa_R^2}\right)^{1/2}\left(\prod_s\frac{2\pi}{\lambda_s^T+\kappa_R^2}\right)^{(n-1)/2}$$
$$\times(\langle\beta^2\rangle_T)^{-(n-1)/2}\left(\prod_{\mu=1}^4\langle\gamma^\mu\gamma^\mu\rangle\right)^{-1/2}[N\langle\gamma^0\gamma^0\rangle+\langle\omega^2\rangle$$
$$\times\langle\gamma^0\gamma^0\rangle-\langle\omega\gamma^0\rangle^2]^{-1/2}\exp\Bigg\{-N\ln g_c-H\{\kappa_R,g_c,\varphi_c\}$$
$$+\frac{1}{2}\langle\sigma^2\rangle-\frac{1}{2}\frac{\langle\sigma\omega\rangle^2}{N+\langle\omega^2\rangle}$$
$$-\frac{1}{2}\frac{[\langle\sigma\gamma^0\rangle(N+\langle\omega^2\rangle)-\langle\sigma\omega\rangle\langle\omega\gamma^0\rangle]^2}{(N+\langle\omega^2\rangle)[\langle\gamma^0\gamma^0\rangle(N+\langle\omega^2\rangle)-\langle\omega\gamma^0\rangle^2]}\Bigg\}, \tag{91}$$

where the following notation has been introduced:

$$\langle fg\rangle=\sum_s\frac{f_sg_s}{\lambda_s^L+\kappa_R^2},\quad \langle fg\rangle_T=\sum_s\frac{f_sg_s}{\lambda_s^T+\kappa_R^2}. \tag{92}$$

The average $\langle fg\rangle$ is expressed in terms of the Green function of the operator $\hat{M}_L+\kappa_R^2$, which, given the obvious symmetry, can be used to prove that (as already used in Eq. (91)) the following quantities vanish:

$$\langle\sigma\gamma^\mu\rangle=\langle\omega\gamma^\mu\rangle=0,\quad \mu\neq0;\quad \langle\gamma^\mu\gamma^{\mu'}\rangle=0,\quad \mu\neq\mu', \tag{93}$$

For a ''regular'' instanton that satisfies Eq. (71) with $\kappa\to\kappa_R$, the coefficients $\sigma_s\equiv0$ and the exponent of Eq. (88) contains no terms linear in the deviations. The insolubility of Eq. (71) means that the coefficients σ_s cannot be taken equal to zero. For a correct transition from (88) to (83) to Eq. (91) they must be sufficiently small that the shifts in the variables C_s^L during diagonalization of the quadratic form do not take the expansion (88) beyond its limits of applicability. The question arises as to how to choose φ_c so as to ensure the required smallness of σ_s. When the instanton is chosen in accordance with Section 7.3, the sum $\Sigma_s\sigma_sC_s^L$ turns out to be proportional to the sum $\Sigma_s\gamma_s^0C_s^L$, whose magnitude is fixed at zero owing to the presence in Eq. (88) of an appropriate δ-function. In that way, terms linear in the deviations are eliminated exactly from the exponent of Eq. (88).

7.3. Choice of instanton

We choose the function $\varphi_c(x)$ by minimizing $H\{\kappa_R,g_c,\varphi\}$ with the additional condition (85) fixing the instanton radius. This yields

$$-\Delta\varphi_c(x)+\kappa_R^2\varphi_c(x)+g_c\varphi_c^3(x)+\mu\varphi_c^3(x)\ln x^2=0 \tag{94}$$

(μ is a Lagrange multiplier[23]) with which it is easy to show that

$$\sigma_s=-\frac{\mu}{4}\gamma_s^0,\quad 2\omega_s-\frac{\mu}{4}\gamma_s^0=(\lambda_s^L+\kappa_R^2)$$
$$\times\int d^4x\varphi_c(x)e_s^L(x),\quad H\{\kappa_R,g_c,\varphi_c\}=N, \tag{95}$$

from which we have

$$\langle\sigma^2\rangle=\left(\frac{\mu}{4}\right)^2\langle\gamma^0\gamma^0\rangle,\quad \langle\sigma\omega\rangle=-\frac{\mu}{4}\langle\omega\gamma^0\rangle,$$

$$\langle\sigma\gamma^0\rangle=-\frac{\mu}{4}\langle\gamma^0\gamma^0\rangle,\quad \langle\omega^2\rangle=-2N+\frac{\mu}{8}\langle\omega\gamma^0\rangle,$$

$$\langle\omega\gamma^0\rangle=\frac{\mu}{8}\langle\gamma^0\gamma^0\rangle, \tag{96}$$

with which Eq. (91) is greatly simplified and Eq. (88) takes the form

$$[G_M]_{N-1}=\left(\int d^4x\varphi_c(x)^4\right)^5\int d^4x_0\int_0^\infty d\ln R^2$$
$$\times\int d^nu\,\delta(|\mathbf{u}|-1)u_{\alpha_1}\ldots u_{\alpha_M}R^{-4-M}$$
$$\times\left(\int d^4x\varphi_c^{l+1}(x)\right)^{n-1}\varphi_c\left(\frac{x_1-x_0}{R}\right)$$
$$\ldots\varphi_c\left(\frac{x_M-x_0}{R}\right)\left(\frac{D_0}{D_T}\right)^{(n-1)/2}$$
$$\left(-\frac{D_0}{D_L}\right)^{1/2}g_c(2\pi)^{-(n+5)/2}N^{-1/2}$$
$$\times\prod_{\mu=0}^4\langle\gamma^\mu\gamma^\mu\rangle^{-1/2}(\langle\beta^2\rangle_T)^{-(n-1)/2}$$
$$\times\exp(-N-N\ln g_c), \tag{97}$$

where the following notation for the determinants has been introduced:

$$D_L=\prod_s\ (\lambda_s^L+\kappa_R^2),\quad D_T=\prod_s\ (\lambda_s^T+\kappa_R^2),$$

$$D_0=\prod_s\ (\lambda_s^0+\kappa_R^2). \tag{98}$$

7.4. Explicit form of the instanton

The substitution $\mu=(-g_c)\mu_0$ and the transition to the function $\phi_c(x)$ in accordance with the first of Eqs. (72) eliminates g_c from Eq. (94). For small κ_R, when $\mu_0\sim\kappa_R^2\ln\kappa_R$ (see below), Eq. (94) shares two scale lengths: a length $|x|\sim 1$ which determines the localization radius of the instanton ''core'' and a length $|x|\sim\kappa_R^{-1}$ to which the instanton ''tail'' extends. This makes it possible to carry out the analysis in two overlapping regions, $|x|\ll\kappa_R^{-1}$ and $|x|\gg 1$, and match the solutions.

The region $|x|\ll\kappa_R^{-1}$. For $\kappa_R=0$ and $\mu=0$, Eq. (94) has the exact solution (92) in which the solution (85) fixes the choice $R=1$. Treating the terms containing κ_R^2 and μ as a perturbation, we have

$$\phi_c(x)=\frac{2\sqrt{2}}{z+1}\left[1+\frac{1-z}{1+z}\,v(z)\right]_{z=x^2},$$

$$v(z)=\frac{\kappa_R^2}{4}\int_0^z dz\,\frac{(1+z)^4}{(1-z)^2z^2}\left[-\ln(1+z)+\frac{z+2z^2}{(1+z)^2}\right]$$

$$+\mu_0\,\frac{z}{z-1}\left[-\ln z-\frac{z}{6}+\frac{3}{2}\right]. \tag{99}$$

Calculating the asymptote $v(z)$ for $z\gg 1$ and including only the terms that increase with z, for the region $1\ll|x|\ll\kappa_R^{-1}$ we have

$$\phi_c(x)=\frac{2\sqrt{2}}{x^2}\left\{1+\frac{1}{2}\,\kappa_R^2x^2\,\ln|x|+\left[\frac{1}{6}\,\mu_0-\frac{3}{4}\,\kappa_R^2\right]x^2\right.$$

$$\left.+3\kappa_R^2\,\ln^2|x|+\left[2\mu_0-\frac{11}{2}\,\kappa_R^2\right]\ln|x|-\frac{1}{x^2}\right\}. \tag{100}$$

The region $|x|\gg 1$. When the terms that are nonlinear in $\phi_c(x)$ are neglected, Eq. (94) has the solution $B|x|^{-1}K_1(\kappa_R|x|)$, where $K_1(x)$ is the modified Bessel function of the second kind. Treating the neglected terms as a perturbation, we have

$$\phi_c(x)=B|x|^{-1}K_1(\kappa_R|x|)$$

$$\times\left\{1-B^2\int_{|x|}^\infty\frac{dy}{yK_1^2(\kappa_Ry)}\int_y^\infty z^{-1}K_1^4(\kappa_Rz)dz\right\}, \tag{101}$$

which for the appropriate choice of B leads to the following result in the region $|x|\ll\kappa_R^{-1}$:

$$\phi_c(x)=\frac{2\sqrt{2}}{x^2}\left\{1+\frac{1}{2}\,\kappa_R^2x^2\,\ln|x|\right.$$

$$+\frac{2C-1+2\ln(\kappa_R/2)}{4}\,\kappa_R^2x^2+3\kappa_R^2\,\ln^2|x|$$

$$\left.+\kappa_R^2\left(6C+\frac{1}{2}+6\ln\left(\frac{\kappa_R}{2}\right)\right)\ln|x|-\frac{1}{x^2}\right\}, \tag{102}$$

where C is Euler's constant. Equations (100) and (102) coincide when

$$\mu_0=3\kappa_R^2(\ln\,\kappa_R+C+1-\ln 2). \tag{103}$$

Using Eq. (99) for calculating the integral in Eq. (70), which is determined by the region $|x|\lesssim 1$, we have

$$N\,\ln\,g_c=N\,\ln\left(-\frac{I_4}{4N}\right)+Nf(\kappa_R),$$

$$f(x)\equiv 3x^2\left(\ln 2-C-\frac{1}{2}-\ln\,x\right), \tag{104}$$

Here we have introduced the notation

$$I_p=\int d^4x\,\phi_c^p(x) \tag{105}$$

for the integrals in the massless theory (i.e., for $\phi_c(x)$ of the form (72) with $R=1$).

7.5. Transformation of the coefficient of the exponential Eq. (97)

Substituting Eq. (104) in Eq. (97) shows that the exponential limits the integral with respect to R to the region $\kappa_R^2\ln\kappa_R\lesssim N^{-1}$ and thereby allows us to calculate the coefficient of the exponential in the limit $\kappa_R\to 0$. Then the solution of Eq. (94) transforms into the instanton of the massless theory (72) with $R=1$. Because the operators $\hat{M}_L$ and $\hat{M}_T$ have the zero modes (75)–(77), the averages in Eq. (97) contain the divergences

$$\langle\gamma^\mu\gamma^\mu\rangle\approx\frac{(\gamma_\mu^\mu)^2}{\lambda_\mu^L+\kappa_R^2},\quad\langle\beta^2\rangle_T\approx\frac{\beta_0^2}{\lambda_0^T+\kappa_R^2}, \tag{106}$$

which cancel the corresponding factors in the determinants D_L and D_T. According to Brezin and Parisi[15] (see details in Ref. 6), it is convenient to express the latter in terms of the function

$$D(z)=\det\left[1-\frac{3z\phi_c^2(x)}{\hat{p}^2+\kappa_R^2}\right]=\prod_s\left(1-\frac{z}{\mu_s}\right), \tag{107}$$

where the μ_s are the eigenvalues of the problem

$$[\hat{p}^2+\kappa_R^2-3\mu_s\phi_c^2(x)]\psi_s(x)=0. \tag{108}$$

Constructing a perturbation theory near $z=1$ and $z=1/3$, it is easy to show that

$$\frac{D_L}{D_0}=\left[3\int d^4x\,\phi_c^2(x)e_0^{L^2}(x)\right]^{-1}\left[\frac{4}{I_6}\int d^4x\left(\frac{\partial\phi_c}{\partial x_\mu}\right)^2\right]^4\overline{D(1)}$$

$$\times\prod_{\mu=0}^4\ (\lambda_\mu^L+\kappa_R^2),\quad\frac{D_T}{D_0}=\frac{I_2}{I_4}\,\overline{D\left(\frac{1}{3}\right)}(\lambda_T^0+\kappa_R^2), \tag{109}$$

where the bar denotes elimination of the zero cofactors from the product (107) for $z=1$ and $z=1/3$.

The product (107) contains divergences determined by the divergence of the sums $\Sigma_s \mu_s^{-1}$ and $\Sigma_s \mu_s^{-2}$. The first is eliminated by renormalizing κ,[15] while the second satisfies

$$\sum_s \frac{1}{\mu_s^2} = 9 \int_0^{\Lambda R} \frac{d^4k}{(2\pi)^4} \times \int_0^{\Lambda R} \frac{d^4q}{(2\pi)^4} \frac{\langle \phi_c^2 \rangle_q \langle \phi_c^2 \rangle_{-q}}{(k^2+\kappa_R^2)[(k+q)^2+\kappa_R^2]},$$

$$\langle f \rangle_q \equiv \int d^4x f(x) e^{iqx}, \tag{110}$$

which is obtained by calculating $\ln D(z)$ order z^2 using perturbation theory. For $\kappa_R = 0$ we have

$$\sum_s \frac{1}{\mu_s^2} = 9 K_4 I_4 \left[\ln \Lambda R - \ln 2 + C + \frac{1}{3} \right]. \tag{111}$$

The divergence for $\Lambda \to \infty$ in Eq. (111) can be eliminated by renormalizing the charge;[4)] however, we are interested in an expansion like (8) which contains a bare charge g_0 and explicit logarithmic divergences. Introducing the renormalized function

$$D_R(z) = \prod_s \left(1 - \frac{z}{\mu_s}\right) \exp\left(\frac{z}{\mu_s} + \frac{z^2}{2\mu_s^2} \right), \tag{112}$$

substituting Eqs. (106), (109), and (111) in Eq. (97), and using the relationships among the integrals obtained by differentiating with respect to the parameters and integrating by parts, we obtain

$$[G_M(x_1, \alpha_1, \ldots, x_M, \alpha_M)]_N = c(-1)^N \left(\frac{4}{I_4}\right)^{N+M/2+5/2} \Gamma\left(N + \frac{M+n+4}{2}\right) \times \int d^n u \, \delta(|\mathbf{u}|-1) u_{\alpha_1} \ldots u_{\alpha_M} \int_0^\infty d \ln R^2 \times \int d^4x_0 R^{-4-M} \phi_c\left(\frac{x_1 - x_0}{R}\right) \cdots \left(\frac{x_M - x_0}{R}\right) \times \exp\left\{ \frac{n+8}{3} \ln(\Lambda R) - N f(\kappa R) \right\}, \tag{113}$$

where

$$c = \frac{2^{n-2} 3^{1/2}}{(2\pi)^{3+n/2}} \left(\frac{I_6}{4}\right)^2 J^{1/2} \exp\left\{ -\frac{3(n+4)}{4} + \frac{n+8}{3} \times [-\ln 2 + C + 1/3] \right\} \left(-\overline{D_R}(1) \overline{D_R^n}^{-1}\left(\frac{1}{3}\right) \right)^{-1/2}, \tag{114}$$

$$J = \int d^4x \phi_c^2(x) \left(\frac{\partial \phi_c(x)}{\partial R} \right)^2 \Bigg|_{R=1}. \tag{115}$$

The values of the integrals which we require are

$$I_3 = 4\sqrt{2} S_4, \quad I_4 = \frac{16}{3} S_4, \quad I_6 = \frac{64}{5} S_4,$$

$$J = \frac{16}{15} S_4; \quad S_4 = 2\pi^2. \tag{116}$$

7.6. Calculating the determinants

An expression for the d-dimensional Laplace operator in spherical coordinates $(r, \varphi_1, \ldots, \varphi_{d-1})$ is obtained through the standard procedure (Section 3 of Vladimirov[24]) by induction with respect to the number of dimensions:

$$\Delta = \frac{\partial^2}{\partial r^2} + \frac{d-1}{r} \frac{\partial}{\partial r} - \frac{\hat{l}^2}{r^2}, \tag{117}$$

where $\hat{l}^2$ is a differential operator acting on the angular variables. The spherical function Y_l of lth order is a homogeneous harmonic polynomial $u_l(x)$ of degree l on the unit sphere $|x|=1$.[24] Substituting $u_l(x) = r^l Y_l(s)$ and $s = x/|x|$ in the Laplace equation, we obtain an eigenvalue problem

$$\hat{l}^2 Y_l(s) = l(l+d-2) Y_l(s), \tag{118}$$

which is soluble only for integral l, since the Laplace equation has no solutions that are not polynomials.[24] A homogeneous polynomial of degree l in d variables has C_{l+d-1}^l coefficients (the number of combinations of d different objects chosen l at a time with repetitions allowed[25]). Acted on by the Laplace operator, it is transformed into a homogeneous polynomial of degree $(l-2)$, which, when set equal to zero, yields C_{l+d-3}^{l-2} conditions. Thus, the degree of degeneracy N_l of the l-th eigenvalue is determined by the difference $C^l - l + d - 1 - C_{l+d-3}^{l-2}$, i.e.,

$$N_l = \frac{(l+d-3)!}{(d-2)!\,l!} (d+2l-2). \tag{119}$$

Separation of variables in Eq. (108) for $\kappa_R = 0$ leads to

$$\left[\frac{\partial^2}{\partial r^2} + \frac{3}{r} \frac{\partial}{\partial r} + \frac{24\mu}{(r^2+1)^2} - \frac{l(l+2)}{r^2} \right] \psi(r) = 0 \tag{120}$$

for the radial equation $\psi(r)$. Setting $\mu = s(s+1)/6$ and making the substitutions $\psi = y \cosh^{-s} t$ and $t = \ln r$, we obtain

$$F\{y\} \equiv \cosh t \, y''_{tt} + [2 \cosh t - 2s \sinh t] y'_t + \{[s^2 - l(l+2)] \cosh t - 2s \sinh t\} y = 0. \tag{121}$$

The functional $F\{y\}$ acting on the exponential e^{kt} yields a linear combination of $e^{(k+1)t}$ and $e^{(k-1)t}$. It is easy to see that the nontrivial solution of Eq. (121) is a superposition of n exponentials with exponents that differ by $2t$ and coefficients chosen so as to satisfy Eq. (121). For the eigenvalues and eigenfunctions of Eq. (120) we obtain

$$\psi_{nl}(r) = \left(\frac{r}{r^2+1} \right)^{n+l} [A_1 r^{-n} + A_2 r^{-n+2} + \ldots + A_n r^{n-2}],$$

$$\mu_{nl} = (n+l)(n+l+1)/6, \quad n = 1,2,3,\ldots \quad l = 0,1,2,\ldots, \tag{122}$$

where n is the radial and l the orbital quantum number. There is an obvious accidental degeneracy like that seen in

the hydrogen atom. The substantially different μ_s cover the range of values $s(s+1)/6$ with a degree of degeneracy $s(s+1)(2s+1)/6$ $(s=1,2,\ldots)$. For the determinants in Eq. (114) we obtain

$$-\overline{D_R}(1)=2\exp\left\{\frac{15}{2}+\sum_{s=3}^{\infty}\frac{s(s+1)(2s+1)}{6}\times\left[\ln\left(1-\frac{6}{s(s+1)}\right)+\frac{6}{s(s+1)}+\frac{18}{s^2(s+1)^2}\right]\right\}\approx 578,$$

$$\overline{D_R}\left(\frac{1}{3}\right)=\exp\left\{\sum_{s=2}^{\infty}\frac{s(s+1)(2s+1)}{6}\left[\ln\left(1-\frac{2}{s(s+1)}\right)+\frac{2}{s(s+1)}+\frac{2}{s^2(s+1)^2}\right]\right\}\approx 0.872. \tag{123}$$

7.7. Vertex part and nonperturbative contribution

For the integral over $d^n u$ in Eq. (113) we have[16]

$$\int d^n u\,\delta(|\mathbf{u}|-1)u_{\alpha_1}\ldots u_{\alpha_{2M}}=\frac{2\pi^{n/2}}{2^M\Gamma(M+n/2)}I_{\alpha_1\ldots\alpha_{2M}}, \tag{124}$$

where $I_{\alpha_1,\ldots,\alpha_{2M}}$ represents the sum of the terms $\delta_{\alpha_1\alpha_i}\ldots\alpha_{\alpha_j\alpha_k}$ obtained by all possible pairings (in the following we exclude $I_{\alpha_1,\ldots,\alpha_{2M}}$ from the definition of G_{2M}). Using the algebra of factorial series[6] it is easy to show that the transition to the vertex part of $\Gamma^{(0,M)}$ proceeds according to the formula

$$[\Gamma^{(0,M)}(p_1,\ldots,p_M)]_N=[G_M(p_1,\ldots,p_M)]_N\times(p_1^2+\kappa^2)\ldots(p_M^2+\kappa^2). \tag{125}$$

Taking the Fourier transform of Eq. (113) and using the relation

$$\langle\phi_c\rangle_p=\frac{\langle\phi_c^3\rangle_p-\mu_0\langle\phi_c^3\ln x^2\rangle_p}{p^2+\kappa_R^2}\approx\frac{\langle\phi_c^3\rangle_p}{p^2+\kappa_R^2} \tag{126}$$

for the Fourier components, which follows from the instanton equation (94), we have

$$[\Gamma^{(0,2M)}(p_1,\ldots,p_{2M})]_N=c\,\frac{2\pi^{n/2}}{2^M\Gamma(M+n/2)}\left(\frac{4}{I_4}\right)^{M+5/2}\left(-\frac{4}{I_4}\right)^N\times\Gamma\left(N+\frac{2M+n+4}{2}\right)\int_0^\infty d\,\ln R^2R^{-4+2M}\times\langle\phi_c^3\rangle_{R_{p_1}}\ldots\langle\phi_c^3\rangle_{R_{p_{2M}}}\times\exp\left\{\frac{n+8}{3}\ln(\Lambda R)-Nf(\kappa R)\right\}. \tag{127}$$

Calculating the integral to logarithmic accuracy, for $p_i=0$ we obtain

$$[\Gamma^{(0,2M)}(p_i=0,\kappa)]_N=c_{2M}(\ln N)^{-\gamma}\Gamma\left(N+\frac{n+8}{3}\right)\times\left(-\frac{4}{I_4}\right)^N\kappa^{4-2M}\exp\left(\frac{n+8}{3}\ln\frac{\Lambda}{\kappa}\right),$$

$$c_{2M}=c\left(\frac{4}{I_4}\right)^{M+5/2}\left(\frac{2}{3}\right)^{\gamma}(I_3)^{2M}\frac{2\pi^{n/2}\Gamma(\gamma)}{2^M\Gamma(M+n/2)},$$

$$\gamma=M+\frac{n-4}{6}. \tag{128}$$

For $\kappa=0$ and $p_i=p$, and noting that

$$\langle\phi_c^3\rangle_p=8\sqrt{2}\,\pi^2pK_1(p), \tag{129}$$

we have

$$[\Gamma^{(0,2M)}(p)]_N=\tilde{c}_{2M}\Gamma\left(N+\frac{n+2M+4}{2}\right)\times\left(-\frac{4}{I_4}\right)^N p^{4-2M}\exp\left(\frac{n+8}{3}\ln\frac{\Lambda}{p}\right),$$

$$\tilde{c}_{2M}=c\,\frac{4\pi^{n/2}(8\pi^2)^{2M}}{\Gamma(M+n/2)}\left(\frac{4}{I_4}\right)^{M+5/2}\times\int_0^\infty dy\;y^{4M-5+(n+8)/3}K_1(y)^{2M}. \tag{130}$$

We define the nonperturbative contribution to the vertex $\Gamma^{(0,2M)}$ as

$$[\Gamma^{(0,2M)}]_{\text{nonpert}}=\sum_{N=N_0}^{\infty}[\Gamma^{(0,2M)}]_N(g_0-i0)^N,\quad N_0\gg 1. \tag{131}$$

The imaginary addition to g_0 originates in the need for analytic continuation from positive g_0 to negative,[2] which for $\mathrm{Im}\,\kappa^2<0$ extends through the lower half plane. We obtain the nonperturbative contribution for the Lipatov asymptote by substituting Eq. (127) in Eq. (131), eliminating the imaginary part of κ from the sum over N by making the substitution $b\to be^{i\varphi}$, and summing in accordance with Eq. (90) of Ref. 6:

$$[\Gamma^{(0,2M)}(p_1,\ldots,p_{2M})]^{\text{Lipatov}}_{\text{nonpert}}=i\pi c\,\frac{2\pi^{n/2}}{2^M\Gamma(M+n/2)}\left(\frac{4}{I_4}\right)^{M+5/2}\left(\frac{I_4}{4|g_0|}\right)^{M+(n+4)/2}\times\exp\left(-\frac{I_4}{4|g_0|}\right)\int_0^\infty d\,\ln R^2R^{-4+2M}\langle\phi_c^3\rangle_{R_{p_1}}\ldots\times\langle\phi_c^3\rangle_{R_{p_{2M}}}\exp\left\{\frac{n+8}{3}\ln(\Lambda R)-\frac{I_4}{4|g_0|}f(\kappa R)\right\}. \tag{132}$$

For $p_i=0$ this yields

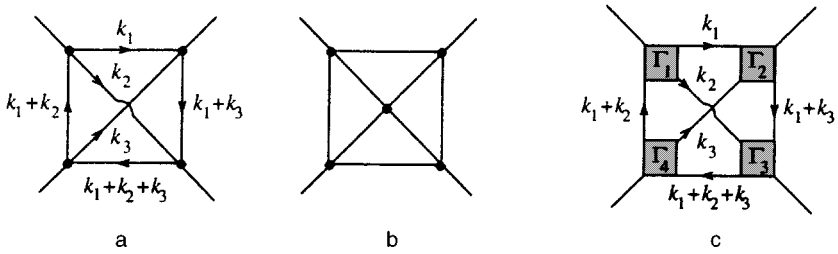

FIG. 5. Examples of skeleton (a,b) and nonskeleton (c) diagrams for a vertex R^0. The arrangement of the internal momenta in graphs *a* and *c* corresponds to zero internal momentum.

$$[\Gamma^{(0,2M)}(p_i=0,\kappa)]^{\text{Lipatov}}_{\text{nonpert}}=i\pi c_{2M}\left(\frac{I_4}{4|g_0|}\right)^{(n+8)/3}\times\exp\left(-\frac{I_4}{4|g_0|}\right)\left(\ln\frac{1}{|g_0|}\right)^{-\gamma}\kappa^{4-2M}\times\exp\left(\frac{n+8}{3}\ln\frac{\Lambda}{\kappa}\right). \tag{133}$$

The vertex $\Gamma^{(0,2)}$ coincides with the self energy and Eqs. (128) and (133) imply Eqs. (21) and (47). Equation (130) with $M=2$ can be used to recover the results of Refs. 14 and 16 for the expansion coefficients for the Gell-Mann–Low function (see Appendix 1).

The author thanks the participants in seminars at the Institute of Physical Problems and at the Physics Institute of the Academy of Sciences for their interest in this work.

This work has been supported financially by the International Science Foundation (Grants MOH 000 and MOH 300) and the Russian Fund for Fundamental Research (project No. 96-02-19527).

APPENDIX 1

Interrelation of the various normalizations

The definitions of the Gell-Mann–Low functions for the Λ- and μ-renormalizations are[10]

$$W^{(\Lambda)}(g_0)=\left.\frac{\partial g_0}{\partial\ln\Lambda}\right|_{g_\mu,\mu=\text{const}},\qquad W^{(\mu)}(g_\mu)=\left.\frac{\partial g_\mu}{\partial\ln\mu}\right|_{g_0,\Lambda=\text{const}}, \tag{A1}$$

and the relation between the renormalized and bare charges is determined by logarithmic expansions like (54),

$$g_\mu=\sum_{N=1}^{\infty}B_N g_0^N=\sum_{N=1}^{\infty}g_0^N\sum_{K=0}^{N-1}A_N^K\left(\ln\frac{\Lambda}{\mu}\right)^K, \tag{A2}$$

$$g_0=\sum_{N=1}^{\infty}\widetilde{B}_N g_\mu^N=\sum_{N=1}^{\infty}g_\mu^N\sum_{K=0}^{N-1}\widetilde{A}_N^K\left(\ln\frac{\mu}{\Lambda}\right)^K, \tag{A3}$$

where $B_1=\widetilde{B}_1=1$. The function $g_\mu(g_0,\Lambda/\mu)$ satisfies an equation like (15) with $V(g_0)\equiv 0$, and the coefficients A_N^K in Eq. (A2) satisfy Eqs. (55) with $W_M\equiv W_M^{(\Lambda)}$ and $V_M\equiv 0$. $W_N^{(\mu)}$ and $\widetilde{A}_N^K$ are related in the same way. By finding the relationship between $\widetilde{A}_N^K$ and A_N^K for small N, it is easy to confirm that the coefficients $W_N^{(\Lambda)}$ and $W_N^{(\mu)}$ coincide for $N=2,3$ but differ in the higher orders. For large N the coefficients B_N are defined by Eq. (130) with $p=\mu$ and $M=2$, since by definition $-2g_\mu=\Gamma_R^{(0,4)}(\mu)=Z^2\Gamma^{(0,4)}(\mu)$ (the coefficient -2 is introduced because of the condition $B_1=1$) and a Z factor does not have to be included for large N because of the slower rise in its coefficients. Reversion of the factorial series (A2) yields

$$\widetilde{B}_N\approx-\sum_{M=0,1,2,\ldots}B_{N-M}\frac{(N\widetilde{B}_2)^M}{M!}\approx-B_N\exp\left(-\frac{B_2}{a}\right), \tag{A4}$$

for large N and this makes it possible to determine the $\widetilde{A}_N^K$. Given that $A_2^1=-K_4(n+8)$, from Eq. (55) we have

$$W_N^{(\mu)}\approx-\widetilde{A}_N^1-W_2^{(\mu)}N\widetilde{A}_{N-1}^0\simeq\frac{n+8}{6}\widetilde{c}_4\Gamma\left(N+\frac{n+8}{2}\right)a^N\exp\left(-\frac{A_2^0}{a}\right), \tag{A5}$$

and the substitution $A_2^0=-(n+8)K_4K_4(1-\ln(4/3))/2$ reproduces the results of Ref. 14 and 16, where the definitions of g_μ and g_0 differ by a factor of 3!

APPENDIX 2

Properties of the irreducible vertex R^0

Let us introduce the three-momentum notation $R^0(p,k,q)$ for the irreducible vertex $R^0(p_1,p_2,p_3,p_4)$ with $\kappa=0$, where

$$2p=p_4-p_3,\quad 2k=p_1-p_2,\quad q=p_1+p_2=-p_3-p_4, \tag{A6}$$

and the numbers of the ends are chosen so that $p\geqslant k\geqslant q\geqslant 0$. In general, when $p\gg k\gg q$ the following logarithmic expansion is valid for R^0,

$$R^0(p,k,q)=\sum_{N=1}^{\infty}g_0^N\sum_{\substack{K,L,M,\\ K+L+M\leqslant N-1}}A_N^{K,L,M}\left(\ln\frac{\Lambda}{p}\right)^K\times\left(\ln\frac{\Lambda}{k}\right)^L\left(\ln\frac{\Lambda}{q}\right)^M \tag{A7}$$

and in order to prove that the vertex R^0 depends on only the maximum momentum, it is sufficient to establish its finiteness for $k=q=0$ and $p\neq 0$. Then $p_4=p$, $p_3=-p$, and $p_1=p_2=0$ and it can be said that the momentum p ''passes'' from vertex 4 to vertex 3.

The proof is based on the fact that it is necessary to distinguish skeleton graphs of type *a* and *b* (Fig. 5) from

nonskeleton graphs c obtained from the skeleton graphs by replacing the simple vertices by four-tail blocks. For the case of the contribution of graph a,

$$R^0_{(a)}(p_i=0)\sim g_0^4\int d^4k_1\int d^4k_2\int d^4k_3 \times G_{k_1}G_{k_2}G_{k_3}G_{k_1+k_2}G_{k_1+k_3}G_{k_1+k_2+k_3}, \tag{A8}$$

it is easy to see that the skeleton graphs for the zero external momenta contain only singly logarithmic divergences originating from the region of integration where all the internal momenta are of the same order of magnitude and are small. The absence of other divergence is related to the impossibility of finding a single momentum k_i that determines the arguments of the two G-functions, two momenta k_i and k_j that determine the arguments of the four G-functions, etc. When momentum p passes through any pair of vertices, the singly logarithmic divergences are cut off at momentum p, since it enters the argument of at least one G-function. In this way, the graph is finite for $k=q=0$. The divergences of nonskeleton graphs are cut off just as are the divergences of the skeleton graphs from which they are obtained.

We proceed to formalize the remarks. A graph with E external lines in the Nth order of perturbation theory has $I=2N=E/2$ internal lines and $L=N-E/2+1$ independent integrations (loops), and diverges for $d-4$ at large momenta as k^{4-E}.[10] In the following we are concerned with four-tail graphs ($E=4$) with L loops, $2L$ internal lines, and $L+1$ logarithmically divergent vertices.

Definition. A graph is a skeleton graph if it is impossible to choose L' independent integrations in it such that $L'<L$ and the integration momenta $k_1,k_2,\ldots,k_{L'}$ fully determine the arguments of the $2L'$ or more Green functions.

Lemma 1. A skeleton graph contains only singly logarithmic divergences, which are removed when the momentum p passes through any pair of vertices.

The proof is evident from the definition and explanations given after Eq. (A8).

Lemma 2. In a skeleton graph it is impossible to isolate a subdiagram with the form of a four-tail block.

Assume, on the contrary, that this is possible. In the isolated block there will be $M<L$ independent integrations with respect to the momenta $k_1,k_2,\ldots,k_M$ which will enter only in the $2M$ Green functions corresponding to the internal lines of the block. The remaining $L'=L-M$ integration momenta will fully determine the arguments of the $2L-2M=2L'$ Green functions, which contradicts the definition of a skeleton diagram.

Lemma 3. In a graph which is not a skeleton diagram it is always possible to isolate a subgraph in the form of a four-tail block.

In a nonskeleton graph there are L' integration momenta which completely determine the arguments of the $2L'$ Green functions. The remaining $M=L-L'$ integration momenta enter only in $2L-2L'=2M$ Green functions. The corresponding $2M$ internal lines will, in general, lie in separate clusters. Let us isolate one such cluster (the i-th) containing N_i vertices, L_i loops, and I_i lines and remove it from the diagram, breaking E_i lines. Obviously, $I_i=2N_i-E_i/2$ and $L_i=N_i-E_i/2_1$, so that

$$I_i-2L_i=E_i/2-2. \tag{A9}$$

Obviously, all the E_i are even. The cases $E_i=0$ and $E_i=2$ correspond to disconnected diagrams and self-energy inserts and are assumed to be excluded. Then $E_i\geqslant 4$ and, in view of Eq. (A9), we have

$$I_i-2L_i\geqslant 0. \tag{A10}$$

Summing over all i and noting that $\Sigma_i I_i=2M$ and $\Sigma_i L_i=M$, we see that the equality holds in Eq. (A10), so that (see Eq. (A9)) $E_i=4$ and all the removed clusters are four-tailed. Since at least one cluster exists, the assertion is proven.

Lemma 4. A nonskeleton graph can be obtained from some skeleton graph by replacing all or part of the simple vertices with four-tail blocks.

By successively isolating the four-tail blocks in a nonskeleton graph and replacing them with simple vertices, we ultimately arrive at a skeleton graph. Following this procedure in opposite order, we obtain a proof of the assertion.

Lemma 5. A nonskeleton graph of order N obtained from a skeleton graph of order M contains a logarithmic divergence of order no greater than $N-M+1$, which is cut off by passage of momentum P through any pair of vertices.

Let us write down as an example the contribution of the graph c (Fig. 5) obtained from graph a:

$$\begin{aligned}R^0_{(B)}(p_i=0)\sim&\int d^4k_1\int d^4k_2\int d^4k_3 G_{k_1}G_{k_2}G_{k_3}G_{k_1+k_2}\\&\times G_{k_1+k_3}G_{k_1+k_2+k_3}\Gamma_1(0,-k_1,-k_2,k_1+k_2)\\&\times\Gamma_2(0,k_1,k_3,-k_1-k_3)\Gamma_3(0,k_1+k_3,k_2,-k_1-k_2\\&-k_3)\Gamma_4(0,-k_1-k_2,-k_3,k_1+k_2+k_3).\end{aligned}$$

The divergence originates from the region $k_i\sim k$, for which arguments of all the vertices are $\sim k$:

$$R^0_{(B)}(p_i=0)\sim\int\frac{dk}{k}\,\Gamma_1(k)\Gamma_2(k)\Gamma_3(k)\Gamma_4(k).$$

The block Γ_i containing N_i simple vertices has a maximum divergence $\sim(\ln\Lambda/k)^{N_i-1}$ if it is included in the parquet sequence of Fig. 4a. Since $\Sigma_i N_i=N$, a graph with M blocks diverges no more rapidly than $(\ln\Lambda/k)^{N-M+1}$, so the divergence is eliminated when momentum p passes through any pair of vertices. There are no other divergences. If not all the momenta are small ($\sim k$), then a graph diverges exponentially as $k\to 0$ and suppresses the logarithmic divergences of the blocks.

Thus, all the graphs are finite for $k=q=0$ and $p\neq 0$, and $R^0(p,k,q)$ depends only on the maximum momentum p.

[1)]The renormalized energy E enters into expressions of the type (5).[13]

[2)]The functions W and η_2 are calculated in Ref. 10 for μ-renormalization and differ from the Λ-renormalization used here, but have the same leading coefficients (see Appendix 1); the definitions of charge and the Gell-Mann–Low function differ in Ref. 10 by a factor of $6K_4$.

[3)]In Refs. 14 and 16 the coefficients W_N have been calculated in a

μ-renormalization, for which this assumption is not correct (see Appendix 1).

[4)]This can be done following the arguments of Section 4.6 of Ref. 6, using the most general form of the counterterms (see Eqs. (3.26)–(3.28) of Ref. 10).

[1] S. Ma, *Modern Theory of Critical Phenomena* Addison-Wesley, Redwood City (1976).
[2] A. Nitzan, K. F. Freed, and M. N. Cohen, Phys. Rev. B **15**, 4476 (1977).
[3] M. V. Sadovskii, Sov. Sci. Rev. A Phys. **7**, 1 (1986).
[4] D. J. Thouless, J. Phys. C **9**, L603 (1976).
[5] I. M. Suslov, Zh. Éksp. Teor. Fiz. **102**, 1951 (1992) [JETP **75**, 1049 (1992)].
[6] I. M. Suslov, Zh. Éksp. Teor. Fiz. **106**, 560 (1994) [JETP **79**, 307 (1994)].
[7] I. M. Lifshits, Usp. Fiz. Nauk **83**, 617 (1964) [Sov. Phys. Uspekhi **7**, 549 (1964)].
[8] I. M. Lifshits, S. A. Gredeskul, and L. A. Pastur, *Introduction to the Theory of Disordered Systems* [in Russian], Nauka, Moscow (1982).
[9] N. N. Bogolyubov and D. V. Shirkov, *Introduction to the Theory of Quantized Fields* [in Russian], Nauka, Moscow (1976).
[10] E. Brezin, J. C. Le Guillou, and J. Zinn-Justin, in *Phase Transitions and Critical Phenomena* C. Domb and M. S. Green (eds.), Academic, NY (1976), Vol. VI.
[11] S. L. Ginzburg, Zh. Éksp. Teor. Fiz. **66**, 647 (1974) [Sov. Phys. JETP **39**, 312 (1974)].
[12] J. L. Cardy, J. Phys. C **11**, L321 (1978).
[13] E. Brezin and G. Parisi, J. Phys. C **13**, L307 (1980).
[14] L. N. Lipatov, Zh. Éksp. Teor. Fiz. **72**, 411 (1977) [Sov. Phys. JETP **45**, 216 (1977)].
[15] E. Brezin and G. Parisi, J. Stat. Phys. **19**, 269 (1978).
[16] E. Brezin, J. C. Le Guillou, and J. Zinn-Justin, Phys. Rev. D **15**, 1544 (1977).
[17] A. O. Gel'fond, *Calculus of Finite Differences* [in Russian], Nauka, Moscow (1977)
[18] A. Z. Patashinskiĭ and V. L. Pokorovskiĭ, *Fluctuation Theory of Phase Transitions* [in Russian], Nauka, Moscow (1982), pp. 317, 333.
[19] I. T. Dyatlov, V. V. Sudakov, and K. A. Ter-Marirosyan, Zh. Éksp. Teor. Fiz. **32**, 767 (1957) [Sov. Phys. JETP **5**, 631 (1957)].
[20] V. V. Sudakov, Dokl. Akad. Nauk SSSR **111**, 338 (1956) [Sov. Phys. Dokl. **1**, 662 (1956)].
[21] A. M. Polyakov, Zh. Éksp. Teor. Fiz. **57**, 271 (1969) [Sov. Phys. JETP **30**, 151 (1969)].
[22] V. G. Makhankov, Phys. Lett. A **61**, 431 (1977).
[23] L. D. Kudryavtsev, *Mathematical Analysis, Vol. 1* [in Russian], Vysshaya Shkola, Moscow (1973).
[24] V. S. Vladimirov, *Equations of Mathematical Physics* [in Russian], Nauka, Moscow (1967).
[25] G. Korn and T. Korn, *Mathematical Handbook for Scientists and Engineers*, Mc Graw-Hill, New York (1961).

Translated by D. H. McNeill

Semiclassical approach to resonance-optics polarization effects in coherent and squeezed fields

A. M. Basharov

Moscow State Institute of Engineering Physics, 115409 Moscow, Russia
(Submitted 15 May 1996)
Zh. Éksp. Teor. Fiz. **111**, 25–43 (January 1997)

Equations are derived for the atomic density matrix and relaxation operator for a broadband squeezed field in an arbitrary polarization state and resonance atomic energy levels with an arbitrary degree of degeneracy. It is shown that suppression of the relaxation of the quadrature component of the atomic polarization depends strongly on the type of resonance transition and the polarization state of the squeezed and coherent perturbing fields. When the resonance levels are strongly degenerate, the relaxation of the quadrature component of the atomic polarization under conditions of maximum suppression is nonexponential in character. The mathematical apparatus developed here makes it possible to calculate polarization-related aspects of the multifrequency optical behavior of atomic and molecular systems resonantly excited both by coherent light and by broadband squeezed fields. [S1063-7761(97)00201-1]

1. INTRODUCTION

Recently there has been increased interest in nonlinear optics phenomena arising from the combined action of electromagnetic fields that are in both coherent and squeezed states. In his groundbreaking paper,[1] Gardiner showed that in a squeezed vacuum, the real and imaginary parts of the atomic polarization are attenuated with different decay constants. References 2–8 were devoted to investigating the influence of this effect on various optical phenomena. In Refs. 2–4 the authors considered spectral features of the absorption of a weak signal by a two-level system in a squeezed vacuum which simultaneously interacted with an intense coherent wave. In Ref. 5, Parkins *et al.* discussed photon echos formed by pulses of coherent and squeezed fields that were separated in time. References 6, 7 discuss the optical bistability that accompanies the interaction of a coherent wave with an optical resonator filled with resonant atoms simultaneous illuminated by an electromagnetic wave in a squeezed state. The authors of Ref. 8 analyzed optical bistability of a thin film of resonant atoms in a squeezed vacuum.

A distinctive feature of Refs. 1–8 is their authors' use of the semiclassical approach to describe the observed effects and to take into account the quantum properties of the electromagnetic pumping; this approach is grounded in the classical Maxwell equations for an intense electric field and a corresponding treatment[9–11] of the generalized quantum mechanical equations for the atomic density matrix. By doing so, these authors elucidated the important manifestations of the ''squeezed'' nature of the pump light. Moreover, they also demonstrated that the standard semiclassical approach to nonlinear optics problems (see, e.g., Refs. 12–14), which has been used with great success in laser physics, can after a suitable generalization be applied to a wide class of problems that involve an intense broadband optical field in a squeezed state as well. In this latter case, as Gardiner and his coauthors showed,[9–11] the nonclassical properties of the pump are ''hidden'' in the relaxation part of the quantum mechanical equations for the atomic density matrix, and the statistical properties of the induced light are not considered.

In this article, the semiclassical approach of Refs. 9–11 is generalized to include degeneracy of the atomic energy levels with respect to the projection of the total angular momentum and the polarization state of the squeezed field. Degeneracy of the atomic levels with respect to angular momentum projection must be taken into account if the polarization properties of the optical phenomena are to be treated properly. Moreover, real states of atoms and molecules are degenerate with respect to the direction of the total angular momentum. In order to obtain equations for the atomic density matrix, a quantum stochastic Ito equation is derived that takes into account the degeneracy of the levels and states of polarization of the quantized fields. Since the formalism of Refs. 9–11, 15 is not of interest here, a derivation of the Ito equation is given that is simpler than that used in Ref. 9, despite the complications introduced by the Zeeman structure of the atomic levels and polarization of the photons. In addition, a relaxation operator is obtained whose structure clearly reveals that the state of polarization of the electromagnetic wave determines both the relaxation matrix for optical coherence and the Zeeman sublevels in a significant way, and that squeezing of the electromagnetic wave changes the character of the former. This latter change (when the matrix for optical coherence is excited coherently) in turn affects the distribution of atomic level populations with respect to the direction of the angular momentum.

The example of an atomic transition between levels with values of the angular momentum 0 and 1 shows that, in contrast to the nondegenerate case,[1,9–11] for an arbitrary state of the polarization of the squeezed field the Zeeman structure will in general increase the minimum possible relaxation constant for the quadrature components of the atomic polarization. The physical reason for this is that two alternative paths are available for a transition from a Zeeman sublevel of one energy level to another with participation of differently polarized photons. The case of an atomic transition between

energy levels with the same value 1/2 of the total angular momentum is exceptional, since the system splits into two independent subsystems, each of which interacts only with left- or right-circularly-polarized photons, and thus mathematically the problem separates into two independent problems which are equivalent to the nondegenerate case investigated previously.[1,9–11] It is established that maximum suppression of the relaxation must be expected for a squeezed field consisting of photons with the same circular polarization, for any degree of degeneracy of the resonance levels.

For large values of the angular momenta of the resonance levels, the relaxation operator reduces to the simpler form corresponding to a quasiclassical description of the total angular momentum. In this paper we discuss the distribution of level occupation numbers with respect to the direction of the total angular momentum when the atomic system interacts with polarized coherent radiation. The presence of a squeezed field leads to narrow angular structures in these distributions, and these depend both on the type of atomic transition and on the state of polarization of the coherent and squeezed fields. It is established that strong degeneracy of the resonance levels modifies the exponential character of the relaxation of atomic polarizations. For the case of maximum suppression of the relaxation and a resonant transition between levels with the same values of the total angular momentum, the relaxation rate is further decreased, whereas for transitions where the angular momentum changes, the relaxation rate increases (compared to the nondegenerate case).

The equations obtained here provide a basis for a semiclassical approach to the polarization properties of (nonlinear) optical phenomena created by polarization-coherent and squeezed fields interacting with atomic systems that are degenerate with respect to projection of the total angular momentum.

In the next section the initial equations are formulated. Then in Secs. 3 and 4 the Ito equation is derived, as is the equation for the atomic density matrix, which contains a relaxation operator that takes into account degeneracy of the resonance levels and the polarization state of the squeezed field. In Sec. 5 matrix elements of the relaxation operator are derived for small values of the angular momenta of the resonance levels, and those polarization states of the squeezed field are analyzed that correspond to the maximum suppression of the atomic relaxation. In Sec. 6 a representation is obtained for the relaxation operator using the quasiclassical description of the angular momentum. Sections 7 and 8 discuss the distribution of population differences of the levels with respect to various orientations of the total angular momentum and the decay law for the atomic polarization under conditions of maximum suppression of the relaxation. In the Conclusion it is emphasized that in order to observe the effects of squeezing experimentally in atomic relaxation,[1] the absorption spectra of a probe signal,[2–4] or in optical bistability,[6–8] it is necessary to choose the polarization properties of both the coherent excitation signal and the squeezed field for each specific transition.

2. INITIAL EQUATIONS

We describe the system, which consists of an ensemble of noninteracting atoms and a classical electromagnetic field with intensity **E**, using the ordinary semiclassical approach in the electric-dipole approximation by means of the Hamiltonian

$$H_{sys}=\sum_{\mathbf{p}\alpha}\left(E_\alpha+\frac{\hbar^2p^2}{2M}\right)a^+_{\mathbf{p}\alpha}a_{\mathbf{p}\alpha}$$
$$-\frac{1}{V}\sum_{\mathbf{pq}\alpha\alpha'}\mathbf{E}(\mathbf{q},t)\mathbf{d}_{\alpha\alpha'}a^+_{\mathbf{p}\alpha}a_{\mathbf{p}-\mathbf{q}\alpha'} \tag{1}$$

and the Maxwell equation

$$\left(\nabla^2-\frac{1}{c^2}\frac{\partial^2}{\partial t^2}\right)\mathbf{E}(\mathbf{r},t)=\frac{4\pi}{c^2}\frac{\partial^2}{\partial t^2}\mathbf{P}. \tag{2}$$

Here $a_{\mathbf{p}\alpha}$ is an operator that annihilates an atom with momentum $\hbar\mathbf{p}$ and mass M in the quantum state $|\alpha\rangle$; V is the system volume. The labels α, α' enumerate eigenstates of the Hamiltonian H_0 of an isolated atom at rest:

$$H_0|\alpha\rangle=E_\alpha|\alpha\rangle,\quad \langle\alpha|\alpha'\rangle=\delta_{\alpha\alpha'},\quad \sum_\alpha|\alpha\rangle\langle\alpha|=1.$$

For an atomic (molecular) gas, these states are distinguished from one another by their energy E_α, and total angular momentum j_α and (or) its projection m_α onto the axis of quantization; the energy levels are degenerate with respect to different orientations of the total angular momentum. We denote by $\mathbf{d}_{\alpha\alpha'}$ the matrix elements of the dipole moment operator of an atom, and write the matrix elements of a given atomic operator A, in the following equivalent forms:

$$\langle\alpha|A|\alpha'\rangle=\langle E_\alpha,j_\alpha,m_\alpha|A|E_{\alpha'},j_{\alpha'},m_{\alpha'}\rangle$$
$$=A_{\alpha\alpha'}=A_{m_\alpha m_{\alpha'}}.$$

The quantity $\mathbf{E}(\mathbf{q},t)$ is the spatial Fourier component of the electric field intensity:

$$\mathbf{E}(\mathbf{q},t)=\int\mathbf{E}(\mathbf{r},t)e^{-i\mathbf{q}\cdot\mathbf{r}}d\mathbf{r}.$$

The polarization **P** of the atomic medium is defined in the usual way:

$$\mathbf{P}=N\int\mathrm{Tr}(\rho\mathbf{d})d\mathbf{v}, \tag{3}$$

where ρ is the density matrix of atoms moving with velocities in the range from $\mathbf{v}$ to $\mathbf{v}+d\mathbf{v}$, and N is the density of two-level atoms.

We derive equations for the atomic density matrix ρ for the case in which the atoms also interact with a quantized one-dimensional electromagnetic field propagating along the z axis. For simplicity we neglect depletion during the absorption/emission of a photon, Raman effects with the participation of the classical and quantum fields,[16] and Stark shifts of the levels. We first obtain an equation for the density matrix of a single atom at rest, which we then generalize to an ensemble of atoms. In this case we treat the atom as a two-level system with quantum numbers E_a, j_a, m and

E_b, j_b, μ, which characterize the upper and lower levels respectively. The total Hamiltonian of this problem has the form

$$H=H_s+H_b+V_b,$$

$$H_s=\sum_m E_a a_m^+ a_m+\sum_\mu E_b a_\mu^+ a_\mu$$

$$-\sum_{m\mu}\mathbf{E}(\mathbf{r},t)\cdot(\mathbf{d}_{m\mu}a_m^+a_\mu+\mathbf{d}_{\mu m}a_\mu^+a_m),$$

$$H_b=\sum_\lambda\int d\omega\hbar\omega b_{\lambda\omega}^+ b_{\lambda\omega},$$

$$V_b=-i\hbar\sum_{\lambda\mu m}\int d\omega K(\omega)(\mathbf{e}_{\lambda\omega}\cdot\mathbf{d}_{\mu m})a_\mu^+ a_m b_{\lambda\omega}+\text{H.c.} \tag{4}$$

Here $b_{\lambda\omega}^+$ and $b_{\lambda\omega}$ are creation and annihilation operators of a photon of frequency ω with a polarization unit vector $\mathbf{e}_{\lambda\omega}$, and $K(\omega)$ is the coupling constant. In deriving the operator V_b for the interaction of an atom with a quantum field, we use the rotating-wave approximation.

3. QUANTUM ITO EQUATION

We assume that the quantized electromagnetic field represents ideal squeezed white noise, which implies that

$$\langle b_\lambda^+(t)b_{\lambda'}(t')\rangle=N_{ph}\tau_{\lambda\lambda'}\delta(t-t'),$$
$$\langle b_{\lambda'}(t)b_\lambda^+(t')\rangle=(\delta_{\lambda\lambda'}+N_{ph}\tau_{\lambda\lambda'})\delta(t-t'),$$
$$\langle b_\lambda(t)b_{\lambda'}(t')\rangle=M_{ph}\eta_{\lambda\lambda'}\delta(t-t'),$$
$$\langle b_{\lambda'}^+(t')b_\lambda^+(t)\rangle=M_{ph}^*\eta_{\lambda\lambda'}^*\delta(t-t'), \tag{5}$$

where

$$b_\lambda(t)=\frac{1}{\sqrt{2\pi}}\int d\omega\ \exp[-i\omega(t-t_0)]b_{\lambda\omega}(t_0), \tag{6}$$

the angle brackets imply averaging over the squeezed photonic heat bath, the matrices $\tau_{\lambda\lambda'}=\tau_{\lambda'\lambda}^*$ and $\eta_{\lambda\lambda'}=\eta_{\lambda'\lambda}$ characterize the polarization state of the squeezed field, the parameter $|M_{ph}|$ represents the degree of compression, and N_{ph} represents the intensity of this field. We also assume that $M_{ph}=|M_{ph}|\exp(-2i\omega_\Gamma t)$, where the center frequency of the squeezed heat bath is denoted by ω_Γ. For a squeezed field prepared in an ideally degenerate parametric amplifier, the quantity ω_Γ is the center frequency of the amplifier.[1] Generally speaking, the center frequency ω_Γ can be separated into right- and left-circularly-polarized photons. All such features are taken into account by the phases of the quantities $\eta_{\lambda\lambda'}$ and the off-diagonal elements $\tau_{\lambda\lambda'}$. The annihilation operator for photons $b_{\lambda\omega}(t_0)$ is referenced to a certain initial time t_0.

We write the Heisenberg equation of motion for a given atomic operator A:

$$\dot{A}=-\frac{i}{\hbar}[A,H_s]+\sum_{\lambda q}\int d\omega K(\omega)[A,R_+^q]e_{\lambda\omega}^q b_{\lambda\omega}$$

$$-\sum_{\lambda' q'}\int d\omega K(\omega)[A,R_-^{q'}]e_{\lambda'\omega}^{q'*}b_{\lambda'\omega}^+. \tag{7}$$

Here we have introduced the operators

$$R_+^q=\sum_{\mu m}a_\mu^+ a_m d_{\mu m}^{-q},\quad R_-^q=-\sum_{\mu m}a_m^+ a_\mu d_{m\mu}^q=(R_+^q)^+.$$

The labels q, q', etc., specify the spherical components of a vector. We next adopt the following definitions. For an arbitrary vector $\mathbf{d}$, the spherical components d^q, $q=0,\pm1$ are

$$d^0=d_z,\quad d^{\pm1}=\mp\frac{1}{\sqrt{2}}(d_x\pm id_y).$$

Here d_x, d_y, and d_z are projections of $\mathbf{d}$ on Cartesian axes; the z axis is taken as the axis of quantization. The matrix elements for the dipole moment $\mathbf{d}$ are related to the reduced dipole moment d_{ba} of an atomic transition $j_b\to j_a$ by

$$d_{\mu m}^q=(-1)^{j_b-\mu}d_{ba}\begin{pmatrix} j_b & 1 & j_a\\ -\mu & q & m\end{pmatrix},$$

$$d_{m\mu}^q=(-1)^{j_b-m}d_{ba}^*\begin{pmatrix} j_a & 1 & j_b\\ -m & q & \mu\end{pmatrix}.$$

The definition of the $3j$ symbols is standard.[17]

We assume that there is no feedback of the atoms to the photonic heat bath, so that the Heisenberg operators for annihilation of photons in (7) are given by the expression for free evolution

$$b_{\lambda\omega}=b_{\lambda\omega}(t_0)\exp[-i\omega(t-t_0)],$$

and that the operator $b_{\lambda\omega}$ commutes with the atomic operators referenced to the same instant of time.

Following Ref. 9, we assume that the coupling constant $K(\omega)$ does not depend on frequency ω, which corresponds to the Markov approximation:

$$K(\omega)=\sqrt{\kappa/2\pi}.$$

Moreover, we assume that the polarization vector $\mathbf{e}_{\lambda\omega}$ also does not depend on the frequency ω: $\mathbf{e}_{\lambda\omega}=\mathbf{e}_\lambda$. Then the quantum Langevin equation follows from Eq. (7):

$$\dot{A}=-\frac{1}{\hbar}[A,H_s]+\sqrt{\kappa}\sum_{\lambda q}[A,R_+^q]e_\lambda^q b_\lambda(t)$$

$$-\sqrt{\kappa}\sum_{\lambda' q'}[A,R_-^{q'}]e_{\lambda'}^{q'*}b_{\lambda'}^+(t). \tag{8}$$

We introduce the quantum Wiener processes $B_\lambda(t,t_0)$ in the following way:

$$B_\lambda(t,t_0)=\int_{t_0}^t dt' b_\lambda(t'),$$

where $[B_\lambda(t,t_0),B_{\lambda'}^+(t,t_0)]=(t-t_0)\delta_{\lambda\lambda'}$. Defining the Ito integral and differential in the standard way,[9,10] we seek the quantum Ito equation for the atomic operator A in the form

$$dA=-\frac{i}{\hbar}[A,H_s]dt+\sqrt{\kappa}\sum_{\lambda q}[A,R_+^q]e_\lambda^q dB_\lambda(t)$$

$$-\sqrt{\kappa}\sum_{\lambda' q'}[A,R_-^{q'}]e_{\lambda'}^{q'*}dB_{\lambda'}^+(t)+Idt, \tag{9}$$

where

$$dB_\lambda^+(t)dB_{\lambda'}(t)=N_{ph}\tau_{\lambda\lambda'}dt,$$

$$dB_{\lambda'}(t)dB_\lambda^+(t)=(\delta_{\lambda\lambda'}+N_{ph}\tau_{\lambda\lambda'})dt,$$

$$dB_\lambda(t)dB_{\lambda'}(t)=M_{ph}\eta_{\lambda\lambda'}dt,$$

$$dB_{\lambda'}^+(t)dB_\lambda^+(t)=M_{ph}^*\eta_{\lambda\lambda'}^*dt,$$

$$dtdt=dtdB_\lambda(t)=dtdB_\lambda^+(t)$$
$$=dB_\lambda(t)dt=dB_\lambda^+(t)dt=0,$$

and the term Idt in Eq. (9) is determined by satisfying the Ito differentiation rule: for any atomic operators A_1 and A_2,

$$d(A_1A_2)=(dA_1)A_2+A_1dA_2+(dA_1)(dA_2). \tag{10}$$

We seek I in the form

$$I=\psi_1\sum_{qq'}(R_+^q[A,R_-^{q'}]+[R_+^q,A]R_-^{q'})(\delta_{qq'}+T_{q'q})$$
$$+\psi_2\sum_{qq'}(R_-^q[A,R_+^{q'}]+[R_-^q,A]R_+^{q'})T_{qq'}$$
$$+\psi_3\sum_{qq'}(R_+^q[A,R_+^{q'}]+[R_+^q,A]R_+^{q'})M_{q'q}$$
$$+\psi_4\sum_{qq'}(R_-^q[A,R_-^{q'}]+[R_-^q,A]R_-^{q'})M_{q'q}^*), \tag{11}$$

where

$$T_{q'q}=N_{ph}\sum_{\lambda\lambda'}e_\lambda^q e_{\lambda'}^{q'*}\tau_{\lambda'\lambda}=T_{qq'}^*,$$

$$M_{qq'}=M_{ph}\sum_{\lambda\lambda'}e_\lambda^q\eta_{\lambda\lambda'}e_{\lambda'}^{q'}=M_{q'q},$$

and the parameters ψ_1, ψ_2, ψ_3, and ψ_4 are defined by using Eq. (10). The structure of Eq. (11) is prompted by the form of the expression $(dA_1)(dA_2)$ when $I_1=I_2=0$, where I_1dt and I_2dt are the corresponding terms of the Ito equation for atomic operators A_1 and A_2. It is not difficult to show that

$$\psi_1=\psi_2=-\psi_3=-\psi_4=\kappa/2. \tag{12}$$

Thus, Eqs. (9), (11), and (12) are the Ito equations required for this problem. Note that this method can be used to address the case in which degeneracy and polarization effects are absent, in which case we obtain the Ito equation of Ref. 9.

4. EQUATIONS FOR THE ATOMIC DENSITY MATRIX

The transition from the Ito equation to equations for the atomic density matrix is accomplished in the standard way[9–11]: since the coefficients of $dB_\lambda(t)$ and $dB_{\lambda'}^+(t)$ are unspecified functions, by averaging (9) we obtain

$$\frac{\langle dA\rangle}{dt}=-\left\langle\frac{i}{\hbar}[A,H_s]\right\rangle+\left\langle\frac{\kappa}{2}\sum_{qq'}(R_+^q[A,R_-^{q'}]\right.$$
$$\left.+[R_+^q,A]R_-^{q'})(\delta_{qq'}+T_{q'q})\right\rangle$$
$$+\left\langle\frac{\kappa}{2}\sum_{qq'}(R_-^q[A,R_+^{q'}]+[R_-^q,A]R_+^{q'})T_{qq'}\right\rangle$$
$$-\left\langle\frac{\kappa}{2}\sum_{qq'}(R_+^q[A,R_+^{q'}]+[R_+^q,A]R_+^{q'})M_{q'q}\right\rangle$$
$$-\left\langle\frac{\kappa}{2}\sum_{qq'}(R_-^q[A,R_-^{q'}]+[R_-^q,A]R_-^{q'})M_{q'q}^*\right\rangle.$$

On the other hand,

$$\langle A\rangle=\mathrm{Tr}\{A(t_0)\rho(t)\},\quad \frac{d\langle A\rangle}{dt}=\mathrm{Tr}\left\{A(t_0)\frac{d\rho(t)}{dt}\right\}.$$

Let us write $\langle dA\rangle/dt=d\langle A\rangle/dt$ in the form

$$\frac{d\langle A\rangle}{dt}=\mathrm{Tr}\left\{A(t_0)\left[\frac{i}{\hbar}[\rho,H_s]+\frac{\kappa}{2}\sum_{qq'}(2R_-^{q'}\rho R_+^q\right.\right.$$
$$-\rho R_+^qR_-^{q'}-R_+^qR_-^{q'}\rho)(\delta_{qq'}+T_{q'q})$$
$$+\frac{\kappa}{2}\sum_{qq'}(2R_+^{q'}\rho R_-^q-\rho R_-^qR_+^{q'}-R_-^qR_+^{q'}\rho)T_{qq'}$$
$$-\frac{\kappa}{2}\sum_{qq'}(2R_+^{q'}\rho R_+^q-\rho R_+^qR_+^{q'}-R_+^qR_+^{q'}\rho)M_{q'q}$$
$$-\frac{\kappa}{2}\sum_{qq'}(2R_-^{q'}\rho R_-^q-\rho R_-^qR_-^{q'}$$
$$\left.\left.-R_-^qR_-^{q'}\rho)M_{q'q}^*\right]\right\}=\mathrm{Tr}\left\{A(t_0)\frac{d\rho(t)}{dt}\right\}.$$

These equations are valid for any atomic operator; therefore, we obtain the following equation for the density matrix:

$$\frac{d\rho}{dt}+\hat\Gamma\rho=\frac{i}{\hbar}[\rho,H_s], \tag{13}$$

where we have introduced the relaxation operator

$$\hat\Gamma\rho=-\frac{\kappa}{2}\sum_{qq'}(2R_-^{q'}\rho R_+^q-\rho R_+^qR_-^{q'}-R_+^qR_-^{q'}\rho)(\delta_{qq'}+T_{q'q})$$
$$-\frac{\kappa}{2}\sum_{qq'}(2R_+^{q'}\rho R_-^q-\rho R_-^qR_+^{q'}-R_-^qR_+^{q'}\rho)T_{qq'}$$
$$+\frac{\kappa}{2}\sum_{qq'}(2R_+^{q'}\rho R_+^q-\rho R_+^qR_+^{q'}-R_+^qR_+^{q'}\rho)M_{q'q}$$
$$+\frac{\kappa}{2}\sum_{qq'}(2R_-^{q'}\rho R_-^q-\rho R_-^qR_-^{q'}-R_-^qR_-^{q'}\rho)M_{q'q}^*. \tag{14}$$

The matrix elements of the relaxation operator (14) have the form

$$(\hat{\Gamma}\rho)_{mm'}=\frac{\kappa}{2}\sum_{m''\mu qq'}\rho_{mm''}d^{q}_{m''\mu}d^{-q'}_{\mu m'}(-1)^{q}T_{qq'}$$

$$+\frac{\kappa}{2}\sum_{m''\mu qq'}d^{q}_{m\mu}d^{-q'}_{\mu m''}\rho_{m''m'}(-1)^{q}T_{qq'}$$

$$-\kappa\sum_{\mu\mu' qq'}d^{q'}_{m\mu}\rho_{\mu\mu'}d^{-q}_{\mu' m'}(-1)^{q}(\delta_{qq'}+T_{q'q}),$$

$$(\hat{\Gamma}\rho)_{\mu\mu'}=\frac{\kappa}{2}\sum_{m\mu'' qq'}\rho_{\mu\mu''}d^{-q}_{\mu'' m}d^{q'}_{m\mu'}(-1)^{q}(\delta_{qq'}+T_{q'q})$$

$$+\frac{\kappa}{2}\sum_{m\mu'' qq'}d^{-q}_{\mu m}d^{q'}_{m\mu''}\rho_{\mu''\mu'}(-1)^{q}$$

$$\times(\delta_{qq'}+T_{q'q})-\kappa\sum_{mm' qq'}d^{-q'}_{\mu m}\rho_{mm'}d^{q}_{m'\mu'}$$

$$(-1)^{q}T_{qq'},$$

$$(\hat{\Gamma}\rho)_{\mu m}=\frac{\kappa}{2}\sum_{m'\mu' qq'}d^{-q}_{\mu m'}d^{q'}_{m'\mu'}\rho_{\mu' m}(-1)^{q}(\delta_{qq'}+T_{q'q})$$

$$+\frac{\kappa}{2}\sum_{m'\mu' qq'}\rho_{\mu m'}d^{q}_{m'\mu'}d^{-q'}_{\mu' m}(-1)^{q}T_{qq'}$$

$$-\kappa\sum_{m'\mu' qq'}d^{-q'}_{\mu m'}\rho_{m'\mu'}d^{-q}_{\mu' m}(-1)^{q}M_{q'q},$$

$$(\hat{\Gamma}\rho)_{m\mu}=\frac{\kappa}{2}\sum_{m'\mu' qq'}\rho_{m\mu'}d^{-q}_{\mu' m'}d^{q'}_{m'\mu}(-1)^{q}(\delta_{qq'}+T_{q'q})$$

$$+\frac{\kappa}{2}\sum_{m'\mu' qq'}d^{q}_{m\mu'}d^{-q'}_{\mu' m'}\rho_{m'\mu}(-1)^{q}T_{qq'}$$

$$-\kappa\sum_{m'\mu' qq'}d^{q'}_{m\mu'}\rho_{\mu' m'}d^{q}_{m'\mu}(-1)^{q}M^{*}_{q'q}. \qquad (15)$$

When $T_{qq'}=M_{qq'}=0$ and the summation with respect to q includes the value $q=0$, the relaxation operator (15) coincides with the relaxation operator for spontaneous radiative decay under conditions where the energy level E_a is the ground state.[13] If $M_{qq'}=0$ while $T_{qq'}\neq 0$ and $q\neq 0$, then (15) describes relaxation processes in the field of a noisy light wave that is structured and polarized in a certain way. Interaction with such a wave alters the distribution of atoms with respect to the Zeeman sublevels from the case of spontaneous radiative decay[13] (see Sec. 7 of the present article). Although squeezing of the electromagnetic wave directly affects only the optical coherence matrix, which determines transitions between Zeeman sublevels of different energy levels, in the final analysis this also affects the equilibrium distribution of atoms in the field of a coherent wave with respect to Zeeman sublevels of both the upper and lower energy levels (see Sec. 7). Moreover, the rate of relaxation of the real and imaginary parts of each optical coherence matrix element is explicitly changed, which in turn leads to different attenuation laws for the imaginary and real parts of each projection of the atomic polarization (see the next section).

It is important to emphasize that by virtue of the geometry of the quantized field we have chosen, the relaxation operator $\hat{\Gamma}\rho$ does not contain terms with $q=0$ if we do not specifically require it to, and consequently does not take into account the spontaneous decay of an atom with emission of a photon perpendicular to the direction of propagation of the wave (5). Such processes, and also other channels for relaxation and/or cases in which the lower energy level E_a is not the ground state, can be described with the help of the simplest generalization of Eq. (13):

$$\frac{d\rho}{dt}+\hat{\Gamma}\rho+\hat{\Gamma}_0\rho=\frac{i}{\hbar}[\rho,H_s], \qquad (13')$$

where we have introduced a phenomenological relaxation operator $\hat{\Gamma}_0\rho$ with the following matrix elements:

$$(\hat{\Gamma}_0\rho)_{mm'}=\gamma_a\rho_{mm'}-W_{mm'},$$

$$(\hat{\Gamma}_0\rho)_{\mu\mu'}=\gamma_b\rho_{\mu\mu'}-W_{\mu\mu'},$$

$$(\hat{\Gamma}_0\rho)_{\mu m}=\gamma_0\rho_{\mu m}.$$

Here γ_a, γ_b, and γ_0 are relaxation constants, while the terms $W_{mm'}$ and $W_{\mu\mu'}$ take pumping processes into account. As usual, we assume for simplicity that

$$W_{mm'}=\frac{\gamma_a N_a\delta_{mm'}}{2j_a+1},\quad W_{\mu\mu'}=\frac{\gamma_b N_b\delta_{\mu\mu'}}{2j_b+1},$$

where N_a and N_b are the steady-state densities of atoms that populate the energy levels E_a and E_b. Here and in what follows we assume the density matrix is normalized by the atomic density.

If the matrix ρ describes atoms (molecules) moving with velocities lying in the interval from v to $v+\Delta v$, then it is necessary to replace[12–14] the derivative $d\rho/dt$ by $(\partial/\partial t+v\nabla)\rho$ in Eqs. (13) and (13′), and to make the following replacement in the matrix elements of the operator $\hat{\Gamma}_0\rho$: $N_a\to N_aF(v)$, $N_b\to N_bF(v)$, where $F(v)$ is the distribution function of the atoms with respect to velocity.

5. RELAXATION OPERATOR FOR SMALL VALUES OF THE TOTAL ATOMIC ANGULAR MOMENTUM

The simplest form of the relaxation operator is obtained for atomic transitions between levels with small values of the angular momentum: $j_a=j_b=1/2$ and $j_a=0=j_b-1$.

For a resonant atomic transition with $j_a=j_b=1/2$ we have

$$\hat{\Gamma}\rho^{a}_{1/2\,1/2}=\frac{\kappa|d_{ba}|^2}{3}[\rho^{a}_{1/2\,1/2}T_{11}-\rho^{b}_{-1/2-1/2}(1+T_{11})], \qquad (16a)$$

$$\hat{\Gamma}\rho^a_{-1/2-1/2}=\frac{\kappa|d_{ba}|^2}{3}\,[\rho^a_{-1/2-1/2}T_{-1-1}$$

$$-\rho^b_{1/2\,1/2}(1+T_{-1-1})], \tag{16b}$$

$$\hat{\Gamma}\rho^a_{1/2-1/2}=\frac{\kappa|d_{ba}|^2}{6}\,\rho^a_{1/2-1/2}(T_{11}+T_{-1-1})$$

$$-\frac{\kappa|d_{ba}|^2}{3}\,\rho^b_{-1/2\,1/2}T_{-1-1}, \tag{16c}$$

$$\hat{\Gamma}\rho^b_{1/2\,1/2}=\frac{\kappa|d_{ba}|^2}{3}\,[\rho^b_{1/2\,1/2}(1+T_{-1-1})$$

$$-\rho^a_{-1/2-1/2}T_{-1-1}], \tag{17a}$$

$$\hat{\Gamma}\rho^b_{-1/2-1/2}=\frac{\kappa|d_{ba}|^2}{3}\,[\rho^b_{-1/2-1/2}(1+T_{11})-\rho^a_{1/2\,1/2}T_{11}], \tag{17b}$$

$$\hat{\Gamma}\rho^b_{1/2-1/2}=\frac{\kappa|d_{ba}|^2}{6}\,\rho^b_{1/2-1/2}(2+T_{11}+T_{-1-1})$$

$$-\frac{\kappa|d_{ba}|^2}{3}\,\rho^a_{-1/2\,1/2}T_{1-1}, \tag{17c}$$

$$\hat{\Gamma}\rho^{ba}_{1/2-1/2}=\frac{\kappa|d_{ba}|^2}{6}\,\rho^{ba}_{1/2-1/2}(1+2T_{-1-1})$$

$$+\frac{\kappa d^2_{ba}}{3}\,\rho^{ba*}_{1/2-1/2}M_{-1-1}, \tag{18a}$$

$$\hat{\Gamma}\rho^{ba}_{-1/2\,1/2}=\frac{\kappa|d_{ba}|^2}{6}\,\rho^{ba}_{-1/2\,1/2}(1+2T_{11})$$

$$+\frac{\kappa d^2_{ba}}{3}\,\rho^{ba*}_{-1/2\,1/2}M_{1\,1}, \tag{18b}$$

$$\hat{\Gamma}\rho^{ba}_{1/2\,1/2}=\frac{\kappa|d_{ba}|^2}{6}\,\rho^{ba}_{1/2\,1/2}(1+T_{11}+T_{-1-1})$$

$$+\frac{\kappa d^2_{ba}}{3}\,\rho^{ba*}_{-1/2-1/2}M_{-1\,1}, \tag{18c}$$

$$\hat{\Gamma}\rho^{ba}_{-1/2-1/2}=\frac{\kappa|d_{ba}|^2}{6}\,\rho^{ba}_{-1/2-1/2}(1+T_{11}+T_{-1-1})$$

$$+\frac{\kappa d^2_{ba}}{3}\,\rho^{ba*}_{1/2\,1/2}M_{1-1}. \tag{18d}$$

Here, the density matrices are furnished with appropriate labels that describe atomic levels b,a and transitions between them for the sake of convenience.

When linearly polarized coherent light propagates in such a medium, interacting with the system of Zeeman sublevels of the resonant atomic levels, two independent subsystems separate out, one of which interacts with left-handed circularly-polarized photons of the coherent field only, the other with right-handed circularly-polarized photons only. If the atomic medium is initially in thermodynamic equilibrium, then only relaxation operators (16a), (16b), (17a), (17b), and (18a), (18b) turn out to be important.

We now discuss the relaxation of the amplitude

$$p^q=\sum_{\mu m}\,\rho_{\mu m}d^q_{m\mu}\,\exp(i\omega_\Gamma t) \tag{19}$$

of the atomic polarization

$$\mathbf{P}=\sum_{\mu m}\,\rho_{\mu m}\mathbf{d}_{m\mu}+\text{c.c.}$$

It is not difficult to show that the corresponding relaxation operators for the real (p^q_{real}) and imaginary (p^q_{im}) parts of the polarization amplitude have the form

$$\hat{\Gamma}p^q_{\text{real}}=\frac{\kappa|d_{ba}|^2}{3}\,p^q_{\text{real}}\left(T_{qq}+|M_{qq}|+\frac{1}{2}\right),$$

$$\hat{\Gamma}p^q_{im}=\frac{\kappa|d_{ba}|^2}{3}\,p^q_{im}\left(T_{qq}-|M_{qq}|+\frac{1}{2}\right).$$

(repeated indices here do not imply summation!) Since $|M_{qq}|\leqslant\sqrt{T_{qq}(T_{qq}+1)}$, when $T_{qq}\gg 1$, and under certain conditions where $|M_{qq}|\approx T_{qq}$, it is clear that there is appreciable suppression of the relaxation of p^q_{im} and enhancement of the attenuation rate of p^q_{real}:

$$\hat{\Gamma}p^q_{im}\approx\frac{\kappa|d_{ba}|^2}{6}\,\frac{1}{T_{qq}}\,p^q_{im}\approx 0,$$

$$\hat{\Gamma}p^q_{\text{real}}\approx\frac{2\kappa|d_{ba}|^2}{3}\,T_{qq}p^q_{\text{real}}.$$

The picture we obtain of the density relaxation agrees with the solution of the problem without taking into account degeneracy of the resonant levels and polarization states of the coherent and squeezed waves.[1]

Entirely different relaxation effects occur for the atomic transition $j_a=0=j_b-1$. We first write the following expressions for the relaxation operator:

$$\hat{\Gamma}\rho^a=\frac{\kappa|d_{ba}|^2}{3}\,\rho^a\sum_q\,T_{qq}-\frac{\kappa|d_{ba}|^2}{3}$$

$$\times\left(\sum_q\,\rho^b_{qq}+\sum_{qq'}\,\rho^b_{qq'}T_{-q-q'}\right),$$

$$(\hat{\Gamma}\rho^b)_{\mu\mu'}=\frac{\kappa|d_{ba}|^2}{3}\,\rho^b_{\mu\mu'}+\frac{\kappa|d_{ba}|^2}{6}\sum_q\,(\rho^b_{\mu q}T_{-\mu'-q}$$

$$+\rho^b_{q\mu'}T_{-q-\mu})-\frac{\kappa|d_{ba}|^2}{3}\,\rho^aT_{-\mu'-\mu},$$

$$(\hat{\Gamma}\rho^{ba})_{\mu 0}=\frac{\kappa|d_{ba}|^2}{6}\,\rho^{ba}_{\mu 0}\left(1+\sum_q\,T_{qq}\right)$$

$$+\frac{\kappa|d_{ba}|^2}{6}\sum_q\,\rho^{ba}_{q0}T_{-q-\mu}$$

$$+\frac{\kappa d^2_{ba}}{3}\sum_q\,\rho^{ab}_{0q}M_{-\mu-q}. \tag{20}$$

For a squeezed field with the simplest polarization structure

$$T_{qq'}=\delta_{qq'}N_q,\quad M_{qq'}=\delta_{qq'}M_q,$$
$$|M_q|\leqslant\sqrt{N_q(N_q+1)},\qquad(21)$$

the relaxation operator for the transition $j_a=0=j_b-1$ takes the form

$$\hat{\Gamma}\rho^a=\frac{\kappa|d_{ba}|^2}{3}\rho^a(N_{-1}+N_1)-\frac{\kappa|d_{ba}|^2}{3}[\rho^b_{-1-1}(1+N_1)+\rho^b_{11}(1+N_{-1})],$$
$$(\hat{\Gamma}\rho^b)_{\mu\mu'}=\frac{\kappa|d_{ba}|^2}{3}\rho^b_{\mu\mu'}+\frac{\kappa|d_{ba}|^2}{6}(\rho^b_{\mu\mu'}N_{-\mu'}+\rho^b_{\mu\mu'}N_{-\mu})-\frac{\kappa|d_{ba}|^2}{3}\rho^a\delta_{\mu\mu'}N_{-\mu},$$
$$(\hat{\Gamma}\rho^{ba})_{\mu 0}=\frac{\kappa|d_{ba}|^2}{6}\rho^{ba}_{\mu 0}(1+N_{-1}+N_1)+\frac{\kappa|d_{ba}|^2}{6}\rho^{ba}_{\mu 0}N_{-\mu}+\frac{\kappa d^2_{ba}}{3}\rho^{ab}_{0\mu}M_{-\mu}.\qquad(22)$$

From the last of Eqs. (22) we obtain the next term, which determines the attenuation of the real and imaginary parts of the spherical components of the atomic polarization amplitude vector for the transition $j_a=0=j_b-1$ (when (21) is satisfied and the phases of the quantities M_{-1} and M_1 are equal):

$$\hat{\Gamma}p^q_{\rm real}=\frac{\kappa|d_{ba}|^2}{6}(1+N_1+N_{-1}+N_q+2|M_q|)p^q_{\rm real},$$
$$\hat{\Gamma}p^q_{im}=\frac{\kappa|d_{ba}|^2}{6}(1+N_1+N_{-1}+N_q-2|M_q|)p^q_{im}.\qquad(23)$$

It is clear that the suppression of relaxation of the imaginary part of the polarization is maximized only when a squeezed field is used, consisting of photons with the same circular polarization. For example when $N_{-1}=M_{-1}=0$, $|M_1|=\sqrt{N_1(N_1+1)}$, $N_{-1}\gg 1$, we can say that

$$\hat{\Gamma}p^q_{im}\approx\frac{\kappa|d_{ba}|^2}{6}\frac{1}{N_1}p^q_{im}\approx 0$$

compared to

$$\hat{\Gamma}p^q_{\rm real}\approx 2\frac{\kappa|d_{ba}|^2}{3}N_1p^q_{\rm real}.$$

If the squeezed field contains both left- and right-hand polarized photons, then because there are two possible transitions from level E_a to sublevels of level E_b with $\mu=1$ and $\mu=-1$, the smallest possible relaxation is determined by the expression

$$\hat{\Gamma}p^q_{im}=\frac{\kappa|d_{ba}|^2}{6}\left(N_{\min}+\frac{1}{N_{\max}}\right)p^q_{im},$$

where $N_{\min}=\min\{N_1,N_{-1}\}$, $N_{\max}=\max\{N_1,N_{-1}\}$. Thus, we may conclude that for an arbitrary polarization state of the squeezed field, the Zeeman structure of the resonance levels increases the smallest possible value for the relaxation (compared to the nondegenerate case and the specific case $j_a=j_b=1/2$) of any quadrature component of the atomic polarization amplitude. Note that a definition different from (19) for the amplitude of the atomic polarization will change the form of the relaxation operators $\hat{\Gamma}p^q_{\rm real}$ and $\hat{\Gamma}p^q_{im}$, but will not affect quantities that characterize the limiting parameters of the polarization relaxation in a squeezed field.

6. RELAXATION OPERATOR FOR THE ATOMIC ANGULAR MOMENTUM: QUASICLASSICAL DESCRIPTION

Let us assume that $j_a\gg 1$, $j_b\gg 1$. Then we can use the semiclassical representation of the $3j$ symbol (Ref. 17, par. 223, Eq. (1)) and assume that the matrix elements of the spherical components of the dipole moment operator are given by

$$d^q_{\mu m}\approx\frac{d_{ba}}{\sqrt{2j}}\mathscr{D}^1_{qj_b-j_a}(0,\vartheta,0)\delta_{\mu-mq},$$
$$d^q_{m\mu}\approx\frac{d^*_{ba}}{\sqrt{2j}}(-1)^q\mathscr{D}^1_{-qj_b-j_a}(0,\vartheta,0)\delta_{mq+\mu},$$

where $j=(j_a+j_b)/2$, $\cos\vartheta\approx K/j$, $K=(\mu+m)/2$, while $\mathscr{D}^{\kappa}_{qq'}(\alpha,\beta,\gamma)\mathscr{D}$ is the Wigner $\mathscr{D}$-function.[17]

Following Ref. 18, let us go to a new representation for the matrix elements of the atomic density matrix:

$$\rho_a(\vartheta,\varphi)=\sum_\xi\rho^a_{K+\xi/2K-\xi/2}e^{-i\xi\varphi},\quad K=(m+m')/2,\quad\xi=m-m',$$
$$\rho_b(\vartheta,\varphi)=\sum_\xi\rho^b_{K+\xi/2K-\xi/2}e^{-i\xi\varphi},\quad K=(\mu+\mu')/2,\quad\xi=\mu-\mu',$$
$$\rho_{ba}(\vartheta,\varphi)=\sum_\xi\rho^{ba}_{K+\xi/2K-\xi/2}e^{-i\xi\varphi},\quad K=(\mu+m)/2,\quad\xi=\mu-m,\qquad(24)$$

with $\cos\vartheta\approx K/j$, $j=(j_a+j_b)/2$ everywhere. Let us assume that the effective interval where the density matrix is nonzero with respect to the variable ξ is much smaller than the characteristic scale of variation of the density matrix with respect to the variable K. Then the summation over ξ in Eq. (24) can be extended to infinity and

$$\rho_{K+\xi/2K-\xi/2}=\frac{1}{2\pi}\int_0^{2\pi}e^{i\xi\varphi}\rho(\vartheta,\varphi)d\varphi.$$

Thus, the transformation (24) can be regarded as analogous to the Wigner transformation for the incoming degrees of freedom. Assuming that quantities of type K are the same when in the same expression, we obtain semiclassical representations of the relaxation operators:

$$\hat{\Gamma}\rho_a(\vartheta,\varphi)=\frac{\kappa|d_{ba}|^2}{2j}\rho_a(\vartheta,\varphi)\mathscr{T}_\sigma(\vartheta,\varphi)-\frac{\kappa|d_{ba}|^2}{2j}\rho_b(\vartheta,\varphi)[\tau_\sigma(\vartheta)+\mathscr{T}_\sigma(\vartheta,\varphi)],$$

$$\hat{\Gamma}\rho_b(\vartheta,\varphi)=\frac{\kappa|d_{ba}|^2}{2j}\,\rho_b(\vartheta,\varphi)[\tau_\sigma(\vartheta)+\mathscr{T}_\sigma(\vartheta,\varphi)]-\frac{\kappa|d_{ba}|^2}{2j}\,\rho_a(\vartheta,\varphi)\mathscr{T}_\sigma(\vartheta,\varphi),$$

$$\hat{\Gamma}\rho_{ba}(\vartheta,\varphi)=\frac{\kappa d_{ba}^2}{4j}\,\rho_{ba}(\vartheta,\varphi)[\tau_\sigma(\vartheta)+2\mathscr{T}_\sigma(\vartheta,\varphi)]+\frac{\kappa d_{ba}^2}{2j}\,\rho_{ba}^*(\vartheta,\varphi)\mathscr{T}_\sigma(\vartheta,\varphi). \tag{25}$$

The angles ϑ and φ characterize the direction of the total angular momentum, while the quantity $\sigma=j_b-j_a$ identifies the type of resonant transition. The following functions are introduced:

$$\mathscr{T}_0(\vartheta,\varphi)=\frac{1}{2}\,(T_{11}+T_{-1-1})\sin^2\vartheta-\frac{1}{2}(e^{-2i\varphi}T_{1-1}+e^{2i\varphi}T_{-11})\sin^2\vartheta,$$

$$\mathscr{T}_{\pm1}(\vartheta,\varphi)=\frac{1}{4}\,(1+\cos^2\vartheta)(T_{11}+T_{-1-1})\mp\frac{1}{2}(T_{11}-T_{-1-1})\cos\vartheta+\frac{1}{4}(e^{-2i\varphi}T_{1-1}+e^{2i\varphi}T_{-11})\sin^2\vartheta,$$

$$\mathscr{T}_0(\vartheta,\varphi)=\frac{1}{2}\,(M_{11}e^{2i\varphi}+M_{-1-1}e^{-2i\varphi})\sin^2\vartheta-\frac{1}{2}\,(M_{1-1}+M_{-11})\sin^2\vartheta,$$

$$\mathscr{T}_{\pm1}(\vartheta,\varphi)=\frac{1}{4}\,(1+\cos^2\vartheta)(M_{11}e^{2i\varphi}+M_{-1-1}e^{-2i\varphi})\mp\frac{1}{2}\,(M_{11}e^{2i\varphi}-M_{-1-1}e^{-2i\varphi})\cos\vartheta+\frac{1}{4}\,(M_{1-1}+M_{-11})\sin^2\vartheta,$$

$$\tau_0(\vartheta)=\sin^2\vartheta,\quad \tau_{\pm1}(\vartheta)=\frac{1}{2}\,(1+\cos^2\vartheta).$$

7. DISTRIBUTION OF LEVEL POPULATIONS WITH RESPECT TO ORIENTATION OF THE TOTAL ANGULAR MOMENTUM FOR STATIONARY COHERENT AND SQUEEZED FIELDS

Assume that an atom that interacts resonantly both with the coherent field

$$\mathbf{E}=\varepsilon\,\exp[i(kz-\omega t)]+\text{c.c.}, \tag{26}$$

and with the squeezed field (5) is characterized by many values of the angular momentum, so that in the resonance approximation Eq. (13′) can be written in the form

$$\left(\frac{d}{dt}+\gamma_a\right)r_a(\vartheta,\varphi)=\gamma_a\,\frac{N_a}{2j}+\frac{i|\mathscr{E}|}{\hbar}\,[r_{ba}^*(\vartheta,\varphi)\mathscr{D}_\sigma(\vartheta,\varphi)-r_{ba}(\vartheta,\varphi)\mathscr{D}_\sigma^*(\vartheta,\varphi)]-\gamma r_a(\vartheta,\varphi)\mathscr{T}_\sigma(\vartheta,\varphi)+\gamma r_b(\vartheta,\varphi)[\tau_\sigma(\vartheta)+\mathscr{T}_\sigma(\vartheta,\varphi)],$$

$$\left(\frac{d}{dt}+\gamma_b\right)r_b(\vartheta,\varphi)=\gamma_b\,\frac{N_b}{2j}-\frac{i|\mathscr{E}|}{\hbar}\,[r_{ba}^*(\vartheta,\varphi)\mathscr{D}_\sigma(\vartheta,\varphi)-r_{ba}(\vartheta,\varphi)\mathscr{D}_\sigma^*(\vartheta,\varphi)]-\gamma r_b(\vartheta,\varphi)[\tau_\sigma(\vartheta)+\mathscr{T}_\sigma(\vartheta,\varphi)]+\gamma r_a(\vartheta,\varphi)\mathscr{T}_\sigma(\vartheta,\varphi),$$

$$\left(\frac{d}{dt}-i\Delta+\gamma_0\right)r_{ba}(\vartheta,\varphi)=\frac{i}{\hbar}\,\frac{|d_{ba}|^2|\mathscr{E}|}{2j}\,[r_b(\vartheta,\varphi)-r_a(\vartheta,\varphi)]\mathscr{D}_\sigma(\vartheta,\varphi)-\frac{\gamma}{2}\,r_{ba}(\vartheta,\varphi)[\tau_\sigma(\vartheta)+2\mathscr{T}_\sigma(\vartheta,\varphi)]-\gamma r_{ba}^*(\vartheta,\varphi)f_\sigma(\vartheta,\varphi). \tag{27}$$

Here the following notation has been used:

$$r_a(\vartheta,\varphi)=\rho_a(\vartheta,\varphi),\quad r_b(\vartheta,\varphi)=\rho_b(\vartheta,\varphi),$$

$$r_{ba}(\vartheta,\varphi)=\rho_{ba}(\vartheta,\varphi)\,\frac{d_{ba}^*}{\sqrt{2j}}\exp[i(\omega t-kz)],$$

$$\Delta=\omega-\omega_0,\quad \gamma=\frac{\kappa|d_{ba}|^2}{2j},$$

$$\mathscr{D}_\sigma(\vartheta,\varphi)=\sum_q\,\mathscr{D}^1_{-q\sigma}(0,\vartheta,0)e^{iq\varphi}l^q,\quad l^q=\mathscr{E}^q/|\mathscr{E}|;$$

the function $f_a(\vartheta,\varphi)$ differs from the function $\mathscr{T}_\sigma(\vartheta,\varphi)$ by the substitution of $M_{qq'}=m_{qq'}\exp[2i(kz-\omega t)]$ for $m_{qq'}$. Depending on the relation between frequencies ω and ω_Γ, the quantity $m_{qq'}$ can be an oscillatory function.

The steady-state solution (27) for the population difference in the simplest case (21), where $\omega=\omega_\Gamma=\omega_0$ and $\gamma_a=\gamma_b=\gamma_\parallel$, can easily be written in the form

$$\frac{r_a(\vartheta,\varphi)-r_b(\vartheta,\varphi)}{(N_a-N_b)/2j}=\left\{1+\frac{2\gamma\mathscr{T}_\sigma(\vartheta,\varphi)}{\gamma_\parallel}+\Lambda([1+(\gamma/\gamma_0)\mathscr{T}_\sigma(\vartheta,\varphi)]|\mathscr{D}_\sigma(\vartheta,\varphi)|^2+(\gamma/2\gamma_0)[f_\sigma(\vartheta,\varphi)\mathscr{D}_\sigma^{*2}(\vartheta,\varphi)+f_\sigma^*(\vartheta,\varphi)\mathscr{D}_\sigma^2(\vartheta,\varphi)])([1+(\gamma/\gamma_0)\mathscr{T}_\sigma(\vartheta,\varphi)]^2-(\gamma/\gamma_0)^2|f_\sigma(\vartheta,\varphi)|^2)^{-1}\right\}^{-1}, \tag{28}$$

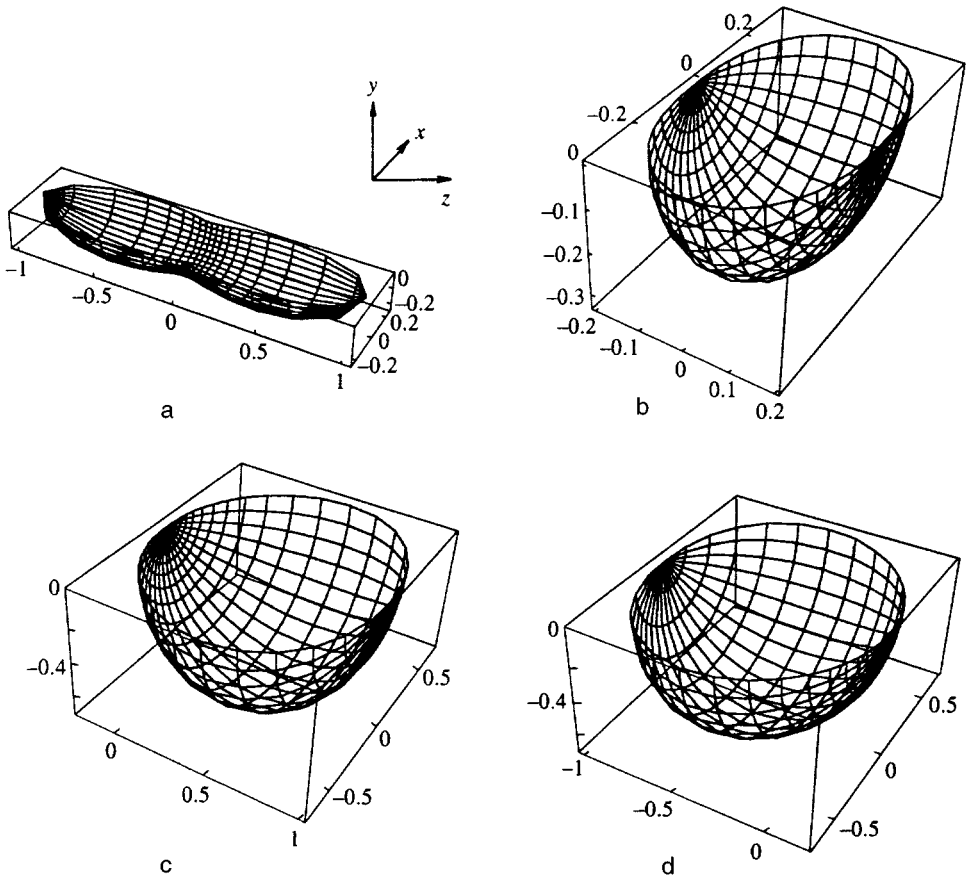

FIG. 1. Plots of the distribution (28) of population differences between lower and upper resonance levels as a function of the direction of the total angular momentum for resonant excitation by a noisy quantized field (5) under conditions (21) for the transitions $j \to j$, $N_1 = N_2 = 2$ (a) and $j+1 \to j$ with parameters $N_1 = N_2 = 2$ (b), $N_1 = 2$, $N_2 = 0$ (c), and $N_1 = 0$, $N_2 = 2$ (d). Other parameters are $\gamma = \gamma_\parallel = 1$, $j \gg 1$; the transition is denoted by $j_b \to j_a$. The ranges over which the angular orientation of the total angular momentum varies are $\pi \leqslant \varphi \leqslant 2\pi$ and $0 \leqslant \vartheta \leqslant \pi$.

where $\Lambda = 4|\mathscr{E}|^2 |d_{ba}|^2 / \hbar^2 \gamma_0 \gamma_\parallel 2j$ is the ratio of the square of the Rabi frequency to the product of the phenomenological relaxation constants.

In the absence of a quantized field (5), i.e., when $\gamma = 0$, the solution (28) coincides with the solution of Nasyrov and Shalagin.[18] In the absence of a coherent field, i.e., for $\Lambda = 0$, Eq. (28) describes steady-state atomic level population differences in the field of a resonant noisy polarized wave described quantum mechanically by (5). As in Ref. 18, a striking dependence of the distribution (28) on the type of resonance transition is observed. This is evident from the fact that for the transition $j \to j$, molecules with angular momentum directed along the z axis essentially fail to interact with the field, whereas molecules whose angular momentum is close to the plane perpendicular to the z axis interact so strongly with the field that their population differences reduce to zero as the field strength increases. For the transition $j+1 \leftrightarrow j$, for which the field contains the same number of left- and right-hand circularly-polarized photons, the molecules interact with it in essentially the same way, independent of the orientation of the total angular momentum and the type of molecular transition ($j+1 \to j$ or $j \to j+1$). However, this situation is considerably changed when the light is circularly polarized: although there is no narrow selectivity with respect to orientation of the angular momentum as happens in the case of the $j \to j$ transitions, the molecules that interact most strongly with the field are those whose angular momentum points in the direction of propagation of the field or opposite to it, depending on the direction of rotation of the photon polarization and the type of transition ($j+1 \to j$ or $j \to j+1$) (see Figs. 1c, 1d). Examining the $j+1 \to j$ transitions instead of the $j \to j+1$ transitions for the same circular polarization of the field, we find that the molecules that interact more intensely with the field rotate opposite to those which would interact strongly with the field for the other type of transition.

For these special cases, the distribution of populations does not depend on the squeezing of the field. Introducing a coherent field does lead to such a dependence, but the change in the distribution of atomic level population differences

$$\Delta\mathscr{N} = \frac{r_a(\vartheta,\varphi) - r_b(\vartheta,\varphi)}{(N_a - N_b)/2j} - \left.\frac{r_a(\vartheta,\varphi) - r_b(\vartheta,\varphi)}{(N_a - N_b)/2j}\right|_{M_{-1} = M_1 = 0}$$

is numerically insignificant, as Fig. 2 illustrates. As before, the change depends on the type of transition and polarization state of both the squeezed and the coherent fields.

8. DECAY OF ATOMIC POLARIZATIONS IN A SQUEEZED VACUUM

The polarization of an atom with degenerate energy levels is made up of polarizations from each individual transition between the Zeeman sublevels of the resonant levels (19). Since each of these transitions is characterized by its own relaxation constant due to the different values of the

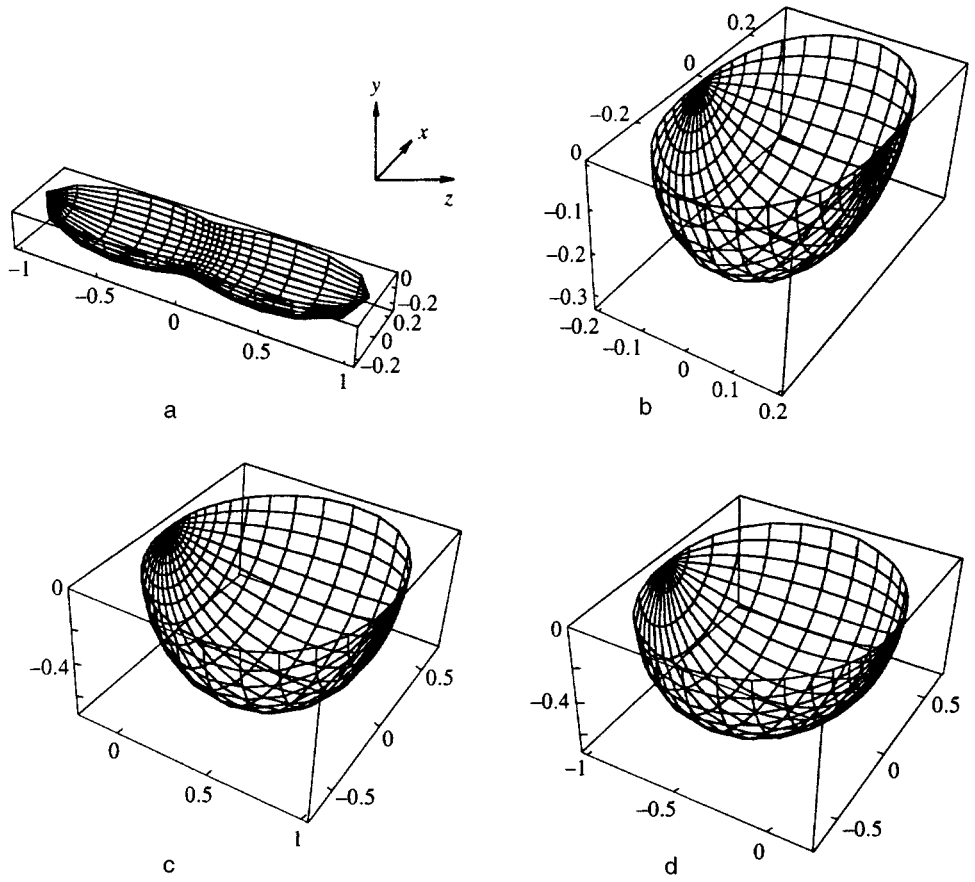

FIG. 2. Variation of the distribution of population differences $\Delta\mathcal{N}$ plotted as a function of the polar φ and azimuthal ϑ orientation angles of the total angular momentum of a resonant atom driven simultaneously at resonance by a coherent and a squeezed electromagnetic field under conditions (21). Figures (a) and (c) correspond to an induced transition when both the excitation fields are linearly and circularly polarized; Figs. (b) and (d) correspond to the transition $j+1\to j$. The values of the parameters are as follows: for (a), (b), $\mathbf{l}=\mathbf{e}_x$, $N_1=N_{-1}=M_1=M_{-1}=2$; for (c), (d), $\mathbf{l}=-(\mathbf{e}_x-i\mathbf{e}_y)/\sqrt{2}$, $N_1=M_1=2$, $N_{-1}=M_{-1}=0$. The other parameters are: $\gamma=\gamma_\parallel=\gamma_0=1$, $\Lambda=5$, $j\gg 1$. The ranges over which the orientation angles of the total angular momentum vary are $0\leqslant\vartheta\leqslant\pi$ and $-\pi\leqslant\varphi\leqslant\pi$.

dipole moments of the Zeeman transitions, for large values of the total angular momentum the attenuation law for the total atomic polarization in the squeezed vacuum that results from adding up all these partial polarizations will differ from the simple exponential law obtained for atomic transitions between nondegenerate levels[1–11] and levels with small values of the total angular momenta (see Sec. 5).

In what follows we illustrate this fact for the case in which the atomic relaxation is maximally suppressed. As we established in Sec. 5, this occurs for a squeezed field consisting of photons all of which have the same circular polarization, for example

$$T_{qq'}=\delta_{qq'}N_q,\quad M_{qq'}=\delta_{qq'}M_q,\quad N_{-1}=M_{-1}=0. \tag{29}$$

Furthermore, let us assume for simplicity that the atom is initially excited by an ultrashort coherent field pulse (26) with the same polarization as the squeezed field in the time interval $0\leqslant t\leqslant\tau_1$. When the coherent field ceases to act, the atom remains in a squeezed field with parameters (29). As a result, for times $\tau_1\leqslant t$ and for a small-area excitation pulse, we obtain the following expression for the atomic density matrix:

$$r_{ba}(\vartheta,\varphi)=-\frac{i|d_{ba}|^2}{2j}\,|\mathscr{E}|\tau_1\,\frac{N_a-N_b}{2j}\,\mathscr{D}^1_{-1\sigma}(0,\vartheta,0)\times e^{i\varphi}\exp\{-[\gamma_0+\Gamma_{\sigma\,\min}(\vartheta)](t-\tau_1)\},$$

where

$$\Gamma_{0\,\min}(\vartheta)=\frac{\gamma}{2}\,(N_1-|M_1|)\sin^2\vartheta,$$

$$\Gamma_{\pm 1\,\min}(\vartheta)=\frac{\gamma}{4}\,(N_1-|M_1|)(1\mp\cos\vartheta)^2,$$

and we set $\omega=\omega_\Gamma=\omega_0$.

In a semiclassical description of the angular momentum, the spherical component of the atomic polarization p^q (19) is given by the expression

$$p^q=-\frac{j}{2\pi}\int_0^{2\pi}d\varphi\int_0^{\pi}\sin\vartheta\times d\vartheta\mathscr{D}^1_{-q\sigma}(0,\vartheta,0)e^{-iq\varphi}r_{ba}(\vartheta,\varphi). \tag{30}$$

Then we can write the spherical component $p^1(t)$ of the atomic polarization in the form

$$p^1(t)=p^1(\tau_1)\exp[-\gamma_0(t-\tau_1)]\times\Gamma(\xi(N_1-|M_1|)(t-\tau_1)),$$

where for the atomic transition $j\to j$, $j\gg 1$ we have

$$\Gamma(x)=\frac{3}{4}\left\{-\frac{1}{x}+\frac{\sqrt{\pi}(e^{-x}+2xe^{-x})\mathrm{Erf}(\sqrt{x})}{2x^{3/2}}\right\},$$

$$\xi=\frac{\gamma}{2},$$

while for the atomic transition $j+1\leftrightarrow j$, $j\gg 1$ we have

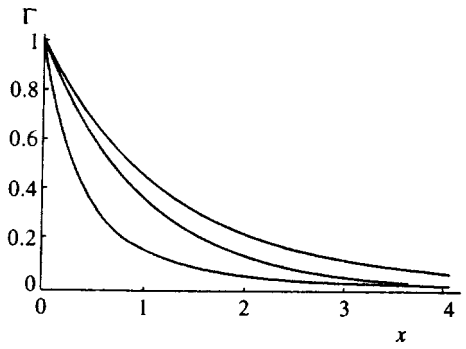

FIG. 3. Relaxation function $\Gamma(x)$ for the case of maximum suppression of the relaxation for transitions $j\to j$, $j\gg 1$ (upper curve), for a nondegenerate transition (middle curve—ordinary exponential), and for the transition $j+1\to j$, $j\gg 1$ (lower curve).

$$\Gamma(x)=\frac{3}{8}\left\{-\frac{1}{x}\,e^{-4x}+\frac{\sqrt{\pi}\,\mathrm{Erf}(2\sqrt{x})}{4x^{3/2}}\right\},\quad \xi=\frac{\gamma}{4}.$$

Here $\mathrm{Erf}(z)=(2/\sqrt{\pi})\int_0^z e^{-x^2}dx$ is the error function, $\mathrm{Erf}(ix)=i\ \mathrm{Erf}\ i(x)$.

For comparison recall that for an atomic transition $1\to 0$, the quantity $\Gamma(x)$ is a simple exponential:

$$\Gamma(x)=e^{-x},\quad \xi=\frac{\kappa|d_{ba}|^2}{3}.$$

Spontaneous relaxation during the transition between resonance levels is everywhere neglected.

Thus, for transitions with $j\to j$, $j\gg 1$, relaxation in a squeezed field for the case of maximum suppression is a weaker effect than it is for the nondegenerate case (and/or the transition $1\to 0$), whereas for the transition $j+1\leftrightarrow j$, $j\gg 1$ it is slightly enhanced (see Fig. 3).

9. CONCLUSION

The results of this article show that in order to ensure maximum suppression of the relaxation for one of the quadrature components of the atomic polarization, it is necessary to choose the polarization states of both the excitation coherent field and the squeezed field in a particular way. For any experiment involving a squeezed field where the effect observed in Ref. 1, i.e., suppression of the atomic relaxation, is manifested in some way, be it measurement of atomic polarization relaxation, the absorption spectrum of a probe coherent signal, or observation of novel effects in optical bistability, it is necessary that certain polarization conditions be satisfied both for coherent and squeezed fields. These conditions can be obtained if the effects are analyzed by using the mathematical apparatus developed in this article. The specific constraints on the polarization state of the excitation fields explain the current lack of convincing experimental studies of mechanisms for suppression of atomic relaxation by a squeezed field.

The author is grateful to the organization ''Russian Gold'' for material support in carrying out these investigations.

[1] C. W. Gardiner, Phys. Rev. Lett. **56**, 1917 (1986).
[2] H. J. Carmichael, A. S. Lane, and D. F. Walls, Phys. Rev. Lett. **58**, 2539 (1987).
[3] H. Ritsch and P. Zoller, Opt. Commun. **64**, 523 (1987).
[4] S. An, M. Sargent III, and D. F. Walls, Opt. Commun. **67**, 373 (1988).
[5] A. S. Parkins and C. W. Gardiner, Phys. Rev. A **40**, 2534 (1989).
[6] P. Galatola, A. Lugiato, M. G. Porreca, and P. Tombesi, Opt. Commun. **81**, 175 (1991).
[7] J. Bergou and D. Zhao, Phys. Rev. A **52**, 1550 (1995).
[8] A. M. Basharov, Zh. Éksp. Teor. Fiz. **108**, 842 (1995) [JETP **81**, 459 (1995)].
[9] C. W. Gardiner and M. J. Collett, Phys. Rev. A **31**, 3761 (1985).
[10] C. W. Gardiner, A. S. Parkins, and P. Zoller, Phys. Rev. A **46**, 4363 (1992).
[11] C. W. Gardiner and A. S. Parkins, Phys. Rev. A **50**, 1792 (1994).
[12] V. S. Letokhov and V. P. Chebotaev, *Principles of Optical Spectroscopy* [in Russian], Nauka, Moscow (1975); *Nonlinear Ultrahigh-Resolution Laser Spectroscopy* [in Russian], Nauka, Moscow (1975).
[13] S. G. Rautian, G. I. Smirnov, and A. M. Shalagin, *Nonlinear Resonances on Atoms and Molecules* [in Russian], Nauka, Novosibirsk (1979).
[14] A. M. Basharov, *Photonics. A Method of Unitary Transformations in Nonlinear Optics* [in Russian], MIFI, Moscow (1990).
[15] M. I. Kolobov and I. V. Sokolov, Opt. Spektrosk. **62**, 112 (1987) [Opt. Spectrosc. (USSR) **62**, 69 (1987)].
[16] A. M. Basharov, Zh. Éksp. Teor. Fiz. **102**, 1126 (1992) [Sov. Phys. JETP **74**, 606 (1992)].
[17] D. A. Varshalovich, A. N. Moskalev, and V. K. Khersonskiĭ, *Quantum Theory of Angular Momentum* [in Russian], Nauka, Leningrad (1975).
[18] K. A. Nasyrov and A. M. Shalagin, Zh. Éksp. Teor. Fiz. **81**, 1649 (1981) [Sov. Phys. JETP **54**, 877 (1981)].

Translated by Frank J. Crowne

Capabilities of a muon method for studying the diamagnetic domains accompanying the de Haas–van Alphen effect

Yu. M. Belousov and V. P. Smilga

Moscow Physicotechnical Institute, 141700 Dolgoprudnyĭ, Moscow Region, Russia
(Submitted 20 June 1996)
Zh. Éksp. Teor. Fiz. **111**, 250–261 (January 1997)

This paper analyzes the capabilities of a muon (μSR) method for studying the de Haas–van Alphen effect and the diamagnetic domain structure accompanying it. It is shown that, unlike the NMR method, the μSR method makes it possible to observe the formation of a diamagnetic domain structure in all metals. It is not currently known what type of domain structure accompanies the de Haas–van Alphen effect: one-dimensional (laminar) or two-dimensional. It is shown that the line shape of the Fourier spectrum of the signal makes it possible to determine both the character of the domain structure (two-dimensional or laminar) and the magnetic field distribution in the domains. © *1997 American Institute of Physics.* [S1063-7761(97)01501-1]

1. The de Haas–van Alphen (dHvA) effect was discovered in 1930.[1,2] Using the classical Faraday–Curie method, de Haas and van Alphen observed oscillations of the macroscopic magnetic moment of a sample as they varied the external magnetic field. A number of modifications of the measurement scheme were later proposed that substantially improved the accuracy of the measurements (see, for example, Ref. 3), but until now they all fundamentally reduced in essence to the measurement of the total magnetic moment, and the question of the structure of the magnetic field distribution in the sample during the dHvA effect has remained open.

This situation is quite understandable if we recall that, until the muon (μSR) method appeared, there were no magnetic microprobes capable of investigating the internal magnetic fields inside a metal. The region of application of EPR and NMR is limited to the depth of the skin layer. Although it is true that Mössbauer γ optics makes it possible to study samples with thicknesses of the order of several micrometers, difficulties arise when resolving effects of the order of $10^{-4}-10^{-5}$ of the value of the external magnetic field and when monitoring the implantation of the Mössbauer isotopes. It should also be pointed out that, when macroscopic measurements of the dHvA effect are made, considerable difficulties arise in processing the results.[3]

The muon method has no restrictions on the sample thickness and makes it easy to directly measure the magnetic field with an accuracy of 10^{-5}. In principle, it is simple to obtain a measurement accuracy substantially greater than that of macroscopic methods. The limitations of the available methods are epitomized by the fact that, even though the existence of diamagnetic domains was theoretically predicted as long ago as 1962,[4] until Ref. 5 distinctly observed domain structure in Be by a muon method in 1995, there was only a single experiment in which diamagnetic domains were observed, in Ag.[6] The measurements were made by the NMR method, and, accordingly, Condon and Walstedt studied only a thin surface layer, where the laminar structure of the domains is strongly distorted, and in fact only the ''shadows'' of the domains themselves were studied. Moreover, they noted[6] that it was impracticable to use the NMR method to study metals with nuclear spins of $I>1/2$.

In 1979, Ref. 7 showed that the muon method makes it possible to investigate diamagnetic domains, and obtained the main formulas for analyzing the domain structure. We should also note that, following the classic work of Landau and Lifshitz, everyone tacitly assumes that the domain structure accompanying the dHvA effect has a laminar character. However, no one has proven that this structure is energetically more favorable than a two-dimensional domain lattice similar in its geometry to Abrikosov's vortex lattice in type-II superconductors. The muon method makes it possible to give an experimental answer to this question. An analysis is carried out below of the use of the muon method to study the dHvA effect. In what follows, for simplicity, we shall confine ourselves everywhere to the case in which the sample target is a thin plate and the external magnetic field is perpendicular to the plane of the sample. The muon spin is parallel to the sample plane, and thus transverse polarization is considered.

2. Transverse polarization of the muon spin in a metal is determined by the general formula (see, for example, Ref. 8)

$$P_+(t)=P_x(t)+iP_y(t)=G(t)\exp(-i\omega_\mu t)P(0), \qquad (1)$$

where $\omega_\mu=\gamma_\mu b$, $\mathbf{b}$ is the local field at the muon, and $G(t)$ is a relaxation function. As is well known (see, for example, Ref. 8), function $G(t)$ is determined by the spins of the lattice nuclei and is different for diffusing and nondiffusing muons. For nondiffusing muons in metals, the relaxation is determined by the Gaussian exponential

$$G(t)=\exp(-\sigma^2t^2), \qquad (2)$$

where the second moment σ is proportional to μ_h, the magnetic moment of the lattice nuclei. The picture is more complex for diffusing muons, but, in the case of rapid diffusion (diffusion rate $\nu\gg\sigma$), the relaxation function has the form

$$G(t)=\exp(-\Lambda t), \qquad (3)$$

where $\Lambda\propto\sigma^2/\nu$. In any case, for an ideal lattice, the depolarization rate is determined by the magnetic moments of the

TABLE I. Nuclear spins and magnetic moments of the stable isotopes of certain metals.

Element	Atomic number	Concentration, %	I	μ_h/μ_N
Mg	24, 26	89.89	0	0
	25	10.11	5/2	−0.85532
Ca	40	99.92	0	0
	43	0.129	7/2	−1.31720
Ti	46, 48, 50	86.74	0	0
	47	7.75	5/2	−0.788130
	49	5.51	7/2	−1.10377
Cr	50, 52, 54	90.45	0	0
	53	9.55	3/2	−0.74391
Fe	54, 56, 58	97.79	0	0
	57	2.21	3/2	+0.05
Ni	58, 60, 62, 64	98.75	0	0
	61	1.25	3/2	−0.74868
Zn	64, 66, 68, 70	95.89	0	0
	67	4.11	5/2	+0.87571
Sr	84, 86, 88	93.04	0	0
	87	6.96	9/2	−1.09302
Zr	90, 92, 93, 94	88.77	0	0
	91	11.23	5/2	−1.9
Mo	92, 94, 96, 98, 100	74.82	0	0
	95	15.72	5/2	−0.9327
	97	9.46	5/2	−0.9523
Pd	102, 104, 106, 108, 110	87.4	0	0
	105	22.6	5/2	−0.57
Tc	all		0	0
Ce	all		0	0

lattice nuclei. The simplest case corresponds to $I=1/2$, where there are no effects associated with quadrupole interactions. The principal isotopes of a large number of metals have a spin of $I=0$ (see the table in Ref. 9).

The depolarization rate is small for most metals, which makes it possible to make precise measurements of the precession frequency and to study small field inhomogeneities. This last point is essential, since inhomogeneities can also arise because of magnetic-susceptibility anisotropy effects. In this case, it is convenient to study the field inhomogeneities from the appearance of weak damping of the longitudinal polarization of the muon spin.

3. The most interesting case is that in which diamagnetic domain structure appears in the sample. When this happens, two close-lying frequencies appear in the transverse polarization.

Let v_1 and v_2 be the relative volumes of the phases with fields b_1 and b_2, respectively: $v_1+v_2=1$. We shall initially assume that the thickness of the domain walls is negligible. Let $\mathbf{P}(0)\|\mathbf{x}$ and $P(0)=1$; then the precession of the muon-spin polarization is determined by the formulas

$$P_x(t)=v_1\cos(\omega_1 t)+v_2\cos(\omega_2 t),$$
$$P_y(t)=-v_1\sin(\omega_1 t)-v_2\sin(\omega_2 t), \tag{4}$$

where $\omega_{1,2}=\gamma_\mu b_{1,2}$. We introduce the notation $(\omega_1+\omega_2)/2=\omega_0$ and $(\omega_1-\omega_2)/2=\Delta\omega$. Introducing complex polarization, we can write Eq. (4) in compact form as

$$P_+(t)=G(t)(v_1 e^{-i\Delta\omega t}+v_2 e^{i\Delta\omega t})e^{-i\omega t}. \tag{5}$$

Let $v_1-v_2=\Delta v>0$, and then Eq. (5) can be rewritten as

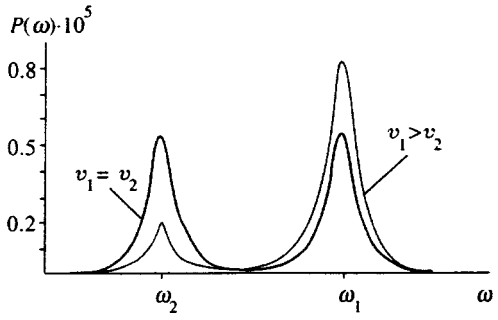

FIG. 1. Qualitative behavior of the Fourier spectrum of the polarization for a diffusing muon and a one-dimensional domain structure for $v_1=v_2$ and $v_1>v_2$.

$$P_+(t)=[\cos(\Delta\omega t)+i\Delta v\ \sin(\Delta\omega t)]e^{-i\omega t}. \tag{6}$$

As can be seen, the time dependence of the transverse polarization for $v_1=v_2$ experiences beats at frequency $\Delta\omega$. When $v_1\neq v_2$, the time dependence does not reduce only to beats.

Let us now explicitly take into account the depolarization effects associated with the magnetic moments in the nuclei of the metal. If the muon rapidly diffuses, we have

$$P_x(t)=[\cos(\Delta\omega t)+i\Delta v\ \sin(\Delta\omega t)]e^{-(\Lambda+i\omega)t}. \tag{7}$$

The presence of depolarization can make it difficult to observe two frequencies. Actually, the Fourier transform of the polarization component $P_x(t)$ is

$$P_x(\omega)=\frac{\Lambda v_1}{\Lambda^2+(\omega-\omega_1)^2}+\frac{\Lambda v_2}{\Lambda^2+(\omega-\omega_2)^2}. \tag{8}$$

Obviously, when $\Lambda\sim\Delta\omega$, one line should be observed. However, as a rule, when diffusion is rapid, $\Lambda\leqslant 10^5\ \mathrm{sec}^{-1}$. It is expected that $\Delta\omega\geqslant 10^5\ \mathrm{sec}^{-1}$, and therefore the two lines can be well resolved. Figure 1 shows a typical Fourier spectrum for a diffusing muon in the case of one-dimensional domain structure. In writing Eqs. (7) and (8), we neglected the possibility that the muon might undergo a transition as it diffuses from one domain to another. This effect can be neglected for the usual size of the diamagnetic domains, but qualitatively it simply causes some broadening of the lines in Fig. 1.

If the muon does not diffuse, we have

$$P_x(t)=[v_1\cos(\omega_1 t)+v_2\cos(\omega_2 t)]\exp(-\sigma^2 t^2). \tag{9}$$

The Fourier transform of the polarization is

$$\begin{aligned}P_x(\omega)&=\mathrm{Re}\int_{-\infty}^{\infty}[v_1\exp\{i(\omega-\omega_1)t\}\\&\quad+v_2\exp\{i(\omega-\omega_2)t\}]\exp(-\sigma^2t^2)dt\\&=\sqrt{\frac{\pi}{\sigma}}\left\{v_1\exp\left[-\left(\frac{\omega-\omega_1}{2\sigma}\right)^2\right]\right.\\&\quad\left.+v_2\exp\left[-\left(\frac{\omega-\omega_2}{2\sigma}\right)^2\right]\right\}.\end{aligned} \tag{10}$$

In this case, it is harder to resolve the two frequencies in the Fourier spectrum. Indeed, after simple transformations, Eq. (10) takes the form

$$P_x(\omega)=\sqrt{\frac{\pi}{\sigma}}\exp\left[-\frac{(\omega-\omega_0)^2+\Delta\omega^2}{4\sigma^2}\right]\times\left\{v_1\exp\left[\frac{(\omega-\omega_0)\Delta\omega}{2\sigma^2}\right]+v_2\exp\left[-\frac{(\omega-\omega_0)\Delta\omega}{2\sigma^2}\right]\right\}. \tag{11}$$

The Fourier transform has the simplest form when $v_1=v_2=1/2$:

$$P_x(\omega)=\sqrt{\frac{\pi}{\sigma}}\exp\left[-\frac{(\omega-\omega_0)^2+\Delta\omega^2}{4\sigma^2}\right]\cosh\frac{(\omega-\omega_0)\Delta\omega}{2\sigma^2}. \tag{12}$$

The function $P_x(\omega)$ has two maxima relative to the dip ω_0, at the points $\pm\Delta\omega$. If $\sigma\sim\Delta\omega$, the two frequencies are unresolvable. However, as noted above, one can expect $\sigma<\Delta\omega$ for most metals.

4. Let us now take into account the finite width of the domain walls. We first consider a one-dimensional laminar (layered) structure whose period is a. Obviously, the width of domains of the first and second kinds is, respectively, $v_{1,2}a$. We shall neglect the depolarization caused by interaction with the nuclear magnetic moments. This is the case that will be of interest for the study of the field distribution in the domain walls. As is well known, the Fourier transform of the polarization makes it possible to directly study the magnetic field distribution in the sample:

$$P_+(t)=\int P_\omega e^{-i\omega t}\frac{d\omega}{2\pi}. \tag{13}$$

Let the field in the plate vary only along the x coordinate. Since the spin polarization of each muon precesses with a definite frequency, which depends on the position of the muon in the sample, the Fourier transform of the polarization of an ensemble of muons is determined by the obvious formula

$$P_\omega=\frac{2\pi}{a}\int\delta(\omega-\omega(x))dx=\frac{4\pi}{a}\int_{-v_1a/2}^{v_2a/2}\delta(\omega-\omega(x))dx. \tag{14}$$

Accordingly,

$$P_+(t)=\frac{2}{a}\int_{-\delta a/2(1+\delta)}^{a/2(1+\delta)}\exp[-i\omega(x)t]dx, \tag{15}$$

where $\delta=v_1/v_2$.

The field inhomogeneity in the sample when the dHvA effect occurs is small by comparison with the mean field in the sample, and the function $\omega(x)$ can be written as

$$\omega(x)=\omega_0+\Omega f(x), \tag{16}$$

where ω_0 is defined above, Ω is the field-inhomogeneity parameter ($\Omega\approx\Delta\omega$), and $f(x)\to\pm1$ as $x\to\pm a/2$. The polarization of Eq. (15) takes the form

$$P_+(t)=2\exp(-i\omega_0t)\int_{-\delta/2(1+\delta)}^{1/2(1+\delta)}\exp[-i\Omega f(\tilde{x})t]d\tilde{x}. \tag{17}$$

5. Let us now estimate the period of a one-dimensional laminar structure. A qualitative estimate of the period can be found in any reference (see, for example, Ref. 10), but it is of interest to obtain estimates containing the dependences on various parameters (temperature, magnetic field). Until now, there has been no good calculation of the field distribution in the domain walls. In a recently published work,[11] calculations were carried out of the magnetic field distribution and the period of the domain structure, based on minimization of the total energy of a sample with an inhomogeneous magnetic field distribution. The magnetic field distribution in the sample was determined on the basis of a standard functional. The calculations showed that the magnetic field distribution in the domains strongly depends on the external magnetic field and the temperature. However, as will be seen below, Itskovy *et al.*[11] wrote the boundary conditions for determining the magnetization incorrectly, and this led to a nonphysical result: a discontinuity of the magnetization gradient at the center of the domains. Thus, we shall obtain the magnetic field distribution in the thin-wall limit, where it is possible to use Kittel's model,[12] which is quite satisfactory in our case. For simplicity, let us consider the situation in which the phase volumes are identical: $v_1=v_2$. The magnetization of the paramagnetic phase (''I'') equals $+M_0$, while that of the diamagnetic phase equals $-M_0$. We shall expand the magnetization of the sample, which depends only on coordinate x on the surface $z=0$, in a Fourier series:

$$M(x)=\sum_{n=0}^{\infty}c_n\sin\frac{2\pi(2n+1)x}{a}, \tag{18}$$

where $c_n=4M_0/\pi(2n+1)$.

Since $\nabla\times\mathbf{B}=0$ in our problem, we can introduce a scalar potential: $\mathbf{B}=-\nabla\psi$, $\nabla^2\psi=0$. In a problem with laminar structure, potential ψ is independent of the y coordinate, and therefore

$$\frac{\partial^2\psi}{\partial x^2}+\frac{\partial^2\psi}{\partial z^2}=0 \tag{19}$$

with the boundary condition

$$-\left.\frac{\partial\psi}{\partial z}\right|_{z=+0}+\left.\frac{\partial\psi}{\partial z}\right|_{z=-0}=4\pi M(x). \tag{20}$$

A solution of Eq. (19) is sought in the form of a series:

$$\psi(x,z)=\sum_{n=0}^{\infty}b_n\sin\frac{2\pi(2n+1)x}{a}\times\exp\left[-\frac{2\pi(2n+1)z}{a}\right]. \tag{21}$$

From the boundary condition given by Eq. (20), we get

$$b_n=\frac{a}{2n+1}c_n=\frac{4aM_0}{\pi(2n+1)}. \tag{22}$$

In addition to the magnetic field energy, a nonuniformly magnetized sample creates an energy of

$$\delta U_1=\frac{1}{2}\oint \varphi\mathbf{M}\cdot d\mathbf{f}. \tag{23}$$

Since $\mathbf{M}\|\mathbf{B}\|\mathbf{z}$, integration over the entire surface reduces to integration over the surfaces $z=0$ and $z=-L_z$, where L_z is the thickness of the sample. The energy density per cm^2 of sample surface is

$$\delta\mathscr{U}_1=\frac{1}{a}\int_{-a/2}^{a/2}M(x)\varphi(x)dx=\frac{4aM_0^2}{\pi^2}\times\sum_n\frac{1}{(2n+1)^3}=\frac{7M_0^2a}{2\pi^2}\zeta(3). \tag{24}$$

Along with the field-output energy, an additional contribution will be introduced by the energy associated with the inhomogeneous field distribution in the finite although thin transitional region between domains of different kinds. Although this region is called a domain wall, it is essentially different in its properties from a domain wall of a ferromagnetic substance: here the field does not change its direction, but only negligibly varies in magnitude. To estimate the inhomogeneity energy, we shall use the simplest representation, in which the magnetization oscillates with a single frequency. In other words, there is only one extremal cross section of the Fermi surface for a given field direction. In this case, taking into account the inhomogeneity, the addition to the thermodynamic potential has the form[3,13]

$$\widetilde{\Omega}=\int\left\{2\pi M^2+A(T)\cos\left[\frac{2\pi F}{H_0^2}(h+4\pi M)\right]+\frac{\alpha}{2}(\nabla M)^2\right\}dV, \tag{25}$$

where

$$A(T)=\frac{1}{2\sqrt{2}(\pi\hbar)^3}\left(\frac{e\hbar}{c}B\right)^{5/2}\left|\frac{\partial^2S}{\partial p_z^2}\right|^{-1/2}\times\frac{1}{m^*}\frac{2\pi^2T/\hbar\omega}{\sinh(2\pi^2T/\hbar\omega)},$$

m^* is the cyclotron mass, S_m is the area of the extremal cross section of the Fermi surface, and $|\partial^2S/\partial p_z^2|\sim 1$. The oscillation frequency of the magnetization is $F=cS_m/2\pi e\hbar$; H_0 is the field for which the phase is a multiple of 2π; $F/H_0=n$, where n is a natural number. The phenomenological parameter $\alpha\geqslant r_L^2$, where $r_L\sim cp_F/eB$ is the Larmor radius. In Refs. 14–17, as a result of microscopic calculations, for the parameter α we obtain values $\alpha\approx 2\pi FA(T)r_L^2/4H_0^2$. The field in the sample (the plate) is $\mathbf{B}=\mathbf{H}+4\pi\mathbf{M}$.

For the value $H=H_0$, the volumes of the phases are identical, $v_1=v_2$; therefore, $\langle\mathbf{B}\rangle=\mathbf{H}_0$ for thin walls. Since $M\ll H_0$, it is possible to have $B\approx H_0$ everywhere. In the general case, $\mathbf{H}=\mathbf{H}_0+\mathbf{h}$.

From the functional in Eq. (25) we obtain Lagrange's equation for magnetization, and, for a homogeneous domain structure,

$$\alpha\frac{d^2M}{dx^2}-4\pi M+\frac{2\pi F}{H_0^2}A(T)\sin\left(\frac{8\pi^2F}{H_0^2}M\right)=0. \tag{26}$$

The inhomogeneity energy is determined from the last term in the functional of Eq. (25). In order to compute it, it is necessary, first of all, to solve Eq. (26). The nonlinear Eq. (26) can be solved in quadratures, but it has no simple analytic solution, and therefore we seek $M(x)$ in the limit of a thin transitional layer whose thickness is $\delta\ll a$. We put the coordinate origin $x=0$ at $M(0)=0$, and then $M(x)<0$ for $-a/2<x<0$, and $M(x)>0$ for $0<x<a/2$.

We introduce the dimensionless variables[3]

$$\frac{2\pi F}{H_0^2}=k\quad(k\gg 1),\quad 4\pi kM=m,\quad k^2A=\mathscr{A}, \tag{27}$$

and then Eq. (26) takes the form

$$\widetilde{\alpha}m''-m+\mathscr{A}\sin m=0, \tag{28}$$

where $\widetilde{\alpha}=\alpha/4\pi$.

As can be seen from this equation, when $\mathscr{A}>1$, the solution is $m=$ const and, consequently, there is no homogeneous state. Boundary conditions must be set for Eq. (28). Obviously, the magnetization has an extremum at the center of the domains, and therefore

$$\left.\frac{dm}{dx}\right|_{x=\pm a/4}=0\left(\left.\frac{dM}{dx}\right|_{x=\pm a/4}=0\right) \tag{29}$$

and, accordingly,

$$M(\pm a/4)=\pm M_0. \tag{30}$$

The first integral of Eq. (28), with the boundary conditions of Eqs. (29) and (30), can be found in the standard form:

$$[m'(x)]^2=\frac{1}{\widetilde{\alpha}}[\mathscr{A}(\cos m_0-\cos m)+(m^2-m_0^2)]. \tag{31}$$

We carry out the subsequent integration in the approximation of small values of $m\ll 1$. This is the case if $\mathscr{A}\geqslant 1$ but can fail to hold when $\mathscr{A}\gg 1$. Unfortunately, this case, which is simplest to investigate, cannot be considered the general case. The most general case is that for which $m\sim 1$, for which as has been pointed out, there is no simple analytic solution, even though Eq. (28) can be solved in quadratures in the general case. We shall obtain an analytic solution in a special case that includes the dependence on all the necessary parameters.

Equation (31) can be solved for $|x|\ll a$ by using the expansion $\cos m\approx 1-m^2/2$. We get

$$m'^2-\frac{\mathscr{A}-2}{2\widetilde{\alpha}}(m_0^2-m^2)=0. \tag{32}$$

From the simplified Eq. (32), we immediately find the solution

$$m=m_0\sin\left(x\sqrt{\frac{\mathscr{A}-2}{2\widetilde{\alpha}}}\right), \tag{33}$$

which is valid in the region where the argument of the sine is small. The solution given by Eq. (33) differs substantially from the standard form of a domain wall. However, it should be emphasized that even when the equation externally resembles that for the magnetization in the domain wall of a ferromagnetic substance (see Ref. 18), they describe quite different behavior of the magnetization and have different boundary conditions. Since $a^2/\tilde{\alpha} \gg 1$, we obtain a constraint for which the solution of Eq. (33) describes the field inhomogeneity in the transitional layer:

$$x \leqslant \frac{\pi}{2} x_0, \quad x_0 = \sqrt{\frac{2\tilde{\alpha}}{\mathscr{H}-2}}. \tag{34}$$

Let us now compute the field inhomogeneity energy per unit area:

$$\delta\mathscr{U}_2 = \frac{L_z}{a} \int_{-\pi x/2}^{\pi x/2} \frac{\alpha}{2} \left(\frac{dM}{dx}\right)^2 dx = \frac{L_z}{a} \frac{\pi\alpha}{4x_0} M_0^2. \tag{35}$$

To find the period of the domain structure, one must, as usual, minimize the total energy associated with the field distribution,

$$\mathscr{U} = \delta\mathscr{U}_1 + \delta\mathscr{U}_2 = \frac{7M_0^2 a}{2\pi^2}\,\zeta(3) + \frac{L_z}{a}\frac{\pi\alpha}{4x_0} M_0^2, \tag{36}$$

in terms of parameter a. For the period of the structure, we get

$$a = \sqrt{\frac{\pi^2 L_z \alpha}{7x_0\zeta(3)}} = \pi \sqrt{\frac{L_z}{7\zeta(3)}}\,\sqrt{\frac{\alpha(\mathscr{H}-2)}{2}}. \tag{37}$$

In the limit $\mathscr{H} \gg 1$, we find

$$a \approx \frac{\pi}{H_0}\,\sqrt{\frac{\pi L_z F}{7\zeta(3)}}\,\sqrt{2\alpha A(T)}. \tag{38}$$

The resulting estimate gives the same dependence on parameters L_z and α as follows from the simple qualitative treatment of Ref. 10, but also contains a dependence on field H_0 that is not obtained from the qualitative considerations. It is interesting that the domain size $a \propto H_0^{-1}$ and increases with decreasing field, but it is precisely at relatively weak fields that the condition for the formation of domain structure is also satisfied.

6. Let us now consider the behavior of the polarization, taking into account the field distribution of Eq. (33). Then we have in Eq. (16)

$$f(x) = \sin\sqrt{\frac{\mathscr{H}-2}{2\tilde{\alpha}}}\,x, \quad \Omega = 4\pi\gamma_\mu M_0. \tag{39}$$

Furthermore, it should be taken into account that Eq. (39) is valid for $x \leqslant \pi x_0/2 \ll a/2$, whereas the integration in Eq. (16) is carried out over the interval $|x| \leqslant a/2$. Therefore, Eq. (16) should transform to

$$P_+(t) = \left(\frac{1}{2} - \frac{x_0}{a}\right)[\exp(-i\omega_1 t) + \exp(-i\omega_2 t)] + \exp(-i\omega_0 t)\int_{-1}^{1} \exp(-i\Omega t\,\sin\varphi)\,d\varphi$$

$$= \exp(-i\omega_0 t)\left\{\left(1 - \frac{2x_0}{a}\right)\cos(\Delta\omega t) + \pi J_0(\Omega t)\right\}. \tag{40}$$

As can be seen, another oscillating term decreasing in time is added to the two-frequency picture (to the beats). Accordingly, the Fourier spectrum is described by

$$P_\omega = \frac{\pi}{a}\left\{\delta(\omega-\omega_1) + \delta(\omega-\omega_2) + \frac{2x_0}{a\sqrt{\Omega^2 - (\omega-\omega_0)^2}}\right\}. \tag{41}$$

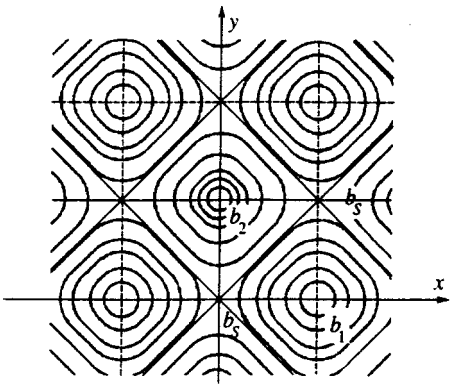

FIG. 2. Qualitative diagram of the field distribution in a two-dimensional domain structure (a square lattice).

7. We now consider the features of the spin-polarization behavior of the muon if a two-dimensional periodic structure is formed (see Fig. 2).

In this case, the magnetic field distribution has a form similar to Abrikosov's vortex structure in the mixed state of type-II superconductors. However, it should be kept in mind that $b_{\max} - b_{\min} = b_1 - b_2 \ll B$ in our case. As is well known (see, for example, Ref. 19), the character of the Fourier spectrum is determined by the Van Hove singularities. The Fourier spectrum of the spin polarization of the muon in Abrikosov's two-dimensional vortex structure has a logarithmic divergence (see, for example, Ref. 20). In our case, the corresponding Eqs. (16) and (17) for a one-dimensional structure should be rewritten in the form

$$P_\omega = \frac{2\pi}{S}\int \delta(\omega - \omega(x,y))\,dx\,dy,$$

$$P_+(t) = \frac{1}{S}\int \exp[-i\omega(x,y)t]\,dx\,dy, \tag{42}$$

where the integration is carried out over the area of a unit cell.

When integrating the first of Eqs. (42), it is convenient to transform, as usual (see, for example, Ref. 19), to curvilinear coordinates:

$$\omega(x,y) = \omega(l,h), \quad \omega(l) = \omega = \text{const}, \tag{43}$$

so that $dS = dl\,dh$, and accordingly, in the neighborhood of a line of constant frequency,

$$\omega(l,h)=\omega(l)+\frac{\partial\omega}{\partial h}\,h. \tag{44}$$

Here $\partial\omega/\partial h=|\nabla\omega|$. For the Fourier amplitude we get

$$P_\omega=\frac{2\pi}{S}\int\delta(|\nabla\omega|h)dl\;dh=\frac{2\pi}{S}\int\frac{dl}{|\nabla\omega|_{\omega(l)=\omega}}. \tag{45}$$

Consider the isotropic case, in which a triangular or square lattice is formed. We emphasize that elucidating the conditions for forming a one-dimensional or two-dimensional structure is a special, separate problem. Here we explain how to distinguish a one-dimensional from a two-dimensional structure experimentally. Taking into consideration the equal-areas rule when forming the domain structure (see, for example, Refs. 3 and 10), we arrive at the conclusion that $b_{\max}$ and $b_{\min}$ remain constant as the external field varies. Accordingly, a singularity corresponding to a saddle point will lie halfway between $\omega_1=\gamma_\mu b_{\max}$ and $\omega_2=\gamma_\mu b_{\min}$ if the volumes of the phases are identical, and will shift toward the field in the stable phase if $v_1\neq v_2$. Let us consider the possible picture for the Fourier spectrum in more detail.

The expansion in Eq. (44) is invalid close to the extrema, since $\nabla\omega=0$, and one must write (we assume $\omega_{xx}\neq 0$ and $\omega_{yy}\neq 0$)

$$\omega(x,y)|_{1,2}=\omega_{1,2}+\frac{1}{2}\left(\frac{\partial^2\omega}{\partial x^2}\,x^2+\frac{\partial^2\omega}{\partial y^2}\,y^2\right). \tag{46}$$

Here ω_{xx} and $\omega_{yy}<0$ in a paramagnetic domain, and ω_{xx} and $\omega_{yy}>0$ in a diamagnetic domain.

For the Fourier component, we have

$$P_{\omega\to\omega_{1,2}}=\frac{4\pi^2}{S}\left.\frac{1}{\sqrt{\omega_{xx}\omega_{yy}}}\right|_{1,2}. \tag{47}$$

When the volumes occupied by the fields $b>b_S$ (v_1) and $b<b_S$ (v_2) are identical, the Fourier amplitudes are $P_{\omega_1}=P_{\omega_2}$. If $v_2>v_1$, then

$$\omega_{xx}\omega_{yy}|_2<\omega_{xx}\omega_{yy}|_1,$$

and we get $P_{\omega_1}<P_{\omega_2}$. Correspondingly, if $v_2<v_1$, we get $P_{\omega_1}>P_{\omega_2}$.

Now let us consider the neighborhood of the saddle point at the origin in Fig. 2. At this point, we have the expansion

$$\omega=\omega_S+\frac{1}{2}\frac{\partial^2\omega}{\partial x^2}\,x^2+\frac{1}{2}\frac{\partial^2\omega}{\partial y^2}\,y^2$$

$$=\omega_S-\frac{1}{2}\,|\omega_{xx}|x^2+\frac{1}{2}\,|\omega_{yy}|y^2. \tag{48}$$

For the Fourier spectrum in the neighborhood of ω_S, logarithmic divergence is observed, with

$$P_{\omega<\omega_S}\sim\frac{1}{\sqrt{|\omega_{xx}\omega_{yy}|}}\ln\frac{\omega_S-\omega}{|\omega_{yy}|}, \tag{49}$$

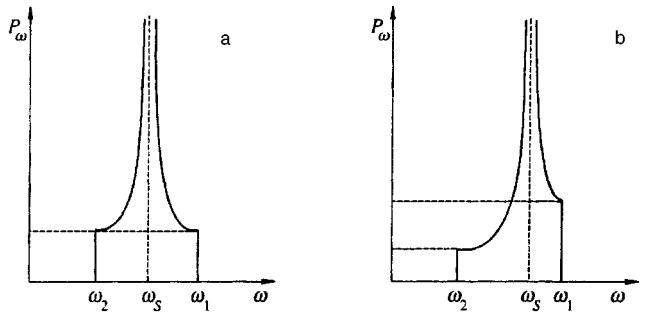

FIG. 3. Qualitative behavior of the Fourier spectrum of the polarization for a two-dimensional structure: (a) for $v_1=v_2$, (b) for $v_1>v_2$.

$$P_{\omega>\omega_S}\sim\frac{1}{\sqrt{|\omega_{xx}\omega_{yy}|}}\ln\frac{\omega-\omega_S}{|\omega_{xx}|}. \tag{50}$$

The qualitative behavior of the Fourier spectrum of the polarization is shown in Fig. 3.

As can be seen, the Fourier spectrum makes it possible to unambiguously identify whether a one-dimensional or two-dimensional structure was formed. The behavior of P_ω close to the singularities makes it possible to test the validity of the equal-areas rule for both one-dimensional and two-dimensional structures. In the experiment of Ref. 5, the Fourier spectrum P_ω has two characteristic maxima, the positions of which are independent of the external field within one period of the dHvA oscillations. This supports the assumption that, under the experimental conditions of Ref. 5, a one-dimensional laminar structure was observed and the equal-areas rule was satisfied.

8. There is currently no reliable calculation of the field distribution in the domains. Obviously, at $(T_c-T)/T_c\ll 1$, relatively large magnetic field fluctuations $(\sim\Delta b)$ should be observed, and the domain-wall thickness can be expected to be comparable to the period of the domain structure. Moreover, rather than a domain structure, a structure with a periodically inhomogeneous magnetic field distribution can be established in the sample.[13] It is these cases that are of significant interest, since the μSR method is probably the only instrument for identifying such structures. It is therefore extremely crucial to do experiments for different magnetic fields, temperatures, and sample sizes.

[1] W. J. de Haas and P. M. van Alphen, Proc. Netherlands R. Acad. Sci. **33**, 1106 (1930).
[2] W. J. de Haas and P. M. van Alphen, Proc. Netherlands R. Acad. Sci. **35**, 454 (1932).
[3] D. Shoenberg, *Magnetic Oscillations in Metals*, Cambridge Univ. Press, (1984).
[4] J. H. Condon, Phys. Rev. **145**, 526 (1966).
[5] G. Solt, C. Baines, V. S. Egorov *et al.*, Phys. Rev. Lett. **76**, 2575 (1996).
[6] J. H. Condon and R. E. Walstedt, Phys. Rev. Lett. **21**, 612 (1968).
[7] Yu. M. Belousov and V. P. Smilga, Fiz. Tverd. Tela (Leningrad) **21**, 2459 (1979) [Sov. Phys. Solid State **21**, 1416 (1979)].
[8] V. P. Smilga and Yu. M. Belousov, *A Muon Method for Studying Matter* [in Russian], Nauka, Moscow, (1991).
[9] S. V. Vonsovskiĭ, *Magnetism of Microparticles*, [in Russian], Nauka, Moscow, (1973).
[10] A. A. Abrikosov, *Fundamentals of the Theory of Metals*, Nauka, Moscow, (1987); [North-Holland, Amsterdam, 1988].

[11] M. A. Itskovy, G. F. Kventsel, and T. Maniv, Phys. Rev. B **50**, 6779 (1994).
[12] C. Kittel, Phys. Rev. **70**, 965 (1946).
[13] I. M. Lifshits, M. Ya. Azbel', and M. I. Kaganov, *Electron Theory of Metals* Nauka, Moscow (1971); [Consultants Bureau, New York, 1973]
[14] I. A. Privorotskiĭ, Zh. Éksp. Teor. Fiz. **52**, 1755 (1967) [Sov. Phys. JETP **25**, 1167 (1967)].
[15] M. Ya. Azbel', Zh. Éksp. Teor. Fiz. **53**, 2131 (1967) [Sov. Phys. JETP **26**, 1203 (1968)].
[16] S. C. Ying, B. J. McIntyre, and J. J. Quinn, Phys. Rev. B **6**, 1801 (1970).
[17] R. S. Markiewicz, Phys. Rev. B **34**, 4172 (1986).
[18] L. D. Landau and E. M. Lifshitz, *Electrodynamics of Continuous Media* Nauka, Moscow (1982); [Pergamon Press, Oxford, 1960].
[19] L. D. Landau and E. M. Lifshitz, *Statistical Physics*, Nauka, Moscow, (1976); [Pergamon Press, Oxford, 1980].
[20] Yu. M. Belousov, V. N. Gorbunov, V. P. Smilga, and V. I. Fesenko, Usp. Fiz. Nauk **160**, No. 11, 55 (1990) [Sov. Phys. Usp. **33**, 911 (1990)].

Translated by W. J. Manthey

Energy spectrum and phase transitions in C_{70} fullerite crystals at high pressure

K. P. Meletov, A. A. Maksimov, and I. I. Tartakovskiĭ

Institute of Solid-State Physics, Russian Academy of Sciences, 142432 Chernogolovka, Moscow Region, Russia

(Submitted 10 July 1996)
Zh. Éksp. Teor. Fiz. **111**, 262–273 (January 1997)

Measurements have been made of the Raman, optical absorption, and luminescence spectra of single crystals and pellets of the fullerite C_{70} at $T=300$ K and at pressures up to 12 GPa. The baric shift $d\omega/dP$ and the Grüneisen parameters of the Raman-active intramolecular phonon modes have been determined. It has been established that the $d\omega/dP$ value for certain phonon modes abruptly changes at pressures of $P_1\approx 2$ GPa and $P_2\approx 5.5$ GPa, as do the half-widths of the Raman lines. These features in the Raman spectrum are associated with phase transitions at high pressure. The baric shifts of the absorption and luminescence edges of C_{70} crystals have been determined and are -0.12 eV/GPa and -0.11 eV/GPa, respectively, for absorption and luminescence. The baric shift of the absorption edge decreases significantly with increasing pressure and is -0.03 eV/GPa at 10 GPa. These data have been used to determine the deformation potential of the fullerite C_{70}, which is about 2.1 ± 0.1 eV. © *1997 American Institute of Physics.* [S1063-7761(97)01601-6]

1. INTRODUCTION

The discovery of the family of multiatomic carbon molecules known as the fullerites has resulted in intensive study of the physical properties both of the molecules and crystals themselves and of various compounds based on them.[1,2] The fact that most of the attention in this case has been devoted to the fullerite C_{60} is mainly associated with the discovery of superconductivity at relatively high temperatures in compounds of C_{60} with the alkali metals.[3,4] A definite role in this is played by the circumstance that the method developed for synthesizing the fullerenes preferentially yields C_{60} and that it is more available than the other representatives of the family, in particular C_{70}.[5]

Nevertheless, a fairly great amount of attention has been paid to the study of the properties of the fullerene C_{70}. This is associated both with the high intensity of the studies of many-atom carbon clusters as a whole and with the successes in obtaining fairly pure starting material and single-crystal samples of C_{70}. Unlike C_{60}, the C_{70} molecule has the shape of a rugby ball and consists of twelve pentagons and twenty-five hexagons.[6] The molecule belongs to the D_{5h} point group, and the C_{70} crystal has hcp structure with parameters $a_0=1.01$ nm and $c_0=1.68$ nm and belongs to the space group P_{6_3}/mmc.[7] Annealing crystals with the hexagonal structure in high vacuum causes it to be altered, and it becomes predominantly cubic, with a small concentration of the hexagonal phase.[8] It should be pointed out that most C_{70} single crystals grown from the vapor phase have a cubic structure, although about 10% of the crystals are obtained with a hexagonal structure.[9]

Much interest and attention have been devoted to the molecular dynamics and the phonon spectrum of C_{70} crystals, which have been studied in a number of theoretical and experimental papers.[10–14] According to theoretical calculations of the molecular dynamics, the C_{70} spectrum contains fifty-three Raman-active vibrations, classified in the D_{5h} point group as $12A_1'+22E_2'+19E_1'$. In a C_{70} crystal, which contains four molecules per unit cell, the number of active modes increases significantly because of lowering of the symmetry and Davydov splitting. The first detailed measurements of the Raman and IR absorption spectra in C_{70} films made it possible to determine the frequencies of the intramolecular vibrations active in Raman scattering and IR absorption and to compare them with the results of numerical calculations.[14] Measurements of the temperature dependence of the Raman spectra of C_{70} single crystals made it possible to determine the frequencies of the intermolecular phonon modes and the critical variations of the Raman spectra associated with the orientational-ordering phase transition at $T=276$ K.[10,15] The structural aspects of the orientational-ordering phase transitions were studied by x-ray and electron diffraction.[9] Detailed studies of the thermodynamics of these transitions were carried out by differential thermal analysis.[16]

In our opinion, there is special interest in studying the energy spectrum and the phase transitions in C_{70} crystals at high pressure. They are a source of additional information on the intermolecular interaction and are needed for qualitative numerical calculations of the band structure and the energy spectrum of C_{70}. The first measurements of the Raman spectrum at high pressure were made on a powdered mixture of C_{60}/C_{70} fullerenes.[17] Measurements of the Raman spectra of C_{70} single crystals at high pressure made it possible to establish the features in the baric dependence of the phonon frequencies associated with phase transitions of the orientational ordering of the molecules in the crystal.[18] Measurements of the IR absorption spectra of C_{70} at high pressure made it possible to determine the baric shift coefficients and the Grüneisen parameters of the IR active modes.[19] The baric shift of the fundamental absorption edge was studied in Ref. 20.

This paper presents the results of detailed measurements of the Raman spectra and the optical absorption and luminescence spectra of single crystals of the fullerite C_{70} at high

TABLE I.

ω_i, cm^{-1}	$d\omega_i/dP$, cm^{-1}/GPa $P<2.0$	$d\omega_i/dP$, cm^{-1}/GPa $2.0<P<5.5$	$d\omega_i/dP$, cm^{-1}/GPa $P>5.5$	γ_i	ω_i, cm^{-1} (Ref. 14)	ω_i, cm^{-1} (Ref. 15)	$d\omega_i/dP$, cm^{-1}/GPa (Ref. 17)
256	3.2	3.2	3.2	0.226	261	257	1.65
412	0.1	0.1	0.1	0.004	411	410	-
509	-	1.0	1.0	0.036	501	506	0.38
570	−0.3	−0.3	−0.3	−0.01	573	570	−0.06
708	−0.3	−0.3	−0.3	−0.008	704	710	-
737	0.9	0.9	0.9	0.022	739	738	0.12
776	0.8	0.8	0.8	0.019	770	768	-
1061	3.7	5.4	1.5	0.063	1062	1062	1.1
1181	7.1	9.4	3.5	0.109	1186	1184	4
1228	5.3	6.3	3.1	0.078	1231	1229	3.2
1254	7.8	7.5	0.9	0.113	1260	1258	-
1367	6.3	8.2	5.3	0.083	1370	1369	1.1
1432	5.2	4.5	3.0	0.066	-	1438	-
1445	6.0	7.6	3.6	0.075	1448	1448	-
1468	6.0	6.3	5.0	0.074	1471	1469	-
1511	3.8	7.8	2.2	0.046	1517	1517	4.5
1565	4.2	5.9	3.3	0.049	1569	1566	2.73

pressure. The baric shifts and the Grüneisen parameters are determined for a large number of intramolecular phonon modes. The baric shift of the fundamental absorption and luminescence edge is determined, as well as the deformation potential of crystalline C_{70}. Characteristic singularities caused by phase transitions are revealed in the baric dependence of the phonon frequencies at pressures of about 2 GPa and about 5.5 GPa.

2. EXPERIMENT

Single crystals of the fullerene C_{70} were grown from solution in toluene. The starting C_{70} material was obtained by the method described in Ref. 5, and, according to the data of a mass-spectrometric analysis, its purity was at least 98.5%. The Raman and luminescence spectra were measured on single-crystal samples of C_{70} with a size of $100\times80\times20$ μm^3. The optical absorption spectra were measured on thin polycrystalline pellets of C_{70}, fabricated from separate crystallites of the starting material. The pellets were fabricated in a high-pressure chamber with diamond anvils whose working areas are parallel to within arc minutes. To do this, a crystallite placed between the parallel working areas was squeezed with no gasket in a sequential loading cycle until its coloration in the unloaded state became clear red. Measurements show that pellets with a uniform thickness from 1 to 5 μm are obtained in this case.

The optical measurements at high pressure were made by means of a high-pressure chamber with diamond anvils of Merill–Basset type.[21] The working area of the anvils was 600 μm across, the diameter of the working opening of the stainless steel gasket was 250 μm, and the thickness of the gasket after preliminary compression was 80 μm. A 4:1 methanol–ethanol mixture was used as a medium to transmit the pressure. The pressure in the working volume of the chamber was determined with an accuracy of 0.05 GPa from the shift of the R_1 luminescence line of ruby microcrystals.[22]

The Raman and luminescence spectra were measured by means of a Dilor-XY triple spectrometer with an optical multichannel recording system. An argon laser ($\lambda=488$ nm) and a He–Ne laser ($\lambda=632.8$ nm) were used as radiation sources. The radiation power directly in front of the high-pressure chamber was $\lesssim0.5$ mW, and the excitation spot diameter, allowing for defocusing by the diamond anvils, equalled about 10 μm. The absorption spectra were measured on an MDR-23 monochromator by the technique described in Ref. 20.

3. RESULTS AND DISCUSSION

In the Raman spectra of C_{70} single crystals at normal pressure and room temperature, seventeen vibrational modes were observed, whose frequencies ω_i are given in the first column of Table I. These frequencies are essentially identical with the data of Refs. 14 and 15 for C_{70} films, shown in the right-hand part of the table. They are also very close to the phonon frequencies in the Raman spectra of C_{70} crystals of hexagonal modification, measured at $T=23$ K and normal pressure.[10] Some of the frequency difference of the separate modes is possibly associated with the presence of stresses in the C_{70} films and with heating of the crystals by the argon laser radiation at $\lambda=488$ nm, in the strong-absorption region of the C_{70}. The presence of stresses in the C_{70} films increases the phonon frequencies somewhat, whereas heating the crystals has the opposite effect. It should be pointed out that a reversible decrease of the phonon frequencies in the Raman spectra of fullerite as the laser radiation power increases was observed earlier in C_{60} crystals.[23] It was associated with the formation of a large number of excited triplet states; however, in our opinion, it is not impossible that it can be associated with significant local heating of the crystal. We observed a similar effect in C_{70} crystals. To explain it, it is necessary to specially investigate the value of the local heating in the laser excitation spot and its effect on the Ra-

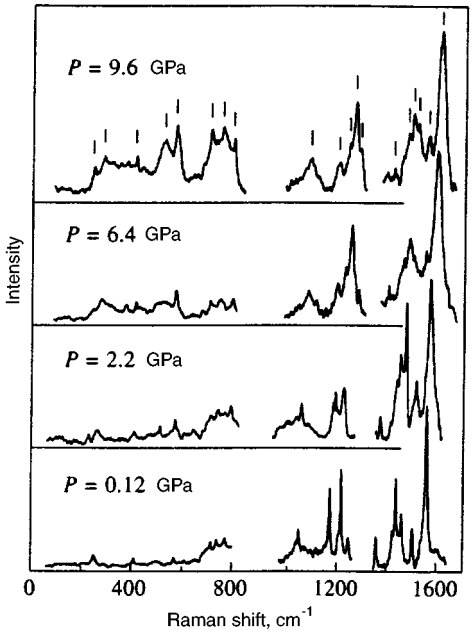

FIG. 1. Raman spectra of C_{70} single crystals at various pressures, $T=300$ K.

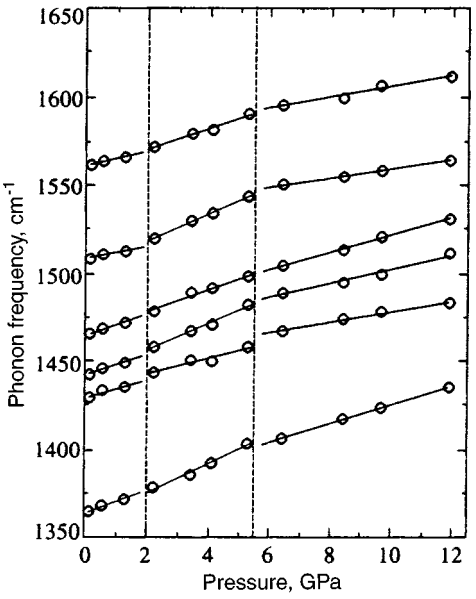

FIG. 2. Baric dependence of frequencies of the phonon modes of C_{70} single crystals in the interval 1350–1650 cm^{-1}.

man spectra. In this paper, we strove to set the laser power at the minimum possible level in order to reduce the effect of laser heating.

All the observed Raman modes relate to intramolecular modes; the intermolecular, rotational, and vibrational modes are located in the 10–60-cm^{-1} frequency interval[10] and were not considered in this work. Figure 1 shows segments of the Raman spectra of C_{70} crystals in the 200–800-cm^{-1} and 1000–1650-cm^{-1} frequency regions at several pressures. No spectra were recorded in the 800–1000-cm^{-1} region, since there are no Raman-active phonon modes of C_{70} in this region. The region close to $\omega\approx1332$ cm^{-1} has also been eliminated from the Raman spectrum, since a very strong diamond vibration is located in this region, and the contribution to the Raman spectrum from the diamond anvils is dominant. The experiments were done at room temperature, but, as indicated above, some local heating of the crystal in the laser-excitation spot is not excluded. The phonon modes of C_{70} observed in experiment at all pressures are noted on the upper spectrum of Fig. 1 by dashes. The frequencies of the overwhelming majority of the phonons increase with increasing pressure. The two phonon modes at 570 and 708 cm^{-1} are exceptions, since their frequencies decrease with increasing pressure. A relative redistribution of the intensity of the phonon modes with increasing pressure is also observed in the Raman spectra and is associated with a change in the resonance conditions of the excitation because of a significant baric shift of the optical absorption spectrum.[20] Most importantly, a significant strengthening of the low-frequency part of the Raman spectrum should be noted. A similar effect was also observed in the Raman spectra of C_{60} crystals. Changing the excitation wavelength from $\lambda=488$ nm to $\lambda=632.8$ nm in these spectra at $P\gtrsim3.4$ GPa partially cancels the negative baric shift of the absorption spectrum and at first causes a partial reconstruction of the initial intensity distribution. However, increasing the pressure further again changes the resonance conditions of the excitation and alters the intensity of the lines in the Raman spectrum.

The baric dependence of the phonon frequencies is shown in Figs. 2–4, corresponding to three different energy intervals. The vertical dashed lines in these figures indicate the pressures of 2.0 and 5.5 GPa, at which the slope of the baric dependence of virtually all the phonon modes abruptly changes. When $P\approx2.0$ GPa, new phonon modes also appear in the spectrum and are indicated in Figs. 3 and 4 by black dots. The solid straight lines are linear approximations of the experimental baric dependences of the phonon frequencies,

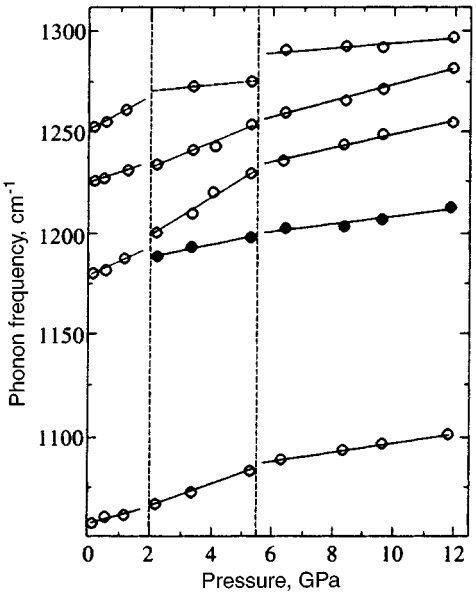

FIG. 3. Baric dependence of frequencies of the phonon modes of C_{70} single crystals in the interval 1050–1300 cm^{-1}.

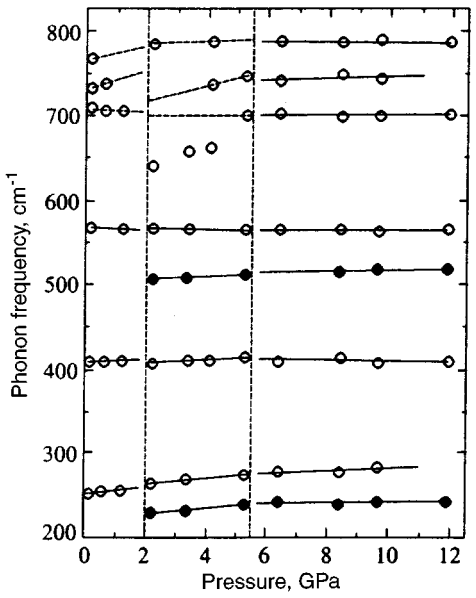

FIG. 4. Baric dependence of frequencies of the phonon modes of C_{70} single crystals in the interval 200–800 cm^{-1}.

drawn independently in three pressure ranges: $P<2.0$ GPa, $2.0<P<5.5$ GPa, and $P>5.5$ GPa. For some phonon modes, these lines are shown by a dashed line, which reflects inadequate statistics of the experimental data.

Figure 5 shows the pressure dependence of the width of the most intense line, for the 1565-cm^{-1} phonon. It clearly shows the abrupt increases in the line width at the boundaries of the three pressure regions, whereas the dependence is described by a virtually identical linear function in the intermediate regions. These data are unambiguous evidence that there are two phase transitions in the C_{70} crystal in the $P_1=2.0\pm0.2$ GPa and $P_2=5.5\pm0.5$ GPa regions. It should be pointed out that the measurements at high pressure were made in two loading cycles with direct application of pressure. In the first loading cycle, measurements were made for pressures of 0.55 and 4.1 GPa (the black dots in Fig. 5); then the pressure was dropped to zero and a second loading cycle

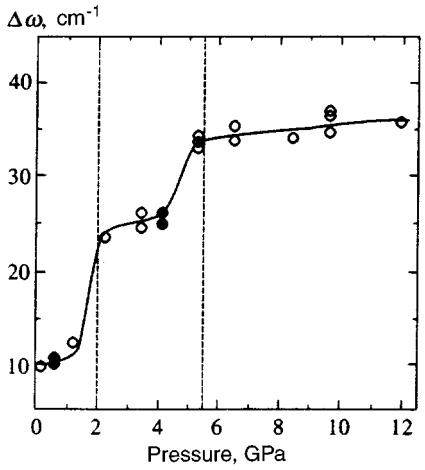

FIG. 5. Raman line width for the phonon with frequency 1565 cm^{-1} vs. pressure.

was carried out on the same sample. The closeness of the data obtained for the position and half-width of the line in the two loading cycles indicates that the phase transition in the $P=2.0\pm0.2$ GPa region, at least, is reversible with respect to pressure.

The Raman data from the C_{70} crystals at high pressure do not make it possible to unambiguously determine the nature of the observed phase transitions. As is well known, orientational-ordering phase transitions that occur in two stages take place in C_{70} crystals, as in C_{60} crystals. In a C_{60} crystal at normal pressure, the first stage of the orientational-ordering phase transition occurs at $T\approx260$ K and corresponds to freezing out of the random rotations of the molecule.[24] After this, the molecules occupy two energetically equivalent orientational positions, between which they can jump. These jumps completely freeze out at $T\approx85$ K, which corresponds to the second stage of the orientational-ordering phase transition.[25] The orientational phase transitions at high pressure and $T=300$ K also occur in two stages, at $P_1\approx0.4$ GPa and $P_2\approx2.4$ GPa, with the baric shift coefficient of the phase-transition temperature being equal to about 100 K/GPa for both stages.[26–30] According to x-ray and electron diffraction data, the orientational ordering in C_{70} crystals at normal pressure also occurs in two stages, which presumably correspond to freezing out of the rotations of the molecule along the short and long axes at $T_1\approx335$ K and $T_2\approx276$ K, respectively.[9]

It is tempting to associate the phase transitions that we observed at high pressure with orientational ordering of the molecules. However, to do this, it must be assumed that the laser radiation heats the crystal to a fairly high temperature, the value of which we estimated earlier as about 100 K.[18] In this case, an estimate of the baric shift coefficient of the phase-transition temperature gives a value significantly lower than in the C_{60} crystal. The observed data do not rule out the possibility that both phase transitions that we observed at high pressure are associated with orientational ordering, but additional studies, using other methods, are needed to reliably explain their nature.

The baric shift coefficients $d\omega_i/dP$ of the phonon modes are given in Table I for three pressure intervals. Their values varied between -0.3 and 9.4 cm^{-1}/GPa for various modes and pressure intervals. The Grüneisen parameters γ_i of the intramolecular phonon modes are determined from these data:

$$\gamma_i=-\frac{\partial\omega_i/\omega_i}{\partial V/V}=\frac{B_0}{\omega_i^0}\frac{\partial\omega_i}{\partial P}. \tag{1}$$

It was assumed in this case that the equation of state of crystalline C_{70} is described by a Murnaghan-type dependence:

$$P=\frac{B_0}{B_0'}\left[\left(\frac{V_0}{V}\right)^{B_0'}-1\right] \tag{2}$$

(where V_0/V is the relative variation of the volume of the crystal) with a bulk modulus of $B_0=18.1\pm1.8$ GPa and that $B_0'=dB_0/dP=5.7\pm0.6$ is the same as in the case of crys-

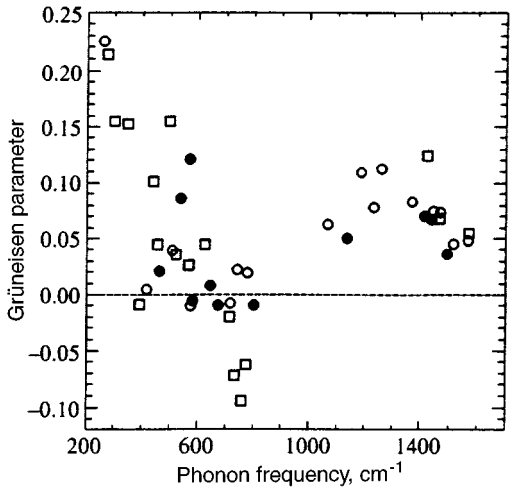

FIG. 6. Grüneisen parameters γ_i of various intramolecular phonon modes of the fullerites C_{60} and C_{70}.

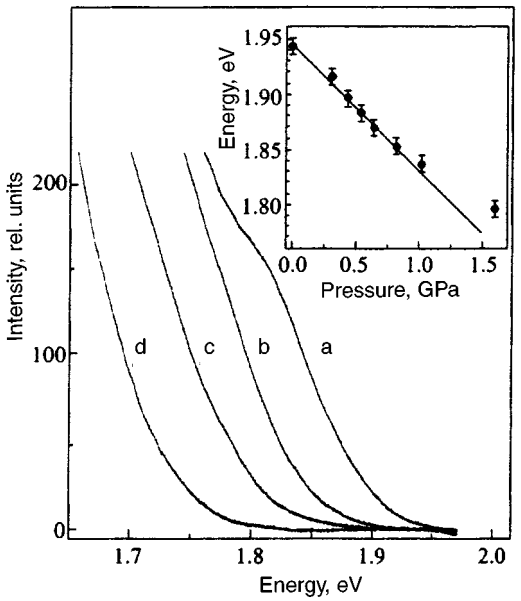

FIG. 7. Initial sections of the luminescence spectra of a C_{70} crystal at various pressures, GPa: *a*) 0, *b*) 0.44, *c*) 0.82, *d*) 1.6. The inset shows the baric dependence of the position of the luminescence edge.

talline C_{60}.[31] The values of the Grüneisen parameters for the intramolecular phonon modes of C_{70}, determined for the initial pressure region, are given in Table I.

Figure 6 shows the dependence of the Grüneisen parameters of fullerite crystals on the frequency of the intramolecular phonon modes. The open dots show the data of this paper, the black dots show the data from IR absorption in C_{70} films,[19] and the squares show the data from Raman scattering in C_{60} crystals.[32] As can be seen from the figure, a distinct correlation is observed between the results of the work using Raman scattering and the IR absorption in C_{70} crystals. This dependence, on which three characteristic regions can be distinguished, also agrees well with the data from Raman scattering in C_{60} crystals. The vibrations are stiffest in the initial region of phonon frequencies, from 200 to 350 cm^{-1}, and correspond to the maximum values of the Grüneisen parameters. Several vibrations in which the Grüneisen parameters are close to zero occur in the frequency region close to 400 cm^{-1}. Next, another group of vibrations, in which the Grüneisen parameters again assume rather large values, occurs in the 450–600-cm^{-1} region. A large group of the highest-frequency vibrations, in the region from 1100 to 1600 cm^{-1}, has approximately the same parameters. Finally, a group of vibrations with negative Grüneisen parameters occurs in the frequency region from 700 to 800 cm^{-1}, whose values for C_{60} are higher in absolute value than the corresponding values for C_{70}.

Negative values of the Grüneisen parameters for crystal phonon modes are evidence of structural instability of the crystal and closeness of the phase transition. In the case of intramolecular modes, they can be evidence of changes of the conformation and instability of the molecule. Negative Grüneisen parameters in the C_{60} molecule characterize the $H_g(3)$ and $H_g(4)$ modes, which correspond to flattening of the molecules (the squashing mode).[12] From this viewpoint, it is not especially surprising that the absolute value of the negative values of the Grüneisen parameters is significantly greater in C_{60} crystals than in C_{70}. This is possibly associated with the initially higher symmetry of the C_{60} molecule and the stronger influence of weak variations of the conformation of the molecule on the spectrum of intramolecular vibrations.

Figure 7 shows the initial sections of the luminescence spectra of C_{70} crystals at $T=300$ K and various pressures. Curve a corresponds to normal pressure, and curves b, c, and d correspond to pressures 0.44, 0.82, and 1.6 GPa, respectively. The luminescence spectrum is very extensive, and its low-frequency edge lies beyond the limits of spectral sensitivity of the optical multichannel analyzer. C_{60} crystals are likewise characterized by photoluminescence spectra that extend to 1 eV in the low-frequency region. The spectra were measured at constant laser-excitation power density and were corrected for the spectral sensitivity of the recording apparatus. Thus, the intensity distribution in the luminescence spectra reflects the true picture, and its scale is identical for all pressures. This makes it possible to determine the position of the edge of the spectrum accurately at any pressure.

The luminescence spectrum shifts toward the red as pressure increases, while its shape changes little. However, we are mainly interested in the baric shift of the luminescence edge. It was determined as follows: the initial section of the spectrum was approximated by a parabola, and the part adjacent to it in the higher-energy region was approximated by a straight line parallel to the x axis. The intersection of these two curves was taken as the point from which the luminescence edge was measured for each pressure. The spectral edge is at about 1.94 eV at normal pressure, and it shifts toward lower energies as pressure increases. The baric shift of the luminescence spectrum is thus negative, which is characteristic of molecular crystals, whose molecules in the electron ground state possess a center of inversion and zero dipole moment. The baric dependence of the position of the luminescence edge, determined by the method indicated above, is shown in the inset to Fig. 7. The straight line in the

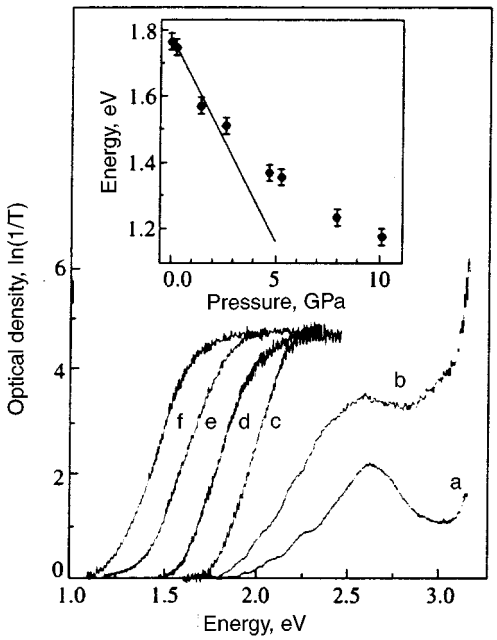

FIG. 8. Absorption spectra of the fullerite C_{70} at various pressures. Curve a shows the absorption of a solution of C_{70} in toluene; curve b shows the absorption of a thin pellet of C_{70} at normal pressure. Curves c, d, e, and f show the absorption of a thin pellet of C_{70} at pressures of 0.2, 1.4, 4.7, and 8.0 GPa, respectively. The inset shows the baric dependence of the position of the absorption edge.

inset is the tangent to the initial region of this dependence, and its slope defines the baric shift of the spectrum, whose value is about -0.11 eV/GPa.

Figure 8 shows absorption spectra of the fullerite C_{70} at $T=300$ K and various pressures. Curve a corresponds to the absorption of a solution of C_{70} in toluene and is given for comparison with the absorption spectrum of a thin pellet of C_{70} (curve b), obtained by the method explained above (in the section on experimental technique). As can be seen from the figure, these two spectra have identical structure, which reflects the rather low level of mechanical stresses in the pellet that unavoidably arise in the process of fabricating it. Curves c, d, e, and f correspond to the absorption of a thinner pellet at pressures of 0.2, 1.4, 4.4, and 8.0 GPa, respectively. The position of the absorption edge, determined by the same method as for the luminescence spectrum, is about 1.8 eV for normal pressure. This value is about 1.84 eV, however, for the solution of C_{70} in toluene, and the difference of ~ 0.04 eV between them determines the so-called crystal shift of the electron terms in molecular crystals.[20] The difference between the position of the absorption edge and the beginning of the luminescence spectrum, corresponding to 0.14 eV, can be a consequence of the chosen method of determining the spectral edge. It is also not impossible that it has a well-defined physical meaning. We cannot assert that the chosen procedure of determining the position of the spectral edge is sufficiently accurate when the spectra have no clearcut edge structure. All the same, there is no doubt that it can be used to accurately determine the baric shift of the spectrum, which is our main goal.

The absorption spectrum of crystalline C_{70}, like the luminescence spectrum, shifts toward lower energies as pressure increases. The baric dependence of the position of the absorption edge is shown in the inset of Fig. 8, where the straight line is the tangent to this dependence at the beginning region of pressures, and its slope defines the baric slope of the spectrum. This value equals about -0.12 eV/GPa and agrees fairly well with the baric shift of the luminescence spectrum. The baric shift of the absorption spectrum strongly decreases with increasing pressure and is about -0.03 eV/GPa at $P=10$ GPa. The same behavior is characteristic of C_{60} crystals, as it is for molecular crystals as a whole.[33]

As is well known, molecular crystals of the fullerites C_{60} and C_{70} are semiconductors with a rather large band gap. Its value can be determined by the position of the optical absorption edge and by the beginning of the luminescence spectrum of the crystal. Our data on the baric shift of the absorption edge and the beginning of the luminescence spectrum essentially determine the pressure dependence of the band gap of the C_{70} crystal. They make it possible to determine the deformation potential of the fullerite C_{70}:

$$\mathscr{D}=\frac{\partial E_g}{\partial \ln(V_0/V)}=-B_0\frac{dE_g}{dP}. \tag{3}$$

Its value, determined from Eq. (3) with parameters $B_0=18.1\pm 1.8$ GPa and $dE_g/dP=-0.115\pm 0.005$ eV/GPa, is $\mathscr{D}=2.1\pm 0.1$ eV.

This value of the deformation potential is somewhat less than the value $\mathscr{D}\approx 1.3$ eV determined in Ref. 32 for C_{60}. Unlike C_{60}, for which there are theoretical band structure calculations at normal and high pressures, and the deformation potential has been determined both numerically and experimentally, there are no such data for the C_{70} crystal. For this reason, it is not currently possible to compare experimental results for the baric dependence of the electron and phonon spectrum of the C_{70} crystal with the results of other papers. Nevertheless, we assume that our results can be useful for further development of theoretical and experimental studies of the energy spectrum of C_{70}.

This work was supported by the Russian Fund for Fundamental Research (Project No 96-02-17489) and the State Scientific–Technical Program ''Fullerenes and Atomic Clusters'' (Project No. 97016). One of the authors (K.P.M.) is grateful to NATO for support of scientific collaboration with Aristotle University in Salonika, Greece (Project NATO CRG No. 960556), and the other two authors (A.A.M. and I.I.T.) are grateful for support to the State Scientific–Technical Program on high-temperature superconductors (Project No. 93193).

[1] E. Rohlfing, D. M. Cox, and A. J. Kaldor, J. Chem. Phys. **81**, 3322 (1984).
[2] H. W. Kroto, J. R. Heath, S. C. O'Brien *et al.*, Nature **318**, 162 (1985).
[3] K. Holczer, O. Klein, Sh.-M. Huang *et al.*, Science **252**, 1154 (1991).
[4] P. W. Stephens, L. Mihaly, P. L. Lee *et al.*, Nature **351**, 632 (1991).
[5] W. Kratschmer, K. Fostiropulos, and D. Huffman, Chem. Phys. Lett. **170**, 167 (1990).
[6] J. R. Heath, S. C. O'Brien, Q. Zhang *et al.*, J. Opt. Soc. Am. **107**, 7779 (1985).
[7] V. P. Dravid, S. Liu, and N. M. Kappes, Chem. Phys. Lett. **185**, 75 (1991).
[8] J. E. Fischer, P. A. Heiney, A. R. McGhie *et al.*, Science **252**, 1288 (1991).

[9] M. A. Verheijen, H. Meekes, G. Meijer *et al.*, Chem. Phys. **166**, 287 (1992).
[10] P. H. M. van Loosdrecht, M. A. Verheijen, H. Meekes *et al.*, Phys. Rev. B **47**, 7610 (1993).
[11] R. E. Stanton and M. D. Newton, J. Phys. Chem. **92**, 2141 (1988).
[12] D. E. Weeks and W. G. Harter, J. Chem. Phys. **90**, 4744 (1989).
[13] Z. Slanina, J. M. Rudzinski, M. Togasi *et al.*, J. Mol. Struct. **202**, 169 (1989).
[14] D. S. Bethune, G. Meijer, W. C. Tang *et al.*, Chem. Phys. Lett. **179**, 181 (1991).
[15] N. Chandrabhas, K. Jayaram, D. V. S. Muthy *et al.*, Phys. Rev. B **47**, 10 963 (1993).
[16] E. Grivei, B. Nysten, M. Gassart *et al.*, Phys. Rev. B **47**, 1705 (1993).
[17] D. W. Snoke, Y. S. Raptis, and K. Syassen, Phys. Rev. B **45**, 14 419 (1992).
[18] A. A. Maksimov, K. P. Meletov, Yu. A. Osipyan *et al.*, JETP Lett. **57**, 816 (1993).
[19] H. Yamawaki, M. Yoshida, Y. Kakudate *et al.*, J. Phys. Chem. **97**, 11 161 (1993).
[20] K. P. Meletov, V. K. Dolganov, and Yu. A. Ossipyan, Solid State Commun. **87**, 639 (1993).
[21] A. Jayaraman, Rev. Sci. Instrum. **57**, 1013 (1986).
[22] D. Barnett, S. Block, and G. J. Piermarini, Rev. Sci. Instrum. **44**, 1 (1973).
[23] P. H. M. van Loosdrecht, P. J. M. van Bentum, M. A. Verheijen *et al.*, Chem. Phys. Lett. **198**, 587 (1992).
[24] P. A. Heiney, J. E. Fischer, A. R. McGhie *et al.*, Phys. Rev. Lett. **66**, 2911 (1991).
[25] W. I. F. David, R. M. Iberson, T. J. S. Dennis *et al.*, Europhys. Lett. **18**, 219 (1992).
[26] G. A. Samara, J. E. Schirber, B. Morosin *et al.*, Phys. Rev. Lett. **67**, 3136 (1991).
[27] N. Chandrabhas, M. N. Shashikala, D. V. S. Muthy *et al.*, Chem. Phys. Lett. **197**, 319 (1992).
[28] K. Meletov, D. Christofilos, G. Kourouklis, and S. Ves, Phys. Lett. **236**, 265 (1995).
[29] K. Meletov, D. Christofilos, S. Ves, and G. Kourouklis, Phys. Rev. B **52**, 10 090 (1995).
[30] A. P. Jephcoat, J. A. Hriljac, L. W. Finger *et al.*, Europhys. Lett. **25**, 429 (1994).
[31] S. J. Duclos, K. Brister, R. G. Haddon *et al.*, Nature **351**, 380 (1991).
[32] K. P. Meletov, G. Kourouklis, D. Christofilos, and S. Ves, Zh. Éksp. Teor. Fiz. **108**, 1456 (1995) [JETP **81**, 798 (1995)].
[33] K. P. Meletov, V. K. Dolganov, O. V. Zharikov *et al.*, J. Phys. (Paris) **2**, 2097 (1992).

Translated by W. J. Manthey

Dielectric enhancement of excitons in semiconducting quantum wires

E. A. Mulyarov and S. G. Tikhodeev

Institute of General Physics, Russian Academy of Sciences, 117942 Moscow, Russia
(Submitted 5 May 1996)
Zh. Éksp. Teor. Fiz. **111**, 274–282 (January 1997)

The energy of the exciton ground state in a semiconducting cylindrical quantum wire surrounded by a dielectric has been calculated using a variational technique accounting for the effect of dielectric enhancement. The effect of dielectric enhancement in such a system has been clearly demonstrated. Exciton parameters have been calculated for an intercalated leadiodide-based quasi-one-dimensional semiconductor and GaAs wires in asbestos nanotubes. © *1997 American Institute of Physics.* [S1063-7761(97)01701-0]

1. INTRODUCTION

The binding energy of excitons in semiconducting films and semiconductor/insulator quantum wells is considerably higher than that of three-dimensional excitons in bulk semiconductors. In addition to dimensional quantization effects, which make an exciton quasi-two-dimensional, image potentials due to the large difference between dielectric constants of the semiconductor and dielectric (or vacuum in case of a semiconducting film) also play an important role. They notably intensify the attraction between the electron and hole, hence the strengthening of excitons (so-called dielectric confinement or dielectric enhancement).[1,2]

In a semiconducting quantum wire surrounded by a dielectric, an electron and a hole are bound even more tightly. The dielectric environment in case of a quantum wire is more important than around a quantum well, since a larger fraction of electric field is contained in the dielectric, thus the attraction between the electron and hole is intensified. As concerns the effect of dimensional quantization, it is known that the binding energy in a one-dimensional Coulomb potential is infinite,[3] therefore we expect a larger binding energy of a quasi-one-dimensional exciton. The effect of exciton enhancement in wires was previously studied theoretically by Babichenko *et al.*[4] They obtained an asymptotic (with a logarithmic accuracy) expression for the exciton binding energy in the limit of a quantum wire of a small radius. This expression yields an estimate of the exciton enhancement within an order of magnitude, but cannot be used in calculating binding energies of real systems.

In the present paper we have developed a variational technique for calculating the binding energy and dimension of a quasi-one-dimensional exciton confined in a thin semiconducting wire inside a bulk dielectric. The calculation has been applied to two systems which can be studied experimentally, namely (1) intercalated lead iodide-based compound $C_5H_{10}NH_2PbI_3$,[5] in which PbI_3 semiconducting wires are surrounded by a bulk organic dielectric, and (2) GaAs wires inside asbestos nanotubes.[6]

2. EXCITONS IN A THIN DIELECTRIC WIRE. RENORMALIZATION OF THE COULOMB POTENTIAL AND VARIATIONAL CALCULATION OF THE BINDING ENERGY

Consider a thin semiconducting wire shaped as a cylinder with a radius R and surrounded by a dielectric. We assume that charge carriers are confined in the semiconductor. In order to determine the ground state of the Wannier–Mott exciton, we will vary the energy functional

$$H\{\Psi\}=\frac{\hbar^2}{2}\int\int d\mathbf{r}_e d\mathbf{r}_h\Bigg\{\frac{1}{m_{\|e}}\left|\frac{\partial}{\partial z_e}\Psi\right|^2+\frac{1}{m_{\perp e}}\left|\nabla_{\rho_e}\Psi\right|^2+\frac{1}{m_{\|h}}\left|\frac{\partial}{\partial z_h}\Psi\right|^2+\frac{1}{m_{\perp h}}\left|\nabla_{\rho_h}\Psi^2\right\}+\int\int d\mathbf{r}_e d\mathbf{r}_h V(\mathbf{r}_e,\mathbf{r}_h)|\Psi|^2, \tag{1}$$

where $m_{\|e,h}$ are the electron and hole effective masses in the direction of the z-axis aligned with the wire, $m_{\perp e,h}$ are the masses in the perpendicular direction, $V(\mathbf{r}_e,\mathbf{r}_h)$ is the potential of the electron–hole interaction, $\mathbf{r}=(\rho,z)$, z_e and z_h are the electron and hole coordinates along the z-axis, $\boldsymbol{\rho}_e$ and $\boldsymbol{\rho}_h$ are radius vectors of the electron and hole in the xy-plane. The trial function of the exciton ground state in the thin semiconducting wire surrounded by the dielectric is selected in the form

$$\Psi(\mathbf{r}_e,\mathbf{r}_h)=\sqrt{\frac{1}{L}\frac{a}{\sqrt{\pi}}}\exp\left[-\frac{1}{2}a^2(z_e-z_h)^2\right]\times\mathscr{R}_e(\rho_e)\mathscr{R}_h(\rho_h), \tag{2}$$

where L is the wire length, a is the variational parameter, $\mathscr{R}_{e,h}(\rho_{e,h})$ are normalized one-particle wave functions of the electron and hole ground states in the two-dimensional confining potential of the wire. The choice of the trial function in this form will be justified below.

The most important assumption in our reasoning is that the length of the quasi-one-dimensional exciton is much larger than the wire radius,[1)] i.e.,

$$aR \ll 1. \tag{3}$$

Another necessary condition is that the radius R has to be sufficiently small so that the energy distance between dimensionally quantized levels is much larger than the exciton binding energy. This condition allows us to separate the variables ρ and z in the wave function defined by Eq. (2). On the other hand, we assume that the wire is sufficiently thick so that the macroscopic dielectric constant of the semiconductor can be used. Below we will see that the result weakly depends on the shapes of the functions $\mathscr{R}_{e,h}(\rho)$ if the confining potential is sufficiently strong (which is the case in a semiconductor/dielectric structure) so that the wave functions decay rapidly beyond the interface. Finally, it follows from the shape of the trial function (2), in which the variables z and ρ are separated, that the second and fourth terms in the braces in the energy functional [Eq. (1)], i.e., the components describing the kinetic energy and not containing derivatives with respect to $z_{e,h}$, are independent of a and can be omitted.

The potential of the electron–hole interaction has the form

$$V(\mathbf{r}_e, \mathbf{r}_h) = -e\varphi(\mathbf{r}_e, \mathbf{r}_h), \tag{4}$$

where $\varphi(\mathbf{r}, \mathbf{r}_0)$ is the electrostatic potential at $\mathbf{r}$ of a charge e placed at $\mathbf{r}_0$. Using the axial symmetry of the system and performing Fourier transform with respect to z, along which the structure is uniform, we can express the potential as

$$\varphi(\mathbf{r}, \mathbf{r}_0) = \int_{-\infty}^{\infty} dk e^{ik(z-z_0)} \sum_{n=-\infty}^{\infty} e^{in\vartheta} \Phi_n(k, \rho, \rho_0), \tag{5}$$

where ϑ is the angle between the vectors ρ and ρ_0, and the expressions for the functions Φ_n are given in Appendix.

After averaging the potential energy (4) over the wave function, Eq. (2), only the zeroth harmonic in the Fourier series in Eq. (5) remains, since the wave functions of the electron and hole ground states are axially symmetric and independent of the angle. Thus the potential energy as a function of a takes the form

$$V(a) = \langle \Psi | V(\mathbf{r}_e, \mathbf{r}_h) | \Psi \rangle = -e \int_{-\infty}^{\infty} dk \, \exp\left(-\frac{k^2}{4a^2} \right) \Phi_0(k), \tag{6}$$

where

$$\Phi_0(k) = (2\pi)^2 \int_0^{\infty} \int_0^{\infty} \Phi_0(k, \rho_e, \rho_h) \times \mathscr{R}_e(\rho_e) \mathscr{R}_h(\rho_h) \rho_e \rho_h d\rho_e d\rho_h. \tag{7}$$

We can see that only $k \leqslant a$ is important in the integral in Eq. (6). Given that

$$\frac{1}{\eta} (aR)^2 |\ln(aR)| \ll 1, \tag{8}$$

we can use the expansion (A.7) in the limit of small k. After averaging over the dimensionally quantized wave functions, we have

$$\Phi_0(k) = -\frac{e}{\pi \varepsilon_b} \left(\ln \frac{|k| R^*}{2} + C \right), \tag{9}$$

where C is Euler's constant. In this case $\eta = \varepsilon_b / \varepsilon_w$, where ε_b and ε_w are the dielectric constants of the dielectric and semiconductor, respectively,

$$\ln \frac{R^*}{R} = \eta \sigma(R) + \sigma(\infty) - \sigma(R), \tag{10}$$

$$\sigma(x) = (2\pi)^2 \int_0^x \rho d\rho \, \ln \frac{\rho}{R} \int_0^{\rho} \rho' d\rho' \{ \mathscr{R}_e^2(\rho) \mathscr{R}_h^2(\rho') + \mathscr{R}_e^2(\rho') \mathscr{R}_h^2(\rho) \}. \tag{11}$$

The function defined by Eq. (9) is none other than the Fourier transform of the potential in the range of small k (or large z). We can see that, with due account of the finite exciton dimension in the quantization plane, the Coulomb potential is smooth over intervals of $z \sim R^*$. This potential is finite around the point $z = 0$, and its variation is proportional to z^2, irrespective of the shape of the trial function. Therefore, we select the function in Eq. (2) in the shape of the quantum harmonic oscillator wave function, rather than the Coulomb function. As concerns the contribution of the image potentials, it is equivalent to a renormalization of the electron–hole interaction constant and the effective wire radius R^*.

After calculating the integral in Eq. (6) and the average kinetic energy, we obtain the exciton ground-state energy

$$E(a) = \frac{\hbar^2}{4\mu} a^2 + \frac{2e^2}{\varepsilon_b} \frac{a}{\sqrt{\pi}} \left\{ \ln \frac{aR}{2} + \frac{1}{2} C + \eta \sigma(R) + \sigma(\infty) - \sigma(R) \right\}, \tag{12}$$

where $\mu^{-1} = m_{\|e}^{-1} + m_{\|h}^{-1}$ and μ is the exciton reduced mass. The exciton binding energy depends primarily on the dielectric constant of the environment because the electrostatic interaction energy between two charged particles confined to the narrow wire is concentrated mostly in the dielectric.

The functions $\mathscr{R}_e$ and $\mathscr{R}_h$ may be very different. This is essential, for example, for the oscillator strength of the excitonic transition. In this paper, however, we calculate only the ground-state energy. Owing to its weak dependence on the shapes of the functions $\mathscr{R}_e$ and $\mathscr{R}_h$, these functions can be expressed in the simplest form and considered identical. Actually, since the functions $\mathscr{R}_{e,h}(\rho)$ vanish rapidly outside the quantum wire, the difference $\sigma(\infty) - \sigma(R)$ in Eq. (10) can be neglected. Irrespective of the shapes of the functions $\mathscr{R}_{e,h}(\rho)$, the parameter $\sigma(R)$ is of the order of unity, therefore, given the condition (3), the function $\eta\sigma(R)$ is smaller than $\ln(aR)$. It follows from Eq. (3) and Eq. (12) that the exciton energy should depend weakly on the shapes of the functions $\mathscr{R}_{e,h}(\rho)$. Therefore we assume hereafter these functions is the simplest form:

$$\mathscr{R}_e(\rho) = \mathscr{R}_h(\rho) = \begin{cases} \dfrac{1}{\sqrt{\pi} R}, & \rho \leqslant R, \\ 0, & \rho \geqslant R, \end{cases} \tag{13}$$

and $\sigma(R)=\sigma(\infty)=-1/4$. Then the exciton ground-state energy as a function of the variational parameter finally takes the form

$$E(a)=\frac{\hbar^2}{4\mu}a^2+\frac{2e^2}{\varepsilon_b}\frac{a}{\sqrt{\pi}}\left\{\ln\frac{aR}{2}+\frac{1}{2}C-\frac{\eta}{4}\right\}. \qquad (14)$$

In the next section we will use Eq. (14) to calculate the exciton binding energy in specific semiconducting structures. By using the expansion of the electrostatic potential at small k [Eq. (A.7)], we can, however, estimate the exciton binding energy with the logarithmic accuracy, regardless of the shape of the trial function $f(\alpha\xi)$, where α is the dimensionless variational parameter, $\xi=z/a_B^*$, and $a_B^*=\hbar^2\varepsilon_b/\mu e^2$.

Let the trial function be normalized so that

$$\int_{-\infty}^{\infty}f^2(\xi)d\xi\int_{-\infty}^{\infty}f'^2(\xi)d\xi=f^4(0).$$

Then the exciton ground-state energy can be expressed as

$$\frac{E(\alpha)}{\mathrm{Ry}^*}=\alpha^2\frac{\int_{-\infty}^{\infty}f'^2(\xi)d\xi}{\int_{-\infty}^{\infty}f^2(\xi)d\xi}+4\alpha\frac{f^2(0)}{\int_{-\infty}^{\infty}f^2(\xi)d\xi}\ln\left(\alpha\frac{R}{a_B^*}\omega\right), \qquad (15)$$

where $\mathrm{Ry}^*=\mu e^4/2\hbar^2\varepsilon_b^2$,

$$\ln\omega=C+\frac{1}{2}\eta+f^{-2}(0)\int_{-\infty}^{\infty}F_k[f^2]\ln|k|dk, \qquad (16)$$

and $F_k[f^2]$ is the Fourier transform of the function $f^2(\xi)$. The exciton binding energy can be estimated with the logarithmic accuracy:

$$E_{\mathrm{ex}}\approx 4\mathrm{Ry}^*\ln^2\frac{R}{a_B^*}. \qquad (17)$$

Equation (17) is identical to the formula obtained in Ref. 4 for a thin quantum wire.

Excitons in the quasi-one-dimensional lead iodide-based compound and in GaAs wires in asbestos nanotubes

In $C_5H_{10}NH_2PbI_3$ compound, abbreviated as pp-PbI_3, which is produced by intercalating piperidinium organic molecules into a PbI_2 semiconducting substrate, excitons with a very large binding energy estimated by experimenters at about 700 meV were observed.[5]

The structure of pp-PbI_3 is a superlattice of Pb-I semiconducting chains with an ordered dielectric medium of $C_5H_{10}NH_2$ molecules among them.[7] Iodine atoms are clustered around lead atoms to form octahedra, which have common sides and thus are united in one-dimensional arrays. The distance between a lead atom and closest iodine atoms is 3.2 Å on an average, therefore the geometrical radius of the chain (the distance between an I atom and the chain axis) is $R_0\approx 2$ Å. The superlattice has a rectangular unit cell with two semiconducting wires. Its dimensions are $d_x=8.69$ Å and $d_y=18.36$ Å, so that the wire radius is much smaller than the typical separation between wires, $d\sim d_x,d_y$. Therefore the exciton parameters can be calculated in a fairly good approximation by taking an isolated semiconducting cylinder surrounded by the dielectric, instead of the periodic structure of quantum wires. Moreover, the small parameter for the image potential due to other quantum wires is not the ratio R_0/d, as in the case of a superlattice of plane quantum wells (i.e., the ratio of the well width to the lattice period), but its square. This statement has been confirmed by numerical estimates, which we do not give in this paper. It naturally follows, however, from a simple consideration, namely, that the contribution to the image potential due to other quantum wells or wires is proportional to the fraction of the volume where the electric field is significantly redistributed, i.e., the fraction of the volume occupied by the semiconductor.

The radius R of the semiconducting wire, however, can differ from its geometrical radius R_0 by a value of the order of the iodine ionic radius R_I, i.e., $R=R_0+R_I$, and R_I can be considered as a fitting parameter in the model. It cannot be larger than the iodine ionic radius, which is approximately 2.2 Å.

In order to obtain a reasonable agreement between our calculations and the experimentally determined exciton binding energy in pp-PbI_3, we set the iodine radius at 2 Å, i.e., $R=4$ Å. The dielectric constant of the quantum barrier, ε_b, is taken equal to the high-frequency dielectric constant of pure piperidinium[8]: $\varepsilon_b=2.1$.

The crystal structure of semiconducting wires is very similar to the trigonal structure of PbI_2, which is used, by the way, as a starting material for fabricating intercalated compounds. PbI_2 is a very anisotropic material because it is composed of one-dimensional arrays of iodine and lead atoms united by common iodine atoms in planar layers, and the anisotropy axis is perpendicular to these layers.[9] In the process of intercalation, the chains are separated and the space between them is filled with piperidinium molecules to form pp-PbI_3. This similarity between the two structures allows us to assume that the parameters of PbI_2 and of semiconducting wires in pp-PbI_3 should be close. Therefore, we take $\varepsilon_w=6.1$.[10]

As concerns the exciton reduced mass in the plane of PbI_2 layers, the experimental data on the electron and hole masses vary over a wide range,[9,11,12] and the reduced mass is in the range of $(0.1-0.5)m_0$, where m_0 is the free-electron mass.

Figure 1 shows the binding energy and averaged length of the exciton in quasi-one-dimensional pp-PbI_3 as a function of the exciton reduced mass μ calculated by varying a to minimize the energy, Eq. (14). The exciton binding energy is up to 900 meV at a reduced mass of $\mu=0.1m_0$, which is in reasonable agreement with the experimental data[5] (taking into account that the exciton luminescence line width is quite large, of the order of 230 meV). Note that in the range of large μ, the condition (3) does not hold. The potential energy in this case is notably larger than the kinetic energy, and the selected wave function given by Eq. (2) is no longer appropriate.

Figure 1 also shows parameters of the exciton calculated without the image potential, i.e., when $\varepsilon_b=\varepsilon_w$ (dashed

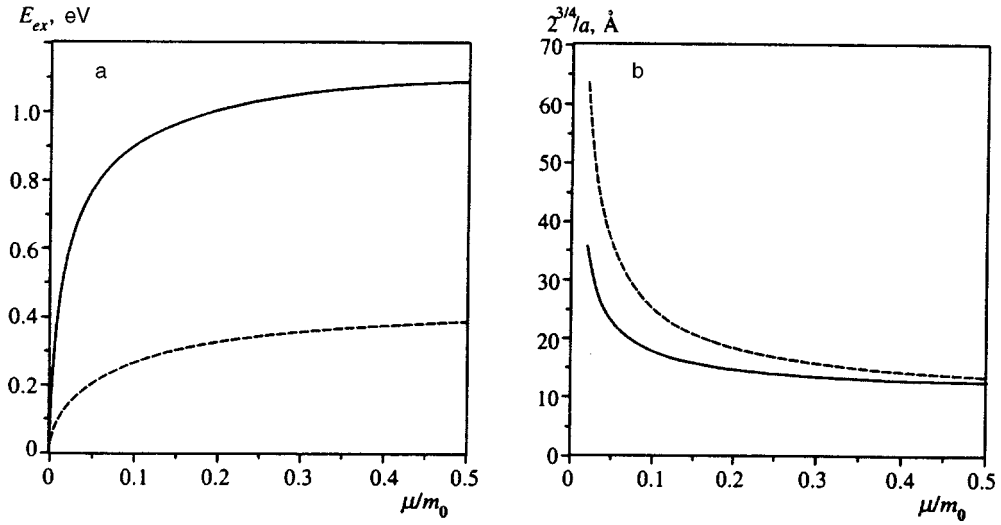

FIG. 1. Variational calculations of (a) the binding energy and (b) mean length $2^{3/4}/a$ of the exciton, as functions of the exciton reduced mass μ in pp-PbI_3 quasi-one-dimensional semiconductor, allowing for image potentials (solid lines) and without them (dashed lines).

lines). These curves demonstrate that the dielectric enhancement effect of the exciton in a semiconducting wire is essential.

In recent years GaAs quantum wires filling cylindrical pores in asbestos nanotubes have been fabricated.[6,13] The diameter of the channel filled with the semiconductor varies between 20 and 100 Å in different samples. Owing to the effect of dielectric enhancement of quasi-one-dimensional excitons, the binding energy may be dozens of times higher than in bulk GaAs. No direct measurements of the binding energy are available, therefore it is interesting to obtain a numerical estimate.

Figure 2 shows the exciton binding energy as a function of the semiconducting-wire radius calculated variationally at different dielectric constants ε_b of the barrier (dielectric) labeling the corresponding curves. The semiconductor dielectric constant ε_w and the exciton reduced mass are taken equal to those of bulk GaAs, namely $\varepsilon_w=13$ and $\mu=0.038m_0$ $\times(m_e=0.067m_0$ and $m_{lh}=0.087m_0$[14]), respectively. The curve for $\varepsilon_b=13$ corresponds to the case in which the image charges are ignored. Thus the exciton binding energy in a semiconducting quantum wire embedded in a bulk dielectric can be increased by the dielectric enhancement effect to 200 meV when the wire radius is 20 Å and $\varepsilon_b=2$ (compare with 24 meV in the wire without accounting for the image potential and 4 meV in bulk GaAs).

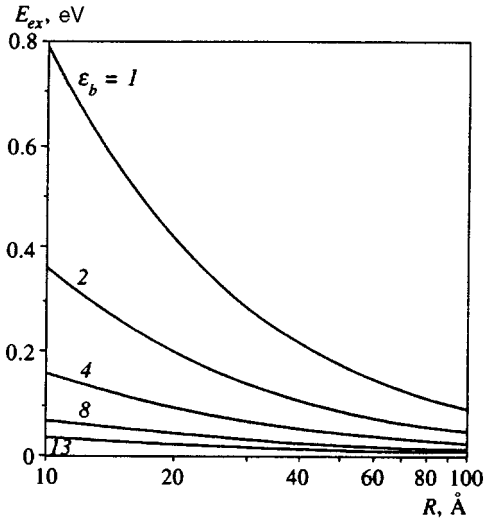

FIG. 2. Variational calculations of the exciton binding energy in a GaAs wire as a function of the wire radius R at several dielectric constants of the barrier.

Thus the dielectric enhancement effect of excitons in quantum wires is quite evident. The variational approach developed for this model allows one to calculate exciton parameters in quasi-one-dimensional dielectric structures. Calculations have been performed for specific examples of the $C_5H_{10}NH_2PbI_3$ intercalated semiconductor and GaAs wires in asbestos nanotubes.

We acknowledge helpful discussions with V. S. Dneprovskiĭ, E. A. Zhukov, A. V. Kvit, G. N. Mikhailova, V. V. Poborchiĭ, A. M. Prokhorov, and A. P. Silin. This work was supported by the Russian Fund for Fundamental Research (Grant No. 095-02-06062a), the Nanostructures program financed by the Ministry of Science and Technological Policy (Grant No. 1-041), and INTAS (Grant No. 94-2112).

APPENDIX

Electrostatic potential

In a cylindrical configuration, the solution $\varphi(\mathbf{r},\mathbf{r}_0)$ of the Poisson equation for an electrostatic potential generated at the point $\mathbf{r}$ by a point charge at the point $\mathbf{r}_0$ can be expressed as

$$\varphi(\mathbf{r},\mathbf{r}_0)=\int_{-\infty}^{\infty}dke^{ik(z-z_0)}\sum_{n=-\infty}^{\infty}e^{in\vartheta}\Phi_n(k,\rho,\rho_0), \quad \text{(A1)}$$

where ϑ is the angle between the vectors $\boldsymbol{\rho}$ and $\boldsymbol{\rho}_0$. If the charge is inside the cylinder, $\rho_0\leqslant R$, then

$$\Phi_n=(-1)^n\gamma\Bigg[\mu_nI_n(k\rho_0)I_n(k\rho)+\begin{cases}I_n(k\rho)K_n(k\rho_0), & \rho\leqslant\rho_0,\\ I_n(k\rho_0)K_n(k\rho), & \rho\geqslant\rho_0,\end{cases}\Bigg], \quad \rho\leqslant R,$$

$$\Phi_n=(-1)^n\gamma\lambda_nI_n(k\rho_0)K_n(k\rho), \quad \rho\geqslant R, \quad \text{(A2)}$$

where

$$\mu_n=\frac{(1-\eta)K_n(kR)K_n'(kR)}{\eta I_n(kR)K_n'(kR)-I_n'(kR)K_n(kR)},$$

$$\lambda_n=\frac{I_n(kR)K_n'(kR)-I_n'(kR)K_n(kR)}{\eta I_n(kR)K_n'(kR)-I_n'(kR)K_n(kR)}, \tag{A3}$$

$$\gamma=\frac{e}{\pi\varepsilon_w}, \quad \eta=\frac{\varepsilon_b}{\varepsilon_w}. \tag{A4}$$

I_n and K_n are the modified Bessel function, ε_w and ε_b are the dielectric constants of the semiconductor and dielectric, respectively. If the charge is outside the cylinder, $\rho_0 \geqslant R$, then

$$\Phi_n=(-1)^n\gamma\lambda_n I_n(k\rho)K_n(k\rho_0), \quad \rho\leqslant R,$$

$$\Phi_n=(-1)^n\frac{\gamma}{\eta}\left[\nu_n K_n(k\rho_0)K_n(k\rho) + \begin{cases} I_n(k\rho)K_n(k\rho_0), & \rho\leqslant\rho_0, \\ I_n(k\rho_0)K_n(k\rho), & \rho\geqslant\rho_0, \end{cases}\right], \quad \rho\geqslant R, \tag{A5}$$

where

$$\nu_n=\mu_n\frac{I_n(kR)I_n'(kR)}{K_n(kR)K_n'(kR)}. \tag{A6}$$

At $kR\ll 1$ and $n=0$, Eqs. (A.2)–(A.6) take the form

$$\Phi_0(k,\rho,\rho_0)=-\frac{e}{\pi\varepsilon_b}\left(\ln\frac{|k|R}{2}+C\right)-\frac{e}{\pi\varepsilon}\ln\frac{\max(\rho,\rho_0)}{R} + O\left(\frac{1}{\eta}(kR)^2\ln(|k|R)\right), \tag{A7}$$

where $\varepsilon=\varepsilon_w$ (if ρ, $\rho_0\leqslant R$) and $\varepsilon=\varepsilon_b$ in the outside region, and C is Euler's constant.

[1)]The condition on the exciton size is even more strict, see Eq. (8) below.

[1] N. S. Rytova, Dokl. Akad. Nauk SSSR **163**, 1118 (1965) [Sov. Phys. Dokl. **10**, 754 (1965)].
[2] L. V. Keldysh, JETP Lett. **29**, 658 (1979).
[3] L. D. Landau and E. M. Lifshitz, *Quantum Mechanics. Nonrelativistic-Theory*, Pergamon Press, New York (1976).
[4] V. S. Babichenko, L. V. Keldysh, and A. P. Silin, Fiz. Tverd. Tela (Leningrad) **22**, 1238 (1980) [Sov. Phys. Solid State **22**, 723 (1980)].
[5] E. A. Muljarov, N. A. Gippius, A. V. Kvit *et al.*, in *Nanostructures: Physics and Technology*, Int. Symp. Abs., St. Petersburg (1994), p. 127.
[6] V. V. Poborchiĭ, M. S. Ivanova, and I. A. Salamatina, Superlattices and Microstructures **16**, 133 (1994).
[7] G. V. Gridunova, E. A. Ziger, V. M. Koshkin *et al.*, Dokl. Akad. Nauk SSSR **278**, 656 (1984) [*sic*].
[8] *CRC Handbook of Chemistry and Physics*, 63rd Ed., Chem. Rubber Comp., Boca Raton, FL (1983).
[9] R. Minder, G. Ottaviani, and C. Canali, J. Phys. Chem. Sol. **37**, 417 (1976).
[10] G. Lucovsky, R. M. White, M. Y. Liang *et al.*, Solid State Commun. **18**, 811 (1976).
[11] E. Tosatti and G. Harbekke, Nuovo Cimento B **22**, 87 (1974).
[12] P. D. Bloch, J. W. Hodby, T. E. Jenkins *et al.*, J. Phys. C **11**, 4997 (1978).
[13] V. Dneprovskiĭ, N. Gushina, O. Pavlov *et al.*, in *Nanostructures: Physics and Technology*, Int. Symp. Abs., St. Petersburg (1995), p. 180.
[14] A. L. Mears and R. A. Stradling, J. Phys. C **4**, L22 (1971).

Translation was provided by the Russian Editorial office.

Field-induced phase transitions in magnetooptical films with a small positive anisotropy constant

F. V. Lisovskiĭ, E. G. Mansvetova, and Ch. M. Pak

Institute of Radio Engineering and Electronics, Russian Academy of Sciences, 141120 Fryazino, Moscow Region, Russia

(Submitted 22 May 1996)
Zh. Éksp. Teor. Fiz. **111**, 283–297 (January 1997)

We study phase transitions induced by a static magnetic field in magnetically uniaxial films with a small positive anisotropy constant. The phase diagram of these objects is determined in the $H_{\parallel}-H_{\perp}$ plane, where $H_{\parallel}$ and $H_{\perp}$ are, respectively, the components of the magnetizing field along and perpendicular to the surface normal. The stability boundary is located for all of the main types of domain configurations observed: a simple stripe domain structure, a stripe domain structure with periodic bending by surface distortions in the profile of the domain walls, and hexagonal lattices of cylindrical magnetic bubbles. © *1997 American Institute of Physics.* [S1063-7761(97)01801-5]

1. INTRODUCTION

The results of the investigations described in this paper pertain to magnetically uniaxial films with an anisotropy constant $\beta_u>0$ and an easy axis parallel to the surface normal. Among the enormous number of magnetically uniaxial thin film samples available to experimentalists at the present time, the favorites are epitaxial films of magnetic garnets. This choice is dictated by the following considerations. First, the parameters of the epitaxial films of mixed rare-earth iron garnets can readily be varied by the appropriate choice of composition and growth conditions, and therefore they can exhibit nearly all possible types of domain structures that exist in any uniaxial ferromagnet. Second, the change in the state of these films in phase transitions can be observed directly by ordinary polarization microscopy, since all the garnets have a rather large specific Faraday rotation in the visible and near infrared.

A thermodynamic equilibrium distribution of the magnetization vector **M** corresponds to the absolute minimum of the free energy, which for the present case is equal to

$$W=2\pi M^2\int_V dv[\alpha(\nabla\cdot\mathbf{m})^2-\beta_u(\mathbf{m}\cdot\mathbf{n})^2-2(\mathbf{m}\cdot\mathbf{h}) -(\mathbf{m}\cdot\mathbf{h_M})] \quad (1)$$

with the standard boundary conditions on the film surface $z=\pm L/2$, where L is the film thickness ($\mathbf{e}_z\|\mathbf{n}$), **M** is the magnetization vector, $\mathbf{m}=\mathbf{M}/M$; α is the inhomogeneous exchange interaction constant, $\mathbf{h}=\mathbf{H}/4\pi M$ and $\mathbf{h_M}=\mathbf{H_M}/4\pi M$ are the normalized external field strength and the magnetostatic field, respectively.[1)] In the general case, variation of expression (1) yields an equation that cannot be solved analytically; approximation methods are based on the Ritz variational principle with trial functions chosen on the basis of experimental data.

For $\beta_u\gg 1$, a good approximation over a wide range of the variables $(h_{\parallel},h_{\perp})$, where $h_{\parallel}=H_{\parallel}/(4\pi M)$ and $h_{\perp}=H_{\perp}/(4\pi M)$, are the normalized components of the magnetizing field parallel and perpendicular to the surface normal, is the approximation of structureless (geometric) domain walls, where the walls are considered to be infinitely thin and to have a constant surface energy density $\sigma_w=\text{const}$ that depends only on the angle between the magnetization vector in adjacent domains.[1,2] It is also assumed that the effective domain wall width is $\Delta_w\ll d$, where d is the period of the domain structure. The models of domain structures with ''geometric'' domain walls have been widely used in the physics of magnetic phenomena in the early studies of inhomogeneous magnetic states, and interest in these models has not waned to the present time (a review of the present-day state of the problem can be found in Ref. 3). One must, however, bear in mind that the domain walls in magnetically uniaxial films are not simply planar interface surfaces between neighboring domains, but are in fact three-dimensional objects supporting a highly nonuniform vortical distribution of the **M** vector (so-called ''twisted'' domain walls; see Refs. 4 and 5). Two types of domain walls are possible: those with the same polarity and those with the opposite polarity of the domain boundaries (the vector **M** in the centers of adjacent domain walls are parallel and antiparallel to one another, respectively). Structures with opposite-polarity domain structures in thin films with infinite lateral dimensions are metastable.

In the problem we are considering, the model of geometric domain walls, even with $\beta_u\gg 1$, is inapplicable over the range of values $(h_{\parallel},h_{\perp})\approx(0,\beta_u)$, corresponding to the neighborhood of lines of second-order phase transitions (or first-order phase transitions close to second-order) from the uniformly magnetized state to the state with the stripe domain structure. The latter in the present case is a frozen-out soft mode,[6–11] i.e., the distribution of the magnetization vector in the film can be described by simple harmonic functions, and the partition of the magnet into domains and domain walls is no longer meaningful. We note that the function $\mathbf{M}(\mathbf{r})$ undergoes no qualitative changes due to the increase in the magnetic field $h_{\perp}$ near the line of phase transitions, but the vortices, which in zero field were localized in the narrow domain walls, are broadened to the point of being comparable in size to the period of the domain structure. A similar situation has also been observed in the demagnetized

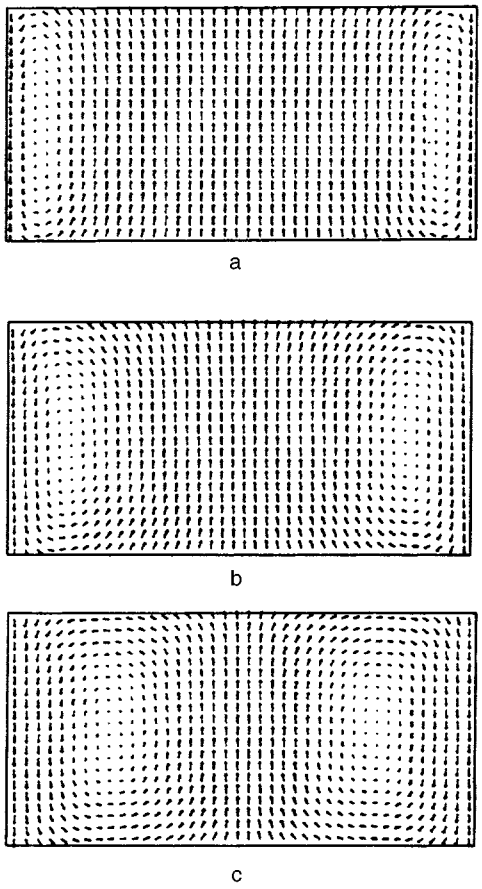

FIG. 1. Distribution of the magnetization in domains and domain walls of magnetically uniaxial films of thickness $L=20l_w$ with $\beta_u=1.5$ (a), 1.1 (b), and 0.7 (c)

state with a lowered anisotropy constant β_u. A most convincing demonstration of this statement was recently obtained by Antonov and coworkers in computer calculations of the equilibrium distribution of $\mathbf{M}(\mathbf{r})$ for a class of singly periodic functions by the method of dynamic iteration.[12,13] By way of example, Fig. 1, borrowed from Antonov *et al.*, shows the distribution of the transverse (to the domain wall surfaces) components of the vector **M** in films with different anisotropy constants and the same thickness $L=20l_w$, where l_w is the so-called characteristic length of the material, equal to

$$l_w=\frac{\sigma_w^{(B)}}{2\pi M^2}=2\pi\sqrt{\alpha\beta_u}.$$

Here $\sigma_w^{(B)}=4\pi^2M^2\sqrt{\alpha\beta_u}$ is the surface energy density of a simple 180° Bloch domain wall.

Figure 1 shows that the subdivision of a magnet into domains and domain walls is entirely meaningless if $\beta_u\leqslant 1$. Moreover, when the anisotropy constant decreases, those regions that, for $\beta_u>1$, belong to a domain wall, become considerably wider than the regions that were initially regarded as domains (compare Figs. 1a, 1c), and the distribution of the magnetization vector throughout the volume of the film is highly nonuniform. For these reasons the use of the Ritz variation principle for solving this micromagnetic problem encounters considerable difficulties, and is not very successful, despite the many attempts to choose a trial function adequate to describe the distribution of **M** over a wide range of film parameters.[2)] The use of inadequate trial functions frequently leads to absurd conclusions, for example, the existence of a phase transition for a value $\beta_u=1$.[23] For biperiodic domain structures, which under certain conditions also exist in magnetic uniaxial films with a positive anisotropy constant (see below), no success has been had in calculating the distribution profile of the magnetization even by computer simulation.

Unlike films with strong anisotropy ($\beta\gg 1$), for which the phase diagram in the $(h_\parallel,h_\perp)$ plane has been studied in great detail both experimentally and theoretically (see, e.g., Ref. 10 and the literature cited therein), the analogous problem for films with weak anisotropy is essentially unsolved, although their domain structures have been intensely studied experimentally over a period of decades. The majority of the experiments were carried out on metal films (iron, nickel, cobalt, Permalloy, and other alloys), on single-crystal wafers of magnetoplumbite and barium ferrites, and epitaxial films of spinel ferrites (the references to the corresponding original papers can be found in Refs. 13–18, 20 and 22). The iron garnets have been studied in only a few publications[24–26]; and the special features of domain structures in garnet films with weak uniaxial anisotropy have also been discussed in a monograph.[27]

It has been established that in magnetically uniaxial films with a small value of β_u with no applied magnetizing field, the following types of ordered distributions of the vector **M** can exist (see Fig. 2): I—a uniformly magnetized state, which corresponds to the absolute minimum in the thermodynamic potential only in sufficiently thin films ($L<L_{cr1}$); II—a stripe domain structure with vertical stripe domain walls, which occurs for $L_{cr1}<L<L_{cr1}^*$; III—a stripe domain structure with in-phase harmonic surface distortions of the domain wall profile ($L_{cr1}^*<L<L_{cr2}$); IV—a complex domain structure with stripe domains penetrating the film alternating with conical domains that do not penetrate; this occurs only for thick films ($L>L_{cr2}$). Experiments carried out with wafers of magnetoplumbite have shown[28] that when the thickness is changed, the transformation of a domain structure of type III to one of type II proceeds as a second-order phase transition (the amplitude of the harmonic distortions of the domain wall profile goes to zero as $L\to L_{cr1}^*+0$), while the transformation of a domain structure of type III into type IV proceeds as a first-order phase transition.[3)] The phase transitions between the various domain configurations when the orientation and the strength of the magnetizing field are changed have scarcely been studied at all (with few exceptions).

2. EXPERIMENTAL CONDITIONS

To study the field-induced phase transitions between the various domain structures, we selected as samples epitaxial films of magnetic garnets with the composition $(BiLu)_3Fe_5O_{12}$, in which, with single-crystal wafers of gadolinium–gallium garnet $Gd_3Ga_5O_{12}$ used as the sub-

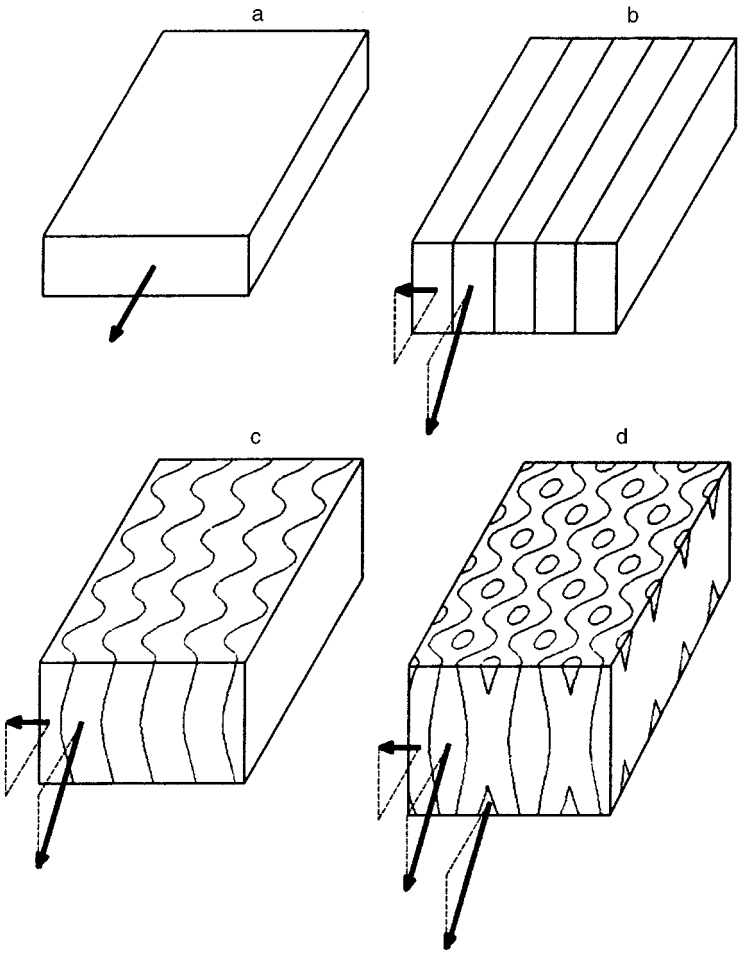

FIG. 2. Main types of ordered domain structures in magnetically uniaxial films for $H=0$.

strates, one can relatively simply obtain low values of the induced uniaxial anisotropy constant. In addition, these films have a low optical absorption coefficient α and a high specific Faraday rotation θ_F at visible wavelengths ($\alpha=20$ cm^{-1} and $\theta_F=1.5\times10^4$ deg/cm at $\lambda=0.63$ μm), which makes it possible to monitor visually in real time the changes in the form of the domain structure during phase transitions.

The films of the lutetium–bismuth system used in our experiments, with a thickness 1 μm$<L<30$ μm, were grown by isothermal liquid-phase epitaxy on (111)-oriented gadolinium–gallium garnet, with zero film–substrate lattice mismatch obtained at the composition $Lu_{2.1}Bi_{0.9}Fe_5O_{12}$. To prepare the films we used two fluxes of garnet-forming oxides: Bi_2O_3 (type I film) and PbO–Bi_2O_3 (type II film). For the growth of the type I films we added a small amount of magnesium oxide MgO to the charge, in addition to the Lu_2O_3 and Fe_2O_3, to reduce the optical absorption of the film. The synthesis temperature for the type I films was varied between 780 and 790 °C, and for the type II films between 720 and 730 °C, and the substrate was rotated in the melt at $\approx$100 rpm, with the direction of rotation of the rod changed every 10 rotations. The growth time was dictated by the required thickness of the film and was from 15 s to 45 min, with the upper limit corresponding to a film thickness of about 30 μm. We were not able to grow thicker films by extending the growth time.

The saturation magnetization of the films was $\simeq$1800 G, the Curie temperature T_C was 560 K, and the specific Faraday rotation θ_F, which varied only slightly with film thickness, was in the range $(1–1.5)\times10^4$ deg/cm at a wavelength $\lambda=0.6328$ μm. When the samples were magnetized by a field along the normal and by a field perpendicular to it, a field $H_\parallel^*=$(1500–1750) Oe and $H_\perp^*=$(24–200) Oe, respectively, were required to erase the domain structure in the type I films, while in type II films these fields were, respectively, (1600–1750) Oe and (300–500) Oe, where the saturation magnetization of the films, as a rule, increased with increasing film thickness. For a preliminary estimate of the uniaxial anisotropy constant we used the relation $\beta_u=H_\perp^*/H_\parallel^*$. The film thickness was determined from a transverse cleave by means of a microscope with a micrometer ocular, and the geometrical parameters of the domain structures were measured either by the same means or from the diffraction patterns. The absolute error in determining the parameters characterizing the periodicity of the magnetization vector was no higher than 0.05 μm in the two cases.

The investigations of the magnetic phase transitions in the films were carried out at room temperature by a magnetooptical method like that described in Ref. 10. The light from the source (an incandescent lamp or a laser) was sent though a polarizer and focused by a lens on the surface of the

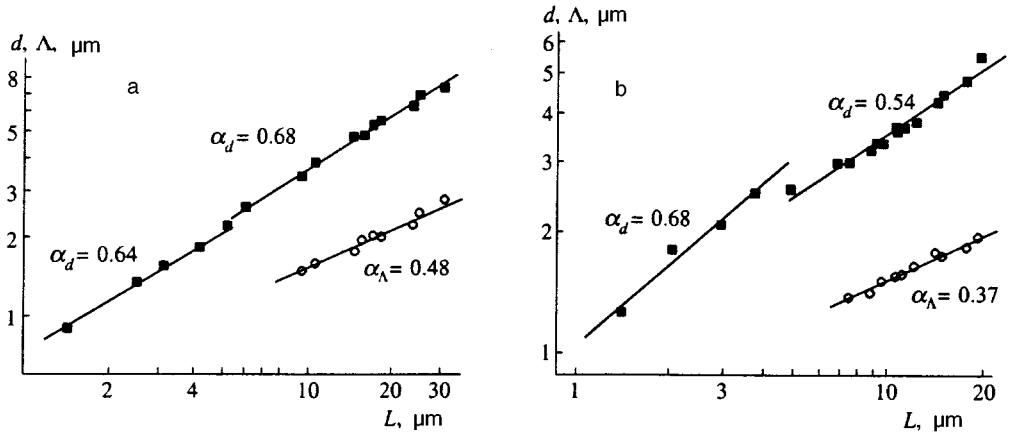

FIG. 3. Geometric parameters of domain structures (d—■, Λ—○ as functions of the thickness of a $Lu_{2.1}Bi_{0.9}Fe_5O_{12}$ film, with the thickness varied by growth (a) and by mechanical polishing (b).

sample, which was affixed to a mount by which it could be rotated relative to the optical axes of the system by an arbitrary angle ϕ_H. The image of the domain structure in the films was examined by a polarization microscope with its objective placed within the mount containing the sample, while the analyzer and the ocular were placed independently on the optical bench. To generate the magnetic field we used an electromagnet with two pairs of orthogonal coils, with which, by varying the operating current, we could change the angle θ_H between the direction of the magnetic field and the film surface and select the necessary relation between the projections of **H** on the normal and on the film surface. The maximum field strengths $H_\parallel$ and $H_\perp$ in the working gap were 10 kOe and 2 kOe, respectively. To measure the magnetic fields we used a sensitive transducer, which in its operating range gave an absolute error of less than 0.1 Oe; however, the nonuniformity of the film and the resultant diffuseness of the phase transition reduced the accuracy in determining the position of the lines on the phase diagram, especially for the first-order phase transitions. A statistical analysis of the results of a sampling of experiments showed that for the second-order phase transitions, the error in the critical fields was no more than 1 Oe, while for first-order phase transitions over the range 200–2000 Oe of the magnetic field, it was 2–20 Oe.

3. EXPERIMENTAL RESULTS

In the absence of a magnetic field the ground state of these films corresponded to a non-labyrinthine domain structure with randomly oriented domain walls, as in the films with $\beta_u \geqslant 1$, and an ordered two-dimensional lattice of stripe domains with modulated or unmodulated domain walls (depending on the thickness). The reason for this result is the large projection of the **M** vector on the film surface, which prevents kinking of the domain walls. Structures with additional closure domains were not observed, since the thickest films that could be grown by the liquid-phase epitaxy method were still thinner than L_{cr2}.

To study how the period d of the stripe domain structure and the period Λ of the wave-like distortions in the domain walls on the sample surface depended on the thickness L, we carried out two groups of experiments on type II films. For the first group of experiments we grew a series of films of different thicknesses (1–30 μm), while in the second group of experiments we used a single film with an initial thickness of 20 μm, which then was reduced in stages to 1.5 μm by mechanical polishing. The results for $d(L)$ and $\Lambda(L)$ for the first and second groups of experiments are shown in Figs. 3a and 3b, respectively, on a log–log plot. The critical thickness L^*_{cr1}, corresponding to the onset of harmonic surface distortions in the domain wall profile, was about 6 μm in both cases.

Approximating $d(L)$ and $\Lambda(L)$ by power laws, $d \propto L^{\alpha_d}$ and $\Lambda \propto L^{\alpha_\Lambda}$ and using the method of least squares, we find that for $L < L^*_{cr1}$ the exponent α_d is equal to 0.64 for the films with thicknesses determined by varying the growth time, and 0.68 for films whose thickness was varied by mechanical polishing. In both cases these values are quite different from that predicted by the theory of Kittel, $\alpha_d = 0.5$. For films with a wave-like distortion of the domain wall profile ($L > L^*_{cr1}$), the value of α_d in the first case increased slightly (to 0.68) and in the second case it decreased to 0.54. This difference can be accounted for by the presence of surface layers formed in the epitaxial films at the final stage of growth,[29] which in the second group of experiments were removed in the first mechanical polishing. This same cause presumably explains the substantial difference in the exponents α_Λ in the function $\Lambda(L)$ for the experiments with the first and second groups (see Fig. 3).

Although the experimental data in Fig. 3 are well represented by a straight line (on the log–log plot), we cannot rule out the possibility that the functions $d(L)$ and $\Lambda(L)$ might not be described by a simple power law, but by more complicated functions. We can state with confidence only that the nature of the functional dependence $d(L)$ changes when the harmonic distortions of the domain wall profile appear in the simple stripe domain structure.

The form of the phase diagram on the $H_\parallel - H_\perp$ plane for films with a small uniaxial anisotropy constant β_u depends on the thickness L and becomes more complicated with increased thickness. An example of the increased complexity of the diagram for a type I film having an anisotropy constant $\beta_u \simeq 0.08$, a thickness $L^*_{cr1} < L = 10$ μm $< L_{cr2}$, and a composition $Lu_{2.1}Bi_{0.9}Fe_{4.96}Mg_{0.04}O_{12}$ (designated No. 1) is

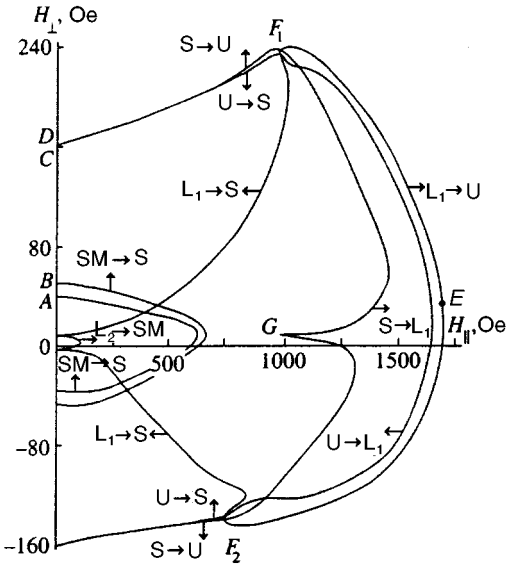

FIG. 4. Phase diagram of a film of $Lu_{2.1}Bi_{0.9}Fe_{4.94}Mg_{0.04}O_{12}$ with $\beta_u \approx 0.08$ and $L = 10$ μm (designated film No. 1) for $\phi_H = 30$ deg.

shown in Fig. 4 with the following notation: U is the uniform state, S is the stripe domain structure with planar (unmodulated) domain walls, SM is the stripe domain structure with modulated domain walls, and $\mathbf{L}_1$ and $\mathbf{L}_2$ are the opposite-polarity lattices of magnetic bubbles; the arrows on the curves show the direction of variation of the field. The origin of the coordinate system is at the center of symmetry of the diagram; therefore the stability boundary of the various domain structures are not shown for negative values of $H_\parallel$.

In the demagnetized state the film, No. 1 contains a periodic stripe domain structure ($d = 3.9$ μm) with a modulated domain wall ($\Lambda = 1.7$ μm), which maintains its stability even over a certain range of the external field **H**. The wavelike surface distortions in the profile of the domain boundaries have disappeared from the line SM→S and the domain structure has become a simple stripe structure. The subsequent evolution of the collection of domains as the magnetic field is increased depended on the direction of the field: for small angles θ_H we observed a transition into the uniformly magnetized state (on the curves S→U), and for large angles, a transition to a hexagonal lattice of magnetic bubbles (on the curves S→L_1 and S→L_2).

If we start with a uniformly magnetized state and reduce the magnetic field, then the type of nucleating domain structure also depends on the direction of **H**: for **H** near the surface normal, a lattice of magnetic bubbles is formed (curves U→L_1 and U→L_2), while for small angles θ_H, a stripe domain structure is formed (curve U→S). The period of the nucleating magnetic bubble lattice is maximum at the point E on the diagram (11.3 μm), and decreases monotonically (to 2.5 μm) as the region of nucleation of the stripe domain structure is approached. The change in the type of nucleating domain structure occurs smoothly, and over a certain range of magnetic field strength and orientation a mixed configuration exists: alternating blocks of stripe domains and magnetic bubbles.

The locations of all the lines in the phase diagram corresponding to the regions of stability of the domain structures of various kinds were determined visually by observing the development of the magnetic state of a small ($\simeq 100 \times 100$ μm^2) region of the film.[4)] The first and simplest step is to locate the curve of loss of stability of the uniformly magnetized state (the curve with the arrows U→L_1, U→L_2, and U→S) and to identify the type of nucleating domain structure. Then we must find the boundaries L_1 and L_2 of the region of stability of the hexagonal magnetic bubble lattice. To do this, we first establish the saturation magnetic field in this direction in order that the angle θ_H correspond to the nucleation of a lattice of magnetic bubbles with the maximum domain density (for example, points $F_{1,2}$ on the diagram in Fig. 4 for the lattice $L_{1)}$, and then make the transition from the uniformly magnetized state to the magnetic bubble lattice by a small reduction in the field $H_\parallel$. Then by a coordinated variation in the fields $H_\parallel$ and $H_\perp$, we move to a point with other coordinates in such a way that the trajectory of the points on the diagram are as close as possible to the curve U→L_1 (or U→$L_{2)}$. In this way we ensured the maximum ordering of the magnetic bubbles without excess change in the density of bubbles (over the equilibrium value) by way of collapse and without transformation of the round magnetic bubbles into elliptical ones.

After a close-packed lattice of magnetic bubbles is obtained, it is necessary at each point of the diagram to increase the magnetizing field smoothly until the bubbles collapse (this corresponds to the points on the curve L_1→U (or L_2→U), while maintaining the angle θ_H in such a way that the image of the point on the diagram moves approximately on the curve U→L_1 or U→L_2. To obtain the next point on the curve L_1→U or L_2→U, all the operations described above must be repeated, and so on. A similar procedure of multiply repeated operations to create the close-packed equilibrium lattice of magnetic bubbles is also used to determine the other stability boundary corresponding to the transition to the stripe domain structure, i.e., the development of an elliptical instability. The only difference is that this transition occurs by reducing the magnetizing field.

The region of existence of a stripe domain structure is determined in a similar way. In zero field $H_\parallel$, a stripe domain structure is nucleated with a period close to the minimum possible, and then a transition is made close to the curve U→S to any other desired point. Then by an increase in the field strength we obtain either a transition to the uniformly magnetized state (the point on the curve S→U) or to the hexagonal magnetic bubble lattice (the point on the curve S→$L_{1,2)}$. The direction of the field must correspond to the normal to the desired curve, since that ensures the greatest accuracy in the measurements. When the field is reduced the point determined is on the curve S→SM corresponding to the suppression of surface modulation of the domain wall profile in a simple stripe domain structure. The procedure for determining the location of the curve SM→S does not require explanation; we merely note that the initial step in this procedure is the nucleation of a modulated stripe domain structure in zero magnetizing field.

When $H = 0$, one frequently observes some preferred di-

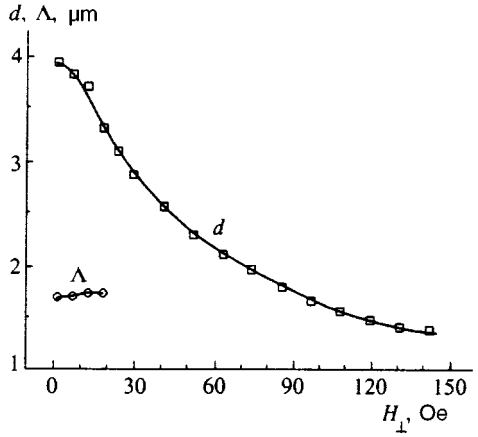

FIG. 5. Dependence of the geometrical parameters (d—□,Λ—○ of the domain structure on the field $H_\perp$ for film No. 1.

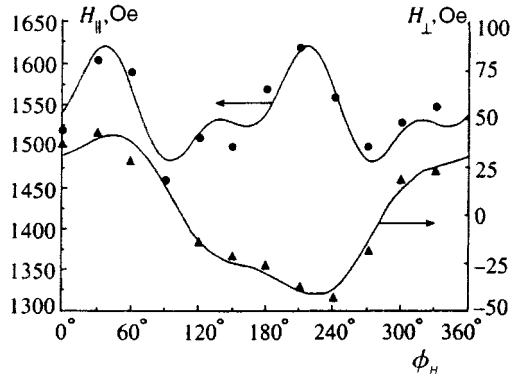

FIG. 6. Position of the point E on the phase diagram for film No. 1 versus the orientation of the field $H_\perp$.

rections along which the stripe domain walls are oriented. This preferred orientation is due to a cubic and, possibly, orthorhombic anisotropy. For a sufficiently large component $H_\perp$ not coinciding with the orientation of the naturally preferred directions, the domain walls become reoriented. When the magnetic field is varied over ranges corresponding to the inner regions of the phase diagram, the period of the stripe domain structure and of the two-dimensional lattices is reorganized by the generation, annihilation, and motion of magnetic defects such as dislocations and disclinations. In some cases, multiple clustering of magnetic dislocations occurs in the form of dislocation walls. Various instabilities of stripe domain structures also occur with the formation of penetrating sinusoidal or sawtooth distortions in the domain boundaries. The transformation of hexagonal lattices into stripe domain structures takes place via the development of an elliptical instability in round magnetic bubbles. In summary, we note that all these processes are similar to those observed in films with $\beta_u \gg 1$.[10,30,31] An important difference, however, is that in the films with a low β_u, global amorphization of the ordered stripe domain structure does not occur in the vicinity of the phase transition (but is typical of films with a dominant uniaxial anisotropy[32]), since the effective stiffness of the system is high.

Figure 5 gives an idea of the modification of the geometric parameters of stripe domain structures as the field strength $H_\perp$ is varied; this figure also shows $d(H_\perp)$ and $\Lambda(H_\perp)$ for film No. 1 for $H_\parallel = 0$. It can be seen that the period of the domain structure depends strongly on the field strength[5)] and falls off with increasing field, whereas the period of the wave-like distortions of the domain walls reacts only weakly to the change in the magnetic field and increases with increasing $H_\perp$.

The dips in the curves $S \rightarrow L_1$ and $L_1 \rightarrow S$ near the horizontal axis (the point G and the apex of the curve $L_2 \rightarrow SM$ in Fig. 4) may be due to the following causes. First, this region of the diagram corresponds to symmetric stripe domain structures ($d_1 = d_2 = d/2$, where d_1 and d_2 are the widths of the domains with different directions of the projection M_z); here is where the greatest difficulty is encountered in the generation and annihilation of magnetic dislocations, through which occur transitions between the stripe domain structure and the lattice of magnetic bubbles. Second, this is the region of the diagram where polarization reversal of the domain walls occurs with a change in the direction of the field $H_\perp$.

The transitions $SM \rightarrow L_1$ and $SM \rightarrow L_2$ are not observed, since out-of-phase distortions are required to nucleate magnetic bubbles from a stripe domain structure. The reverse transformation, nonetheless, does take place, since harmonic distortions of the profile of the closed domain walls are not forbidden. The phase transitions $U \rightarrow S$ and $S \rightarrow U$ are close to second order, and the others are close to first order. Unfortunately, there is no sufficiently precise experimental criterion for the identification of first-order phase transitions in films with $\beta_u \leqslant 1$, unlike the case with $\beta_u \gg 1$, where an inherent attribute of these transformations is the formation of the so-called ''mixed state'' in the nucleation of the domain structure, which is characterized by the coexistence of blocks of opposite-polarity magnetic bubbles and patches of stripe domains.[10,33] Nevertheless, other very good criteria can be used, including the fact that, first, the second-order phase transitions occur with essentially no hysteresis (within the accuracy of the measurements), and second, they are charac-

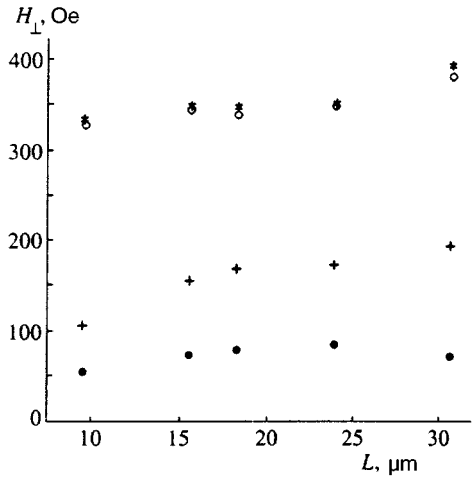

FIG. 7. Position of the points A(●), B(+), C(o) and D(*) as functions of the thickness of a film of composition $Lu_{2.1}Bi_{0.9}Fe_5O_{12}$.

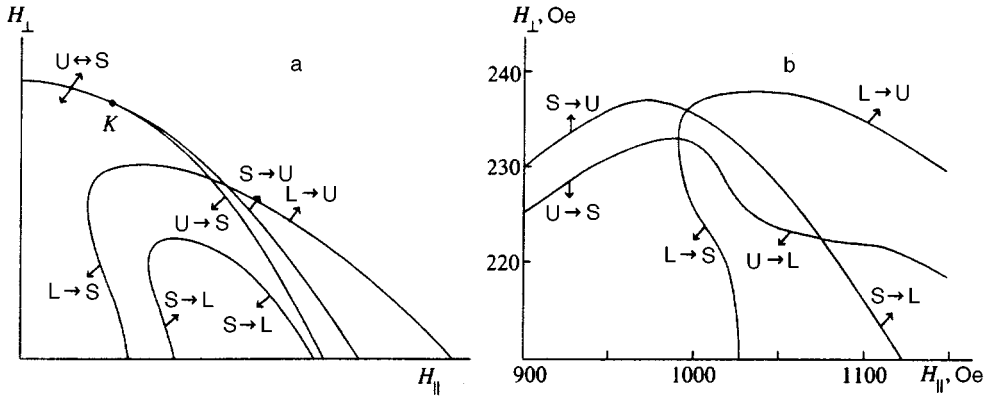

FIG. 8. Schematic plot of the theoretical phase diagram (for $\beta_u \gg 1$) in the neighborhood of a tricritical point (a) and the analogous part of the experimental phase diagram for film No. 1 (b).

terized by nucleation uniformity, the disappearance or transformation of the domain structure over the area of the film, and a relative insensitivity to microscopic defects.

The vertical axis is not a symmetry axis in the diagram because of the effect of the crystallographic (cubic) and induced orthorhombic anisotropy. The change in the position of the film relative to the field $\mathbf{H}_\perp$, which can be characterized by the azimuthal rotation angle ϕ_H from a reference direction, does not result in any qualitative changes in the form of the phase diagram. The entire diagram is topologically similar, for various values of the angle ϕ_H, and the only change is in the position of the characteristic points of the diagram (the points $A-G$ in Fig. 4). By way of example, Fig. 6 shows a plot of the coordinate of the point **E** (the vertex of the diagram with the vertical tangent) versus the angle ϕ_H; the points that are shown are experimental data and the solid curves are the approximating Fourier series, which for $H_\perp$ contain only even harmonics, while for $H_\parallel$ they contain only odd harmonics. For films with a large uniaxial anisotropy constant, similar curves for the points of uniform domain structure nucleation corresponding to a second-order phase transition from a uniformly magnetized state into a nonuniformly magnetized state are used to determine the anisotropy constant, and the orthorhombic and cubic anisotropies are determined by comparison with the results of a calculation.[10,33] In the present case this cannot be done because of the lack of an analytic theory.

As the film thickness is steadily reduced, the only qualitative change in the phase diagram is the disappearance of the region of existence of a stripe domain structure with modulated domain walls in the range of thicknesses $L<L^*_{cr1}$; the positions of the other points on the diagram depend only slightly on the thickness (Fig. 7).

4. CONCLUSIONS

A comparison of the form of the phase diagram for films with $\beta_u<1$ (Fig. 4) with that for $\beta\gg1$ (Fig. 2) of Ref. 10 for a field-induced phase transition shows that they are topologically similar. This cannot be regarded as unexpected because, as mentioned in the Introduction, the distribution of magnetization in the films does not undergo any qualitative changes when β_u passes through unity. Moreover, in films with weak uniaxial anisotropy, one can see ''fine structure'' in the phase diagram, which can scarcely be seen in highly anisotropic uniaxial films. We now discuss this problem in greater detail.

The phenomenological theory of orientational phase transitions in films that has been developed for $\beta_u\gg1$ shows[7,10] that the direct nucleation of hexagonal lattices of magnetic bubbles from the uniformly magnetized state is possible only for $\beta_u\to\infty$, and for $h_\parallel\neq0$ the transformation occurs as a first-order phase transition. The point with coordinates $h_\parallel=0$ and $h_\perp\approx\beta_u$ corresponds to a second-order phase transition and is multicritical, since the line of phase transitions between the uniformly magnetized state and the stripe domain structure terminates there. For finite values of β_u, the line of stability loss of the uniformly magnetized state relative to a transition to a lattice of magnetic bubbles (the $U\to L_{1,2}$ line in the notation of Fig. 4) splits into a line of a second-order phase transitions between the uniform state and the stripe domain structure (the U↔S line) and a line of stability loss of the latter relative to a transition into a magnetic bubble lattice (the line $S\to L_{1,2}$), while the multicritical point divides into two tricritical points R_1 and R_2 located on the curve U↔S symmetrically about the $h_\perp$ axis, where all the effects described here occur more intensely, the lower the value of β_u. Finally, the phase diagram near the tricritical point assumes the form shown in Fig. 8a.[6)] If we now examine in detail the structure of the phase diagram for film No. 1 in the neighborhood of, for example, the F_1 point (Fig. 8b) then it becomes obvious that the main conclusions of the theory developed for highly anisotropic uniaxial films provide a qualitative explanation of the properties of the phase diagram for films with a low value of β_u.

This work was carried out with the financial support of the Russian Fund for Fundamental Research (Project No. 96-02-16082-a) and Korean Science and Engineering Foundation, under the auspices of the Korea–Russia Joint Research Program. The authors are grateful to L. I. Antonov for sharing with us his results on the calculation of the magnetization distribution and for valuable discussions.

Certain results of this work were published in abridged form in Ref. 34.

1)By magnetostatic we mean the field satisfying the equations of magnetostatics that is induced by the desired magnetization vector, and that coincides with the demagnetizing field inside the sample and the fringing field

outside the sample. This explanation is required, since in the Russian scientific literature (unlike the foreign literature) this terminology is not standardized.

[2)]The list of original publications on this subject is very long, and therefore we mention only the monographs[11,14,15] and articles[13,16–22] where a complete bibliography can be found.

[3)]Attempts have been made to calculate the critical thicknesses L_{cr1}, L^*_{cr1} and L_{cr2} (see Refs. 13–22 and the references cited therein); however, reliable estimates were obtained only for the first critical thickness, corresponding to a second-order phase transition.

[4)]Limiting the area of visual observation is necessary to reduce the effect of local inhomogeneities in the film on the measurement results. It must be noted, however, that the films of the chosen composition have considerably more uniform parameters than do films with $\beta_u \geqslant 1$, for which results have been published in Ref. 10. The reason is that in a film with $\beta_u \leqslant 1$, the magnetic sublattice formed by the iron ions are not diluted by gallium or aluminum ions; specifically, fluctuations in the distribution function of these ions are the main cause of the nonuniformity in the magnetization and the effective induced anisotropy field.

[5)]The curve shown in Fig. 5 refers to domain walls oriented parallel to the vector $\mathbf{H}_\perp$, which is always the case in strong enough fields. If the experiment is carried out so that the direction of the field $\mathbf{H}_\perp$ does not initially coincide with the orientation of the domain walls, then increasing the field causes nucleation of blocks of stripe domains within the initial stripe domain structure, with domain walls along the field, which then expand and displace the previous structure.

[6)]The diagram also qualitatively reflects the fact that when the field $\mathbf{H}_\perp$ is reduced, the phase transition between the uniformly magnetized state and the stripe domain structure becomes a first-order phase transition at the point K (Ref. 9).

[1] L. D. Landau and E. M. Lifshitz, Phys. Z. SU **8**, 153 (1935).
[2] C. Kittel, Rev. Mod. Phys. **21**, 541 (1949).
[3] V. G. Bar'yakhtar, A. N. Bogdanov, and D. A. Yablonskiĭ, Usp. Fiz. Nauk **156**, 47 (1988) Usp. Fiz. Nauk **156**, 47 (1988) [Sov. Phys. Usp. **31**, 810 (1988)].
[4] E. Schlömann, J. Appl. Phys. **44**, 1837 (1973).
[5] A. P. Malozemoff and J. C. Slonczewski, *Magnetic Domain Walls in Bubble Materials*, Academic Press, New York (1979).
[6] R. M. Goldstein and M. W. Muller, Phys. Rev. B **2**, 4585 (1970).
[7] V. V. Tarasenko, E. V. Chenskiĭ, and I. E. Dikshteĭn, Zh. Éksp. Teor. Fiz. **70**, 2178 (1976) [Sov. Phys. JETP **43**, 1136 (1976)].
[8] V. G. Bar'yakhtar and B. A. Ivanov, in *Physics of the Condensed State and the Use of Nuclear-Physics Methods in Biology* [in Russian], Leningrad Institute of Nuclear Physics, Leningrad (1979).
[9] V. V. Tarasenko, Fiz. Tverd. Tela (Leningrad) **22**, 503 (1980) [Sov. Phys. Solid State **22**, 294 (1980)].
[10] I. E. Dikshteĭn, F. V. Lisovskiĭ, E. G. Mansvetova *et al.*, Zh. Éksp. Teor. Fiz. **86**, 1473 (1984) [Sov. Phys. JETP **59**, 863 (1984)].
[11] B. N. Filippov and A. P. Tankeev, *Dynamic Effects in Ferromagnets with a Domain Structure* [in Russian], Nauka, Moscow (1987).
[12] L. I. Antonov, S. V. Zhuyravlev, E. V. Lukasheva *et al.*, Fiz. Met. Metalloved. **74**, 23 (1992).
[13] E. V. Lukasheva, Dissertation, Moscow State University, Moscow (1995).
[14] N.M. Sakanskiĭ and M. Sh. Erukhimov, *Physical Properties and Applications of Magnetic Films* [in Russian], Nauka, Novosibirsk (1975).
[15] A. I. Mitsek and V. N. Pushkar', *Real Crystals with Magnetic Ordering* [in Russian], Naukova Dumka, Kiev (1978).
[16] J. Kaczer IEEE Trans. Magnetics **MAG-6**, 442 (1970).
[17] T. I. Nestrelyaĭ, Dissertation, Kuĭbyshev Pedagogical Institute (1971).
[18] L. I. Antonov, Dissertation, Kuĭbyshev Pedagogical Institute (1972).
[19] Yu. G. Lebedev, I. G. Tityakov, and B. N. Filippov, Fiz. Tverd. Tela (Leningrad) **17**, 3149 (1975) [Sov. Phys. Solid State **17**, 2082 (1975)].
[20] G. S. Kandaurova and L. G. Onoprienko, *Fundamental Problems in the Theory of Magnetic Domain Structures* [in Russian], Ural State University, Sverdlovsk (1977).
[21] E. P. Antonets, B. M. Stepanov, and V. A. Fabrikov, Fiz. Met. Metalloved. **49**, 510 (1980).
[22] E. E. Shalygina, Dissertation, Kuĭbyshev Pedagogical Institute (1990).
[23] A. Holst and H. Kronmüller Phys. Stat. Solidi **31**, 787 (1969).
[24] G. A. Jones, T. M . Lacey, and I B. Puchalska, J. Appl. Phys. **53**, 7870 (1982).
[25] R. M. Grechishkin, Yu. M. Zukov, and D. I. Sementsov, Pis'ma Zh. Tekh. Fiz. **15**(5), 45 (1989) [Sov. Tech. Phys. Lett. **15**, 349 (1989)].
[26] M. Grechishkin, Yu. M. Zukov, D. I. Sementsov *et al.*, Kristallographiya **36**, 1484 (1991) [Sov. Phys. Crystallogr. **36**, 842 (1991)].
[27] A. H. Bobeck and E. Della Torre, *Magnetic Bubbles*, North-Holland, Amsterdam (1975).
[28] J. Kaczer and R. Gemperle, Czech. J. Phys. B **11**, 510 (1961).
[29] F. V. Lisovskiĭ and E. G. Mansvetova, Mikroelektronika **8**, 331 (1979).
[30] I. E. Dikshteĭn, F. V. Lisovskiĭ, E. G. Mansvetova *et al.*, Zh. Éksp. Teor. Fiz. **98**, 2158 (1990) [Sov. Phys. JETP **71**, 1213 (1990)].
[31] I. E. Dikshteĭn, F. V. Lisovskiĭ, E. G. Mansvetova *et al.*, Zh. Éksp. Teor. Fiz. **100**, 205 (1991) [Sov. Phys. JETP **73**, 114 (1991)].
[32] I. E. Dikshteĭn, F. V. Lisovskiĭ, E. G. Mansvetova *et al.*, Fiz. Tverd. Tela (Leningrad) **25**, 3591 (1983) [Sov. Phys. Solid State **25**, 2066 (1983)].
[33] A. Hubert, A. P. Malozemoff, and J. C. De Luca, J. Appl. Phys. **45**, 3562 (1974).
[34] F. V. Lisovskiĭ, E. G. Mansvetova, and Ch. M. Pak, in *Abstracts of the 14th All-Union School-Seminar '' New Magnetic Materials for Microelectronics,''* Part II, Moscow (1994), p. 85.

Translated by J. R. Anderson

Anisotropic structure of the gap in high-T_c superconductors: competition between *s*- and *d*-type symmetry

É. A. Pashitskiĭ and V. I. Pentegov

Institute of Physics, Ukrainian National Academy of Sciences, 252650 Kiev, Ukraine
(Submitted 28 May 1996; resubmitted 1 August 1996)
Zh. Éksp. Teor. Fiz. **111**, 298–317 (January 1997)

We show that the anisotropic structure, observed in angle-resolved photoemission spectroscopy experiments, of the gap in high-T_c superconductors based on layered cuprate metal-oxide compounds is the result of the strong anisotropy of the electronic spectrum in the plane of the layers, an anisotropy caused by the hybridization between the overlapping broad and anomalously narrow bands. Depending on the values of the electron–phonon coupling constants and the Coulomb repulsion, which in certain conditions is balanced almost perfectly by the attraction caused by the electron–plasmon interaction, either the $d_{x^2-y^2}$ or the s_{xy} symmetry is realized in the superconducting order parameter. When the initial C_{v4} symmetry of the band spectrum of the Bi(2212) single crystal with a superlattice or the Y(123) single crystal with one-dimensional chains is broken, an anomalous temperature dependence of the anisotropic-gap width Δ is observed, and this dependence differs dramatically from the standard $\Delta(T)$ dependence of the BCS theory.
[S1063-7761(97)01901-X]

1. INTRODUCTION

Recently experiments in angle-resolved photoemission spectroscopy (the ARPES method)[1–6] involving single crystals of layered cuprate metal-oxide compounds of the $Bi_2Sr_2CaCuO_2{+}O_{8+x}$ and $YBa_2Cu_3O_{7-\delta}$ type have revealed a strong anisotropy in the electronic spectrum and the superconducting gap in the plane of the CuO_2 layers. In particular, Shen *et al.*[1] and Dessau *et al.*[6] used the ARPES method to study cuprate metal-oxide compounds with hole conductivity, $YBa_2Cu_3O_{7-\delta}$(123), $YBa_2Cu_4O_{8-\delta}$(124), $Bi_2Sr_2CuO_{6+x}$(2201), and $Bi_2Sr_2CaCu_2O_{8+x}$(2212), and found near the Fermi level what became known as ''flat'' (nondispersive) bands narrower than 45 meV in the vicinity of the symmetric Y- and M-points near the edges of the Brillouin zone.[1)] More accurate measurements by King *et al.*[7] and Gofron *et al.*,[8] who used polarized beams of synchrotron radiation with high energy resolution (better than 3 meV), revealed that these bands are saddles with an infinite effective mass in the $\Gamma-M$ direction for bismuth crystals and in the $\Gamma-M$ direction for yttrium crystals, and with a quasi-one-dimensional electronic spectrum with a positive effective mass in the perpendicular directions. According to Abrikosov *et al.*,[9,10] these quasi-one-dimensional sections of the spectrum and the related Van Hove root singularities in the electron density of states are the reason for the high T_c of the superconductivity transition, $T_c \geqslant 100$ K, due to ordinary Cooper pairing caused by electron–phonon interaction. However, the width of the saddle sections observed by King *et al.*[7] and Gofron *et al.*[8] below the Fermi level, a width corresponding to the Fermi energy $E_{F1} \approx 20-30$ meV, is comparable in order of magnitude to the width of the superconducting gap in high-T_c superconductors ($\Delta_0 \geqslant 20$ meV as $T \to 0$), and is much smaller than the characteristic energy of high-frequency optical phonons corresponding to vibrations of oxygen ions ($\widetilde{\omega}_{ph} \geqslant 50$ meV) in cuprate metal-oxide compounds. For this reason the Coulomb repulsion between electrons in the given case is not weakened, in comparison to the electron–phonon interaction, by the large Bogolyubov-Tolmachev logarithm $\ln(E_{F1}/\widetilde{\omega}_{ph})$, as it is in common superconductors,[11] and the effective coupling constant λ is equal to $\lambda_{ph}-\mu_C$, where λ_{ph} is the dimensionless electron–phonon coupling constant, and μ_C is the Coulomb repulsion constant. Since the screening of the Coulomb repulsion is weak and there is no contribution from transfer processes in the electron–phonon interaction due to the small value of the Fermi momentum ($k_{F1} < \pi/a$), it is difficult to expect a high value for T_c, which with allowance for the root singularity in the density of states is given by the relationship $T_c \approx E_1 \lambda^2$ (see Ref. 9), without any additional attraction mechanism, which to a great extent would balance the large value of μ_C. In particular, the retarded electron–plasmon interaction,[12–14] with low-frequency collective excitations of the electron density (excited by acoustic plasmons) and an acoustic dispersion law, could produce such attraction.[15]

In their photoemission experiments with high angular resolution, Ding *et al.*[16] studied a Bi(2212) single crystal and discovered anisotropic structure in the superconducting gap in the plane of the ($\mathbf{a}-\mathbf{b}$) layers with maxima of different sizes in the directions $\Gamma-M$, $\Gamma-X$, and $\Gamma-Y$ and deep minima (almost reaching zero) in certain intermediate directions. As noted in Refs. 17 and 18, such a Δ vs. θ dependence does not agree with the model of d-wave Cooper pairing of current carriers because of their interaction with spin-density fluctuations,[19–21] a model that predicts the existence of maxima in the gap size in the $\Gamma-M$ direction and zero values for Δ in the $\Gamma-X$ and $\Gamma-Y$ directions.

Ferenbacher and Norman[17] have analyzed the anisotropic structure of the superconducting gap $\Delta(\theta)$ in $Bi_2Sr_2CaCu_2O_{8+x}$ single crystals, observed by Ding *et al.*,[16] on the basis of a phenomenological BCS model with an

electron–electron interaction potential of a special type, which reflects the symmetry properties of the crystal lattice and can be written as a linear combination of separable potentials, $V(\mathbf{k},\mathbf{k}')=\Sigma_i \widetilde{V}_i \eta_i(\mathbf{k})\eta_i(\mathbf{k}')$, where the functions $\eta_i(\mathbf{k})$ form the basis of an irreducible representation of the symmetry group C_{v4}. As Ferenbacher and Norman showed,[17] the best agreement with the experimental data of Ding *et al.*[16] is achieved in the case of singlet s_{xy} wave pairing, with the gap parameter $\Delta(\mathbf{k})\sim\cos k_x \cos k_y$, although such an approximation cannot describe the asymmetry of $\Delta(\theta)$ in different quadrants of the Brillouin zone, an asymmetry related to the superlattice in the $\Gamma-Y$ direction with a wave vector $\mathbf{Q}\approx 0.21(\pi/a,\pi/a)$, where a is the lattice constant in the plane of the layers.[2)] Norman *et al.*[18] arrived at the same conclusion as a result of a detailed analysis of various types of Cooper pairing, including $d_{x^2-y^2}$-wave pairing with an anisotropic gap $\Delta(\mathbf{k})\sim\cos k_x-\cos k_y$ in the field of a periodic superlattice potential and with allowance for layer-to-layer anisotropic s^* pairing, for which $\Delta(\mathbf{k})\sim\cos k_x+\cos k_y$.

However, recent publications[23,24] reported an error in setting up the ARPES experiment of Refs. 16–18 and in the subsequent interpretation of the experimental data. Measurements of the superconducting gap in the X-quadrant of the Brillouin zone were made with the synchrotron radiation polarized in the $\Gamma-X$ direction, while the selection rules for the matrix elements forbid the photoemission of electrons in the $\Gamma-X$ direction for such polarization. Hence the gap maximum observed in this direction by Ding *et al.*[16] is an artifact, caused by parasitic reflexes (''ghosts'') that are related to the transfer processes on the periodic distortions of the crystal (superlattice) in the $\Gamma-Y$ direction.

More accurate measurements by Ding *et al.*[24] of the gap in the X- and Y-quadrants of the Brillouin zone with the light polarized in the $\Gamma-Y$ and $\Gamma-X$ directions, respectively, have shown that there is no superconducting gap along the diagonals of the Brillouin zone, which suggests $d_{x^2-y^2}$ symmetry in the order parameter. An independent argument in favor of the d-wave type of Cooper pairing in high-T_c superconductors is the result of interference tunneling experiments in observing a spontaneous Josephson current in systems of the SQUID type[25–27] and in generating half-integral magnetic-flux quanta in rings with an odd number of weak bonds.[28,29]

Note, however, that the $d_{x^2-y^2}$ symmetry in the superconducting order parameter is not a firm indication of a specific mechanism of Cooper pairing of current carriers and, in particular, cannot serve as proof of the validity of the mechanism of high-T_c superconductivity suggested in Refs. 19–21, in which superconductivity is caused by the exchange of virtual quanta of spin-density excitations (paramagnons) in an almost totally antiferromagnetic Fermi liquid.

In the present paper we show that the extended saddle-like anomalies observed near the edges of the Brillouin zone in the Bi(2212) and Y(123) single crystals[7–9] may be caused by hybridization between overlapping wide and narrow $2D$-bands near the Fermi level. This leads to strong anisotropy of the cylindrical Fermi surface, which tentatively can be separated into ''electron'' and ''hole'' sections with positive and negative curvature (effective mass). As a result of competition between electron–electron attraction (caused by the electron–phonon and electron–plasmon interactions) and Coulomb repulsion, both symmetries of the gap, the $d_{x^2-y^2}$ symmetry and the s_{xy} symmetry (or the s^* symmetry) can be realized, and because of the dependence of the coupling constants on the carrier concentration, a transition from one type of symmetry to the other is possible as doping increases. We also show that when the C_{v4} symmetry of the electronic spectrum is broken because of the emergence of a superlattice in Bi(2212) or because of formation of ordered one-dimensional ($1D$) chains in Y(123), the temperature dependence of the gap size may become anomalous, differing dramatically from the standard dependence of ΔT in the BCS theory.[11]

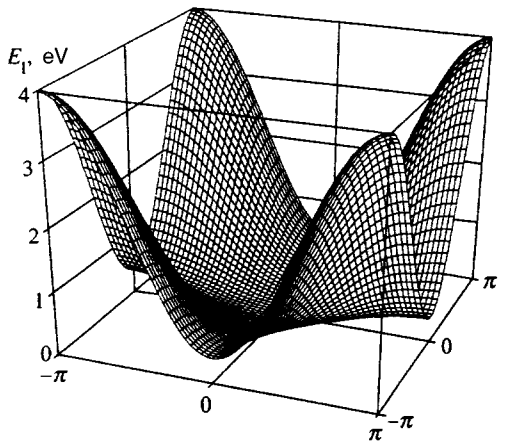

FIG. 1. Dispersion of the wide $2D$-band $E_1(k_x,k_y)$ in cuprate layers of CuO_2 at $t_1=1$ eV and $\tilde{t}_1=0.8$ eV.

2. THE STRUCTURE OF Bi(2212) AND Y(124) SINGLE CRYSTALS

We start our investigation by showing that the saddle-like sections observed in photoemission experiments[7–9] near the M- and Y-points of the Brillouin zone in the electronic spectrum of Bi(2212) and Y(123) single crystals within an extremely narrow energy range (less than 20 meV) can be the result of hybridization between the overlapping wide and anomalously narrow $2D$-bands. Indeed, let us assume that near the Fermi level, in addition to a fairly wide conduction band (wider than 1eV) caused by the overlap of, and hybridization between, the $d_{x^2-y^2}$ orbitals of the copper ions and the $p_{x,y}$ orbitals of the oxygen ions in the plane of the CuO_2 layers[30] and characterized by the following dispersion law (Fig. 1):

$$E_1(k_x,k_y)=-t_1(\cos k_x a+\cos k_y b-2)+\tilde{t}_1(\cos k_x a\ \cos k_y b-1), \quad (1)$$

with a and b the lattice constants in the plane of the layers, there exists a much narrower band (narrower than 0.1 eV) caused, for instance, by the slight overlap of the $d_{3z^2-r^2}$ orbitals of the copper ions Cu^{2+} with a similar dispersion law

$$E_2(k_x,k_y)=-t_2(\cos k_x a+\cos k_y b-2)+\tilde{t}_2(\cos k_x a\ \cos k_y b-1)+E_0, \quad (2)$$

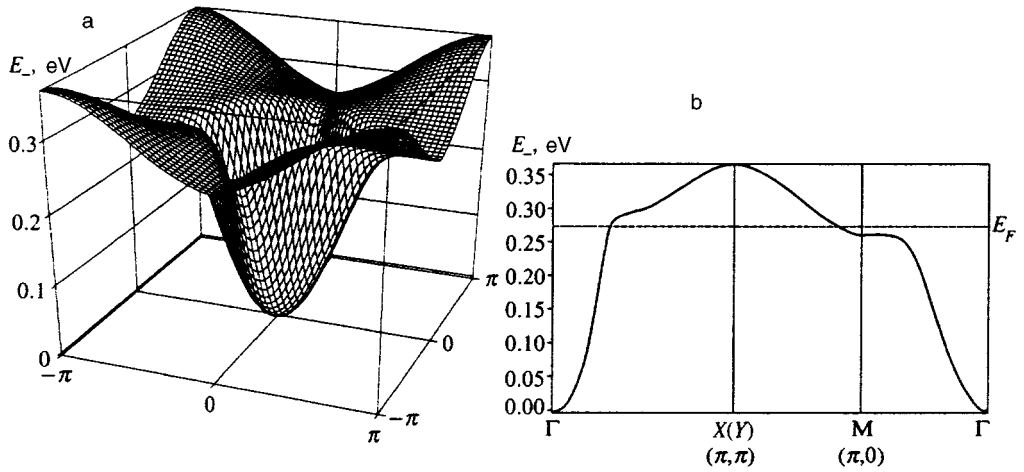

FIG. 2. (a) Dispersion of the lower hybrid branch $E_-(k_x,k_y)$ at $t_1=1$ eV, $\tilde{t}_1=0.8$ eV, $E_0=0.3$ eV, $t_2=0.016$ eV, $\tilde{t}_2=0.032$ eV, and $|V_h|=0.025$ eV. (b) Dispersion of the lower branch along the three principal directions in the Brillouin zone.

where $t_2 \ll t_1$, $\tilde{t}_2 \ll \tilde{t}_1$, and E_0 is the distance between the minima of the overlapping bands ($E_0>0$). Then the electronic spectrum that emerges as a result of hybridization between bands (1) and (2) is given by the following expression:

$$E_\pm(k_x,k_y)=\frac{1}{2}\,[E_1(k_x,k_y)+E_2(k_x,k_y)] \pm \sqrt{\frac{1}{4}\,[E_1(k_x,k_y)-E_2(k_x,k_y)]^2+|V_h|^2}, \tag{3}$$

where V_h is the matrix element of the interaction (repulsion) of crossed branches.

Figure 2(a) depicts the dependence of the energy on k_x and k_y for the lower branch, $E_-(k_x,k_y)$, of the hybrid spectrum (3), and Fig. 2(b) the dispersion relation of this branch along the three principal directions of the Brillouin zone with parameter values ensuring the best agreement (within the given model) with the experimental data of King *et al.*[7] and Gofron *et al.*[8] The upper hybrid branch $E_+(k_x,k_y)$ lies above the Fermi level and hence does not show up in photoemission spectra (it can only be observed in inverse-photoemission spectra).

As Figs. 2a and b show, the electronic spectrum contains two saddle-like structures that sketch in the $\Gamma-M$ directions and have an infinitely large effective mass near the M-points and a finite positive effective mass in the transverse directions $X-M-Y$ if the Fermi level lies fairly close to the bottom of the saddle. At the same time, in the $\Gamma-X$ and $\Gamma-Y$ directions the curvature of the branch $E-(k_x,k_y)$ and, correspondingly, the effective quasiparticle mass are negative. This agrees with Kubo's conclusion,[31] which follows from an analysis of numerical band calculations, states that the sign of the transport mass of the current carriers may be different for different sections of the Fermi surface (with the sign of their cyclotron mass remaining unchanged), and explains the negative sign of the thermoelectromotive force with a positive (hole) sign of the Hall constant in cuprate metal-oxide compounds.[32,33] Thus, the anisotropic Fermi surface determined by the conditions $E_-(k_x,k_y)=E_F$ is divided into ''electron'' and ''hole'' sections corresponding to the hybridization between different orbitals of the Cu^{2+} and O^{2-} ions in the plane of the CuO_2 layers.

By selecting the parameters in a certain way the model spectrum (3) with (1) and (2) can be made to agree both quantitatively and quantitatively with the experimental data[7–9] for Bi(2212) near the M-points and for Y(123) near the Y-points of the Brillouin zone. Note that for a spectrum with a single wide $2D$-band (see Fig. 1) there can be no flat (to within 10^{-3} eV) extended saddle-like sections (observed by King *et al.*[7] and Gofron *et al.*[8]) in the spectrum for fairly broad regions of the Brillouin zone. These saddle-like anomalies emerge only in the case of crossing and hybridization between a wide band and an anomalously narrow $2D$-band whose relative position depends on many parameters—in particular, on the electrostatic interaction of the negatively charged ion clusters $(CuO_2)^{-2}$ clusters and the positively charged ions Ca^{2+} (or Y^{3+}), and on the Coulomb respulsion energy of the electrons at a single site, and these parameters may change with doping (because the extent to which the ions of the crystal lattice are screened changes with the level of doping).

In Y(123) or Y(124) single crystals with CuO chains aligned with the axis $\mathbf{b}\|\mathbf{y}$, near the X-points of the Brillouin zone there emerges additional hybridization between the $2D$-bands and a narrow $1D$-band with a spectrum $E_{1D}(k_y)=W_1\cos \mathrm{k}_y b$, so that the hybrid spectrum for the lower branch in (3) assumes the form

$$\tilde{E}_\pm(k_x,k_y)=\frac{1}{2}\,[E_{1D}(k_y)+E_-(k_x,k_y)] \pm \sqrt{\frac{1}{4}\,[E_{1D}(k_y)-E_-(k_x,k_y)]^2+|\tilde{V}_h|^2}. \tag{4}$$

This implies that in the vicinity of the X-points of the Brillouin zone there are no saddle-like anomalies near the Fermi level, but the extent to which the spectrum becomes one-dimensional grows in the $\Gamma-Y$ direction. The saddle-like structures in the vicinity of the Y-points of the Brillouin zone are retained (see Ref. 8). Note that Combescot and

Leyronas[34] examined the effect of hybridization between the $1D$-band E_{1D} and a wide $2D$-band with a spectrum of type (1), but the existence of the narrow $2D$-band (2), which leads to saddle-like anomalies in the spectrum, was not taken into account.

3. THE SYSTEM OF EQUATIONS FOR A MULTICOMPONENT GAP PARAMETER

When the electronic spectrum is highly anisotropic, one cannot use the standard Éliashberg equation[35] for a gap size that depends only on the energy ω to describe the superconducting state. On the other hand, when the electron–electron interaction is strong ($\lambda \geqslant 1$), one cannot use the BCS model, which correspond to the loose-binding approximation ($\lambda \ll 1$). Furthermore, the BCS theory[11] lacks the rigorous macroscopic justification for using a separable potential $V(\mathbf{k},\mathbf{k}')=V\eta(\mathbf{k})\eta(\mathbf{k}')$ or a combination of such potentials[17] in describing an anisotropic gap $\Delta(\mathbf{k})$.

In view of this, we believe it is advisable to employ the model of a multiband (multivalley) superconductor[36–38] with a multicomponent order parameter Δ_{ij}, which is defined as a set of gaps in different parts of an anisotropic (multiply-connected) cylindrical Fermi surface:

$$\Delta_{ij}(\mathbf{k},\omega)=T\sum_{\omega'}\int\frac{d^2k'}{(2\pi)^2}\sum_{l,m}W_{ij,lm}(\mathbf{k},\mathbf{k}',\omega-\omega')F_{lm}(\mathbf{k}',\omega'), \tag{5}$$

where ω and ω' are discrete Matsubara frequencies, $W_{ij,lm}$ are the matrix elements of the retarded electron–electron interaction calculated with electronic wave functions belonging to different bands, and F_{lm} are the anomalous Green's functions. Of course such an approach cannot yield an explicit angular dependence of the anisotropic gap size, $\Delta(\theta)$, and takes into account only the average values of $|\Delta|$ and the gap sign in different sections of the Fermi surface as a function of the coupling constants (see below).

If we ignore the ''crossed'' Cooper pairing of electrons from different sections of the anisotropic Fermi surface and set $\Delta_{ij}=0$ for $i\neq j$, the system of equations (5) for the gap sizes $\Delta_i=\Delta_{ii}$ after averaging over the momenta (within each section of the Fermi surface) assumes the form

$$\Delta_i(\omega)=-T\sum_{\omega'}\int d\xi\sum_j\nu_j(\xi)\widetilde{W}_{ij}(\omega-\omega')F_{jj}(\xi,\omega'), \tag{6}$$

where ξ is the electron energy measured from the common Fermi level, and ν_j and $\widetilde{W}_{ij}$ are the density of states and the matrix elements $W_{ii,jj}$ averaged over the area of the jth section of the Fermi surface (the matrix elements describe both the retarded electron–electron attraction near the Fermi surface caused by electron–phonon interaction and screened Coulomb repulsion). Here $\widetilde{W}_{ij}$ for $i\neq j$ determine the probability of virtual two-particle transitions between the different sections of the Fermi surface.

Note that ''crossed'' Cooper pairing with $\Delta_{ij}\neq 0$ $(i\neq j)$ can be ignored, since for sections of the Fermi surface with different curvatures, such pairing leads to the formation of pairs with finite momentum $q\sim\pi/a$ whose binding energy is either small or zero (see Ref. 11). However, the system of equations (6) is valid only for extremely pure superconductors, where the scattering of current carriers by imperfections in the crystal lattice and impurities with a characteristic time τ does not mix electronic states belonging to different sections of the Fermi surface in the process of Cooper pairing, i.e., $\tau>\Delta_i^{-1}$. In the case of ''impure'' superconductors, $\tau\Delta_i\leqslant 1$, we must allow for the gap becoming isotropic in the plane of layers ($\mathbf{a}-\mathbf{b}$) because of electron relaxation, i.e., the existence of finite off-diagonal components in the order parameter. In what follows we examine the case of a pure superconductor ($\tau\Delta_{ii}\gg 1$).

The retarded electron–electron interaction in Eqs. (6) in different sections of the Fermi surface, with allowance for electron–phonon interaction and Coulomb repulsion, can be written as

$$\widetilde{W}_{ij}(\omega)=\langle|\widetilde{g}_{ph}(\mathbf{k},\mathbf{k}')|^2D_{ph}(\mathbf{k}-\mathbf{k}',\omega)+\widetilde{\Gamma}_{ee}(\mathbf{k}-\mathbf{k}',\omega)\rangle_{ij}, \tag{7}$$

where $\widetilde{g}_{ph}$ and D_{ph} are the matrix element of the electron–phonon interaction and the phonon Green's function (for nonpolar phonons), $\widetilde{\Gamma}_{ee}$ is the vertex part (a four-prong diagram) of the screened electron–electron Coulomb interaction in the multicomponent Fermi liquid of multiband metals,[36] and angle brackets $\langle\cdots\rangle_{ij}$ stand for averaging over $\mathbf{k}$ in the ith section of the Fermi surface and over $\mathbf{k}'$ in the jth section.

Because of the low concentration of degenerate current carriers in $2D$-layers of CuO_2 in cuprate metal-oxide compounds, and hence the relatively low values of the Fermi momentum $k_F<\pi/a$, for virtual phonons participating in the Cooper pairing of current carriers, transfer processes are unimportant, since the momentum transfer $q\leqslant 2k_F$ lies within the first Brillouin zone, in contrast to the case of ordinary polyvalent metals with $k_F\gg\pi/a$ (in the extended-band scheme). Hence, in ionic crystals of metal-oxide compounds, all phonon branches are either polar (dipole-active) or nonpolar (both acoustic and optical), and polar optical phonons (in particular, high-frequency oxygen vibrational modes) can be incorporated into the dispersion of the effective dielectric constant of the ionic crystal, as is the case with multivalley semiconductors.[39–41].

Furthermore, as shown in Refs. 42 and 43, when a layered crystal contains an anomalously narrow $2D$-band near the Fermi level, partially filled by ''heavy'' (h) charge carriers that are almost totally localized at lattice sites, the entire Brillouin zone contains a slowly decaying branch of acoustic plasmons that hybridizes with longitudinal optical phonons. The electron–electron attraction caused by the exchange of virtual quanta of hybrid phonon–plasma vibrations to a great extent balances the Coulomb repulsion near the Fermi surface in ionic crystals with a large DC dielectric constant. Indeed, in view of the Kramers–Kronig relation for the reciprocal dielectric constant of a crystal, $\widetilde{\varepsilon}^{-1}(q,\omega)$, the electron–plasmon coupling constant is given by[43]

$$\lambda_{pl}=-\frac{2}{\pi}\nu(0)\int_0^\infty\frac{d\omega}{\omega}\langle V_C(q)\mathrm{Im}\,\widetilde{\varepsilon}^{-1}(q,\omega)\rangle=\mu_C^\infty-\mu_C^0, \tag{8}$$

where angle brackets $\langle\cdots\rangle$ stand for averaging over q (momentum transfer), $V_C(q)$ is the matrix element of the unscreened Coulomb interaction, and $\mu_C^{\infty}=\nu(0)\langle V_C(q)/\varepsilon_{\infty}(q)\rangle$ and $\mu_C^{0}=\nu(0)\langle V_C(q)/\varepsilon_0(q)\rangle$ are the dimensionless Coulomb repulsion constants at high ($\omega\to\infty$) and low ($\omega\to 0$) frequencies, with $\varepsilon_{\infty}(q)$ and $\varepsilon_0(q)$ the high- and low-frequency lattice dielectric constants. As (8) implies, when $\varepsilon_0\gg\varepsilon_{\infty}(0)$, i.e., when $\mu_C^{0}\ll\mu_C^{\infty}$, the coupling constant λ_{pl} is approximately equal to μ_C^{∞}, i.e., the combination of the electron–plasmon interaction and the polar electron–phonon interaction balances Coulomb repulsion almost perfectly.

On the other hand, one must bear in mind that in the ''electron'' and ''hole'' sections of the anisotropic Fermi surface with different signs of the effective mass, the Bloch wave functions of the band states, $\Psi_{kj}(\mathbf{r})=u_{kj}(\mathbf{r})e^{ikr}$, are determined by the overlap of, and hybridization between, different orbitals of the Cu^{2+} and O^{2-} ions in the CuO_2 layers, so that the off-diagonal matrix elements $\widetilde{W}_{i,j}$ $(i\neq j)$ must contain the matrix elements of the electron–phonon and electron–plasmon interactions and of unscreened Coulomb repulsion, calculated using different (and almost orthogonal) wave functions:

$$\widetilde{g}_{ij}^{ph}(\mathbf{k},\mathbf{k}')=\sum_{\nu}\int d\mathbf{r}\Psi_{ki}^{*}(\mathbf{r})(\mathbf{e}_{\mathbf{k}-\mathbf{k}'}^{\nu}\nabla\widetilde{V}_{ei}(\mathbf{r}))\Psi_{k'j}(\mathbf{r}), \tag{9}$$

$$\widetilde{g}_{ij}^{pl}(\mathbf{k},\mathbf{k}')=\int d\mathbf{r}\Psi_{ki}^{*}(\mathbf{r})\left(\frac{\widetilde{V}_{ei}^{C}(\mathbf{r})}{Z_i\sqrt{\widetilde{V}_C(q)}}\right)\Psi_{k'j}(\mathbf{r}), \tag{10}$$

$$V_{ij}^{C}(\mathbf{k}-\mathbf{k}')=\int d\mathbf{r}\int d\mathbf{r}'\Psi_{ki}^{*}(\mathbf{r})\Psi_{k'j}^{*}(\mathbf{r}')\frac{e^2}{|\mathbf{r}-\mathbf{r}'|}\times\Psi_{k'j}(\mathbf{r}')\Psi_{ki}(\mathbf{r}), \tag{11}$$

where $\mathbf{e}_{\mathbf{q}}^{\nu}$ is the polarization vector of the νth phonon branch, $\widetilde{V}_{ei}(\mathbf{r})$ and $\widetilde{V}_{ei}^{C}(\mathbf{r})$ are the screened pseudopotential of the electron–ion interaction and its Coulomb part, Z_i is the average charge (valence) of an ion, and $\widetilde{V}_C(q)$ is the matrix element of screened Coulomb repulsion (see Appendix).

Because the nonpolar electron–phonon interaction is local and the wave functions in the electron and hole sections of the Fermi surface are practically orthogonal, the off-diagonal matrix elements (19) can be assumed negligible, so that the matrix elements of the non-local (long-range) Coulomb interaction, Eq. (11), and of the electron–plasmon interaction, Eq. (10), remain finite.

Thus, on the Fermi surface the dimensionless coupling constants can be written as

$$\widetilde{\lambda}_{ii}\equiv-\nu_i\widetilde{W}_{ii}(0)=\lambda_{ii}^{ph}+\lambda_{ii}^{pl}-\mu_{ii},$$
$$\widetilde{\lambda}_{ij}\equiv-\nu_j\widetilde{W}_{ij}(0)=\lambda_{ij}^{pl}-\mu_{ij}, \tag{12}$$

where $\lambda_{ii}^{ph}=\nu_i\langle|g_{ii}^{ph}|^2\rangle$ are the nonpolar electron–phonon coupling constants, $\lambda_{ij}^{pl}=\nu_j\langle|g_{ij}^{pl}|^2\rangle$ are the electron–plasmon and polar electron–phonon coupling constants (which allow for hybridization between acoustic plasmons and dipole-active optical phonons), and $\mu_{ij}=\nu_j\langle V_{ij}^{C}\rangle$ are the corresponding Coulomb repulsion constants at high energies $\omega\geqslant E_{Fi}$, with $\lambda_{ij}^{pl}<\mu_{ij}$ (see Eq. (8)). This implies that $\widetilde{\lambda}_{ij}$ is negative, while λ_{ii} can be either positive or negative depending on the values of the nonpolar electron–phonon coupling constant λ_{ii}^{pb} and the static screened Coulomb repulsion constant $\mu_{ii}^{0}\equiv\mu_{ii}-\lambda_{ii}^{pl}>0$.

4. SYMMETRY OF THE MULTICOMPONENT ORDER PARAMETER IN A Bi(2212) SINGLE CRYSTAL

As noted earlier (see also Ref. 44), because of strong hybridization between the overlapping wide and anomalously narrow $2D$-bands, the electronic spectrum of a layered crystal of the Bi(2212) type contains extended saddle-like structures in the $\Gamma-M$ directions. These structures have been observed in ARPES experiments[7–9] with high energy resolution. As a result of this, at a certain level of doping, when the Fermi level lies above the bottom of the saddle-like structure (Fig. 2), the anisotropic cylindrical Fermi surface can be divided into four pairs of quasi-one-dimensional ''electron'' sections and four ''hole'' sections with, respectively, positive and negative curvature (effective mass). Here the density of states in the quasi-one-dimensional ''electron'' sections near the M-point of the Brillouin zone has a Van Hove root singularity, which strengthens the electron–electron interaction and drives the superconducting transition temperature T_c up.[9,10]

If we ignore the breaking of the C_{v4}-symmetry of the initial spectrum and Fermi surface caused by the appearance of a superlattice in the $\Gamma-Y$ direction,[1] the system of equations (6) allows for four types of solution:

(1) the gaps in the mutually perpendicular ''electron'' sections of the Fermi surface are equal in absolute value but have opposite signs, while the gaps in the ''hole'' sections (along the diagonals of the Brillouin zone) vanish; such a solution corresponds to the $d_{x^2-y^2}$-wave type of Cooper pairing;

(2) the gaps Δ_1 in all the ''electron'' sections of the Fermi surface are equal in absolute value and have the same sign, while the gaps Δ_2 in the ''hole'' sections are nonzero and have a sign (a phase shift by π) opposite to that of Δ_1; such a solution corresponds to the s_{xy}- (or s^*-) type of symmetry in the superconducting order parameter;

(3) the gaps in all sections of the Fermi surface are of the same sign (say $\Delta_1>0$ and $\Delta_2>0$) but differ in magnitude ($\Delta_1\neq\Delta_2$) because of a difference in the densities of states; this corresponds to a quasi-isotropic solution of the s-type; and

(4) the solution with the d_{xy}-type of symmetry of the gap: $\Delta(k)\sim\sin k_x\sin k_y$.

The last solution is probably possible only if the Fermi level is near the bottom of the saddle-like sections, where these sections of the band spectrum contribute little to the effective coupling constant, irrespective of the high density of states.

In the case of $d_{x^2-y^2}$ symmetry (Fig. 3a) the system of equations (6) in the loose-binding approximation leads to a simple equation for the absolute value of the gap size Δ_1:

$$1=(\lambda_{11}-2\lambda_{11}'+\lambda_{11}'')L_1, \tag{13}$$

where

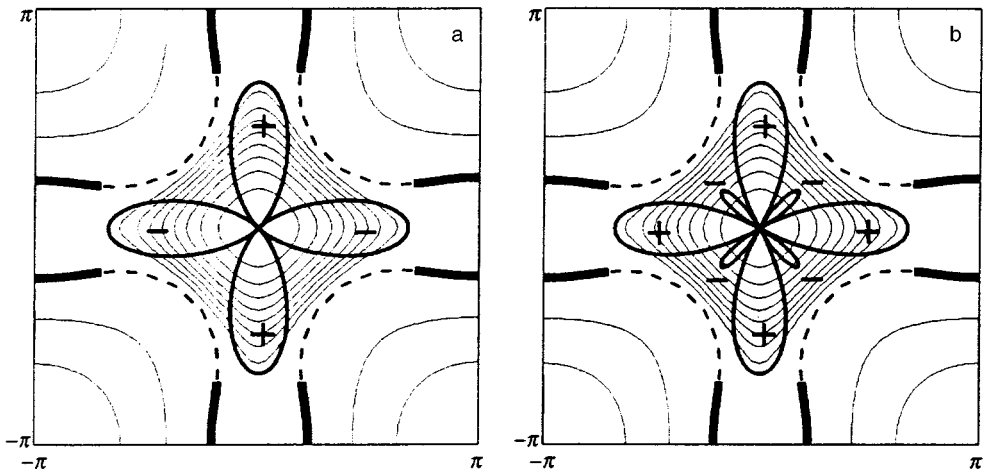

FIG. 3. The structure of the anisotropic superconducting gap for a $d_{x^2-y^2}$-symmetric order parameter and the constant-energy lines of the lower hybrid branch of the spectrum, $E_-(k_x,k_y)$. The thick solid curves in the section of the cylindrical Fermi surface indicate the ''electron'' sections, and the dashed curves the ''hole'' sections. (b) The structure of the anisotropic superconducting gap for a s_{xy}-symmetric order parameter.

$$L_1(|\Delta_1|)=\frac{1}{2}\int_{-E_{F1}}^{E_{F1}}\frac{d\xi}{\sqrt{\xi^2+|\Delta_1|^2}}\sqrt{\frac{E_{F1}}{\xi+E_{F1}}}\times\tanh\frac{\sqrt{\xi^2+|\Delta_1|^2}}{2T},\qquad(14)$$

E_{F1} and λ_{11} are the Fermi energy and the dimensionless coupling constant in the quasi-one-dimensional ''electron'' section of the Fermi surface with a root singularity in the density of states,[9,10] and λ'_{11} and λ''_{11} are the constants of the interaction between electrons in different saddle-like sections of the Fermi surface near the M-points of the Brillouin zone separated by the wave vectors $(\pi/a,\ \pi/a)$ and $(0,2\pi/a)$, respectively.

Note that the case where all coupling constants are negative ($\lambda_{11}<0, \lambda'_{11}<0$, and $\lambda''_{11}<0$) corresponds to the magnon mechanism of Cooper pairing in an almost totally antiferromagnetic Fermi liquid,[11–13] so that a superconducting transition is possible, as Eq. (13) implies, only when the interaction is highly anisotropic, when the absolute value of the coupling constant λ'_{11} along a diagonal of the Brillouin zone satisfies the condition $|\lambda'_{11}|>(1/2)(|\lambda_{11}|+|\lambda''_{11}|)$.

On the other hand, when near the Fermi level the electron–electron attraction caused by the electron–phonon and electron–plasmon interactions is predominant in each of the ''electron'' sections of the Fermi surface, $\lambda_{11}=\lambda_{11}^{ph}-\mu_{11}^0>0$, but there is also Coulomb repulsion between electrons in neighboring sections ($\lambda'_{11}<0$ and $\lambda''_{11}<0$), and Cooper d-pairing is possible, according to (13), if

$$\Lambda_d=\lambda_{11}+2|\lambda'_{11}|-|\lambda''_{11}|>0.$$

In (14), we have allowed here for the fact that when the Fermi level is close to the bottom of the saddle-like structures, the Fermi energy E_{F1} is much lower than the average phonon energy $\bar{\omega}_{ph}\geqslant 50$ meV and, what is more, it is much lower than the energy of the bound (hybrid) phonon–plasma vibrations $\tilde{\Omega}\geqslant 0.1$ eV (see Ref. 43), so that with allowance for the root singularity in the density of states and d-pairing the superconducting transition temperature is, in order of magnitude, equal to $T_c^d\approx E_{F1}\Lambda_d^2$ (see Ref. 9).

In the case of an s-type of symmetry in the order parameter, the system of equations (6) for the gaps Δ_1 and Δ_2 assumes the form

$$\Delta_1=\Delta_1(\lambda_{11}+2\lambda'_{11}+\lambda''_{11})L_1+2\Delta_2(\lambda_{12}+\lambda'_{12})L_2,\qquad(15)$$

$$\Delta_2=\Delta_2(\lambda_{22}+2\lambda'_{22}+\lambda''_{22})L_2+2\Delta_1(\Lambda_{21}+\lambda'_{21})L_1,\qquad(16)$$

where

$$L_2(|\Delta_2|)=\int_0^{\tilde{\Omega}}\frac{d\xi}{\sqrt{\xi^2+|\Delta_2|^2}}\tanh\frac{\sqrt{\xi^2+|\Delta_2|^2}}{2T},\qquad(17)$$

with $\tilde{\Omega}$ the interaction-energy cutoff in the ''hole'' section of the Fermi surface. Here we assume that the Fermi energy in the ''hole'' sections, E_{F2}, is higher than $\tilde{\Omega}$, so that in addition to allowing for the electron–phonon and electron–plasmon interactions the constants λ_{22}, λ'_{22}, and λ''_{22} allow for the Coulomb pseudopotential (see Ref. 11),

$$\mu_{22}^*=\mu_{22}\left[1+\mu_{22}\ln\frac{E_{F2}}{\tilde{\Omega}}\right]^{-1},\qquad(18)$$

while the constants λ_{11}, λ'_{11}, and λ''_{11} contain the unrenormalized Coulomb repulsion constant μ_{11}, since $E_{F1}<\tilde{\Omega}$.

An analysis of the system of equations (15) and (16) shows that for negative values of the cross constants, $\lambda_{ij}<0$ and $\lambda'_{ij}<0$ for $i\neq j$ $(i,j=1,2)$, which means that Coulomb repulsion between the ''electron'' and ''hole'' sections of the Fermi surface is predominant, the solution that is energetically favored and has the highest superconducting transition temperature T_c^s is the one with gaps Δ_1 and Δ_2 of opposite sign (say, $\Delta_1>0$ and $\Delta_2<0$), which is equivalent to the eight-lobe s_{xy}-type of symmetry in the superconducting order parameter (Fig. 3b). When $\lambda_{ij}>0$ and $\lambda'_{ij}>0$ (attraction), the favored solution is the one in which Δ_1 and Δ_2 are of the same sign, which corresponds to quasi-isotropic s pairing.

If for the sake of simplicity we ignore the root singularity in the density of states in (14) and assume that $L_1=L_2=\ln(1.134\tilde{\Omega}/T_c^s)$ as $T\to T_c^s$, then the condition that the system of equations (15) and (16) linearized for $\Delta_{1,2}\to 0$ has a solution yields the following exponential formula for T_c^s of the BCS type:

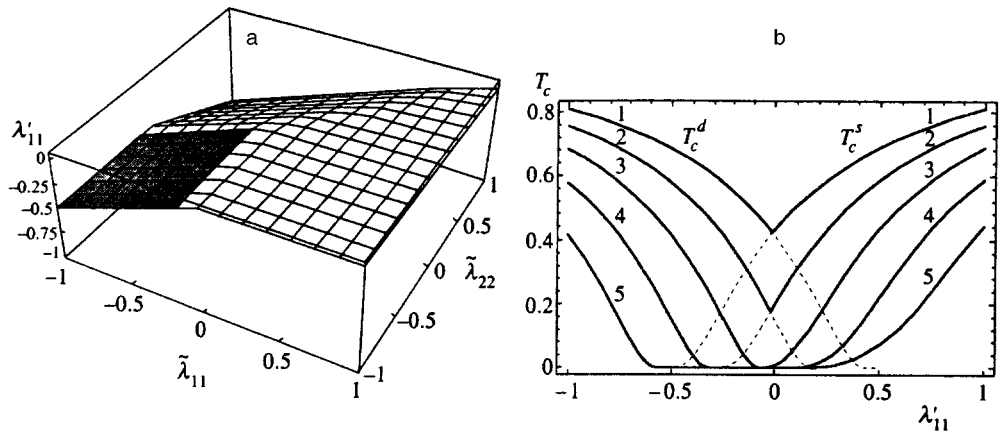

FIG. 4. (a) The surface that separates the regions of d and s pairing in the space of parameters $\tilde{\lambda}_{11} \equiv \lambda_{11} + \lambda''_{11}$, $\tilde{\lambda}_{22} \equiv \lambda_{22} + 2\lambda'_{22} + \lambda''_{22}$, and λ'_{11} at $\lambda_{12}=0.1$. Under the surface $T_c^d > T_c^s$, and above the surface $T_c^s > T_c^d$ except for a shaded area above which s pairing is impossible in the given model. (b) The curves representing the dependence of T_c^s and T_c^d on λ'_{11} at $\tilde{\lambda}_{22}=0.5\tilde{\lambda}_{11}$ and $\tilde{\lambda}_{12}=0.1$ for $\tilde{\lambda}_{11}=1$ (curve *1*), $\tilde{\lambda}_{11}=0.5$ (curve *2*), $\tilde{\lambda}_{11}=0$ (curve *3*), $\tilde{\lambda}_{11}=-0.5$ (curve *4*), and $\tilde{\lambda}_{11}=-1$ (curve *5*). The dashed sections are the continuations of curves *1* and *2* into the regions where the corresponding values of T_c^s and T_c^d are smaller than the maximum value of T_c.

$$T_c^s = 1.134\tilde{\Omega}\,\exp\left[-\frac{1}{\Lambda_s}\right], \tag{19}$$

where

$$\Lambda_s = \frac{2(\lambda_{11}\Lambda_{22} - \tilde{\lambda}_{12}^2)}{(\Lambda_{11}+\Lambda_{22}) \pm \sqrt{(\Lambda_{11}-\Lambda_{22})^2 + 4\tilde{\lambda}_{12}^2}}, \tag{20}$$

$$\Lambda_{ii} = \lambda_{ii} + 2\lambda'_{ii} + \lambda''_{ii}, \quad i = 1,2,$$

$$\lambda_{12}^2 = (\lambda_{12}+\lambda'_{12})(\lambda_{21}+\lambda'_{21}). \tag{21}$$

In (20) we must select the larger of the two solutions, which corresponds to the maximum value of T_c^s.

A comparison of the superconducting transition temperatures T_c^d and T_c^s calculated on the basis of Eqs. (13) and (14), on the one hand, and on the basis of Eqs. (15)–(17), on the other, makes it possible to find the range of parameters in which the gap is either d-symmetric or s-symmetric.

Figure 4a depicts the surface that separates the regions of d- and s-pairing in the space of the parameters $\tilde{\lambda}_{11} \equiv \lambda_{11} + \lambda''_{11}$, $\tilde{\lambda}_{22} \equiv \Lambda_{22}$, and λ'_{11} for a value of the constant of cross interaction between the ''electron'' and ''hole'' sections on the Fermi surface, $\tilde{\lambda}_{12}$, equal to 0.1. Under this surface lies the region of d pairing, where $T_c^s < T_c^d$, and above it the region of s pairing, where $T_c^s > T_c^d$. (Note that within a certain range of λ'_{11}, above the shaded section of the surface there lies a region where there is neither s nor d pairing.)

We see that d pairing is possible only for negative values of the constant λ'_{11}, which describes the interaction between the neighboring ''electron'' sections of the Fermi surface with a momentum transfer $q \approx \pi\sqrt{2}/a$. The smallness of $\tilde{\lambda}_{12}$ is due to the smallness of the matrix element $|g_{12}^{ph}|$ caused, on the one hand, by the local nature of the electron–phonon interaction and the orthogonality of the electronic wave functions in different sections of the Fermi surface and, on the other, by the almost perfect balance between the weakly screened Coulomb repulsion and the retarded electron–plasmon interaction (see Eq. (8)).[3)] As $\tilde{\lambda}_{12}$ increases, the boundary between the regions with s and d pairing shifts in the direction of larger absolute values of the negative coupling constant λ'_{11}.

When there is attraction between electrons belonging to the same quasi-one-dimensional (saddle-like) section of the Fermi surface produced by the electron–phonon and electron–plasmon interactions, i.e., $\tilde{\lambda}_{11} > 0$, even a weak Coulomb repulsion between the electrons in different sections of the Fermi surface, when $\lambda'_{11} < 0$ and $\lambda''_{11} < 0$ (but $|\lambda''_{11}| < \lambda_{11}$ and $\tilde{\lambda}_{11} > 0$), is sufficient for d pairing to emerge. Such repulsion can be the result of either the electron–magnon interaction or incomplete balance between screened Coulomb repulsion and the attraction caused by electron–phonon and electron–plasmon interactions.

On the other hand, Fig. 4a shows that when repulsion in the saddle-like sections is predominant ($\tilde{\lambda}_{11} < 0$), d pairing is possible only for large absolute values of the negative coupling constant λ'_{11}, which corresponds to an anisotropic interaction of current carriers and paramagnons.[19–21]

Figure 4b presents T_c^s and T_c^d as functions of λ'_{11}. The functions were calculating using the linearized equations (13), (15), and (16) for different values of $\tilde{\lambda}_{11}$ at $\tilde{\lambda}_{22}=0.5\tilde{\lambda}_{11}$ and $\tilde{\lambda}_{12}=0.1$. Clearly, when $\tilde{\lambda}_{11} < 0$, there is a range of values of λ'_{11} within which both T_c^s and T_c^d vanish (curves *4* and *5*). At the same time, attraction in the ''electron'' sections of the Fermi surface ($\tilde{\lambda}_{11} > 0$), even against the background of repulsion, which forms the d symmetry of the gap ($\lambda'_{11} < 0$), drives T_c up in comparison to the effect produced by the electron–magnon interaction ($\tilde{\lambda}_{11} < 0$).

Thus, the competition between attraction (caused by the electron–phonon and electron–plasmon interactions) and Coulomb repulsion, combined with the high anisotropy of the electron spectrum, may lead either to a d-symmetric or an s-symmetric superconducting gap, depending on the values of the various parameters. Note that the values of the coupling constant may change considerably as a result of variation of the level of doping (by holes or electrons), as suggested by the strong concentration dependence of T_c in cuprate metal-oxide compounds (see, e.g., Ref. 47). This means that in high-T_c superconductors, such as Bi(2212) single crystals, the order parameter may change symmetry under a changing dopant concentration.

5. BREAKING OF THE SYMMETRY OF THE SPECTRUM AND THE TEMPERATURE DEPENDENCE OF THE GAP WIDTH IN Bi(2212) AND Y(123) SINGLE CRYSTALS

As shown in Refs. 16 and 22, Bi(2212) single crystals contain a long-wave superlattice aligned with one of the diagonals of the Brillouin zone (in the $\Gamma-Y$ direction). This superlattice breaks the C_{v4} symmetry of the electronic spectrum in the plane of the layers. In the case of d pairing, this should not greatly affect the symmetry of the superconducting order parameter $\Delta_d(k)\sim\cos k_x a-\cos k_y a$, which vanishes in the $\Gamma-X$ and $\Gamma-Y$ directions.

However, in the case of s_{xy} pairing, the presence of a superlattice may lead to symmetry breaking in the spectrum and the superconducting gap (for instance, to different values of the gap size in the $\Gamma-X$ and $\Gamma-Y$ directions). Such symmetry of the spectrum and gap has been observed in ARPES experiments.[3–5] In this case, within the model of an anisotropic superconductor with a multicomponent order parameter[36–38] the system of equations (6) can be written as follows ($i,j=1,2,3$):

$$\Delta_1(1-\tilde{\lambda}_{11}L_1)=\Delta_2\tilde{\lambda}^*_{12}L_2+\Delta_3\tilde{\lambda}^*_{13}L_3, \tag{22}$$

$$\Delta_2(1-\tilde{\lambda}^*_{22}L_2)=\Delta_1\tilde{\lambda}_{21}L_1+\Delta_3\tilde{\lambda}^*_{23}L_3, \tag{23}$$

$$\Delta_3(1-\tilde{\lambda}^*_{33}L_3)=\Delta_1\tilde{\lambda}_{31}L_1+\Delta_2\lambda^*_{32}L_2, \tag{24}$$

where Δ_2 and Δ_3 are the gaps in the nonequivalent ''hole'' sections of the Fermi surface (in the $\Gamma-X$ and $\Gamma-Y$ directions), L_3 is defined in (17) with $|\Delta_2|$ replaced by $|\Delta_3|$, and the parameters $\tilde{\lambda}^*_{ij}$ differ from the constants $\tilde{\lambda}_{ij}$ in that the Coulomb constants μ_{ij} are replaced by the pseudopotential $\mu^*_{ij}=\mu_{ij}[1+\mu_{ij}\ln(E_{Fj}/\tilde{\Omega})]^{-1}$. Here the diagonal coupling constants $\tilde{\lambda}_{11}$, $\tilde{\lambda}^*_{22}$, and $\tilde{\lambda}^*_{33}$ are positive because of the strong electron–phonon and electron–plasmon interactions, while the off-diagonal coupling constants $\tilde{\lambda}_{21}$ and $\tilde{\lambda}_{31}$ are negative because of suppression of the electron–phonon interaction caused by the dominant nature of Coulomb repulsion (see Eq. (12)). The constants $\tilde{\lambda}^*_{ij}$ at $i\neq j$ ($j=2,3$) can be either negative or positive thanks to the weakening of repulsion by the factor $[1+\mu_{jj}\ln(E_{Fj}/\tilde{\Omega})]$, although in the given case the Bogolyubov–Tolmachev logarithm is much smaller than in common superconductors.[11]

Equations (22)–(24) imply that for $\tilde{\lambda}_{11}>0$ and $\tilde{\lambda}^*_{ii}>0$ ($i=2,3$) but $\tilde{\lambda}_{21}<0$ and $\tilde{\lambda}_{31}<0$ (with $\tilde{\lambda}^*_{ij}$ of arbitrary sign) the absolute values of Δ_1, Δ_2, and Δ_3 attain their maxima when the signs of Δ_2 and Δ_3 are opposite to the sign of Δ_1 (say, $\Delta_2<0$ and $\Delta_3<0$ for $\Delta_1>0$), which corresponds to the breaking ($\Delta_2\neq\Delta_3$) of the symmetry of the s_{xy}-type in the superconducting order parameter (Fig. 5a).

Note that such a many-lobed gap structure, with the ''lobes'' in the $\Gamma-M$ and $\Gamma-X(Y)$ directions having different signs (opposite phases), can, at least in principle, lead to generation of spontaneous magnetic fluxes in superconducting Bi(2212) rings for certain patterns of the weak (Josephson) bonds.[29] On the other hand, because the signs of the gap ''lobes'' in the $\Gamma-M$ directions in the case of s_{xy} symmetry are the same, no spontaneous Josephson current should appear in interference experiments with tunneling junctions on the mutually perpendicular faces of a layered Bi(2212) single crystal[25–27] (see also below). At the same time, if one of the tunneling junctions is aligned with a diagonal of the Brillouin zone (say, $\Gamma-X$), then in such a circuit there should, at least in principle, be a phase shift by π because the signs (phases) of the ''lobes'' of the order parameter in the $\Gamma-M$ and $\Gamma-X$ directions are opposite (see Fig. 5a). Such tunneling experiments should resolve the problem of the type of symmetry of the superconducting order parameter in Bi(2212) for different doping levels.

In Y(123) and Y(124) single crystals the quartic symmetry C_{v4} is broken because of the $1D$-chains of CuO forming along the axis $\mathbf{b}\|\mathbf{y}$ when oxygen content is at its maximum. Here to approximately describe the structure of the anisotropic superconducting gap we can use the system of equations (22)–(24), provided that Δ_1, and Δ_2 are interpreted as the gap sizes in the cylindrical sections of the Fermi surface that are coupled with the $2D$-layers of CuO_2 by the Cooper pairing of the electrons on, respectively, the ''banks'' of the quasi-one-dimensional extended saddle-like structures in the vicinity of the Y-points of the Brillouin band and in the region of strong hybridization between the $1D$- and $2D$-bands in the vicinity of the X-points of the Brillouin zone, and Δ_3 is interpreted as the gap size in the flat sheets of the Fermi surface that are coupled to the $1D$-chains of CuO. Allowing for the Van Hove root singularity in the density of states of the wide $1D$-band, we can write the integral L_3 as

$$L_3=\frac{1}{2}\int_{-\tilde{\Omega}}^{\tilde{\Omega}}\frac{d\xi}{\sqrt{\xi^2+\Delta_3^2}}\sqrt{\frac{E_{F3}}{\xi+E_{F3}}}\tanh\sqrt{\frac{\xi^2+\Delta_3^2}{2T}}, \tag{25}$$

where E_{F3} is the Fermi energy of the electrons in the $1D$-chains ($E_{F3}\gg\tilde{\Omega}$). Combescot and Leyronas[34] found that Δ_1 and Δ_2 have opposite signs ($\Delta_1>0$ and $\Delta_2<0$), and the sign of the principal ''lobe'' of Δ_3 in the $\Gamma-Y$ direction (along the $1D$-chains) coincides with the sign of Δ_2. The corresponding structure of a gap with opposite signs in the $\Gamma-X$ and $\Gamma-Y$ directions is shown in Fig. 5b.

Note that the possibility that such a gap structure exists in Y(123) and imitates the d-wave type of symmetry in the superconducting order parameter in the tunneling experiments of Wollman *et al.*,[25] Iguchi and Wan,[26] and Browner and Ott[27] was pointed out independently in Refs. 48 and 49.

To determine the temperature dependence of the parameters $\Delta_1<0$, $\Delta_2<0$, and $\Delta_3<0$, we solved the system of nonlinear equations (22)–(24) numerically. Figure 6 depicts the results of calculations obtained with $\tilde{\lambda}_{21}<0$, $\tilde{\lambda}_{31}<0$, and $\tilde{\lambda}^*_{ij}<0$ (for $i\neq j$) but $\tilde{\lambda}_{11}>0$ and $\tilde{\lambda}^*_{ii}>0$ ($i=2,3$). Clearly, in this case the temperature behavior of the negative gaps Δ_2 and Δ_3 differs dramatically from the behavior predicted by BCS theory. In particular, a ''step'' dependence of Δ_2 on T, which qualitatively agrees with the experimental data of Ref. 50, can be achieved by proper selection of the values of the parameters in the problem. Figure 6 shows that the anisotropy of the absolute value of $\Delta(\theta)$ is temperature-dependent and increases as T_c is approached.

6. CONCLUSIONS

Using the model of a superconductor with a multicomponent order parameter, we found that the anisotropic struc-

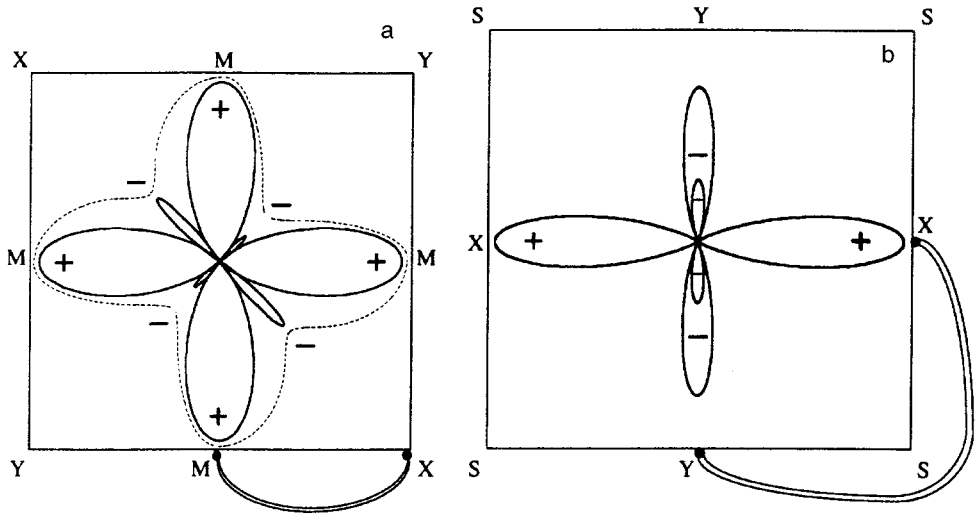

FIG. 5. (a) The structure of the gap in Bi(2212) with broken s_{xy} symmetry of the ''butterfly'' type.[48] (b) The structure of the anisotropic gap in Y(123) imitating d pairing.

ture of the superconducting gap, observed through ARPES experiments with high-T_c superconductors based on cuprate metal-oxide compounds, is a consequence of the strong anisotropy of the electronic spectrum in the plane of the layers. Such anisotropy may be the result, on the one hand, of hybridization between overlapping wide and narrow bands and, on the other, of competition between effective attraction caused by electron–phonon and electron–plasmon interactions and Coulomb repulsion. Depending on the values of the coupling constants, the superconducting gap is either d-symmetric or s-symmetric. Furthermore, since the coupling constants and the characteristic interaction energies (in particular, the Fermi energy E_{F1} in the saddle-like sections of the Fermi surface, and the energy of acoustic plasmons hybridizing with optical phonons) depend on the carrier concentration, a fact revealed by a strong concentration dependence of T_c for cuprate metal-oxide compounds,[47] it becomes possible, at least in principle, to initiate a transition from one type of symmetry to the other by varying the doping level. According to a recent report,[51] a change in the symmetry of the order parameter in Tl(2201) and Bi(2212) occurs under variations of oxygen content.

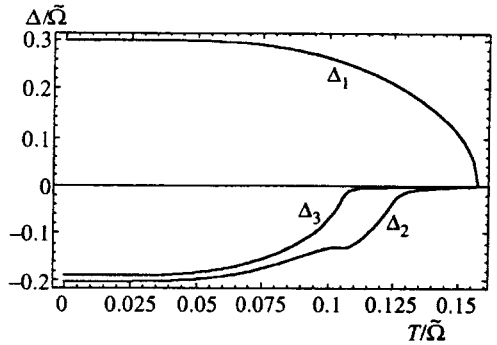

FIG. 6. The temperature curves of the positive (Δ_1) and negative (Δ_2 and Δ_3) parameters of the superconducting gap for the following values of the coupling constants: $\tilde{\lambda}_{11}=0.58$, $\tilde{\lambda}^*_{22}=0.45$, $\tilde{\lambda}^*_{33}=0.42$, $\tilde{\lambda}^*_{12}=-0.01$, $\tilde{\lambda}^*_{13}=-0.0$, $\tilde{\lambda}_{21}=-0.0015$, $\tilde{\lambda}^*_{23}=-0.021$, $\tilde{\lambda}_{31}=-0.001$, and $\tilde{\lambda}^*_{32}=-0.001$; here $E_{F1}/\tilde{\Omega}=0.7$.

When in Bi(2212) single crystals with a superlattice or in Y(123) single crystals with ordered $1D$-chains the initial C_{v4} symmetry of the band spectrum in the plane of the layers is broken, one may observe asymmetric structures in the anisotropic superconducting gap and an anomalous temperature behavior of the gap size differing dramatically from the standard temperature behavior of Δ in the BCS theory.

APPENDIX

In the case of ''heavy'' (h) charge carriers in the anomalously narrow band, which are almost totally localized at crystal lattice sites, the matrix element of electron–plasmon coupling can be calculated by using the Hamiltonian of the electron–ion interaction,

$$H_{int}^{(ei)}=\sum_n \left[\delta\mathbf{R}_n \nabla \tilde{V}_{ei}(\mathbf{r}-\mathbf{R}_n^0) + \frac{\delta Z_i(\mathbf{r}-\mathbf{R}_n^0)}{Z_i}\, \tilde{V}_{ei}^C(\mathbf{r}-\mathbf{R}_n^0)\right], \tag{A1}$$

where $\tilde{V}_{ei}$ and $\tilde{V}_{el}^C$ is the screened electron–ion interaction pseudopotential and its Coulomb part, $\delta\mathbf{R}_n$ is a small displacement of an ion from its equilibrium position $\mathbf{R}_n^0$, and δZ_i is the deviation of the charge of an ion with a varying (fluctuating) valence from its average value Z_i at the nth site caused by the longitudinal field $\varphi(\mathbf{r})$ of the collective vibrations of the number density of the h-carriers. The first term on the right-hand side of Eq. (A1) describes the ordinary electron–phonon interaction with acoustic and optical phonons in the harmonic approximation with matrix elements (12). The second term corresponds to the adiabatic electron–plasmon interaction and, with allowance for the Poisson equation

$$\Delta\varphi(\mathbf{r})=-4\pi e\sum_n \delta Z_i(\mathbf{r}-\mathbf{R}_n^0)$$

in the Fourier representation, by analogy with (12) assumes the form

$$\tilde{g}_{ij}^{pl}(\mathbf{k},\mathbf{k}')=\int d\mathbf{r}\Psi_{ik}^{*}(\mathbf{r})\,\frac{(\mathbf{k}-\mathbf{k}')^2\varphi_{\mathbf{k}-\mathbf{k}'}}{4\pi Z_i e}\,\tilde{V}_{ei}^{C}(\mathbf{r})\Psi_{jk'}(\mathbf{r}), \tag{A2}$$

where $\varphi_{\mathbf{q}}$ is the Fourier transform of the potential $\varphi(\mathbf{r})$, which is related to the Fourier transform of the perturbation $\delta Z_i(\mathbf{q})$ of the ion charge density by the formula $q^2\varphi_{\mathbf{q}}=4\pi e\,\delta Z_i(\mathbf{q})$.

On the other hand, the field operators of the collective excitations of the charge density are defined as $\hat{\varphi}_{\mathbf{q}}^{+}\equiv\varphi_{\mathbf{q}}^{*}c_{\mathbf{q}}^{+}$ and $\hat{\varphi}_{\mathbf{q}}\equiv\varphi_{\mathbf{q}}\hat{c}_{\mathbf{q}}$, where $\varphi_{\mathbf{q}}^{*}=\varphi_{-\mathbf{q}}$, and $\hat{c}_{\mathbf{q}}^{+}$ and $\hat{c}_{\mathbf{q}}$ are the creation and annihilation Bose operators, which are related to the electron density operators $\hat{\rho}_{\mathbf{q}}=\Sigma\hat{a}_{\mathbf{k}+\mathbf{q},\sigma}^{+}\hat{a}_{\mathbf{k},\sigma}$ by

$$\hat{\rho}_{\mathbf{q}}=\frac{q^2}{4\pi e}\,\hat{\varphi}_{\mathbf{q}}=\frac{q^2\varphi_{\mathbf{q}}}{4\pi e}\,\hat{c}_{\mathbf{q}},\quad \hat{\rho}_{-\mathbf{q}}=\frac{q^2}{4\pi e}\,\hat{\varphi}_{\mathbf{q}}^{+}=\frac{q^2\varphi_{\mathbf{q}}^{*}}{4\pi e}\,\hat{c}_{\mathbf{q}}^{+}. \tag{A3}$$

In view of this, the Coulomb Hamiltonian

$$H_C=\frac{1}{2}\sum_{\mathbf{q}}V_C(\mathbf{q})\hat{\rho}_{\mathbf{q}}\hat{\rho}_{-\mathbf{q}} \tag{A4}$$

in the self-consistent field approximation, with allowance for adiabatic screening of low-frequency perturbations of the charge density of h-carriers by almost free ''light'' (l) current carriers within a broad conduction band, can be written to high accuracy in a form similar to the Fröhlich Hamiltonian:

$$\tilde{H}_C\cong\sum_{\mathbf{q},\mathbf{k},\sigma}\frac{q^2}{4\pi e}\,\varphi_{\mathbf{q}}\tilde{V}_C(\mathbf{q})(\hat{a}_{\mathbf{k}+\mathbf{q},\sigma}^{+}\hat{a}_{\mathbf{k},\sigma}\hat{c}_{\mathbf{q}}^{+}+\text{H.c}),$$

$$\tilde{V}_C(\mathbf{q})=\frac{4\pi e^2}{q^2+\kappa_l^2}, \tag{A5}$$

with κ_l the reciprocal radius of screening by the l-carriers.

At the same time, the vertex part (a four-prong diagram) of the retarded screened Coulomb interaction in the regions where there are slowly decaying acoustic plasmons ($qv_{Fh}\ll\omega\ll qv_{Fl}$) has the form[13,43]

$$\Gamma_{ee}(\mathbf{q},\omega)\equiv\frac{4\pi e^2}{q^2\varepsilon(\mathbf{q},\omega)}\cong\tilde{V}_C(\mathbf{q})\,\frac{\omega^2}{\omega^2-\omega_{pl}^2(\mathbf{q})}, \tag{A6}$$

where $\omega_{pl}(\mathbf{q})\approx q\Omega_h/\sqrt{q^2+\kappa_l^2}$, with Ω_h the plasma frequency of the h-carriers.

By analogy with the electron–phonon interaction, we can introduce the plasma Green's function

$$D_{pl}(\mathbf{q},\omega)=\frac{\omega_{pl}(\mathbf{q})}{2}\left[\frac{1}{\omega-\omega_{pl}(\mathbf{q})+i\delta}-\frac{1}{\omega+\omega_{pl}(\mathbf{q})-i\delta}\right], \tag{A7}$$

so that Eq. (A6) assumes the form

$$\Gamma_{ee}(\mathbf{q},\omega)=\tilde{V}_C(\mathbf{q})[D_{pl}(\mathbf{q},\omega)+1]. \tag{A8}$$

The first term on the right-hand side corresponds to the retarded electron–electron interaction caused by the exchange of virtual acoustic plasmons, and the corresponding effective electron–plasmon interaction Hamiltonian can be written

$$\hat{H}_{e-pl}=\sum_{\mathbf{k},\mathbf{q},\sigma}g_{pl}(\mathbf{q})\hat{a}_{\mathbf{k}+\mathbf{q},\sigma}^{+}\hat{a}_{\mathbf{k},\sigma}(\hat{c}_{\mathbf{q}}^{+}+\hat{c}_{-\mathbf{q}}), \tag{A9}$$

where $g_{pl}^2(\mathbf{q})=\tilde{V}_C(\mathbf{q})$. Comparing (A9) and (A5), we find that

$$\frac{q^2\varphi_{\mathbf{q}}}{4\pi e}=\frac{g_{pl}(\mathbf{q})}{\tilde{V}_C(\mathbf{q})}=\frac{1}{\sqrt{\tilde{V}_C(\mathbf{q})}}, \tag{A10}$$

from which Eq. (13) follows. Note that because of the singularity of the Coulomb part of the pseudopotential, $\tilde{V}_{ei}^{C}(\mathbf{r})$, at the point $r=0$, in the electronic wave functions $\Psi_{\mathbf{k},i}(\mathbf{r})$ we can replace the smooth Bloch factors $u_{\mathbf{k},i}(\mathbf{r})$ by $u_{\mathbf{k},i}(0)$ and take the latter outside the integral with respect to $\mathbf{r}$. If we also bear in mind that the Fourier transform of $\tilde{V}_{ei}^{C}(\mathbf{r})$ is

$$\tilde{V}_{ei}^{C}(\mathbf{q})=\frac{4\pi e^2 Z_i}{q^2+\kappa_l^2},$$

we can write the matrix element of the electron–plasmon interaction in a partially factorized form,

$$\tilde{g}_{ij}^{pl}(\mathbf{k},\mathbf{k}')\cong u_{\mathbf{k},i}^{*}(0)u_{\mathbf{k},j}(0)g_{pl}(\mathbf{k}-\mathbf{k}'), \tag{A11}$$

which reflects the anisotropy of the band spectrum in single crystals of cuprate metal-oxide compounds.

[1)] In $Nd_{2-x}Ce_xCuO_4$ compounds, where conductivity is of the electron type, there are no ''flat'' bands near the Fermi level.[1]

[2)] Note that Withers *et al.*[22] were the first to point out the existence of a superstructure in Bi(2212).

[3)] Earlier in the double-band superconductor model it was assumed[45,46] that the off-diagonal band-to-band coupling constant is at its maximum.

[1] Z.-X. Shen, D. S. Dessau, B. O. Wells, D. M. King, W. E. Spicer, A. J. Arko, D. Marshall, L. W. Lombardo, A. Kapitulnik, P. Dickinson, S. Doniach, J. DiCarlo, T. Loeser, and C. H. Park, Phys. Rev. Lett. **70**, 1553 (1993).

[2] W. N. Hardy, D. A. Bonn, D. C. Morgan, Ruixing Liang, and Kuan Zhang, Phys. Rev. Lett. **70**, 3999 (1993).

[3] R. J. Kelley, Jian Ma, C. Quitmann, G. Margaritondo, and M. Onellion, Phys. Rev. B **50**, 590 (1994).

[4] R. J. Kelley, Jian Ma, G. Margaritondo, and M. Onellion, in *Proc. 4th Int. Conf. M^2S HTSC*, Grenoble (France), July 1994, p. 268.

[5] Jian Ma, P. Almeras, R. J. Kelley, H. Berger, G. Margaritondo, X. Y. Cai, Y. Feng, and M. Onellion, Phys. Rev. B **51**, 9271 (1995).

[6] D. S. Dessau, Z.-X. Shen, D. M. King, D. S. Marshall, L. W. Lombardo, P. H. Dickinson, A. G. Loeser, J. DiCarlo, C.-H. Park, A. Kapitulnik, and W. E. Spicer, Phys. Rev. Lett. **71**, 2781 (1993).

[7] D. M. King, Z.-X. Shen, and D. S. Dessau, Phys. Rev. Lett. **73**, 3298 (1994).

[8] K. Gofron, J. C. Campuzano, A. A. Abrikosov, M. Lindroos, A. Bansil, H. Ding, D. Koelling, and B. Dabrowski, Phys. Rev. Lett. **73**, 3302 (1994).

[9] A. A. Abrikosov, J. C. Campuzano, and K. Gofron, Physica C **214**, 73 (1993).

[10] A. A. Abrikosov, Physica C **214**, 107 (1993); **222**, 191 (1994); **244**, 243 (1995).

[11] J. R. Schrieffer, *Theory of Superconductivity*, W. A. Benjamin, New York (1964).

[12] H. Fröhlich, Phys. Lett. A **26**, 169 (1968); J. Phys. C **1**, 544 (1968).

[13] É. A. Pashitskiĭ, Zh. Éksp. Teor. Fiz. **55**, 2387 (1968) [Sov. Phys. JETP **28**, 1267 (1969)]; **56**, 662 (1969) [Sov. Phys. JETP **29**, 362 (1969)].

[14] J. Ruvalds, Adv. Phys. **30**, 677 (1981).

[15] D. Pines and J. R. Schrieffer, Phys. Rev. **124**, 1387 (1961).

[16] H. Ding, J. C. Campuzano, A. F. Bellman, T. Yokoya, M. R. Norman, M. Randeria, T. Takahashi, H. Katayama-Yoshida, T. Mochiku, K. Kadowaki, G. Jennings, Phys. Rev. Lett. **74**, 2784 (1995); **75**, 1425 (1995).

[17] R. Ferenbacher and M. R. Norman, Phys. Rev. Lett. **74**, 3884 (1995).

[18] M. R. Norman, M. Randeria, H. Ding, and J. C. Campuzano, Phys. Rev. B **52**, 615 (1995).

[19] A. J. Millis, H. Monien, and D. Pines, Phys. Rev. B **42**, 167 (1990).
[20] P. Monthoux, A. V. Balatsky, and D. Pines, Phys. Rev. B **46**, 14803 (1992).
[21] P. Monthoux and D. Pines, Phys. Rev. B **47**, 6069 (1993).
[22] R. L. Withers *et al.*, J. Phys. C **21**, 6067 (1988).
[23] M. R. Norman, M. Randeria, H. Ding, J. C. Campuzano, and A. F. Bellman, Phys. Rev. B **52**, 15107 (1995).
[24] H. Ding, M. R. Norman, J. C. Campuzano *et al.*, E-prints archive cond-mat/9603044.
[25] D. A. Wollman, D. J. Van Harlingen, W. C. Lee, D. M. Ginsberg, and A. J. Leggett, Phys. Rev. Lett. **71**, 2134 (1993); D. A. Wollman, D. J. Van Harlingen, J. Giapintzakis, and D. M. Ginsberg, Phys. Rev. Lett. **74**, 797 (1995).
[26] I. Iguchi and Z. Wan, Phys. Rev. B **49**, 12388 (1994).
[27] D. A. Browner and H. R. Ott, Phys. Rev. B **50**, 6530 (1994).
[28] C. C. Tsuei, J. R. Kirtley, C. C. Chi, Lock See Yu-Jahnes, A. Gupta, T. Shaw, J. Z. Sem, and M. B. Ketchen, Phys. Rev. Lett. **73**, 593 (1994).
[29] J. R. Kirtley, C. C. Tsuei, Martin Rupp, J. Z. Sun, Lock See Yu-Jahnes, A. Gupta, M. B. Ketchen, K. A. Moler, and M. Bhushan, Phys. Rev. Lett. **76**, 1336 (1996).
[30] J. Yu, S. Massida, and A. J. Freeman, Physica C **152**, 273 (1988).
[31] Y. Kubo, Phys. Rev. B **50**, 3181 (1994).
[32] P. Mandal, A. Poddar, P. Choudhury *et al.*, Indian J. Pure and Appl. Phys. **30**, 531 (1992).
[33] N. L. Wang, Y. Chong, C. Y. Wang, D. J. Huang, Z. Q. Mao, L. Z. Cao, and Z. J. Chen, Phys. Rev. B **47**, 3347 (1993).
[34] R. Combescot and X. Leyronas, Phys. Rev. Lett. **75**, 3732 (1995).
[35] G. M. Éliashberg, Zh. Éksp. Teor. Fiz. **38**, 966 (1960) [Sov. Phys. JETP **11**, 696 (1960)]; **39**, 1437 (1960) [Sov. Phys. JETP **12**, 1000 (1961)].
[36] B. T. Geĭlikman, Zh. Éksp. Teor. Fiz. **48**, 1194 (1965) [Sov. Phys. JETP **21**, 796 (1965)]; Usp. Fiz. Nauk **88**, 327 (1973) [Sov. Phys. Usp. **9**, 142 (1973)].
[37] É. A. Pashitskiĭ and A. S. Shpigel', Ukr. Fiz. Zh. (Russ. Ed.) **23**, 669 (1978).
[38] A. M. Gabovich, É. A. Pashitskiĭ, and A. S. Shpigel', Zh. Éksp. Teor. Fiz. **77**, 1157 (1979) [Sov. Phys. JETP 50, 583 (1979)].
[39] V. L. Gurevich, A. I. Larkin, and Yu. A. Firsov, Fiz. Tverd. Tela (Leningrad) **4**, 185, (1962).
[40] M. L. Cohen, Phys. Rev. **134**, 511 (1964).
[41] É. A. Pashitskiĭ, V. L. Makarov, and S. D. Tereshchenko, Fiz. Tverd. Tela (Leningrad) **16**, 427 (1974).
[42] É. A. Pashitskiĭ, Yu. M. Malozovskiĭ, and A. V. Semenov, Zh. Éksp. Teor. Fiz. **100**, 465 (1991) [Sov. Phys. JETP **73**, 255 (1991)]; Ukr. Fiz. Zh. (Russ. Ed.) **36**, 889 (1991); Supercond. Sci. Technol. **5**, 507 (1992).
[43] E. A. Pashitskiĭ, Zh. Éksp. Teor. Fiz. **103**, 867 (1993) [JETP **76**, 425 (1993)]; Fiz. Nizk. Temp. **19**, 140, 355 (1993) [Low Temp. Phys. **19**, 100, 249, 607 (1993)]; **21**, 995, 1091 (1995) [**21**, 763, 837 (1995)].
[44] É. A. Pashitskiĭ and V. I. Pentegov, Pis'ma Zh. Éksp. Teor. Fiz **63**, 553 (1996) [JETP Lett. **63**, 583 (1996)].
[45] V. A. Moskalenko, Fiz. Met. Metalloved. **8**, 503 (1959).
[46] H. Suhl, B. T. Matthias, and L. R. Walker, Phys. Rev. Lett. **3**, 552 (1959).
[47] J. L. Tallon, R. G. Buckley, E. M. Haines *et al.*, Physica C **185–189** (1991).
[48] É. A. Pashitskiĭ, Pis'ma Zh. Éksp. Teor. Fiz **61**, 264 (1995) [JETP Lett. **61**, 275 (1995)].
[49] A. A. Golubov and I. I. Mazin, Physica C **243**, 153 (1995).
[50] Jian Ma, C. Quitmann, R. J. Kelley *et al.*, Physica C **235–240**, 1875 (1994).
[51] C. Kendziora, R. J. Kelley, and M. Onellion, Phys. Rev. Lett. **77**, 727 (1996).

Translated by Eugene Yankovsky

Anisotropy of the magnetic properties of the cuprates Dy_2BaCuO_5 and Ho_2BaCuO_5: magnetic and spectroscopic investigations

M. Baran, and H. Szymczak

Institute of Physics, Polish Academy of Sciences, 02-668 Warsaw, Poland

S. A. Klimin and M. N. Popova

Institute of Spectroscopy, Russian Academy of Sciences, 142092 Troitsk, Moscow Region, Russia

R. Z. Levitin and B. V. Mill'

Physics Department, Moscow State University, 119899 Moscow, Russia
(Submitted 13 June 1996)
Zh. Éksp. Teor. Fiz. **111**, 318–331 (January 1997)

The magnetization of single crystals of the cuprates Dy_2BaCuO_5 and Ho_2BaCuO_5 along different crystallographic directions is measured using a SQUID magnetometer in fields up to 54 kOe. Spectroscopic investigations of the exchange splitting of the levels of Er^{3+} probe ions in these cuprates are also performed. It is shown that the cuprates investigated are highly anisotropic antiferromagnets, which display quasi-Ising behavior in a magnetic field. The nature of the two spontaneous magnetic phase transitions detected in Dy_2BaCuO_5 and Ho_2BaCuO_5 is analyzed. It is shown that the low-temperature transition is due to an increase in rare-earth–copper exchange. [S1063-7761(97)02001-5]

1. INTRODUCTION

Rare-earth cuprates having the general formula R_2BaCuO_5 with R=La, Nd–Gd, Dy–Lu, and Y are known as attendant components in 1-2-3 high-T_c superconductors. The compounds with La and Nd (the so-called ''brown phase'') are tetragonal and belong to the $P4/mbm$ space group.[1] The compounds with the smaller rare-earth ions (Sm–Gd, Dy–Lu, and Y), which have been termed the ''green phase,'' crystallize in the orthorhombic system with the $Pbnm$ space group.[2,3]

The crystal structure of the green phase of R_2BaCuO_5 can be described as a three-dimensional framework of RO_7 polyhedrons (monocapped triangular prisms) joined by common faces and edges, whose cavities are occupied by Cu^{2+} and Ba^{2+} ions. The Cu^{2+} ions are located in isolated CuO_5 tetragonal pyramids, and the Ba^{2+} ions are found in BaO_{11} polyhedrons. All the cations occupy fourfold sites with C_s symmetry, there being two inequivalent sites R1 and R2 for the rare earth. The cations are located at the $z=1/4$, and 3/4 levels,[1)] through which mirror symmetry planes of the local C_s symmetry point group of the cation site pass. The O3 oxygen ions are found in these planes.

The oxygen coordination polyhedrons for the rare-earth ions in the two sites differ only slightly; however, their local environments differ significantly. The rare-earth ion in the first site is bonded by means of oxygen ions to six nearby copper ions, five of the six R–O–Cu bond angles being close to 180°, while the ion in the other site is bonded to only three copper ions at bond angles close to 90°.

Figure 1 shows the two inequivalent rare-earth ions R1 and R2 together with their local environments projected onto the $z=1/4$ plane in the case of Dy_2BaCuO_5.

The presence of two magnetic subsystems formed by the Cu^{2+} and R^{3+} ions is responsible for the complicated magnetic behavior of R_2BaCuO_5. The most characteristic property of most of these compounds with magnetic rare earths, particularly Dy_2BaCuO_5 and Ho_2BaCuO_5, which were investigated in the present work, is that they have two magnetic ordering temperatures or Néel points T_{N1} and T_{N2} (Refs. 4–11). The high-temperature transition at T_{N1} is a second-order phase transition, while the transition at the lower temperature T_{N2} occurs abruptly and is apparently a first-order phase transition.

According to the results of different investigations (measurements of the magnetization, magnetic susceptibility, specific heat, and Young's modulus, as well as spectroscopic measurements),[4–11] $T_{N1}=18-20$ K, and $T_{N2}=9-11$ K for Dy_2BaCuO_5, while $T_{N1}=17$ K, and $T_{N2}=7-8$ K for Ho_2BaCuO_5. According to the spectroscopic data, the low-temperature transition splits into two in the dysprosium cuprate.[7]

It was presumed in the early studies[4,5] that the high-temperature transition at T_{N1} is caused by antiferromagnetic ordering of the copper subsystem, while antiferromagnetic ordering of the rare-earth subsystem occurs at T_{N2}. However, neutron diffraction[3] and spectroscopic[7] investigations showed that the low-temperature transition is accompanied not only by an increase in the degree of magnetic order in the rare-earth subsystem, but also by a change in the type of antiferromagnetic ordering. For example, in dysprosium cuprate the wave vector (the propagation vector) of the magnetic structure, which equals $\mathbf{k}=[0,0,1/2]$ in the temperature range $T_{N1}>T>T_{N2}$ (the magnetic unit cell is doubled in comparison with the crystallographic unit cell along the c axis), transforms into the wave vector $\mathbf{k}=[0,0,0]$ below T_{N2} (the magnetic unit cell coincides with the crystallographic unit cell). In addition, the directions of the magnetic moments also change at T_{N2}. Above T_{N2} the copper mag-

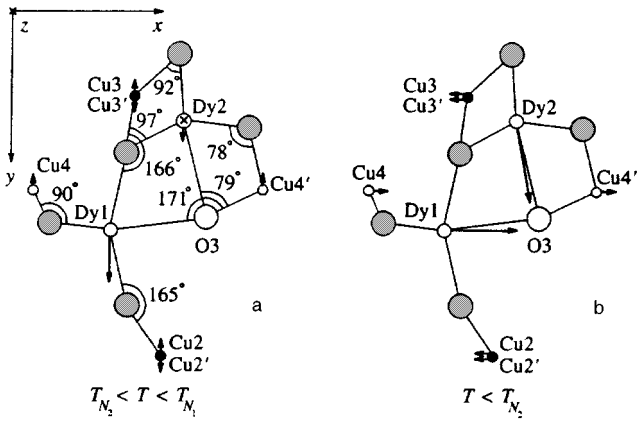

FIG. 1. Fragment of the structure of Dy_2BaCuO_5 together with the directions of the magnetic moments in the high-temperature (a) and low-temperature (b) phases (according to the data in Ref. 3) projected onto the $z=1/4$ plane. The atoms lying in this plane (Dy1, Dy2, O3, Cu4, and Cu 4′) are denoted by unfilled circles. Each blackened circle corresponds to a pair of copper atoms positioned over one another (in the $z=3/4$ and $z=-1/4$ planes); each gray circle corresponds to a pair of oxygen atoms arranged symmetrically above and below the $z=1/4$ plane. The cross in the left-hand drawing corresponds to the presence of the z projection of the Dy2 magnetic moment. A primed number refers to the respective copper site in a neighboring cell. The Dy–O–Cu bonds are depicted by lines. The bond angles calculated from the structural data in Ref. 3 are indicated.

netic moments, like the Dy1 magnetic moment, are collinear with the b axis of the crystal, and the Dy2 magnetic moment lies in the bc plane. Below that temperature the copper magnetic moments are collinear with the a axis, while the Dy1 and Dy2 magnetic moments are preferentially oriented along the a and b axis, respectively (there are small components of the magnetic moment along the b axis for Dy1 and along the a axis for Dy2). The magnetic structures of Dy_2BaCuO_5 above and below T_{N2} are shown in Figs. 1a and 1b.

The magnetic structure of Ho_2BaCuO_5 has been studied less thoroughly. It has been reported[3] that above T_{N2} the wave vector $\mathbf{k}=[0,0,1/2]$ and that below this temperature there are two wave vectors: $\mathbf{k}_1=[0,0,1/2]$ and $\mathbf{k}_2=[0,0,0]$. Assuming that the copper magnetic moments are ordered just as in Dy_2BaCuO_5 and that the wave vectors $\mathbf{k}_1$ and $\mathbf{k}_2$ describe different components of the magnetic moments in a single magnetic phase, Golosovskiĭ *et al.*[3] found that below T_{N2} the holmium magnetic moments in the two structural sites differ strongly in magnitude and that, in contrast to Dy_2BaCuO_5, there is a projection of the Ho2 magnetic moment onto the c axis.

We note that all the studies enumerated above were performed on polycrystalline samples, and we do not know of any research in which the magnetic properties of R_2BaCuO_5 single crystals were investigated. Nevertheless, the low crystal symmetry of these cuprates, as well as the results of neutron diffraction investigations of their magnetic structure[3] and investigations employing rare-earth spectroscopic probes,[7,10] suggest that the anisotropy of the magnetic properties should be significant.

For this reason, we undertook an investigation of the magnetic properties of Dy_2BaCuO_5 and Ho_2BaCuO_5 single crystals. Measurements of the spectra of Er^{3+} ions introduced as probes into Dy_2BaCuO_5 and Ho_2BaCuO_5 were also performed.

2. SAMPLES AND EXPERIMENTAL METHODS

Single crystals of R_2BaCuO_5 (R=Dy and Ho) of length 3–4 mm and transverse dimensions 0.1–0.2 mm were grown from nonstoichiometric melts of the R_2O_3–BaO–CuO systems by cooling the melts from 1200–1300 °C at the rate of 2 °C per hour in aluminum oxide crucibles. According to Ref. 12, the long axis of the crystals is parallel to the c axis of the unit cell. On the lateral facets of the crystals there are {110} and {010} faces, so that the cross section of each crystal is an irregular hexagon. In determining the demagnetizing factor, we regarded the cross section of the sample as a circle.

An analysis of the magnetic neutron diffraction data,[3] as well as preliminary measurements of the magnetization, showed that there is considerable anisotropy of the magnetic properties in the ab plane. We determined the a and b axes of the crystals from their habit. The orientation of the axes was verified by the symmetry of the magnetic properties in the ab plane, and, as can be seen from Fig. 2, the various directions in this plane could be determined quite accurately (to within 3–4 °).

The magnetization measurements were performed in fields up to 54 kOe over the temperature range 2–100 K using a SQUID magnetometer. The error in the measurement of the absolute value of the magnetization was 5–10%. Such low accuracy is attributable mainly to the small mass and dimensions of the sample (the error in the measurement of the absolute value of the magnetic moment of a sample using a SQUID magnetometer did not exceed 0.1%).

The magnetic susceptibility was determined from magnetization measurements in fields up to 1 kOe.

Polycrystalline samples of $Dy_{1.98}Er_{0.02}BaCuO_5$ and $Ho_{1.98}Er_{0.02}BaCuO_5$ obtained from the oxides by solid-phase synthesis at 1030 °C, and which were phase-pure to x-rays, were used for the spectroscopic measurements.

The diffuse transmission spectra were recorded in the region of the intense $^4I_{15/2}\rightarrow{}^4I_{13/2}$ magnetic-dipole allowed optical transition of the free Er^{3+} ion (near 6500 cm^{-1}) using a Bomem DA3.002 FT spectrometer with a spectral resolution to 0.1 cm^{-1}. The samples were immersed in helium vapor at temperatures from 2.1 to 100 K.

3. EXPERIMENTAL RESULTS

3.1. Magnetic susceptibility

Figure 3 presents the temperature dependence of the magnetic susceptibility of Dy_2BaCuO_5 and Ho_2BaCuO_5 single crystals along the a, b, and c axes of the crystals. The arrows in these figures show the temperatures for antiferromagnetic ordering of the copper subsystem (T_{N1}) and the rare-earth subsystem (T_{N2}) determined in Ref. 8 via specific heat measurements. It is seen that the transition of the copper subsystem to the antiferromagnetic state is barely noticeable: it is accompanied only by slight variation of the slope of the χ versus T curve along the a axis of the crystal. As we first noted in Ref. 4, this is because the contribution of the copper

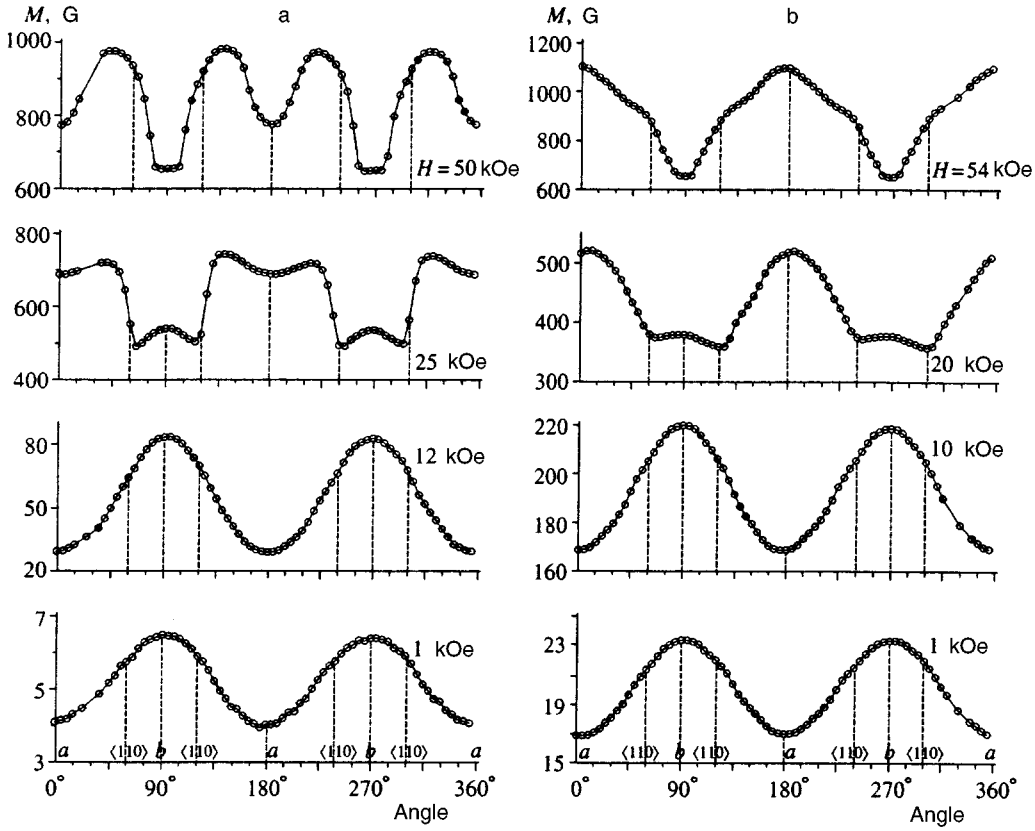

FIG. 2. Angular dependence of the magnetization of Dy_2BaCuO_5 (a) and Ho_2BaCuO_5 (b) single crystals in various external magnetic fields at 5 K.

subsystem to the total magnetic susceptibility is small. The contribution of the ith magnetic subsystem to the total paramagnetic susceptibility is determined by the Curie constant of that subsystem:

$$C_i = n_i g_i^2 J_i(J_i+1)\mu_B^2/3k_B, \tag{1}$$

where n_i is the number of ions of type i in a formula unit, g_i is the g factor, k_B is Boltzmann's constant, J_i is the total angular momentum of the ion, and μ_B is the Bohr magneton. For the copper subsystem ($n_{Cu}=1$, $g_{Cu}=2$, $J_{Cu}=1/2$) we have $C_{Cu}=1\mu_B^2/k_B$, which is two orders of magnitude smaller than the Curie constant of the rare-earth subsystem in the two compounds studied: $C_{Dy}=75.5\cdot\mu_B^2/k_B$ ($n_{Dy}=2$, $g_{Dy}=4/3$, $J_{Dy}=15/2$), $C_{Ho}=75\mu_B^2/k_B$ ($n_{Ho}=2$, $g_{Ho}=5/4$, $J_{Ho}=8$). Although the values just presented are approximate, since the magnetic moments in a crystal can differ from the magnetic moments of the free ions, it is seen that the anomalous susceptibility associated with the magnetic ordering of the copper subsystem is negligible against the background of the large susceptibility of the rare-earth subsystem.

The transition to the antiferromagnetic state of the rare-earth subsystem at T_{N2} is accompanied by a decrease in the susceptibility. In Dy_2BaCuO_5 this decrease is observed along

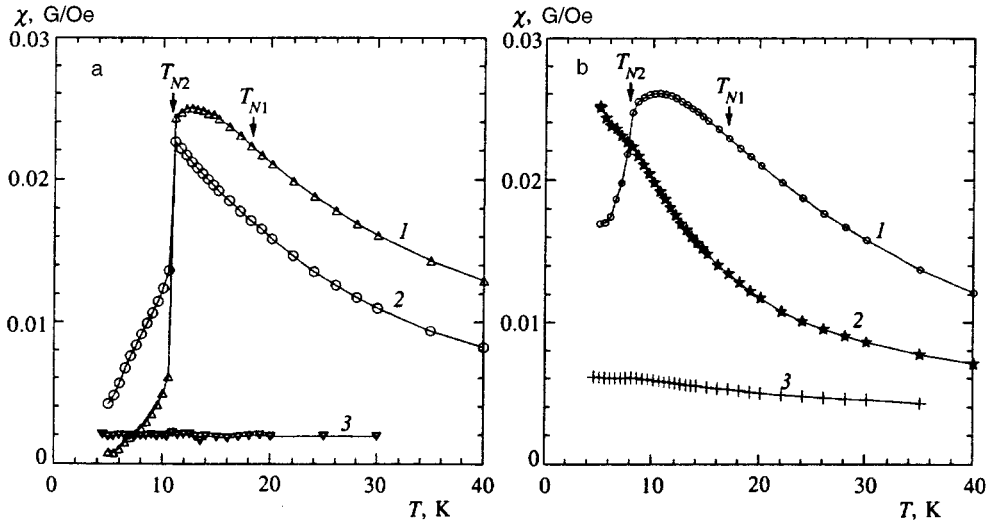

FIG. 3. Temperature dependence of the magnetic susceptibility of Dy_2BaCuO_5 (a) and Ho_2BaCuO_5 (b) along the a (*1*), b (*2*), and c (*3*) axes.

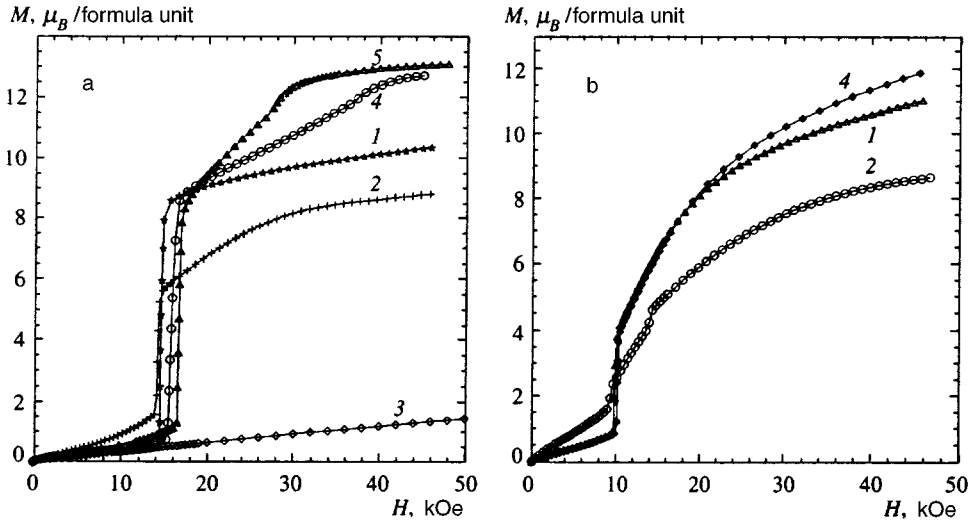

FIG. 4. Field dependence of the magnetization of a Dy_2BaCuO_5 single crystal at 5 K (a) and 9 K (b) along the *a* (*1*), *b* (*2*), and *c* (*3*) axes, the ⟨110⟩ direction (*4*), and at a 45° angle to the *a* axis (*5*).

the *a* and *b* axes and is very abrupt, while in Ho_2BaCuO_5 only the magnetic susceptibility along the *a* axis exhibits an anomaly at T_{N2}, and the transition to the antiferromagnetic state of the Ho subsystem is more diffuse.

For both compounds the susceptibility along the *c* axis is considerably smaller than the susceptibility in the *ab* plane and depends weakly on the temperature in the temperature range investigated.

3.2. Magnetization

Dy_2BaCuO_5. Figure 4a presents the dependence of the magnetization on the field in different directions at 5 K. It is seen that in the range of fields investigated, the magnetization along the *c* axis of the crystal is small and nearly linearly dependent on the field. At the same time, the magnetization in the *ab* plane undergoes a metamagnetic transition in all the directions investigated. The critical fields for the metamagnetic transitions are approximately the same for field directions along the *a* and *b* axes of the crystal, and are somewhat greater when the field is oriented along intermediate directions. In these directions the magnetization undergoes one more diffuse metamagnetic transition in stronger fields. The appreciable anisotropy of the magnetization in strong magnetic fields greater than the fields of the metamagnetic transitions is noteworthy (see also Fig. 2).

As the temperature rises, the character of the magnetization curves does not vary significantly except for the fact that the metamagnetic transition in a field oriented along the *b* axis of the crystal also bifurcates (Fig. 4b). At the same time, the second metamagnetic transition in the ⟨110⟩ direction quickly becomes diffuse and then negligible as the temperature rises.

The temperature dependence of the critical fields of the metamagnetic transitions in different directions is shown in Fig. 5. It is noteworthy that the values of the critical fields decrease as the temperature rises, and that they tend to zero as the Néel point T_{N2} of the low-temperature transition is approached. Metamagnetism vanishes above that temperature.

Ho_2BaCuO_5. Figure 6a presents plots of $M(H)$ at 5 K for various directions. It is seen that the magnetization along the *a* axis and in the ⟨110⟩ direction has a metamagnetic character, there being two metamagnetic transitions in the latter case. At the same time, no metamagnetic transitions are observed in the plot of *M* versus *H* along the *b* axis. There is also strong anisotropy of the magnetization in the *ab* plane in strong magnetic fields (see also Fig. 2).

The magnetization along the *c* axis (perpendicular to the *ab* plane) is considerably weaker than that in the *ab* plane and depends almost linearly on the field, exhibiting a weak tendency to saturate in strong fields.

The metamagnetic transitions are diffuse by 5 K. They rapidly become more diffuse as the temperature rises, and metamagnetic behavior is not observed above T_{N2}, as is clearly seen from Fig. 6b, which shows plots of *M* versus *H* in different directions at 8 K.

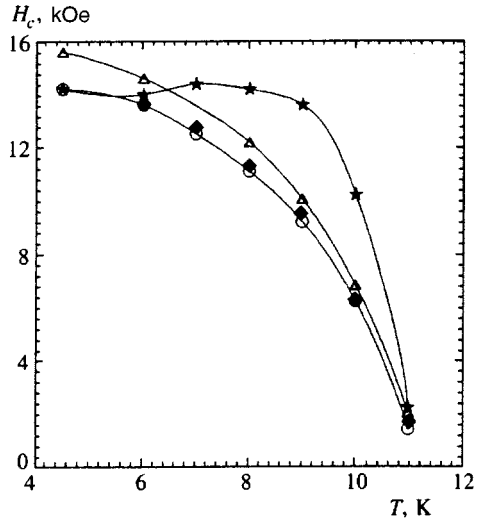

FIG. 5. Temperature dependence of the fields for the metamagnetic transitions of Dy_2BaCuO_5 along the *a* (◆) and *b* (○,⋆) axes and in the ⟨110⟩ direction (△).

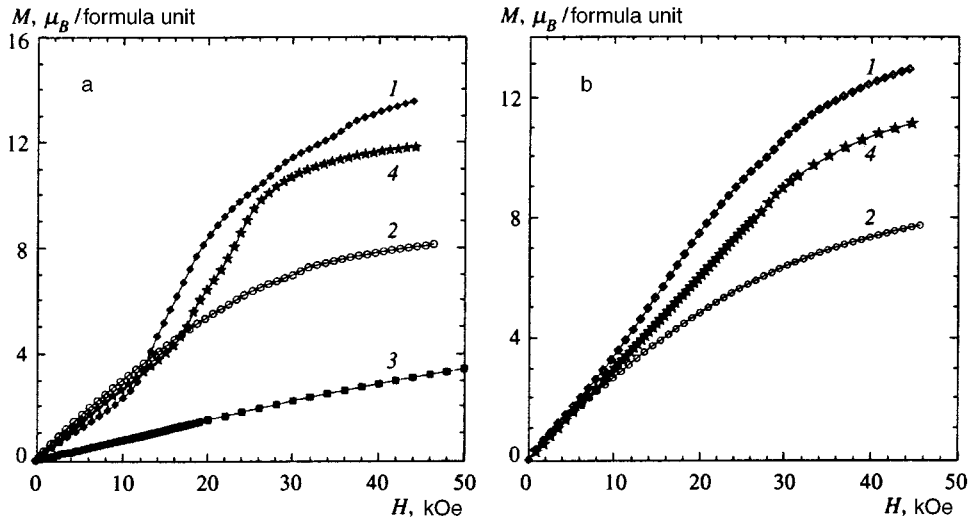

FIG. 6. Field dependence of the magnetization of a Ho_2BaCuO_5 single crystal at 5 K (a) and 8 K (b) along the *a* (*1*), *b* (*2*), and *c* (*3*) axes and the ⟨110⟩ direction (*4*).

3.3. Optical spectra of Er^{3+} probe ions

The low-symmetry crystal field in the compounds R_2BaCuO_5 completely removes the degeneracy, except for the Kramers degeneracy, of the levels of Er^{3+} probe ions replacing R1 and R2 ions. In the magnetically ordered state, the Kramers doublets split because of magnetic interactions, and, as a result, each spectral line splits into a maximum of four components (see the scheme in the upper part of Fig. 7). The experimental data show that these splittings are determined mainly by the Er–Cu exchange interaction, while the Er–R interactions are insignificant, and that the Er–Cu exchange is highly anisotropic.[13–15] Therefore, the spectrum of the probe ions depends on the orientation of the copper magnetic moments closest to them.

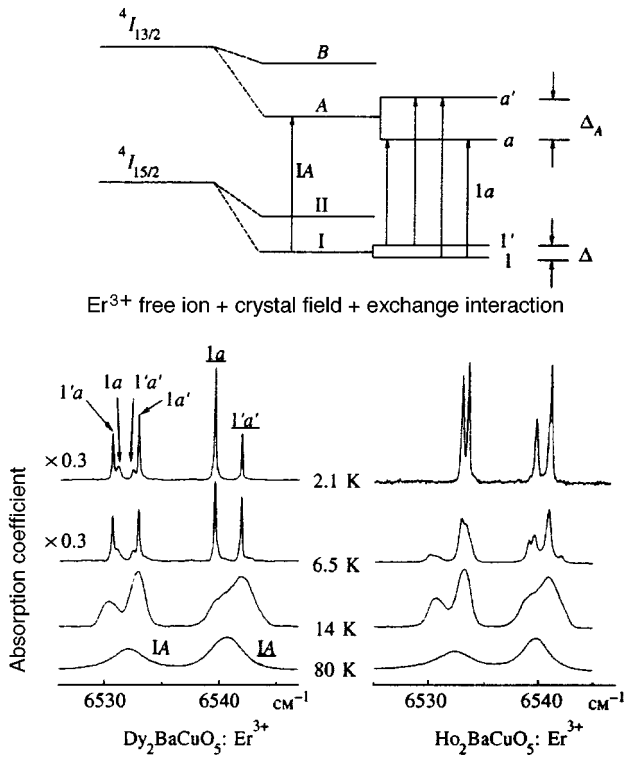

FIG. 7. Two lines of the spectrum of Er^{3+} in Dy_2BaCuO_5:Er(1%) and Ho_2BaCuO_5:Er(1%) corresponding to two inequivalent sites of the rare earth at different temperatures. The scheme in the upper part of the figure elucidates the splitting of the spectral lines observed upon magnetic ordering. The labels of the transitions in one of the structural sites are underlined, and those for the other site are not.

Figure 7 shows how the two spectral lines at 6532 and 6540 cm^{-1} (see the spectra at 80 K in the paramagnetic phase), which correspond to the two inequivalent structural sites of the erbium probe ions in the dysprosium and holmium cuprates, split as the temperature is lowered.

In the temperature range $T_{N2}<T<T_{N1}$ the spectra for both compounds are essentially identical (see the spectra at 14 K), in agreement with the conclusions in Ref. 3 regarding the identical magnetic structures of the copper subsystem in this temperature range.

At T_{N2} the spectral lines for both Dy_2BaCuO_5 and Ho_2BaCuO_5 narrow sharply as a consequence of the ordering of the rare-earth subsystem. However, the form of the spectrum of the erbium probe ions at $T<T_{N2}$ is significantly different for the dysprosium and holmium compounds (see the spectra at 6.5 and 2.1 K). While the picture for Dy_2BaCuO_5 is faithfully described by a simple scheme with one set of splittings of the Er^{3+} levels for each structural site (at 2.1 K $\Delta=0.5$ cm^{-1} and $\Delta_A=1.8$ cm^{-1} for the structural site corresponding to the line at 6532 cm^{-1}; $\Delta=1.3$ cm^{-1} and $\Delta_A=3.7$ cm^{-1} for the other site corresponding to the line at 6540 cm^{-1}), there are at least two such sets for Ho_2BaCuO_5, and each of them differs significantly from the set just described for Dy_2BaCuO_5.

The appearance of inequivalent spectroscopic sites for erbium probe ions in Ho_2BaCuO_5 at $T<T_{N2}$ can be associated either with the establishment of a complicated magnetic structure in the copper subsystem or with the appearance of two different magnetic phases. The analysis of the magnetic structure of Ho_2BaCuO_5 proposed in Ref. 3 gives one spectroscopic site for an Er^{3+} probe ion in each of two structurally inequivalent sites. Golosovskiĭ *et al.*,[3] however, point out that because of the weakness of the magnetic reflections from copper, inaccuracies are possible in the determination of the magnetic structure of the copper subsystem, and that

the possibility of the two wave vectors detected for Ho_2BaCuO_5 belonging to two different magnetic phases has not been ruled out. It should also be borne in mind that the experimental data from the powder neutron diffraction of polyatomic compounds can usually be described equally well by several different magnetic structures.[16,17]

Thus, the spectroscopic data are consistent with the magnetic structure of Dy_2BaCuO_5 proposed in Ref. 3 and are not consistent with the low-temperature magnetic structure of Ho_2BaCuO_5 from the same report. The magnetic structure of Ho_2BaCuO_5 is more complicated than that of Dy_2BaCuO_5 and is in need of refinement.

4. DISCUSSION

Some general features that are characteristic of the magnetic behavior of both cuprates investigated here can be noted.

First, these compounds exhibit two spontaneous magnetic transitions at T_{N1} and T_{N2}.

Second, there are no (or very small) anomalies of the magnetic susceptibility at the high-temperature Néel point T_{N1}, and a considerable decrease in the magnetic susceptibility is observed upon the low-temperature phase transition at T_{N2}.

Third, there is distinct anisotropy of the magnetic properties: the magnetization and the magnetic susceptibility are considerably greater in the ab plane than along the c axis.

Fourth, metamagnetic transitions are observed when the samples are magnetized in the ab plane at low temperatures (below T_{N2}).

As follows from the data presented, the susceptibility along the c axis of the Dy_2BaCuO_5 and Ho_2BaCuO_5 crystals is considerably smaller than the susceptibility in the ab plane (except for the case of very low temperatures in Dy_2BaCuO_5, at which the susceptibilities along the a and c axes are comparable). In weakly anisotropic antiferromagnets this finding would indicate that the antiferromagnetism vector is collinear with the c axis. However, the neutron diffraction data[3] show that the magnetic moments lie preferentially in the ab plane of the crystal, and, therefore, the transverse magnetic susceptibility is measured when the magnetic field is oriented along the c axis of the crystal.

Thus, it can be concluded from the experimental magnetic susceptibility data that the anisotropic magnetic interactions leading to preferential orientation of the magnetic moments in the ab plane significantly exceed the isotropic exchange interactions in the cuprates investigated.

The cuprates studied, however, cannot be regarded as easy-plane antiferromagnets, since the occurrence of metamagnetic transitions at $T<T_{N2}$ when the samples are magnetized in the ab plane is evidence that at low temperatures the anisotropic interactions in this plane are comparable in magnitude to the isotropic exchange interactions.

The structure of the dysprosium subsystem at $T<T_{N2}$ in zero magnetic field indicated by the data from the neutron diffraction studies in Ref. 3 is shown in Fig. 8a. In the simplest Ising model, the metamagnetic transitions observed along the a and b axes of the crystal can be represented as shown in Figs. 8b and 8c, i.e., the magnetic moments which

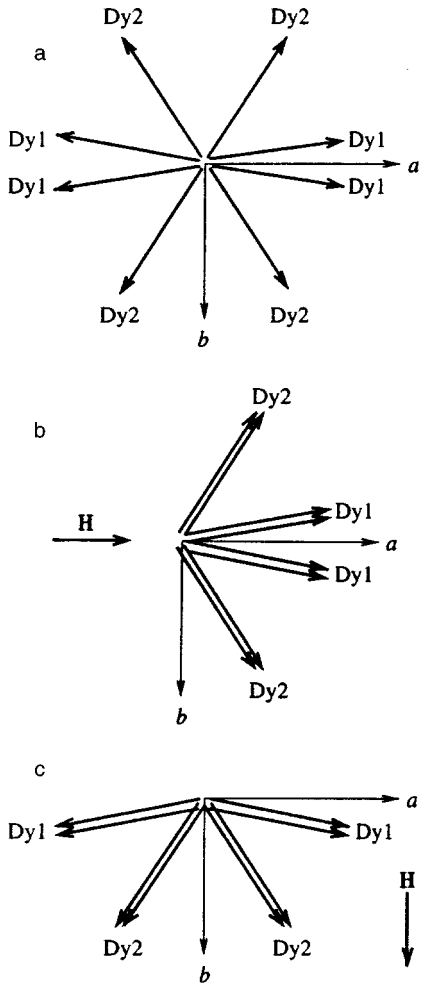

FIG. 8. Magnetic structure of the dysprosium subsystem in Dy_2BaCuO_5 at $T<T_{N2}$: a) $0\leqslant H<H_c$; b) $H>H_c$, **H**||**a**; c) $H>H_c$, **H**||**b**.

form an obtuse angle with the field are reoriented by 180° during these transitions. Such a simple model also allows us to attribute the presence of the two metamagnetic transitions observed in some cases in Dy_2BaCuO_5 to the fact that reorientation of the magnetic moments in the two inequivalent positions does not occur simultaneously. In addition, such a model qualitatively explains why the saturation magnetization is greater along the a axis than along the b axis of the crystal. The magnitude of the saturation magnetic moment along the other directions in the crystal is also consistent with the model under consideration (from our experimental data we have $M_a:M_b:M_{45°}=1:0.875:1.3$, and from Ref. 3 it follows that this ratio is 1:0.93:1.37 in the Ising model). The strength of the critical transition field when the field is oriented at a 45° angle relative to the a and b axes is also explained in the Ising model: according to this model the strength of this field at 5 K should be 16.6 kOe, while the experimental value equals 17 kOe.

The qualitative arguments presented above can probably be applied to the description of the magnetic behavior of the holmium cuprate. However, in this case the situation is more complicated, since the low-temperature antiferromagnetic structure of Ho_2BaCuO_5 is presumably described, as we

have already noted above, by the two wave vectors $\mathbf{k}_1=[0,0,1/2]$ and $\mathbf{k}_2=[0,0,0]$ and, in contrast to Dy_2BaCuO_5, in the holmium cuprate there is a projection of the holmium magnetic moment onto the c axis of the crystal at low temperatures. In addition, the spectroscopic data that we obtained cannot be described within the magnetic structure proposed in Ref. 3, and additional research is needed.

It should be stressed that the simple Ising model considered above is very approximate, since the copper subsystem is neglected and the relationship between the copper and rare-earth subsystems is not considered in it. At the same time, the available experimental data show that the rare-earth–copper exchange interaction has a significant influence on the properties of the cuprates in the low-temperature phase. This follows, first, from the fact that as our magnetic and spectroscopic investigations of the isomorphous compounds R_2BaZnO_5 showed, the rare-earth–rare-earth exchange interaction is weak (no magnetic ordering was observed in these compounds in the temperature range investigated, $T\geqslant 2.1$ K) and cannot account for the values of T_{N2} observed in the dysprosium and holmium cuprates. Second, as was shown above, it follows from the results of the spectroscopic[7] and neutron diffraction[3] investigations that the magnetic ordering of the rare-earth subsystem at T_{N2} is accompanied by alteration of the magnetic structure not only in the rare-earth subsystem, but also in the copper subsystem.

Thus, the rare-earth–copper exchange interaction along with the magnetic anisotropy specifies the behavior of the rare-earth subsystem. It would seem that below T_{N1}, at which an antiferromagnetic structure with the wave vector $\mathbf{k}=[0,0,1/2]$ appears in the copper subsystem, the copper subsystem interacts weakly with the rare-earth subsystem, only partially polarizing it. Upon further cooling to T_{N2} a change occurs in the type of magnetic ordering in the copper subsystem under the influence of the isotropic and anisotropic interactions between the copper and rare-earth subsystems, which in turn leads to enhancement of the rare-earth–copper exchange interaction and a sharp increase (by means of a first-order phase transition) in the degree of magnetic order in the rare-earth subsystem.

Qualitatively, the change in the strength of the dysprosium–copper exchange interaction in response to the change in the magnetic structure of the copper subsystem at the Néel point T_{N2} of the low-temperature phase transition can be understood by analyzing Fig. 1, which depicts the environments of the two inequivalent dysprosium ions and shows the orientations of the dysprosium and copper magnetic moments in the high-temperature and low-temperature magnetic phases on the basis of the data in Ref. 3.

As we have already pointed out, the environment of Dy1 is such that the angles of most of the Dy–O–Cu bonds are close to 180°. This generally promotes symmetric exchange, i.e., leads to large values of the exchange integrals I_{ij} in the expression for the symmetric part of the exchange interaction:

$$E_{\text{ex}}^{\text{sym}}=\sum_{ij} I_{ij}M_i m_{ij}, \tag{2}$$

where $i=x, y, z$, and M_i and m_{ij} are the components of the magnetic moments of the rare-earth ion and the copper ions closest to it, which are labeled by the subscript j.

Above T_{N2}, at which the wave vector of the magnetic structure $\mathbf{k}=[0,0,1/2]$, the copper magnetic moments in neighboring cells along the c axis are oppositely directed (see Fig. 1a), and the exchange interaction of Dy1 with each of the Cu3–Cu3′ and Cu2–Cu2′ pairs vanishes. In this temperature range the main contribution to the ordering of the Dy1 magnetic moments probably comes from the antiferromagnetic Dy1–Cu4′ exchange interaction.

Below T_{N2} we have $\mathbf{k}=[0,0,0]$, and the spins in the Cu3–Cu3′ and Cu2–Cu2′ pairs are parallel. Thus, at $T<T_{N2}$ the strength of the Dy1–Cu exchange increases with a resultant increase in the degree of magnetic order in the dysprosium subsystem.

Note that the decisive factor influencing the orientation of the dysprosium magnetic moments at temperatures below T_{N2} is probably the anisotropy caused by the crystal field. This is evinced by the fact that in this temperature range the magnetic moments of dysprosium in each of its inequivalent sites have approximately the same orientation with respect to the corresponding DyO_7 coordination polyhedron.

We note that below T_{N2} the dysprosium magnetic moments in one of the sites (Dy1) are almost collinear with the copper magnetic moments, while the magnetic moments in the other site (Dy2) are almost perpendicular to them. Hence it follows that at low temperatures the symmetric part of the exchange interaction involving the Dy2 site is small. In addition, it follows from Fig. 1 that the Dy2–Cu symmetric exchange constants must be small because of the nearly 90° Dy–O–Cu bond angles, i.e., the symmetric exchange apparently does not have a significant influence on the ordering of the Dy2 magnetic moments. However, it follows from the experimental data in Ref. 3 that values of the Dy1 and Dy2 magnetic moments above and below T_{N2} are approximately the same, i.e., approximately equal to the molecular fields from the copper subsystem that act on the dysprosium magnetic moments in these positions. For Dy2 the decisive interaction is probably the Dzyaloshinskii–Moriya antisymmetric exchange interaction, which can be represented in the form

$$E_{\text{ex}}^{\text{antisym}}=\sum_j \mathbf{D}_j\cdot[\mathbf{M}\times\mathbf{m}_j], \tag{3}$$

where the antisymmetric exchange parameter $\mathbf{D}_j$ can be expressed (see, for example, Ref. 18) as

$$\mathbf{D}_j=d_j[\mathbf{r}_{0j}\times\mathbf{r}_j]. \tag{4}$$

Here $\mathbf{r}_{0j}$ and $\mathbf{r}_j$ are vectors that join the intermediate oxygen ion to the Dy2 and Cu_j ions, respectively, and d_j is a constant.

As follows from Eq. (4), the nearly 90° bond angles promote the large value of the Dy2–Cu antisymmetric exchange parameter, and it is seen from Eq. (3) that antisymmetric exchange orients the dysprosium and copper magnetic moments perpendicularly to one another, as is observed for the Dy2 site (Fig. 1).[2)]

Also, as can easily be seen from Fig. 1, above T_{N2} the antisymmetric exchange interaction of the Dy2 ion with the Cu4′ ion is equal to zero, and the interaction with the

Cu3–Cu3′ pair fails to vanish only because this ion has a projection onto the *c* axis. Below this temperature all the nearby copper ions make comparable contributions to the antisymmetric exchange, and, therefore the molecular field from the nearby copper ions that acts on Dy2 also increases in the low-temperature phase.

Summarizing the foregoing discussion, we briefly formulate what is, in our opinion, the nature of the two magnetic phase transitions in Dy_2BaCuO_5 and Ho_2BaCuO_5. In R_2BaCuO_5 cuprates the exchange interaction within the copper subsystem is dominant, the rare-earth–copper interaction is considerably weaker, and the rare-earth–rare-earth interaction can be neglected. Because each copper atom is isolated and there are no direct Cu–O–Cu bonds through a single oxygen ion, the different Cu–O–O–Cu and Cu–O–R–O–Cu bonds cause the two magnetic structures in the copper subsystem with the wave vectors $\mathbf{k}=[0,0,1/2]$ and $\mathbf{k}=[0,0,0]$ and copper magnetic moments directed along the *a* and *b* axis, respectively, to have similar energies. At T_{N1}, ordering occurs in the structure with $\mathbf{k}=[0,0,1/2]$ under the influence of the copper–copper interaction in the copper subsystem, and the copper magnetic moment is parallel to the *b* axis. The rare earth is weakly polarized. When the temperature is lowered, the role of the single-ion anisotropy caused by the crystal field increases, leading to a definite orientation of the rare-earth magnetic moments in the two inequivalent positions relative to the coordination polyhedron. At T_{N2}, reorientation to the structure with $\mathbf{k}=[0,0,0]$ occurs under the influence of the copper–rare-earth exchange interactions in the copper subsystem, and the copper magnetic moment is parallel to the *a* axis. The energy loss in the copper subsystem relative to the energy of the high-temperature phase is offset by the gain due to enhancement of the copper–rare-earth exchange interaction.

This work was partially supported by the Russian Fund for Fundamental Research (Grant 96-02-19474a and 95-02-03796-a), as well as by the State Committee for Institutes of Higher Education of the Russian Federation (Grant 95-0-74-157).

[1)] From here on we use the notation of the axes in the *Pbnm* configuration. Other configurations, in which the order of the axes is different, are used in some publications.

[2)] The small component of the Dy2 magnetic moment that is collinear with the copper magnetic moments is clearly due to weak symmetric antiferromagnetic exchange.

[1] J. K. Stalick and W. Wong-ng, Mater. Lett. **9**, 401 (1990).
[2] C. Michel and B. Raveau, J. Solid State Chem. **43**, 73 (1982).
[3] I. V. Golosovskiĭ, V. P. Plakhtiĭ, V. P. Kharchenkov *et al.*, Fiz. Tverd. Tela (Leningrad) **34**, 1473 (1992) [Sov. Phys. Solid State **34**, 782 (1992)].
[4] R. Z. Levitin, B. V. Mill, V. V. Moshchalkov *et al.*, Solid State Commun. **73**, 433 (1990).
[5] R. Z. Levitin, B. V. Mill, V. V. Moshchalkov *et al.*, J. Magn. Magn. Mater. **90–91**, 536 (1990).
[6] A. Salinas-Sanchez, R. Saez-Puche, and M. A. Lario-Franco, J. Solid State Chem. **89**, 361 (1990).
[7] M. N. Popova and G. G. Chepurko, JETP Lett. **52**, 562 (1990).
[8] V. V. Moshchalkov, N. A. Samarin, I. O. Grishchenko *et al.*, Sverkhprovodimost: Fiz., Khim., Tekh. **4**, 1892 (1991) [Supercond., Phys. Chem. Technol. **4**, 1800 (1991)].
[9] V. V. Moshchalkov, N. A. Samarin, I. O. Grishchenko *et al.*, Solid State Commun. **73**, 879 (1991).
[10] M. N. Popova and I. V. Paukov, in *Excited States of Transition Elements*, W. Strek, W. Ryba-Romanowski, J. Legend-Ziewicz, and B. Jezowska-Trzebiatowska (eds.), World Scientific, Singapore (1992), p. 211.
[11] R. Burriel, M. Castro, C. Pique *et al.*, J. Magn. Magn. Mater. **104–107**, 627 (1992).
[12] T. Kobayashi, H. Katsuda, K. Hayashi *et al.*, Jpn. J. Appl. Phys. **27**, L670 (1988).
[13] M. N. Popova and I. V. Paukov, Opt. Spektrosk. **76**, 285 (1994) [Opt. Spectrosc. **76**, 258 (1994)].
[14] M. N. Popova, Proc. SPIE **2706**, 182 (1995).
[15] I. V. Paukov, M. N. Popova, and B. V. Mill, Phys. Lett. A **169**, 301 (1992).
[16] I. V. Golosovsky, P. Boni, and P. Fischer, Solid State Commun. **87**, 1035 (1993).
[17] I. V. Golosovsky, P. Boni, and P. Fischer, in Progress Report 1992, Labor. für Neutronenstrenung LNS-167 (February, 1993), p. 110.
[18] K. P. Belov, A. K. Zvezdin, A. M. Kadomtseva, and R. Z. Levitin, *Orientational Transitions in Rare-Earth Magnets* [in Russian], Nauka, Moscow (1979).

Translated by P. Shelnitz

Field dependence of spin–lattice relaxation of Nd^{3+} ions in $Y_3Al_5O_{12}$ crystals

L. K. Aminov, I. N. Kurkin, S. P. Kurzin, D. A. Lukoyanov, I. Kh. Salikhov, and R. M. Rakhmatullin

Kazan' State University, 420008 Kazan', Russia
(Submitted 29 May 1996)
Zh. Éksp. Teor. Fiz. **111**, 332–343 (January 1997)

Our studies involve measuring spin–lattice relaxation times for Nd^{3+} ions in yttrium–aluminum garnets over the temperature range 4–50 K at 9.25 and 36.4 GHz for different orientations of the external magnetic field in relation to the crystallographic axes. The temperature dependence of the relaxation rate is described by $T_1^{-1}=AT^n+b\ \exp(-\Delta/kT)$, where n varies from sample to sample, with $n=1$ for ''perfect'' samples (i.e., with the longest relaxation times). Here Δ is approximately 130 cm^{-1}, which is the energy of the excited Kramers doublet of the neodymium ion closest to the ground state, and this makes it possible to interpret the second term in T_1^{-1} as the contribution of two-stage relaxation proceeding through the intermediate level Δ. A strong field dependence of these processes has been discovered: when the frequency was increased fourfold, the relaxation rate increased by a factor of 10. The effect is a specific manifestation of the degeneracy of the excited level, breaking of the symmetry of the crystalline field due to lattice defects, and the prevalence of deformations of a certain type in the spin–lattice interaction. [S1063-7761(97)02101-X]

1. INTRODUCTION

$Y_3Al_5O_{12}$ crystals (yttrium–aluminum garnets, or YAG) have found wide application as active media in lasers and in other devices of radio electronics and engineering. Such physical properties of YAG crystals as a wide transparency range, high thermal conductivity, hardness, and resistance to laser light make it possible to use this material as a matrix for building solid-state lasers with unique characteristics. Among trivalent rare-earth ions, Nd^{3+} ensure the most effective lasing in YAG crystals. YAG:Nd lasers have low lasing thresholds and high outputs. Hence the literature devoted to the study of the optical properties of these crystal is vast (see Kaminskiĭ's monograph[1] and the literature cited therein).

In investigating the physical properties of impurity paramagnetic crystals, attention must be focused on EPR spectra and the processes of spin–lattice relaxation of the lower energy levels of the paramagnetic ions. However, there are only a few papers devoted to the study of the spin–lattice relaxation of rare-earth ions in garnets, and the results are inconsistent.

Svare and Seidel[2] studied the spin–lattice relaxation of some rare-earth ions (Er^{3+}, Dy^{3+}, Yb^{3+}, and Nd^{3+}) whose concentration in various insulator garnet crystals ($Y_3Al_5O_{12}$, $Lu_3Al_5O_{12}$, $Y_3Ga_5O_{12}$, and $Lu_3Ga_5O_{12}$) was 1%. For the relaxation rate of Nd^{3+} in $Y_3Ga_5O_{12}$ they found that

$$T_1^{-1}=17T+9.0\times10^{10}\ \exp(-85\times1.44/T)[s^{-1}],$$

but they observed systematic deviations that exceeded the range of experimental errors in measuring T_1 (the YAG:Nd system was not examined).

Huang[3] studied the spin–lattice relaxation of Nd^{3+} in $Y_3Al_5O_{12}$ by the method of pulsed saturation at 8.9 GHz in a magnetic field $H=1900$ Oe directed along the [110] crystallographic axis. The temperature dependence of the spin–lattice relaxation rate was:

$$T_1^{-1}=34T+4.5\times10^{10}\ \exp(-75\times1.44/T)[s^{-1}].$$

The presence of the second term on the right-hand side can be explained by relaxation processes resulting from optical lattice vibrations with an energy $\Delta=75$ cm^{-1}. Note, however, that studies of IR and Raman spectra have revealed no vibrations with such energies in YAG.[1,4–6] Huang[3] also studied Yb^{3+} ions. The spin–lattice relaxation of these ions at high temperatures was found to result from Raman processes: $T_1^{-1}\propto T^9$.

Bagdasarov *et al.*[7] studied the relaxation of Nd^{3+} in $Y_3Al_5O_{12}$ using a device with an operating frequency of 9.34 GHz and an operating temperature in the liquid-helium range. Measurements on a single line in a magnetic field $H=3875$ Oe revealed a complicated temperature dependence of the relaxation rate, which varied with concentration. The effect was attributed to cross-relaxation among the levels of Nd^{3+} and the excited levels of foreign impurity ions that had landed in the crystal during the growth process.

To establish the precise relaxation mechanisms of rare-earth ions in garnets, we carried out a detailed study of the temperature dependence of the spin–lattice relaxation rate for a specific YAG:Nd system. The measurements were made over a broad temperature range on samples (prepared by different techniques) at different frequencies, with different EPR lines, and in different external fields. By the time the first measurements were complete, we had discovered a strong field dependence of the contribution of two-stage relaxation processes, and we specifically studied this dependence at a fixed temperature of 11.4 K. In Sec. 2 we present data on the samples used in the measurements, the experimental conditions, and the results of relaxation-time measurements. In Sec. 3 we discuss experimental results and the possibility of describing the field dependence of the relaxation rate in terms of existing theories. Finally, in Sec. 4 we draw conclusions concerning our study.

2. EXPERIMENT

$Y_3Al_5O_{12}$ single crystals exhibit the cubic symmetry O_h^{10}. The unit cell contains eight molecules, and rare-earth ions (R^{3+}) are activated at the positions of Y^{3+}. The nearest neighbors of the yttrium ions are eight O^{2-} ions, forming a distorted cube (the local symmetry D_2). The yttrium ions can occupy six magnetically inequivalent positions, and for an arbitrary orientation of an external magnetic field in relation to the crystal, the EPR spectrum of an R^{3+} ion consists of six lines. If the magnetic field is directed along the [100] axis, the EPR spectrum consists of only two lines. Since in our work we studied the spin–lattice relaxation of Nd^{3+} ions in $Y_3Al_5O_{12}$, we list the gyromagnetic ratio for this ion: according to Ref. 8, $g_x=1.743$, $g_y=1.160$, and $g_z=3.908$.

The measurements were made via the pulsed saturation method in the X-band (using an IRÉS-1003 relaxometer at 9.25 GHz) and Q band (at 36.4 GHz) in the 4–15 K temperature range, primarily with the magnetic field $\mathbf{H}\|[100]$. For this orientation of the magnetic field, the resonant magnetic field at 9.25 GHz is $H=1685$ Oe (double line) and $H=4480$ Oe (quadruple line). At 36.4 GHz, measurements of spin–lattice relaxation were made only on the double line with $H=6660$ Oe. The magnetization restoration kinetics in most cases (always at high temperatures) was strictly single-exponential. Errors in measuring the spin–lattice relaxation rate by this method did not exceed 10%. At $T>20$ K, the EPR lines of Nd^{3+} begin to broaden considerably because of rapid spin–lattice relaxation, and disappear above 50 K. The temperature dependence of the linewidth (ΔH_{pp}) makes it possible to estimate the spin–lattice relaxation times in the 25–50 K range.

The method of determining these times is as follows. The formula

$$\Delta H_{pp}^2=\Delta H_{pp}H'_{pp}+(\Delta H_{pp}^0)^2 \tag{1}$$

relates the observed linewidth ΔH_{pp}, the part of the linewidth $\Delta H'_{pp}$ due to spin–lattice relaxation (Lorentzian lineshape), and ΔH_{pp}^0, which is the temperature-independent (at $T<20$ K) linewidth (Gaussian profile).[9] Using (1), we find $\Delta H'_{pp}$ and then determine T_1[10]

$$T_1^{-1}=\frac{\sqrt{3}g\beta}{2\hbar}\,\Delta H'_{pp}. \tag{2}$$

For our samples $\Delta H_{pp}^0=15$–20 Oe, and the values at $T\sim 50$ K exceed ΔH_{pp}^0 by a factor of approximately 20. The accuracy of the spin–lattice relaxation rate in this case was at worst 20%. The YAG samples used to measure the spin–lattice relaxation times were prepared by different techniques: sample A was grown at the Institute of Crystallography of the Russian Academy of Sciences by the method of horizontal oriented crystallization, and samples B and B′ were grown by the Czochralski method at the ''Polyus'' company.

The results of measuring T_1 are presented in Figs. 1–4.

Figure 1 shows the results of measuring T_1 for samples A and B at 1685 Oe (the double line corresponding to the g_z component) and 4480 Oe (quadruple line) at 9.25 GHz. The results will be discussed later. Here we give only the functional dependences of the spin–lattice relaxation rates on temperature, which are in good agreement with the experimental data.

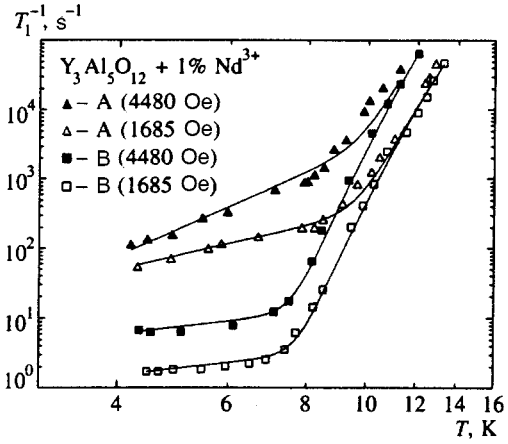

FIG. 1. Temperature dependence of the spin–lattice relaxation rate for Nd^{3+} ions in single-crystal samples of $Y_3Al_5O_{12}$ of type A and B. The magnetic field was directed along [100]. The solid curves represent calculations with Eqs. (3)–(6).

Sample A:

$$H=1685\ \text{Oe},\quad T_1^{-1}=[2.7T^{2.1}+5.2\times 10^{10}\times\exp(-128\times 1.44/T)]\ \text{s}^{-1}, \tag{3}$$

$$H=4480\ \text{Oe},\quad T_1^{-1}=[0.3T^{4}+3.1\times 10^{11}\times\exp(-128\times 1.44/T)]\ \text{s}^{-1}. \tag{4}$$

Sample B:

$$H=1685\ \text{Oe},\quad T_1^{-1}=[0.38T+5.2\times 10^{10}\times\exp(-128\times 1.44/T)]\ \text{s}^{-1}, \tag{5}$$

$$H=4480\ \text{Oe},\quad T_1^{-1}=[1.5T+3.1\times 10^{11}\times\exp(-128\times 1.44/T)]\ \text{s}^{-1}. \tag{6}$$

Figure 2 depicts the results of measuring T_1 at different fre-

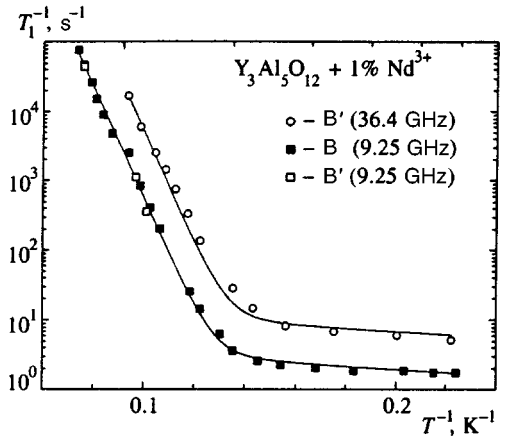

FIG. 2. Temperature dependence of the spin–lattice relaxation rate for Nd^{3+} ions in $Y_3Al_5O_{12}$. The measurements were made for the weak-field EPR line with $\mathbf{H}\|[100]$. The solid curves represent calculations using Eqs. (5) and (7).

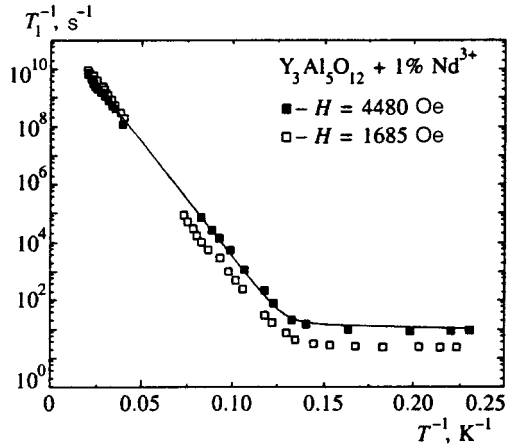

FIG. 3. Spin–lattice relaxation rate for Nd^{3+} ions in $Y_3Al_5O_{12}$. The measurements were made for weak-field and strong-filed EPR lines with $\mathbf{H} \parallel [100]$ at 9.25 GHz. The solid curve represents the results of calculations using Eq. (6).

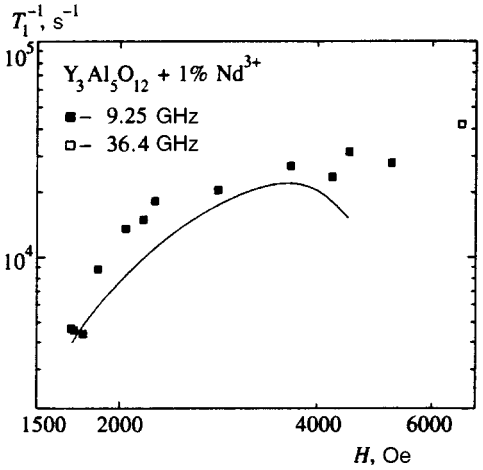

FIG. 4. Field dependence of the spin–lattice relaxation rate for Nd^{3+} ions in $Y_3Al_5O_{12}$. The magnetic field was oriented arbitrarily in a plane with [100], and the temperature was roughly 11.4 K. The solid curve represents the results of calculations using Eqs. (11) and (19) with $\gamma = 2\times10^{11}$ s^{-1}.

quencies (9.25 and 36.4 GHz) for the same orientation of the magnetic field (namely g_z) and, naturally, in different magnetic fields (1685 and 6660 Oe, respectively) for samples B and B′. The observed temperature dependence at 9.25 GHz is given in Eq. (5), and at 36.4 GHz it is:

$$T_1^{-1} = [1.33T + 4.6\times10^{11} \exp(-128\times1.44/T)] \ \text{s}^{-1}. \tag{7}$$

Figure 3 depicts the results of measuring the spin–lattice relaxation rate for sample B at 9.25 GHz both in the weak-field and strong-field EPR lines, obtained by using the pulsed saturation method (4–12 K), and from the temperature broadening of the lines (25–50 K). The solid curve corresponds
to (6).

Clearly, in the high-temperature range (where processes exponentially dependent on the reciprocal temperature dominate), there is a strong dependence of spin–lattice relaxation on the magnitude of the external magnetic field, both in measurements at different frequencies for the same orientation of the magnetic field and in measurements at a single frequency but on lines in different fields. For a detailed study of this dependence we measured T_1 at 9.25 GHz with $T \cong 11.4$ K for arbitrary orientations of the field in relation to crystallographic axes in EPR lines corresponding to different field strengths (Fig. 4). Note that when the EPR lines coincided, no jumps in the relaxation rates were observed. Figure 4 also depicts the result obtained at 36.4 GHz and 6660 Oe.

Let us discuss the results.

3. THEORY AND DISCUSSION

The temperature range over which the measurements were made can be tentatively divided into two regions: the high-temperature ($T > 8$ K), in which relaxation processes with rates exponentially depending on the reciprocal temperature dominant, and the low-temperature ($T < 8$ K), where $T_1^{-1} \propto AT^n$. For ''perfect'' samples B with the longest relaxation times we have $n = 1$; a linear dependence of rate on temperature usually indicates the presence of direct relaxation processes involving a single phonon with a frequency equal to the EPR frequency.[11] This assumption is in qualitative agreement with the increase in the coefficient A with field strength, although such an increase is not as rapid as might be expected from the Kronig–Van Vleck mechanism ($A \propto H^4$). This can probably be explained by the fact that at impurity ion concentrations of about 1%, two-particle relaxation mechanisms of the Waller type begin to operate.

For samples A we have $n > 1$, which qualitatively makes this situation resemble low-temperature relaxation of impurity rare-earth ions in KY_3F_{10} single crystals.[12] Possibly, in imperfect garnet crystals, rapidly relaxing centers like those in two-level systems in glasses are formed. The interaction of rare-earth ions with these centers can explain, at least in principle, the complicated temperature dependence of relaxation times. Ashurov *et al.*[13] studied the possible types of disorder in garnet crystals doped with rare-earth elements. They found that in crystals synthesized from the melt at high temperatures, additional impurity centers may appear. A fraction of the rare-earth ions occupy the positions of Al^{3+} ions and generate internal stresses, which reduces the quality of the crystal.

Unfortunately, in the case considered here, as in Ref. 12, the ''anomalous'' temperature behavior of the relaxation rate is observed only over a narrow temperature range, with temperatures differing by roughly one order of magnitude. Within this range one can establish fairly good agreement with the experimental data by approximating the measured rate T_1^{-1} by a sum of several exponential terms. Bagdasarov *et al.*[7] reasoned along approximately these lines and used a sum consisting of a term linear in temperature and an exponential term. They explained the presence of the second term as an effect of foreign impurity ions. Here we can merely state that the ''anomalous'' behavior of the rate at low temperatures is due to the imperfect nature of the crystal, and do not provide a concrete mechanism that would explain such behavior.

Now let us examine the high-temperature range. Here

the results for samples A and B under similar conditions of observation are essentially identical, i.e., the difference in the quality of the samples has little effect on the spin–lattice relaxation of the impurity ion. The relaxation rate can be written $T_1^{-1}=B\exp(-\Delta/T)$, with the coefficient B strongly dependent on the magnetic field strength: for the same line in the EPR spectrum (the weak-field line, corresponding to g_z) the rate at 36.4 GHz is approximately eight times the rate at 9.25 GHz (see Fig. 2). Of the same nature is the dependence in sample B on the magnetic field strength when we go from the weak-field (double) line to the strong-field (quadruple) line at the same frequency of 9.25 GHz (see Fig. 1), so that we can expect to obtain detailed data on the field dependence of the relaxation rate by changing the orientation of the magnetic field in relation to the crystallographic axes and measuring the rate at a fixed frequency on EPR lines in different fields (the results of such measurements are shown in Fig. 4).

The value of the parameter Δ, determined in spin–lattice relaxation studies, is close to the interval of 130 cm^{-1} separating the closest excited doublet from the principal doublet of Nd^{3+} in YAG,[1,14] which indicates the presence of a two-stage relaxation process of the resonance-fluorescence type through this excited level. We also note that studies of the IR spectrum of YAG have revealed the presence of vibrations with an energy of approximately 120 cm^{-1} (see Refs. 4–6). Hence, one cannot ignore the possibility that Nd^{3+} ions may relax by an ordinary Raman process involving optical phonons with an energy that might also lead to an exponential dependence of the spin–lattice relaxation rate on the reciprocal temperature, with the dispersion of this branch of lattice vibrations being small. We see that there can be two mechanisms of spin–lattice relaxation of the Nd^{3+} ion in YAG at high temperatures.

The literature suggests a field dependence of the spin–lattice relaxation rate due to distinctive lattice vibrations with a narrow frequency spectrum near Δ. A quadratic field dependence of the relaxation rate, $T_1^{-1}\propto H^2\exp(-\Delta/T)$ was discovered in studies of the spin–lattice relaxation of Yb^{3+} ions in BaY_2F_8 (see Ref. 15). Calculations demonstrated that one of the prerequisites for such a dependence is the proximity of the two excited levels of Yb^{3+}. The second excited level of Nd^{3+} in YAG is separated from the ground level by 199 cm^{-1}, which is rather far from the first, i.e., the condition is not met. A field dependence of the relaxation rate of the form $T_1^{-1}\propto H^{-2}\exp(-\Delta/T)$ was discovered in studies of spin–lattice relaxation of Tb^{3+} ions in $CaWO_4$ (see Ref. 16), and this was attributed to crystal lattice vibrations with an extremely narrow spectrum (of the order of EPR frequencies). This field dependence is the opposite of the one observed in YAG:Nd.

These facts lead one to doubt the effectiveness of the second relaxation mechanism, which assumes a strong link between the impurity Nd^{3+} ion in YAG and the branch of optical vibrations, which has a sharp maximum of the distribution density $\rho(\omega)$ at $\Delta\sim 120$ cm^{-1}. If this mechanism were effective for YAG:Nd^{3+}, it would show up in other rare-earth ions. For instance, in KY_3F_{10} the high-temperature relaxation rate for all three studied ions of Ce, Nd, and Yb follows the pattern $T_1^{-1}=B\exp(-\Delta/T)$ with $\Delta=87.5$ cm^{-1}, which means we are justified in believing this behavior to be due to the interaction of the ions and optical vibrations with energy Δ (see Ref. 12). On the other hand, in garnets the relaxation of Yb^{3+} obeys a $T_1^{-1}\propto T^9$ law, as noted earlier. We conclude that the optical vibrations of a garnet lattice at frequencies of approximately 120 cm^{-1} either do not strongly interact with the impurity ions, or their spectrum is extremely blurred. In both cases, the specific way in which they show up in spin–lattice relaxation is lost in comparison to acoustic vibrations: they only slightly modify the frequency distribution density of the vibrations, $\rho(\omega)\propto\omega^2$, characteristic of acoustic branches. Thus, the most probable relaxation process in YAG:Nd^{3+} at high temperatures is a two-stage process through an intermediate level with an excitation energy of 130 cm^{-1}. These assumptions also agree with our estimates of the relaxation rate based on the approximate Orbach–Jeffries scheme (see Ref. 17).

In calculating the spin–lattice relaxation rates, we used the values of the crystalline-field parameters for $Y_3Al_5O_{12}$:Nd^{3+} obtained by Morrison *et al.*:[18]

$$B_{20}=-208\ \text{cm}^{-1},\quad B_{22}=-306\ \text{cm}^{-1},$$

$$B_{40}=-339\ \text{cm}^{-1},\quad B_{42}=-410\ \text{cm}^{-1},$$

$$B_{44}=1065\ \text{cm}^{-1},\quad B_{60}=70\ \text{cm}^{-1},$$

$$B_{62}=197\ \text{cm}^{-1},\quad B_{64}=1116\ \text{cm}^{-1},$$

$$B_{66}=41\ \text{cm}^{-1}.$$

Calculations were carried out for the case in which the magnetic field was parallel to the [100] crystallographic axis for the weak- and strong-field lines. In both cases we arrived at the following temperature dependence for the relaxation rate:

$$T_1^{-1}=1.11\times 10^{11}\exp(-130\times 1.44/T).$$

Note that the calculations do not reflect the dependence of the spin–lattice relaxation rate on the magnetic field strength that we established experimentally. Obviously, this is due to the approximate nature of the formulas used in the Orbach–Jeffries method. However, such an approximation was thought of as being quite satisfactory, because the existing experimental data did not suggest any appreciable field dependence of the relaxation times due to two-stage processes.

Allowance for the effect of variations in the magnetic field strength on Δ, a quantity contained in the exponent in the expression for T_1^{-1} and in the pre-exponential factor B (through the distribution density $\rho(\Delta)$), leads to corrections to the rate of the order of $(\mu_B H/kT)^2$ and $(\mu_B H/\Delta)^2$ (here μ_B is the Bohr magneton); both are unimportant at high temperatures and values of Δ of order 100 cm^{-1}. More important corrections emerge when one allows for the specific features of the Kramers degeneracy of the Stark levels of rare-earth ions.[19–22] The authors of these papers have demonstrated that in relatively weak magnetic fields (the splitting of an excited doublet, $\Delta\omega$, is comparable to the doublet's width γ resulting from the finiteness of the respective lifetime), the rate T_1^{-1} consists of terms with and without the factors $(\Delta\omega/\gamma)^2$, and since $\Delta\omega\propto H$, a field dependence of the rate may emerge. We illustrate this dependence by using a simple approach in

which the rate of two-stage processes is obtained by slightly modifying the expression for the probability of two-phonon Raman processes (cf. Refs. 11 and 22).

Let us write that part of the probability of a Raman transition between the states n and n' of the principal doublet of a paramagnetic ion that without allowance for the width of the intermediate level (γ_m) would be represented by a divergent integral:

$$w_{nn'}=\frac{1}{72\pi^3\hbar^2 d^5 v^{10}}\sum_{ij} q_i q_j \int \omega^6 n_\omega(n_\omega+1) \times\left|\sum_m \frac{\langle n|V_i|m\rangle\langle m|V_j|n'\rangle}{\omega-\omega_{mn}+i\gamma_m/2}\right|^2 d\omega. \tag{8}$$

Here d is the crystal density, v is the average speed of sound, q_i and q_j are numerical factors of order 1, and $n_\omega=[\exp(\hbar\omega/kT)-1]^{-1}$ is the average number of phonons of frequency ω. The expression (8) was written by using the Debye model of crystal vibrations, and the spin–lattice Hamiltonian is

$$\mathscr{H}_{SL}=\sum_i V_i e_i, \tag{9}$$

where the e_i are the components of the displacement tensor $\tilde{e}=\partial\mathbf{u}/\partial\mathbf{r}$, which transforms as real-valued spherical harmonics ($e_1\sim e_{xx}+e_{yy}+e_{zz}$, $e_2\sim e_{xx}+e_{yy}-2e_{zz}$, $e_3\sim e_{xx}-e_{yy}$, $e_4\sim e_{yz}+e_{zy}$, $e_7\sim e_{yz}-e_{zy}$, etc.), with $\mathbf{u}(\mathbf{r})$ the displacement at the point $\mathbf{r}$ of the crystal lattice under a deformation. We allow only for the level closest to the ground level, the m,m' doublet with excitation energy Δ. For Kramers-conjugate states m and m', the ''widths'' are almost the same, $\gamma_m=\gamma_{m'}=\gamma$, but the matrix elements $u_{ij}=\langle n|V_i|m\rangle\langle m|V_j|n'\rangle$ and $v_{ij}=\langle n|V_i|m'\rangle\langle m'|V_j|n'\rangle$ are not necessarily equal; for instance, $u_{ii}=-v_{ii}$. We retain only the contribution of the ''resonant'' part of the integral in (8), associated with frequencies $\omega\sim\Delta$. Here it is important to allow for the splitting of the states m and m' by the magnetic field: $\Delta\omega=\omega_{mn}-\omega_{m'n}$. *Direct calculations of this contribution yield*

$$w_{nn'}\approx\frac{\Delta^6 n_\Delta(n_\Delta+1)}{36\pi^2\hbar^2 d^2 v^{10}\gamma}\sum_{ij} q_i q_j\{|v_{ij}|^2+|u_{ij}|^2 + \frac{2}{\Delta\omega^2+\gamma^2}[\gamma^2\ \mathrm{Re}(u_{ij}v_{ij}^*)+\gamma\Delta\omega\ \mathrm{Im}(u_{ij}v_{ij}^*)]\}, \tag{10}$$

where $*$ stands for complex conjugation. The usual expression for the probability of a two-stage process can be obtained in the approximation $(\gamma/\Delta\omega)\to 0$ by dropping the terms in braces that contain γ. Bearing in mind that $kT\ll\Delta$, we can write the following formula for the relaxation rate due to two-stage processes:

$$T_1^{-1}=w_{nn'}+w_{n'n}=\frac{\Delta^6}{18\pi^2\hbar^2 d^2 v^{10}\gamma} \times\left(B_1+B_2\frac{\Delta\omega^2}{\Delta\omega^2+\gamma^2}\right)\exp\left(-\frac{\Delta}{kT}\right). \tag{11}$$

The splitting of the excited doublet is $\Delta\omega=g_m\mu_B H$, where $g_m^2=g_{mx}^2 n_x^2+g_{my}^2 n_y^2+g_{mz}^2 n_z^2$ is the effective gyromagnetic ratio of the excited doublet of the Nd^{3+} ion, with the field orientation determined by the direction cosines n_α. For a fixed line in the EPR spectrum and a given orientation of the field, the splitting $\Delta\omega$ is proportional to the magnetic field strength or the resonance frequency ω_0. For a fixed frequency ω_0 and different components of the spectrum, or a fixed component but different field orientations, the value of the effective ratio g_m changes, as well.

The coefficients B_1 and B_2 in (11) also depend on the orientation of the field. For local D_2 symmetry they can be expressed in terms of the four parameters $A_{1,2,3,4}$ as follows:

$$B_1=\sum_{i\neq j} A_i A_j-\frac{2}{g^2}[(A_1A_2+A_3A_4)g_z^2 n_z^2 + (A_1A_3+A_2A_4)g_x^2 n_x^2+(A_1A_4+A_2A_3)g_y^2 n_y^2], \tag{12}$$

$$2(B_2+B_1)=(A_1+A_2+A_3+A_4)^2 - \frac{1}{g^2 g_m^2}[(A_1+A_2-A_3-A_4)g_z g_{mz} n_z^2 + (A_1+A_3-A_2-A_4)g_x g_{mx} n_x^2 + (A_1+A_4-A_2-A_3)g_y g_{my} n_y^2]^2. \tag{13}$$

The parameters A_i are combinations of the matrix elements of the operators V_i in (9) between the states (N,N') and (M,M') of the principal and excited doublets, respectively, the states being selected in such a way that they diagonalize the component J_z of the angular momentum operator. The functions $|N'\rangle$ and $|M'\rangle$ are the result of time reversal of the functions $|N\rangle$ and $|M\rangle$, respectively, so that under a rotation of 180° about the z axis, $|N\rangle$ and $|M\rangle$ are multiplied by i and $|N'\rangle$ and $|M'\rangle$ by $-i$. Then

$$A_1=q_1|U_1|^2+q_2|U_2|^2+q_3|U_3|^2,$$
$$A_2=q_6|U_6|^2+q_9|U_9|^2,$$
$$A_3=q_4|W_4|^2+q_7|W_7|^2,\quad A_4=q_5|W_5|^2+q_8|W_8|^2, \tag{14}$$

where

$$U_i=\langle N|V_i|M\rangle,\quad W_i=\langle N|V_i|M'\rangle. \tag{15}$$

If the parameters A_i are approximately equal in magnitude, the relaxation rates contain essentially no orientational dependence. This dependence can show up quite clearly if one parameter is much larger than the others, i.e., if the paramagnetic ion is effectively related to a definite type of deformation.

The fact that magnetic ions are firmly related to a definite type of deformation is a characteristic feature of many phenomena in crystals. We note, for instance, that magnetostriction in $LiTmF_4$ in a magnetic field parallel to a crystallographic axis ($\mathbf{H}\|\mathbf{c}$) resulting from the totally symmetric deformations e_{zz} and $e_{xx}+e_{yy}$, is weaker by a factor of 1000 than magnetostriction in a magnetic field $\mathbf{H}\perp\mathbf{c}$, due to deformations $e_{xx}-e_{yy}$ and e_{xy} (see Ref. 23). Hence we can make

an assumption that makes it possible to describe the orientational dependence of the relaxation rate observed in experiments:

$$A_1 = na, \quad A_2 = A_3 = A_4 = a, \quad n \approx 10^3. \tag{16}$$

For estimates we also used the calculated values of the components of tensor g_m obtained by using the parameters (given above) of the crystalline field with allowance for all the j-multiplets of the ground state term ^{4}I of the Nd^{3+} ion:

$$g_{mx} = 0.765, \quad g_{my} = 0.609, \quad g_{mz} = 4.355. \tag{17}$$

Note that the calculated values of the gyromagnetic ratios of the principal doublet,

$$g_x = -1.249, \quad g_y = 1.83, \quad g_z = -3.973 \tag{18}$$

obtained in a similar manner agree fairly well with the experimental data given at the beginning of Sec. 2. For the width of the intermediate level we take $\gamma = 2 \times 10^{11}$ s^{-1} (the average pre-exponential factor in Eqs. (3)–(7)) and examine the dependence of the relaxation rate on the orientation of the external field in the (100) plane of the crystal (this plane contains the z axis and the bisectrix of the angle between the local x and y axes, i.e., $n_x = n_y$).

In this case

$$B_1 = 4(n+1)a^2,$$

$$B_2 = 0.5(n-1)^2 a^2 \{1 - g^{-2} g_m^{-2} (17.1 \cos^2 \theta - 0.08)^2\},$$

$$\Delta\omega^2 = \omega_0^2 g_m^2 g^{-2},$$

$$g^2 = 13.1 \cos^2 \theta + 2.19, \quad g_m^2 = 18.49 \cos^2 \theta + 0.48, \tag{19}$$

where θ is the angle between the z axis and the field, and ω_0 is the fixed frequency of the variable field ($2\pi \times 9.25$ GHz). By adjusting the parameter a in such a way that for the z-orientation the calculated relaxation rate coincides with the experimental value, and plotting the relaxation rate for each orientation as a function of the corresponding value of the external magnetic field strength, we were able to adequately represent the pattern of the experimental points in Fig. 4 (the solid curve depicts the result of relaxation rate calculations).

When the field is oriented along the principal axes of the g-tensor, the coefficient B_2 vanishes, and, according to our theory, in perfect crystals there should be no field dependence of the relaxation rate for such orientations (cf. Refs. 19 and 21). One can expect, however, that the crystal contains a number of positions of impurity centers of lower symmetry, and that there is a noticeable deviation of the axes of the g-tensors from the crystallographic axes. Already at $B_2 \approx B_1$ the relaxation of such centers is strongly dependent on $|\mathbf{H}|$. The reason for such distortions may be the imperfection of the crystals discussed above and the paramagnetic impurities proper, whose concentration ($\approx 1\%$) is fairly high. For such a concentration, the spins are strongly coupled and relax as a single system, which imposes the overall field dependence of the relaxation rate. To verify this point it would be desirable to study the concentration dependence of the relaxation rate, especially at extremely low concentrations.

Note that there is one more possible explanation of the dependence of the relaxation rate on the magnetic field strength: the proximity of the optical phonon frequencies to the frequency Δ of the transition of an impurity ion into the excited state. If the edge of the phonon band is close to Δ, the extent to which optical phonons participate in two-stage relaxation processes is determined by the overlap of this band and the profile of the line of excitation of the ion. As the magnetic field strength increases, this line, whose width is γ, moves inside a small interval of 2–3 cm^{-1}, but this can be sufficient for an appreciable increase in the above-mentioned overlap and, accordingly, for an increase in the rate of relaxation with participation of optical phonons. Perhaps this mechanism is an addition to the one mentioned earlier, and facilitates a more clearcut manifestation of the field dependence of the spin–lattice relaxation rate.

Thus, the field dependence of the spin–lattice relaxation rate of Nd^{3+} ions in YAG discovered in the high-temperature range can probably be interpreted as a specific manifestation of the degeneracy of the excited level participating in the two-stage relaxation process. This is also in full agreement with the fact that the temperature-dependent part of the EPR linewidth does not depend on the field strength, since it is determined by the probability of direct transitions from the ground states to the excited and, therefore, does not depend on whether the latter are degenerate or not. For the same reason, the estimates of relaxation times done by using the linewidth is in better agreement with the pulsed measurements of T_1^{-1} at large values of the magnetic field strength.

According to Eq. (11), several conditions must be met for the field dependence of the spin–lattice relaxation time to show up: the lifetime of the intermediate level must be sufficiently short ($\gamma \geqslant \omega_0$), and the coefficient B_2 must be large ($B_2 > B_1$). The quantity γ is proportional to the phonon distribution density $\rho(\Delta)$, and an increase in the Debye value of the density due to optical vibrations at a frequency close to the energy Δ of ion excitation may also play a role in that the YAG:Nd system proves to be a convenient object for observing this dependence.

4. CONCLUSION

We now summarize the main results of our investigation of the spin–lattice relaxation of the impurity Nd^{3+} ions in YAG.

1. Low-temperature relaxation is determined to a great extent by the method of sample preparation. In the most ''perfect'' crystals, relaxation results from direct energy transfer to the phonon system. The existence of defects markedly increases the relaxation rate.

2. At high temperatures, the difference in relaxation rates for different samples becomes smaller. The transfer of ion energy to the lattice is a two-stage process through an intermediate level with excitation energy $\Delta \sim 130$ cm^{-1}. We found that here relaxation strongly depends on the external magnetic field. We know of no reports of such a dependence in experiments involving various systems.

3. The probable reason for such a dependence is the quasidegeneracy of the excited doublet level of the ion, for which the doublet splitting is comparable to the reciprocal

lifetime of the state. The presence in the YAG lattice of optical vibrations with frequencies close to Δ probably reduces this lifetime, and results in a more clearcut manifestation of the field dependence of the relaxation rate.

The authors are grateful to B. Z. Malkin for discussions and data on gyromagnetic ratio calculations, and to G. A. Ermakov and E. V. Antonov for providing the single crystals for the experiments.

[1] A. A. Kaminskiĭ, *Laser Crystals. Their Physics and Properties*, 2nd ed., Springer, Berlin (1990).
[2] I. Svare and G. Seidel, in *Paramagnetic Resonance*, W. Low, (Ed.), Vol. 2, Academic Press, New York (1963).
[3] C. Y. Huang, Phys. Rev. **139**, A241 (1965).
[4] N. T. McDevitt, J. Opt. Soc. Am. **59**, 1240 (1969).
[5] J. P. Hurrell, S. P. S. Porto, I. F. Chang *et al.*, Phys. Rev. **173**, 851 (1968).
[6] G. A. Slack, D. W. Oliver, R. M. Chrenko *et al.*, Phys. Rev. **177**, 1308 (1969).
[7] Kh. S. Bagdasarov, D. M. Daraseliya, and A. A. Manenkov, JETP Lett. **2**, 329 (1965).
[8] É. P. Nikolova and B. L. Timan, Zh. Prikl. Spektrosk. **36**, 479 (1982).
[9] G. M. Zhidomirov, Ya. S. Lebedev, S. N. Dobryakov *et al.*, *Interpretation of Complex EPR Spectra* [in Russian], Nauka, Moscow (1975).
[10] Gh. Cristea, T. L. Bohan, and H. J. Stapleton, Phys. Rev. B **4**, 2081 (1971).
[11] S. A. Al'tschuler and B. M. Kozyrev, *Electron Paramagnetic Resonance in Compounds of Transition Elements*, 2nd ed., Wiley, New York (1975).
[12] L. K. Aminov and I. N. Kurkin, Fiz. Tverd. Tela (St. Petersburg) **37**, 2684 (1995) [Phys. Solid State **37**, 1476 (1995)].
[13] M. Kh. Ashurov, Yu. K. Voron'ko, V. V. Osiko *et al.*, in *The Spectroscopy of Crystals* [in Russian], Nauka, Leningrad (1978).
[14] R. K. Watts and W. C. Holton, J. Appl. Phys. **45**, 873 (1974).
[15] I. N. Kurkin and K. P. Chernov, Zh. Éksp. Teor. Fiz. **83**, 1072 (1982) [Sov. Phys. JETP **56**, 607 (1982)].
[16] L. K. Aminov, V. A. Ivan'shin, and I. N. Kurkin, in *Paramagnetic Resonance* [in Russian], No. 23, Kazan Univ. Press, Kazan (1990).
[17] C. D. Jeffries, *Dynamic Nuclear Orientation*, Wiley, New York (1963).
[18] C. A. Morrison, D. E. Wortman, and N. Karayianis, J. Phys. C **9**, L191 (1976).
[19] J. W. Culvahouse and P. M. Richards, Phys. Rev. **178**, 485 (1969).
[20] I. V. Aleksandrov and K. K. Pukhov, Fiz. Tverd. Tela (Leningrad) **9**, 1159, (1967) [Sov. Phys. Solid State **9**, 906 (1967)].
[21] I. V. Aleksandrov and K. K. Pukhov, in *Paramagnetic Resonance (1944–1969)* [in Russian], Nauka, Moscow (1971).
[22] S. K. Lyo, Phys. Rev. B **5**, 795 (1972).
[23] S. A. Al'tshuler, V. I. Krotov, and B. Z. Malkin, JETP Lett. **32**, 214 (1980).

Translated by Eugene Yankovsky

Instability of single-electron memory at low temperatures in Al/AlO$_x$/Al structures

V. A. Krupenin, S. V. Lotkhov, and D. E. Presnov

M. V. Lomonosov Moscow State University, 119899 Moscow, Russia
(Submitted 4 July 1996)
Zh. Éksp. Teor. Fiz. **111**, 344–357 (January 1997)

A nanostructure based on a uniform one-dimensional array of ultrasmall tunnel junctions (a single-electron trap) characterized by an ability to maintain an excess charge of several electrons in an island is fabricated and investigated. Changes in the state of the trap are detected by a single-electron transistor. At the working temperature $T=35$ mK the storage time of a charge state is more than 8 h (which is the duration of the experiment). It is demonstrated that the possible factors limiting the lifetime of a state at temperatures below the typical temperatures for thermal activation include the influence of the random distribution and drift of the effective background charges of the metal islands, as well as the reverse influence discovered here of the transistor on the trap. As the current passing through the transistor increases, the hysteresis loop in the dependence of the charge in the trap on the control voltage narrows. It is noted that an increase in the current from 5 to 300 nA is equivalent to raising the working temperature to 250 mK. © *1997 American Institute of Physics.* [S1063-7761(97)02201-4]

1. INTRODUCTION

The development of nanolithographic methods has made it possible to fabricate single-electron systems of submicron tunnel junctions, whose behavior is based on the Coulomb blockade. In order for the charge effects to predominate over the background of thermal fluctuations and the quantum spreading of the energy levels, the parameters of the structure must satisfy the following conditions:[1]

$$C \ll e^2/2kT, \quad R \gg R_q, \tag{1}$$

where C and R are the characteristic capacitance and tunnel resistance of the junctions, k is Boltzmann's constant, T is the temperature of the sample, e is the electron charge, h is Planck's constant, and $R_q=h/4e^2\approx 6.5$ kΩ is the quantum resistance. Remarkably, the conditions (1) do not lead to fundamental restrictions on the minimum topological dimensions of single-electron structures. This makes single-electron structures promising for further miniaturization of the basic cells of microelectronic structures.[2]

The present research is devoted to an experimental investigation of a prototype single-electron memory cell or, stated differently, a single-electron trap. The simplest form of a single-electron trap is depicted schematically in Fig. 1a.

The metal island A, which is under the electrostatic influence of a control electrode (gate), is connected to a grounded electrode by a uniform one-dimensional array of N tunnel junctions with capacitance C_t. In energy terms the presence of this array is represented by the presence of an electrostatic barrier controlled by the gate voltage V_g (Fig. 2):

$$\Delta E_i = e^2/2C_\Sigma^i - eV_i(V_g), \tag{2}$$

where C_Σ^i is the total capacitance of the ith intermediate island in the array ($0<i\leqslant N$), defined to be the charge of the island produced by unit potential when all external electrodes are grounded, and $V_i(V_g)$ is the contribution to the potential of the ith island from the field created by the voltage applied to the gate. Depending on its height, the barrier is capable of isolating an excess charge ne in the island, where n is an integer in a certain range of values: $n_{\min}(V_g)<n<n_{\max}(V_g)$. The discrete number of stable charge states M in the trap as a function of the gate voltage V_g is[3]

$$M=\left[\frac{NC_\Sigma}{C_t}-1\right]+\frac{1}{2}\pm\frac{1}{2}, \tag{3}$$

where C_Σ is the total capacitance of the island A. By asymmetrizing (''tilting'') the barrier by means of one of the increments $(\Delta V_g)_{\text{in}}$ or $(\Delta V_g)_{\text{out}}$ we can cause the tunneling of an electron into or out of the island, respectively, with the resultant change $n\rightarrow n\pm 1$. For the reverse transition $n\pm 1\rightarrow n$ to occur, the direction of the asymmetrization (''tilting'') of the barrier must be reversed by an opposite change in V_g. Thus, the dependence of the island charge on V_g has a hysteretic character (see Fig. 6 in Sec. 3.2). The width of the hysteresis loop depends on the height of the barrier, the temperature, the V_g sweep rate, and the influence of external excitations. The state in which the system is found at the current time is determined by the history of the variation of V_g, i.e., the system has memory. A pair of adjacent states with n and $n+1$ electrons in the island can be assigned to logical 0 and 1 (or low and high), and such a single-electron trap can be used to store a single bit of digital information.

Unfortunately, there are several mechanisms that lead to undesirable switching between the charge states of the trap and thereby reduce the accuracy of stored digital information. They include the thermal activation of tunneling (the influence of this effect on a single-electron trap was thoroughly examined in Ref. 4), macroscopic quantum tunneling,[5] and tunneling due to photon excitation.[6] The behavior of the experimental structure is also influenced significantly by the random drift of the background effective charges of the islands in the structure, on which we shall dwell in detail in this paper.

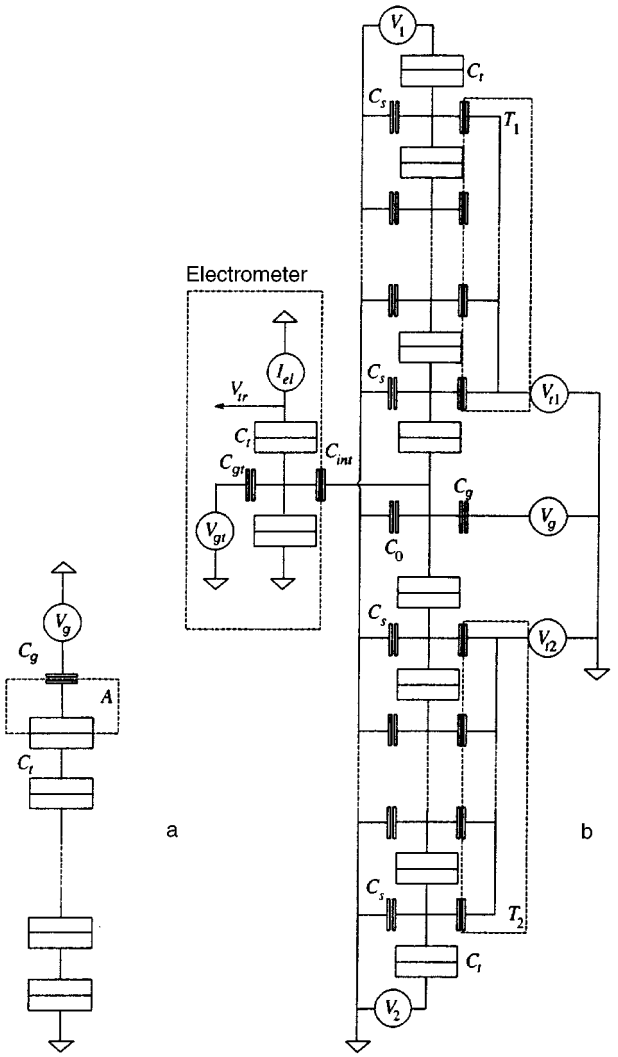

FIG. 1. Equivalent circuits of a very simple single-electron trap (a) and of the experimental structure investigated (b).

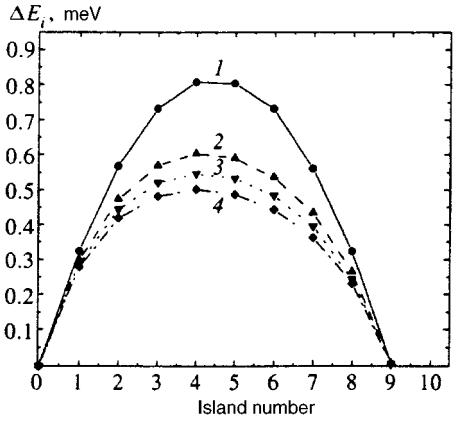

FIG. 2. Dependence of the free energy ΔE_i on the position of the electrode in the array for various values of the self-capacitance of the intermediate islands: *1)* $C_s=0$, *2)* $C_s=10$ aF, *3)* $C_s=15$ aF, *4)* $C_s=20$ aF. The data were obtained numerically, using Eq. (2), $C_t=200$ aF, $C_\Sigma=240$ aF, and $V_g=e/2C_g=1.14$ mV.

We observed a reverse influence of the single-electron electrometer used to detect the tunnel events on the charge dynamics of the trap. It was discovered that the width of the hysteresis loop in the dependence of the trap island charge on the gate voltage decreases as the constant current supplied to the single-electron transistor is increased, shortening the lifetime of the states.

2. EXPERIMENTAL METHOD

The equivalent circuit of the experimental structure is depicted in Fig. 1b. The structure includes an additional similar one-dimensional array of tunnel junctions connected to the trap island, making it possible for current to flow along two one-dimensional series arrays. For this reason, the principal electrical parameters can be determined in this circuit directly from measurements without enlisting topological calculations of the capacitances. It is known[7] that the current–voltage characteristic of a one-dimensional array of tunnel junctions has a Coulomb-blockade segment at voltages less than a certain threshold ($V<V_{\rm th}$) and that it tends to a linear asymptote at $V\gg V_{\rm th}$. Thus, by supplying a bias voltage several times the threshold voltage of the Coulomb blockade of each array or, in other words, by selecting a nearly asymptotic regime, we can neglect the nonlinearity of the current–voltage characteristic of each array in evaluations and calculate the voltage on the central island using Ohm's law. This permits the direct determination of both the ratio between the asymptotic resistances of the arrays and the mutual capacitance $C_{\rm int}$ of the central islands of the transistor and the trap from measurements. Knowing $C_{\rm int}$, we can evaluate the total capacitance of the trap island C_Σ, which is needed to calculate the height of the electrostatic barrier.

In our experiment, variations in the state of the island in the single-electron trap were detected because of the capacitive coupling of the trap island to the single-electron transistor alongside it.[8] The need to compensate for the influence of the background charge called for the introduction of additional tuning gates T_1 and T_2 for the arrays.

A system of small-area (80×80 nm^2) Al/AlO$_x$/Al tunnel junctions was fabricated on a silicon substrate with an insulating Al_2O_3 coating of thickness 200 nm by the two-shadow deposition of Al through a two-layer electron-beam lithographic mask with suspended segments and intermediate *in situ* oxidation (see, for example, Ref. 9). A photomicrograph of the experimental structure is presented in Fig. 3.

The measurements of the electrical characteristics were performed in a dilution refrigerator at temperatures from 30 to 200 mK. The parts of the cryostat and the measuring circuit that are at higher temperatures, the electromagnetic background in the laboratory, and the ''noisy'' power supplies of the measuring instruments can be sources of electromagnetic excitations capable of provoking a tunnel event. External noise is capable of reaching the single-electron structure both along the electrical conductors and through leaks in the shielding of the sample. To protect the sample from noise, it was enclosed in a hermetically sealed metal capsule, and the electrical connecting lines from the sample to the measuring instruments were interrupted by coaxial cable microwave filters,[10] which were located in the same

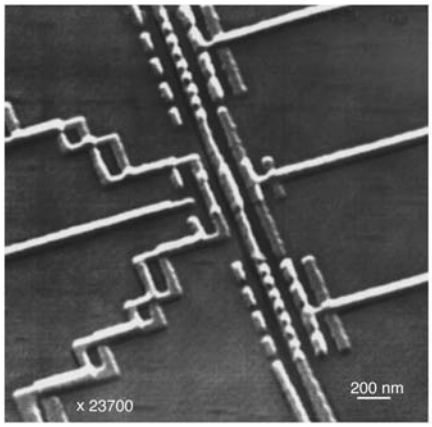

FIG. 3. Photomicrograph of the experimental structure.

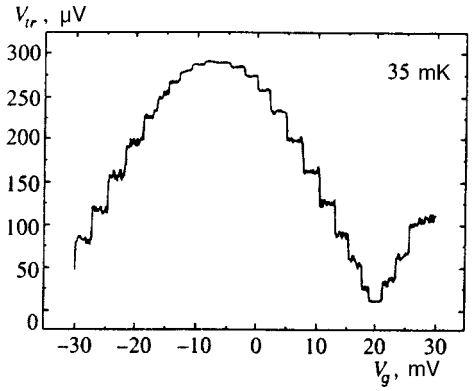

FIG. 4. Period of the modulation characteristic $V_{tr}(V_g)$ of the electrometer by the trap gate in the ''compensated'' regime. There are $m=24$ tunnel events in one modulation period.

capsule with the sample in direct proximity to it and were at the same temperature. Special low-noise measuring instruments were used in the experiment. The power sources of the control circuits and preamplifiers were storage batteries. The typical noise level of the measuring instruments was $V_{rms}\sim 30$ nV/Hz$^{1/2}$ at a frequency of 10 Hz.

3. EXPERIMENTAL RESULTS

3.1. Determination of the parameters of the structure

1. To determine the resistance ratio, the arrays must be brought into a conducting (unblocked) state by applying a potential difference V_1-V_2 several (~ 10) times greater than the blockade voltage to their ends. In this case the potential of the central island in the trap is determined by the ratio between the total resistances of the arrays R_1/R_2 and the applied voltages V_1 and V_2 at the ends. We record the signal from the electrometer and supply a small positive voltage increment ΔV_1 to one end of the structure. The amplitude of the signal from the electrometer varies. By applying a negative voltage increment ΔV_2 to the other end of the structure, we can restore the original ''reading'' of the electrometer. It is clear that

$$R_1/R_2=|\Delta V_1/\Delta V_2|. \tag{4}$$

The ratio between the resistances of the arrays $R_1/R_2=0.88$ justifies considering them to be the same to within the accuracy of our evaluations (approximately 20%).

2. The period ΔV_{tr} of the modulation characteristic $V_{tr}(V_{gt})$ of the transistor is determined by the mutual capacitance between the island of the transistor and the modulating electrode C_{gt} and is equal to 21 mV, whence $C_{gt}=e/\Delta V_{tr}=7.6$ aF. The capacitances C_t of the tunnel junctions evaluated from the offset voltage $V_{off}=e/C_{sum}$ of the current–voltage characteristic of the transistor (under the assumption that $C_{sum}\approx 2C_t$, where C_{sum} is the total capacitance of the transistor island) are approximately equal to 200 aF.

3. When the mutual capacitances of the islands in the arrays with the island of the transistor are neglected (modulating the conductivity of the transistor by the gates T_1 and T_2 to the arrays, we estimated that together they amount to about 20% of C_{int}), it can be assumed that the electrometer ''senses'' only the potential of the trap island. Applying identical increments $\Delta V_1=\Delta V_2$ to the voltages at the ends of the arrays, which have been shifted into the conducting state by the fixed potential difference V_1-V_2, we find the mutual capacitance C_{int} of the transistor island and the trap island from the period of the plot of $V_{tr}(V_1)$.

4. If the effective electrostatic influence of the trap gate on the transistor island is balanced by applying a corresponding voltage to the ''transistor's'' gate, the modulation of the transistor will be stepwise (Fig. 4) and will occur exclusively as a result of electron tunneling events from its island to the trap island. This permits evaluation of the total capacitance of the trap island C_Σ (which is defined in analogy to C_Σ^i, see the Introduction).

The passage of one modulation period corresponds to variation of the trap island charge by me, where m is the number of electrons that entered the island. The change in the trap island potential not balanced by the ''electrometer's'' gate equals

$$\Delta V_0=me/C_\Sigma. \tag{5}$$

On the other hand, this voltage change led to variation of the effective charge of the transistor island by e; therefore,

$$C_{int}\Delta V_0=e. \tag{6}$$

Comparing (5) and (6), we obtain

$$C_\Sigma=mC_{int}. \tag{7}$$

5. The increment of the voltage V_g between two successive jumps in Fig. 4 equals e/C_g (see, for example, Ref. 3), whence we can easily determine C_g, i.e., the mutual capacitance of the island and the gate.

6. Let us define the total nontunnel capacitance of an intermediate island in an array C_s as the sum of the self-capacitance (the ''capacitance to ground'') of the island and the mutual capacitances of the island to all the electrodes surrounding it, except those separated from it by tunnel barriers. Starting with the assumption that the structure under consideration is one-dimensional and linear (see Fig. 3) and taking into account that the length of the central island of the trap is 10 times the effective length of an intermediate island

TABLE I. Numerical values of the parameters of the experimental structure.

			Capacitance, aF						
Parameter	R_1+R_2	R_1/R_2	C_{gt}	C_g	C_{int}	C_t	C_Σ	C	C_s
Value	2 MΩ	0.88	7.6	70	10	200	240	45	15

in an array, we have $C_{\text{nt}} \cong 10C_s$, where C_{nt} is the total nontunnel capacitance of the trap island, which is defined by analogy to C_s. Using the obvious relation

$$C_\Sigma = 2C + C_{\text{nt}} \approx 2C + 10C_s \tag{8}$$

where C is the capacitance of one array of junctions, which is numerically equal to the charge of the right-hand end of the array induced by unit potential when the left-hand end is grounded, and taking $C \sim C_t/N \approx 22$ aF as a zeroth approximation, we obtain the rough estimate $C_s \sim 20$ aF.

For a more accurate determination of C with consideration of the finite values of C_s we consider a ''semi-infinite'' array of metal islands with a total nontunnel capacitance C_s, which are separated by tunnel barriers with a capacitance C_t. The capacitance C_x of the ''semi-infinite'' array, being equal to the capacitance of any semi-infinite segment thereof, satisfies the equation

$$(C_x)^{-1} = (C_t)^{-1} + (C_s + C_x)^{-1}. \tag{9}$$

The potential V_i of the ith island from the end of the array is related to the potential of the end of the array V_0 by the expression

$$V_i = V_{i-1}\,\frac{C_x}{C_x+C_s} = V_{i-2}\left(\frac{C_x}{C_x+C_s}\right)^2 = \ldots = V_0\left(\frac{C_x}{C_x+C_s}\right)^i. \tag{10}$$

Eliminating C_x by plugging the solution of Eq. (9) into (10) and taking into account that $C_t/C_s \gg 1$, we obtain

$$V_i \approx V_0\,\exp(-i/\lambda), \tag{11}$$

where $\lambda = \sqrt{C_t/C_s}$ is the characteristic electrostatic shielding length in the array. The physical meaning of Eq. (11) is[7] that the electrostatic field in the array is localized within a sequence of λ junctions counted from the voltage source. The remaining tunnel junctions are scarcely polarized and are under the influence of a nearly zero potential. The estimates of C_t and C_s presented above give $\lambda \sim 3-4$ for a ''semi-infinite'' array with the parameters of the structure that we investigated. The field damping coefficient for $N=9$ equals $\exp(-N/\lambda) \approx 0.06$. Clearly, grounding the Nth island of the array, which transforms it from a ''semi-infinite'' array into a real array, does not lead to significant redistribution of the potential and the polarized charges in the array, and to within $V_N/V_0 \approx \exp(-N/\lambda)$ Eq. (9) is also applicable to the determination of the capacitance of a finite array C:

$$(C)^{-1} = (C_t)^{-1} + (C_s + C)^{-1}. \tag{12}$$

Solving the system of equations (8) and (12), we find the values $C_s \approx 15$ aF and $C \approx 45$ aF.

The approximate values obtained for the parameters of our experimental structure are presented in Table I.

3.2. Lifetime of a charge state

The height of the energy barrier and therefore the number of stable states and their lifetimes are greatly dependent on the electrostatic influence of the distribution of the uncompensated charge in the substrate and the space surrounding the structure, i.e., on the electrostatic environment. This can be seen indirectly after taking into account that the height of the energy barrier ΔE also specifies the value of the threshold voltage of the Coulomb blockade in an array of tunnel junctions: $(V_1 - V_2)_T \sim \Delta E/e$. Figure 5 presents an experimental plot of the dependence of the voltage at a small current through the array, which is thus close to $(V_1 - V_2)_T$, on the voltage on the gate T_1 for zero voltages on the remaining gates.

As is seen from Fig. 5, the maximum threshold voltage and, therefore, the maximum barrier height are achieved at a nonzero value of the compensating voltage on T_1. Moreover, the form of the dependence varies with the passage of time, demonstrating the drift of the distribution of the effective background charges Q_{0i}, where i labels the islands. In the ideal case, complete compensation of the drift phenomena requires the inclusion of $N-1$ tuning gates in the structure (in accordance with the number of intermediate islands), which is not feasible in complicated applied systems. For this reason, the search for methods of overcoming the background charge in single-electron structures takes on special urgency.

Figure 6 shows two $V_{\text{tr}}(V_g)$ hysteresis loops, which were recorded by the electrometer with a time interval for optimal

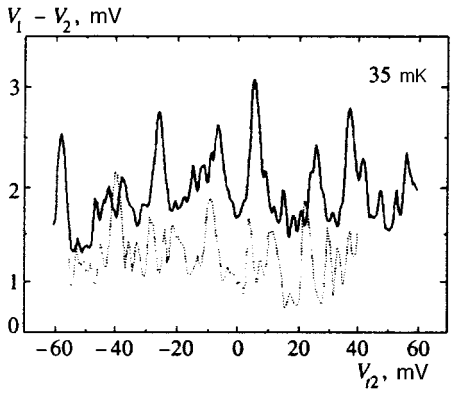

FIG. 5. Dependence of the voltage at the small current $I=5$ pA through an array as a function of the voltage on the tuning gate T_2. The time interval between the measurements of the plots depicted by the dotted line and the solid line was 70 h.

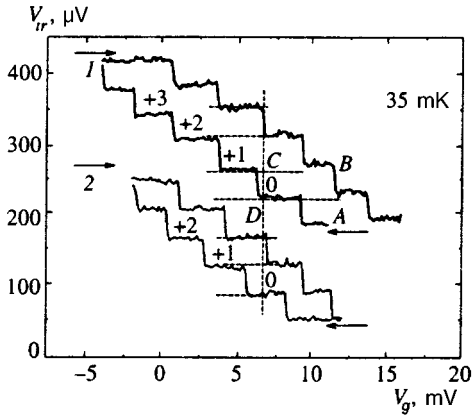

FIG. 6. Narrowing of the hysteresis loop with the passage of time ($I=5$ pA). Pair of curves *2*, which were obtained 2 h after curves *1*, is displaced downward along the vertical axis by 150 μV for the sake of clarity.

tuning of the gates T_1 and T_2 and are actually diagrams of the charge states of the island. The number of stable states can be determined from the number of steps in the diagram of states intersected by the single vertical straight line $V_g=V_{g0}$. When the temperature, sweep rate, operating conditions of the electrometer, and voltages on the tuning gates were fixed, gradual narrowing of the hysteresis loop with a decrease in the number of states from 4 (curve *1* in Fig. 6) to 3 (curve *2*) was observed with the passage of time, attesting to lowering of the electrostatic barrier, which is, in all likelihood, due to the redistribution of the Q_{0i}.

For the two neighboring states 0 and 1 corresponding to the hysteresis loop *ABCD* (Fig. 6), the ratio between the mean lifetimes τ_0 and τ_1 depends on the choice of V_g in the range $V_{CD}<V_g<V_{AB}$. The temperature T was fixed in the range 150–200 mK, in which the characteristic lifetimes are convenient for measurement (Fig. 7). It is clear that $\tau_0 \gg \tau_1 \approx 0$ at the point $V_g=V_{AB}$ and that $\tau_1 \gg \tau_0 \approx 0$ at the point $V_g=V_{CD}$. Therefore, there is an intermediate value of V_g for which $\tau_1=\tau_0$.

If the lifetime of a state is governed by the thermal mechanism for activating electron tunneling, we have[4]

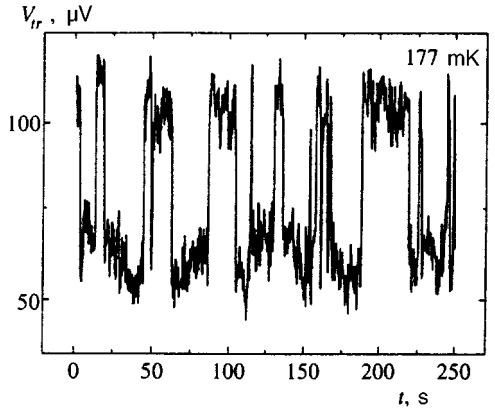

FIG. 7. Alternating random switching of the charge states of a single-electron trap recorded on a background of noise using an electrometer with a current in the transistor $I=5$ pA.

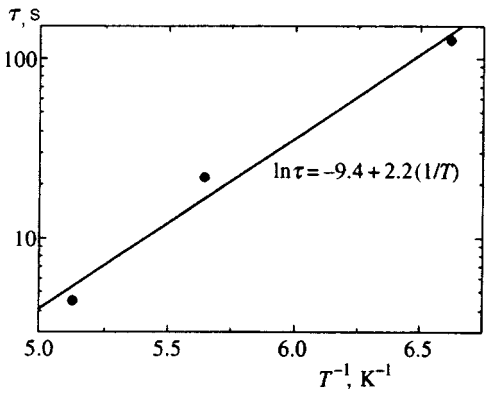

FIG. 8. Temperature dependence of the mean lifetime of a charge state.

$$\langle\tau\rangle \propto \exp(\Delta E/kT), \tag{13}$$

where ΔE is the height of the energy barrier. In other words, the tunneling rate is proportional to the probability of the thermal excitation of an electron to a level exceeding the height of the electrostatic barrier. The barrier height at which $\tau_1=\tau_0=\tau$, as determined from the slope of the semilog plot of $\tau(1/T)$ in Fig. 8, is 0.19 ± 0.3 meV.

The estimate of the lifetime of the state at 35 mK, obtained by extrapolating the data in Fig. 8, is $\exp 53 \approx 10^{23}$ s, which is much greater than the experimental observation time.

Macroscopic quantum tunneling of a charge (cotunneling) is also known to be one of the channels for the decay of a state. The time constant $\tau_{\rm cot}$ of the cotunneling process in an array of N tunnel junctions can be estimated (13) to be

$$\tau_{\rm cot}=2R_tC_t[(N-1)!]^2N^{-2N}(2N-1)! \times\left(\frac{\pi^2R_t}{R_q}\right)^{N-1}\left(\frac{E_C}{eV}\right)^{2N-1}, \tag{14}$$

where $E_C=e^2/2C_t$ is the characteristic Coulomb energy and V is the potential difference across the array of tunnel junctions.

According to (14), the cotunneling rate drops significantly under the condition $E_C/eV \gg 1$. The inequality $E_C/eV>3$, at least, holds for a symmetrized ($\tau=\tau_1=\tau_0$) barrier, giving the estimate $\tau_{\rm cot}>10^{20}$ s.

To demonstrate the memory effect, we stored an electron for more than 8 h. After this time, the voltage $V_{\rm tr}$ varied significantly (by more than the height of a step) due to the drift of the effective background charge of the electrometer island. Therefore, in order to demonstrate the constancy of the state, we took a ''reading'' of the trapped electron after raising the value of V_g above V_{AB}, which caused a jump in $V_{\rm tr}$.

As we have already stated, the hysteresis loop $\Delta V_{\rm loop}$ in the dependence of the trap island charge on the gate voltage can narrow under the influence of external excitations that are capable of provoking a random tunnel event. We discovered that the single-electron electrometer used to detect events in the trap is one of the sources of such excitations: the width of the hysteresis loop (Fig. 9) decreases as the current $I_{\rm el}$ through the electrometer increases (Fig. 10). At a

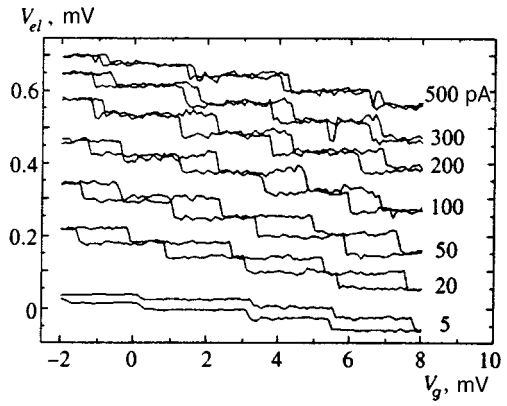

FIG. 9. Hysteresis curves corresponding to different current values (labeling the curves). The curves have been displaced in the vertical direction with a spacing of 120 μV for clarity.

working temperature of 35 mK, an increase in current from 5 to 300 pA narrows the loop to the value characteristic of 250 mK. Thus, even at low temperatures, the transistor itself can still be one of the factors limiting the storage time of a trap state. In our opinion, the increase in the absolute value of the derivative $|d(\Delta V_{\rm loop})/d(I_{\rm el})|$ of the dependence presented in Fig. 10 at low current is a significant feature of the effect. It distinguishes the current dependence of the loop width from the temperature dependence, which is characterized by flattening at small values of T, thereby setting it apart from a number of temperature-induced effects. As a working hypothesis to explain the effect, we suggest that the activation of the trap by the transistor is associated with broadband noise in the voltage of the transistor island due to the influence of tunnel events on the spectrum of states of the trap island.

On the other hand, the estimates of the warming of the trap ΔT by the transistor current [Ref. 11, Eq. (3.1)] at the helium bath temperature $T_0=35$ mK and an electric power $P=200$ nA$\times$1 mV as a function of the effective heat dissipation area S

S, μm^2	300×300	20×20	2×2
ΔT, mK	0.6	40	190

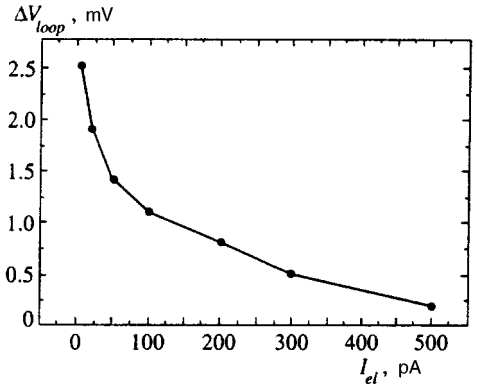

FIG. 10. Dependence of the width of the hysteresis loop on the current passing through the electrometer.

do not allow us to unequivocally rule out that the effect is due to heating.

At the present time additional experiments are being set up, and a model which describes the phenomenon is being developed.

4. DISCUSSION

The lifetime of the charge state of the trap depends on the maximum height of the electrostatic barrier. When the intrinsic capacitances of the intermediate islands in the array are neglected, the maximum barrier height ΔE in the symmetric case of equal heights of the barriers to the entry and departure of an electron, i.e., $\Delta E_{\rm in}=\Delta E_{\rm out}$, is determined[3] by the capacitance C_t of the tunnel junctions, how many there are in the array N, and the total capacitance of the island C_Σ:

$$\Delta E=\frac{e^2}{8C_\Sigma}\frac{NC_\Sigma}{C_t}-1. \tag{15}$$

Substituting the values of C_Σ and C_t obtained above into (15), we have $\Delta E\approx 0.8$ meV for $N=9$.

Consideration of the intrinsic capacitances of the intermediate islands (Fig. 2) leads to an increase in the capacitance C of the array and lowering of the barrier. For $C_t\cong 200$ aF and $C_s\cong 15$ aF the barrier is lowered by one-third, i.e. to approximately 0.5 meV, which is still almost twice the experimental value.

In our opinion, one possible reason for the decrease in barrier height is the nonzero effective background charges Q_{0i} of the intermediate islands. For a simple estimate of the magnitude of this effect, we place a negative charge $q=-e/20$ on one of the intermediate small islands in the array. This charge fully characterizes the actual scale of the drifting of the background charges of the islands in the structure and, in particular, can be determined from the drift of the working point of the electrometer. When $C_\Sigma \gg C$, the contribution of the electrostatic field of the charge q

$$\Delta E^q\approx eq/4C\approx -0.1\Delta E \tag{16}$$

amounts to 10% of the height of the idealized barrier. Taking into account the total number of intermediate islands in the array and the possible correlation between the Q_{0i} (Ref. 12), we can estimate the overall effect to be several tenths of an meV.

At low temperatures (below 50 mK), where thermal activation is suppressed, one of the factors restricting the lifetime and number of states is excitation of the trap by the transistor. The data in Fig. 10 suggest that even a small current passing through the transistor is capable of significantly narrowing the hysteresis loop and thereby shortening the storage time of a state.

Estimates of the time constants of the processes leading to the decay of states as a result of cotunneling and thermal activation yield values significantly exceeding the observation times accessible in the experiment. The drift variations of the characteristics were recorded experimentally. We assume that they are related to the redistribution of uncompensated charge in the local electromagnetic environment,

mainly in the substrate, which alters the effective background charges Q_{0i} of the metal islands (including the central islands of the trap and the electrometer) in the single-electron structure. This results, first, in the lower energy barrier mentioned above, second, in displacement of the optimum working point of the trap with respect to the control voltage V_g, and third, in instability of the ''output'' voltage of the single-electron sensing transistor. Despite the fact that the overall effect of the drifts did not result in switching during the 8 h of experimental storage of a charge state, we assume that random switching of the states is possible during the significantly longer time interval needed for practical applications of the single-electron memory effect.

In our opinion, there are three principal ways to address the negative influence of drift phenomena.

1. Develop a topology that provides for electrostatic shielding of the islands in the single-electron structure by electrodes at fixed potentials. An example of such a solution is the fabrication of an array of tunnel junctions in the form of a vertical multilayered ($Al/AlO_x/AO/AlO_x/\ldots$) column located on an external power-supply electrode with an area considerably greater than the area of the base of the column.

2. Search for substrate materials with a minimum number of structural features in the surface layers, on which the formation of charge traps that participate in the chaotic movement of the charge carriers and create fluctuations of the electromagnetic environment is possible. Here attention can be focused on substrates with a single-crystal structure.

3. Increase the height of the energy barrier by diminishing the capacitances of the junctions and the islands in the array by fabricating structures with small characteristic dimensions—for example, end-surface tunnel junctions.

5. CONCLUSIONS

The device described in this paper is a single-electron trap. Having multiple-valued charge states, it is a prototype of a single-electron memory cell. To demonstrate the memory effect we observed the storage of an electron in the trap island for more than 8 h.

It has been demonstrated that the drift of the distribution of the effective background charges of the islands can be one of the dominant factors limiting the storage time at low temperatures (at which the thermal activation mechanism is suppressed).

Another factor influencing the activation of tunneling in the trap is the reverse influence discovered here of the sensing electrometer on the trap. With respect to its influence on charge hysteresis, an increase in the current supplied to the transistor is similar to an increase in temperature, although it is possibly not associated with direct heating of the structure by the current flowing through the transistor.

We thank our colleagues from the Physikalisch-Technische Bundesanstalt (Braunschweig, Germany) for their assistance in performing the low-temperature measurements. We also thank A. B. Zorin for several valuable critical remarks during the preparation of this paper. The experimental investigations that formed the foundation of the present work were partially supported by the Russian Fund for Fundamental Research (Grant No. 95-02-04151A), the Russian Physics of Solid-State Nanostructures Program (Grant no. 1-033), and the German BMFT (Grant no. 13N6260).

[1] D. V. Averin and K. K. Likharev, in *Mesoscopic Phenomena in Solids*, B. L. Altshuler, P. A. Lee, and R. A. Webb (eds.), Elsevier, Amsterdam (1991), p. 173.
[2] A. N. Korotkov, submitted to *Molecular Electronics*, J. Jortner and M. A. Ratner (eds.), Blackwell, Oxford.
[3] K. Nakazato, R. J. Blaikie, and H. Ahmed, J. Appl. Phys. **75**, 5123 (1994).
[4] J. E. Lukens, P. D. Dresselhaus, Siyuan Han, L. Ji, K. K. Likharev, and W. Zheng, Physica B (Amsterdam) **203**, 354 (1994).
[5] D. V. Averin and A. A. Odintsov, Phys. Lett. A **140**, 251 (1989).
[6] J. M. Martinis and M. Nahum, Phys. Rev. B **48**, 18 316 (1993).
[7] N. S. Bakhvalov, G. S. Kazacha, K. K. Likharev, and S. I. Serdyukova, Zh. Éksp. Teor. Fiz. **95**, 1010 (1989) [Sov. Phys. JETP **68**, 581 (1989)].
[8] T. A. Fulton and G. C. Dolan, Phys. Rev. Lett. **59**, 109 (1987).
[9] V. A. Krupenin, S. V. Lotkhov, and D. E. Presnov, in *Nanostructures: Physics and Technology. Abstracts of Invited Lectures and Contributed Papers. 26–30 June 1995*, St. Petersburg, Russia (1995), p. 354.
[10] A. B. Zorin, Rev. Sci. Instrum. **66**, 4296 (1995).
[11] F. C. Wellstood, C. Urbina, and J. Clarke, Phys. Rev. B **49**, 5942 (1994).
[12] A. B. Zorin, F. J. Ahlers, J. Niemeyer *et al.*, Phys. Rev. B **53**, 13682 (1996).
[13] D. V. Averin and Yu. V. Nazarov, Phys. Rev. Lett **65**, 2446 (1990).

Translated by P. Shelnitz

Nonequilibrium noise-induced phase transitions in simple systems

P. S. Landa and A. A. Zaikin

M. V. Lomonosov Moscow State University, 119899 Moscow, Russia
(Submitted 19 April 1996; resubmitted 3 June 1996)
Zh. Éksp. Teor. Fiz. **111**, 358–378 (January 1997)

The theory and the results of an investigation of nonequilibrium noise-induced phase transitions in the simple example of a physical pendulum with a randomly oscillating pivot are presented. It is shown that such transitions lead to the appearance of a more ordered state of the system. The possibility of a difference between noise-induced oscillations and chaotic oscillations of dynamic origin is discussed. © *1997 American Institute of Physics.* [S1063-7761(97)02301-9]

1. INTRODUCTION

Noise-induced phase transitions similar to those discussed below were considered theoretically by Van den Broeck *et al.*[1,2] for systems described by finite-difference models of partial differential equations of a certain form. Noise-induced two-dimensional structures, which can be regarded as a distinctive form of turbulence, were discovered numerically in Ref. 3. This indirectly confirmed the opinion previously advanced by one of us[4,5] that the turbulence in open flows is not the result of self-induced oscillations, but is induced by noise.

The transitions that we are speaking about here differ fundamentally from those considered by other investigators (see, for example, Refs. 6 and 7), who used this term for the appearance of additional maxima in a probability distribution due to multiplicative noise, mainly in systems having the property of multistability. We note that this fact was also mentioned in Refs. 1 and 2.

It is very interesting that the noise-induced phase transitions under consideration are possible in very simple systems, for example, in a physical pendulum with a randomly oscillating pivot. Investigating just such simple systems is convenient, because, on the one hand, it is possible to perform an approximate analytic treatment, and, on the other hand, a pendulum is a perfectly real physical object, which offers the possibility, in principle, of performing an experiment.

2. THEORETICAL TREATMENT OF PENDULUM OSCILLATIONS CAUSED BY RANDOM OSCILLATIONS OF THE PIVOT

The possibility of exciting an oscillator under a random parametric influence was first demonstrated analytically by Stratonovich and Romanovskiĭ.[8,9] The same problem was subsequently solved by Dimentberg.[10] To obtain a constraint on the amplitude of the oscillations excited, those investigators took into account nonlinear friction. However, as will be shown below, the inclusion of nonlinear friction is not obligatory, since the amplitude can be constrained by means of a nonlinear restoring force. On the other hand, its inclusion is convenient, since nonlinear friction of sufficiently large magnitude makes it possible to eliminate random full turns of the pendulum through angles that are multiples of 2π. Such full turns complicate the analysis of the results obtained.

When nonlinear friction is taken into account, the equation of motion of a pendulum with a randomly oscillating pivot can be written in the form

$$\ddot{\varphi}=2\beta(1+\alpha\dot{\varphi}^2)\dot{\varphi}+\omega_0^2(1+\xi(t))\sin\varphi=0, \tag{1}$$

where φ is the angular deviation of the pendulum relative to the equilibrium position, $\omega_0=\sqrt{mbg/J}$ is the frequency of small natural oscillations of the pendulum, J and m are, respectively, the moment of inertia and the mass of the pendulum, b is the distance from the center of mass to the pivot, g is the acceleration of gravity, $\beta=H/2J$ is the damping coefficient of the oscillations, $H\dot{\varphi}$ is the frictional tongue in the linear approximation, α is the coefficient of nonlinear friction, and $g\xi(t)$ is the acceleration of the pivot, which is a comparatively broadband random process with nonzero spectral density at the frequency $2\omega_0$. We assume that the intensity of the oscillations of the pivot is small enough that $\sin\varphi$ can be represented in the form

$$\sin\varphi\approx(1-\gamma\varphi^2)\varphi, \tag{2}$$

where $\gamma=1/6$.

An approximate analytic solution of the problem of interest to us can be obtained, if it is assumed that $\beta/\omega_0\sim\epsilon$ and $\gamma\varphi^2\sim\epsilon$, where ϵ is a certain provisional small parameter, which can be set equal to unity in the final expressions. Now it is convenient to rewrite Eq. (1) with consideration of (2) in the following form:

$$\ddot{\varphi}+\omega_0^2\varphi=\epsilon(-2\beta(1+\alpha\dot{\varphi}^2)\dot{\varphi}+\omega_0^2\gamma\varphi^3)$$
$$-\sqrt{\epsilon}\xi(t)(1-\epsilon\gamma\varphi^2)\varphi. \tag{3}$$

Here $\sqrt{\epsilon}$ in front of the noise term has the same meaning as on p. 346 of the Russian edition of Stratonovich's book.[9] This way of writing the term is useful, because the spectral density of the noise, which appears in the final expressions, is of order ϵ.

We solve Eq. (3) by the Krylov–Bogolyubov method to the accuracy of a second approximation with respect to the small parameter ϵ. For this purpose we set $\varphi=A\cos\psi+\epsilon u_1+\epsilon^2u_2+\ldots$, where $\psi=\omega_0t+\phi$,

$$\dot{A}=\epsilon f_1+\epsilon^2 f_2+\ \ldots,$$

$$\dot{\phi}=\epsilon F_1+\epsilon^2 F_2+\ \ldots\ . \tag{4}$$

and $u_1,u_2,\ldots,\ f_1,f_2,\ldots,$ and $F_1,F_2,\ldots$ are unknown functions. Using the Krylov–Bogolyubov procedure for stochastic equations (see Refs. 9 and 11), we can easily find expressions for the unknown functions f_1, f_2, and F_1 (F_2 introduces only small corrections to F_1 and is therefore not of interest). Leaving only the nonlinear term in f_2 and substituting the expressions found into Eq. (4), we obtain

$$\dot{A}=\left(-\beta\left(1+\frac{3}{4}\ (\alpha\omega_0^2+\gamma)A^2\right)+\frac{\omega_0}{2}\ \overline{\xi\ \sin 2\psi}\right)A, \tag{5}$$

$$\dot{\phi}=-\frac{3}{8}\ \omega_0\gamma A^2+\omega_0\overline{\xi\ \cos^2\ \psi}, \tag{6}$$

where the line over an expression denotes averaging with respect to time. As was shown in Ref. 9, in Eq. (5)

$$\overline{\xi\ \sin 2\psi}=\overline{\langle\xi\ \sin 2\psi\rangle}+\zeta_1(t), \tag{7}$$

where the angle brackets denote averaging over a statistical ensemble, and $\zeta_1(t)$ is a random process, which can be regarded as white noise with zero mean and intensity K_1 equal to

$$K_1=\frac{1}{2}\ \kappa(2\omega_0). \tag{8}$$

In (8)

$$\kappa(2\omega_0)=\int_{-\infty}^{\infty}\langle\xi(t)\xi(t+\tau)\rangle\cos 2\omega_0\tau\ d\tau$$

is the spectral density of the process $\xi(t)$ at the frequency $2\omega_0$. Because there is a correlation between ξ and ϕ, the quantity $\overline{\langle\xi\ \sin 2\psi\rangle}$ in Eq. (7) is nonzero and equal to

$$\overline{\langle\xi\ \sin 2\psi\rangle}=\frac{\omega_0}{4}\ \kappa(2\omega_0)=\frac{\omega_0}{2}K_1. \tag{9}$$

Similarly, in Eq. (6)

$$\overline{\xi\ \cos^2\ \psi}=\overline{\langle\xi\ \cos^2\ \psi\rangle}+\zeta_2(t), \tag{10}$$

where

$$\overline{\langle\xi\ \cos^2\ \psi\rangle}=\frac{\omega_0}{4}\ \int_{-\infty}^{0}\langle\xi(t)\xi(t+\tau)\rangle\sin 2\omega_0\tau\ d\tau\equiv M, \tag{11}$$

$\zeta_2(t)$, as in (7), can be regarded as white noise with zero mean and intensity K_2 equal to

$$K_2=\frac{1}{4}\left(\kappa(0)+\frac{1}{2}\ \kappa(2\omega_0)\right). \tag{12}$$

The value of M depends on the character of the random process $\xi(t)$: if $\xi(t)$ is white noise, then $M=0$; if, on the other hand, $\xi(t)$ has a finite correlation time, as, for example, when its spectral density is

$$\kappa(\omega)=\frac{\alpha^2\kappa(2\omega_0)}{(\omega-2\omega_0)^2+\alpha^2},$$

then

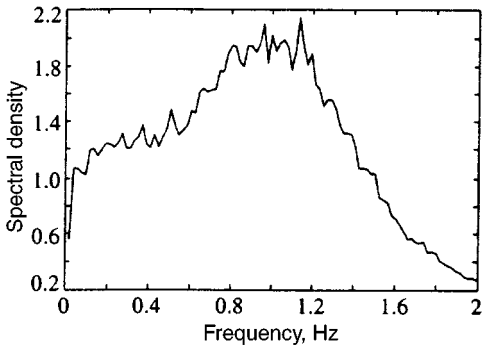

FIG. 1. Spectral density of the noise $\xi(t)$.

$$M=-\frac{\alpha\omega_0^2\kappa(2\omega_0)}{4(16\omega_0^2+\alpha^2)}.$$

Taking into account (7)–(12), we rewrite Eqs. (5) and (6) in the form

$$\dot{A}=\left(-\beta-\frac{3}{4}\ \beta\tilde{\gamma}A^2+\frac{\omega_0^2}{4}\ K_1\right)A+\frac{\omega_0}{2}\ A\zeta_1(t), \tag{13}$$

$$\dot{\phi}=-\frac{3}{8}\ \omega_0\gamma A^2+\omega_0 M+\omega_0\zeta_2(t),$$

where $\tilde{\gamma}=\gamma+\alpha\omega_0^2$.

The following Fokker–Planck equation corresponds to Eqs. (13):

$$\begin{aligned}\frac{\partial w(A,\phi)}{\partial t}=&-\frac{\partial}{\partial A}\left(\left(\frac{\omega_0^2K_1}{4}\ \eta-\frac{3}{4}\ \beta\tilde{\gamma}A^2\right)Aw(A,\phi)\right)\\&-\omega_0\left(\frac{3}{8}\ \gamma A^2-M\right)\ \frac{\partial w(A,\phi)}{\partial\phi}\\&+\frac{K_1\omega_0^2}{8}\frac{\partial^2}{\partial A^2}\ (A^2w(A,\phi))\\&+\frac{K_2\omega_0^2}{2}\frac{\partial^2 w(A,\phi)}{\partial\phi^2},\end{aligned} \tag{14}$$

where

$$\eta=1-\frac{4\beta}{\omega_0^2K_1}.$$

The stationary solution of Eq. (14) satisfying the condition that the probability flux equal zero does not depend on ϕ. It is convenient to write it in the form

$$w(A,\phi)=\frac{C}{2\pi A^2}\ \exp\left\{\int_1^A\frac{2\eta}{A}\ dA-\int_0^A\frac{6\beta\tilde{\gamma}}{\omega_0^2K_1}\ A\ dA\right\}. \tag{15}$$

The constant C is determined from the normalization condition

$$\int_0^{2\pi}\int_0^{\infty}w(A,\phi)A\ dA\ d\phi=1.$$

After integrating (15) over ϕ and calculating the integral in the exponential, we find the expression for the density distribution of the oscillation amplitudes:

$$w(A)=CA^{2\eta-1}\exp\left\{-\frac{3\beta\tilde{\gamma}}{\omega_0^2K_1}A^2\right\}. \tag{16}$$

From the normalization condition we find

$$C=2\begin{cases}\left(\dfrac{\omega_0^2K_1}{3\beta\tilde{\gamma}}\right)^{-\eta}\dfrac{1}{\Gamma(\eta)} & \text{for } \eta>\\ 0 & \text{for } \eta\leqslant 0\end{cases}$$

and, therefore,

$$w(A)=2\begin{cases}\left(\dfrac{\omega_0^2K_1}{3\beta\tilde{\gamma}}\right)^{-\eta}\dfrac{1}{\Gamma(\eta)}A^{2\eta-1} & \\ \quad\times\exp\left\{-\dfrac{3\beta\tilde{\gamma}}{\omega_0^2K_1}A^2\right\} & \text{for } \eta>0\\ \delta(A) & \text{for } \eta\leqslant 0\end{cases}. \tag{17}$$

The distribution density of the amplitudes turned out to be delta-shaped when $\eta \leqslant 0$ because we did not take into account additive noise.[1)]

Using (17), we can find $\langle A\rangle$ and $\langle A^2\rangle$:

$$\langle A\rangle=\begin{cases}\sqrt{\dfrac{\omega_0^2K_1}{3\beta\tilde{\gamma}}}\dfrac{\Gamma(\eta+1/2)}{\Gamma(\eta+1)}\eta & \text{for } \eta>0\\ 0 & \text{for } \eta\leqslant 0\end{cases},$$

$$\langle A^2\rangle=\begin{cases}\dfrac{\omega_0^2K_1}{3\beta\tilde{\gamma}}\eta & \text{for } \eta>0\\ 0 & \text{for } \eta\leqslant 0\end{cases}. \tag{18}$$

Hence, it is clear that parametric excitation of pendulum oscillations due to the noise influence occurs when $\eta>0$. This is manifested by the fact that the average values of the amplitude and the square of the amplitude become nonzero. If such oscillations are observed and their cause is not known, it can be concluded that they are chaotic self-induced oscillations. This naturally raises the question of whether the process observed can be distinguished from such oscillations. This question is the subject of Sec. 4.

3. NUMERICAL SIMULATION OF THE EQUATION DESCRIBING THE OSCILLATIONS OF A PENDULUM WITH AN OSCILLATING PIVOT

Since the theoretical results obtained, first, do not make it possible to find the form of the noise-induced oscillations of the pendulum and, second, are approximate, we numerically investigated the solution of the equation

$$\ddot{\varphi}+0.2(1+\alpha\dot{\varphi}^2)\dot{\varphi}+(1+\xi(t))\sin\varphi=0, \tag{19}$$

where $\xi(t)$ is sufficiently broad-band noise, whose spectral density is shown in Fig. 1.

A term describing nonlinear friction was included in Eq. (19) in order to avoid rotation of the pendulum at noise intensities significantly exceeding the critical value. The investigation showed that, as the noise intensity increases above the critical value [$\kappa_{cr}(2)=0.8$], the average values of the instantaneous amplitude of the pendulum oscillations calculated using a Hilbert transform (see, for example, Refs. 12 and 13) and of its square become nonzero and then increase, as follows from the theory. The corresponding dependences are shown in Fig. 2. We see that their initial segments coincide quite well with the theoretical dependences specified by Eq. (18), which we calculated under the assumption that the noise intensity is close to the critical value.

In the immediate vicinity of the threshold, the oscillations excited are very reminiscent of the chaotic self-induced oscillations that result from loss of stability of the equilibrium state due to merging, for example, with an unstable limit cycle, and therefore exhibit intermittency.[14] The form of such oscillations and the projections of their phase portrait in the $\varphi(t),\dot{\varphi}(t)$ plane are shown in Fig. 3. We note that turbulence in a region of transitional Reynolds numbers also exhibits intermittency.[15–17] It is no accident that the first detailed analyses of these phenomena were published specifically by specialists in turbulence.[18]

If nonlinear friction is not introduced, the pendulum begins to undergo full turns through angles that are multiples of 2π from time to time when the noise intensity deviates only very slightly from the critical value (see Fig. 3b). In order to avoid this unacceptable phenomenon, we performed the calculations at these noise intensities allowing for nonlinear friction. As the deviation from the critical value increases, the duration of the segments during which the pendulum oscillates near the equilibrium position gradually decreases,

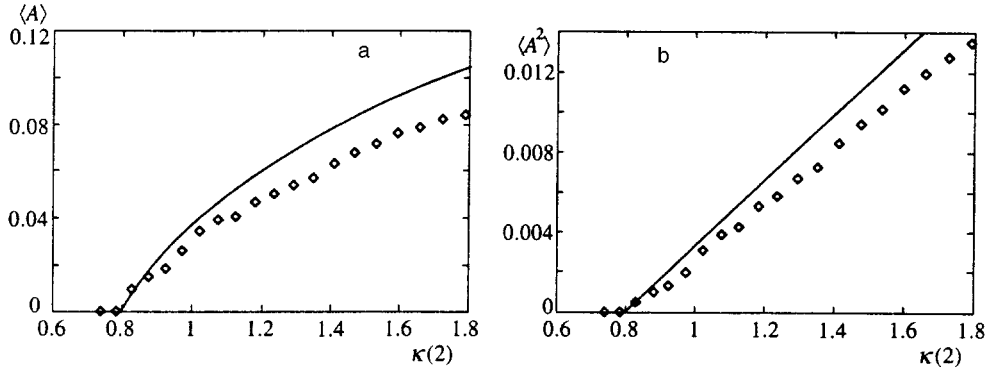

FIG. 2. Dependence of $\langle A\rangle$ (a) and $\langle A^2\rangle$ (b) on the spectral density of the noise $\kappa(2)$ (points). The solid curves show the corresponding theoretical dependences calculated using Eq. (18).

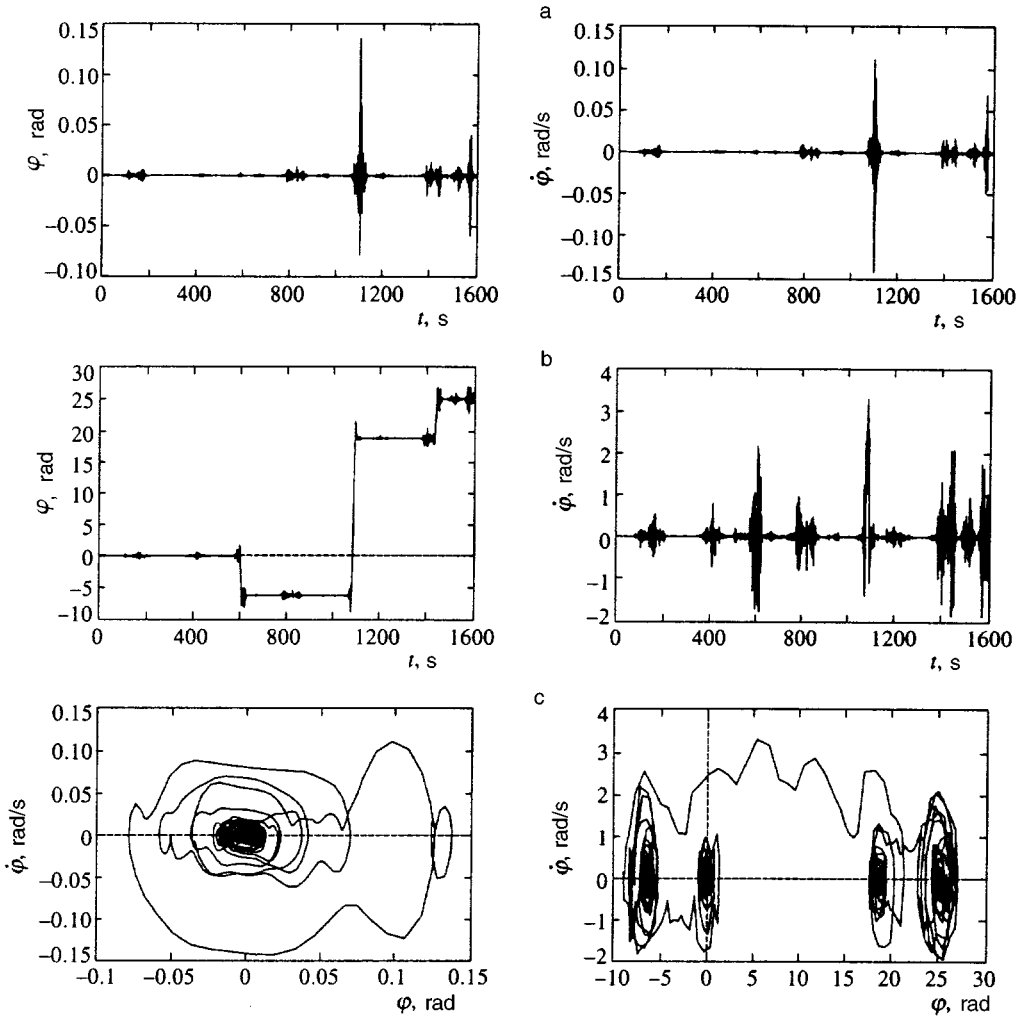

FIG. 3. Plots of $\varphi(t)$ and $\dot{\varphi}(t)$ for $\alpha=0$ when $\kappa(2)/\kappa_{cr}(2)=1.01$ (a) and $\kappa(2)/\kappa_{cr}(2)=1.06$ (b), and projections of the corresponding phase portraits in the $\varphi(t),\dot{\varphi}(t)$ plane (c).

and when the noise intensity is sufficiently greater, these segments vanish. This is illustrated in Fig. 4.

Since the observed oscillations of the pendulum are caused exclusively by noise influences, it might have been expected that they should exhibit the infinitely high dimension of the corresponding set constructed in some infinite-dimensional space. However, our calculations of the correlation dimension both in an ordinary Takens space and using the well-fit basis technique[19] showed that the dimension is finite. This is evidenced by saturation of the correlation dimension as the dimension of the embedding space increases. An example of such saturation is shown in Fig. 5. As the noise intensity increases, the dimension increases slightly, but remains finite [see Fig. 6, which presents the dependence of the correlation dimension ν on the relative spectral density of the noise $\kappa(2)/\kappa_{cr}(2)$].

Thus, as our investigation showed, the dimension does not make it possible to distinguish noise-induced oscillations from chaotic oscillations of dynamical origin, for which the dimension should be finite. An example of such oscillations is considered below. We stress that this result contradicts some widely accepted theories, according to which the dimension, in particular, can be used to distinguish chaotic oscillations in dynamical systems from random noise-induced oscillations (see Ref. 14). Granted that several papers have recently appeared (see, for example, Refs. 20 and 21), in which it was shown that noise signals with a $1/f^{\alpha}$ spectrum can have a finite correlation dimension (at least for $1 \leqslant \alpha \leqslant 3$). However, as we shall see below, the spectrum of the observed noise-induced oscillations does not always have the $1/f_{\alpha}$ form; nevertheless, their dimension was always found to be finite.

Because the dimension corresponding to the noise-induced oscillations of a pendulum is finite, it can be asserted that an attractor is induced in a certain phase space characterizing the motion of the pendulum, for example, in a Takens space, under the influence of noise.

For comparison, we consider the chaotic oscillations of a pendulum caused by sufficiently large periodic oscillations of the pivot. When nonlinear friction is taken into account, these oscillations are described by the equation

$$\ddot{\varphi}+2(1+\alpha\dot{\varphi}^2)\beta\dot{\varphi}+(1+B\cos 2t)\sin\varphi=0, \qquad (20)$$

where B is the relative amplitude of the oscillations in the acceleration of the pivot. The behavior of the solution of Eq. (20) for $\alpha=0$ and varying B was studied in detail in Ref. 22 by numerical simulation. We repeated the calculations performed in that work for several values of B, at which the oscillations of the pendulum are chaotic. An example of such

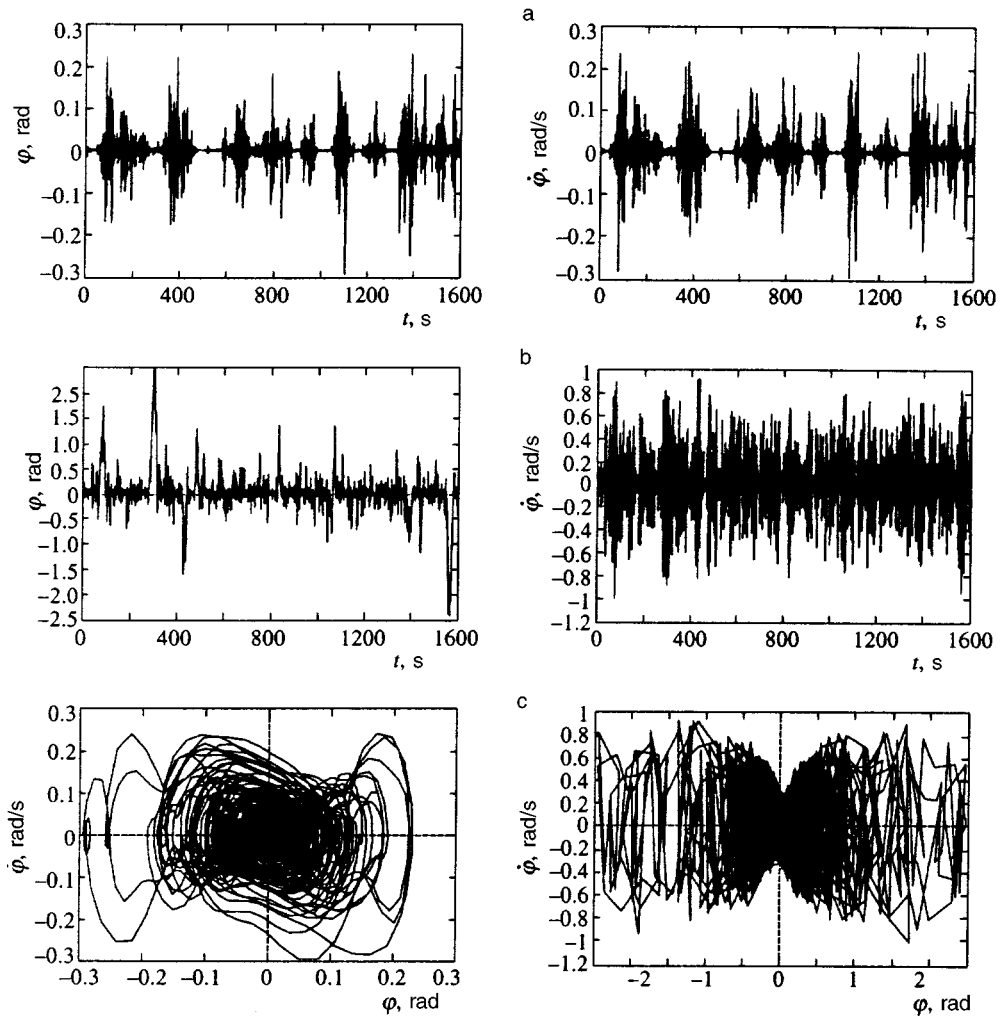

FIG. 4. Plots of $\varphi(t)$ and $\dot{\varphi}(t)$ for $\alpha=100$ when $\kappa(2)/\kappa_{cr}(2)=1.25$ (a) and $\kappa(2)/\kappa_{cr}(2)=14$ (b), and projections of the corresponding phase portraits in the $\varphi(t),\dot{\varphi}(t)$ plane (c).

oscillations is presented in Fig. 7. It can be seen from the figure that the pendulum performs irregular rotations in either direction, which result in slow drifting of the rotation angle φ. The presence of nonlinear friction, if it has sufficient magnitude, causes the rotation to vanish, and the pendulum executes only chaotic oscillations relative to the equilibrium position (Fig. 8). When $B=3$ and $\alpha=0$, the correlation dimension of the attractor corresponding to these chaotic oscillations equals 2.51 ± 0.05, and when $B=3.5$ and $\alpha=2$, it equals 2.09 ± 0.03. We see that the presence of nonlinear friction significantly reduces the dimension.

The spectra of the oscillations excited are also of considerable interest. In the case of excitation of the pendulum by a harmonic influence in the absence of nonlinear friction, in which the pendulum performs irregular rotations, the spectrum of its oscillations contains a low-frequency part due to

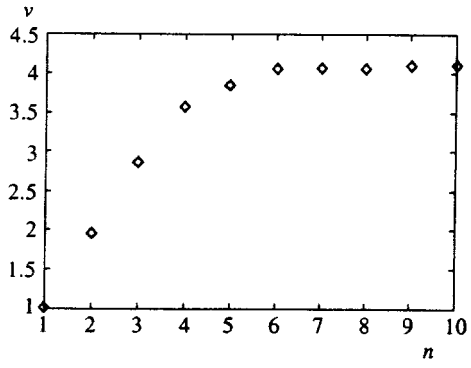

FIG. 5. Dependence of the correlation dimension ν on the dimension of the embedding space n for $\kappa(2)/\kappa_{cr}(2)=14$ and $\alpha=100$.

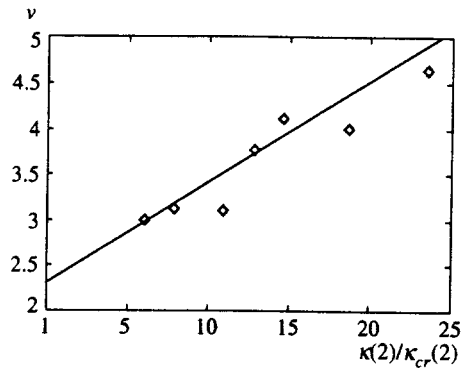

FIG. 6. Dependence of the correlation dimension ν on the relative spectral density of the noise $\kappa(2)/\kappa_{cr}(2)$ for $\alpha=100$ (diamonds). The solid line is a linear approximation of this dependence.

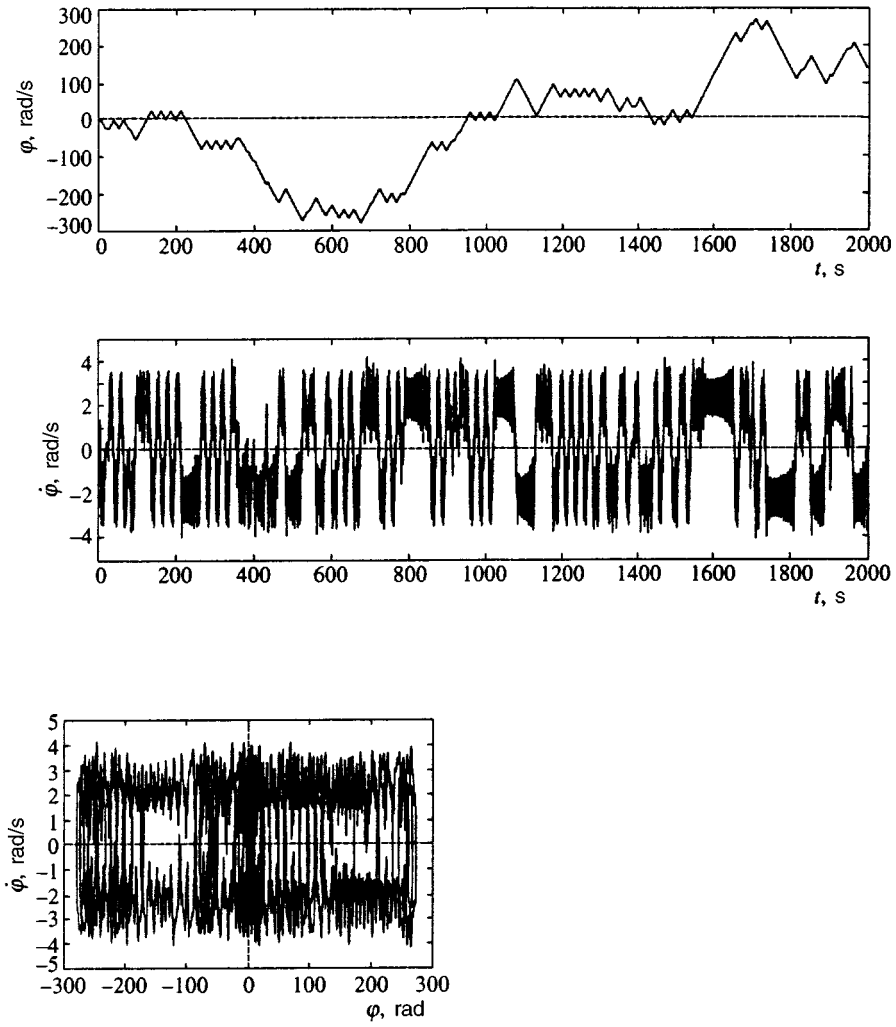

FIG. 7. Solution of Eq. (20) and projection of the phase portraits onto the $\varphi,\dot{\varphi}$ plane for $B=3$ and $\alpha=0$.

these slow rotations, the spectral density decreasing with increasing frequency, but not monotonically (see Fig. 9a). When nonlinear friction is present, the low-frequency portion of the spectrum is significantly smaller, and the spectrum contains pronounced maxima at frequencies which are multiples of the natural frequencies (Fig. 9b).

In the case of a pendulum excited by noise, the oscillation spectrum calculated without allowing for nonlinear friction has a maximum at a frequency close to the natural value when the noise intensity is close to the critical value (Fig. 10a). As the noise intensity increases, this maximum decreases and ultimately vanishes (Fig. 10b). As a result, the spectrum takes on a monotonically decreasing form similar to a flicker noise spectrum. At high noise intensities the spectrum can be approximated by a $1/f^n$ power function, in which we obtained $n=12$ for $\kappa(2)/\kappa_{cr}(2)=22$ (Fig. 10c). When nonlinear friction is present, the behavior of the spectrum remains qualitatively unchanged (see Figs. 9d, 9e, and 9f). Only when the noise intensity is sufficiently large and the spectrum takes on a monotonically decreasing form can it be approximated by two linear segments on a semilogarithmic scale (Fig. 10g). The correlation functions of the signals for the parameters corresponding to Figs. 10d and 10f are presented in Fig. 11. We see that the correlation time of the signals determined from the width of the correlation at half-height is small enough that the assertion in Refs. 20 and 21 that noise signals with a $1/f^{\alpha}$ spectrum have a finite dimension, because the correlation time for them is very small, is in need of refinement in our case.

4. THE RYTOV–DIMENTBERG CRITERION

Let us now turn to the question of whether noise-induced oscillations can be distinguished from chaotic oscillations of dynamical origin. A similar question was posed by S. M. Rytov[12] and subsequently by M. F. Dimentberg[23,10] in reference to the problem of distinguishing between a noise signal passed through a linear narrow-band filter and periodic noise-contaminated self-induced oscillations.[2)] It was shown in their work that in the latter case, the probability density for the square of the instantaneous amplitude, which can be determined using a Hilbert transform in the case of a broadband process, should have a maximum at a certain finite value of the amplitude, while in the case of noise that passed through a filter it should decrease monotonically. It can be expected that in the case of chaotic oscillations of dynamical origin, the probability density for the square of the instantaneous amplitude should also have a maximum at one or more finite values of the amplitude.

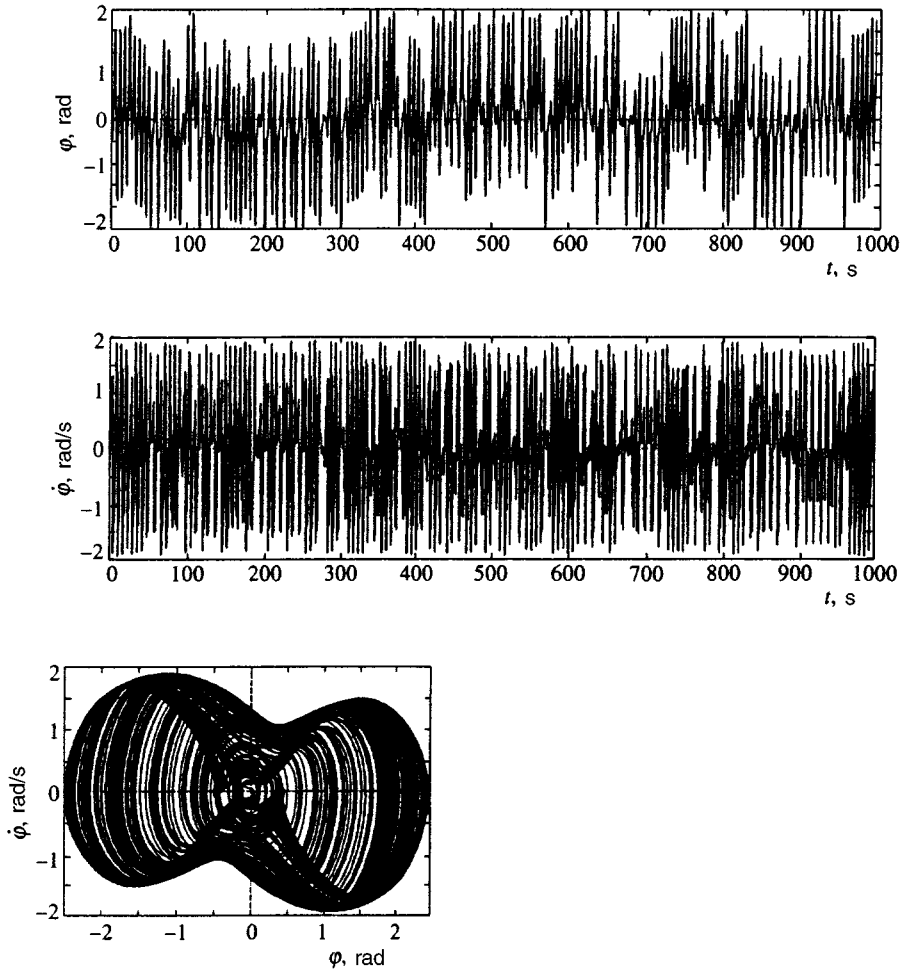

FIG. 8. Solution of Eq. (20) and projection of the phase portraits onto the $\varphi,\dot{\varphi}$ plane for $B=3.5$ and $\alpha=2$.

Such a result was, in fact, obtained by us for the chaotic pendulum oscillations resulting from periodic oscillations of the pivot that we considered above. Figure 12 shows a histogram of the probability distribution of the square of the instantaneous amplitude of the oscillations determined using a Hilbert transform. It is clear that the probability density is not a monotonically decreasing function and that it has several weak maxima.

As follows from the theoretical results presented in Sec. 2, in the case of the excitation of pendulum oscillations as a result of random oscillations of the pivot, the probability distribution for $x=\tilde{\gamma}A^2$ is $\tilde{w}(x)=w(\sqrt{x/\tilde{\gamma}})/2\sqrt{\tilde{\gamma}x}$, where $w(\sqrt{x/\tilde{\gamma}})$ is specified by Eq. (17). A plot of $\tilde{w}(x)$ for $\eta=0.2$ is presented in Fig. 13a. We see that the analytically calculated probability density for the square of the amplitude decreases monotonically with increasing amplitude. The same result was also obtained as a result of the numerical simulation of Eq. (19) (Figs. 13b and 13c).

Dimentberg also proposed another version of his criterion,[10] which is based on the notion that the probability density $x(t)$ for the process under investigation can be ana-

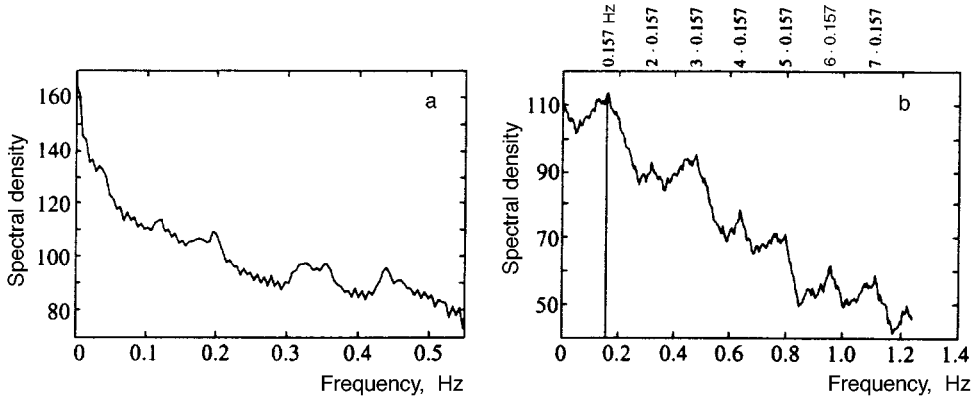

FIG. 9. Spectral densities of the solution of Eq. (20) on a logarithmic scale for $B=3$ and $\alpha=0$ (a) and for $B=3.5$ and $\alpha=2$ (b).

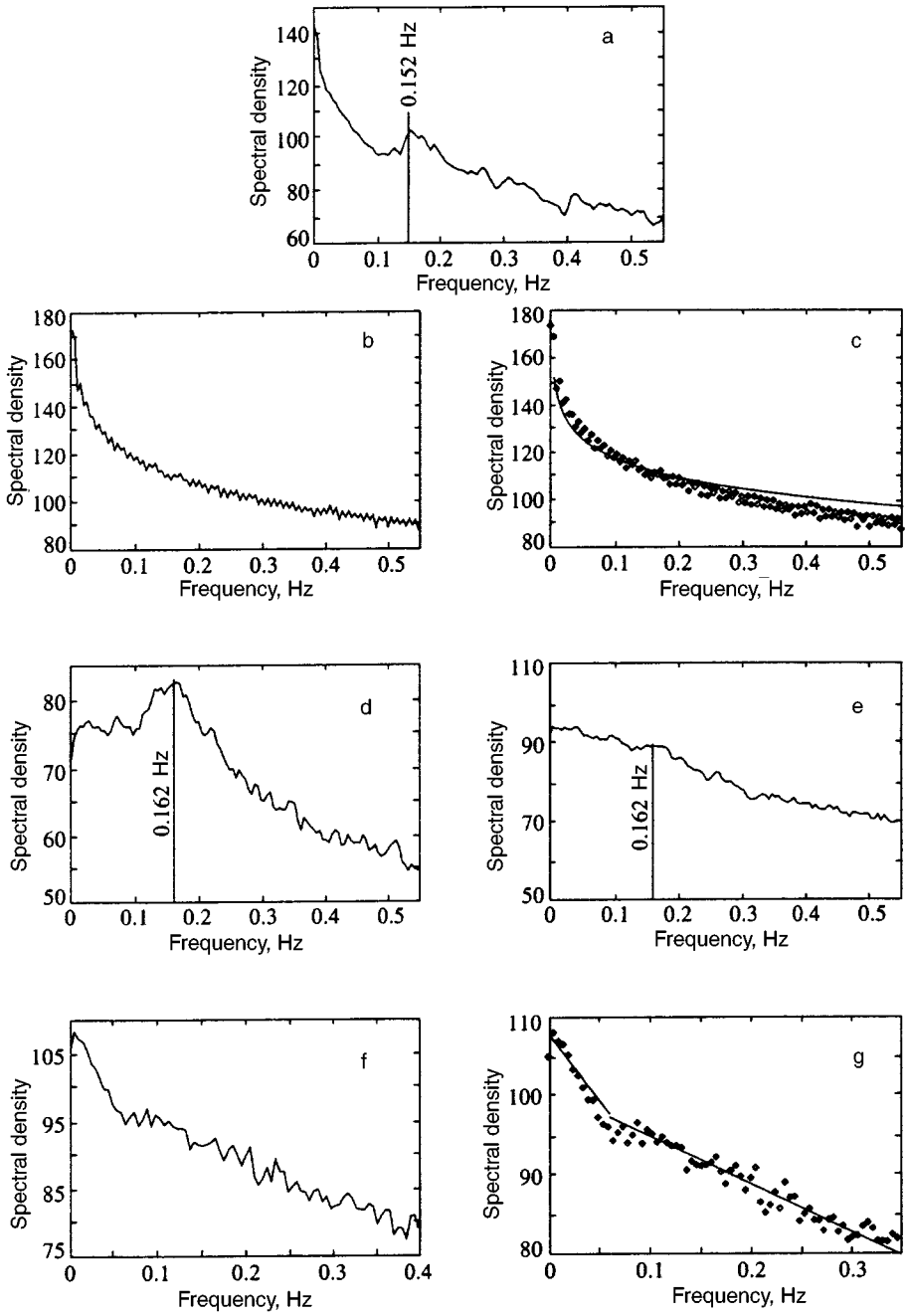

FIG. 10. Spectral densities of the solution of Eq. (19) on a logarithmic scale for $\alpha=0$ when $\kappa(2)/\kappa_{cr}(2)=1.06$ (a) and $\kappa(2)/\kappa_{cr}(2)=22$ (b) and for $\alpha=100$ when $\kappa(2)/\kappa_{cr}(2)=1.25$ (d), $\kappa(2)/\kappa_{cr}(2)=4.6$ (e), and $\kappa(2)/\kappa_{cr}(2)=14$ (f); approximation of the logarithm of the spectral density for $\alpha=0$ and $\kappa(2)/\kappa_{cr}(2)=22$ by the function $90-12\log f$ (c); approximation of the logarithm of the spectral density for $\alpha=100$ and $\kappa(2)/\kappa_{cr}(2)=14$ by segments of two straight lines: $108-170f$ for $f \leqslant 0.06$ and $101-60f$ for $f \geqslant 0.06$ (g).

lyzed instead of the probability density for the square of the instantaneous amplitude. Dimentberg showed in a particular example that if the probability density for positive values of x is not a monotonically decreasing function, the process $x(t)$ is auto-oscillatory. However, if the probability density for $x>0$ decreases monotonically, no unequivocal answer can be given: the process $x(t)$ can be either noise that has passed through the filter or strongly noise-contaminated self-induced oscillations. Although the authors make no mention of this fact, it should be noted that the use of either form of

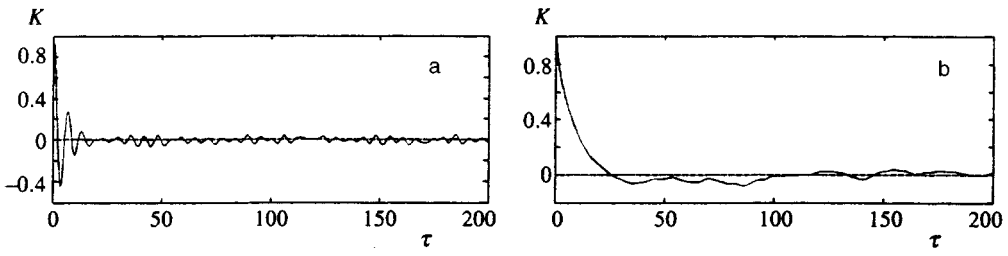

FIG. 11. Correlation functions for the solutions of Eq. (19) for $\alpha=100$ when $\kappa(2)/\kappa_{cr}(2)=1.25$ (a) and $\kappa(2)/\kappa_{cr}(2)=14$ (b).

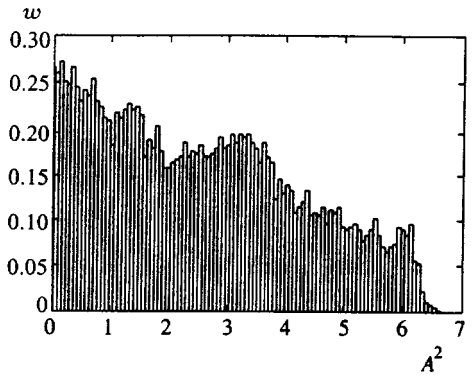

FIG. 12. Probability distribution of the square of the instantaneous oscillation amplitude for $\alpha=2$ and $B=3.5$.

this criterion is likely to be possible only if the probability density for x is an even function.

We tested the second form of Dimentberg's criterion for both noise-induced pendulum oscillations and chaotic oscillations caused by a harmonic parametric influence. Despite the ambiguity and the incomplete symmetry of the distributions indicated by the author, it was found that this form of the criterion also gives correct results. This is illustrated in Fig. 14, which shows the probability distributions for the rotation angle φ of the pendulum in the two cases indicated above.

Thus, despite the essentially nonlinear transformation of the noise, the Rytov–Dimentberg criterion is valid in the examples that we considered. Of course, the question of the validity of this criterion in the general case and the possibility of using it when the probability distribution for the process under consideration is not an even function calls for a more detailed investigation.

5. EXCITATION OF OSCILLATIONS OF A PENDULUM WITH A RANDOMLY OSCILLATING PIVOT AS A NOISE-INDUCED PHASE TRANSITION. KLIMONTOVICH CRITERION FOR ORDERED MOTION

The excitation of pendulum oscillations as a result of a parametric noise influence can be interpreted as the onset of a nonequilibrium second-order phase transition in the system under consideration when $\eta=0$. Either $\langle A\rangle$ or $\langle A^2\rangle$ can be taken as the order parameter characterizing this transition. As follows from (18) and Fig. 2, under such a choice of the order parameter the critical index equals 1.

To demonstrate that the motion in the system becomes more ordered following the transition under consideration, we utilize the criterion proposed by Klimontovich,[24,25] the essence of which can be described as follows. Two states corresponding to different values of a certain control parameter a are selected in the system under investigation. One of these states, which corresponds to $a=a_0$, is provisionally taken as the state of physical chaos. The probability density for the set of variables X describing the state of the system is denoted by $w(X,a)$. We represent $w(X,a_0)\equiv w_0(X)$ in the form of a canonical Gibbs distribution

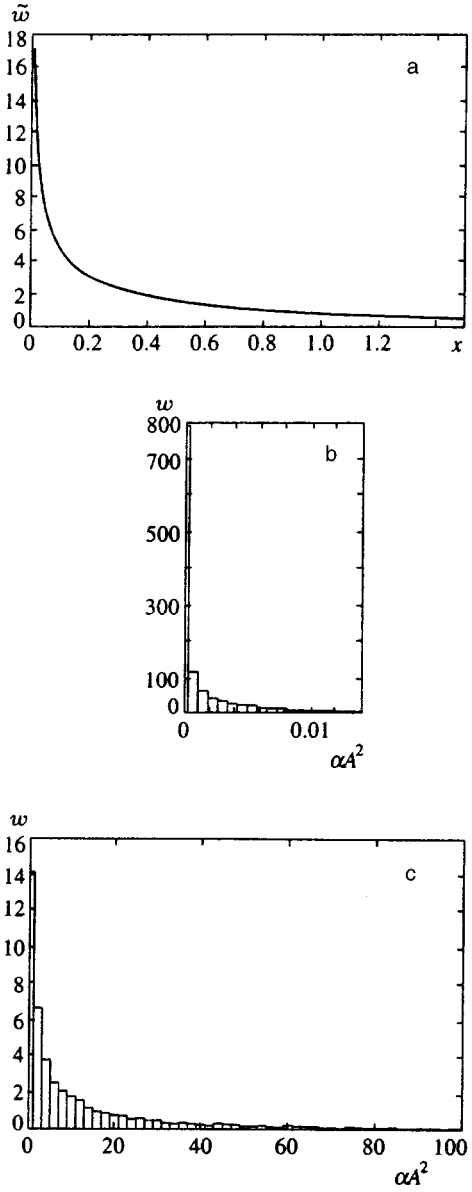

FIG. 13. Dependence of $\tilde{w}(x)=(2\tilde{\gamma}^{\eta}/C)w(x)$ for $\eta=0.2$ (a) and probability distribution for αA^2 obtained by numerically solving Eq. (19) for $\kappa(2)/\kappa_{cr}(2)=1.25$ (b) and $\kappa(2)/\kappa_{cr}(2)=14$ (c).

$$w_0(X)=\exp\left\{\frac{F_0(D_0)-H(X,a_0)}{D_0}\right\}, \tag{21}$$

where F_0 is the free energy, $H(X,a_0)$ is the Hamiltonian function, and D_0 is the temperature, which can be set equal to unity. We introduce the notation

$$F_0(1)-H(X,a_0)=-H_{\text{eff}},$$

and we take H_{eff} as the effective Hamiltonian, which does not depend on a. Clearly, the mean value of the effective Hamiltonian, which is equal to the effective energy, depends on a in the general case. Klimontovich proposed renormalizing the initial probability distribution in such a manner that the effective energies in the initial state (when $a=a_0$) and

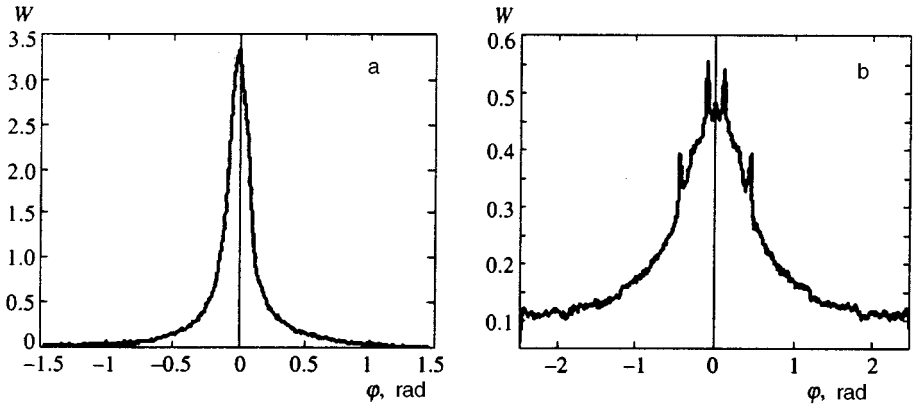

FIG. 14. Probability density of the angle φ [$W(\varphi)$] in the case of noise-induced oscillations of a pendulum for $\kappa(2)/\kappa_{cr}(2)=14$ (a) and chaotic oscillations induced by a harmonic parametric influence (b).

final state (when $a=a_0+\Delta a$)coincide. For this purpose, the renormalized probability density $\tilde{w}_0(X,a,\Delta a)$, which satisfies the condition

$$\int H_{\text{eff}}\tilde{w}_0(X,a,\Delta a)dX=\int H_{\text{eff}}w(X,a_0+\Delta a)dX, \quad (22)$$

is introduced. In Eq. (22) the probability density $\tilde{w}_0(X,a,\Delta a)$, like $w_0(X)$, can be represented in the form of a canonical Gibbs distribution:

$$\tilde{w}_0(X,a,\Delta a)=\exp\left\{\frac{F(D)-H_{\text{eff}}}{D}\right\}, \quad (23)$$

where $F(D)$ is the effective free energy, and D is the effective temperature, which depends on Δa. The unknown function $F(D)$ is determined from the normalization condition

$$\int \tilde{w}_0(X,a,\Delta a)dX=1, \quad (24)$$

and the dependence of D on Δa is found from Eq. (22). Comparing (21) and (23), we see that $D(0)=1$ and $F(1)=0$.

Klimontovich claimed that if the value of $D(\Delta a)$ thus found is greater than unity, the state of the system with $a=a_0+\Delta a$ will be more ordered than the state with $a=a_0$, i.e., in this case we correctly took the latter as the state of physical chaos.[3)] After the state of physical chaos is determined (we shall assume that it corresponds to a value of a equal to a_0), Klimontovich proposes introducing the difference between the entropies

$$\tilde{S}_0=-\int \tilde{w}_0(X,a,\Delta a)\ln \tilde{w}_0(X,a,\Delta a)dX$$

and

$$S=-\int w(X,a_0+\Delta a)\ln w(X,a_0+\Delta a)dX$$

as a quantitative measure of the degree of ordering of the motion when a varies from a_0 to $a_0+\Delta a$. It follows from the normalization conditions and Eq. (22) that

$$\Delta S=\tilde{S}_0-S=\int w\ln\frac{w}{\tilde{w}_0}dX. \quad (25)$$

We note that ΔS, which is defined by (25), cannot be negative, even if we incorrectly chose the state of physical chaos, i.e., even if we found that $D<1$. However, it would then not characterize the degree of ordering of the motion. Thus, as we have already stated, the criterion for a transition to a more ordered state is $D(\Delta a)>1$ and not $\Delta S>0$.

Let us now turn to our problem and take the state corresponding to $\eta=\eta_0$ as physical chaos and the state corresponding to $\eta>\eta_0$ as the state whose degree of order we wish to determine. Assuming that $\eta,\eta_0\ll 1$ and performing all the calculations indicated above, we find that $D=1+2(\eta-\eta_0)(1+2\eta+3\eta^2+\ldots)$, i.e., we correctly selected the state of physical chaos.[4)] The calculation of the entropy difference δS is fairly cumbersome, but it can be shown that $\delta S\sim\eta^2(\eta-\eta_0)$. The expressions found are also valid for $\eta_0=0$.

Thus, we have found that upon the phase transition considered above, the motion becomes more ordered from the standpoint of Klimontovich's criterion, although the degree of ordering varies only slightly. From the standpoint of pure common sense this result seems paradoxical (as does Klimontovich's well-known finding that the transition from laminar to turbulent flow is accompanied by an increase in the degree of ordering of the motion). For this reason, Klimontovich's criterion has aroused and still arouses strenuous resistance among many investigators, especially those who deal exclusively with dynamical systems and do not consider fluctuations. However, in our opinion, Klimontovich's criterion contains a rational core when it is applied to systems in which fluctuations play a decisive role.

Klimontovich interpreted his results with respect to turbulence in the following manner. When turbulence develops, an increasingly larger part of the energy of the chaotic motion of the molecules is transformed into the energy of the considerably more ordered, large-scale motion of eddies, i.e, the fraction of the energy in the small-scale chaotic motion decreases. Therefore, the degree of ordering of the motion as a whole increases. It is difficult not to agree with this interpretation. A similar interpretation can be given for the noise-induced phase transition in a pendulum considered here. We question both the feasibility and utility of applying Klimontovich's criterion to systems in which the presence of fluctuations is not fundamental, for example, self-excited oscillators.

6. STABILIZATION OF THE UPPER EQUILIBRIUM POSITION OF A PENDULUM WITH A RANDOMLY OSCILLATING PIVOT

It is widely known that when the pivot of a pendulum undergoes rapid periodic oscillations, its upper equilibrium position can become stable under certain conditions (see, for example, Refs. 26–29). This phenomenon was observed experimentally by P. L. Kapitsa.[30,31] It will be shown below that a similar phenomenon occurs when the pivot undergoes sufficiently high-frequency random oscillations. For this purpose we consider the equation

$$\ddot{\varphi}+2\beta\dot{\varphi}+(1+\xi(t))\sin\varphi=0. \tag{26}$$

If the spectrum of the random process $\xi(t)$ is concentrated in a sufficiently high-frequency region and does not contain components in zones of parametric resonance, fluctuations of the variable φ due to random oscillations of the pivot will be small. Setting $\varphi=\langle\varphi\rangle+\delta\varphi$, where $\delta\varphi\ll\langle\varphi\rangle$, in (26), we obtain

$$\langle\ddot{\varphi}\rangle+2\beta\langle\dot{\varphi}\rangle+\sin\langle\varphi\rangle+\cos\langle\varphi\rangle\langle\xi(t)\,\delta\varphi\rangle=0,$$

$$\delta\ddot{\varphi}+2\beta\,\delta\dot{\varphi}+\cos\langle\varphi\rangle\,\delta\varphi+\xi(t)\sin\langle\varphi\rangle=0. \tag{27}$$

One of the stationary solutions of Eqs. (27) has the form

$$\langle\varphi\rangle=\pi,\quad \delta\varphi=0. \tag{28}$$

This solution corresponds to the upper equilibrium position of the pendulum, in whose stability we are interested.

To investigate this stability, we can write linearized equations for small deviations from the steady-state solution (28). Setting $\langle\varphi\rangle=\pi+\psi$, from (27) we obtain the following linearized equations for ψ and $\delta\varphi$:

$$\delta\ddot{\psi}+2\beta\dot{\psi}-\psi-\langle\xi(t)\,\delta\varphi\rangle=0, \tag{29}$$

$$\delta\ddot{\varphi}+2\beta\,\delta\dot{\varphi}-\delta\varphi-\xi(t)\psi=0. \tag{30}$$

Under steady-state conditions the solution of Eq. (30) has the form

$$\delta\varphi(t)=\frac{1}{2\sqrt{1+\beta^2}}\int_{-\infty}^{t}[\exp(p_1(t-t'))-\exp(p_2(t-t'))]\xi(t')\psi(t')dt', \tag{31}$$

where $p_{1,2}=-\beta\pm\sqrt{1+\beta^2}$ are the roots of the characteristic equation $p^2+2\beta p-1=0$. Hence we find

$$\langle\xi(t)\,\delta\varphi\rangle=\frac{1}{2\sqrt{1+\beta^2}}\int_{-\infty}^{t}[\exp(p_1(t-t'))-\exp(p_2(t-t'))]\langle\xi(t)\xi(t')\rangle\psi(t')dt'. \tag{32}$$

Setting $t'-t=\tau$ in this expression and noting that the value of ψ does not vary significantly during the correlation time of the random process $\xi(t)$, we rewrite (32) in the following form:

$$\langle\xi(t)\,\delta\varphi\rangle=-\frac{1}{2\sqrt{1+\beta^2}}\,\psi(t)\int_0^{\infty}[\exp(-p_1\tau)-\exp(-p_2\tau))]\langle\xi(t)\xi(t+\tau)\rangle d\tau. \tag{33}$$

To calculate the integral in this expression, we specify the correlation function of the process $\xi(t)$ in the form

$$\langle\xi(t)\xi(t+\tau)\rangle=\sigma^2e^{-\alpha\tau}\cos\omega\tau,$$

where $\sigma^2=\alpha\kappa(\omega)/2$ is the variance of the random process $\xi(t)$, $\kappa(\omega)$ is the value of the spectral density of this process at its center frequency, and α is the half-width of the spectrum of the process $\xi(t)$. From (33) we find

$$\langle\xi(t)\,\delta\varphi\rangle=-\frac{\sigma^2(\omega^2-(p_1+\alpha)(p_2+\alpha))}{(\omega^2+(p_1+\alpha)^2)(\omega^2+(p_2+\alpha)^2)}\,\psi(t). \tag{34}$$

Under the condition $\omega\gg1,\beta,\alpha$ we thus obtain

$$\langle\xi(t)\,\delta\varphi\rangle\approx-\frac{\sigma^2}{\omega^2}\,\psi(t). \tag{35}$$

Substituting (35) into (29), we obtain the approximate equation

$$\ddot{\psi}+2\beta\dot{\psi}+\omega_0^2\psi=0, \tag{36}$$

where $\omega_0=\sqrt{\sigma^2/\omega^2-1}$ is the natural frequency of small oscillations of the pendulum about the upper equilibrium position when $\beta=0$. It follows from Eq. (36) that the mean deviation of the pendulum from the upper equilibrium position will decay, i.e., the equilibrium position will be stable, if the frequency ω_0 is real.

The transition to a regime with stabilization of the upper equilibrium position of the pendulum due to either periodic or random high-frequency vibration of the pivot can be regarded as the creation of an averaged system [the deviation of the upper equilibrium position for this system is described by Eq. (36)] of some new attractor induced by the high-frequency vibration in phase space. In some sense we can forget about the high-frequency vibration and consider a new dynamical system with two stable equilibrium states. Just such an approach was developed by I. I. Blekhman.[29] A procedure for obtaining equations that describe this new system was also given in his monograph. On the other hand, the process of stabilizing the upper equilibrium position of a pendulum by means of high-frequency random vibration of the pivot, as well as the process of exciting vibrations considered above, can be interpreted as a noise-induced second-order phase transition, in which the parameter σ^2 plays the role of the ''temperature,'' and the real part of the frequency ω_0 plays the role of the order parameter. It follows from the expression for ω_0 that the corresponding critical index equals 1/2.

7. CONCLUSIONS

We have thus shown that nonequilibrium second-order phase transitions, which lead to the appearance of an induced attractor of finite dimension, are possible even in such a simple system as a physical pendulum under the influence of multiplicative noise. The investigation of such transitions in other, more complicated systems will undoubtedly be of great physical interest.

We thank M. G. Rosenblum, A. B. Potapov, and D. A. Gribkov for kindly supplying programs for calculating the dimensionality by various methods, and for their assistance in performing several calculations. We would like to express our special thanks to R. L. Stratonovich for extremely useful remarks and advice.

[1)]It was, however, taken into account by Dimentberg.[10]

[2)]The noise source leading to noise contamination of the self-induced oscillations can be either additive or multiplicative.

[3)]All this is true if the value of D following the reverse transition from a to $a-\Delta a$ is less than unity; otherwise, the situation is more complicated. As follows from the results obtained below, the former simple situation exists in the case under consideration.

[4)]It follows from this expression that if we set $\eta < \eta_0$, the value of D will be less than unity. Thus, the simple situation referred to above does in fact come to pass.

[1] C. Van den Broeck, J. M. R. Parrondo, J. Armero, and A. Hernández-Machado, Phys. Rev. E **49**, 2639 (1994).
[2] C. Van den Broeck, J. M. R. Parrondo, and R. Toral, Phys. Rev. Lett. **73**, 3395 (1994).
[3] J. M. R. Parrondo, C. Van den Broeck, J. Buceta, and F. Javier de la Rubia, Physica A (Amsterdam) **224**, 153 (1996).
[4] P. S. Landa, *Nonlinear Oscillations and Waves in Dynamical Systems*, Kluwer, Dordrecht–Boston (1996).
[5] A. S. Ginevskiĭ and P. S. Landa, Izv. Vyssh. Uchebn. Zaved., Prikl. Nelin. Dyn. **3**, 42 (1995).
[6] W. Horsthemke and R. Lefever, *Noise-Induced Transitions. Theory and Application in Physics, Chemistry, and Biology*, Springer, Berlin (1984).
[7] I. I. Fedchenia, Physica A (Amsterdam) **125**, 577 (1984).
[8] R. L. Stratonovich and Yu. M. Romanovskiĭ, Nauchn. Dokl. Vyssh. Shk., Ser. Fiz.-Mat. **3**, 221 (1958).
[9] R. L. Stratonovich, *Topics in the Theory of Random Noise, Vol. 1*, Gordon and Breach, New York (1963).
[10] M. F. Dimentberg, *Nonlinear Stochastic Problems of Mechanical Vibrations* [in Russian], Nauka, Moscow (1980).
[11] P. S. Landa, *Sustained Oscillations in Systems with a Finite Number of Degrees of Freedom* [in Russian], Nauka, Moscow (1980).
[12] S. M. Rytov, Yu. A. Kravtsov, and V. I. Tatarskiĭ, *Principles of Statistical Radiophysics*, 2nd ed., Springer-Verlag, Berlin–New York (1987–1989) [Russ. original of 1st ed., Nauka, Moscow (1966), p. 264].
[13] L. A. Vaĭnshteĭn and D. E. Vakman, *Separation of Frequencies in the Theory of Vibrations and Waves* [in Russian], Nauka, Moscow (1983).
[14] Yu. I. Neimark and P. S. Landa, *Stochastic and Chaotic Oscillations*, Kluwer, Dordrecht (1992).
[15] S. Corrsin, NACA Advis. Conf. Rep., 3123 (1943).
[16] J. Rotta, Ing.-Arch. **24**, 258 (1956).
[17] N. V. Nikitin, Izv. Ross. Akad. Nauk, Mekh. Zhidk. Gaza, 14 (1994).
[18] Y. Pomeau and P. Manneville, Commun. Math. Phys. **74**, 189 (1980).
[19] P. S. Landa and M. G. Rosenblum, Physica D (Amsterdam) **48**, 232 (1991).
[20] A. R. Osborne and A. Provenzale, Physica D (Amsterdam) **35**, 357 (1989).
[21] J. Theiler, Phys. Lett. A **155**, 480 (1991).
[22] J. B. McLaughlin, J. Stat. Phys. **34**, 375 (1981).
[23] M. F. Dimentberg, Izv. Akad. Nauk SSSR, Mekh. Tverd. Tela, (6) (1969).
[24] Yu. L. Klimontovich, *Turbulent Motion and the Structure of Chaos*, Kluwer, Dordrecht (1991).
[25] Yu. L. Klimontovich, Usp. Fiz. Nauk **158**, 59 (1989).
[26] N. N. Bogolyubov, Inst. Mekh. Akad. Nauk Ukr. SSR **14**, 9 (1950).
[27] L. D. Landau and E. M. Lifshitz, *Mechanics*, 2nd ed., Pergamon Press, Oxford–New York (1969).
[28] V. V. Bolotin, V. I. Vorob'ev, V. A. Semenov, and V. K. Chernov, Izv. Akad. Nauk SSSR, Mekh. Tverd. Tela, 36 (1979).
[29] I. I. Blekhman, *Vibrational Mechanics* [in Russian], Nauka, Moscow (1994).
[30] P. L. Kapitsa, Zh. Éksp. Teor. Fiz. **21**, 588 (1951).
[31] P. L. Kapitsa, Usp. Fiz. Nauk **44**, 7 (1951).

Translated by P. Shelnitz

Erratum: Logarithmic radiative corrections to the dipole matrix elements in the hydrogen atom [JETP 82, 656–663 (1996)]

V. G. Ivanov

Main Astronomical Observatory, Russian Academy of Sciences, 196140 Pulkovo, Russia

S. G. Karshenboĭm

D. I. Mendeleev Scientific-Research Institute of Metrology, 198005 St. Petersburg, Russia

[S1063-7761(97)02401-3]

The following corrections were reported by the authors:

1. Table I should read as follows:

TABLE I. Analytic and numerical values of $S_{n'n}$.

n	$n'=2$	$n'=3$	$n'=4$	$n'=\infty$
1	$\frac{131}{48}+\ln\frac{4}{3}$ 3.0168	$\frac{55}{36}+\ln\frac{3}{2}$ 1.9332	$\frac{1103}{960}+\ln\frac{8}{5}$ 1.6190	$\ln 2-\frac{3}{8}-\mathscr{C}_2+\frac{5}{8}e^2$ 1.2524
2	$\frac{1}{12}$ 0.0833	$\frac{2351}{720}+\ln\frac{6}{5}$ 3.4476	$\frac{1843}{960}+\ln\frac{4}{3}$ 2.2075	$\ln 2-\frac{235}{128}-\mathscr{C}_4+\frac{47}{128}e^4$ 1.2376
3	$-\frac{451}{80}-\ln\frac{5}{4}$ -5.8606	$\frac{1}{18}$ 0.0556	$\frac{676223}{190400}+\ln\frac{8}{7}$ 3.6851	$\ln 2-\frac{541}{216}-\mathscr{C}_6+\frac{325}{1512}e^6$ 1.2836
4	$-\frac{875}{192}-\ln\frac{3}{2}$ −4.9628	$-\frac{21107}{4032}-\ln\frac{7}{6}$ −5.3890	$\frac{1}{24}$ 0.0417	$\ln 2-\frac{413551}{141312}-\mathscr{C}_8+\frac{6973}{47104}e^8$ 1.3269
∞	$\mathscr{C}'_4-\frac{7}{16}e^4$ −4.2558	$\mathscr{C}'_6-\frac{2}{9}e^6$ −3.6611	$\mathscr{C}'_8-\frac{181}{1216}e^8$ −3.3318	

2. Equation (10) should read as follows:

$$\delta d_{zn'n}=-\frac{2A(Z\alpha)m^2}{\pi}\,d_{zn'n}\left[\sum_{n''\neq n}\frac{1}{n''^3}\,\frac{1}{1/n^2-1/n''^2}\,\frac{\mathscr{D}_{n''n'}}{\mathscr{D}_{nn'}}+\int_0^\infty\frac{dt}{t^3(1/n^2+1/t^2)}\,\frac{1}{1-e^{-2\pi t}}\,\frac{\mathscr{D}_{tn'}}{\mathscr{D}_{nn'}}\right]. \tag{10}$$

3. Equation (21) should read as follows:

$$\overline{G_n}(E_n;0,\mathbf{r})=-\frac{Z\alpha m^2}{2\pi r}\,\frac{e^{-z_n/2}}{n!}\sum_{s=0}^{n}\frac{(-z_n)^{n-s}}{s!}\left[\frac{n!}{(n-s)!}\right]^2\left\{(n-s)\left[(\psi(n+1)-2\psi(n-s+1))\right.\right.$$
$$\left.\left.-\frac{2(n-s)+3-z_n}{2n}+\ln z_n\right]+1\right\}. \tag{21}$$

4. The second equation in Appendix C (Section A), p. 662, should be numbered as ''(C1).''

 3-378/97/010209-02$10.00

5. The first equation in Appendix C (Section B), p. 662, should read as follows:

$$Q_{\nu n'}=\xi_\nu^4\sum_{t=0}^{n'-2}\frac{(-1)^t\xi_\nu^t}{t!}\frac{\Gamma(n'-1)}{\Gamma(n'-1+t)}\frac{\Gamma(4)}{\Gamma(t+4)}\sum_{s=0}^{n}\frac{(-1)^s(\nu-s)\eta_\nu^{\nu-s}}{s!}\frac{\Gamma(\nu+1)\Gamma(\nu-s+4+t)}{[\Gamma(\nu+1-s)]^2}.$$

6. Table IV on p. 661 should read as follows:

TABLE IV. Corrections to the line intensities and partial and total line widths corresponding to transitions in the lower levels, in units of $A(Z\alpha)m^2/\pi$.

Level	Corrections to the intensities and widths		
	Transition	$\delta I/I$	Partial and total $\delta\Gamma/\Gamma$
$2p$	$2p\to 1s$	−4.6331	−1.9664 } −1.9664
$3s$	$3s\to 2p$	−9.5879	−10.121 } −10.121
$3p$	$3p\to 1s$	−5.1336	−2.8836 } −2.3654
	$3p\to 2s$	−0.3048	1.4952 }
$4s$	$4s\to 2p$	−9.2589	−9.4256 } −9.1860
	$4s\to 3p$	−8.2066	−8.8494 }
$4p$	$4p\to 1s$	−5.2953	−3.1620 } −2.4981
	$4p\to 2s$	−0.9183	0.4150 }
	$4p\to 3s$	1.2750	2.7988 }
	$4p\to 3d$	0	0 }

Vacuum splitting of the energy levels of a system consisting of an atom and a dielectric microsphere

V. V. Klimov

P. N. Lebedev Institute of Physics, Russian Academy of Sciences, 117294 Moscow, Russia

V. S. Letokhov

Institute of Spectroscopy, Russian Academy of Sciences, 142092 Troitsk, Moscow Region, Russia
(Submitted 13 June 1996)
Zh. Éksp. Teor. Fiz. **111**, 44–51 (Janaury 1997)

Expressions are found for the vacuum splitting of the energy levels of a system consisting of a two-level atom and a dielectric microsphere. These expressions coincide with those obtained from a purely classical approach. © *1997 American Institute of Physics.* [S1063-7761(97)00301-6]

1. INTRODUCTION

Contemporary technology has progressed to the point where various structures (microspheres, sharp points[1]) can be fabricated with characteristic dimensions in the hundreds or even tens of nanometers. For this reason, there has been more and more interest in the investigation of optical phenomena near such nanostructures.

Nanostructure optics is a very specialized area of optics and spectroscopy, because it involves optics over dimensions that are comparable to or even smaller than a wavelength. This implies that many of the concepts of ordinary optics and spectroscopy are subject to considerable modification.

One of the most interesting directions of inquiry in this area is the investigation of how the spectroscopic characteristics of an atom change near a nanostructure. In this case, the formal quantum mechanical problem can be solved if we limit ourselves to first order in perturbation theory, yielding both the level shift[2] and the change in linewidth.[3] In Ref. 4 this problem was discussed and applied to an atom near a dielectric microsphere, and the shift in frequency and change in linewidth were found.

A more interesting case is that of strong electromagnetic coupling, where perturbation theory cannot be applied. In this case a situation can arise where the radiation of an atom is absorbed by the resonator and the radiation of the resonator is absorbed by the atom, i.e., the case of Rabi splitting. Although this effect has been discussed in a number of papers (see, e.g., Refs. 3 and 5) from a general point of view, in specific situations its treatment is a complicated problem. In Ref. 6, Dutta *et al.* discussed vacuum Rabi splitting in a model problem where the interaction of an atom with a sphere was approximated by distributing a dielectric permittivity with resonance properties uniformly over the latter; the coupling strength of the atom to the sphere was controlled by varying the resonant part of the dielectric constant.

In Refs. 4 and 7, Klimov *et al.* discussed the classical problem of the resonant effect of a dielectric microsphere on the radiative properties of an oscillator located near its surface. In this paper we discuss this problem from a quantum mechanical point of view for a two-level atom interacting with the resonant modes of a dielectric microsphere. The geometry of the problem is shown in Fig. 1.

2. QUANTIZATION OF THE ELECTROMAGNETIC FIELD IN THE PRESENCE OF A MICROSPHERE

In order to solve this problem we must first quantize the electromagnetic field properly. For the most part, this procedure is well understood; however, a special approach is required for each specific case. In our problem, we choose as the quantization volume a perfectly conducting sphere with large but finite radius $\Lambda \to \infty$ (see Fig. 1). The classical expansion of the electromagnetic field and its vector potential over a complete set of eigenstates can be written in the form

$$\mathbf{E}=\sum_s \frac{a_s-a_s^+}{i\sqrt{2}}\,\mathbf{e}(s,\mathbf{r}), \quad \mathbf{B}=\sum_s \frac{a_s+a_s^+}{\sqrt{2}}\,\mathbf{b}(s,\mathbf{r}),$$

$$\mathbf{A}=-\frac{c}{\omega_s}\sum_s \frac{a_s+a_s^+}{\sqrt{2}}\,\mathbf{e}(s,\mathbf{r}),$$

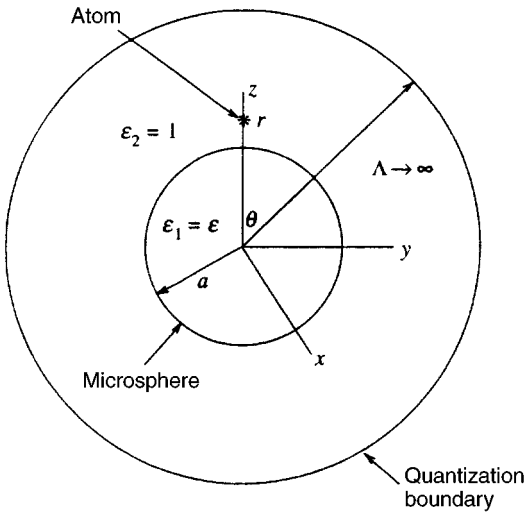

FIG. 1. Geometry of the problem.

$$\nabla\times\mathbf{e}(s,\mathbf{r})=-\frac{\omega_s}{c}\,\mathbf{b}(s,\mathbf{r}). \tag{1}$$

Here a_s, a_s^+ are the photon annihilation and creation operators for the corresponding modes with the usual commutation relations; ω_s are the frequencies of these modes.

For the case of interest to us, i.e., TM modes, it is easy to obtain expressions for $\mathbf{e}(s,\mathbf{r})$ and $\mathbf{b}(s,\mathbf{r})$ (see, e.g., Ref. 8) in terms of spherical harmonics Y and spherical Hankel functions h:[9]

$$\mathbf{b}(n,m,\nu)=[\alpha_{TM,n}^{(1)}h_n^{(1)}(kr)+\alpha_{TM,n}^{(2)}h_n^{(2)}(kr)]\times\hat{\mathbf{L}}Y_{nm}(\vartheta,\varphi),\quad r>a,$$

$$\mathbf{e}(n,m,\nu)=-\frac{1}{k}\,[\nabla\times\mathbf{b}(n,m,\nu)]. \tag{2}$$

Here $k=\omega_s/c$ is the wave vector outside the sphere, and $s=\{n,m,\nu\}$, where n is the orbital quantum number, m is the azimuthal quantum number, and ν is the radial quantum number; $\mathbf{L}=-i\mathbf{r}\times\nabla$ is the angular momentum operator, and a is the radius of the microsphere. Within the microsphere analogous representations apply with the spherical functions h_n replaced by spherical Bessel functions j_n, and $\alpha_{TM,n}^{(1,2)}$ replaced by $\beta_{TM,n}$.

The coefficients $\alpha_{TM,n}^{(1,2)}$ and $\beta_{TM,n}$ can be found in the usual way from the continuity conditions on the tangential components of the field at the boundary of the sphere, and normalization of the wave functions in a sphere with radius Λ to one photon per mode:

$$\alpha_{TM,n}^{(1)}=\left[\varepsilon\,\frac{d}{dz_2}\,[z_2h_n^{(2)}(z_2)]j_n(z_1)-\frac{d}{dz_1}\,[z_1j_n(z_1)]h_n^{(2)}(z_2)\right]\frac{iz_2\beta_{TM,n}}{2\varepsilon},$$

$$\alpha_{TM,n}^{(2)}=-\left[\varepsilon\,\frac{d}{dz_2}\,[z_2h_n^{(1)}(z_2)]j_n(z_1)-\frac{d}{dz_1}\,[z_1j_n(z_1)]h_n^{(1)}(z_2)\right]\frac{iz_2\beta_{TM,n}}{2\varepsilon},$$

$$|\alpha_{TM,n}^{(1)}|^2=|\alpha_{TM,n}^{(2)}|^2=\frac{2\pi\hbar c}{\Lambda}\,\frac{k^3}{n(n+1)}. \tag{3}$$

In (3) and in what follows $z_1=\sqrt{\varepsilon}ka$, $z_2=ka$, and ε is the dielectric constant of the microsphere. Note that the contribution to the normalization of the wave function from the region within the dielectric microsphere is negligible compared to the contribution from the region with $r\sim\Lambda$.

In order to find the effective mode amplitudes it is also necessary to know the density of final states. The requirement that the tangential components of the electric field vanish on the interior surface of this sphere leads to the transcendental equation

$$\frac{d}{dr}\,(rZ)\bigg|_{r=\Lambda}=0,$$

$$Z=\left[\alpha_{TM,n}^{(1)}h_n^{(1)}\left(\frac{\omega_s}{c}\,r\right)+\alpha_{TM,n}^{(2)}h_n^{(2)}\left(\frac{\omega_s}{c}\,r\right)\right], \tag{4}$$

which has the asymptotic solution

$$\omega_s=\left(\nu+\frac{n+1}{2}\right)\frac{\pi c}{\Lambda}+\ldots \tag{5}$$

From this it follows that the density of final states will be given by the simple expression

$$\rho_{TM}(\omega)=\frac{\Lambda}{\pi\hbar c}. \tag{6}$$

3. CALCULATION OF THE EFFECTIVE ELECTRIC FIELD AMPLITUDE OF A RESONANT MODE AND THE EFFECTIVE RABI FREQUENCY

In the most interesting case of resonant interaction of an atom with one of the long-lived modes of the electromagnetic field in the microsphere (the so-called whispering gallery modes[10]), the effective Hamiltonian for the dipole interaction of the atom and the radiation[11] can be written in the form

$$H=H_A+H_F+H_I, \tag{7}$$

where the Hamiltonians of the atom H_A, the field H_F, and the interaction H_I have the following forms for a two-level atom:

$$H_A=\frac{\hbar\omega_A}{2}\,\sigma_3,\quad H_F=\hbar\omega_{res}\left[a^+a+\frac{1}{2}\right],$$

$$H_I=-\hat{\mathbf{d}}\cdot\hat{\mathbf{E}}=-\mathbf{e}\cdot\mathbf{d}\sigma_3\,\frac{a-a^+}{i\sqrt{2}}=\hbar\Omega_R\sigma_I i(a-a^+). \tag{8}$$

Here a^+ and a are the usual creation and annihilation operators for photons with frequency ω_{res} in the resonant mode of the microsphere, $\mathbf{e}$ is the amplitude of the resonant mode, $\mathbf{d}$ is the matrix element for the dipole moment, and σ_1, σ_3 are Pauli matrices:

$$\sigma_3=\begin{bmatrix}1&0\\0&-1\end{bmatrix},\quad \sigma_1=\begin{bmatrix}0&1\\1&0\end{bmatrix}. \tag{9}$$

The Rabi frequency Ω_R in (8) can be determined in the usual way in terms of the transition dipole moment $\mathbf{d}$ and the amplitude of the electric field in the resonant mode:

$$\Omega_R=\frac{\mathbf{d}\cdot\mathbf{e}}{\sqrt{2}\hbar}. \tag{10}$$

The frequency of the resonant mode ω_{res} and the magnitude of the transition dipole moment d must be set equal to their values for no interaction. As for the atomic transition frequency ω_A, it seems logical to include in it the shift caused by the pure electrostatic interaction with the microsphere:[4,7]

$$\omega_A^2=\omega_0^2-\delta\omega_0^2,\quad \delta\omega_0^2=\frac{3}{8}\,\frac{\varepsilon-1}{\varepsilon+1}\,\frac{\gamma_0\omega_0}{[k_0(r-a)]^3}. \tag{11}$$

In (11), ω_0, γ_0 are the frequency and linewidth of the transition for the case where no microsphere is present, and $k_0=\omega_0/c$.

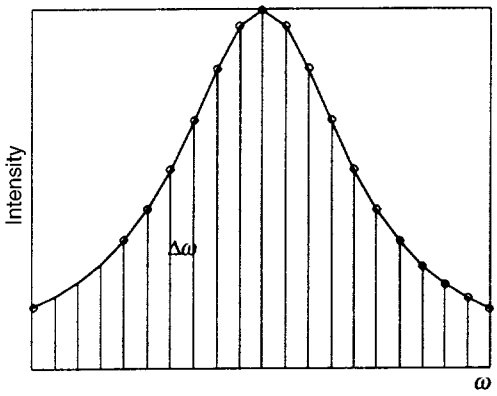

FIG. 2. Distribution of quantized frequencies over the resonance line shape. The spacing between discrete lines is $\hbar\Delta\omega = 1/\rho(\omega) = \pi\hbar c/\Lambda$.

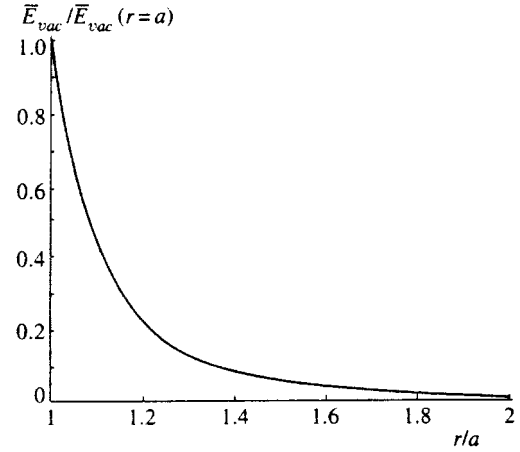

FIG. 3. Dependence of the effective electric field on radius (TM mode, $n=9$, $\varepsilon=6$, $k_{res}a=5.548731$).

In (8) the interaction energy is expressed in terms of the amplitude of the resonant mode. However, the width of the resonance line is finite, and it is necessary to take into account the contribution of all profile discrete modes ω_s lying under the resonance profile (see Fig. 2), including modes that are degenerate with respect to azimuthal angle. In this paper all modes are included by mean square averaging. The results obtained confirm the correctness of this approach.

If we consider as a specific example the case in which the element of the transition dipole moment is oriented along the radius, then it can only interact with TM modes of the dielectric microsphere, and consequently the quantity to examine is the mean square of the radial component of the electric field in the TM mode.

The radial component of the sth TM mode, which is of interest to us, can be easily found from Eq. (2)

$$e_r(n,m,\nu) = -\frac{in(n+1)}{kr}\,[\alpha^{(1)}_{TM,n}h^{(1)}_n(kr) + \alpha^{(2)}_{TM,n}h^{(2)}_n(kr)]Y_{nm}(\vartheta,\varphi). \tag{12}$$

Summing the squares of the modulus (12) over the azimuthal quantum number m with the help of the familiar relation

$$\sum_m Y^2_{nm} = \frac{2n+1}{4\pi},$$

we obtain the following expression for the mean square of the electric field due to all degenerate TM modes:

$$\overline{E^2_{r,TM}} = n(n+1)(2n+1)\,\frac{2k\hbar c}{\Lambda r^2}\,|j_n(kr) - q_n h^{(1)}_n(kr)|^2, \tag{13}$$

where the q_n are the Mie coefficients:

$$q_n = \frac{1}{2}\left(1 - \frac{\alpha^{(1)}_{TM,n}}{\alpha^{(2)}_{TM,n}}\right) = \frac{\left[\varepsilon\,\frac{d}{dz_2}[z_2 j_n(z_2)]j_n(z_1) - \frac{d}{dz_1}[z_1 j_n(z_1)]j_n(z_2)\right]}{\left[\varepsilon\,\frac{d}{dz_2}[z_2 h^{(1)}_n(z_2)]j_n(z_1) - \frac{d}{dz_1}[z_1 j_n(z_1)]h^{(1)}_n(z_2)\right]}. \tag{14}$$

Under the assumption of resonant interaction of the atom with the microsphere, the expression for the Mie coefficient can be written in the form

$$q_n \approx -i\,\frac{\mathrm{Im}\,Q_{res}}{\omega - \Omega_{res}}, \tag{15}$$

where Ω_{res} is the complex frequency that characterizes the resonant mode: $\Omega_{res} = \omega_{res} - i\Gamma^{(n)}_{res}/2$, while $\Gamma^{(n)}_{res}$ characterizes the width of the resonance mode.

Using elementary relations, Eq. (13) is easily reduced to the form

$$\overline{E^2_{r,TM}} = n(n+1)(2n+1)\,\frac{2k\hbar c}{\Lambda r^2}\,[j^2_n(kr) - \mathrm{Re}(q_n(h^{(1)}_n)^2(kr)^2)]. \tag{16}$$

This expression involves only the degenerate modes of one of the discrete frequencies ω_s (see (5) in Fig. 2). In order to obtain the effective value of the electric field associated with the mode, it is necessary to sum $\overline{E^2_{r,TM}}$ over all frequencies within the mode under discussion, i.e., the final expression for the square of the effective value of the mode amplitude must be written in the form

$$\overline{E^2_{vac}} = \int_{\omega_{res}-\Delta\omega}^{\omega_{res}+\Delta\omega} \overline{E^2_{r,TM}}(\omega)\rho(\omega)\,d\omega, \tag{17}$$

where $\Delta\omega \sim \Gamma^{(n)}_{res}$ determines the averaging interval. The effective Rabi frequency will accordingly be given by

$$\Omega_R = \frac{d\overline{E}_{vac}}{\sqrt{2}\hbar}. \tag{18}$$

After substituting (15) into (16), the integration in the second term of (16) can be extended to the interval $-\infty$ to ∞, as a result of which we obtain the final expression for the mean square of the electric field:

$$\overline{E^2_{vac}} = n(n+1)(2n+1)\,\frac{\hbar\Gamma^{(n)}_{res}}{2r^3}\left[Y^2_{n+1/2}(k_{res}r) + J^2_{n+1/2}(k_{res}r)\left(\frac{4\Delta\omega}{\pi\Gamma^{(n)}_{res}} - 1\right)\right], \tag{19}$$

where J_n, Y_n are Bessel functions of the first and second kind respectively,[9] and $k_{res} = \omega_{res}/c$. For long-lived modes, the value of n is large and the term with J^2_n is small compared to the term Y^2_n. Furthermore, by choosing the interval of frequency averaging to be

$$\Delta\omega = \frac{\pi\Gamma^{(n)}_{res}}{4}, \tag{20}$$

we can set the term with J^2_n to zero identically, as a result of which the expression for the effective mean-square amplitude of the resonant mode takes the form

$$\overline{E^2_{vac}} = n(n+1)(2n+1)\,\frac{\hbar\Gamma^{(n)}_{res}}{2r^3}\,Y^2_{n+1/2}(k_{res}r). \tag{21}$$

Figure 3 shows the dependence of the effective mode amplitude on the distance from the microsphere to the atom for a TM resonance with $n=9$, $\varepsilon = 6$, and $k_{res}a = 5.5487$.

4. DETERMINING THE ENERGY LEVEL SPLITTING; DISCUSSION OF RESULTS

Once we have found the effective Rabi frequency, the problem reduces to diagonalizing the Hamiltonian (8), which in the occupation number representation has the form

$$H/\hbar = \begin{bmatrix} \frac{\omega_{res}+\omega_A}{2} & 0 & 0 & i\Omega_R & 0 & \dots \\ 0 & \frac{\omega_{res}-\omega_A}{2} & i\Omega_R & 0 & \dots & 0 \\ 0 & 0 & \frac{3\omega_{res}+\omega_A}{2} & \dots & 0 & i\sqrt{n+1}\Omega_R \\ 0 & -i\Omega_R & \dots & \frac{(2n+1)\omega_{res}-\omega_A}{2} & i\sqrt{n+1}\Omega_R & 0 \\ -i\Omega_R & \dots & 0 & -i\sqrt{n+1}\Omega_R & \frac{(2n+3)\omega_{res}+\omega_A}{2} & 0 \\ \dots & 0 & -i\sqrt{n+1}\Omega_R & 0 & 0 & \dots \end{bmatrix}. \tag{22}$$

In the rotating-wave approximation, which is valid for small values of the Rabi frequency, we have instead of (22) the matrix

$$H/\hbar = \begin{bmatrix} \frac{\omega_{res}+\omega_A}{2} & 0 & 0 & i\Omega_R & 0 & \dots \\ 0 & \frac{\omega_{res}-\omega_A}{2} & 0 & 0 & \dots & 0 \\ 0 & 0 & \frac{3\omega_{res}+\omega_A}{2} & \dots & 0 & i\sqrt{n+1}\Omega_R \\ 0 & 0 & \dots & \frac{(2n+1)\omega_{res}-\omega_A}{2} & 0 & 0 \\ -i\Omega_R & \dots & 0 & 0 & \frac{(2n+3)\omega_{res}+\omega_A}{2} & 0 \\ \dots & 0 & -i\sqrt{n+1}\Omega_R & 0 & 0 & \dots \end{bmatrix}, \tag{23}$$

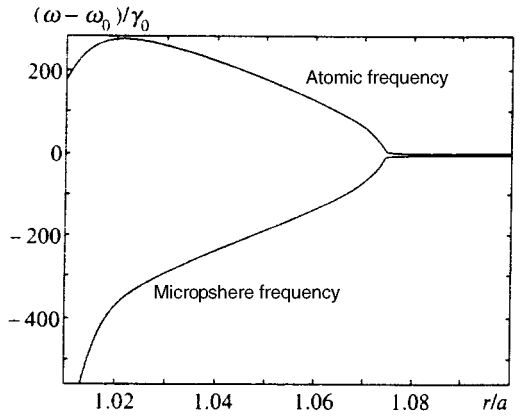

FIG. 4. Dependence of the relative shift in frequency on the position of the radially oscillating atom (for $k_0a=5.548733$, $\omega_0/\gamma_0=10^7$) for a dielectric sphere with $\varepsilon=6$, $n=9$, $k_{res}a=5.548731$.

whose diagonalization is elementary. As a result, the structure of the energy spectrum of the system under study has the form

$$E_{g0}=-\frac{\hbar}{2}(\omega_A-\omega_{res}),\quad E_{\pm,n}=(n+1)\hbar\omega_{res}$$
$$\pm\frac{\hbar}{2}\sqrt{(\omega_A-\omega_{res})^2+4\Omega_R^2(n+1)},\quad n=0,1,\ldots \tag{24}$$

Equation (24), together with the expressions for the effective Rabi frequency (18) and effective field amplitude (21), is a complete solution for the energy spectrum of a system consisting of a two-level atom and a dielectric microsphere.

It is easy to obtain from (24) an expression for the vacuum Rabi splitting of the transition frequency from the first excited state to the ground state:

$$\omega_{\pm}=\frac{\omega_A+\omega_{res}}{2}\pm\sqrt{\frac{(\omega_A-\omega_{res})^2}{4}+\Omega_R^2}. \tag{25}$$

In order to determine the physical meaning of these frequencies, we must use the fact that as the interaction between the atom and the sphere decreases ($r\to\infty$), one of the solutions reduces to the frequency of the atomic transition in free space ($\omega_1\to\omega_0$), while the other reduces to the resonant frequency in the microsphere ($\omega_2\to\omega_{res}$).

A clear illustration of these results is shown in Fig. 4, where the dependence of the frequency splitting on the distance to the microsphere is plotted.

A remarkable feature of Eq. (25) is the fact that it coincides up to negligibly small terms with the expression obtained from purely classical relations[4,7] by the usual replacement $d^2_{\text{quantum}}\sim\overline{d^2_{\text{class}}}/2$. Thus, all the analysis of the Rabi splitting of the energy spectrum carried out in (4) and (7) can be taken over without change to the quantum mechanical case. On the other hand, this agreement verifies the correctness of the procedure we have used for finding the effective mode amplitudes.

The dissipative characteristics of this system can be determined with the help of the density matrix.[3]

The authors are grateful to the Russian Fund for Fundamental Research (Grant 96-02-19753) and to the Department of Defense of the United States of America (through the University of Arizona) for financial support of this work.

[1] D. W. Pohl and D. Courjon, *Near-Field Optics*, Kluwer, Dordrecht (1992).
[2] J. M. Wylie and J. E. Sipe, Phys. Rev. A **30**, 1185 (1984); Phys. Rev. A **32**, 2030 (1985).
[3] S. Haroche, in *Fundamental Systems in Quantum Optics*, Elsevier, Amsterdam (1992), p. 771.
[4] V. V. Klimov, M. Ducloy, and V. S. Letokhov, submitted to J. Mod. Optics (1996).
[5] A. N. Oraevskiĭ, Usp. Fiz. Nauk **164**, 415 (1994).
[6] S. Dutta Gupta and Girish S. Agarwal, Opt. Commun. **115**, 597 (1995).
[7] V. V. Klimov, V. S. Letokhov, and M. Ducloy, submitted to J. Mod. Optics.
[8] J. D. Jackson, *Classical Electrodynamics*, Wiley, New York (1975).
[9] *Handbook of Special Functions*, M. Abramowitz and I. R. Stegun (eds.), Dover, New York (1965).
[10] L. A. Vaĭnshteĭn, *Electromagnetic Waves* [in Russian], Radio i Svyaz', Moscow (1988).
[11] E. Power and T. Thiunamachandran, Phys. Rev. A **25**, 2473 (1982).

Translated by Frank J. Crowne

Photon splitting in an ultrastrong magnetic field

V. N. Baĭer, A. I. Mil'shteĭn, and R. Zh. Shaĭsultanov

G. I. Budker Institute of Nuclear Physics, Siberian Branch of the Russian Academy of Sciences, 630090 Novosibirsk, Russia

(Submitted 20 June 1996)
Zh. Éksp. Teor. Fiz. **111**, 52–62 (January 1997)

We analyze the splitting of a photon with energy ω below the e^+e^- pair-production threshold in an ultrastrong magnetic field. We use the amplitudes found by employing the operator diagrammatic technique. In a field considerably above the critical values the process amplitudes become independent of the field strength. A study of the polarization operator of a photon in an external field of arbitrary strength in the energy range considered in the present investigation shows that there is only one set of polarizations of the initial and final photons for which the splitting amplitude is nonzero. © *1997 American Institute of Physics.* [S1063-7761(97)00401-0]

1. INTRODUCTION

The creation and annihilation of virtual electron–positron pairs induces nonlinear self-action of the electromagnetic field. The splitting of a photon in an external field is a process of nonlinear QED, and observing it is still a challenge for the experimenter.

Theoretical studies of photon splitting in an external field have a long history. In the early 1970s, the process of photon splitting in a uniform, constant magnetic field was studied in Refs. 1–4, where one can also find references to earlier work that proved erroneous. In Refs. 1 and 3 the process was examined as a possible mechanism for the production of linearly polarized photons in the strong magnetic fields of neutron stars. For low-energy photons ($\omega \ll m$, with m the electron mass; in what follows we use a system of units in which $c=\hbar=1$), the splitting process can be examined by introducing the effective Heisenberg–Euler Lagrangian (see, e.g., Ref. 5). In the limit of weak fields $H \ll H_0$ ($H_0=m^2/e=4.41\times 10^{13}$ Oe is the critical magnetic field, and e is the electron charge), the effective Lagrangian can be expanded in a power series, with only the first term in the expansion, which is represented by hexagonal diagrams, contributing to the amplitude of the process (see Refs. 1 and 2).

What is important here is the selection rules in photon polarizations, including those that emerge when one allows for the dispersion of photons in the magnetic field. These were examined by Adler *et al.*[1] (see also Ref. 5, Secs. 129 and 130), who gave a detailed study of the process with $\omega \ll m$ and $H \ll H_0$. A thorough analysis of the problem was done in Ref. 3, where a formula was derived for the photon splitting amplitude by using the complete expression for the effective Heisenberg–Euler Lagrangian. Naturally, the formula was valid for $\omega \ll m$, but the magnetic field strength can be arbitrary.

For astrophysical applications, one must know the amplitude in the general case of arbitrary photon energies and external magnetic field strengths. Such a calculation was also done in Ref. 3, where the amplitude of the transition allowed by selection rules was found for $\omega < 2m$. This is the energy range that is most interesting for applications.

At higher photon energies, electron–positron pair production by a photon in an external magnetic field becomes important, a process that effectively leads to photon absorption. The probability of this process in a strong enough field exceeds that of photon splitting by many orders of magnitude.

Adler[3] used the Green's function of an electron in an external magnetic field in Schwinger's proper-time representation. The expression for the amplitude obtained in this manner proved extremely cumbersome, which hinders further use. Nevertheless, numerical results were obtained for this amplitude at $\omega=m$ and $\omega \ll m$ over a broad range of magnetic field strengths $H \leqslant H_0$.

Papanyan and Ritus[4] also used the electron Green's function in the proper-time representation to study photon splitting in crossed fields $\mathbf{E}\perp\mathbf{H}$, $E=H$. Stoneham[6] used a different representation for the electron Green's function and obtained a different representation for the photon splitting amplitude.

Later, photon splitting in a uniform, constant electromagnetic field for arbitrary values of the two field invariants $\mathcal{F}$ and $\mathcal{G}$, with $\mathcal{F}=(\mathbf{E}\cdot\mathbf{H})$ and $\mathcal{G}=(\mathbf{E}^2-\mathbf{H}^2)/2$, was examined in Ref. 7. The paper employed the operator diagrammatic technique developed by Katkov, Strakhovenko, and one of the present authors (V.N.B.) in Ref. 8. As a result we were able to considerably simplify this intricate problem. The amplitudes obtained for the special case of zero electric (or magnetic) field have a form that is more compact than the one in Ref. 3. In the limiting cases where $\omega \ll m$ and/or $H \ll H_0$, the amplitudes found in Ref. 7 agree with those found in Refs. 1–3. While in Ref. 3 the numerical calculations were done for photon energies below the electron–position pair production threshold, in Ref. 7 the case $\omega \gg m$ was examined. We were interested in the possibility of observing photon splitting in strong electric fields of oriented single crystals at high energies.[9] All the research cited so far used Lorentz-covariant and gauge-invariant formulations of QED.

Lately the process of photon splitting has been once more investigated in Ref. 10. The motivation for this re-

search was the new discoveries in x-ray astronomy. The calculations of Mentzel *et al.*[10] were done within the framework of noncovariant perturbation theory and the Landau gauge. Their results strikingly contradict all those of previous research. Nevertheless, attempts have been made to use them in astrophysics.[11] The results of Refs. 10 and 11 have been severely criticized by Adler.[12]

Since the process may have important astrophysical applications (see, e.g., Ref. 13), we conducted numerical calculations and analyzed the photon splitting amplitude, basing our reasoning on the results of analytic calculations done in Ref. 7. Here we consider the most interesting energy range $\omega<2m$ and an arbitrary magnetic field strength H.

The results of the present work were briefly reported in Ref. 14. Two papers appeared after that publication, Refs. 15 and 16. Adler and Schubert[15] suggested another way of deriving the expression for the amplitude obtained in Ref. 3. They also pointed out that in the expressions for the amplitude given in Refs. 3, 6, and 14, which are similar integral representations, the integrands coincide numerically. Wilke and Wunner[16] acknowledged an error in Ref. 10, with the new results agreeing with those of Ref. 14.

2. POLARIZATION OPERATOR IN A MAGNETIC FIELD

Concerning the propagation of electromagnetic waves, we can say that a region of space occupied by a magnetic field can be interpreted as a medium with a refractive index that differs from unity. The value of the refractive index is crucial to the selection rules in the polarizations of the initial and final photons in the splitting process. For $\omega\ll m$ and $H\ll H_0$ this has been analyzed in Ref. 1 (see also Ref. 5). Here we are interested in the selection rules for an arbitrary value of the magnetic field and a photon energy $\omega<2m$. The refractive index is found from the photon polarization operator. The contribution to the polarization operator $\Pi_{\mu\nu}(k)$ of the electron loop in an external uniform, constant electromagnetic field was found in Refs. 3, 8 and 17.

We consider the case where $\mathbf{E}=0$ and $k^2=0$. The polarization operator $\Pi_{\mu\nu}(k)$ has four mutually orthogonal eigenvectors b_i^ν defined by the equation

$$\Pi_{\mu\nu}(k)b_i^\nu=\kappa_i b_{i\mu}, \quad i=1,\ 2,\ 3,\ 4. \tag{2.1}$$

The eigenvalues κ_i act as the square of the mass of a photon in the field in the corresponding mode. The solution of this equation in the special case considered here is[8]

$$b_1^\mu=b_4^\mu=k^\mu, \quad b_2^\mu=(Bk)^\mu, \quad b_3^\mu(Ck)^\mu, \tag{2.2}$$

with the tensors B and C introduced in Ref. 18 (see Eqs. (A2), (A3), and (A8) in Ref. 18). At $\mathbf{E}=0$ we have

$$C_{\mu\nu}=\frac{F^*_{\mu\nu}}{H}, \quad B_{\mu\nu}=\frac{F_{\mu\nu}}{H}, \tag{2.3}$$

where $F_{\mu\nu}$ is the electromagnetic field-strength tensor, $F^*_{\mu\nu}$ is the dual field-strength tensor, and H is the magnetic field strength.

The eigenvalues κ_i have the form (see Ref. 8)

$$\begin{aligned}
&\kappa_1=\kappa_4=0, \quad \kappa_{2,3}=-\frac{\alpha}{4\pi}\,\omega^2\sigma^2 R_{2,3},\\
&R_{2,3}=\int_{-1}^{1}dv\int_0^\infty \frac{dx}{\sinh x}\,a_{2,3}\exp(-\psi),
\end{aligned} \tag{2.4}$$

where $\alpha=e^2=1/137$, $\sigma^2=k_\perp^2/\omega^2=\sin^2\vartheta$, with ϑ the angle between the direction of the magnetic field and that of the photon's wave vector $\mathbf{k}$,

$$\begin{aligned}
&a_1=\cosh(xv)-v\ \coth x\ \sinh(xv),\\
&a_2=-2\,\frac{\cosh x-\cosh(xv)}{\sinh^2 x}+a_1,\\
&a_3=(1-v^2)\cosh x-a_1,\\
&\psi=\frac{H_0}{H}\left[2r\,\frac{\cosh x-\cosh(xv)}{\sinh x}+x(1-r(1-v^2))\right],
\end{aligned} \tag{2.5}$$

and $r=\omega^2\sigma^2/4m^2$. In (2.4) and (2.5) we allowed for the fact that below the electron–positron pair-production threshold ($r<1$), the contour of integration with respect to x in the integrals determining the functions R_2 and R_3 in Ref. 8 can be rotated: $x\to -ix$. As a result the resulting representations for R_2 and R_3 are real, which is convenient for numerical calculations, since the integrands contain no oscillating functions. Note that these functions depend only on $k_\perp=\omega\sigma$.

The photon splitting amplitude is nonzero only if $\sigma\neq 0$ ($k_\perp\neq 0$). In view of gauge invariance, the modes 1 and 4 contribute nothing to the amplitude. For mode 2 the zeroth component b_2^0 is zero, and the vector $\mathbf{b}_2/\omega=\mathbf{e}_2$ is perpendicular to the plane containing the vectors $\mathbf{H}$ and $\mathbf{k}$. For mode 3 the zeroth component b_3^0 is nonzero, and $\mathbf{b}_3\|\mathbf{H}$. In calculating the photon splitting amplitude, one can employ the gauge-invariance property, and subtract from the vector b_3^μ a vector proportional to k^μ so that the zeroth component of the vector difference vanishes. After this, the spatial component of the resulting vector lies in the above-mentioned plane and is perpendicular to $\mathbf{k}$. As noted earlier, the region occupied by a magnetic field can be considered a medium whose refractive index is a function of κ_i. For modes 2 and 3 we have

$$n_{2,3}^2=1-\frac{\kappa_{2,3}}{\omega^2}=1+\frac{\alpha}{4\pi}\,\sigma^2 R_{2,3}. \tag{2.6}$$

Let us analyze the behavior of the functions R_2 and R_3 in the limiting cases. When $H\ll H_0$, the main contribution to the integrals determining these functions is provided by the region $x\ll 1$. Expanding the hyperbolic functions in power series and calculating the integrals, we obtain

$$n_2=1+\frac{2\alpha}{45\pi}\left(\frac{H}{H_0}\right)^2\sigma^2, \quad n_3=1+\frac{7\alpha}{90\pi}\left(\frac{H}{H_0}\right)^2\sigma^2. \tag{2.7}$$

When $k_\perp\ll m(r\ll 1)$, the exponent ψ in the exponential function in (2.4) tends to H_0x/H, the integrals with respect to v can easily be evaluated, and we get

$$\begin{aligned}
R_2=2\int_0^\infty &\frac{dx}{x^2\sinh^3 x}\exp\left(-\frac{x}{b}\right)\\
&\times[\cosh x(\sinh^2 x-2x^2)+x\ \sinh x],
\end{aligned}$$

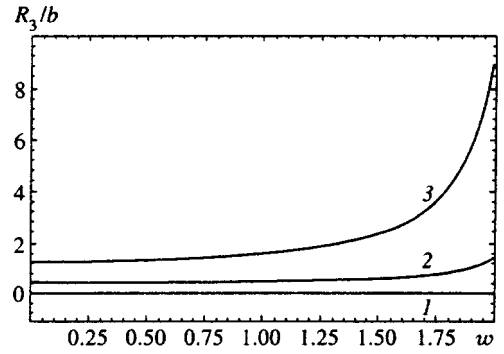

FIG. 1. R_3/b vs $w=\omega\sigma/m$ for different values of the parameter $b=H/H_0$: 0.1 (curve *1*), 1 (curve *2*), and 30 (curve *3*).

$$R_3=\int_0^\infty \frac{dx}{3x^2\sinh^2 x}\exp\left(-\frac{x}{b}\right)\times[\sinh 2x(2x^2-3)+6x], \tag{2.8}$$

where $b=H/H_0$. Plugging (2.8) into (2.6) yields formulas for the refractive indices coinciding with those that follow from the effective Heisenberg–Euler Lagrangian, which can be used at low frequencies and arbitrary external fields.

In the two limiting cases the integrals in (2.8) can be evaluated exactly:

$$b\ll 1:\ R_2=\frac{16b^2}{45},\quad R_3=\frac{28b^2}{45},$$
$$b\gg 1:\ R_2=\frac{4}{3},\quad R_3=\frac{4b}{3}. \tag{2.9}$$

The asymptotic behavior of R_2 and R_3 in the limit $b\ll 1$ has been thoroughly discussed (see Refs. 3 and 5), and it agrees with (2.7). We see that while for $b\ll 1$, the functions R_2 and R_3 differ only by a numerical factor, but $b\gg 1$ the situation is different: R_2 is field-independent, but R_3 increases linearly with field strength. Our results are valid when $n_{2,3}-1\ll 1$, which is equivalent to

$$\frac{\alpha}{3\pi}\frac{H}{H_0}\ll 1.$$

For arbitrary values of the parameters $b=H/H_0$ and r, the functions R_2 and R_3 were calculated numerically. Figure 1 illustrates the dependence of R_3/b on $w=k_\perp/m$ for different values of the parameter b. Clearly, near the pair-production threshold this function rapidly increases at high field strengths. For $w<0.5$ and any value of b, the function R_3/b is essentially independent of w, and its values for different b's coincide with those obtained by using the effective Heisenberg–Euler Lagrangian.

As for R_2, its dependence on w is extremely weak. This is especially evident if one looks at Figure 2, which depicts the dependence of R_2 on b for values $w=0.1$ and $w=1.9$. At intermediate values of the parameter w, the curves lie in the region between the two curves in Fig. 2. Figure 3 depicts R_2 and R_3 as functions of b for different values of w, with R_2 taken at $w=1.9$. Clearly, $R_3>R_2$ for all values of w, i.e., $n_3>n_2$.

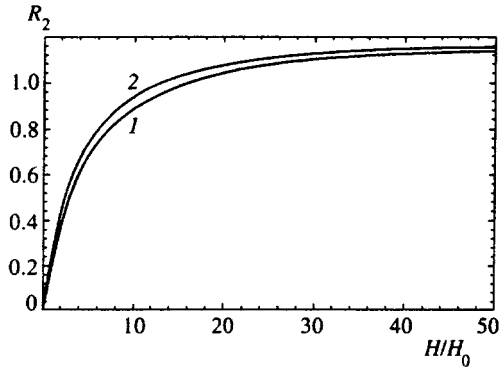

FIG. 2. R_2 vs. $b=H/H_0$ for different values of $w=\omega\sigma/m$: 0.1 (curve *1*) and 1.9 (curve *2*).

3. PHOTON SPLITTING IN A MAGNETIC FIELD

Now let us examine the splitting of a photon with energy ω into two photons with energies ω_1 and ω_2. In the collinear approximation (see, e.g., Ref. 5), the photon splitting rate (probability per unit time) below the pair-production threshold is expressed in terms of the splitting amplitude as follows:

$$dW=\frac{1}{32\pi}|T|^2\frac{d\omega_1}{\omega^2}\,\theta(\omega_1 n_{(1)}^2+\omega_2\omega_{(2)}^2-\omega n^2), \tag{3.1}$$

where $n_{(1)}$, $n_{(2)}$, and n are the polarization-dependent refractive indices for the energies ω_1, ω_2, and ω. The θ-function in (3.1) is a reflection of CP-invariance and the selection rules in photon polarizations (see Ref. 3). Below, as in Ref. 7, we denoted mode 2 by B and mode 3 by C.

The CP-allowed transitions are $B\to CC$, $C\to BC$, and $B\to BB$. The formulas and figures of Sec. 2 imply that for a magnetic field of arbitrary strength, the refractive index of B is smaller than the refractive index of C at any frequency ratio. From this, it follows that for all the CP-allowed transitions the argument of the θ-function is positive only for the $B\to CC$ transition. This rule was obtained in Ref. 1 for fields $H\ll H_0$ and photon energies $\omega\ll m$.

The amplitude T of photon splitting in a magnetic field for the allowed transition can be found from the general ex-

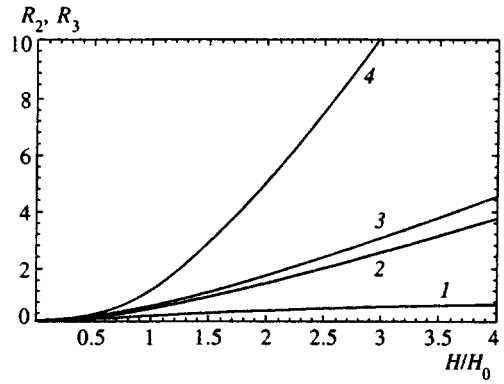

FIG. 3. R_2 vs. $b=H/H_0$ at $w=1.9$ (curve *1*), and R_3 vs. $b=H/H_0$ at $w=0.1$ (curve *2*), $w=1$ (curve *3*), and $w=1.9$ (curve *4*).

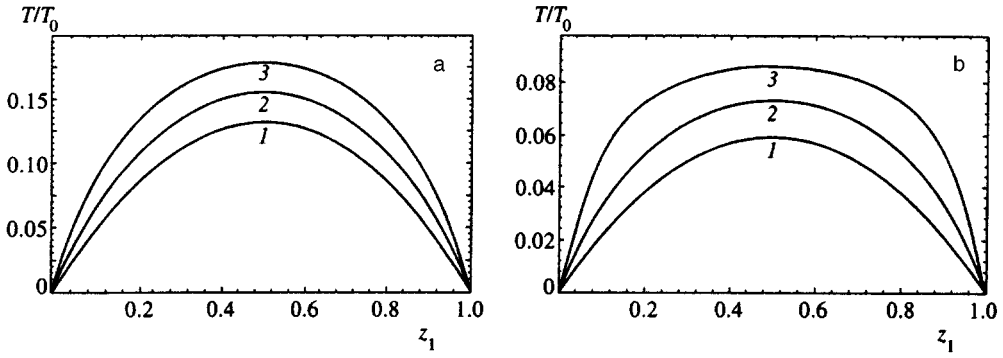

FIG. 4. The photon splitting amplitude as a function of the energy of one of the final photons ($z_1=\omega_1/\omega$) at $H=\mathrm{H}_0/2$ (a) and $H=H_0$ (b) for different initial-photon energies: $\omega/m=0.1$ (curve *1*), $\omega/m=1.5$ (curve *2*), and $\omega/m=1.9$ (curve 3). The amplitude T is normalized to the amplitude T_0 given by (3.4).

pression (Eqs. (2.16)–(2.18)in Ref.7) by substituting $E=0$:

$$T=\frac{(4\pi\alpha)^{3/2}\omega\sigma}{2\pi^2}\int_0^\infty dx\,\frac{\exp(-H_0x/H)}{x\,\sinh^2 x}\int_0^x dt_2 \times\left[\int_0^{t_2}dt_1 G\,\exp(c\Phi)+\sinh^2 t_2\,\exp(c\Phi_0)\right], \quad (3.2)$$

where

$$c=\frac{H_0}{H}\left(\frac{\omega\sigma}{m}\right)^2,$$

$$\Phi_0=\frac{t_2(x-t_2)}{x}-\frac{\cosh x-\cosh(2t_2-x)}{2\sinh x},$$

$$\Phi=\frac{z_1z_2(t_1-t_2)(t_1-t_2+x)-z_1t_1(t_1-x)-z_2t_2(t_2-x)}{x} -\frac{(1-z_1z_2)\cosh x-z_1\cosh(2t_1-x)-z_2\cosh(2t_2-x)+z_1z_2\cosh(x+2t_1-2t_2)}{2\sinh x},$$

$$G=\frac{1-[z_1\cosh(2t_1-x)+z_2\cosh(2t_2-x)]\cosh x}{x}+2cz_1z_2\sinh^2(t_2-t_1)[z_1\sinh^2 t_1+z_2\sinh^2(t_2-x)]. \quad (3.3)$$

Here $z_{1,2}=\omega_{1,2}/\omega$, and σ was introduced in (2.4). To obtain (3.2) we rotated the contour of integration with respect to each variable: $x\to -ix$ and $t_{1,2}\to -it_{1,2}$. This transformation is applicable if $\omega<2m$. As a result, the integrand in (3.2) contains no oscillating trigonometric functions, which proves convenient in numerical calculations.

Let us discuss the properties of T. Clearly, the amplitude T is symmetric under interchange of the final photons ($\omega_1\leftrightarrow\omega_2$). To prove this we must introduce new variables, $t_1=x-\tau_2$ and $t_2=x-\tau_1$, and interchange the order of integration with respect to τ_1 and τ_2. In view of gauge invariance, as $\omega\to 0$ the amplitude $T\propto\omega\omega_1\omega_2$, and also $T\to 0$ as $\omega_1\to 0$ for all values of ω. This means that there is very strong cancellation in (3.2), a fact that must be taken into account in numerical integration. The calculations simplify if subtractions are performed in the integrand in (3.2): $\exp(c\Phi)\to\exp(c\Phi)-1$ for the first term in G (proportional to $1/x$), and $\exp(c\Phi_0)\to\exp(c\Phi_0)-1$. Direct calculations show that the sum of the subtracted terms is zero.

For $\omega\ll m$, the main contribution to the amplitude is provided by the range of variables where $c\Phi\ll 1$ and $c\Phi_0\ll 1$. By expanding the corresponding exponentials in power series and retaining the terms linear in c, we can evaluate the integrals with respect to t_1 and t_2. The result coincides with the photon splitting amplitude found by using the effective Heisenberg–Euler Lagrangian (Eq. (22) in Ref. 3. At $\omega\sim m$, the integration in (3.2) was done numerically. Since the energy ω and the parameter σ enter into T only as the combination $\omega\sigma$, we can set $\sigma=1$ without loss of generality.

Figure 4 depicts the dependence of T/T_0 on the final-photon energy at $H=H_0/2$ (Fig. 4a) and $H=H_0$ (Fig. 4b) for different initial-photon energies, where

$$T_0=\frac{13}{315}\,\frac{(4\pi\alpha)^{3/2}}{\pi^2}\,\frac{\omega^3}{m^2}\left(\frac{H}{H_0}\right)^3. \quad (3.4)$$

At $\omega/m=0.1$ the result agrees, to extremely high accuracy (better than one part in a thousand), with that obtained by using the effective Heisenberg–Euler Lagrangian.

Figure 5 depicts the total probability of the allowed transition W, expressed in units of W_0, as a function of $w=\omega/m$. Here

$$W_0=\frac{T_0^2}{960\pi\omega}=0.116\left(\frac{\omega}{m}\right)^5\left(\frac{H}{H_0}\right)^6\mathrm{cm}^{-1}. \quad (3.5)$$

Curve *1* corresponds to $H/H_0=1$, and curve *2* to $H/H_0=1/2$. Although the probability changes by many orders of magni-

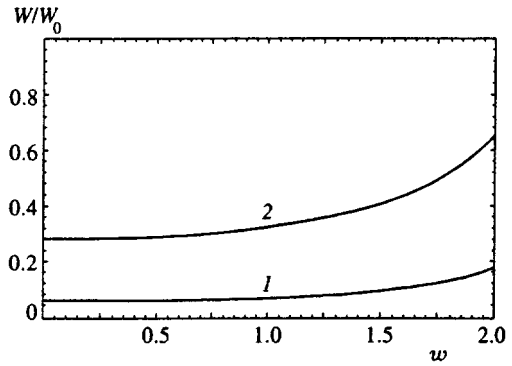

FIG. 5. The total photon-splitting probability W (expressed in terms of the probability W_0 given by (3.5)) as a function of the photon energy ($w=\omega/m$) at $H=H_0$ (curve *1*) and $H=H_0/2$ (curve *2*).

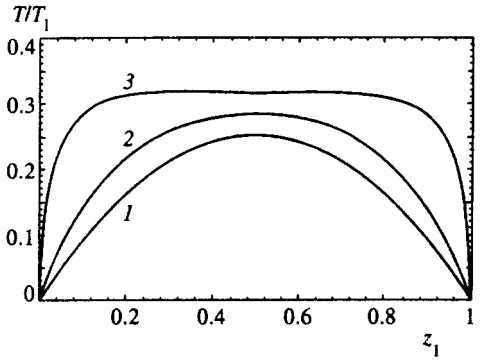

FIG. 7. The amplitude T as function of the final-photon energy for $H\gg H_0$ at different initial-photon energies: $\omega/m=0.1$ (curve *1*), $\omega/m=1.5$ (curve *2*), and $\omega/m=1.99$ (curve *3*).

tude within the parameter range considered here, the main part of its variation is related to W_0, which is simply the contribution of hexagonal diagrams to the photon splitting probability for $\omega\ll m$. Consequently, Fig. 5 demonstrates the difference between the probability calculated exactly in the parameters ω/m and H/H_0 and the probability calculated to lowest order in these parameters. The probability W_{HE}, obtained by using the effective Heisenberg–Euler Lagrangian, is also proportional to $(\omega/m)^5$. Hence the points of intersection of the curves and the vertical axis yield the probability W_{HE}.

Figure 5 shows that at $H\sim H_0$ the probabilities W and W_{HE} are much lower than W_0. At the same time, W/W_{HE} increases appreciably as $\omega\to 2m$. Hence we must take into account the exact dependence on the photon energy. Our numerical results agree (to within several percent) with those of Adler,[3] where the numerical values were given for $\omega=m$.

Figure 6 depicts the total probability of the allowed transition W, expressed in units of W_1, as a function of the magnetic field strength (in units of H_0) for different initial-photon energies. Here

$$W_1=W_0\left(\frac{H_0}{H}\right)^6=0.116\left(\frac{\omega}{m}\right)^5\ \mathrm{cm}^{-1}. \tag{3.6}$$

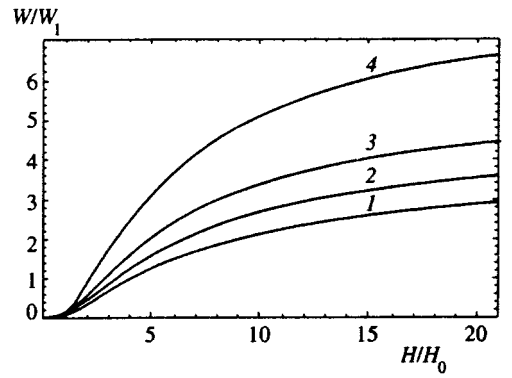

FIG. 6. The total photon-splitting probability W (expressed in terms of the probability W_1 given by (3.6)) as a function of the magnetic field strength (expressed in units of H_0) at different initial-photon energies: $w=\omega/m=0.1$ (curve *1*; this curve coincides, to high accuracy, with the probability found by using the effective Heisenberg–Euler Lagrangian), $w=1.1$ (curve *2*), $w=1.5$ (curve *3*), and $w=1.9$ (curve *4*).

Figure 6 shows that in strong fields the growth in probability slows down considerably. In view of this, the study of the behavior of the amplitude T in very strong magnetic fields $H\gg H_0$ is interesting from the theoretical angle.

When $H\gg H_0$, the main contribution to the double integral in (3.2) is provided by the regions where $x\sim H/H_0$ and $x-t_2\sim 1$. In the triple integral in (3.2) there are two regions that provide the main contribution: $x\sim H/H_0$, $t_1\sim H/H_0$, and $x-t_2\sim 1$; and $x\sim H/H_0$, $t_1\sim 1$, and $t_2\sim H/H_0$. After appropriate expansions the integrals can be evaluated, with the result that

$$T(H\gg H_0)=T_1\,\frac{24m^4}{\omega^3}\left[\frac{\omega_1}{\omega_2\sqrt{4m^2-\omega_2^2}}\arctan\left(\frac{\omega_2}{\sqrt{4m^2-\omega_2^2}}\right)+\frac{\omega_2}{\omega_1\sqrt{4m^2-\omega_1^2}}\arctan\left(\frac{\omega_1}{\sqrt{4m^2-\omega_1^2}}\right)-\frac{\omega}{4m^2}\right], \tag{3.7}$$

where

$$T_1=\frac{(4\pi\alpha)^{3/2}}{12\pi^2}\,\frac{\omega^3}{m^2}. \tag{3.8}$$

We see that for $H\gg H_0$, the amplitude T is independent of the magnetic field strength. The amplitude calculated by using the effective Heisenberg–Euler Lagrangian for $H\gg H_0$ is

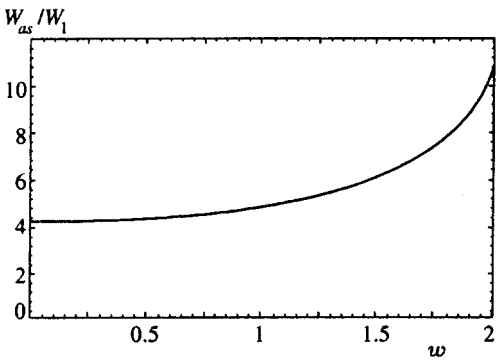

FIG. 8. $W_{as}\equiv W(H\gg H_0)$ vs. the initial-photon energy ($w=\omega/m$).

$$T_{HE}=T_1\,\frac{\omega_1\omega_2}{\omega^2}.$$

The dependence of T on the final-photon energy ($z_1=\omega_1/\omega$) in this limit is shown in Fig. 7 for different initial-photon energies. When the field is strong and $\omega\to 2m$, both Fig. 4 and Fig. 7 display a plateau at the center of the distribution. The probability $W_{as}\equiv W(H\gg H_0)$ is depicted in Fig. 8.

Note that at $\omega=2m$ the amplitude and probability of the process are finite for all magnetic field strengths.

Thus, we have calculated the photon splitting amplitude by using the exact formula applicable for an arbitrary magnetic field strength H and $\omega<2m$. The diagrams demonstrate a dependence of the amplitude and probability on the magnetic field strength and photon energy in their range. For $\omega\ll m$ our results agree with the amplitude obtained by using the effective Heisenberg–Euler Lagrangian. We found that in an ultrastrong field $H\gg H_0$ the amplitude is independent of the magnetic field strength. Since there is only one allowed transition $B\to CC$, a photon cascade develops only if the magnetic field changes sign (over distances much larger than the length at which the splitting process develops).

[1] S. L. Adler, J. N. Bahcall, C. G. Callan, and M. N. Rosenbluth, Phys. Rev. Lett. **25**, 1061 (1970).

[2] Z. Bialynicka-Birula and I. Bialynicka-Birula, Phys. Rev. D **10**, 2341 (1970).

[3] S. L. Adler, Ann. Phys. (N.Y.) **67**, 599 (1971).

[4] V. O. Papanyan and V. I. Ritus, Zh. Éksp. Teor. Fiz. **61**, 2231 (1971) [Sov. Phys. JETP **34**, 1195 (1972)]; **65**, 1756 (1973) [Sov. Phys. JETP **38**, 879 (1974)].

[5] V. B. Berestetskiĭ, E. M. Lifshitz, and L. P. Pitaevskiĭ, *Quantum Electrodynamics*, 3rd ed., Pergamon Press, Oxford (1991).

[6] R. J. Stoneham, J. Phys. A **12**, 2187 (1979).

[7] B. N. Baĭer, A. I. Mil'shteĭn, and R. Zh. Shaĭsultanov, Zh. Éksp. Teor. Fiz. **90**, 1141 (1986) [Sov. Phys. JETP **63**, 665 (1986)].

[8] B. N. Baĭer, V. M. Katkov, and V. M. Strakhovenko, Zh. Éksp. Teor. Fiz. **68**, 405 (1975) [Sov. Phys. JETP **41**, 198 (1975)].

[9] B. N. Baier, A. I. Milstein, and R. Zh. Shaisultanov, Phys. Lett. A **120**, 255 (1987).

[10] M. Mentzel, D. Berg, and G. Wunner, Phys. Rev. D **50**, 1125 (1994).

[11] G. Wunner, R. Sang, and D. Berg, Astrophys. J. **455**, L51 (1995).

[12] S. L. Adler, submitted to Astrophys. J.

[13] M. G. Baring and A. K. Harding, in *High Velocity Neutron Stars and Gamma-Ray Bursts* (Proc. of La Jolla Workshop), AIP, New York (1995).

[14] V. N. Baier, A. I. Milstein, and R. Zh. Shaisultanov, HETP-TH 9604 028, Preprint BINP 96-18. Novosibirsk (April 1996).

[15] S. L. Adler and C. Schubert, HEP-TH 9605 035, Preprint IASSNS-HEP-96/37 (1996).

[16] C. Wilke and G. Wunner, HEP-TH 960 556.

[17] I. A. Batalin and A. E. Shabad, Zh. Éksp. Teor. Fiz. **60**, 894 (1971) [Sov. Phys. JETP **33**, 483 (1971)].

[18] V. N. Baier, V. M. Katkov, and V. M. Strakhovenko, Zh. Éksp. Teor. Fiz. **67**, 453 (1974) [Sov. Phys. JETP **40**, 225 (1975)].

Translated by Eugene Yankovsky

Magnetization of optically polarized gas atoms by an optical pulse train

A. I. Alekseev

Moscow State Engineering Physics Institute, 115409 Moscow, Russia
(Submitted 20 June 1996)
Zh. Éksp. Teor. Fiz. **111**, 63–92 (January 1997)

The properties of the density matrix and the multipole moments arising in oriented and aligned atoms with zero nuclear spin through the interaction with strong resonant ultrashort pulses with wave vector $\mathbf{k}_0$ and circular or linear polarization have been found. Calculations have been made for the time-dependent light-induced magnetization $\boldsymbol{\mu}(t')$ of a gas of pre-oriented and prealigned atoms following the passage of a weak resonant elliptically polarized pulse with frequency ω and wave vector $\mathbf{k}$ collinear with $\mathbf{k}_0$. It is shown that for oriented atoms, $\boldsymbol{\mu}(t')$ is an even function of the detuning from resonance, $\omega-\omega_{ba}$, and can be split into two terms whose directions are a consequence of symmetry and are determined by the vectors $\mathbf{k}_0$ and $\mathbf{k}$ as well as by the direction of rotation of the electric fields corresponding to the pulses. For aligned atoms the vector $\boldsymbol{\mu}(t')$ is collinear with $\mathbf{k}$, and the first term is an even function of $\omega-\omega_{ba}$. However, the second term is an odd function of $\omega-\omega_{ba}$ and reverses direction when the sign of $\omega-\omega_{ba}$ changes, as well as when the orientation of the axes of the polarization ellipse is changed. It is shown that if a series of weak linearly polarized pulses pass through the gas, the light-induced magnetization of the oriented and aligned gas atoms can be decomposed into three factors: the first determines the direction and is a consequence of the symmetry; the second (with the dimensions of magnetic moment) depends on the characteristics of the resonant transitions; and the third is a universal function of t' and $\omega-\omega_{ba}$ that does not depend on the underlying characteristics of the resonant transition. These vector factors and the universal functions are in principle different for oriented and aligned atoms.
 [S1063-7761(97)00501-5]

1. INTRODUCTION

The experiments of Badalyan *et al.*[1,2] demonstrated the light-induced magnetization of potassium and rubidium vapor atoms resulting from the sequential passage of linearly polarized pulses in the presence of a static magnetic field $\mathbf{H}$ and in zero field ($\mathbf{H}=0$). If we bear in mind that for $\mathbf{H}=0$ the magnetization of an isotropic atomic gas by the passage of a single linearly polarized pulse of light violates symmetry (see, e.g., Ref. 3), we see that the magnetization of rubidium and potassium gas in Refs. 1 and 2 by the sequential passage of linearly polarized pulses for $\mathbf{H}=0$ is an extraordinary phenomenon.

The magnetization of an isotropic atomic gas by a circularly polarized pulse with wave vector $\mathbf{k}_0$ and polarization vector $\mathbf{l}_{\mathbf{k}_0 s}$ (where $s=\pm 1$) for $\mathbf{H}=0$ is consistent with symmetry, since in this case there exists a real pseudovector $i[\mathbf{l}_{k_0 s}\mathbf{l}^*_{\mathbf{k}_0 s}]$, which determines the direction of the induced magnetic moment $\boldsymbol{\mu}_{at}$ of the atom.

In this connection a fundamental question arises: what should the direction of the pseudovector $\boldsymbol{\mu}_{at}$ be if it is induced by a train of linearly polarized pulses with $\mathbf{H}=0$? In Ref. 4 the conditions were determined for an atom in a static magnetic field for which a linearly polarized pulse induces a magnetic moment $\boldsymbol{\mu}_{at}$ collinear with $\mathbf{H}$. The magnetization of an atomic gas by a sequence of linearly polarized light pulses with $\mathbf{H}=0$ observed in the experiments of Refs. 1 and 2 is in need of theoretical explanation.

In this paper we study theoretically the magnetization of a gas of atoms with zero nuclear spin by the passage of a series of pulses resonant with the transition frequency $\omega_{ba}=(E_b-E_a)\hbar^{-1}$, where E_a and E_b are the energies of the ground and the excited states of the atom. In order to examine the problem of the magnetization of the atoms by linearly polarized pulses, we must first solve the problem of the optical polarization of the atoms by the passage of a strong ultrashort pulse with frequency ω_0, wave vector $\mathbf{k}_0$, and duration τ_0 under conditions where atomic collisions can be neglected and the relaxation is determined only by the spontaneous emission probability γ of atoms in the excited state (energy E_b) for $\tau_0<t$. For long times, $\gamma^{-1}\ll t$, after the passage of an intense short circularly polarized pulse with polarization vector $\mathbf{l}_{\mathbf{k}_0 s}$ ($s=\pm 1$), oriented atoms are produced in the gas in the steady state, and in the case of a strong linearly polarized pulse with polarization vector $\mathbf{l}_0$, aligned atoms are produced. If then a weak elliptically polarized pulse with wave vector $\mathbf{k}$ collinear with $\mathbf{k}_0$ and with frequency ω and polarization vector $\mathbf{l}_{\mathbf{k}\lambda}$ ($\lambda=\pm 1$) passes through the gas, then because of symmetry the induced time-dependent magnetic moment will have the form

$$\boldsymbol{\mu}^{(0)}_{at}(t')=i[\mathbf{l}_{\mathbf{k}\lambda}\mathbf{l}^*_{\mathbf{k}\lambda}]C^{(0)}(t')+i[\mathbf{l}_{\mathbf{k}_0 s}\mathbf{l}^*_{\mathbf{k}_0 s}]D^{(0)}(t')$$

for a pre-oriented atom and

$$\boldsymbol{\mu}^{(2)}_{at}(t')=i[\mathbf{l}_{\mathbf{k}\lambda}\mathbf{l}^*_{\mathbf{k}\lambda}]C^{(2)}(t')+(\mathbf{k}/k)\mathbf{l}^2_{\mathbf{k}\lambda}\,\sin(2\varphi_{\mathbf{k}})D^{(2)}(t')$$

for a prealigned atom, where the angle $\varphi_{\mathbf{k}}$ ($\varphi_{-\mathbf{k}}=-\varphi_{\mathbf{k}}$), defines the orientation of the axes of the polarization ellipse relative to the vector $\mathbf{l}_0$. The quantities $C^{(q)}(t')$ and $D^{(q)}(t')$ with $q=0, 2$ depend on the time t' with retardation

taken into account, and also depend on the detuning from resonance, $\omega-\omega_{ba}$, the characteristics of the atom, and its velocity $\mathbf{v}$. These formulas imply the fundamental statement that the light pulse magnetizes pre-oriented and prealigned atoms differently.

Analysis of the magnetization of an atom by a strong pulse with fixed frequency ω_0 and a subsequent weak pulse with arbitrary frequency ω and elliptical polarization serves as the basis of solving the more complex problem of the magnetization of an atom by means of a series of weak pulses with parallel wave vectors and identical polarization and amplitude, but different frequencies ω near the transition frequency ω_{ba}.

The results for $\boldsymbol{\mu}_{at}^{(0)}(t')$ and $\boldsymbol{\mu}_{at}^{(2)}(t')$ make it possible to allow for the Maxwellian distribution $f(v)$ of atomic velocity $\mathbf{v}$ in the calculation of the magnetic moment per unit volume of the gas, which is the light-induced magnetization $\boldsymbol{\mu}(t')$. For each successive passage of a weak linearly polarized pulse with wave vector $\mathbf{k}$, the light-induced magnetization at a given point in the gas can be described by the same formula, in which the initial time $t'=0$ is taken to be the time of arrival of this particular pulse; that is,

$$\boldsymbol{\mu}_q(t')=-\mathbf{L}_q[V_qX_{aq}(t',\omega-\omega_{ba})+W_qX_{bq}(t',\omega-\omega_{ba})\times\exp(-\gamma t')],\quad q=0,\ 2,$$

where

$$\mathbf{L}_0=(\mathbf{k}_0/k_0)s\beta,\quad \mathbf{L}_2=(\mathbf{k}/k)\sin(2\varphi_{\mathbf{k}}).$$

Here the quantities with the subscript $q=0$ and $q=2$ refer, respectively, to pre-oriented atoms, with $1\leqslant 2J_a$, and prealigned atoms, with $1\leqslant J_a$, with angular momentum J_a in the ground state, and β is the unit pseudoscalar. The quantities $X_{aq}(t',\omega-\omega_{ba})$ and $X_{bq}(t',\omega-\omega_{ba})$ are universal functions that are even in $\omega-\omega_{ba}$ for $q=0$ and odd in $\omega-\omega_{ba}$ for $q=2$. They depend on γ and the amplitude of the weak pulse in relative units, and on the atomic mass m_{at} and the temperature T of the gas, which enters by way of the most probable velocity of the Maxwellian distribution $f(v)$. The angular momenta J_a and J_b, the g-factors g_a and g_b, the reduced dipole moment d_{ba}, and the atom number density N are subsumed by the constants V_q and W_q, which have dimensions of magnetic moment, and determine the order of magnitude of $\mu_q(t')$. The vectors $\mathbf{L}_0$ and $\mathbf{L}_2$ yield the direction of the light-induced magnetization in the case of successive linearly polarized pulse trains with $\mathbf{H}=0$.

The fundamental properties found for the light-induced magnetization are a consequence of symmetry. They can be observed experimentally by making relative measurements of the light-induced magnetization. The most important characteristics of the resonant transition, such as J_a, J_b, g_a, g_b, and d_{ba} will not have any effect on these measurements, which is an attractive feature for experimental investigations of light-induced magnetization.

2. OPTICAL POLARIZATION OF AN ATOM IN THE PASSAGE OF A STRONG CIRCULARLY POLARIZED PULSE

Let us assume that a circularly polarized pulse of arbitrary intensity and a rotating electric field vector

$$\mathbf{E}_0=\mathbf{l}_{\mathbf{k}_0s}R_0(t-t_0')\exp[i(\mathbf{k}_0\cdot\mathbf{r}-\omega_0t-\alpha_0)]+\text{c.c.},\qquad(1)$$

propagates through a gas of identical atoms, where

$$s=\pm1,\quad t_0'=t_0+\mathbf{k}_0\cdot(\mathbf{r}-\mathbf{r}_0)/\omega_0,$$

and $\mathbf{l}_{\mathbf{k}_0s}$ is the unit complex polarization vector, orthogonal to the wave vector $\mathbf{k}_0$. The real amplitude $R_0(t-t_0)$ is a function that varies slowly compared to $\exp[i(\mathbf{kr}-\omega_0t)]$. The frequency ω_0 is close to the transition frequency $\omega_{ba}=(E_b-E_a)\hbar^{-1}$, and the phase shift α_0 is a constant. The energy levels E_a and E_b belong to the ground state and the excited state of the atom, respectively. The leading edge of the circularly polarized pulse passes through the boundary point $\mathbf{r}_0$ of the volume of gas at time t_0 and arrives at an arbitrary point $\mathbf{r}$ inside this volume at time t with allowance for retardation $\mathbf{k}(\mathbf{r}-\mathbf{r}_0)/\omega_0$. The vector $\mathbf{l}_{\mathbf{k}_0s}$, regardless of the choice of right-handed or left-handed coordinates, can be written as

$$\mathbf{l}_{\mathbf{k}_0s}=2^{-1/2}(s\mathbf{l}_{\mathbf{k}_0}^{(1)}+i\mathbf{l}_{\mathbf{k}_0}^{(2)}),\qquad(2)$$

where for right-handed and left-handed circular polarization we have, $s=1$ and $s=-1$, respectively. The unit vectors $\mathbf{l}_{\mathbf{k}_0}^{(1)}$ and $\mathbf{l}_{\mathbf{k}_0}^{(2)}$ on the right-hand side of Eq. (2) satisfy the necessary conditions

$$\mathbf{k}_0\cdot\mathbf{l}_{\mathbf{k}_0}^{(1)}=\mathbf{k}_0\cdot\mathbf{l}_{\mathbf{k}_0}^{(2)}=\mathbf{l}_{\mathbf{k}_0}^{(1)}\cdot\mathbf{l}_{\mathbf{k}_0}^{(2)}=0,\quad \mathbf{l}_{-\mathbf{k}_0}^{(1)}=\mathbf{l}_{\mathbf{k}_0}^{(1)},$$

$$\mathbf{l}_{-\mathbf{k}_0}^{(2)}=-\mathbf{l}_{\mathbf{k}_0}^{(2)},\quad [\mathbf{l}_{\mathbf{k}_0}^{(1)}\mathbf{l}_{\mathbf{k}_0}^{(2)}]=\mathbf{k}_0/k_0.$$

With the replacement $\mathbf{k}_0\rightarrow-\mathbf{k}_0$ the vector Eq. (2) can be transformed,

$$\mathbf{l}_{\mathbf{k}_0s}\rightarrow-\mathbf{l}_{\mathbf{k}_0,-s},\qquad(3)$$

because of the properties of the unit vectors $\mathbf{l}_{\mathbf{k}_0}^{(1)}$ and $\mathbf{l}_{\mathbf{k}_0}^{(2)}$. We shall also consider inversion, $x\rightarrow-x$, $y\rightarrow-y$, and $z\rightarrow-z$, which transforms the vector (2) differently:

$$\mathbf{l}_{\mathbf{k}_0s}\rightarrow\mathbf{l}_{\mathbf{k}_0,-s}.\qquad(4)$$

The states of the atom are characterized not only by the energies E_a and E_b, but also by the quantum numbers J_a and J_b, the angular momenta $\mathbf{J}_a$ and $\mathbf{J}_b$, and the projections M_a and M_b of these angular momenta on the axis of quantization. Therefore the interaction of an individual gas atom with the field, Eq. (1), can be conveniently described by the quantum mechanical equations for the components of the density matrix ρ in the JM representation,

$$\left(\frac{\partial}{\partial t}+\mathbf{v}\cdot\nabla+i\omega_{ba}+\frac{\gamma}{2}\right)\rho_{M_bM_a}=\frac{i}{\hbar}(\mathbf{E}_0\cdot\mathbf{d}_{M_bM_a'}\rho_{M_a'M_a}-\rho_{M_bM_b'}\mathbf{E}_0\cdot\mathbf{d}_{M_b'M_a}),\qquad(5)$$

$$\left(\frac{\partial}{\partial t}+\mathbf{v}\cdot\nabla+\gamma\right)\rho_{M_bM_b'}=\frac{i}{\hbar}(\mathbf{E}_0\cdot\mathbf{d}_{M_bM_a}\rho_{M_aM_b'}-\rho_{M_bM_a}\mathbf{E}_0\cdot\mathbf{d}_{M_aM_b'}),\qquad(6)$$

$$\left(\frac{\partial}{\partial t}+\mathbf{v}\cdot\nabla\right)\rho_{M_aM'_a}$$

$$=\frac{i}{\hbar}\left(\mathbf{E}_0\cdot\mathbf{d}_{M_aM_b}\rho_{M_bM'_a}-\rho_{M_aM_b}\mathbf{E}_0\cdot\mathbf{d}_{M_bM'_a}\right)$$

$$+\frac{\gamma(2J_b+1)}{|d_{ba}|^2}\,\mathbf{d}_{M_aM_b}\rho_{M_bM'_b}\cdot\mathbf{d}_{M'_bM'_a}, \tag{7}$$

where

$$\gamma=\frac{4|d_{ba}|^2\omega_{ba}^3}{3\hbar c^3(2J_b+1)},$$

where $\mathbf{d}_{M_bM_a}$ is the matrix element of the electric dipole moment operator $\mathbf{d}$ of the atom, d_{ba} is the reduced dipole moment,[5,6] γ is the probability of spontaneous emission of a photon $\hbar\omega_{ba}$ by an isolated atom, $\mathbf{v}$ is the thermal velocity of an atom, and c is the speed of light in vacuum. The term on the right-hand side of Eq. (7) with the factor γ describes the transition of an atom in the ground level E_a to the excited state with energy E_b, as induced by the spontaneous emission of a photon $\hbar\omega_{ba}$. In each matrix product repeated indices imply summation.

Equations (5)–(7) will be solved in the resonance approximation using the inequality $|\omega_0-\omega_{ba}|\ll\omega_0$. The density matrix $\rho=\rho(t-t'_0,s)$ is a function of $t-t'_0$, and depends on the parameter s. The components of the density matrix at time $t=t'_0$ satisfy the initial condition

$$\rho_{M_bM'_b}(0,s)=\rho_{M_bM_a}(0,s)=0,$$

$$\rho_{M_aM'_a}(0,s)=\frac{\delta_{M_aM'_a}}{2J_a+1}. \tag{8}$$

In writing down Eqs. (5)–(8) we have assumed that the gas is sufficiently tenuous so that atomic collisions contribute negligibly to the level broadening, compared to the radiative width $\hbar\gamma$. Therefore the normalization of the density matrix, Tr $\rho=1$, does not vary with time (a closed resonant transition). If atomic collisions are responsible for the width $\hbar\gamma_a$ of the ground level E_a, then Eqs. (5)–(7) and the subsequent discussion are valid over the period of time $0<t-t'_0\ll\gamma_a^{-1}$ with the condition $\gamma_a\ll\gamma$.

We assume that the circularly polarized pulse (1) has duration τ_0 and is ultrashort

$$\gamma\tau_0\ll 1, \tag{9}$$

where γ^{-1} is the radiative lifetime of the excited state. Because of inequality (9), it is possible to neglect relaxation in Eqs. (5)–(7) in the time interval $0<t-t'_0\leqslant\tau_0$, and set $\gamma=0$. In order to solve these equations with $\gamma=0$ we use a right-handed Cartesian coordinate system xyz, and take the z axis (the axis of quantization) collinear with $\mathbf{k}_0$, with the x axis parallel to $\mathbf{l}^{(1)}_{\mathbf{k}_0}$. Then the vector (2) becomes

$$\mathbf{l}_{\mathbf{k}_0 s}=2^{-1/2}(s\mathbf{l}_x+i\sigma_0\mathbf{l}_y),$$

where $\mathbf{l}^{(1)}_{\mathbf{k}_0}=\mathbf{l}_x$ and $\sigma_0=(\mathbf{k}_0\mathbf{l}_z)/k_0$. Here $\mathbf{l}_x$, $\mathbf{l}_y$, and $\mathbf{l}_z$ are the unit vectors of the Cartesian axes x, y, and z. Now Eqs. (5)–(7) can be solved by the methods worked out in Ref. 7 for a two-level atom without degenerate levels, and in Ref. 8 for the case of degeneracy in the projection of the angular momentum. The final solution of Eqs. (5)–(7) for $\gamma=0$ in the time interval $0\leqslant t-t'_0\leqslant\tau_0$, with the use of the initial conditions Eq. (8) can be written as

$$\rho_{M_aM'_a}(t-t'_0,s)$$

$$=\frac{1}{2J_a+1}\{1-[B^{(s)}_{M_a+s}(t-t'_0)]^2\}\delta_{M_aM'_a}, \tag{10}$$

$$\rho_{M_bM'_b}(t-t'_0,s)=\frac{1}{2J_a+1}[B^{(s)}_{M_b}(t-t'_0)]^2\delta_{M_bM'_b}, \tag{11}$$

where

$$B^{(s)}_M(t-t'_0)=\sin\left[\Lambda^{(s)}_M\int_0^{t-t'_0}R_0(\xi)d\xi\right],$$

$$\Lambda^{(s)}_M=(-1)^{J_b-M+s}\begin{pmatrix}J_b & J_a & 1\\ M & s-M & -s\end{pmatrix}\frac{|d_{ba}|}{\hbar},$$

$$M=M_a+s,M_b. \tag{12}$$

Here the $3j$ symbol $\left(\begin{smallmatrix}a & b & c\\ d & e & h\end{smallmatrix}\right)$ is defined in Refs. 5 and 6. The calculation of the quantities Eqs. (10)–(12) used the fact that the detuning from resonance $\Delta_0=\omega_0-\omega_{ba}$ and the velocity $\mathbf{v}$ satisfy the inequality $|\Delta_0-\mathbf{k}_0\mathbf{v}|\tau_0\ll 1$.

After the ultrashort pulse, Eq. (1), has passed it is necessary in the region $t'_0+\tau_0<t$ to take into account relaxation in Eqs. (5) and (7), and the components of the density matrix can be written

$$\rho_{M_aM'_a}(t-t'_0,s)$$

$$=\rho_{M_aM'_a}(\tau_0,s)+\frac{2J_b+1}{|d_{ba}|^2}\,\mathbf{d}_{M_aM_b}\rho_{M_bM'_b}(\tau_0,s)$$

$$\times\mathbf{d}_{M'_bM'_a}\{1-\exp[-\gamma(t-t'_0-\tau_0)]\}, \tag{13}$$

$$\rho_{M_bM'_b}(t-t'_0,s)=\rho_{M_bM'_b}(\tau_0,s)\exp[-\gamma(t-t'_0-\tau_0)]. \tag{14}$$

The solution, Eqs. (10)–(14), does not contain the optical coherence matrix $\rho_{M_bM_a}(t-t'_0,s)$, since it is damped in a time proportional to $\exp[-\gamma(t-t'_0-\tau_0)/2]$, and therefore will not be used in explicit form in subsequent calculations.

If the ultrashort pulse Eq. (1) has a rectangular amplitude profile with constant amplitude R_0 over the time interval $0\leqslant t-t'\leqslant\tau_0$, then for any detuning from resonance Δ_0 and arbitrary velocity $\mathbf{v}$, in formulas (10)–(14) one must use

$$B^{(s)}_M(t-t'_0)=\frac{R_0\Lambda^{(s)}_M}{\Omega^{(s)}_M}\sin[\Omega^{(s)}_M(t-t'_0)],$$

$$\Omega^{(s)}_M=\left[\frac{1}{4}(\Delta_0-\mathbf{k}_0\mathbf{v})^2+R_0^2(\Lambda^{(s)}_M)^2\right]^{1/2}, \tag{15}$$

instead of expression (12), while in the region $t'_0+\tau_0<t$ the quantity Eq. (15) remains constant with the argument $t-t'_0=\tau_0$.

After a long time

$$\gamma^{-1}\ll t-t'_0-\tau_0, \tag{16}$$

the excited level E_b is entirely depleted through spontaneous emission, and the density matrix $\rho(t-t_0',s)$ takes on a constant value $\rho(\infty,s)$ with the following components

$$\rho_{M_aM_a'}(\infty,s)=\rho_{M_a}(s)\,\delta_{M_aM_a'}, \tag{17}$$

$$\rho_{M_bM_b'}(\infty,s)=\rho_{M_bM_a}(\infty,s)=0, \tag{18}$$

where

$$\rho_{M_a}(s)=\frac{1}{2J_a+1}\left\{1-[B^{(s)}_{M_a+s}(\tau_0)]^2-(2J_b+1)\right.$$
$$\times\sum_{\kappa M_b}(-1)^{\kappa-M_a-M_b}(2\kappa+1)$$
$$\times\begin{pmatrix}J_a & J_a & \kappa\\ M_a & -M_a & 0\end{pmatrix}\begin{pmatrix}J_b & J_b & \kappa\\ M_b & -M_b & 0\end{pmatrix}$$
$$\left.\times\begin{Bmatrix}J_a & \kappa & J_a\\ J_b & 1 & J_b\end{Bmatrix}[B^{(s)}_{M_b}(\tau_0)]^2\right\}, \tag{19}$$

and the $6j$ symbol $\{\begin{smallmatrix}a & b & c\\ d & e & h\end{smallmatrix}\}$ is defined in Refs. 5 and 6.

The density matrix (17) describes the stationary state of the atom in the ground level E_a, and has the following fundamental property:

$$\rho_{-M_a,-M_a'}(\infty,s)=\rho_{M_aM_a'}(\infty,-s). \tag{20}$$

According to (3), the sign of the parameter s in formula (19) is reversed by the replacement $\mathbf{k}_0\to-\mathbf{k}_0$ and therefore the density matrix (17) is changed. However, with the simultaneous replacement $\mathbf{k}_0\to-\mathbf{k}_0$ and $s\to-s$ it remains the same. Upon inversion the matrix indices change sign: $M_a=\mathbf{l}_z\mathbf{J}_a\to-M_a$ and $M_a'\to-M_a'$. Also, the parameter s changes sign with the replacement (4). Therefore, according to Eq. (20), this matrix element does not change sign upon inversion. However, after inversion the density matrix (17), by virtue of the replacement (4), describes the stationary state of the atom produced by a circularly polarized pulse with polarization vector $\mathbf{l}_{\mathbf{k}_0,-s}$, whereas before inversion the other polarization $\mathbf{l}_{\mathbf{k}_0 s}$ was involved.

The optical polarization of an atom is characterized by the equality (20). To describe the optical polarization of an atom one can also use the polarization multipole moments $\rho_q^{\kappa}(J_a,s)$, which figure in the expansion of the density matrix (17) in a series in the $3j$ symbols according to the formulas

$$\rho_{M_aM_a'}(\infty,s)=(-1)^{J_a-M_a'}\sum_{\kappa q}\frac{2\kappa+1}{\sqrt{2J_a+1}}$$
$$\times\begin{pmatrix}J_a & J_a & \kappa\\ M_a & -M_a' & q\end{pmatrix}\rho_q^{(\kappa)}(J_a,s), \tag{21}$$

$$\rho_q^{(\kappa)}(J_a,s)=\sqrt{2J_a+1}\sum_{M_aM_a'}(-1)^{J_a-M_a'}$$
$$\times\begin{pmatrix}J_a & J_a & \kappa\\ M_a & -M_a' & q\end{pmatrix}\rho_{M_aM_a'}(\infty,s), \tag{22}$$

where $0\leqslant\kappa\leqslant 2J_a$ and $-\kappa\leqslant q\leqslant\kappa$. The multipole moments of rank $\kappa=0,1,2$ describe the population, the orientation, and the alignment of an atom in the ground level E_a, respectively. The property (20) of the density matrix is reflected in the behavior of the multipole moments as

$$\rho_q^{(\kappa)}(J_a,-s)=(-1)^{\kappa}\rho_{-q}^{(\kappa)}(J_a,s),\quad q=0. \tag{23}$$

Because of the equality (23), the behavior of the multipole moments of arbitrary rank κ under separate transformations $\mathbf{k}_0\to-\mathbf{k}$, $s\to-s$ and inversion can be described with the use of the two equalitIes

$$\rho_q^{(\kappa)}(J_a,s)=\sigma_0 s\beta\rho_0^{(\kappa)}(J_a,1)\,\delta_{0q}\quad\text{for } s=\pm1,\ \kappa\ \text{odd}, \tag{24}$$

$$\rho_q^{(\kappa)}(J_a,s)=\rho_0^{(\kappa)}(J_a,1)\,\delta_{0q}\quad\text{for } s=\pm1,$$
$$\kappa\ \text{even and}\ \kappa=0, \tag{25}$$

where the replacements $\mathbf{k}_0\to-\mathbf{k}_0$ and $s\to-s$ and inversion can be used separately or conjointly. Here $\beta=1$ in a right-handed coordinate system and $\beta=-1$ in a left-handed coordinate system.

From Eqs. (17) and (22) we obtain an explicit expression for the multipole moments of the atom in the ground state:

$$\rho_q^{(\kappa)}(J_a,s)$$
$$=\delta_{0q}\delta_{0\kappa}-\frac{\delta_{0q}}{\sqrt{2J_a+1}}\left\{\sum_{M_a}(-1)^{J_a-M_a}\begin{pmatrix}J_a & J_a & \kappa\\ M_a & -M_a & 0\end{pmatrix}\right.$$
$$\times[B^{(s)}_{M_a+s}(\tau_0)]^2+(2J_b+1)(-1)^{J_a+J_b+\kappa}$$
$$\times\begin{Bmatrix}J_a & \kappa & J_a\\ J_b & 0 & J_b\end{Bmatrix}\sum_{M_b}(-1)^{J_b-M_b}\begin{pmatrix}J_b & J_b & \kappa\\ M_b & -M_b & 0\end{pmatrix}$$
$$\left.\times[B^{(s)}_{M_b}(\tau_0)]^2\right\}, \tag{26}$$

where the sum of all terms in curly brackets vanishes for $\kappa=0$, and therefore the population in the ground state, as in the unperturbed atom, is $\rho_0^{(0)}(J_a,s)=1$ (a closed resonant transition).

The optical polarization of an atom as described by formulas (20) and (23)–(26) is a consequence of the symmetry in the interaction with a circularly polarized pulse when the quantization axis is collinear with $\mathbf{k}_0$. It is characterized by a single axis of axial symmetry and two opposite directions along this axis corresponding to $s=1$ and $s=-1$. This axis is the axis of quantization in the calculation of the density matrix (17) and the multipole moments (26). If we take into account the rotation of the electric field $\mathbf{E}_0$ about the wave vector $\mathbf{k}_0$, then the optical polarization of the atom produced by the circularly polarized pulse is described by a right-handed screw for $s=1$ and a left-handed screw for $s=-1$. This optical polarization is characteristic of an oriented atom in the state with $\rho_0^{(1)}(J_a,s)$.

3. ALIGNMENT OF AN ATOM BY MEANS OF A STRONG LINEARLY POLARIZED PULSE

The electric field vector $\mathbf{E}_0$ of a linearly polarized pulse of duration τ_0 is given by

$$\mathbf{E}_0=\mathbf{l}_0 R_0(t-t_0')\exp[i(\mathbf{k}_0\cdot\mathbf{r}-\omega_0 t-\alpha_0)]+\text{c.c.}, \tag{27}$$

where the unit real vector $\mathbf{l}_0$ satisfies the equalities $\mathbf{l}_0=\mathbf{l}_{\mathbf{k}_0}^{(1)}=\mathbf{l}_{-\mathbf{k}_0}^{(1)}$ and is not changed by the replacement $\mathbf{k}_0\to-\mathbf{k}_0$. The other quantities in Eq. (27) are the same as those used in Eq. (1). Formula (27) and these properties of the vector $\mathbf{l}_0$ do not depend on the choice of left- or right-handed coordinate system.

Besides the right-handed xyz coordinate system chosen in Sec. 2, we shall consider another right-handed coordinate system $\overline{xyz}$ with the $\overline{z}$ axis (the axis of quantization) along the vector $\mathbf{l}_0$ and the $\overline{y}$ axis parallel to the y axis. Since the vector $\mathbf{l}_0$ is unchanged by the replacement $\mathbf{k}_0\to-\mathbf{k}_0$, the direction of the axis of quantization (the $\overline{z}$ axis) remains the same when the direction of $\mathbf{k}_0$ is reversed. Moreover, it is assumed that the length τ_0 of the linearly polarized pulse (27) satisfies the inequality (9). Then for such a pulse we apply the calculation method of Refs. 7 and 8 in the $\overline{xyz}$ coordinate system, and the solution of equations (5)–(7) with the initial condition (8) is the density matrix $\overline{\rho}=\overline{\rho}(t-t_0',0)$ with the components (10)–(14) in which we have made the replacements

$$\rho\to\overline{\rho},\quad M_a\to\overline{M}_a,\quad M_b\to\overline{M}_b,\quad s\to 0, \tag{28}$$

where $\overline{M}_a$ and $\overline{M}_b$ are the projections of the angular momenta on the $\overline{z}$ axis and the density matrix $\overline{\rho}$ has the indices from the set M_a, M_b, M_a' and M_b'. If we make the replacements (28) in formulas (17) and (18) we obtain the components of the constant density matrix $\overline{\rho}(\infty,0)$ in the xyz coordinate system for long times (expression (16)) after the passage of the ultrashort linearly polarized pulse (27).

The optical polarization of an atom in the field (27) must be described in the right-handed xyz system of coordinates with the z axis (the axis of quantization) collinear with $\mathbf{k}_0$ and the x axis along the vector $\mathbf{l}_0$. In this case the x and z axes coincide with the two orthogonal directions in space defined by the linearly polarized pulses independently of the replacement $\mathbf{k}_0\to-\mathbf{k}_0$. The transformation from the $\overline{xyz}$ coordinate system to the xyz system is carried out via three successive rotations by the Euler angles α, β, and γ, as in Ref. 6. For this purpose we first carry out the rotation about the $\overline{z}$ axis by the angle $\alpha=0$ with the transformation to the new coordinate system $x_1y_1z_1$. Then follows the rotation about the new y_1 axis by the angle $\beta=-\pi/2$ with the transformation to the new coordinate system $x_2y_2z_2$. Then the rotation is carried out about the z_2 axis by the angle $\gamma=0$, with the transformation to the new xyz coordinate system. If we take into account the density matrix $\overline{\rho}(\infty,0)$ calculated in the $\overline{xyz}$ coordinate system, and use the law for the transformation of density matrices under rotations of the Cartesian coordinate system by Euler angles α, β, and γ (Ref. 6), then we can find the components of the density matrix of the atom in the stationary state at long times (16) in the xyz coordinate system with the z axis (the axis of quantization) collinear with $\mathbf{k}_0$ and the x axis along the $\mathbf{l}_0$ direction:

$$\begin{aligned}\rho_{M_aM_a'}=\sum_{\overline{M}_a}\overline{\rho}_{\overline{M}_a}(0)\sum_{\kappa q}(2\kappa+1)(-1)^{J_a-\overline{M}_a}\\ \times\begin{pmatrix}J_a & J_a & \kappa\\ \overline{M}_a & -\overline{M}_a & 0\end{pmatrix}(-1)^{J_a-M_a'}\\ \times\begin{pmatrix}J_a & J_a & \kappa\\ M_a & -M_a' & q\end{pmatrix}d_{0q}^{\kappa}\left(-\frac{\pi}{2}\right),\end{aligned} \tag{29}$$

$$\rho_{M_bM_b'}=\rho_{M_bM_a}=0, \tag{30}$$

where $\overline{\rho}_{\overline{M}_a}(0)$ is given by formula (19) with the replacement (28), while $d_{0q}^{\kappa}(-\pi/2)$ is a special case of the real factor $d_{MM'}^{J}(\beta)$ in the Wigner D function

$$D_{MM'}^{J}(\alpha,\beta,\gamma)=e^{-iM\alpha}d_{MM'}^{J}(\beta)e^{-iM'\gamma}.$$

The density matrix (29) describes the stationary state of an atom in the ground level E_a a long time (16) after the passage of the linearly polarized pulse (27), and has the property

$$\rho_{-M_a,-M_a'}=\rho_{M_aM_a'}. \tag{31}$$

By analogy with Eqs. (21) and (22), we expand the density matrix (29) in a series

$$\begin{aligned}\rho_{M_aM_a'}=(-1)^{J_a-M_a'}\sum_{\kappa q}\frac{2\kappa+1}{\sqrt{2J_a+1}}\\ \times\begin{pmatrix}J_a & J_a & \kappa\\ M_a & -M_a' & q\end{pmatrix}\rho_q^{(\kappa)}(J_a),\end{aligned} \tag{32}$$

where, because of the equality (29), the only nonvanishing polarization multipole moments $\rho_q^{\kappa}(J_a)$ are those of even rank κ, including $\kappa=0$. These multipole moments describe the optical polarization of the atom, and according to Eqs. (29) and (32) take the form

$$\begin{aligned}\rho_q^{(\kappa)}(J_a)=\delta_{0\kappa}\delta_{0q}-\frac{1}{\sqrt{2J_a+1}}\left\{\sum_{M_a}(-1)^{J_a-M_a}\right.\\ \times\begin{pmatrix}J_a & J_a & \kappa\\ M_a & -M_a & 0\end{pmatrix}[B_{M_a}^{(0)}(\tau_0)]^2+(2J_b+1)\\ \times(-1)^{J_a+J_b+\kappa}\begin{Bmatrix}J_a & \kappa & J_a\\ J_b & 1 & J_b\end{Bmatrix}\sum_{M_b}(-1)^{J_b-M_b}\\ \left.\times\begin{pmatrix}J_b & J_b & \kappa\\ M_b & -M_b & 0\end{pmatrix}[B_{M_b}^{(0)}(\tau_0)]^2\right\}d_{0q}^{\kappa}\left(-\frac{\pi}{2}\right),\end{aligned} \tag{33}$$

where $\kappa=2n$ with $n=0,1,2,\ldots$. The upper bound of variation of κ in the first and second sums is determined by the inequalities $\kappa\leqslant 2J_a$ and $\kappa\leqslant 2J_a,2J_b$, respectively. The quantity $B_M^{(0)}(\tau_0)$ with $M=M_a,M_b$ is given by formulas (12) and (15) with $s=0$.

One can see that the density matrix does not change with the replacement $\mathbf{k}_0 \rightarrow -\mathbf{k}_0$. On the other hand, the replacement $\mathbf{l}_0 \rightarrow -\mathbf{l}_0$ reverses the direction of the $\bar{z}$ axis according to the calculations (29) and (33). This results in a change in sign of the angle of rotation β, which for Eqs. (29) and (33) means the replacement $-\pi/2 \rightarrow \pi/2$. After this replacement the quantities (29) and (33) will be referred to the xyz coordinate system with the same z axis collinear with $\mathbf{k}_0$ and the x axis antiparallel to $\mathbf{l}_0$. Inversion is accompanied by the replacements $M_a \rightarrow -M_a$, $\mathbf{k}_0 \rightarrow -\mathbf{k}_0$ and $\mathbf{l}_0 \rightarrow -\mathbf{l}_0$ and a reversal of the direction of the $\bar{z}$ axis. If we take the property (31) into account, then we see that after inversion, the density matrix does not change form.

The optical polarization which we have found is a consequence of symmetry. It is characterized by two orthogonal axes, the first of which points in the $\mathbf{l}_0$ direction, while the second is collinear with $\mathbf{k}_0$. These axes are the axes of quantization in the $\bar{x}\bar{y}\bar{z}$ and xyz coordinate systems when the quantities (29) and (33) are calculated. The optical polarization generated in an atom by a linearly polarized pulse is characteristic of an aligned atom.

4. LIGHT-INDUCED MAGNETIZATION OF GAS OF PRE-ORIENTED ATOMS

We now study the magnetization of a gas of pre-oriented atoms during the passage of an elliptically polarized pulse

$$\mathbf{E}=\mathbf{l}_{\mathbf{k}\lambda}a(t')\exp[i(\mathbf{kr}-\omega t)]+\text{c.c.}\,, \tag{34}$$

where

$$\lambda=\pm 1, \quad t'=t-\tilde{t}_0', \quad \tilde{t}'=\tilde{t}_0+\mathbf{k}(\mathbf{r}-\mathbf{r}_0)/\omega.$$

$a(t')$ is the complex amplitude, which is a function that varies slowly compared to $\exp[i(\mathbf{kr}-\omega t)]$, and $\tilde{t}_0$ is the time of arrival of the pulse (34) in the gas at the boundary point $\mathbf{r}_0$. The wave vector $\mathbf{k}$ is collinear with $\mathbf{k}_0$. The electric field vector $\mathbf{E}$ executes right-handed rotation for $\lambda=1$ and left-handed rotation for $\lambda=-1$. The elliptical polarization vector $\mathbf{l}_{\mathbf{k}\lambda}$ in the case of right-handed polarization, $\lambda=1$, can be written as

$$\mathbf{l}_{\mathbf{k}1}=\mathbf{l}_{\mathbf{k}}^{(1)}\cos\psi+i\mathbf{l}_{\mathbf{k}}^{(2)}\sin\psi, \tag{35}$$

while for left-handed polarization, $\lambda=-1$, can be written

$$\mathbf{l}_{\mathbf{k},-1}=-\mathbf{l}_{\mathbf{k}}^{(1)}\sin\psi+i\mathbf{l}_{\mathbf{k}}^{(2)}\cos\psi. \tag{36}$$

In Eqs. (35) and (36) the argument ψ takes values $0\leqslant\psi\leqslant\pi/2$. The ratio of the lengths of the polarization ellipse axes is $\cos\psi/\sin\psi$ and $\sin\psi/\cos\psi$, respectively, in Eqs. (35) and (36). If $\psi=\pi/4$, the polarization ellipse becomes a circle, and formulas (35) and (36) describe right-circular polarization and left-circular polarization. If we set $\lambda=1$ and $\psi=0$ or $\lambda=-1$ and $\psi=\pi/2$, formulas (34)–(35) describe linearly polarized pulses. The unit vectors in expressions (34) and (36) satisfy the equalities

$$\mathbf{kl}_{\mathbf{k}}^{(1)}=\mathbf{kl}_{\mathbf{k}}^{(2)}=\mathbf{l}_{\mathbf{k}}^{(1)}\mathbf{l}_{\mathbf{k}}^{(2)}=0, \quad \mathbf{l}_{-\mathbf{k}}^{(1)}=\mathbf{l}_{\mathbf{k}}^{(1)}, \quad \mathbf{l}_{-\mathbf{k}}^{(2)}=-\mathbf{l}_{\mathbf{k}}^{(2)}, \tag{37}$$

$$[\mathbf{l}_{\mathbf{k}}^{(1)}\mathbf{l}_{\mathbf{k}}^{(2)}]=\mathbf{k}/k, \tag{38}$$

$$\mathbf{l}_{-\mathbf{k}\lambda}=\mathbf{l}_{\mathbf{k}\lambda}^{*}, \quad \mathbf{l}_{\mathbf{k}\lambda}\mathbf{l}_{\mathbf{k}\lambda'}^{*}=\delta_{\lambda\lambda'}, \quad \lambda,\lambda'=\pm 1. \tag{39}$$

The magnetization of a gas in the field (34) cannot be investigated without knowing the rules for transformation of the polarization vectors (35) and (36) under the replacement $\mathbf{k}\rightarrow-\mathbf{k}$ and inversion. In order to find these rules we used the fact that the equalities (35)–(39) are satisfied regardless of the choice of right-handed or left-handed coordinates. This, together with the equality (37), enables us to determine the transformation of the polarization vectors with the replacement $\mathbf{k}\rightarrow-\mathbf{k}$ in the form

$$\mathbf{l}_{\mathbf{k}\lambda}\rightarrow-\mathbf{l}'_{\mathbf{k},-\lambda},$$

where for the new polarization vector $\mathbf{l}_{\mathbf{k},\lambda}$ with $\lambda=1$ and $\lambda=-1$ we have introduced the notation

$$\mathbf{l}'_{\mathbf{k}1}=\mathbf{l}_{\mathbf{k}}^{(1)}\cos\psi'+i\mathbf{l}_{\mathbf{k}}^{(2)}\sin\psi',$$

$$\mathbf{l}'_{\mathbf{k},-1}=-\mathbf{l}_{\mathbf{k}}^{(1)}\sin\psi'+i\mathbf{l}_{\mathbf{k}}^{(2)}\cos\psi', \tag{40}$$

with the new parameter ψ' defined by the formulas

$$\psi'=\pi/2-\psi, \quad 0\leqslant\psi'\leqslant\pi/2,$$

and by the new ratios of the axes of the polarization ellipse $\cos\psi'/\sin\psi'=\sin\psi/\cos\psi$ and $\sin\psi'/\cos\psi'=\cos\psi/\sin\psi$, respectively, for right-handed $(\lambda=1)$ and left-handed $(\lambda=-1)$ polarization. These ratios of the lengths of the polarization ellipse axes for $\lambda=1$ and $\lambda=-1$ are interchanged relative to the initial polarization vectors (35) and (36), which were specified up to the replacement $\mathbf{k}\rightarrow-\mathbf{k}$. If we use the equality (38), then upon the replacement $\mathbf{k}\rightarrow-\mathbf{k}$ we can also find the transformation of the vector product

$$i[\mathbf{l}_{\mathbf{k}\lambda}\mathbf{l}_{\mathbf{k}\lambda}^{*}]=(\mathbf{k}/k)\lambda\sin(2\psi)\rightarrow i[\mathbf{l}'_{\mathbf{k},-\lambda}l'^{*}_{\mathbf{k},-\lambda}]$$
$$=-(\mathbf{k}/k)\lambda\sin(2\psi')=-(\mathbf{k}/k)\lambda\sin(2\psi). \tag{41}$$

Moreover, by virtue of (37) and (38), the polarization vector transforms under inversion according to another rule,

$$\mathbf{l}_{\mathbf{k}\lambda}\rightarrow\mathbf{l}'_{\mathbf{k},-\lambda}, \tag{42}$$

whereas according to Eq. (41) the vector product $i[\mathbf{l}_{\mathbf{k}\lambda}\mathbf{l}_{\mathbf{k}\lambda}^{*}]$ transforms under inversion in the same way as under the replacement $\mathbf{k}\rightarrow-\mathbf{k}$. This important result enables us to write this vector product as

$$i[\mathbf{l}_{\mathbf{k}\lambda}\mathbf{l}_{\mathbf{k}\lambda}^{*}]=(\mathbf{k}/k)\lambda\beta\sin(2\psi), \tag{43}$$

where β is the unit pseudovector, which in right-handed and left-handed coordinate systems is equal to $\beta=1$ and $\beta=-1$, respectively. Formula (43) takes into account the replacements $\mathbf{k}\rightarrow-\mathbf{k}$ and $\lambda\rightarrow-\lambda$ and inversion, which can be carried out individually or in various combinations with one another. According to Eq. (43), the factor in Eq. (24) that takes into account circularly polarized pulses can be written in a different manner:

$$\sigma_0 s\beta=i[\mathbf{l}_{\mathbf{k}_0 s}\mathbf{l}_{\mathbf{k}_0 s}^{*}]\mathbf{l}_z,$$

where $\mathbf{l}_z$ is the unit vector in the direction of the axis of quantization.

The state of the atom in the field, Eq. (34), is described by the density matrix $\rho(t')$, which satisfies Eqs. (5)–(7) with

$\mathbf{E}_0 \to \mathbf{E}$. Its components, which are not diagonal in the energy, have the following characteristic form in the resonance approximation, $|\omega - \omega_{ba}| \ll \omega$:

$$\rho_{M_b M_a}(t') = r_{M_b M_a}(t') \exp[i(\mathbf{kr} - \omega t)],$$

where $t = t' - \tilde{t}'_0$, so that they are functions of t'. In addition, the components $r_{M_b M_a}(t')$, $\rho_{M_a M_a}(t')$, and $\rho_{M_b M_b(t')}$ vary slowly compared to $\exp[i(\mathbf{kr} - \omega t)]$ and satisfy the equations

$$\left(\frac{\partial}{\partial t} + \mathbf{v}\nabla\right) r_{M_b M_a}(t') = \left(1 - \frac{\mathbf{kv}}{\omega}\right) \frac{d}{dt'} r_{M_b M_a}(t') = \frac{d}{dt'} r_{M_b M_a}(t'),$$

$$\left(\frac{\partial}{\partial t} + \mathbf{v}\nabla\right) \rho_{MM'}(t') = \frac{d}{dt'} \rho_{MM'}(t'), \quad M = M_a, M'_b.$$

where we have omitted small terms of order v/c.

In light of this discussion, we can transform Eqs. (5)–(7) in the field (34) into the simpler equations

$$\left(\frac{d}{dt'} - i\Delta + \frac{\gamma}{2}\right) r_{M_b M_a} = \frac{ia(t')}{\hbar} [\mathbf{l}_{\mathbf{k}\lambda} \mathbf{d}_{M_b M'_a} \rho_{M'_a M_a} - \rho_{M_b M'_b} \mathbf{l}_{\mathbf{k}\lambda} \mathbf{d}_{M'_b M_a}], \tag{44}$$

$$\left(\frac{d}{dt'} + \gamma\right) \rho_{M_b M'_b} = \frac{i}{\hbar} [\mathbf{l}_{\mathbf{k}\lambda} \mathbf{d}_{M_b M_a} r_{M_a M'_b} a(t') - a^*(t') r_{M_b M_a} \mathbf{l}^*_{\mathbf{k}\lambda} \mathbf{d}_{M_a M'_b}], \tag{45}$$

$$\frac{d}{dt'} \rho_{M_a M'_a} = \frac{i}{\hbar} [\mathbf{l}^*_{\mathbf{k}\lambda} \mathbf{d}_{M_a M_b} r_{M_b M'_a} a^*(t') - a(t') r_{M_a M_b} \mathbf{l}_{\mathbf{k}\lambda} \mathbf{d}_{M_b M'_a}] + \frac{\gamma(2J_b + 1)}{|d_{ba}|^2} \mathbf{d}_{M_a M_b} \rho_{M_b M'_b} \mathbf{d}_{M'_b M'_a},$$

$$\Delta = \omega - \omega_{ba} - \mathbf{kv}. \tag{46}$$

Equations (44)–(46) and their initial conditions can be conveniently analyzed in the right-handed xyz coordinate system with z axis (the axis of quantization) collinear with $\mathbf{k}_0$ and x axis along the vector $\mathbf{l}^{(1)}_{\mathbf{k}_0}$, since the optical prepolarization of the atom was calculated in those coordinates. The initial conditions at $t' = 0$ then assume the simplest form:

$$r_{M_b M_a}(0) = 0, \quad \rho_{M_b M'_b}(0) = 0,$$

$$\rho_{M_a M'_a}(0) = \rho_{M_a M'_a}(\infty, s), \tag{47}$$

where the right-hand sides of the equalities coincide with the components of the density matrices (17) and (18) of the preoriented atom.

The light-induced magnetization of an atomic gas is represented by a magnetic moment per unit volume, given by

$$\boldsymbol{\mu}(t') = -\mu_B N \int f(v) [g_a \mathbf{J}_{M'_a M_a} \rho_{M_a M'_a}(t') + g_b \mathbf{J}_{M'_b M_b} \rho_{M_b M'_b}(t')] d\mathbf{v}, \tag{48}$$

where

$$\mu_B = |e|\hbar/2mc,$$

$$f(v) = (\sqrt{\pi}u)^{-3} \exp\left(-\frac{v^2}{u^2}\right), \quad u = \left(\frac{2\kappa_B T}{m_{at}}\right)^{1/2},$$

μ_B is the Bohr magneton, e and m are the electron charge and mass, g_a and g_b are the gyromagnetic ratios (the g-factors), N is the concentration of the gas atoms, $f(v)$ is the Maxwell distribution, T is the gas temperature, κ_B is the Boltzmann constant, m_{at} is the mass of the atom, and $\mathbf{J}_{M_a M'_a}$ and $\mathbf{J}_{M_b M'_b}$ are the matrix elements of the angular momentum operators $\mathbf{J}_a$ and $\mathbf{J}_b$, respectively.

The density matrices in Eq. (48) must be calculated by solving Eqs. (44)–(46) by perturbation theory if the elliptically polarized pulse, Eq. (34), has duration τ and low intensity. Then the condition on the range of applicability of time-dependent perturbation theory for a rectangular pulse, Eq. (34), of constant amplitude a can be conveniently written as

$$\tau \ll \tau_{\text{pum}}, \tag{49}$$

where τ_{pum} is the time of optical pumping,

$$\tau_{\text{pum}} = 2[(\omega - \omega_{ba} - ku)^2 + \gamma^2/4](f^2\gamma)^{-1},$$

and $f = |d_{ba} a|/\hbar^{-1}$ is the Rabi frequency.

According to the method of successive approximations in perturbation theory, the density matrix for the first approximation in the field (34) is the solution of Eq. (44) in which the components (47) are used on the right-hand side without taking the field (34) into account. The density matrix elements $\rho^{(2)}_{M_a M'_a}(t')$ and $\rho^{(2)}_{M_b M'_b}(t')$ of second order in the field (34) are the respective solutions of Eqs. (45) and (46) in which the right-hand sides retain the terms quadratic in the field (34). The solution of these latter equations with the initial conditions (47) can be written in the short form

$$\rho_{M_a M'_a}(t') = \rho_{M_a M'_a}(\infty, s) + \rho^{(2)}_{M_a M'_a}(t'),$$

$$\rho_{M_b M'_b}(t') = \rho^{(2)}_{M_b M'_b}(t'). \tag{50}$$

The term $\rho_{M_a M'_a}(\infty, s)$ in Eq. (50) describes the steady state of an atom in the ground state before the passage of the pulse (34). This term, along with formulas (17), (21), (24), and (48), enables us to find the constant light-induced magnetization

$$\boldsymbol{\mu}_a = -(\mathbf{k}_0/k_0) s \beta \mu_B N g_a \sqrt{J_a(J_a + 1)} \int f(v) \rho^{(1)}_0 \times (J_a, 1) d\mathbf{v},$$

where the multipole moment $\rho^{(1)}_0(J_a, 1)$ is defined in Eq. (26) for $\kappa = 1$ and $s = 1$. The light-induced magnetization $\boldsymbol{\mu}_a$ is produced by the preceding strong pulse (1), and if there are no depolarizing collisions it is retained during the time that the following weak pulse (34) passes.

To study the light-induced magnetization in the experiments of Refs. 1 and 2 the light pulses were passed through a cell containing the atomic gas and situated inside the pickup coil. The time-dependent light-induced magnetization

of the atomic gas induced an electric current in the windings of the pickup coil, producing a potential difference $V(t')$ between the ends, as described by the well-known formula

$$V(t')=-C\mathbf{n}\,\frac{d\boldsymbol{\mu}(t')}{dt'}, \tag{51}$$

where the unit vector $\mathbf{n}$ is collinear with $\mathbf{k}$ and the constant C depends on the experimental arrangement. Here $\mathbf{n}$ defines the fixed direction for which the magnetic flux is measured and $V(t')$ is the emf of the pickup coil. The experimentally measured quantity, the projection of the derivative $d\boldsymbol{\mu}(t')/dt'$ in the fixed direction $\mathbf{n}$, provided information on the properties of the time-dependent quantity $\boldsymbol{\mu}(t')$.

According to Eq. (51) the constant light-induced magnetization $\boldsymbol{\mu}_a$ cannot be measured in experiments that use a pickup coil. Therefore, to study the behavior of $\boldsymbol{\mu}(t')$ as the weak pulse (34) passes, it is necessary to calculate the time-dependent light-induced magnetization due to the terms in Eq. (50) quadratic in the field (34). After writing down these terms in Eq. (48), we obtain

$$\mu(t')=\frac{\mu_B N}{\hbar^2}\int d\mathbf{v}f(v)\Big\{g_a I^a(t')\mathbf{S}-g_b I^b(t')\mathbf{Q} - \frac{g_a(2J_b+1)}{|d_{ba}|^2}[I^a(t')-I^b(t')]\mathbf{P}\Big\}+\text{c.c.}, \tag{52}$$

where

$$\mathbf{S}=\mathbf{J}_{M'_aM_a}(\mathbf{l}^*_{\mathbf{k}\lambda}\mathbf{d}_{M_aM_b})(\mathbf{l}_{\mathbf{k}\lambda}\mathbf{d}_{M_bM''_a})\rho_{M''_aM'_a}(\infty,s), \tag{53}$$

$$\mathbf{Q}=\mathbf{J}_{M'_bM_b}(\mathbf{l}_{\mathbf{k}\lambda}\mathbf{d}_{M_bM_a})\rho_{M_aM'_a}(\infty,s)(\mathbf{l}^*_{\mathbf{k}\lambda}\mathbf{d}_{M'_aM'_b}), \tag{54}$$

$$\mathbf{P}=\mathbf{J}_{M'_aM_a}(\mathbf{d}_{M_aM_b}(\mathbf{l}_{\mathbf{k}\lambda}\mathbf{d}_{M_b\tilde{M}_a})\rho_{\tilde{M}_a\tilde{M}'_a}(\infty,s) \times(\mathbf{l}'_{\mathbf{k}\lambda}\mathbf{d}_{\tilde{M}'_aM'_b})\mathbf{d}_{M'_bM'_a}), \tag{55}$$

$$I^a(t')=\int_0^{t'}d\tau_2 a^*(\tau_2)\exp[(-\gamma/2+i\Delta)\tau_2] \times\int_0^{\tau_2}d\tau_1 a(\tau_1)\exp[(\gamma/2-i\Delta)\tau_1], \tag{56}$$

$$I^b(t')=\exp(-\gamma t')\int_0^{t'}d\tau_2 a^*(\tau_2)\exp[(\gamma/2+i\Delta)\tau_2] \times\int_0^{\tau_2}d\tau_1 a(\tau_1)\exp[(\gamma/2-i\Delta)\tau_1]. \tag{57}$$

To sum over the projections of the angular momenta we introduce the notation

$$\mathbf{A}=\mathbf{l}_{\mathbf{k}\lambda}, \quad \mathbf{B}=\mathbf{l}^*_{\mathbf{k}\lambda} \tag{58}$$

in Eqs. (53)–(55) and write the vectors in Eqs. (53)–(55) and (58) as expansions in orthogonal unit vectors

$$\mathbf{A}=\sum_q A_q\mathbf{l}^q, \quad \mathbf{B}=\sum_q B_q\mathbf{l}^q, \tag{59}$$

$$\mathbf{S}=\sum_{\tilde{q}} S_{\tilde{q}}\mathbf{l}^{\tilde{q}}, \quad \mathbf{Q}=\sum_{\tilde{q}} Q_{\tilde{q}}\mathbf{l}^{\tilde{q}}, \quad \mathbf{P}=\sum_{\tilde{q}} P_{\tilde{q}}\mathbf{l}^{\tilde{q}}, \tag{60}$$

where the vectors $\mathbf{l}^q$ with $q=0,\pm1$ are the contravariant unit vectors:[6]

$$\mathbf{l}^{(-1)}=2^{-1/2}(\mathbf{l}_x+i\mathbf{l}_y), \quad \mathbf{l}^{(1)}=2^{-1/2}(-\mathbf{l}_x+i\mathbf{l}_y), \quad \mathbf{l}^{(0)}=\mathbf{l}_z.$$

Using the Wigner–Eckart theorem, the rule for contracting $3j$ symbols,[5,9] and Eqs. (58)–(60), we obtain

$$S_{\tilde{q}}=-\delta_{0\tilde{q}}\frac{|d_{ba}|^2J_{aa}}{\sqrt{2J_a+1}}\sum_\kappa(2\kappa+1)\rho_0^{(\kappa)}(J_a,s) \times\sum_q(-1)^qA_{-q}B_qG_a(q,\kappa), \tag{61}$$

$$Q_{\tilde{q}}=\delta_{0\tilde{q}}\frac{|d_{ba}|^2J_{bb}}{\sqrt{2J_a+1}}\sum_\kappa(2\kappa+1)\rho_0^{(\kappa)}(J_a,s) \times\sum_q(-1)^qA_{-q}B_qG_b(q,\kappa), \tag{62}$$

$$P_{\tilde{q}}=\frac{|d_{ba}|^2J_{aa}}{J_{bb}}(-1)^{J_a+J_b}\begin{Bmatrix}J_a & 1 & J_a\\ J_b & 1 & J_b\end{Bmatrix}Q_{\tilde{q}}, \tag{63}$$

$$G_a(q,\kappa)=\sum_{\kappa'}(2\kappa'+1)(-1)^\kappa\begin{pmatrix}1 & 1 & \kappa'\\ 0 & -q & q\end{pmatrix} \times\begin{pmatrix}\mathbf{1} & \kappa & \kappa'\\ q & 0 & -q\end{pmatrix}\begin{Bmatrix}1 & 1 & \kappa'\\ J_a & J_b & J_a\end{Bmatrix} \times\begin{Bmatrix}1 & \kappa & \kappa'\\ J_a & J_b & J_a\end{Bmatrix}, \tag{64}$$

$$G_b(q,\kappa)=\sum_{\kappa'}(2\kappa'+1)\begin{pmatrix}1 & 1 & \kappa'\\ 0 & -q & q\end{pmatrix}\begin{pmatrix}1 & \kappa & \kappa'\\ -q & 0 & q\end{pmatrix} \times\begin{Bmatrix}1 & 1 & \kappa'\\ J_b & J_a & J_b\end{Bmatrix}\begin{Bmatrix}1 & \kappa & \kappa'\\ J_a & J_b & J_a\end{Bmatrix}, \tag{65}$$

$$J_{aa}=[J_a(J_a+1)(2J_a+1)]^{1/2}, \quad J_{bb}=[J_b(J_b+1)\times(2J_b+1)]^{1/2}.$$

The vectors $\mathbf{A}$ and $\mathbf{B}$, which are orthogonal to the z axis, obey the equality

$$\sum_q(-1)^qA_{-q}B_qG_a(q,\kappa) =\frac{1}{2}\{\mathbf{AB}[G_a(1,\kappa)+G_a(-1,\kappa)]+i[\mathbf{AB}]_z[G_a(1,\kappa) -G_a(-1,\kappa)]\}, \tag{66}$$

where, because of Eqs. (43) and (58), we can set

$$\mathbf{AB}=1, \quad i[\mathbf{AB}]_z=(\mathbf{l}_z\mathbf{k}/k)\lambda\beta\sin(2\psi).$$

Using the formula

$$G_a(-q,\kappa)=(-1)^{\kappa+1}G_a(q,\kappa),$$

we find that the right-hand side of Eq. (66) is equal to $G_a(1,\kappa)$ for odd κ and

$$(\mathbf{l}_z\mathbf{k}/k)\lambda\beta\sin(2\psi)G_a(1,\kappa) \tag{67}$$

for even κ, including $\kappa=0$. These equalities, (66) and (67) are also valid for $G_b(q,\kappa)$ with the change of subscript $a\to b$. In addition, it is necessary to take into account that according to Eqs. (24) and (25) the multipole moments $\rho_0^{(\kappa)}\times(J_a,s)$ have a different form for odd and even κ, including $\kappa=0$. Finally, the time-dependent light-induced magnetization (52) in the time interval $0\leqslant t'$, regardless of the choice of coordinate system, takes the form

$$\boldsymbol{\mu}(t')=-(\mathbf{k}/k)\lambda\beta\,\sin(2\psi)\sum_{\kappa=0,2}\mu^{(\kappa)}(t')$$

$$-(\mathbf{k}_0/k_0)s\beta\sum_{\kappa=1,3}\mu^{(\kappa)}(t'), \tag{68}$$

where

$$\mu^{(\kappa)}(t')=g_aD_a^{(\kappa)}M_a^{(\kappa)}(t')+g_bD_b^{(\kappa)}M_b^{(\kappa)}(t')+g_aD_{ab}^{(\kappa)}\times[M_a^{(\kappa)}(t')-M_b^{(\kappa)}(t')],$$

$$D_a^{(\kappa)}=6(2\kappa+1)\sqrt{2J_a+1}\;J_{aa}G_a(1,\kappa),$$

$$D_b^{(\kappa)}=6(2\kappa+1)\sqrt{2J_a+1}J_{bb}G_b(1,\kappa),$$

$$D_{ab}^{(\kappa)}=6(2\kappa+1)\sqrt{2J_a+1}J_{aa}G_b(1,\kappa)(-1)^{J_a+J_b}\times(2J_b+\mathbf{1})\begin{Bmatrix}J_a & 1 & J_a\\ J_b & 1 & J_b\end{Bmatrix},$$

$$M_a^{(\kappa)}(t')=\frac{\mu_BN|d_{ba}|^2}{6(2J_a+1)\hbar^2}\int f(v)\rho_0^{(\kappa)}(J_a,1)I_0^a(t')d\mathbf{v}, \tag{69}$$

$$M_b^{(\kappa)}(t')=\frac{\mu_BN|d_{ba}|^2}{6(2J_a+1)\hbar^2}\int f(v)\rho_0^{(\kappa)}(J_a,1)I_0^b(t')d\mathbf{v}, \tag{70}$$

$$I_0^a(t')=I^a(t')+I^{a*}(t'),\quad I_0^b(t')=I^b(t')+I^{b*}(t'). \tag{71}$$

Here the quantity $I_0^a(t')$ after the passage of the pulse (34) retains the constant value $I_0^a(\tau)$, in accordance with Eq. (56). In addition, $I_0^b(t')$ because of relaxation falls off in Eq. (57) as

$$I_0^b(t')=I_0^b(\tau)\exp[-\gamma(t'-\tau)],\quad \tau\leqslant t'. \tag{72}$$

For the ultrashort pulse (34) with $\gamma\tau\ll 1$ the criterion for the applicability of perturbation theory is the inequality[8]

$$\left|\hbar^{-1}d_{ba}\int_0^\tau a(t')dt'\right|^2\ll 1. \tag{73}$$

Here the dependence of $\boldsymbol{\mu}(t')$ on the time t' in the range $0\leqslant t'$ is given by Eqs. (71), which take the form

$$I_0^a(t')=I_0(t'),\quad I_0^b(t')=I_0(t')\exp(-\gamma t'), \tag{74}$$

where

$$I_0(t')=\left|\int_0^{t'}a(\xi)\exp(-i\Delta\xi)d\xi\right|^2. \tag{75}$$

In formula (68) the summation index κ coincides with the rank of the multipole moments $\rho_0^{(\kappa)}(J_a,s)$ characterizing the initial state of the atom. This means that $\boldsymbol{\mu}(t')$ depends not only on the population, but also on the optical pre-polarization of the atom produced by the preceding circularly polarized pulse (1). Thus the first term in Eq. (68) with $\kappa=0$ is related only to the population $\rho_0^{(0)}(J_a,s)=1$ of the ground state and is equal to

$$\boldsymbol{\mu}_{pop}(t')=-(\mathbf{k}/k)\lambda\beta\,\sin(2\psi)\{g_aQ_aM_a^{(0)}(t')+g_bQ_bM_b^{(0)}\times(t')+g_aQ_{ab}[M_a^{(0)}(t')-M_b^{(0)}(t')]\}. \tag{76}$$

where

$$Q_a=6^{1/2}J_{aa}(-1)^{J_a+J_b}\begin{Bmatrix}1 & 1 & 1\\ J_a & J_a & J_b\end{Bmatrix},$$

$$Q_b=6^{-1/2}J_{bb}(-1)^{J_a+J_b}\begin{Bmatrix}1 & 1 & 1\\ J_b & J_b & J_a\end{Bmatrix},$$

$$Q_{ab}=6^{1/2}J_{aa}(2J_b+1)\begin{Bmatrix}1 & 1 & 1\\ J_b & J_b & J_a\end{Bmatrix}\begin{Bmatrix}J_a & 1 & J_a\\ J_b & 1 & J_b\end{Bmatrix}.$$

The value of expression (76) coincides with the light-induced magnetization of an isotropic atomic gas resulting from the passage of an elliptically polarized pulse (34) as derived in Ref. 3 if we set $N_a=N$, $N_b=\gamma_a=0$, $\gamma_b=\gamma$, and $\gamma_{ba}=\gamma/2$.

The second term in Eq. (68) with $\kappa=2$ takes into account the optical pre-polarization of the atom, which is characterized by one component of the multipole moment $\rho_0^{(2)}\times(J_a,s)$. The state of the atom with $\rho_0^{(2)}(J_a,s)$ has complete rotational symmetry about the z axis, which is collinear with $\mathbf{k}_0$ and $\mathbf{k}$. According to Eq. (25) this state of the atom is invariant under inversion or with the replacements $k_0\to -k_0$ and $s\to -s$. The state of the atom with $\rho_0^{(0)}\times(J_a,s)$ also has these properties. Therefore the terms in (68) with $\kappa=0,2$ do not depend on the orientation of the axes of the polarization ellipse of the pulse (34). In accordance with the symmetry of the atom in the states with $\rho_0^{(\kappa)}(J_a,s)$ for $\kappa=0,2$ and the properties of the field (34), the first two terms in Eq. (68) with $\kappa=0,2$ are proportional to the only pseudovector (43) that is invariant under the interchange $\mathbf{k}_0\to\mathbf{k}_0$ and $s\to -s$ and vanishes for linearly polarized pulses described by formulas (34) and (35) with $\lambda=1$ and $\psi=0$ or by formulas (34) and (36) with $\lambda=-1$ and $\psi=\pi/2$.

The terms of greatest interest in Eq. (68) are those with $\kappa=1,3$. They take into account the optical pre-polarization of the atom by means of the multipole moments with $\rho_0^{(\kappa)}\times(J_a,s)$ with $\kappa=1,3$. This optical polarization is characteristic of the oriented atom. The states of the atom $\rho_0^{(\kappa)}\times(J_a,s)$ with $\kappa=1,3$ have complete rotational symmetry about the z axis, which is collinear with $\mathbf{k}_0$ and $\mathbf{k}$. Therefore these terms in Eq. (68) with $\kappa=1,3$ do not depend on the orientation of the axes of the polarization ellipse of the pulse (34). However, according to Eq. (24) the quantity $\rho_0^{(\kappa)}\times(J_a,s)$ with $\kappa=1,3$ changes sign under inversion and when $\mathbf{k}_0\to -\mathbf{k}_0$ and $s\to -s$. In this connection the terms in Eq. (68) with $\kappa=1,3$ can be expressed in terms of the only pseudovector

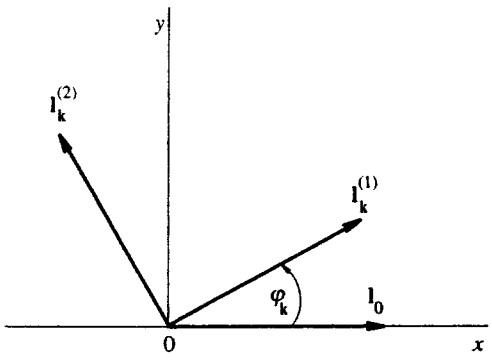

FIG. 1. Orientation of the axes of the polarization ellipse ($\mathbf{l}_{\mathbf{k}}^{(1)}$ and $\mathbf{l}_{\mathbf{k}}^{(2)}$) relative to the polarization vector $\mathbf{l}_0$ in the plane perpendicular to the direction of propagation of the light pulses. The unit vector $\mathbf{l}_{\mathbf{k}}^{(1)}$ is also the polarization vector for a linearly polarized pulse.

$$i[\mathbf{l}_{\mathbf{k}_0 s}\mathbf{l}_{\mathbf{k}_0 s}^{*}]=(\mathbf{k}_0/k_0)s\beta, \tag{77}$$

that takes into account the change in the atomic states under inversion and the separate replacements $\mathbf{k}_0\rightarrow-\mathbf{k}_0$ and $s\rightarrow -s$. It should be noted in particular that these terms are nonzero with the passage of a linearly polarized pulse (34) with the polarization vector (35) and $\lambda=1$ and $\psi=0$, or the polarization vector (36) with $\lambda=-1$ and $\psi=\pi/2$.

A distinguishing feature of the light-induced magnetization, Eq. (68), is also the characteristic dependence on the detuning $\omega-\omega_{ba}$ from resonance when one uses the amplitude

$$a(t')=a_0(t')\exp(-i\alpha) \tag{78}$$

in Eq. (34) with real $a_0(t')$ and α, for which $I_0^a(t')$ and $I_0^b(t')$ are even functions of Δ. For the amplitude (78) the light-induced magnetization (68) is an even function of $\omega-\omega_{ba}$ if the dependence on $\mathbf{kv}$ in Eqs. (71) is negligible or if $\rho_0^{(\kappa)}(J_a,1)$ is an even function of $\mathbf{v}$. The latter is the case, for example, at exact resonance $\omega_0=\omega_{ba}$ for the previous strong pulse. In this case, making the replacement $\mathbf{v}\rightarrow-\mathbf{v}$ for the variable of integration in Eqs. (69) and (70) produces the desired result.

5. LIGHT-INDUCED MAGNETIZATION OF A GAS OF PREALIGNED ATOMS

In a gas of prealigned atoms there exist two preferred orthogonal directions defined by the vectors $\mathbf{k}_0$ and $\mathbf{l}_0$. Therefore when the pulse (34) propagates collinearly with $\mathbf{k}_0$ it is necessary to set the orientation of the axes of the polarization ellipse by means of the formula

$$[\mathbf{l}_0\mathbf{l}_{\mathbf{k}}^{(1)}]=(\mathbf{k}/k)\sin\varphi_{\mathbf{k}}, \tag{79}$$

where the angle $\varphi_{\mathbf{k}}$ is reckoned positive from the vector $\mathbf{l}_0$ to the vector $\mathbf{l}_{\mathbf{k}}^{(1)}$ in the clockwise direction looking along $\mathbf{k}$ (Fig. 1). It can be seen that $\varphi_{\mathbf{k}}$ is a pseudovector, which transforms as $\varphi_{\mathbf{k}}\rightarrow-\varphi_{\mathbf{k}}$ under inversion. In addition, because $\mathbf{l}_{-\mathbf{k}}^{(1)}=\mathbf{l}_{\mathbf{k}}^{(1)}$, the angle $\varphi_{\mathbf{k}}$ changes sign when $\mathbf{k}\rightarrow-\mathbf{k}$, i.e., $\varphi_{-\mathbf{k}}=-\varphi_{\mathbf{k}}$. The pseudovector (79) is of fundamental importance in this problem, since it enables one to determine the direction of $\boldsymbol{\mu}(t')$.

The orientation of the unit vectors $\mathbf{l}_{\mathbf{k}}^{(1)}$ and $\mathbf{l}_{\mathbf{k}}^{(2)}$ relative to $\mathbf{l}_0$ in Fig. 1 is independent of the choice of right- or left-handed coordinates. However the calculation of the light-induced magnetization Eq. (48) is more logically carried out in the right-handed xyz coordinate system with the z axis collinear with $\mathbf{k}_0$ and the x axis along $\mathbf{l}_0$, since this is the system in which the alignment of the atom is given by formulas (29) and (33). Then, according to Fig. 1, the orientation of the axes of the polarization ellipse of the pulse (34) can be written as

$$\mathbf{l}_{\mathbf{k}}^{(1)}=\mathbf{l}_x\cos\varphi_{\mathbf{k}}+\mathbf{l}_y\sigma_{\mathbf{k}}\sin\varphi_{\mathbf{k}}, \tag{80}$$

$$\mathbf{l}_{\mathbf{k}}^{(2)}=-\mathbf{l}_x\sin\varphi_{\mathbf{k}}+\mathbf{l}_y\sigma_{\mathbf{k}}\cos\varphi_{\mathbf{k}}, \tag{81}$$

where $\sigma_{\mathbf{k}}=(\mathbf{l}_z\mathbf{k})/k$ and the conditions (37)–(39) are satisfied. Right- and left-handed polarization is described by the vectors (35) and (36), which after constructing the vectors (80) and (81) can be written

$$\mathbf{l}_{\mathbf{k}1}=\mathbf{l}_x(\cos\varphi_{\mathbf{k}}\cos\psi-i\sin\varphi_{\mathbf{k}}\sin\psi)+\mathbf{l}_y\sigma_{\mathbf{k}}(\sin\varphi_{\mathbf{k}}\cos\psi+i\cos\varphi_{\mathbf{k}}\sin\psi), \tag{82}$$

$$\mathbf{l}_{\mathbf{k},-1}=-\mathbf{l}_x(\cos\varphi_{\mathbf{k}}\sin\psi+i\sin\varphi_{\mathbf{k}}\cos\psi)-\mathbf{l}_y\sigma_{\mathbf{k}}(\sin\varphi_{\mathbf{k}}\sin\psi-i\cos\varphi_{\mathbf{k}}\cos\psi), \tag{83}$$

where the vectors (82) and (83) form the unit polarization vector $\mathbf{l}_{\mathbf{k}\lambda}$ that describes right-handed ($\lambda=1$) and left-handed ($\lambda=-1$) polarization of the pulse (34) with the axes of the polarization ellipse rotated by the angle $\varphi_{\mathbf{k}}$.

In order to calculate the light-induced magnetization, Eq. (48), of a gas of pre-aligned atoms by the propagation of the pulse (34) with polarization vectors (82) and (83), it is necessary to solve equations (44)–(46) with initial conditions at $t'=0$,

$$\tau_{M_bM_a}(0)=0,\quad \rho_{M_bM_b'}(0)=0,\quad \rho_{M_aM_a'}(0)=\rho_{M_aM_a'}, \tag{84}$$

where the right-hand sides of the equations coincide with the components of the density matrices (29) and (30) of the prealigned atoms. For a weak pulse (34), corresponding to the inequality (49), the solution of Eqs. (44)–(46) by successive approximations and with the initial conditions (84) has the form

$$\rho_{M_aM_a'}(t')=\rho_{M_aM_a'}+\rho_{M_aM_a'}^{(2)}(t'),$$

$$\rho_{M_bM_b'}(t')=\rho_{M_bM_b'}^{(2)}(t'), \tag{85}$$

where the term $\rho_{M_aM_a'}$, according to Eq. (29), describes the unperturbed state of the prealigned atom. This term does not contribute to the light-induced magnetization (48), since the series expansion of the density matrix $\rho_{M_aM_a'}$ in the $3j$ symbols (Eq. 32) does not contain any term with a multipole moment of the first rank. Thus, unlike a gas of pre-oriented atoms, a gas of prealigned atoms is not magnetized before the weak pulse (34) arrives. Here the time-dependent light-induced magnetization (48) depends only on the terms in Eq. (85) that are quadratic in the field (34). After summation

over the projections of the angular momenta, and using the notation Eqs. (58)–(60), we can write it in the following way:

$$\boldsymbol{\mu}(t')=\frac{\mu_B N}{\hbar^2}\int d\mathbf{v}f(v)\sum_{\kappa\tilde{q}\tilde{q}}\tilde{\mathbf{I}}^{\tilde{q}}\Big\{g_a F_q^{(\kappa)}(\tilde{q})I^a(t')$$
$$-g_b H_q^{(\kappa)}(\tilde{q})I^b(t')-\frac{g_a J_{aa}}{J_{bb}}H_q^{(\kappa)}(\tilde{q})$$
$$\times(-1)^{J_a+J_b}(2J_b+1)\begin{Bmatrix}J_a & 1 & J_a\\ J_b & 1 & J_b\end{Bmatrix}[I^a(t')$$
$$-I^b(t')]\Big\}+\text{c.c.}, \tag{86}$$

$$F_q^{(\kappa)}(\tilde{q})=\frac{|d_{ba}|^2 J_{aa}}{\sqrt{2J_a+1}}(-1)^{q+\tilde{q}}(2\kappa+1)$$
$$\times\rho_q^{(\kappa)}(J_a)\sum_{\kappa' q' q''}(2\kappa'+1)$$
$$\times(-1)^{q'}A_{q'}B_{q''}\begin{pmatrix}1 & 1 & \kappa'\\ -\tilde{q} & q'' & q+q'\end{pmatrix}$$
$$\times\begin{pmatrix}1 & \kappa & \kappa'\\ q' & q & -q-q'\end{pmatrix}\begin{Bmatrix}1 & 1 & \kappa'\\ J_a & J_b & J_a\end{Bmatrix}$$
$$\times\begin{Bmatrix}1 & \kappa & \kappa'\\ J_a & J_b & J_a\end{Bmatrix}, \tag{87}$$

$$H_q^{(\kappa)}(\tilde{q})=\frac{|d_{ba}|^2 J_{bb}}{\sqrt{2J_a+1}}(-1)^{q+\tilde{q}}(2\kappa+1)$$
$$\times\rho_q^{(\kappa)}(J_a)\sum_{\kappa' q' q''}(2\kappa'+1)$$
$$\times(-1)^{q''}A_{q'}B_{q''}\begin{pmatrix}1 & 1 & \kappa'\\ -\tilde{q} & q' & q+q''\end{pmatrix}$$
$$\times\begin{pmatrix}1 & \kappa & \kappa'\\ -q'' & -q & q+q''\end{pmatrix}\begin{Bmatrix}1 & 1 & \kappa'\\ J_b & J_a & J_b\end{Bmatrix}$$
$$\times\begin{Bmatrix}1 & \kappa & \kappa'\\ J_a & J_b & J_a\end{Bmatrix}. \tag{88}$$

In Eq. (86) the summation index κ coincides with the rank of the multipole moments $\rho_0^{(\kappa)}(J_a)$ associated with the initial state of the atom. Therefore κ assumes even values, including $\kappa=0$. The range of summation over κ and κ' in Eqs. (86)–(88) is dictated by the properties of the $3j$ and $6j$ symbols, and is given by

$$0\leqslant\kappa'\leqslant 2,\quad 0\leqslant\kappa\leqslant 2,\quad \kappa\leqslant 2J_a,$$

and by $\kappa\leqslant 2J_b$ for the third term in Eq. (86).

By virtue of the properties of the $3j$ symbols and the orthogonality of the vectors **A** and **B** to the z axis, the terms in Eq. (86) with $q=0$ and $\kappa=0,2$ are nonzero only for $\tilde{q}=0$. These terms can be calculated in the same way as for oriented atoms, and therefore the summations over the index κ for the principal quantities in Eqs. (87) and (88) in the case $q=0$ have the form

$$\sum_{\kappa=0,2}F_0^{(\kappa)}(\tilde{q})=S_{\tilde{q}},\quad \sum_{\kappa=0,2}H_0^{(\kappa)}(\tilde{q})=Q_{\tilde{q}}, \tag{89}$$

where $S_{\tilde{q}}$ and $Q_{\tilde{q}}$ are given by (61) and (62) with $\rho_0^{(\kappa)}\times(J_a,s)\to\rho_0^{(\kappa)}(J_a)$, which denotes a transition from an oriented atom to an aligned atom.

To calculate the remaining terms in Eq. (86) with $q\neq 0$ and $\kappa=2$, we use the equalities

$$\rho_{\pm 1}^{(2)}(J_a)=0,\quad \rho_{-2}^{(2)}(J_a)=\rho_2^{(2)}(J_a),$$

which follow from the properties of $d_{0q}^{\kappa}(\pm\pi/2)$ with $\kappa=2$ and $q=\pm 1,\pm 2$. In addition, we take advantage of the properties of the $3j$ symbols, which lead to the constraints

$$\tilde{q}=q+q'+q'',\quad |q+q'|\leqslant\kappa',\quad |q+q''|\leqslant\kappa',$$
$$\kappa'=1,\ 2$$

in formulas (87) and (88) with $\kappa=2$. These constraints are satisfied for $q'=\pm 1$ and $q''=\pm 1$ only if $\tilde{q}=0$, $q'=q''=\pm 1$ and $q=-2q'$. Therefore the sums of the principal quantities in (87) and (88) with $\kappa=2$ and $q\neq 0$ become

$$\sum_{q=\pm 2}F_q^{(2)}(\tilde{q})=\delta_{0\tilde{q}}\frac{5|d_{ba}|^2 J_{aa}}{\sqrt{2J_a+1}}\rho_2^{(2)}(J_a)$$
$$\times(A_{-1}B_{-1}-A_1B_1)F, \tag{90}$$

$$\sum_{q=\pm 2}H_q^{(2)}(\tilde{q})=-\delta_{0\tilde{q}}\frac{5|d_{ba}|^2 J_{bb}}{\sqrt{2J_a+1}}\rho_2^{(2)}(J_a)$$
$$\times(A_{-1}B_{-1}-A_1B_1)H, \tag{91}$$

where

$$F=\sum_{\kappa'}(2\kappa'+1)\begin{pmatrix}1 & 1 & \kappa'\\ 0 & 1 & -1\end{pmatrix}\begin{pmatrix}1 & 2 & \kappa'\\ 1 & -2 & 1\end{pmatrix}$$
$$\times\begin{Bmatrix}1 & 1 & \kappa'\\ J_a & J_b & J_a\end{Bmatrix}\begin{Bmatrix}1 & 2 & \kappa'\\ J_a & J_b & J_a\end{Bmatrix},$$
$$H=\sum_{\kappa'}(2\kappa'+1)\begin{pmatrix}1 & 1 & \kappa'\\ 0 & -1 & 1\end{pmatrix}\begin{pmatrix}1 & 2 & \kappa'\\ 1 & -2 & 1\end{pmatrix}$$
$$\times\begin{Bmatrix}1 & 1 & \kappa'\\ J_b & J_a & J_b\end{Bmatrix}\begin{Bmatrix}1 & 2 & \kappa'\\ J_a & J_b & J_a\end{Bmatrix}.$$

Using the explicit form for the vectors **A** and **B** when the axes of the polarization ellipse are rotated, we find, according to Eqs. (82) and (83),

$$A_{-1}B_{-1}-A_1B_1=\imath(A_xB_y+A_yB_x)$$
$$=i\sigma_{\mathbf{k}}\lambda\ \cos(2\psi)\sin(2\varphi_{\mathbf{k}}), \tag{92}$$

where

$$\lambda\ \cos(2\psi)=\mathbf{l}_{\mathbf{k}\lambda}^2,\quad \lambda=\pm 1.$$

After multiplying by $\mathbf{l}^{(0)}=\mathbf{l}_z$, we are able to use Eq. (92) to resolve the issue regarding the direction of $\boldsymbol{\mu}(t')$ in this problem. The appearance of the double angle $2\varphi_{\mathbf{k}}$, in con-

trast to Eq. (79), is a consequence of symmetry. For an aligned atom, only one of the two orthogonal symmetry axes is in this direction $\mathbf{l}_0$. Any direction of the third axis that is orthogonal to the other two is equally probable. Therefore the light-induced magnetization $\boldsymbol{\mu}(t')$ will remain the same regardless of whether $\mathbf{l}_{\mathbf{k}}^{(1)}$ is taken parallel or antiparallel to the third axis. These two directions of $\mathbf{l}_{\mathbf{k}}^{(1)}$ correspond to rotation by $\varphi_{\mathbf{k}}=\pi/2$ and $\varphi_{\mathbf{k}}=-\pi/2$. The invariance of $\boldsymbol{\mu}(t')$ under these rotations is secured by the factor $\sin(2\varphi_{\mathbf{k}})$. The results, Eqs. (89)–(92), allow us to write the light-induced magnetization (86) of a gas of pre-aligned atoms in the following way:

$$\boldsymbol{\mu}(t')=-(\mathbf{k}/k)\lambda\beta\,\sin(2\psi)\sum_{\kappa=0,2}\mu_0^{(\kappa)}(t') -(\mathbf{k}/k)\lambda\,\cos(2\psi)\sin(2\varphi_{\mathbf{k}})\mu_2^{(2)}(t'), \tag{93}$$

where

$$\mu_0^{(\kappa)}(t')=g_aD_a^{(\kappa)}M_{a0}^{(\kappa)}(t')+g_bD_b^{(\kappa)}M_{b0}^{(\kappa)}(t')+g_aD_{ab}^{(\kappa)} \times[M_{a0}^{(\kappa)}(t')-M_{b0}^{(\kappa)}(t')],\quad \kappa=0,\,2,$$

$$\mu_2^{(2)}(t')=g_aD_aM_{a2}^{(2)}(t')+g_bD_bM_{b2}^{(2)}(t')+g_aD_{ab} \times[M_{a2}^{(2)}(t')-M_{b2}^{(2)}(t')],$$

$$D_a=30\sqrt{2J_a+1}J_{aa}F,\quad D_b=30\sqrt{2J_a+1}J_{bb}H,$$

$$D_{ab}=30\sqrt{2J_a+1}J_{aa}H(-1)^{J_a+J_b}(2J_b+1) \times\begin{Bmatrix}J_a & 1 & J_a\\ J_b & 1 & J_b\end{Bmatrix},$$

$$M_{aq}^{(\kappa)}(t')=\frac{\mu_BN|d_{ba}|^2}{6(2J_a+1)\hbar^2}\int f(v)\rho_q^{(\kappa)}(J_a) \times I_q^a(t')d\mathbf{v},\quad \kappa,q=0,\,2,$$

$$M_{bq}^{(\kappa)}(t')=\frac{\mu_BN|d_{ba}|^2}{6(2J_a+1)\hbar^2}\int f(v)\rho_q^{(\kappa)}(J_a) \times I_q^b(t')d\mathbf{v},\quad \kappa,\,q=0,\,2,$$

$$I_2^a(t')=i[I^a{}^*(t')-I^a(t')],\quad I_2^b(t')=i[I^b{}^*(t') -I^b(t')]. \tag{94}$$

The quantities (94) are defined in the region $0\leqslant t'$, but after the pulse (34) passes they assume the characteristic form

$$I_2^a(t')=I_2^a(\tau),\quad I_2^b(t')=I_2^b(\tau)\exp[-\gamma(t'-\tau)],$$

$$\tau\leqslant t'.$$

In the case of an ultrashort pulse satisfying the inequalities $\gamma\tau\ll 1$ and (73), the following relation is true for the quantities (94):

$$I_2^a(t')=I_2(t'),\quad I_2^b(t')=I_2(t')\exp(-\gamma t'),\quad 0\leqslant t'. \tag{95}$$

where

$$I_2(t')=i\Bigg[\int_0^{t'}d\tau_2a(\tau_2) \times\exp(-i\Delta\tau_2)\int_0^{\tau_2}d\tau_1a^*(\tau_1) \times\exp(i\Delta\tau_1)-\int_0^{t'}d\tau_2a^*(\tau_2) \times\exp(i\Delta\tau_2)\int_0^{\tau_2}d\tau_1a(\tau_1)\exp(-i\Delta\tau_1)\Bigg]. \tag{96}$$

The final formula (93) retains the same form in the right-handed and left-handed coordinate systems. It contains the multipole moments $\rho_q^{(\kappa)}(J_a)$ ($\kappa=0,\,2$ and $q=0,\,\pm2$) of the atomic initial state generated by a strong linearly polarized pulse (27). The atomic states with $\rho_0^{(\kappa)}(J_a)$ for $\kappa=0,\,2$ have axial symmetry about the z axis, which is collinear with $\mathbf{k}_0$ and $\mathbf{k}$. Therefore the terms in Eq. (93) with $\kappa=0,\,2$ and $q=0$ do not depend on the orientation of the axes of the polarization ellipse. Moreover, the atomic states with $\rho_0^{(\kappa)}\times(J_a)$ for $\kappa=0,\,2$ are invariant under inversion and when $\mathbf{k}_0\to-\mathbf{k}_0$, and also with the replacement $\mathbf{l}_0\to-\mathbf{l}_0$, by virtue of the equalities $d_{00}^{(0)}(\pm\pi/2)=1$ and $d_{00}^{(2)}(\pm\pi/2)=-1/2$. From these properties of the initial states of an atom with $\rho_0^{(\kappa)}(J_a)$ for $\kappa=0,\,2$ it follows that for a weak pulse (34) there is only a single pseudovector (43) invariant under the replacement $\mathbf{k}_0\to-\mathbf{k}_0$ and $\mathbf{l}_0\to-\mathbf{l}_0$. This pseudovector vanishes for a linearly polarized pulse (34) with a polarization vector (35) for $\lambda=1$ and $\psi=0$, or (36) with $\lambda=-1$ and $\psi=\pi/2$. Here formula (76) and the related comments apply to the first term in Eq. (93) with $\rho_0^{(\kappa)}(J_a)=1$.

The last term in Eq. (93) with $\rho_2^{(2)}(J_a)$ takes into account pre-alignment of the atoms, which does not depend on the replacements $\mathbf{k}_0\to-\mathbf{k}_0$ and $\mathbf{l}_0\to-\mathbf{l}_0$. Here the orientation of the axes of the polarization ellipse is of fundamental importance. With this symmetry there exists a pseudovector $(\mathbf{k}/k)\sin(2\varphi_{\mathbf{k}})$ that is invariant under the replacements $\mathbf{k}_0\to-\mathbf{k}_0$, $\mathbf{k}\to-\mathbf{k}$, $\mathbf{l}_0\to-\mathbf{l}_0$, and $\lambda\to-\lambda$. For the amplitude, Eq. (78), the last term in Eq. (93) is an odd function of $\omega-\omega_{ba}$ if the dependence on $\mathbf{kv}$ in Eq. (94) can be neglected or if $\rho_2^{(2)}(J_a)$ is an even function of the velocity $\mathbf{v}$. Moreover, it vanishes for a circularly polarized pulse with $\psi=\pi/4$ and is nonzero for linear polarization, which is characterized by the vector (35) with $\lambda=1$ and $\psi=0$ or (36) with $\lambda=-1$ and $\psi=\pi/2$.

6. MAGNETIZATION OF A GAS BY AN OPTICAL PULSE TRAIN

To study experimentally the dependence of $\boldsymbol{\mu}(t')$ on the time t' and the detuning from resonance $\omega-\omega_{ba}$ with unchanged initial conditions, it is necessary to pass through the gas a sequence of pulses with the same polarization and amplitude but with different frequencies ω near the transition frequency ω_{ba}. Each successive pulse must pass through the gas under the same initial conditions, Eqs. (47) or (84). This is possible only when the initial conditions are produced by an intense ultrashort pulse and subsequent pulses are weak. The latter must be delayed by more than γ^{-1} in order to

permit the excited state of the atom generated by the intense pulse to decay before the series of weak pulses arrive. Then each weak pulse will make an adjustment to the initial conditions for the density matrix that is proportional to the square of the weak field.

These adjustments to the initial conditions within the framework of perturbation theory can be neglected in the passage of a series of weak pulses with shifted frequencies ω. Therefore, for each weak pulse, the light-induced magnetization $\boldsymbol{\mu}(t')$ at an arbitrary point in the gas will be described by the same formula, (68) or (93), with the initial time $t'=0$ taken at the instant the pulse arrives. Moreover, in order that the previous pulse not distort the time-dependent light-induced magnetization of the preceding pulse, the pulses must be separated by more than γ^{-1}.

In this scheme, in which the frequency ω is scanned, the weak pulse creates a residual static magnetization. However, this magnetization will not contribute to the emf in the pickup coil, Eq. (51), and therefore will not reflect on the results of the experimental investigations of the time-dependent light-induced magnetization created by an individual weak pulse.

It follows from this discussion that for experimental investigations it is advantageous to use a strong ultrashort pulse with circular or linear polarization, frequency ω_0, and pulse width τ_0 that satisfy the inequality $|\omega_0-\omega_{ba}-k_0u|\tau_0\ll 1$, in order that the multipole moments $\rho_0^{(\kappa)}(J_a,s)$ and $\rho_q^{(\kappa)}(J_a)$ of the optically polarized atoms not depend on the velocity $\mathbf{v}$. In addition, it is convenient to use a series of weak pulses with the pulse width (49) and amplitude (78) ordinarily used in experiment. From a fundamental point of view, the most interesting cases are those of a linearly polarized pulse (34) with the polarization vector (35), $\lambda=1$ and $\psi=0$, or (36) with $\lambda=-1$ and $\psi=\pi/2$, since for these cases the symmetry dependence in this problem is quite transparent. Under these conditions the time-dependent light-induced magnetizations, Eqs. (68) and (93), produced by a linearly polarized pulse with polarization vector $\mathbf{l}_{\mathbf{k}}^{(1)}$ (see Fig. 1) for $0\leqslant t'$ can be written as

$$\boldsymbol{\mu}(t')=-(\mathbf{k}_0/k_0)s\beta[V_0X_{a0}(t',\omega-\omega_{ba})+W_0X_{b0}\times(t',\omega-\omega_{ba})\exp(-\gamma t')],\quad 1\leqslant 2J_a, \tag{97}$$

for pre-oriented atoms and

$$\boldsymbol{\mu}(t')=-(\mathbf{k}/k)\sin(2\varphi_{\mathbf{k}})[V_2X_{a2}(t',\omega-\omega_{ba})+W_2X_{b2}(t',\omega-\omega_{ba})\exp(-\gamma t')],\quad 1\leqslant J_a, \tag{98}$$

for prealigned atoms, where

$$X_{a0}(t',\omega-\omega_{ba})=2(\tau a_0)^{-2}\int d\mathbf{v}f(v)\int_0^{t'}d\xi\int_0^{\xi}d\eta a_0(\xi)a_0(\eta)\exp[-\gamma(\xi-\eta)/2]\cos[\Delta(\xi-\eta)], \tag{99}$$

$$X_{b0}(t',\omega-\omega_{ba})=2(\tau a_0)^{-2}\int d\mathbf{v}f(v)\int_0^{t'}d\xi\int_0^{\xi}d\eta a_0\times(\xi)a_0(\eta)\exp[\gamma(\xi+\eta)]\cos[\Delta(\xi-\eta)], \tag{100}$$

$$X_{a2}(t',\omega-\omega_{ba})=2(\tau a_0)^{-2}\int d\mathbf{v}f(v)\int_0^{t'}d\xi\int_0^{\xi}d\eta a_0\times(\xi)a_0(\eta)\exp[-\gamma(\xi-\eta)/2]\times\sin[\Delta(\xi-\eta)], \tag{101}$$

$$X_{b2}(t',\omega-\omega_{ba})=2(\tau a_0)^{-2}\int d\mathbf{v}f(v)\int_0^{t'}d\xi\int_0^{\xi}d\eta a_0\times(\xi)a_0(\eta)\exp[\gamma(\xi+\eta)]\sin[\Delta(\xi-\eta)], \tag{102}$$

$$V_0=g_aM\sum_{\kappa=1,3}\rho_0^{(\kappa)}(J_a,1)(D_a^{(\kappa)}+D_{ab}^{(\kappa)}),$$

$$W_0=M\sum_{\kappa=1,3}\rho_0^{(\kappa)}(J_a,1)(g_bD_b^{(\kappa)}-g_aD_{ab}^{(\kappa)}),$$

$$V_2=g_2M\rho_2^{(2)}(J_a)(D_a+D_{ab}),$$

$$W_2=M\rho_2^{(2)}(J_a)(g_bD_b-g_bD_{ab}),$$

$$M=\frac{\mu_BN|d_{ba}|^2(a_0\tau)^2}{6(2J_a+1)\hbar^2}.$$

Here a_0 is the largest value of the amplitude $a_0(t')$ in the form of Eq. (78), and the quantities (99)–(102) are universal functions of t' and $\omega-\omega_{ba}$.

It can be seen from Eqs. (97) and (98) that for pre-oriented atoms, Eq. (97), $\boldsymbol{\mu}(t')$ is an even function of $\omega-\omega_{ba}$ and reverses direction with the independent replacements $\mathbf{k}_0\to-\mathbf{k}_0$ and $s\to-s$. However, for prealigned atoms, Eq. (98), $\boldsymbol{\mu}(t')$ is an odd function of $\omega-\omega_{ba}$, and reverses direction when the sign of $\omega-\omega_{ba}$ changes and when the angle $\varphi_{\mathbf{k}}$ passes through $0,\pm\pi/2$, and $\pm\pi$, and $\boldsymbol{\mu}(t')$ is proportional to $\sin(2\varphi_{\mathbf{k}})$. This behavior is fundamental, since they result from symmetry; they establish the direction of $\boldsymbol{\mu}(t')$ when a series of linearly polarized pulses pass through the gas.

The emf across the pickup coil, Eq. (51), can also be written in terms of universal functions:

$$U(t')=(\mathbf{nk}_0/k_0)s\beta\{U_0Y_{a0}(t',\omega-\omega_{ba})+\widetilde{U}_0[Y_{b0}(t',\omega-\omega_{ba})-\gamma\tau X_{b0}(t',\omega-\omega_{ba})]\times\exp(-\gamma t')\},\quad 1\leqslant 2J_a, \tag{103}$$

for pre-oriented atoms and

$$U(t')=(\mathbf{nk}/k)\sin(2\varphi_{\mathbf{k}})\{U_2Y_{a2}(t',\omega-\omega_{ba})+\widetilde{U}_2[Y_{b2}(t',\omega-\omega_{ba})-\gamma\tau X_{b2}(t',\omega-\omega_{ba})]\times\exp(-\gamma t')\},\quad 1\leqslant J_a, \tag{104}$$

for prealigned atoms, where

$$Y_{aq}(t',\omega-\omega_{ba})=\tau dX_{aq}(t',\omega-\omega_{ba})/dt', \tag{105}$$

$$Y_{bq}(t',\omega-\omega_{ba})+\tau dX_{bq}(t',\omega-\omega_{ba})/dt', \tag{106}$$

$$U_q=CV_q\tau^{-1}, \quad \widetilde{U}_q=CW_q\tau^{-1}, \quad q=0,2.$$

If the amplitude goes to zero at $t'=\tau$, $a_0(\tau)=0$, then the universal functions (105) and (106) for $\tau\leqslant t'$ are also zero, while the other functions (99)–(102) for $\tau\leqslant t'$ remain constant after $t'=\tau$. In this case the emfs given by Eqs. (103) and (104) at $\tau\leqslant t'$ can be written in relative units as

$$U(t')/\widetilde{U}_0=-(\mathbf{nk}_0/k_0)s\beta\gamma\tau X_{b0}(\tau,\omega-\omega_{ba}) \times\exp(-\gamma t'), \tag{107}$$

$$U(t')/\widetilde{U}_2=-(\mathbf{nk}/k)\sin(2\varphi_{\mathbf{k}})\gamma\tau X_{b2}(\tau,\omega-\omega_{ba}) \times\exp(-\gamma t'). \tag{108}$$

In the other possible case, $a_0(\tau)\neq 0$ and $a_0(t')=0$ at $\tau<t'$, the universal functions (105) and (106) are discontinuous at $t'=\tau$. Then (107) and (108) are valid when $\tau<t'$, without the isolated value $t'=\tau$. In both of these cases, Doppler broadening of the resonant transition changes the value of $X_{bq}(t',\omega-\omega_{ba})$ for $q=0,2$, but does not affect the exponential decay, $\exp(-\gamma t')$, at $\tau<t'$. Therefore the experimental determination of γ using of Eqs. (107) and (108) is an alternate method of Doppler-free spectroscopy[10] thanks to the high sensitivity of the experimental method using a pickup coil.

For small-area ultrashort pulses (Eq. (73)), the strong inequality $\gamma\tau\ll 1$ dictates that

$$X_{aq}(t',\omega-\omega_{ba})=X_{bq}(t',\omega-\omega_{ba})=X_q(t',\omega-\omega_{ba}), \tag{109}$$

$$Y_{aq}(t',\omega-\omega_{ba})=Y_{bq}(t',\omega-\omega_{ba})+Y_q(t',\omega-\omega_{ba}) \tag{110}$$

at $0\leqslant t'\leqslant\tau$, where the universal functions $X_q(t',\omega-\omega_{ba})$ and $Y_q(t',\omega-\omega_{ba})$ with $q=0,\ 2$ are given by (99)–(102), (105), and (106) in the absence of relaxation, $\gamma=0$. They satisfy the inequality

$$Y_q(t',\omega-\omega_{ba})\gg\gamma\tau X_q(t',\omega-\omega_{ba}), \quad q=0,\ 2,$$

which can violate only near $t'=\tau$. Therefore, for ultrashort pulses, the dependence of the emf, Eqs. (103) and (104), on the time t' and $\omega-\omega_{ba}$ at $0\leqslant t'<\tau$ takes the form

$$U(t')/(U_0+\widetilde{U}_0)=(\mathbf{nk}_0/k_0)s\beta Y_0(t',\omega-\omega_{ba}), \tag{111}$$

$$U(t')/(U_2+\widetilde{U}_2)=(\mathbf{nk}/k)\sin(2\varphi_{\mathbf{k}})Y_2(t',\omega-\omega_{ba}). \tag{112}$$

However, over the entire range $0\leqslant t'$, the emf can be calculated by means of (103) and (104), noting that $\gamma\tau\ll 1$.

The light-induced time-dependent magnetization $\boldsymbol{\mu}(t')$ at the initial time $t'=0$ is equal to zero, $\boldsymbol{\mu}(0)=0$, and at remote times $\gamma^{-1}\ll t'$ it becomes constant ($\boldsymbol{\mu}(\infty)$). Using this information and integrating both sides of Eq. (51), we find

$$\int_0^\infty U(t')dt'=-C\mathbf{n}\boldsymbol{\mu}(\infty). \tag{113}$$

Consequently the experimentally determined emf, $U(t')$, as a function of t' for an individual weak pulse of frequency ω permits us to find, by numerical integration, the universal functions (99) and (101) at frequency ω and $t'=\tau$:

$$\frac{\mathbf{nk}_0}{k_0}s\beta X_{a0}(\tau,\omega-\omega_{ba})=\frac{1}{U_0\tau}\int_0^\infty U(t')dt', \quad 1\leqslant 2J_a, \tag{114}$$

$$\frac{\mathbf{nk}}{k}\sin(2\varphi_{\mathbf{k}})X_{a2}(\tau,\omega-\omega_{ba})=\frac{1}{U_2\tau}\int_0^\infty U(t')dt', \quad 1\leqslant J_a, \tag{115}$$

where the left-hand sides of Eqs. (114) and (115) are related to the light-induced magnetization at $\gamma^{-1}\ll t'$ by means of Eq. (113).

Formulas (107)–(115) are suitable for experimental investigations of the vector properties of the light-induced magnetization and its dependence on t', $\omega-\omega_{ba}$, m_{at}, and N, since they relate the experimentally observed quantities in relative units to the universal functions and the factors $(\mathbf{nk}_0/k_0)s\beta$ and $(\mathbf{nk}/k)\sin(2\varphi_k)$, which are a result of symmetry. The universal functions of t' and $\omega-\omega_{ba}$ depend also on the relaxation constant γ, the amplitude $a_0(t')$ in relative units, the atomic mass m_{at}, and the gas temperature T. However, they do not depend on the angular momenta J_a or J_b, the g-factors g_a or g_b, the reduced dipole moment d_{ba}, or the atomic density N. Those latter factors enter into the constants U_q and $\widetilde{U}_q$ with $q=0,\ 2$, which serve as a scale for the experimental measurements of the emf in relative units.

In experiments with inhomogeneously broadened transitions, $\gamma\ll k_0u$, it is possible to realize the conditions $\gamma\ll 1/\tau_0\ll k_0u$, under which $\rho_0^{(\kappa)}(J_a,1)$ and $\rho_0^{(\kappa)}(J_a)$ depend on the velocity $\mathbf{v}$. Then to preserve the form of (107)–(112), (114), and (115), which contain the emf in relative units, it is necessary to use weak ultrashort pulses whose width τ satisfies $\gamma\ll ku\ll 1/\tau$ in order that the Doppler shift in Eqs. (99)–(102), (109), and (110) may be neglected. As a result, we can set $\int f(v)d\mathbf{v}=1$, and make the replacement

$$\rho_0^{(\kappa)}(J_a,1)\to\int f(v)\rho_0^{(\kappa)}(J_a,1)d\mathbf{v},$$

$$\rho_2^{(2)}(J_a)\to\int f(v)\rho_2^{(2)}(J_a)d\mathbf{v}.$$

in all the universal functions, and in the constants U_q and $\widetilde{U}_q$ with $q=0,\ 2$. Then, with the aid of Eqs. (107)–(115) we can study experimentally the vector properties of the light-induced magnetization and its dependence on t', $\omega-\omega_{ba}$, and γ. Other physical quantities enter into the constants U_q and $\widetilde{U}_q$ with $q=0,\ 2$.

In order to get an idea of how the light-induced magnetization and emf vary, we examine the universal functions (109) and (110) for an ultrashort pulse ($\gamma\tau\ll 1$) with a rectangular amplitude profile

$$a_0(t')=a_0 \quad \text{for} \quad 0\leqslant t'\leqslant\tau,$$

$$a_0(t')=0 \quad \text{for} \quad t'<0 \quad \text{and} \quad \tau<t', \tag{116}$$

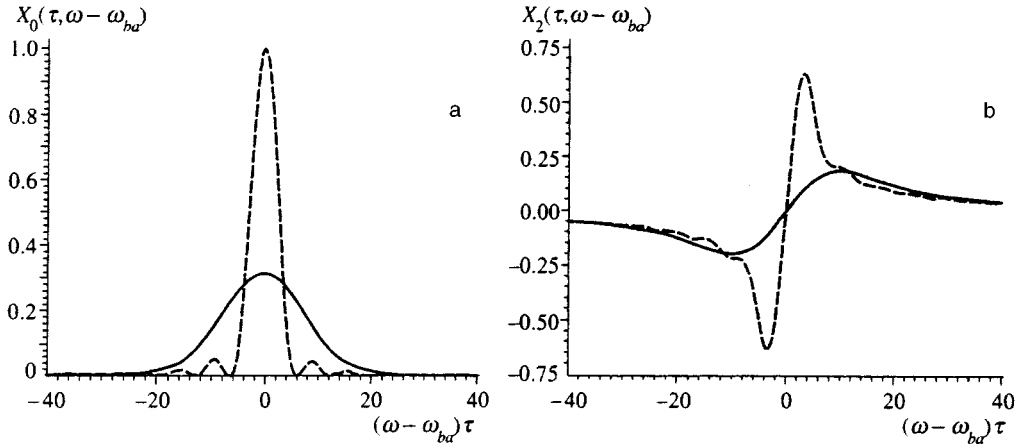

FIG. 2. Universal function $X_q(t',\omega-\omega_{ba})$ for $t'=\tau$ as a function of $\omega-\omega_{ba}$ for a rectangular amplitude profile (Eq. (116)). The solid curve includes the influence of the Doppler effect with $\tau=10\tau_D$. The dashed curves correspond to $10\tau=\tau_D$, where the Doppler effect can be neglected. a) $q=0$; b) $q=2$.

and with a Gaussian amplitude profile

$$a_0(t')=a_0\ \exp[-(t'-\tau/2)^2/(2\tau_p)^2],\quad 0\leqslant t'\leqslant\tau, \tag{117}$$

where $a_0(t')=0$ outside of the interval $0\leqslant t'\leqslant\tau$. Here a_0 and τ_p $(4\tau_p<\tau)$ are constants. The characteristic time τ_p enters into the spectral width $\Delta_\omega=\sqrt{2\ln 2}\,\tau_p^{-1}$ of the Gaussian pulse if the inequality $4\tau_p<\tau$ is sufficiently strong (for example, $8\tau_p\leqslant\tau$). In these examples the universal functions (109) with $q=0,\ 2$ have the form

$$X_0(t',\omega-\omega_{ba})=2\int_0^{t'/\tau}d\xi\int_0^{\xi}d\eta\ \cos[\delta(\xi-\eta)]\times\exp\{-\varepsilon[(\xi-1/2)^2+(\eta-1/2)^2]-(\tau/2\tau_D)^2(\xi-\eta)^2\}, \tag{118}$$

$$X_2(t',\omega-\omega_{ba})=2\int_0^{t'/\tau}d\xi\int_0^{\xi}d\eta\ \sin[\delta(\xi-\eta)]\times\exp\{-\varepsilon[(\xi-1/2)^2+(\eta-1/2)^2]-(\tau/2\tau_D)^2(\xi-\eta)^2\}, \tag{119}$$

$$\delta=(\omega-\omega_{ba})\tau,\quad \tau_D=1/ku,$$

with $\varepsilon=0$ for a rectangular amplitude profile, Eqs. (116), and $\varepsilon=(\tau/2\tau_p)^2$ for a Gaussian profile, Eq. (117). Here τ_D is the Doppler relaxation time. The two other universal functions (110) with $q=0,\ 2$ can be obtained by differentiating (118) and (119) with respect to t', according to Eqs. (105) and (106).

In the case of an inhomogeneously broadened transition, $\gamma\ll ku$, Fig. 2 shows the behavior of the universal function $X_q(\tau,\omega-\omega_{ba})$ with $q=0,\ 2$ as a function of the offset from resonance $\omega-\omega_{ba}$ for the rectangular amplitude profile (116). For an even function $X_0(\tau,\omega-\omega_{ba})$, the Doppler effect lowers and broadens the main bell-shaped maximum of these curves. The maximum of the odd function $X_2(\tau,\omega-\omega_{ba})$ in the absence of the Doppler effect $(10\tau=\tau_D)$ occurs for $\omega-\omega_{ba}=3.2/\tau$, whereas with a strong Doppler effect $(\tau=10\tau_D)$ we have $\omega-\omega_{ba}=9.8/\tau$. Away from resonance the quantity $X_2(\tau,\omega-\omega_{ba})$ goes to zero more slowly than $X_0(\tau,\omega-\omega_{ba})$.

To demonstrate the effect of the shape of the amplitude profile, Fig. 3 shows the behavior of the universal function $Y_q(t',\omega-\omega_{ba})$ with $q=0,\ 2$ as a function of $\omega-\omega_{ba}$ for $t'=\tau/2$ and the Gaussian amplitude profile, (117) with $\tau=8\tau_p$ $(\varepsilon=16)$. The fixed time $t'=\tau/2$ was selected arbi-

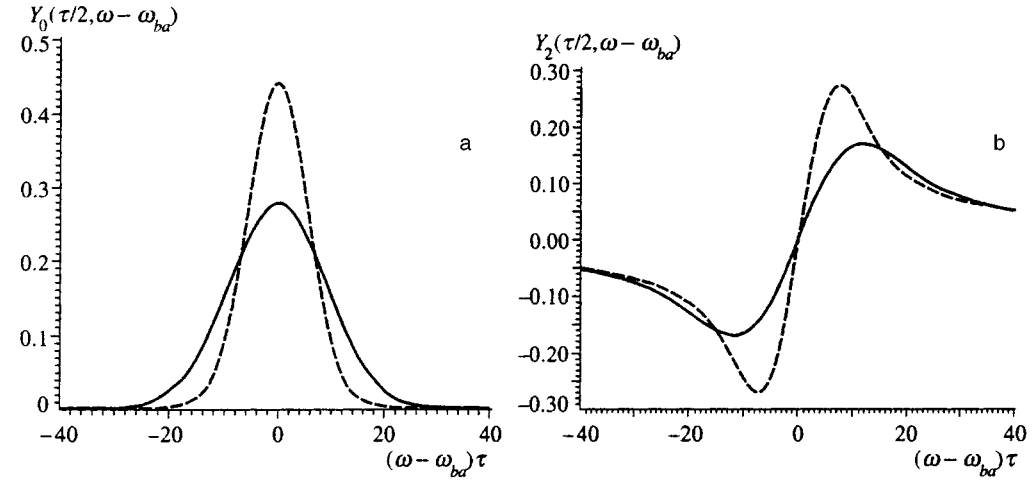

FIG. 3. Universal function $Y_q(t',\omega-\omega_{ba})$ for $t'=\tau/2$ as a function of $\omega-\omega_{ba}$ for a Gaussian amplitude profile (Eq. (117)) with $\tau=8\tau_p$ $(\varepsilon=16)$. The physical meaning of the solid and dashed curves is the same as in Fig. 2. a) $q=0$, b) $q=2$.

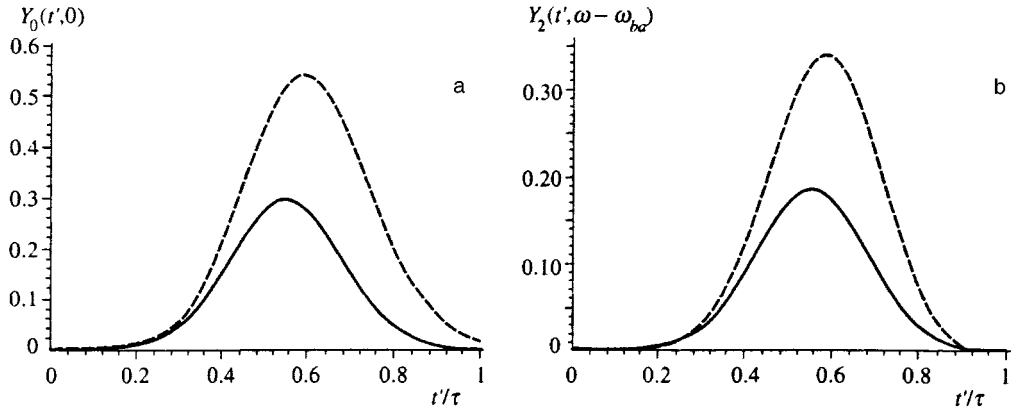

FIG. 4. Universal function $Y_q(t',\omega-\omega_{ba})$ as a function of t' for a fixed offset from resonance, $\omega-\omega_{ba}$, and a Gaussian amplitude profile with $\tau=8\tau_p$ ($\varepsilon=16$). The physical meaning of the solid and dashed curves is the same as in Fig. 2. a) $q=0$ and $\omega-\omega_{ba}=0$; b) $q=2$ and $\omega-\omega_{ba}=11.83/\tau$ (solid curve) and $7.45/\tau$ (dashed curve).

trarily. Here the Doppler effect affects the even functions with $q=0$ and the odd functions with $q=2$ identically, as in Fig. 2. The maximum of $Y_q(\tau/2,\omega-\omega_{ba})$ as an odd function of $\omega-\omega_{ba}$ is obtained in the absence of the Doppler effect ($10\tau=\tau_D$) at $\omega-\omega_{ba}=7.45/\tau$, and when the Doppler effect is strong ($\tau=10\tau_D$) the maximum is at $\omega-\omega_{ba}=11.83/\tau$.

Figure 4 shows the dependence of the universal function $Y_q(t',\omega-\omega_{ba})$ on the time t' for $q=0,\ 2$ and the Gaussian amplitude profile, (117) with $\tau=8\tau_p$ ($\varepsilon=16$). For $q=0$ we assume exact resonance ($\omega=\omega_{ba}$), corresponding to the optimum condition for $Y_q(t',\omega-\omega_{ba})$ as an even function of $\omega-\omega_{ba}$. For $q=2$, fixed offsets from resonance were selected, corresponding to the maximum of $Y_2\ (\tau/2,\omega-\omega_{ba})$ as an odd function of $\omega-\omega_{ba}$, as in Fig. 3. For a Gaussian amplitude profile symmetric about $t'=\tau/2$ the behavior of the universal functions is shown by asymmetric curves that undergo a Doppler effect.

7. DISCUSSION

If the first and second pulses in the train are strong, then the dependence on t' and on $\omega-\omega_{ba}$ in (68) and (93) changes. Nevertheless, the symmetry-related properties of light-induced magnetization are preserved. For example, for a strong linearly polarized second pulse, Eq. (68) retains the term in $(\mathbf{k}_0/k_0)s\beta$ and the even dependence on $\omega-\omega_{ba}$, while Eq. (93) retains the term with $(\mathbf{k}/k)\sin(2\varphi_{\mathbf{k}})$ and the odd dependence on $\omega-\omega_{ba}$, although these dependences on $\omega-\omega_{ba}$ will be described by more complicated functions. The solution of the problem with three strong pulses is quite complex, since the initial conditions for the third pulse change.

In atoms with nonzero nuclear spin I, light-induced magnetization assumes a more complicated form due to the existence of hyperfine levels, and because of optical pumping to nonresonant sublevels of the ground state hyperfine structure.[11,12] Despite these complications, the rules imposed by symmetry are preserved. Moreover, if the components of the hyperfine structure in the ground level E_a and excited level E_b are far enough apart, and if only two sublevels E_{F_a} and E_{F_b} with total angular momentum F_a and F_b are in resonance, then after the replacements

$$\omega_{ba}\to(E_{F_b}-E_{F_a})\hbar^{-1},\quad J_a\to F_a,\quad J_b\to F_b,$$

$$d_{ba}\to d_{F_bF_a},\quad N\to N/(2I+1)$$

the formulas derived in Sections 4–6 are valid over a time interval for which the depletion of the sublevel E_F by optical pumping is negligible. Here $d_{F_bF_a}$ is the reduced dipole moment of the transition $F_a\to F_b$.

In Ref. 1, Badalyan *et al.* published an experimental curve of the emf as a function of offset from resonance in rubidium vapor, with nuclear spin $I=5/2$ for the resonant transitions $5^2S_{1/2}\to5^2P^0_{1/2}$ and $5^2S^0_{1/2}\to5^2P^0_{3/2}$, using fairly weak linearly polarized pulses in the absence of a magnetic field, under the conditions $\gamma\tau\approx1$ and $\gamma\ll ku$. According to the published curve, light-induced magnetization of the rubidium vapor in the vicinity of each resonant frequency of the transition is an even function of $\omega-\omega_{ba}$ with a maximum at $\omega=\omega_{ba}$, which agrees with the magnetization of oriented rubidium atoms interacting with linearly polarized pulses. Additional experimental data are required for a more detailed analysis.

[1] A. M. Badalyan, A. A. Dabagyan, M. E. Movsesyan *et al.*, Izv. Akad. Nauk SSSR Ser. Fiz. **43**, 304 (1979).
[2] A. M. Badalyan, M. E. Movsesyan, and R. E. Movsesyan, JETP Lett. **29**, 534 (1979).
[3] A. I. Alekseev, Opt. Spektrosk. **75**, 842 (1993) [Opt. Spectrosc. J. **75**, 499 (1993)].
[4] A. I. Alekseev, Zh. Éksp. Teor. Fiz. **104**, 2954 (1993) [JETP **77**, 371 (1993)].
[5] I. I. Sobel'man, *Introduction to the Theory of Atomic Spectra* [in Russian], Nauka, Moscow (1977).
[6] D. A. Varshalovich, A. N. Moskalev, and V. K. Khersonskiĭ, *Quantum Theory of Angular Momentum* [in Russian], Nauka, Leningrad (1975).
[7] A. Bambini and P. R. Berman, Phys. Rev. A **23**, 2496 (1981).
[8] A. I. Alekseev, A. M Basharov, and V. N Beloborodov, Zh. Éksp. Teor. Fiz. **84**, 1290 (1983) [Sov. Phys. JETP **57**, 747 (1983)].
[9] L. D. Landau and E. M. Lifshitz, *Quantum Mechanics: Non-Relativisic Theory*, 3rd ed., Pergamon Press, Oxford (1977) [Russ. original 4th ed., Nauka, Moscow (1989)].
[10] V. S. Letokhov and V. P. Chebotaev, *Nonlinear High-Resolution Laser Spectroscopy* [in Russian], Nauka, Moscow (1990).
[11] A. I. Alekseev and N. A. Korotkova, Zh. Éksp. Teor. Fiz. **108**, 118 (1995). [JETP **81**, 63 (1995)].
[12] A. I. Alekseev and N. A. Korotkova, Laser Phys. **5**, 1147 (1995).

Translated by J. R. Anderson

Anomalies in resonant absorption line profiles of atoms with large hyperfine splitting

A. I. Parkhomenko, S. P. Pod'yachev, T. I. Privalov, and A. M. Shalagin

Institute of Automation and Electrometry, Siberian Branch of the Russian Academy of Sciences, 630090 Novosibirsk, Russia
(Submitted 28 June 1996)
Zh. Éksp. Teor. Fiz. **111**, 93–106 (January 1997)

We examine a monochromatic absorption line in the velocity-nonselective excitation of atoms when the components of the hyperfine stricture of the electronic ground states are optically pumped. We show that the absorption lines possess unusual substructures for some values of the hyperfine splitting of the ground state (which exceed the Doppler absorption linewidth severalfold). These substructures in the absorption spectrum are most apparent if the hyperfine structure of the excited electronic state is taken into account. We calculate the absorption spectra of monochromatic light near the D_1 and D_2 lines of atomic rubidium ^{85,87}Rb. With real hyperfine splitting taken into account, the D_1 and D_2 lines are modeled by 4- and 6-level diagrams, respectively. Finally, we show that atomic rubidium vapor can be successfully used to observe the spectral features experimentally. © *1997 American Institute of Physics.*
[S1063-7761(97)00601-X]

1. INTRODUCTION

Even in such simple atoms as those of alkali elements, the electronic ground state consists of a set of sublevels that are hyperfine components and magnetic sublevels. If the orbital angular momentum of the electrons in the ground state is zero (the *s* state), these sublevels are exceptionally long-lived: collisions with the particles of a nonmagnetic buffer gas and even with the walls (provided that the walls are specially treated) almost never lead to mixing of the populations of these sublevels. Because of this, for instance, the so-called effects of optical orientation and optical pumping are apparent in atoms of alkali metals (see, e.g., Ref. 1). The essence of such effects lies in the fact that even weak optical radiation in resonance with the transition to the closest excited electronic state of the atoms can create a pronounced and long-lived nonequilibrium distribution of populations over the sublevels of the ground state. In particular, such radiation can pump practically all the atoms (with which there is effective interaction) to a single component of the hyperfine structure. In a situation in which optical pumping is a minor effect (for example, the radiation intensity is so low that no pumping between the levels of the hyperfine structure occurs in the time it takes an atom to traverse the light beam), the monochromatic absorption line consists of separate lines corresponding to intra-atomic transitions. Under conditions of optical pumping and when other nonlinear effects are present, the absorption line profile can undergo considerable alteration.

Many theoretical and experimental investigations have been conducted in the laser spectroscopy of resonant transitions of atoms initiated by optical pumping within the hyperfine structure of the ground state. A characteristic feature of all such investigations is the velocity-selective excitation of absorbing atoms and, as a rule, hyperfine splitting that is moderate compared to Doppler broadening. Under such conditions, the absorption spectra consist of Doppler-broadened lines with nonlinear resonances, which emerge when two fields of different frequencies or different directions of propagation are employed (see, e.g., Refs. 2–5).

Atoms of alkali metals have served as the objects of such experiments. When only one monochromatic traveling wave is employed, optical pumping leads to formation of a single smooth absorption line occupying a position between the resonant transition frequencies associated with the components of the hyperfine structure (see, e.g., Refs. 3, 6, and 7). As hyperfine splitting grows, the line profile remains smooth, and its width is approximately equal to the size of the hyperfine splitting. The greater the hyperfine splitting in comparison to the Doppler linewidth, the stronger the pumping from one hyperfine component of the ground state to another. In this regard, Cs and Rb are the most typical of the alkali atoms, with hyperfine splitting exceeding Doppler widths by a factor close to 20.

This, briefly, is the picture of the absorption line profile (particularly for a monochromatic line) that the experimenter observes today in the presence of optical pumping between the levels of the hyperfine structure of the electronic ground states of atoms.

In the present investigation, we analyze what we believed to be a simple situation, the absorption of a monochromatic traveling wave by atoms with large hyperfine splitting of the ground state under conditions in which the atom–radiation interaction is velocity-nonselective. We arrived at a curious result: for certain ratios of the homogeneous and Doppler widths and within a certain range of hyperfine splittings (which are large compared to the Doppler width, so that Voigt profiles cannot be approximated by Doppler profiles), the absorption line profile ceases to be smooth and acquires substructure which, in general, is related to no real transitions in the atom. This substructure is even more devious when the hyperfine splitting of an excited electronic state is taken into account: the hyperfine splitting of an excited state adds to the deformation of the absorption line. As a result, the absorption line can acquire really strange shapes. What is characteristic is that strong deformations of the absorption line profile occur over a rather narrow range of values of the

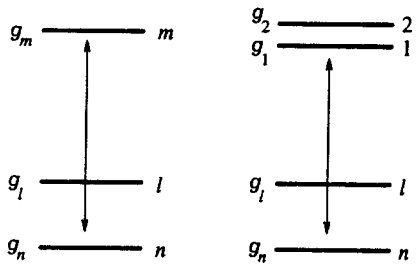

FIG. 1. Level diagrams for the three- and four-level models.

parameters of the problem. Outside this range, the absorption line behaves in full agreement with the picture described earlier. We also show that atomic rubidium vapor provides an appropriate medium in which to observe the predicted spectral anomalies.

The aim of the present work is to demonstrate the existence of anomalies in the absorption line profile of a monochromatic traveling wave under conditions of optical pumping and in velocity-nonselective excitation of the absorbing atoms, and to provide a physical interpretation of these anomalies.

2. THREE-LEVEL SYSTEM

We start our analysis with the simplest situation, in which the hyperfine splitting of the excited state can be ignored (three-level system; Fig. 1). Level m is the excited electronic state, and levels n and l are the components of the hyperfine structure of the ground state. From level m a particle radiatively relaxes only to levels n and l with constants Γ_{mn} and Γ_{ml}, respectively. Additional simplifications, which we use below, consist in the following. Magnetic structure (level degeneracy) is taken into account by introducing statistical weights g_m, g_l, and g_n. Such an approach is justified because even the presence of a weak laboratory magnetic field leads to precession of the magnetic moments and mixes the populations among the magnetic sublevels. We assume that the radiation represented by a traveling wave with frequency ω close to the frequencies of optical transitions, ω_{ml} and ω_{mn}, is so weak that saturation of the optical transitions can be ignored. The probability of absorption per unit time per atom, p, is described by the well-known simple formula

$$p=\sum_{j=n,l} p_j = I \sum_{j=n,l} B \int Y_j(\mathbf{v})\rho_j(\mathbf{v})d\mathbf{v}, \tag{1}$$

$$B=\frac{\pi^2 c^2}{\hbar\omega^3}\,\frac{g_m}{g_l+g_n}\,\Gamma_m,$$

$$Y_j(\mathbf{v})=\frac{1}{\pi}\,\frac{\Gamma}{\Gamma^2+(\omega-\omega_{mj}-\mathbf{k}\cdot\mathbf{v})^2}.$$

Here I and $\mathbf{k}$ are the intensity and wave vector of the radiation, $\Gamma_m=\Gamma_{mn}+\Gamma_{ml}$ is the rate of spontaneous decay of state m, Γ is the homogeneous halfwidth of the absorption line, $\rho_j(\mathbf{v})$ is the velocity distribution of the population of level j $(j=n,l)$, and B is Einstein's second coefficient (here we have allowed for the fact that $\Gamma_{mn}/\Gamma_{ml}=g_n/g_l$ in the selected three-level model[8]).

The absorption coefficient α is related to the absorption probability p:

$$\alpha=\frac{\hbar\omega N p}{I}, \tag{2}$$

where N is the number density of the absorbing particles.

The velocity distribution of the populations for the hyperfine sublevels of the ground state is assumed to be the equilibrium Maxwellian one:

$$\rho_j(\mathbf{v})=w_j W(\mathbf{v}), \quad j=n,\ l, \tag{3}$$

where w_j is the probability of finding the particle in level j. The assumption (3) is valid at least in the presence of a fairly small amount of buffer gas, which ensures rapid collisional Maxwellization in comparison to the time that the atom stays inside the light beam.

With allowance for (3), the partial absorption probability assumes the simple form

$$p_j=\gamma\,\frac{g_m}{g_n+g_l}\,w_j\,f(x_j), \tag{4}$$

$$f(x_j)=\frac{1}{\pi}\int_{-\infty}^{\infty}\frac{y\,\exp(-t^2)dt}{y^2+(x_j-t)^2}, \quad \gamma=\frac{\pi^2c^2}{\hbar\omega^3}\,\frac{\Gamma_m}{\sqrt{\pi}k\overline{v}}I,$$

$$x_j=\frac{\omega-\omega_{mj}}{k\overline{v}}, \quad y=\frac{\Gamma}{k\overline{v}}, \quad \overline{v}=\sqrt{\frac{2k_BT}{M}}.$$

Here $f(x_j)$ is the well-known Voigt profile, x_j is the frequency offset of the radiation from that of the corresponding atomic transition, normalized to the Doppler parameter $k\overline{v}$, and $\overline{v}$ is the most likely velocity (k_B is the Boltzmann constant, T is the temperature, and M is the mass of the atom).

In Eq. (4), not only does f depend on the frequency of the radiation, so does the probability w_j. This constitutes the essence of optical pumping: as the frequency of the radiation changes, the atoms become redistributed among the sublevels of the hyperfine structure of the ground state. The balance equations for w_j have the form

$$\left(\frac{d}{dt}+\Gamma_m\right)w_m=p_l+p_n,$$

$$\frac{d}{dt}\,w_l=\Gamma_{ml}w_m-p_l,$$

$$\frac{d}{dt}\,w_n=\Gamma_{mn}w_m-p_n, \quad w_m+w_n+w_l=1. \tag{5}$$

In the adopted approximation ($w_m\ll 1$ and $w_l+w_n\approx 1$) under steady-state conditions, Eqs. (4) and (5) yield

$$w_l=\frac{f(x_n)/g_n}{f(x_n)/g_n+f(x_l)/g_l}, \quad w_n=1-w_l. \tag{6}$$

The total absorption probability $p=p_l+p_n$ (over the transitions) is given by the well-known expression (see, e.g., Ref. 9)

$$p=\gamma g_m\left[\frac{g_l}{f(x_l)}+\frac{g_n}{f(x_n)}\right]^{-1}. \tag{7}$$

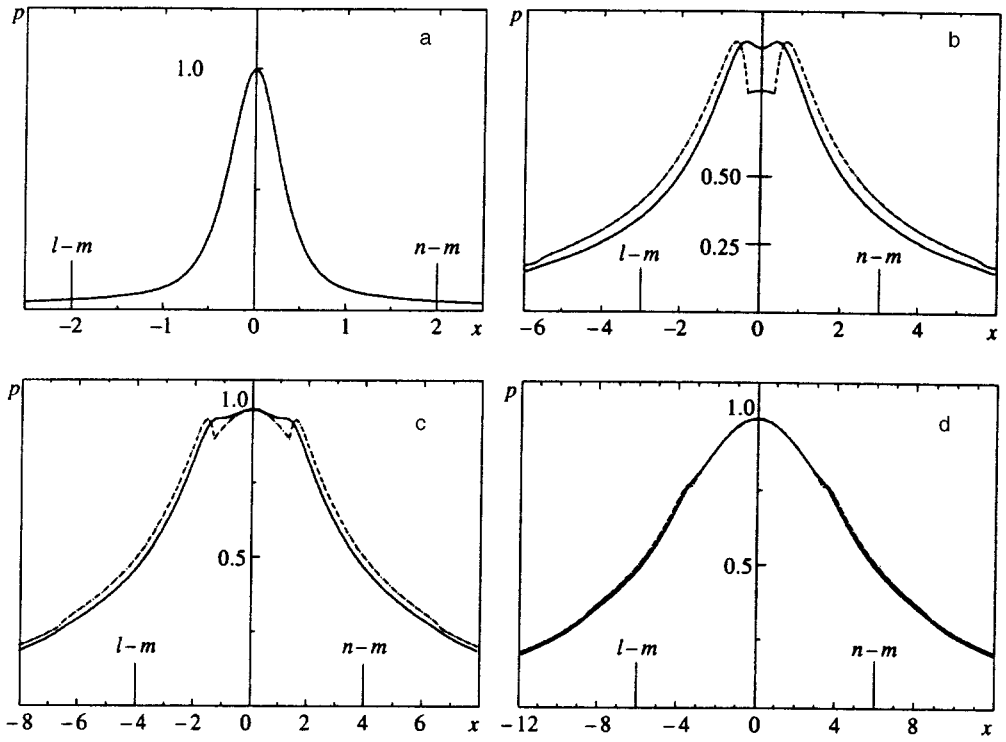

FIG. 2. Absorption probability $p(x)$ (in arbitrary units) given by Eq. (7) for a three-level absorbing particle at (a) $\Delta=4$, (b) 6, (c) 8, and (d) 12, with x the dimensionless relative offset, and $y=0.01$. The solid curves represent calculations that used the Voigt profile $f(x)$, and the dashed curves calculations that used the approximation (8). The vertical lines mark the positions of the transitions.

A formula similar to (7) for Doppler profiles ($f(x)$ is approximated by $\exp(-x^2)$) has been derived by Elbel *et al.*[3]

Let us examine the absorption line profile described by the given formula in the special case $y=\Gamma/(k\overline{v})=0.01$ (large Doppler broadening) and $g_n=g_l$ (symmetric three-level system). Figure 2 depicts $p(x)$, with

$$x=\frac{x_l+x_n}{2}=\left(\omega-\frac{\omega_{ml}+\omega_{mn}}{2}\right)\frac{1}{k\overline{v}},$$

for several characteristic values of the hyperfine splitting $\Delta=\omega_{ln}/(k\overline{v})$. At $\Delta=4$ and smaller, the absorption line has a smooth symmetric profile with a peak at $x=0$ (the average value of the atomic transition frequencies). However, beginning with $\Delta=6$, substructure unexpectedly appears in the absorption line profile. It first shows up as a narrow dip at $x=0$, and then (as Δ increases) two symmetrically disposed small ''bumps'' emerge. As Δ increases, the distance between the bumps grows and they become less and less pronounced. At $\Delta>10$, the profile essentially becomes smooth. What is characteristic here is that the special features of the line profile are not related to actual intra-atomic transitions—they are due entirely to the spectral features of the Voigt profile $f(x)$.

When Doppler broadening is large, $f(x)$ has a clearcut double structure (Fig. 3): a rapidly abating (Gaussian)central part, and smoothly abating Lorentzian wings. Indeed, let us roughly approximate the Voigt profile with the function

$$f(x)\simeq\begin{cases}\exp(-x^2), & |x|\leqslant x_0(y),\\ y/\sqrt{\pi}x^2, & |x|>x_0(y),\end{cases}\tag{8}$$

where the exponential function describes the central part of the Voigt profile ($x\lesssim 1$) for $y\ll 1$, and the function $y/\sqrt{\pi}x^2$ the asymptotic behavior of $f(x)$. The matching point $x_0(y)$ is determined by the condition

$$y=\sqrt{\pi}x_0^2\exp(-x_0^2),\tag{9}$$

where of the two values of x_0, we naturally select the one that is greater than unity. Figure 3 clearly shows that the transition from the central (Gaussian) part of the Voigt profile to the Lorentzian wings takes place right near $x=x_0$. What is characteristic here is that the function rapidly grows as we move from x_0 to the center of the line (it doubles as a result of displacement from x_0 by a distance much smaller than $k\overline{v}$), and slowly decreases as we move away from the center (by a factor of two as a result of a displacement from x_0 by a much greater distance).

The dashed curves in Fig. 2 depict the line profiles (7) with the approximation (8). In this case the substructure of

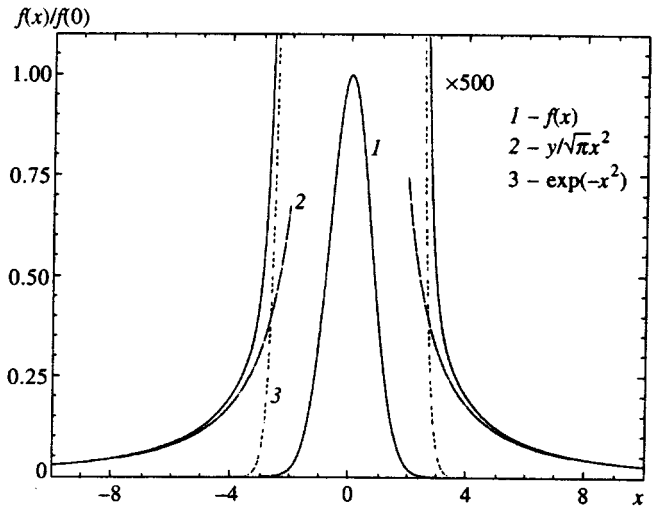

FIG. 3. Illustration of Eq. (8); $y=0.01$.

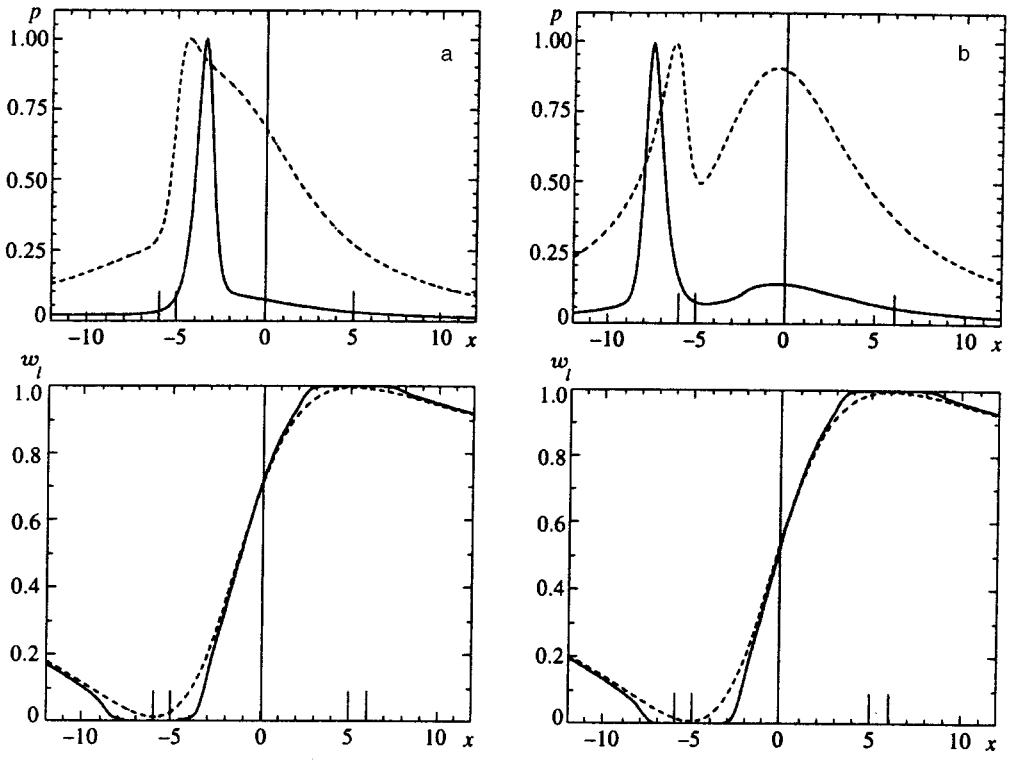

FIG. 4. Absorption probability $p(x)$ (in arbitrary units) given by Eq. (12) for a four-level absorbing particle, with w_l the probability of finding the particle at level l (Eq. (14)). The positions of the transitions are shown by vertical lines from left to right on the horizontal axis (dimensionless offset x): (a) $l\to1$, 2 and $n\to1$; and (b) $l\to1,2$ and $n\to2$.

the absorption line is especially obvious, the frequencies of the spectral features are essentially the same as for the actual profile, and the interpretation of these features is transparent.

If

$$\Delta>2x_0(y), \tag{10}$$

there are two characteristic spectral regions that lie within the absorption line: 1) closer to the line center ($|x|<\Delta/2-x_0$) the radiation interacts with both transitions due to the Lorentzian wings of the Voigt profile, and 2) farther from the line center ($|x|>\Delta/2-x_0$) the radiation interacts with one of the transitions (the closer one) via the Gaussian central part of the Voigt profile, and with the other via a Lorentzian wing. The indicated spectral features occur at the point of transition from one spectral region to another. The distance from these points to the closest atomic transition frequencies is close to x_0. Since $y=0.01$ in the example of Fig. 2, we have $x_0\simeq2.65$. Hence, the absorption line features can only show up when $\Delta>5.3$.

If in Eq. (7) we formally replace the Voigt profile by the Lorentzian profile $y/\sqrt{\pi}(x^2+y^2)$ (with the halfwidth at half-height $y=\sqrt{\ln 2}$), the absorption line spectral features completely disappear.

Note that in an asymmetric three-level system ($g_l\neq g_n$), with the absorption line shifted toward the transition with the greater statistical weight in the lower level, the aforementioned features are qualitatively retained, as is their frequency, but their amplitudes become asymmetric.

3. FOUR-LEVEL SYSTEM

It turns out that if the hyperfine splitting of the excited electronic state is taken into account, then under certain conditions the spectral features in question are considerably enhanced. An additional substructure also appears in the absorption line profile, due to a different physical cause.

In this connection we examine the four-level model system represented by Fig. 4. The components of the hyperfine structure of the excited state m are labeled by i, which assumes the values $i=1$, 2. We keep the previous notation for the hyperfine structure of the ground state: $j=l$, n. The absorption probability p_{ji} for the $j\to i$ transition has the following form (as in Sec. 3, we ignore nonlinear effects in optical transitions and assume that the velocity distribution of the ground-state hyperfine components is close to Maxwellian):

$$p_{ji}=\gamma\xi_{ji}f(x_{ij})w_j, \tag{11}$$

$$\xi_{ji}=\frac{g_i}{g_j}\frac{\Gamma_{ij}}{\Gamma_m},\quad x_{ij}=\frac{\omega-\omega_{ij}}{k\overline{v}},$$

$$\Gamma_m=\sum_j\Gamma_{ij},\quad j=n,\ l,\quad i=1,\ 2.$$

Here Γ_{ij} is the spontaneous decay rate (the first Einstein coefficient) for the transition $i\to j$, and the formulas for γ and ξ_{ji} follow from the expression for the second Einstein coefficient for the transition $j\to i$.[8] The total absorption probability is

$$p=\sum_{ij}p_{ij}=\gamma\sum_{i=1,2}\sum_{j=l,n}\xi_{ji}f(x_{ij})w_j. \tag{12}$$

Under steady-state conditions the balance equations corresponding to (5) for the probabilities w_i and w_j of finding the particle in levels i and j are

$$\Gamma_m w_i = \sum_{j=l,n} p_{ji}, \quad i=1,\ 2,$$

$$\sum_{i=1,2} \Gamma_{ij} w_i = \sum_{i=1,2} p_{ji}, \quad j=l,\ n. \tag{13}$$

Combining these equations with the approximate normalization condition $w_l + w_n \approx 1$, we obtain

$$w_l = \frac{\Gamma_{1l}\xi_{n1} f(x_{1n}) + \Gamma_{2l}\xi_{n2} f(x_{2n})}{\Gamma_{1l}\xi_{n1} f(x_{1n}) + \Gamma_{2l}\xi_{n2} f(x_{2n}) + \Gamma_{1n}\xi_{l1} f(x_{1l}) + \Gamma_{2n}\xi_{l2} f(x_{2l})},$$

$$w_n = 1 - w_l. \tag{14}$$

The rates Γ_{ij} of spontaneous decay of the excited state i via the channel $i \to j$ and the parameters ξ_{ij} in Eqs. (13) and (14) obey the relationships

$$\Gamma_{in} + \Gamma_{il} = \Gamma_m, \quad i=1,\ 2,$$

$$\xi_{j1} + \xi_{j2} = \frac{g_1 + g_2}{g_l + g_n}, \quad j=l,\ n. \tag{15}$$

The first relationship in (15) reflects the well-known fact[8] that the total rate Γ_m of spontaneous decay of an excited hyperfine sublevel i is the same for all hyperfine sublevels i of the excited state m. The second relationship follows from an analysis of the actual decay channels for the hyperfine components i: if the particle distribution over the hyperfine components of the excited state is an equilibrium one, spontaneous decay will also lead to an equilibrium population of the particles among the hyperfine components of the lower state.

In the special case in which the channels for the decay of levels 1 and 2 into levels l and n are proportional, i.e.,

$$\frac{\Gamma_{1l}}{\Gamma_{1n}} = \frac{\Gamma_{2l}}{\Gamma_{2n}}, \tag{16}$$

the formula for the absorption probability acquires the following simple form as a natural generalization of Eq. (7):

$$p = \frac{\gamma(g_1 + g_2)}{g_l[g_1 f(x_{1l}) + g_2 f(x_{2l})]^{-1} + g_n[g_1 f(x_{1n}) + g_2 f(x_{2n})]^{-1}}. \tag{17}$$

The absorption spectrum described by this formula contains features similar to those of the three-level system. There are twice as many because the number of optical transitions doubles, but their contrast remains about the same. The physical reason for the emergence of these features is the same, and derives from the properties of the Voigt profile. Replacing the Voigt functions by Lorentzians of the same characteristic width washes out these spectral structures and smoothes out the absorption line.

It turns out that if condition (16) is not met, i.e., levels 1 and 2 do not decay to levels n and l in the same proportion, the spectral features will be more pronounced. Their contrast becomes higher as the asymmetry of the decay channels for levels 1 and 2 increases. To clarify matters, we now examine instances in which one channel is completely forbidden.

a) $\Gamma_{2n} = 0, \quad \frac{\Gamma_{2l}}{\Gamma_m} = 1, \quad \frac{\Gamma_{1l}}{\Gamma_m} = \frac{1}{3}, \quad \frac{\Gamma_{1n}}{\Gamma_m} = \frac{2}{3}.$

In this case, Eq. (14) is transformed into (6) if x_l is replaced by x_{1l} and x_n by x_{1n}, i.e., the probability of finding the particle in levels n and l is totally insensitive to the existenceof level 2. The situation is straightforward since the action of the radiation on the transition $2 \to l$ can have no effect on optical pumping; level 2 decays and becomes populated via the same channel.

An absorption line meeting all these requirements is shown in Fig. 4a (solid curve) for

$$\Delta = \frac{\omega_{ln}}{k\bar{v}} = 11, \quad \delta = \frac{\omega_{12}}{k\bar{v}} = 1, \quad y = \frac{\Gamma}{k\bar{v}} = 0.01.$$

The substructure is clearly present, especially a narrow high peak. The maximum of this peak is shifted to the right of the lines of the transitions $1 \to l$ and $2 \to l$.

b) $\Gamma_{1n} = 0, \quad \frac{\Gamma_{1l}}{\Gamma_m} = 1, \quad \frac{\Gamma_{2l}}{\Gamma_m} = \frac{1}{3}, \quad \frac{\Gamma_{2n}}{\Gamma_m} = \frac{2}{3}.$

Here levels l and n are populated via the action of the radiation on the transitions $l \to 2$ and $n \to 2$, while level 1 has no effect on the process. The absorption line in Fig. 4b (solid curve) also has a pronounced narrow peak shifted to the left of the frequencies of the transitions $1 \to l$ and $2 \to l$.

If we replace the Voigt functions f by Lorentzians of the same width, the sharp spectral peaks are washed out both in case (a) and case (b). However, certain spectral irregularities near the $1 \to l$ and $2 \to l$ transitions still remain (dashed curves in Figs. 4a and b). The easiest way to understand why spectral features emerge is to examine the distribution of populations over sublevels n and l simultaneously as functions of the radiation frequency (Figs. 4a and b). Typically, because of the special properties of the Voigt function f, level l becomes severely depleted ($w_l \to 0$ and $w_n \to 1$) within a sizable spectral interval near the frequency of the transition $n \to 1$ (case (a)) or $n \to 2$ (case (b)). The population of level n behaves similarly ($w_n \to 0$, $w_l \to 1$) when the frequency of the radiation is in the vicinity of the frequency of the transition $n \to 1$ (case (a)) or $n \to 2$ (case (b)). The limits of this interval are determined precisely by x_0 of Eqs. (8) and (9), i.e., by the offset from resonance at which the Voigt function drastically changes its behavior.

The presence of an additional absorption channel that changes nothing in the behavior of the populations of levels n and l has the following consequences. In case (a), the additional channel (the transition $l \to 2$) is to the right of the transition $l \to 1$ on the frequency scale. Hence, as the radiation frequency moves from right to left, the additional channel affects absorption sooner. When the radiation frequency approaches to within x_0 of the frequency of the transition $l \to 2$, the Voigt function $f(x_{2l})$ increases sharply. At this point the level l is still largely populated. The result is a sharp rise in the absorption probability (specifically, in the $l \to 2$ channel). As the frequency becomes shifted still farther to the left, we land in a frequency interval where the level l is depleted, with the result that absorption drops once more. All this leads to a sharp peak in absorption, which is reflected by Fig. 4a (solid curve). Our reasoning suggests that the peak lies in the frequency range $\omega_{2l} + x_0 k\bar{v} > \omega > \omega_{1l} + x_0 k\bar{v}$, i.e., its position depends on the ratio be-

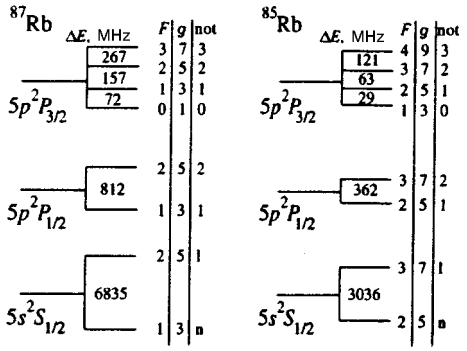

FIG. 5. The transition diagrams for the D_1- and D_2-lines of ^{85,87}Rb; here F is the total angular momentum of the atom, ΔE (MHz) is the distance between the sublevels of the hyperfine splitting, and g designates the statistical weights. The notation for the transitions used in the text is given in the ''not'' column.

tween Γ and $k\overline{v}$ and is in no way related to actual transitions in the atom. The same explanation holds for the peak in the absorption line in case (b), only now the peak is to the left of the frequencies of the $l\rightarrow 1$ and $l\rightarrow 2$ transitions, i.e., in the frequency range $\omega_{2l}-x_0k\overline{v}>\omega>\omega_{1l}-x_0k\overline{v}$.

If the Voigt profiles are replaced by Lorentzians of the same width, levels n and l become severely depleted only in the immediate vicinity of the corresponding transition frequencies. The spectral features then become less pronounced, and are more closely linked to the atomic transition frequencies: the additional absorption channel ($l\rightarrow 2$ in case (a) and $l\rightarrow 1$ in case (b)) leads to an abrupt change in the absorption probability near the frequency of the ''proper'' transition, which is quite natural.

4. ABSORPTION LINES OF RUBIDIUM ISOTOPES

Atomic rubidium vapor serves as a striking example of the experimental realization of the spectral features just discussed. The hyperfine splitting of the ground state of rubidium atoms is 6835 MHz for ^{87}Rb and 3036 MHz for ^{85}Rb, which is much larger than the Doppler linewidth. Figure 5 provides the parameters of the transitions in ^{85,87}Rb needed for calculations.[10] The four-level model considered in Sec. 3 (Eqs. (12) and (14)) is valid for calculating the absorption spectra of the D_1 lines. For the D_2 lines one must allow for the four sublevels of the hyperfine structure of the excited state, of which only two (levels 1 and 2 in the notation of Fig. 5) affect optical pumping (by virtue of the selection rules). Hence, the populations of levels l and n are still described by Eq. (14) of the four-level model. The total probability of absorption in the D_2 lines is given by

$$p=\sum_{ij} p_{ij}=\gamma\left[w_l\sum_{i=1,2,3}\xi_{li}f(x_{il})+w_n\sum_{i=0,1,2}\xi_{ni}f(x_{in})\right], \tag{18}$$

where the parameters were defined earlier. Below we give the ratios of the spontaneous decay constants of the hyperfine sublevels of the excited states in different channels:

$$^{85}\text{Rb}\begin{cases} D_1 \text{ line: } \dfrac{\Gamma_{1l}}{\Gamma_m}=\dfrac{7}{9},\ \dfrac{\Gamma_{1n}}{\Gamma_m}=\dfrac{2}{9},\ \dfrac{\Gamma_{2l}}{\Gamma_m}=\dfrac{4}{9},\ \dfrac{\Gamma_{2n}}{\Gamma_m}=\dfrac{5}{9}, \\ D_2 \text{ line: } \dfrac{\Gamma_{1l}}{\Gamma_m}=\dfrac{2}{9},\ \dfrac{\Gamma_{2l}}{\Gamma_m}=\dfrac{5}{9},\ \dfrac{\Gamma_{1n}}{\Gamma_m}=\dfrac{7}{9},\ \dfrac{\Gamma_{2n}}{\Gamma_m}=\dfrac{4}{9}, \end{cases}$$

$$^{87}\text{Rb}\begin{cases} D_1 \text{ line: } \dfrac{\Gamma_{1l}}{\Gamma_m}=\dfrac{5}{6},\ \dfrac{\Gamma_{1n}}{\Gamma_m}=\dfrac{1}{6},\ \dfrac{\Gamma_{2l}}{\Gamma_m}=\dfrac{1}{2},\ \dfrac{\Gamma_{2n}}{\Gamma_m}=\dfrac{1}{2}, \\ D_2 \text{ line: } \dfrac{\Gamma_{1l}}{\Gamma_m}=\dfrac{1}{6},\ \dfrac{\Gamma_{2l}}{\Gamma_m}=\dfrac{1}{2},\ \dfrac{\Gamma_{1n}}{\Gamma_m}=\dfrac{5}{6},\ \dfrac{\Gamma_{2n}}{\Gamma_m}=\dfrac{1}{2}, \end{cases}$$

$$\frac{\Gamma_{3l}}{\Gamma_m}=1,\quad \frac{\Gamma_{0n}}{\Gamma_m}=1,\quad \Gamma_{0l}=0,\quad \Gamma_{3n}=0. \tag{19}$$

For Γ_m we took the value $\Gamma_m\simeq 5.6$ MHz from Ref. 10. At room temperature the Doppler parameter $k\overline{v}$ for rubidium is roughly 300 MHz, so that the minimum value of $y\equiv\Gamma/(k\overline{v})$ is $\Gamma_m/(2k\overline{v})\simeq 0.01$. The absorption spectra for monochromatic light in the resonant transitions of rubidium for the given values of $k\overline{v}$ and y are depicted in Figs. 6 and 7 (solid

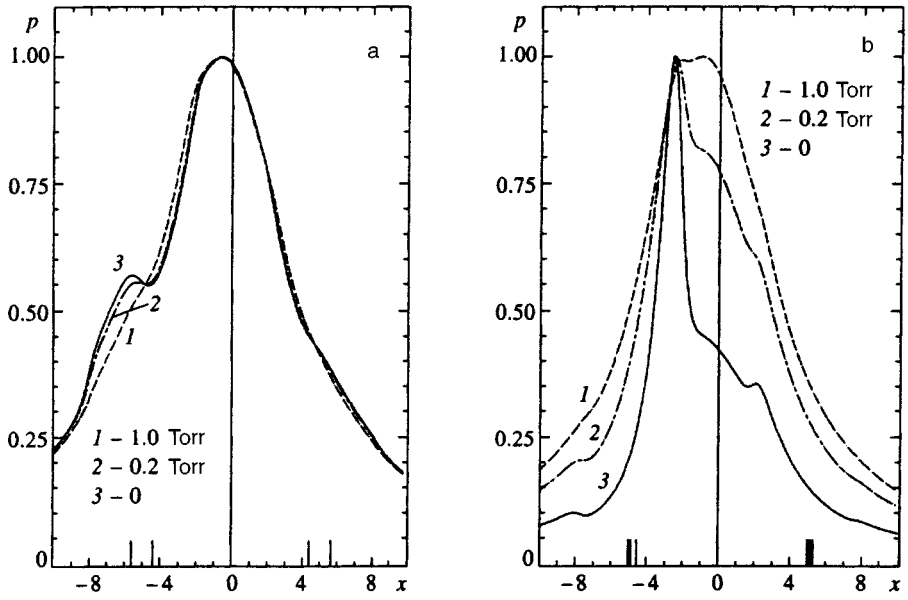

FIG. 6. The absorption probability $p(x)$ (in arbitrary units) for (a) the D_1 line and (b) the D_2 line of ^{85}Rb, with x the dimensionless offset (in units of $k\overline{v}$). The positions of the transitions are shown by vertical lines from left to right along the x axis: (a) $l\rightarrow 1,2$ and $n\rightarrow 1,2$; and (b) $l\rightarrow 1,2,3$ and $n\rightarrow 0,1,2$.

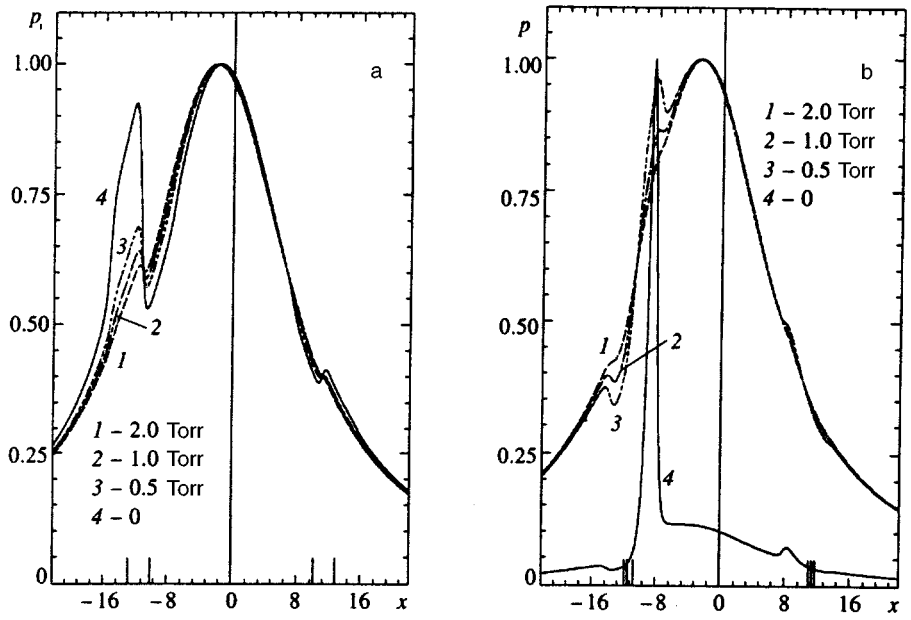

FIG. 7. The same as Fig. 6 for ^{87}Rb. The notation is also the same.

curves), where the spectral features are readily apparent. The number of features proved to be even greater than in the above model. The reason is that in the actual experiment, four absorption channels affect the populations of levels l and n, rather than two. One should therefore expect the spectral features to be present near all frequencies $\omega_{il} \pm x_0 k\overline{v}$ and $\omega_{in} \pm x_0 k\overline{v}$ $(i=1,2)$.quency scale.

Collisions with buffer-gas particles, even at low pressures, lead to significant washing out (smoothing) of the spectral features. Even inert buffer gases initiate efficient exchange within the hyperfine structure of the excited state. To describe this process, instead of Eqs. (13) we take the following equations (which model equilibrium mixing over the components of the hyperfine structure):

$$(\Gamma_m + \nu_m) w_i = \sum_{j=l,n} p_{ji} + \nu_m \frac{g_i}{g_m} w_m,$$

$$\sum_i \Gamma_{ij} w_i = \sum_i p_{ji}, \quad w_m = \sum_i w_i, \quad g_m = \sum_i g_i. \quad (20)$$

The label i assumes two or four values in the case of D_1 or D_2 lines, respectively. Here ν_m is the frequency of collisions that mix the sublevels of the hyperfine structure of the excited state (m). However, it is assumed that collisions have no effect on the distribution of populations over the levels l and n, which is sure to be the case for collisions with atoms of inert gases.

The variation of the linewidth Γ and frequency ν_m of mixing collisions with varying buffer-gas pressure is described by the characteristic parameter 9 MHz Torr^{-1} (see Ref. 11). The resulting transformation of the absorption spectrum is depicted in Figs. 6 and 7, which show that by $P=2$ Torr, all spectral structures become almost entirely washed out, and the spectral line smoothes out. The main reason for the blurring is collisional mixing of the hyperfine components, while colllisional broadening has only a minute effect on this deformation. In becomes clear, therefore, why Hamel *et al.*[6] and Streater *et al.*[7] failed to detect a single spectral feature discussed here. In their research, which involved the study of light-induced drift in rubidium, they also calculated the monochromatic-radiation absorption spectrum. However, they assumed from the start that the components of the hyperfine structure of the excited states are strongly mixed, with the result that the absorption line profile is smooth and featureless.

5. CONCLUSION

We have shown that as a result of optically pumping the hyperfine components of the atomic ground state, the absorption spectrum for monochromatic radiation in resonant transitions acquires unexpected sharp spectral features. This becomes especially evident if the hyperfine splitting of the excited state is taken into account. Collisions, which mix the hyperfine components of the excited electronic state, effectively blur these structures and smooth out the spectrum. One of the most appropriate experimental substances in which the spectral features can be observed is atomic rubidium gas. One must bear in mind, however, that the features show up within a rather narrow range of parameter values. Above all, there must be optical pumping, even in the absorption wings. This imposes lower limits on the radiation intensity and lifetime in a specified sublevel of the ground state hyperfine structure. If no special precautions are taken, the latter is restricted by the time that the atom spends inside the light beam, and increases with buffer-gas pressure. We saw, however, that the buffer gas disrupts the effect. Therefore, we cannot rule out the need to take radical steps in carrying out experiments of this type, for example, by covering the walls of the cell with paraffin. In this case the lifetime of the atom in a hyperfine sublevel increases dramatically.

The authors would like to express their gratitude to Profs. E. B. Aleksandrov, M. Ducloy, and F. Kh. Gel'mukhanov for fruitful discussions. The present work

was made possible by financial support from the International Science Foundation (Grant RCM 300), the Russian Fund for Fundamental Research (Grant No. 93-02-03567), the Netherlands Organization for Scientific Research (NWO), and the Universities of Russia Program.

[1] E. B. Aleksandrov, G. I. Khvostenko, and M. P. Chaĭka, *Interference of Atomic States*, Springer, New York (1993).
[2] T. W. Hänsch, I. S. Shanin, and A. L. Schawlow, Phys. Rev. Lett. **27**, 707 (1971).
[3] M. Elbel, H. Hühnermann, Th. Meier, and W. B. Schneider, Z. Phys. A **275**, 339 (1975).
[4] V. L. Velichanskiĭ, A. S. Zibrov, V. V. Kargopol'skiĭ *et al.*, Kvant. Elektron. (Moscow) **7**, 10 (1980).
[5] A. M. Akul'shin, V. L. Velichanskiĭ, R. G. Gaṃidov, A. Ch. Izmaĭlov, V. V. Popovichev, and V. A. Sautenkov, Zh. Éksp. Teor. Fiz. **99**, 107 (1991) [Sov. Phys. JETP **72**, 58 (1991)].
[6] W. A. Hamel, A. D. Streater, and J. P. Woerdman, Opt. Commun. **63**, No. 1, 32 (1987).
[7] A. D. Streater, J. Mooibroek, and J. P. Woerdman, Opt. Commun. **64**, No. 2, 137 (1987).
[8] I. I. Sobelman, *Introduction to the Theory of Atomic Spectra*, Pergamon Press, Oxford (1973).
[9] S. N. Atutov, A. I. Parkhomenko, S. P. Pod''yachev, and A. M. Shalagin, Zh. Éksp. Teor. Fiz. **99**, 378 (1991) [Sov. Phys. JETP **72**, 210 (1991)].
[10] A. A. Radtsig and B. M. Smirnov, *Reference Data on Atoms, Molecules, and Ions*, Springer, Berlin (1985).
[11] N. Allard and J. Kielkopf, Rev. Mod. Phys. **54**, 4 (1982).

Translated by Eugene Yankovsky

High density current drive by high frequency radiation

V. P. Silin and S. I. Uryupin

P. N. Lebedev Physics Institute, Russian Academy of Sciences, 117924 Moscow, Russia
(Submitted 20 May 1996)
Zh. Éksp. Teor. Fiz. **111**, 107–119 (January 1997)

A self-consistent theory is developed for current drive by intense radiation in the presence of the ion-acoustic instability. The spectrum of ion-acoustic turbulent noise generated by the driven current and concentrated in a limited cone of angles along the propagation direction of the wave is found. Excitation of the instability is accompanied by the establishment of an electron drift that is excited by the electromagnetic wave and has a velocity on the order of the ion acoustic speed. This current drive regime is realized over a wide range of intensities, as long as the region of turbulence in the angles of the acoustic wave vector is expanding. At yet higher intensities, the driven current increases in proportion to the intensity of the fundamental wave. Similar behavior is found for driven heat fluxes. [S1063-7761(97)00701-4]

1. INTRODUCTION

The generation of quasistationary currents by high frequency electromagnetic radiation is of interest in connection with the development of diagnostic techniques for laser plasmas,[1] as well as in connection with the problem of generating megagauss magnetic fields.[2] Many papers have been devoted to theories for the generation of possible quasistationary currents in laminar plasmas, where the main mechanism for electron scattering is on ions.[3–10] Of the types of currents discussed, current drive owing to the pressure of light on the electrons is of special interest. Numerical estimates[3] show that for the laser light intensities presently available, current drive at high densities with a characteristic electron drift velocity u_d comparable to the electron thermal velocity v_T is possible in laminar plasmas. At such high electron drift velocities, however, the plasma is unstable with respect to the ion-acoustic instability. This means that the theory of high density current drive with $u_d \gtrsim v_s$, where v_s is the ion acoustic speed, must, on one hand, take the possible development of the ion-acoustic instability into account and, on the other, account for the reverse effect of turbulence on the formation of the driven current itself. A self-consistent theory of this type for current drive in plasmas with ion-acoustic turbulence is presented in this paper. The need for a new theory arises for radiation intensities that satisfy the condition

$$I\left[\frac{\mathrm{W}}{\mathrm{cm}^2}\right] > 4\cdot 10^{14}\sqrt{\frac{Z}{A}}\,\lambda^{-2}[\mu\mathrm{m}]\sqrt{\frac{T[\mathrm{eV}]}{100}},$$

where Z is the degree of ionization of the ions, A is the mass number, T (eV) is the electron temperature, and λ (μm) is the wavelength of the radiation. As shown in Sec. 2, here the driven current excites the ion-acoustic instability. It is also shown there that along with the ion-acoustic instability the intense radiation causes the Weibel instability to develop. The growth rate for the Weibel instability is found and the conditions under which its effect on current drive can be neglected are formulated. In Sec. 3 a self-consistent theory is presented for the spectrum of the ion-acoustic turbulence excited by a driven current. The quasistationary distribution is found for the density of wave numbers $N(\mathbf{k})$ with respect to wave number $\mathbf{k}$ that develops as a result of the competition between Cherenkov acoustic emission by the driven current, the absorption of sound during a Cherenkov interaction with resonant ions, and stimulated scattering on thermal ions. Here the same type of frequency distribution of the ion-acoustic turbulence is established as in the theory of the anomalous resistance of current-carrying plasmas. The distribution of the turbulent noise over the angles of the wave vector, however, is new. It is unique because, even at high levels above threshold, the turbulent noise region is concentrated within a cone of angles smaller than a maximum of $\theta_m \simeq 43.6°$. This latter property is crucial to the behavior of the driven electron currents studied in Sec. 4. It is shown that the excitation of ion-acoustic turbulence leads to the establishment of a driven current with an electron drift velocity $u_d \sim (1+\delta)v_s$, where the parameter δ characterizes the Cherenkov damping of sound on hot resonant ions. Currents at this level are maintained over a wide range of radiation intensities until, as the excess above threshold increases, the region of turbulence in the angles of the wave vector continues to expand. At still higher intensities, the driven current rises in proportion to the intensity of the laser light, but much more slowly than in a laminar plasma. Similar behavior is found for driven heat fluxes, which are generated much less efficiently owing to the excitation of ion-acoustic turbulence.

2. KINETICS OF LAMINAR PLASMAS

Consider a circularly polarized electromagnetic wave with frequency ω_0 and wave vector $\mathbf{k}_0=(0,0,k_0)$ in a fully ionized plasma,

$$\frac{1}{2}\,\mathbf{E}\,\exp(-i\omega_0 t + i\mathbf{k}_0\cdot\mathbf{r}) + \text{c.c.}, \tag{2.1}$$

where $\mathbf{E}=(E,iE,0)/\sqrt{2}$ and E is the electric field strength. We shall assume that the wave frequency ω_0 is much higher than both the electron plasma frequency ω_{Le} and their collision frequency. Under these conditions the phase and group

velocities of the wave are close to the speed of light, i.e., $\omega_0/k_0 \simeq c$ and the small change in the wave amplitude owing to collisional absorption can be neglected. We assume that the amplitude of the velocity of the oscillations of an electron in the wave field,

$$v_E = |\mathbf{v}_E| = |e\mathbf{E}/m\omega_0|$$

(e and m are the electron charge and mass), is less than the electron thermal speed v_T. Then the action of the wave on the electrons can be described by a perturbation theory, writing the electron distribution function in the form of an expansion in terms of harmonics of the fundamental frequency that decrease with increasing harmonic number. We write down a kinetic equation for the main part of the distribution function $f = f(\mathbf{v},t)$ averaged over the wave period in the form

$$\frac{\partial}{\partial t} f + \left\{ \frac{1}{4} \left(\mathbf{v}_E \cdot \frac{\partial}{\partial \mathbf{v}} \right) \mathrm{St} \left[\left(\mathbf{v}_E^* \cdot \frac{\partial f}{\partial \mathbf{v}} \right) \right] + \mathrm{c.c.} \right\} + \left\{ \frac{1}{4} \left(\mathbf{v}_E \times \frac{\partial}{\partial \mathbf{v}} \right) \mathrm{St} \left[\frac{(\mathbf{k}_0 \cdot \mathbf{v})}{\omega_0} \left(\mathbf{v}_E^* \cdot \frac{\partial f}{\partial \mathbf{v}} \right) \right] + \mathrm{c.c.} \right\} + \left\{ \frac{1}{4} (\mathbf{v} \cdot \mathbf{v}_E) \left(\mathbf{k}_0 \times \frac{\partial}{\partial \mathbf{v}} \right) \frac{1}{\omega_0} \mathrm{St} \left(\mathbf{v}_E^* \cdot \frac{\partial f}{\partial \mathbf{v}} \right) + \mathrm{c.c.} \right\} = \mathrm{St}(f) + \mathrm{St}(f,f), \tag{2.2}$$

where $\mathrm{St}(f,f)$ is the electron–electron collision integral and

$$\mathrm{St}(f) = \frac{1}{2} \nu(v) \frac{\partial}{\partial v_\alpha} (v^2 \delta_{\alpha\beta} - v_\alpha v_\beta) \frac{\partial}{\partial v_\beta} f \tag{2.3}$$

is the electron–ion collision integral. In Eq. (2.3)

$$\nu(v) = 4\pi Z e^4 n \Lambda / m^2 v^3$$

is the electron–ion collision frequency, n is the electron density, and Λ is the Coulomb logarithm. In deriving Eq. (2.2) we have neglected the effect of electron–electron collisions on the high frequency first harmonic of the distribution function, which is justified for $Z \gg 1$. In addition, Eq. (2.2) has been written taking into account the smallness of the field-induced anisotropy in the distribution function f. The difference between f and the isotropic function f_0 is small in view of the smallness of the parameters v_E^2/v_T^2 and $(\mathbf{k}_0 \cdot \mathbf{v})/\omega_0$, i.e., $f = f_0 + \delta f$, where

$$|\delta f| \ll f_0 = \int d\Omega f / 4\pi,$$

and $d\Omega$ is the element of solid angle for the velocity vector. The equation for f_0 is obtained by averaging over the directions of the velocity in Eq. (2.2) and has the form[11,12]

$$\frac{\partial}{\partial t} f_0 = \frac{v_E^2}{6v^2} \frac{\partial}{\partial v} \left[\nu(v) v^2 \frac{\partial f_0}{\partial v} \right] + \mathrm{St}(f_0, f_0). \tag{2.4}$$

In Eq. (2.4) we have left out the small electron–ion collision integral $\mathrm{St}(f_0)$ which describes the slow exchange of energy between the electrons and ions. Subtracting Eq. (2.4) from Eq. (2.2), we obtain an equation for the quasistationary axially symmetric anisotropic correction δf at times greater than the electron momentum relaxation time, $t \gg 1/\nu(v)$,

$$\frac{1}{4} \left(\xi^2 - \frac{1}{3} \right) v_E^2 v \frac{\partial}{\partial v} \left[\frac{\nu(v)}{v} \frac{\partial f_0}{\partial v} \right] - \xi(1-\xi^2) \frac{k_0}{\omega_0} v_E^2 v^2 \frac{\partial}{\partial v} \left[\frac{\nu(v)}{v} \frac{\partial f_0}{\partial v} \right] - \frac{3}{2} \xi \frac{k_0}{\omega_0} v_E^2 \nu(v) \frac{\partial f_0}{\partial v} = \frac{1}{2} \nu(v) \frac{\partial}{\partial \xi} (1-\xi^2) \frac{\partial}{\partial \xi} \delta f, \tag{2.5}$$

where $\xi = \cos\theta$ and θ is the angle between the velocity vector $\mathbf{v}$ and $\mathbf{k}_0$. We seek a solution to Eq. (2.5) in the form of the sum $\delta f = \delta f_+ + \delta f_-$ of even δf_+ and odd δf_- functions of the variable ξ. Then, given that $\xi^2 - 1/3$ is an eigenfunction of the electron collision operator, for δf_+ we have

$$\delta f_+ = \frac{1}{12} \left(\frac{1}{3} - \xi^2 \right) v_E^2 \frac{v}{\nu(v)} \frac{\partial}{\partial v} \left[\frac{\nu(v)}{v} \frac{\partial f_0}{\partial v} \right]. \tag{2.6}$$

In turn, using the regularity condition for the derivative $\partial \delta f_- / \partial \xi$ at $\xi = \pm 1$, for the function δf_- we obtain

$$\frac{\partial}{\partial \xi} \delta f_- = \frac{3}{2} \frac{k_0}{\omega_0} v_E^2 \frac{\partial f_0}{\partial v} + (1-\xi^2) \frac{k_0 v_E^2}{2\omega_0} \frac{v^2}{\nu(v)} \frac{\partial}{\partial v} \left[\frac{\nu(v)}{v} \frac{\partial f_0}{\partial v} \right]. \tag{2.7}$$

Equations (2.6) and (2.7) contain the function f_0, which is a solution of Eq. (2.4). We limit ourselves to examining Eq. (2.4) in the case of frequent electron–electron collisions, for which $v_T^2 \gg Z v_E^2$. Then it is possible to neglect the difference between f_0 and the Maxwellian distribution function f_m. In addition, when Eqs. (2.6) and (2.7) are used, we shall assume that the Coulomb logarithm Λ which enters into the definition of the frequency $\nu(v)$ is independent of the velocity.

The corrections δf_+ and δf_- determine various physical phenomena. In particular, the function δf_+ can be used to find the growth rate for the Weibel instability. Using the general dispersion relation[13] for electromagnetic perturbations of the form $\exp(\gamma t + iqz)$, in the limit $|\gamma| \ll q v_T$ we have the following expression for the growth rate:

$$\gamma = -\sqrt{\frac{2}{\pi}} q v_T \left[\frac{1}{2n} \int d\mathbf{v} (1-\xi^2) \times \left(v \frac{\partial}{\partial v} + \frac{1-\xi^2}{\xi} \frac{\partial}{\partial \xi} \right) \delta f_+ + \frac{q^2 c^2}{\omega_{Le}^2} \right]. \tag{2.8}$$

Taking the explicit form (2.6) for δf_+, from Eq. (2.8) we find

$$\gamma = \gamma_m \frac{q}{2q_m} \left(3 - \frac{q^2}{q_m^2} \right), \tag{2.9}$$

and

$$\gamma_m = \frac{\omega_{Le}}{27} \sqrt{\frac{8}{\pi}} \frac{v_E^3}{c v_T^2}, \quad q_m = \frac{v_E}{3v_T} \frac{\omega_{Le}}{c}. \tag{2.10}$$

According to Eq. (2.9), the instability can develop if the spatial scale length of the perturbations is sufficiently long:

$L_q = 1/q > 1/q_m\sqrt{3}$. Perturbations with a scale length of $1/q_m$ have the maximum growth rate $\gamma = \gamma_m$. Chaotic helical magnetic fields develop in the plasma owing to the Weibel instability. In the nonlinear state, when the level of long wavelength electromagnetic fluctuations attains a maximum value, the intensity of the helical magnetic fields can be estimated using the formula $B^2/4\pi \sim nmv_E^2$. In the following we restrict ourselves to conditions such that the influence of the magnetic fields on the electron kinetics can be neglected. This is clearly possible when the characteristic electron cyclotron frequency $\Omega = |e|B/mc$ is lower than the self-collision rate of the thermal electrons with $v \sim v_T$. The latter condition together with the estimate for the magnetic field strength can be written in the form $\nu(v_T) > \omega_{Le} v_E/c$.

Under the above conditions the electron charge and heat fluxes are oriented in the direction of propagation of the electromagnetic wave and are determined by the function δf_-. By definition, the current density J and the electron heat flux Q_T are

$$J = e\int d\mathbf{v}\xi v\,\delta f_- = e\pi\int_{-1}^{1} d\xi(1-\xi^2)\int_0^\infty dv v^3\,\frac{\partial}{\partial\xi}\,\delta f_-, \tag{2.11}$$

and

$$Q_T = \frac{m}{2}\int d\mathbf{v}\xi v^3\delta f_- = \frac{\pi}{2}\,m\int_{-1}^{1} d\xi(1-\xi^2) \times\int_0^\infty dv v^5\,\frac{\partial}{\partial\xi}\,\delta f_-. \tag{2.12}$$

Using Eq. (2.7), from these we finally have

$$\mathbf{J} = 1.7en\,\frac{\mathbf{k}_0}{\omega_0}\,v_E^2, \tag{2.13}$$

and

$$\mathbf{Q}_T = \frac{25}{4}\,nmv_T^2\,\frac{\mathbf{k}_0}{\omega_0}\,v_E^2. \tag{2.14}$$

Equation (2.14) describes the heat flux driven by the high frequency electromagnetic wave and Eq. (2.13) gives the current density of the driven current. The result (2.13) coincides with that obtained in Ref. 10 and agrees with the prediction of Ref. 3. In Ref. 3 it was stated that, based on an equation of type (2.13) and an increased intensity of the radiation, it is possible to generate anomalously high current densities up to $J \sim env_T$. In a real laser plasma, however, the situation is different. Before a current density $\sim env_T$ can be achieved by raising the radiation intensity, the ion-acoustic instability will be excited. This can be confirmed by calculating the growth rate of the ion-acoustic instability[14]

$$\gamma_e(\mathbf{k}) = \gamma_s\left(\frac{\omega_s}{kv_s}\right)^3\left\{\frac{\sqrt{8\pi}}{nv_s}\,v_T^3\cos\theta_k\int_0^\infty dv \times\int_{-\sin\theta_k}^{\sin\theta_k}\frac{d\xi}{\sqrt{\sin^2\theta_k-\xi^2}}\,\frac{\partial}{\partial\xi}\,\delta f_- - \frac{\omega_s}{kv_s}\right\}, \tag{2.15}$$

where θ_k is the angle of the acoustic wave vector, $v_s = \omega_{Li} r_{De}$, ω_{Li} is the ion plasma frequency, r_{De} is the electron Debye radius, $\gamma_s = \sqrt{\pi/8}kv_s\omega_{Li}/\omega_{Le}$, and $\omega_s = kv_s/\sqrt{1+k^2r_{De}^2}$ is the ion-acoustic frequency. Using Eq. (2.7), we obtain an explicit expression for the growth rate of the ion-acoustic instability from Eq. (2.15),

$$\gamma_e(\mathbf{k}) = \gamma_s\left(\frac{\omega_s}{kv_s}\right)^3\left\{\frac{k_0v_E^2}{\omega_0v_s}\cos\theta_k\,\frac{5\cos^2\theta_k-1}{4} - \frac{\omega_s}{kv_s}\right\}. \tag{2.16}$$

Since $\omega_s/kv_s \leqslant 1$, for $\theta_k = 0$ Cerenkov generation of ion-acoustic waves is possible even when $v_E^2 > v_s\omega_0/k_0 = v_sc$. At the instability threshold, when $v_E^2 = v_s\omega_0/k_0$, the driven current density (2.13) is $1.7env_s$, or much less than env_T. This means that a rigorous description of the generation of high current densities in the range from env_s to env_T will require the development of a theory for current drive under conditions where the ion-acoustic instability is excited. This problem is solved in the following sections.

3. THE SPECTRUM OF ION-ACOUSTIC TURBULENCE

The following assumption is important for a theory of the effect of intense high frequency waves on plasmas when the ion-acoustic instability is present. If the frequency ω_0 of the radiation is much higher than the electron plasma frequency, then the effect of low frequency ion-acoustic fluctuations in the charge density on the rapidly varying electron motion at frequencies $\sim\omega_0$ can be neglected.[15,16] On the contrary, when considering the slow movements described by Eq. (2.2), the latter must be supplemented by the quasilinear collision integral $\mathrm{St}_{QL}(f)$ which accounts for the Cherenkov interaction of the electrons with ion-acoustic waves. When describing the interaction of the circularly polarized wave (2.1), noting the axial symmetry of the excited nonequilibrium electron distribution, we shall use a quasilinear collision integral of the form[14,17]

$$\mathrm{St}_{QL}(f) = \frac{v_T^3}{v^3}\,\frac{\partial}{\partial\xi}\left[(1-\xi^2)\nu_2(\sqrt{1-\xi^2})\,\frac{\partial f}{\partial\xi} + \sqrt{1-\xi^2}\,\nu_1(\sqrt{1-\xi^2})v_s\,\frac{\partial f}{\partial v}\right] + \frac{1}{v^2}\,\frac{\partial}{\partial v}\left(v_T^3\,\frac{v_s}{v}\right)\left[\nu_0(\sqrt{1-\xi^2})v_s\,\frac{\partial f}{\partial v} + \sqrt{1-\xi^2}\,\nu_1(\sqrt{1-\xi^2})\,\frac{\partial}{\partial\xi}\,f\right], \tag{3.1}$$

where the turbulence frequencies $\nu_n(\sqrt{1-\xi^2})$, $n = 0, 1, 2$, depend on the form of the distribution of the number density of the ion-acoustic waves with respect to wave number, $N(\mathbf{k}) = N(k, \cos\theta_k)$:

$$\nu_n(\sqrt{1-\xi^2}) = \frac{e^2}{\pi m^2 v_T^3\omega_{Li}^2}\int_{k_{\min}}^{k_{\max}} dk\,k\omega_s^3\left(\frac{\omega_s}{kv_s}\right)^{2-n} \times\int_{-\sqrt{1-\xi^2}}^{\sqrt{1-\xi^2}} dx\,\frac{N(k,x)}{\sqrt{1-\xi^2-x^2}}\left(\frac{x}{\sqrt{1-\xi^2}}\right)^n. \tag{3.2}$$

In Eq. (3.2), $x=\cos\theta_k$ and $k_{\min}$ and $k_{\max}$ are the boundaries of the turbulence region in the absolute value of the wave number. In writing down Eq. (3.2) we have omitted small corrections of order ω_s/kv. We shall regard the electron–electron collision frequency ν_{ee} as high, such that $\nu_{ee}\gg(\omega_{Li}/\omega_{Le})^2\nu_n(\sqrt{1-\xi^2})$. Then the ion-acoustic turbulence does not cause a significant distortion of the electron distribution from Maxwellian and the solution of Eq. (2.2) combined with the collision integral (3.1), as before for a laminar plasma, can be sought in the form $f=f_m+\delta f_+ +\delta f_-$. Avoiding a discussion of the possible effect of ion-acoustic turbulence on the Weibel instability, we shall not consider the equation for δf_+. We shall dwell on the equation for the odd correction δf_- to the distribution. Neglecting small terms of order $v_s/v_T\ll 1$, for δf_- we have (cf. Eq. (2.5))

$$-\frac{k_0}{\omega_0}v_E^2\nu\left\{\frac{3}{2}\xi\frac{\partial f_m}{\partial v}+\xi(1-\xi^2)v^5\frac{\partial}{\partial v}\left[\frac{1}{v^4}\frac{\partial f_m}{\partial v}\right]\right\}=\frac{\partial}{\partial\xi}\left\{(1-\xi^2)\left[\nu_2(\sqrt{1-\xi^2})+\frac{\nu}{2}\right]\frac{\partial}{\partial\xi}\delta f_- +\sqrt{1-\xi^2}\nu_1(\sqrt{1-\xi^2})v_s\frac{\partial f_m}{\partial v}\right\}, \tag{3.3}$$

where $\nu=\nu(v_T)$. Integrating this equation subject to the regularity condition for the function $\partial\delta f_-/\partial\xi$ for $\xi=\pm 1$, we obtain

$$\frac{\partial}{\partial\xi}\delta f_-=\left[\nu_2(\sqrt{1-\xi^2})+\frac{\nu}{2}\right]^{-1}\left\{\nu\frac{k_0}{\omega_0}v_E^2\left[\frac{3}{4}\frac{\partial f_m}{\partial v}+\frac{1}{4}(1-\xi^2)v^5\frac{\partial}{\partial v}\left(\frac{1}{v^4}\frac{\partial f_m}{\partial v}\right)\right]-[\nu_1(\sqrt{1-\xi^2})/\sqrt{1-\xi^2}]v_s\frac{\partial f_m}{\partial v}\right\}. \tag{3.4}$$

Equation (3.4) allows us to rewrite the expression for the electron growth rate of the ion-acoustic instability (2.15) in the form

$$\gamma_e(\mathbf{k})=\gamma_s\left(\frac{\omega_s}{kv_s}\right)^3\left\{\frac{2}{\pi}\cos\theta_k\int_0^{\sin\theta_k}\frac{d\xi}{\sqrt{\sin^2\theta_k-\xi^2}}\times\left[\nu_2(\sqrt{1-\xi^2})+\frac{\nu}{2}\right]^{-1}\left[\frac{k_0}{\omega_0}\frac{\nu}{v_s}v_E^2\left(\frac{1}{2}-\frac{5}{4}\xi^2\right)+\frac{\nu_1(\sqrt{1-\xi^2})}{\sqrt{1-\xi^2}}\right]-\frac{\omega_s}{kv_s}\right\}. \tag{3.5}$$

In studies of quasistationary ion-acoustic turbulent noise, the main mechanisms for stabilizing the instability are Cherenkov damping of sound on hot resonant ions[18,19] and stimulated scattering on thermal ions.[20,21] According to the self-consistent theory of ion-acoustic turbulence,[19] Cherenkov damping on hot resonant ions has the growth rate

$$\gamma_i(\mathbf{k})=\delta\gamma_s\left(\frac{\omega_s}{kv_s}\right)^3\left\{\frac{2}{\pi}\cos\theta_k\int_0^{\sin\theta_k}\frac{d\xi}{\sqrt{\sin^2\theta_k-\xi^2}}\times\frac{\nu_1(\sqrt{1-\xi^2}}{\sqrt{1-\xi^2}}\left[\nu_2(\sqrt{1-\xi^2})+\frac{\nu}{2}\right]^{-1}-\frac{\omega_s}{kv_s}\right\}, \tag{3.6}$$

where $\delta=(n_h/n_i)(\omega_{Le}/\omega_{Li})v_s^3/v_h^3$, n_h is the hot ion density, v_h is their root mean square velocity, n_i is the total ion density, while the damping rate owing to stimulated scattering is given by

$$\gamma_{NL}(\mathbf{k})=\frac{k^2v_{Ti}^2}{4\pi n_i m_i v_s^2}\left(\frac{kv_s}{\omega_s}\right)^3\frac{\partial}{\partial k}k^4\left(\frac{kv_s}{\omega_s}\right)^3\times\int_{-1}^{1}dx'Q(x,x')N(k,x'), \tag{3.7}$$

where v_{Ti} is the ion thermal speed, m_i is the ion mass, $x=\cos\theta_k$, $x'=\cos\theta_k'$, $Q(x,x')$ is the nonlinear interaction kernel given by

$$Q(x,x')=\int_0^{2\pi}\frac{d\varphi}{2\pi}(\mathbf{k}\cdot\mathbf{k}')^2[\mathbf{k}\cdot\mathbf{k}']^2(kk')^{-4}, \tag{3.8}$$

and φ is the azimuthal angle of the vector $\mathbf{k}$. Here the spectrum of the ion-acoustic turbulence is found from the condition of balance for wave generation, their absorption and repumping over the wave number spectrum,

$$\gamma_e(\mathbf{k})+\gamma_i(\mathbf{k})+\gamma_{NL}(\mathbf{k})=0. \tag{3.9}$$

Using the accepted approximation, from the theory of ion-acoustic turbulence, of the last term in the curly brackets of Eqs. (3.5) and (3.6) by $\omega_s/kv_s\equiv 1$, we write the solution to Eq. (3.9) in the form $N(\mathbf{k})=N(k)\Phi(x)$. Then, as for ion-acoustic turbulence generated by a conduction current or thermal flux, in the range of wave numbers from $k_{min}r_{De}\ll 1$ to $k_{max}r_{De}\gg 1$ the frequency distribution has the form

$$N(k)=4\pi n_i m_i(1+\delta)\gamma_s\left(\frac{r_{De}}{r_{Di}}\right)^2k^{-5}\left(\frac{\omega_s}{kv_s}\right)^3\times\left[\ln\left(\frac{\omega_{Li}}{\omega_s}\right)-0.5\left(\frac{\omega_s}{kv_s}\right)^2-0.25\left(\frac{\omega_s}{kv_s}\right)^4\right], \tag{3.10}$$

where r_{Di} is the ion Debye radius. Under the conditions corresponding to the distribution (3.10), the turbulence frequencies ν_n (3.2) take the form

$$\nu_n(\sqrt{1-\xi^2})=\nu_N(\Lambda_n/\overline{\Lambda})\chi_n(\sqrt{1-\xi^2}), \tag{3.11}$$

where $\overline{\Lambda}=0.5$, $\Lambda_1=0.488$, $\Lambda_2=0.497$,

$$\nu_N=\frac{\overline{\Lambda}}{\sqrt{8\pi}}\omega_{Li}(1+\delta)\frac{r_{De}^2}{r_{Di}^2}, \tag{3.12}$$

and

$$\chi_n(\sqrt{1-\xi^2})=\int_0^{\sqrt{1-\xi^2}}\frac{dx\Phi(x)}{\sqrt{1-\xi^2-x^2}}\left(\frac{x}{\sqrt{1-\xi^2}}\right)^n. \tag{3.13}$$

We shall neglect the small difference of λ_1 and Λ_2 from $\overline{\Lambda}$ in the following. Noting Eqs. (3.10)–(3.13), from Eq. (3.9) we

obtain an equation for determining the distribution of ion-acoustic turbulence with respect to the angle of the wave vector:

$$\frac{2}{\pi}\,x\int_0^{\sqrt{1-x^2}}\frac{d\xi}{\sqrt{1-x^2-\xi^2}}\left[\chi_2(\sqrt{1-\xi^2})+\frac{\nu}{2\nu_N}\right]^{-1}$$
$$\times\left[\frac{\nu_p}{\nu_N}\left(\frac{1}{2}-\frac{5}{4}\,\xi^2\right)+\frac{\chi_1(\sqrt{1-\xi^2})}{\sqrt{1-\xi^2}}\right]$$
$$=1+\int_{-1}^{1}dx'\,Q(x,x')\Phi(x'),\tag{3.14}$$

where $\nu_p=p\nu$ and p is the degree of excess above threshold, given by

$$p=\frac{k_0v_E^2}{\omega_0v_s(1+\delta)}.\tag{3.15}$$

We shall study Eq. (3.14) in the limit $p\ll\nu_N/\nu$, which is of greatest interest for applications. Since for a hot transparent plasma the frequency ν_N is orders of magnitude higher than the electron–ion collision frequency ν, in the limit $p\ll\nu_N/\nu$ extremely high degrees of excess above threshold are possible, i.e., $p\gg1$. For $p\ll\nu_N/\nu$, the function $\Phi(x)$ has a sharp maximum at $x=1$ ($\theta_k=0$), while far from $x=1$ it is so small that the integral terms on the right of Eq. (3.14) are much smaller than unity. This circumstance makes it possible to include the integral term in an approximate way, only for ensuring regularization of the noise at $x=1$, by replacing it with the small constant

$$\varepsilon=\int_{-1}^{1}dx'\,Q(x=1-,x')\Phi(x')$$
$$=\int_{-1}^{1}dx(x^2-x^4)\Phi(x)\ll1.\tag{3.16}$$

Taking the Abel transform of Eq. (3.14) and using Eq. (3.16), we find

$$\frac{\nu_p}{4\nu_N}(5t^2-3)t^2+t\chi_1(t)=(1+\varepsilon)\left[\chi_2(t)+\frac{\nu}{2\nu_N}\right].\tag{3.17}$$

Ion-acoustic turbulence is excited within a limited range of angles, for which $1\geqslant x\geqslant x_0>0$, where $x_0=\cos\theta_0$ and θ_0 is the limiting angle of the cone of angles within which the turbulent noise is concentrated. Then, according to the definition (3.13), the functions $\chi_n(t)$ go to zero for $t\leqslant x_0$. Given this fact and dropping the correction $\varepsilon\ll1$, from Eq. (3.17) we find

$$x_0^2=0.3+\sqrt{0.09+0.4/p}.\tag{3.18}$$

For $p=1$ this implies $x_0=1$ and for $p\gg1$, we have $x_0\simeq\sqrt{0.6}$ or $\theta_0=\theta_m\simeq43.6°$. Recall that in the case of ion-acoustic turbulence excited by a conduction current, for $p\gg1$ the noise was excited over angles from 0 to 90°. Now, however, because of the different angular structure of the instability growth rate (see Eqs. (2.16) and (3.5)), the waves are excited in a narrow cone of angles. In the interval from $x=x_0$ to $x=1$, the solution of Eq. (3.17) has the form

$$\Phi(x)=\frac{\nu_p}{3\pi\nu_Nx}\frac{d}{dx}\left[\frac{x(x^2-x_0^2)^{3/2}}{1+\varepsilon-x}(4x^2+6x_0^2-3)\right].\tag{3.19}$$

Equations (3.10) and (3.19) describe completely the spectrum of the ion-acoustic turbulence excited by the driven current produced by moderately intense high frequency radiation when the degree of excess above threshold varies over the range from $p\geqslant1$ to $p\ll\nu_N/\nu$. This kind of ion-acoustic turbulence can be used to study the reverse effect of turbulence on high density current drive.

4. ELECTRON CURRENT DRIVE

We now turn to an analysis of electron current drive with electron drift velocities greater than the sound speed. First we consider the driven current. Following the definition (2.11) and using Eqs. (3.4) and (3.11), after integration with respect to the speed we obtain

$$J=\frac{3}{2}\,envs\int_0^1\frac{tdt}{\sqrt{1-t^2}}\left[\chi_2(t)+\frac{\nu}{2\nu_N}\right]^{-1}$$
$$\times\left[(1+\delta)\,\frac{\nu_p}{\nu_N}\left(2t^4-\frac{3}{4}\,t^2\right)+t\chi_1(t)\right].\tag{4.1}$$

Since the functions $\chi_n(t)$, which determine the turbulence frequency are nonzero only for $t\geqslant x_0$, the total current (4.1) is conveniently represented as the sum of two currents, $J=J_c+J_t$. The first current J_c is caused by electrons whose velocities are oriented at small angles to the propagation direction of the electromagnetic wave ($\sin\theta<\cos\theta_0$). These electrons are scattered only in collisions with ions and their contribution to the current is

$$J_c=en\,\frac{k_0}{\omega_0}\,v_E^2\left[\frac{17}{10}-\frac{\sin\,\theta_0}{20}\,(34+17\cos^2\,\theta_0\right.$$
$$\left.+24\cos^4\,\theta_0)\right].\tag{4.2}$$

At the threshold for excitation of ion-acoustic turbulence, when $\theta_0=\theta$, Eq. (4.2) transforms to the formula for the driven current in a laminar plasma. Far above threshold, i.e., when $p\gg1$ and the angle θ_0 approaches the maximum possible θ_m, Eq. (4.2) implies

$$J_c=2.9\cdot10^{-2}en\,\frac{k_0}{\omega_0}\,v_E^2.\tag{4.3}$$

Thus, because of the narrowed range of angles within which electron scattering is caused only by the ions, the numerical coefficient in Eq. (4.3) turns out to be almost 60 times smaller than in a laminar plasma.

The second current J_t is associated with electrons moving at large angles to the vector $\mathbf{k}_o$ ($\sin\theta>\cos\theta_0$). These electrons undergo intense scattering on turbulent fluctuations in the charge density and their contribution to the driven current is given by

$$J_t=\frac{3}{2}\,envs\sqrt{1-x_0^2}+\frac{3}{2}\,envs\int_{x_0}^1\frac{t^3dt}{\sqrt{1-t^2}}\,[3t^2+\delta(8t^2-3)]$$

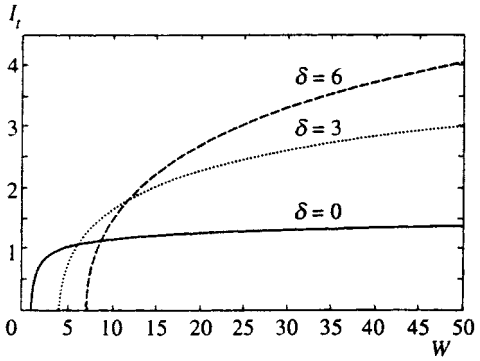

FIG. 1. Contribution to current drive from electrons interacting with turbulent noise as a function of radiation intensity. The dependence of the current on the amount of Cherenkov damping on ions is illustrated by the curves corresponding to different values of δ.

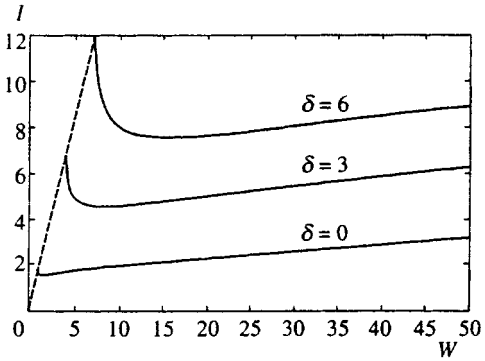

FIG. 2. Driven current as a function of radiation intensity. The dashed line is the current in a laminar plasma. The smooth curves are the current density in plasmas with ion-acoustic turbulence for three levels of Cherenkov damping of sound on the ions ($\delta = 0,3,6$).

$$\times\left\{ t^2(5t^2-3)+\frac{4}{3\pi}\int_{x_0}^{t}\frac{dx}{\sqrt{t^2-x^2}}\frac{\sqrt{x^2-x_0^2}}{1-x}\right.$$
$$\left.\times\left[x^2(20x^2+10x_0^2-9)+\frac{x^2-x_0^2}{1-x}(4x^2+6x_0^2-3)\right]\right\}^{-1}. \tag{4.4}$$

The current $J_t = I_t e n v_s$ (4.4) is found numerically as a function of the parameter

$$W=\frac{E^2}{4\pi n m v_s c}\frac{\omega_{Le}^2}{\omega_0^2}\equiv p(1+\delta), \tag{4.5}$$

which has the significance of a dimensionless energy (intensity) of the high frequency electromagnetic field. Calculations of the function I_t are shown in Fig. 1 for three values of $\delta = 0$, 3, and 6. If Cherenkov damping of sound on resonant ions is negligible ($\delta = 0$), then as the intensity of the radiation increases and the region of turbulence expands, the current density J_t increases monotonically from zero to $\sim 1.9 e n v_s$ with anomalously high W. Similar dependences exist for the current density J_t (4.4) if $\delta \neq 0$. According to Fig. 1 and Eq. (4.4), the larger δ is, the higher the current density J_t will be, but the current itself shows up at high radiation fluxes. The current behaves this way because, as δ increases, the threshold (3.15) for excitation of the ion-acoustic instability rises and the turbulent noise level (3.10), (3.19) decreases, so that there is less electron scattering on the ion-acoustic fluctuations in the charge density.

Let us compare the total driven current obtained taking the excitation of the ion-acoustic instability into account (4.1) with the driven current in a laminar plasma (2.13). The results of this comparison are shown in Fig. 2. The dashed line $I = J/e n v_s = 1.7W$ corresponds to Eq. (2.13). The smooth curves are the current density in a turbulent plasma with different amounts of Cherenkov damping of sound on the ions ($\delta = 0,\ 3,\ 6$). As can be seen from Fig. 2, when the intensity of the radiation exceeds the level corresponding to the instability threshold, the linear current rise characteristic of laminar plasmas ceases. Furthermore, at low levels above threshold, when the turbulent noise is concentrated in a narrow cone of angles along the propagation direction of the wave, where the intensity is anomalously high (see Eq. (3.19)), the driven current density decreases slightly. With increasing distance from the threshold, the turbulence region expands and this is accompanied by a rise in the turbulent part of the current, J_t (4.4) and a fall in the classical part J_c (4.2). The total drive current is maintained at a level $J \sim (1+\delta) e n v_s$ over a wide range of intensities. Finally, at very high intensities, when the turbulence fills the entire cone of angles up to the maximum $\theta_m \simeq 43.6°$ (3.18), the current J_t (4.4) approaches saturation and J_c (4.2) increases in proportion to W (see Eq. (4.3)). In sum, the total current J increases as in a laminar plasma (2.13), linearly with $J \propto W$, but the absolute magnitude of the current is many times lower than might be expected from the classical theory.

Similar behavior occurs for driven heat fluxes. In fact, following the definition (2.12) and using Eqs. (3.4), (3.11), and (3.19), we have

$$Q_T = Q n m v_T^2 v_s = n m v_T^2 v_s (Q_c + Q_t), \tag{4.6}$$

and

$$Q_c = \frac{25}{4} W[1-\sqrt{1-x_0^2}(1+0.5x_0^2+0.6x_0^4)], \tag{4.7}$$

and

$$Q_t = \frac{15}{4}\sqrt{1-x_0^2}+\frac{15}{4}\int_{x_0}^{1}\frac{t^3 dt}{\sqrt{1-t^2}}[5t^2+\delta(10t^2-3)]$$
$$\times\left\{ t^2(5t^2-3)+\frac{4}{3\pi}\int_{x_0}^{t}\frac{dx}{\sqrt{t^2-x^2}}\frac{\sqrt{x^2-x_0^2}}{1-x}\right.$$
$$\left.\times\left[x^2(20x^2+10x_0^2-9)+\frac{x^2-x_0^2}{1-x}(4x^2+6x_0^2-3)\right]\right\}^{-1}, \tag{4.8}$$

where x_0 obeys Eq. (3.18). Numerically calculated heat fluxes Q are plotted in Fig. 3 as functions of the intensity W of the electromagnetic radiation for two values of δ. Like the driven current, the heat flux obeys Eq. (2.14), which is characteristic of laminar plasmas, at radiation intensities be-

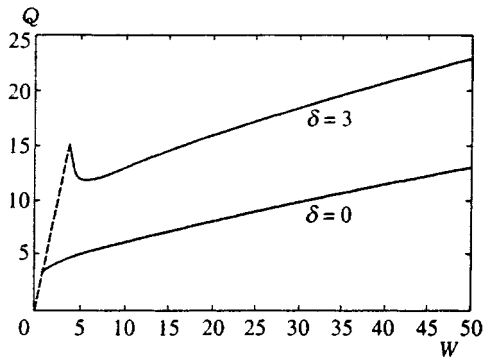

FIG. 3. Driven heat flux as a function of radiation intensity. The dashed line is the flux in a laminar plasma. The smooth curves corresponding to $\delta=0$ and $\delta=3$ are the flux in plasmas with ion-acoustic turbulence.

low threshold. Beyond the threshold for excitation of the ion-acoustic instability, over a wide range of intensities the heat flux is strongly suppressed in absolute magnitude and is maintained at a level $\sim(1+\delta)nmv_T^2v_s$. At very high intensities, when the turbulent noise fills the entire region of accessible angles $\theta\lesssim\theta_m$, the driven heat flux rises $\sim W$, but much more slowly than in a laminar plasma.

5. CONCLUSION

The above results show that, in general, the ion-acoustic instability causes a substantial reduction in the efficiency of current drive by high frequency electromagnetic radiation. Because of the effect of ion-acoustic turbulence on the electron kinetics, radiation intensities two to three times higher than in laminar plasmas are required in order to drive high current densities $\sim envT$. At the same time, it should be noted that experimental verification of the new features of current drive and the spectrum of ion-acoustic turbulence presented above is possible at radiation intensities which are typical of modern laboratory experiments.

This work was supported by the Russian Fund for Fundamental Research (Project No. 94-02-03631) and Project No. 2.46 of the State Program on Optics and Laser Physics.

[1] A. M. Prokhorov, S. I. Anisimov, and P. P. Pashinin, Usp. Fiz. Nauk. **119**, 401 (1976) [Sov. Phys. Usp. **19**, 547 (1976)].
[2] M. G. Haines, Canadian J. Phys. **64**, 912 (1986).
[3] P. P. Pashinin and A. M. Prokhorov, JETP Lett. **26**, 526 (1977).
[4] P. P. Pashinin and M. V. Fedorov, Zh. Éksp. Teor. Fiz. **75**, 454 (1978) [Sov. Phys. JETP **48**, 228 (1978)].
[5] I. B. Bernstein, C. E. Max, and J. J. Thomson, Phys. Fluids **21**, 905 (1978).
[6] I. P. Shkarofsky, Phys. Fluids **23**, 52 (1980).
[7] M. M. Skorich, Laser and Particle Beams **5**, 83 (1987).
[8] A. Fukuyama, S.-I. Itoh, and K. Itoh, J. Phys. Soc. Japan **51**, 1010 (1982).
[9] K. N. Ovchinnikov, V. P. Silin, and S. A. Uryupin, Fiz. Plazmy **17**, 1116 (1991) [Sov. Phys. Plasma Phys. **17**, 648 (1991)].
[10] K. N. Ovchinnikov, V. P. Silin, and S. A. Uryupin, Kr. soobshch. po fizike FIAN, No. 1, 2, 50 (1992).
[11] A. B. Langdon, Phys. Rev. Lett. **44**, 575 (1980).
[12] R. Balescu, J. Plasma Phys. **27**, 553 (1982).
[13] R. Davidson, in *Elements of Plasma Physics* [Russian translation], Vol 1, A. A. Galeev and R. Sudan, (eds.), Energoatomizdat, Moscow (1983), p. 443.
[14] V. P. Silin and S. A. Uryupin, Zh. Éksp. Teor. Fiz. **102**, 78 (1992) [JETP **75**, 41 (1992)].
[15] V. P. Silin, Krat. soobshch. po fizike FIAN, No. 5, 59 (1983).
[16] V. P. Silin and S. A. Uryupin, Zh. Éksp. Teor. Fiz. **98**, 117 (1990) [Sov. Phys. JETP **71**, 64 (1990)].
[17] L. I. Rudakov and L. V. Korblev, Zh. Éksp. Teor. Fiz. **50**, 220 (1966) [Sov. Phys. JETP **23**, 145 (1966)].
[18] L. M. Kovrizhnykh, Zh. Éksp. Teor. Fiz. **52**, 1406 (1967) [Sov. Phys. JETP **25**, 934 (1967)].
[19] V. P. Silin and S. A. Uryupin, Fiz. Plazmy **12**, 2042 (1986) [*sic*].
[20] V. I. Petviashvili, Dokl. Akad. Nauk SSSR **153**, 1295 (1963).
[21] B. B. Kadomtsev, in *Reviews of Plasma Physics* [in Russian], Atomizdat, Moscow (1964), vol. 4, p. 258.

Translated by D. H. McNeill

Isomorphic description of the two-phase region of near-critical binary mixtures

E. E. Gorodetskiĭ,*) V. D. Kulikov, and L. V. Fedyunina,

Institute for Oil and Gas Problems, Russian Academy of Sciences, 117917 Moscow, Russia

M. A. Anisimov

Institute for Physical Science and Technology, University of Maryland at College Park, MD 20742, USA
(Submitted 16 August 1996)
Zh. Éksp. Teor. Fiz. **111**, 120–126 (January 1997)

The paper presents a general approach based on the hypothesis of field mixing designed to describe properties of binary mixtures around critical points, including the region of two-phase states. The efficacy of the technique is illustrated by derivation of an analytic equation for boundary curves of a binary mixture. The shapes of these curves are largely determined by the critical lines $T_c(x)$ and $P_c(x)$. Given the shapes of these curves, one can easily estimate the maximum pressure at which two-phase equilibrium is possible, and the width of the retrograde condensation region. © *1997 American Institute of Physics.* [S1063-7761(97)00801-9]

In this reported work, the equations of curves for binary mixtures (cross-sections of the two-phase region at constant concentration) have been obtained analytically on the basis of a previously developed approach[1–3]; in particular, a relationship has been found between the shapes of these curves and the critical parameters of the mixtures. By taking a methane–ethane mixture as an example, we have demonstrated that the resulting equation provides a qualitatively accurate description of the published experimental data.

In accordance with the general concept of the universality of critical phenomena,[4] we assume that the singular part of the thermodynamic potential of any system near a phase transition of the second kind is a universal function of two scaling fields, namely the ordering field h_1 and temperature-like field h_2, which are thermodynamically conjugate to the parameters φ_1, with the scaling dimension of the order parameter, and φ_2, with the scaling dimension of the energy. In the proposed approach, this function is assumed to be known.

In real liquids, the scaling fields h_1 and h_2 are linear combinations of real fields.[4] In a two-component mixture, these fields are the deviation of the solvent's chemical potential μ_1 and temperature T from their critical values $\mu_{1c}(\mu)$ and $T_c(\mu)$, which are determined by the difference between the chemical potentials of the components $\mu=\mu_2-\mu_1$:

$$h_1=\left(\frac{\partial h_1}{\partial \mu_1}\right)_{T,\mu}\Delta\mu_1+\left(\frac{\partial h_1}{\partial T}\right)_{\mu_1,\mu}\Delta T=a_1\Delta\mu_1+a_2\Delta T,$$
$$h_2=\left(\frac{\partial h_2}{\partial \mu_1}\right)_{T,\mu}\Delta\mu_1+\left(\frac{\partial h_2}{\partial T}\right)_{\mu_1,\mu}\Delta T=b_2\Delta\mu_1+b_1\Delta T, \tag{1}$$

where $\Delta\mu_1=\mu_1-\mu_{1c}(\mu)$ and $\Delta T=T-T_c(\mu)$. Earlier[1–3] we proved that, if the gas–liquid critical curve is continuous,[5] the parameters a_1 and b_1 can be taken equal to $1/RT_c(\mu)$ and $1/T_c(\mu)$. The parameter b_2 is responsible for the asymmetry of the coexistence curve, and is usually small. Its presence in our equations is not essential, and for simplicity we will omit it in our calculations.

Given this choice of variables, the thermodynamic potential density is the pressure

$$P=P^s(h_1,h_2)+P^r(\mu_1,T,\mu), \tag{2}$$

where $P^s=\rho_c(\mu)RT_c(\mu)\tilde{P}^s$, $\rho_c(\mu)$ is the critical density, P^r is the regular part of the pressure, and $\tilde{P}^s$ is the aforementioned known universal function of the scaling fields h_1 and h_2:

$$\tilde{P}^s(h_1,h_2)=h_2^2|h_2|^{-\alpha}[f_0(z)+|h_2|^{\Delta}f_1(z)]. \tag{3}$$

Here $z=h_1/h_2^{\beta+\gamma}$, $\alpha=0.11$, $\beta=0.325$, $\gamma=1.24$, and $\Delta=0.51$ are universal critical exponents,[6] and R is the molar gas constant. The second term in the expression for the singular part of pressure is the first correction to the asymptotic expression for this value. The ''densities'' conjugate to the scaling fields h_1 and h_2 are

$$\varphi_1=\left(\frac{\partial\tilde{P}^s}{\partial h_1}\right)_{h_2},\quad \varphi_2=\left(\frac{\partial\tilde{P}^s}{\partial h_2}\right)_{h_1}. \tag{4}$$

The densities of other thermodynamic parameters can be easily derived from the relation

$$dP=s\ dT+\rho d\ \mu_1+\rho x\ d\mu, \tag{5}$$

where s is the entropy density and x is the molar fraction of the second component. We then obtain the following expressions for the mixture molar density ρ and its concentration x:

$$\rho=\left(\frac{\partial P}{\partial \mu_1}\right)_{T,\mu}=\rho_c(\mu)\varphi_1+\left(\frac{\partial P^r}{\partial \mu_1}\right)_{T,\mu}, \tag{6}$$

$$x=\left(\frac{\partial P}{\partial \mu}\right)_{T,\mu_1}\left(\frac{\partial P}{\partial \mu_1}\right)^{-1}_{T,\mu}$$

$$= \frac{RT_c\left[\left(\frac{\partial h_1}{\partial \mu}\right)_{\mu_1,T}\varphi_1+\left(\frac{\partial h_2}{\partial \mu}\right)_{\mu_1,T}\varphi_2\right]+\rho_c^{-1}\left(\frac{\partial P^r}{\partial \mu}\right)_{\mu_1,T}}{\varphi_1+\rho_c^{-1}\left(\frac{\partial P^r}{\partial \mu_1}\right)_{T,\mu}}. \tag{7}$$

The latter equation determines the mixture concentration as a function of T and μ. If the concentration x is fixed, Eq. (7) determines μ as a function of T and x. Note that similar expressions can be obtained for any thermodynamic parameters as functions of φ_1 and φ_2 that have a certain scaling dimension.

Since the points of the boundary curve belong simultaneously to corresponding points of the liquid–gas coexistence curve, the field $h_1\{\Delta\mu_1(\mu),\Delta T(\mu)\}$ vanishes at these points. Hence the fields $\Delta\mu_1(\mu)$ and $\Delta T(\mu)$ are related on this curve by the linear equation $\Delta\mu_1 = (\partial\mu_1/\partial T)_{h_1=0}\Delta T(\mu)$, and the field $h_2 \propto \Delta T(\mu)$. With due account of this relation, we obtain the following equation for the scaling densities in the two-phase region:

$$\begin{aligned}\varphi_1 &= \pm B_0|\tau(\mu)|^{\beta}(1+B_1|\tau(\mu)|^{\Delta}),\\ \varphi_2 &= \frac{A_0^-}{1-\alpha}\,\tau(\mu)|\tau(\mu)|^{-\alpha},\end{aligned} \tag{8}$$

where A_0^- is the amplitude of the singular part of the isochoric heat capacity in the two-phase region at $\mu=$const;[2,3] B_0 and B_1 are the amplitudes which determine the principal term and Wegner's correction for the coexistence curve, and $\tau(\mu)=T/T_c(\mu)-1$.

Let us express the regular parts of the derivatives in Eq. (7) as

$$\begin{aligned}\rho_c(\mu)^{-1}\left(\frac{\partial P^r}{\partial \mu_1}\right)_{T,\mu} &= 1+d_1\tau(\mu),\\ \rho_c(\mu)^{-1}\left(\frac{\partial P^r}{\partial \mu}\right)_{T,\mu_1} &= x_c(\mu)+d_2\tau(\mu),\end{aligned} \tag{9}$$

where d_1 and d_2 are parameters, and substitute them into Eq. (7). Thus we obtain

$$x \simeq \left[RT_c\left(\frac{\partial h_1}{\partial \mu}\right)_{\mu_1,T}-x_c\right]\varphi_1+RT_c\left(\frac{\partial h_2}{\partial \mu}\right)_{\mu_1,T}\varphi_2 + x_c(\mu)+D\tau(\mu), \tag{10}$$

where $D=d_2-x_cd_1$. If pure components are considered, this coefficient should vanish. The expression $RT_c(\mu)\times(\partial h_1/\partial\mu)_{\mu_1,T} - x_c$ reduces to $-\rho_c^{-1}(\partial P/\partial\mu)_{h_1,T}$. The value of this derivative calculated along the line on which the field h_1 is zero at $\mu=$const at the critical point is

$$\left(\frac{\partial P}{\partial \mu}\right)^c_{h_1=0,T} = \frac{dP_c}{d\mu}-\left(\frac{\partial P}{\partial T}\right)^c_{h_1=0,\mu_c}\frac{dT_c}{d\mu} \equiv -K_0\,\frac{dT_c}{d\mu}. \tag{11}$$

Previously[2,3] the thermodynamic derivative on the left-hand side of Eq. (11) was denoted by K_1. In this work we find it more convenient to isolate the derivative $dT_c/d\mu$ explicitly. Since the coefficient b_2, which is equal to $(\partial h_2/\partial\mu_1)_T$, is small, the derivative $RT_c(\partial h_2/\partial\mu)_T$ in Eq. (10) reduces to $R(dT_c/d\mu)$.

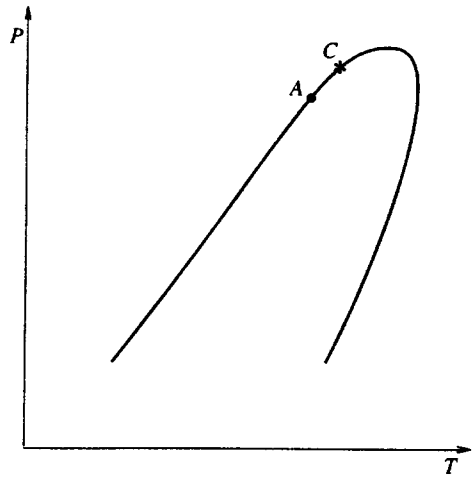

FIG. 1. Typical dew-bubble curve of a binary mixture.

Equation (10) describes both the coexistence curve of the binary mixture[7] and the boundary curve. The equation for the latter curve describes the relationship between the pressure and temperature on the curve that bounds the region of two-phase states at a given average concentration.

In the phase diagram (Fig. 1), the critical point C is determined by the critical value of the chemical potential μ_c and the critical concentration $x_c(\mu_c)$, which is equal to the average concentration x in the mixture. At the same time, the chemical potential μ differs at different points of the boundary curve.

Let us determine the relationship between the pressure at an arbitrary point of the boundary curve, whose chemical potential is μ (point A in Fig. 1), and the pressure $P_c(\mu_c)=P_c(x_c)$. Above all, we take into account that the contribution of the singular part to the pressure, P^s, is always small (it vanishes at the critical point as $|\tau(\mu)|^{2-\alpha}$) in comparison to the linear terms of the regular part. In other words, to a first approximation, the pressure at the boundary curve is determined only by P^r. Expanding the regular part of the pressure in terms of $\Delta T=T-T_c(\mu_c)$ and $\Delta\mu=\mu-\mu_c$, with due account of the condition $h_1=0$, we obtain

$$\Delta P = P-P_c(\mu_c)=\left(\frac{\partial P}{\partial T}\right)^c_{h_1=0,\mu_c}\Delta T-K_0\,\frac{dT_c}{d\mu}\,\Delta\mu. \tag{12}$$

This equation relates the pressure, temperature, and chemical potential at the boundary curve. It is obvious that in order to obtain the equation of the boundary curve, we need an additional equation relating these three variables to each other. This can be derived from the condition of constant concentration at the boundary curve. By substituting $x=x_c(\mu_c)$ on the left-hand side of Eq. (10) and expanding the variables $\tau(\mu)$ and $x_c(\mu)$ in terms of $\Delta\mu$ near $\mu=\mu_c$, we obtain

$$\left(\frac{dx}{d\mu}-\frac{D}{T_c}\frac{dT_c}{d\mu}\right)\Delta\mu+D\tau(\mu_c)+\frac{K_0}{\rho_c}\frac{dT_c}{d\mu}\,\varphi_1$$

$$-R\,\frac{dT_c}{d\mu}\,\varphi_2=0. \tag{13}$$

Here the densities φ_1 and φ_2 are defined by Eq. (8) with

$$\tau(\mu)=\tau(\mu_c)-\frac{1}{T_c}\frac{dT_c}{d\mu}\,\Delta\mu=\frac{1}{T_cK_0}\left(\Delta P-\frac{dP_c}{dT_c}\,\Delta T\right). \tag{14}$$

Equations (8), (12), and (13) determine the relationship between the pressure and temperature at the boundary curve. Equation (13) is, in effect, a parametric equation of that-curve. The resulting solution is two-valued [see Eq. (8)]: the left branch of the dew-bubble curve (AC branch in Fig. 1) corresponds to the plus sign in Eq. (8), and the right branch to the minus sign. In what follows, we will assume that $dx_c/d\mu_c=x(1-x)/RT_c(x)$ on the whole line of critical points.[3] Note, that $K_0=0$ at $x=x_A$ corresponds to the azeotropic point.[1–3] It follows from Eq. (13) that in this case the boundary curve degenerates into the curve defined by

$$P-P_c(x_A)=(\partial P/\partial T)^c_{h_1=0,\mu_c}[T-T_c(x_A)],$$

i.e., an azeotropic mixture behaves in this sense like a pure fluid.

Thus, boundary curves of binary mixtures are determined by the following set of physical parameters:

1) the derivatives dT_c/dx, dP_c/dx, and the related derivative dP_c/dT_c;

2) the amplitudes of asymptotic (B_0) and Wegener's (B_1) terms in the equation of the mixture coexistence curve;

3) the derivative $(\partial P/\partial T)^c_{h_1=0,\mu_c}$ or the parameter K_0 [Eq. (11) indicates that K_0 is not an independent parameter, but a function of the above variables];

4) the amplitude A_0^- of the specific heat;

5) the coefficient of the liquid–gas asymmetry, $D=d_2-xd_1$.

The derivatives dT_c/dx and dP_c/dx can be measured directly. The other parameters are, strictly speaking, adjustable parameters. Only in the simplest cases, in which the amplitudes B_0, B_1, and A_0 and the derivatives $(\partial P/\partial T)^c_{h_1=0}=(\partial P/\partial T)^c_{\rho=\rho_c}$ in pure components are close, can they be determined fairly accurately using additivity rules without additional fitting parameters. This situation is directly related to the example of the methane–ethane mixture discussed below.

Figure 2 shows fits of Eqs. (12) and (13) to experimental data for the methane–ethane mixture. In order to plot the boundary curves, we used the data on the lines of the critical points $T_c(x)$ and $P_c(x)$, coexistence curves, and specific heats of pure components.[9,10] The derivatives $(\partial P/\partial T)^c_{\rho=\rho_c}$ for pure methane and ethane were taken from Ref. 11:

$$\frac{1}{\rho_cR}\left(\frac{\partial P}{\partial T}\right)^{c(\mathrm{CH_4})}_{\rho=\rho_c}=1.72,\quad \frac{1}{\rho_cR}\left(\frac{\partial P}{\partial T}\right)^{c(\mathrm{C_2H_6})}_{\rho=\rho_c}=1.81;$$

$$B_0^{(\mathrm{CH_4})}=1.52,\quad B_0^{(\mathrm{C_2H_6})}=1.61;$$

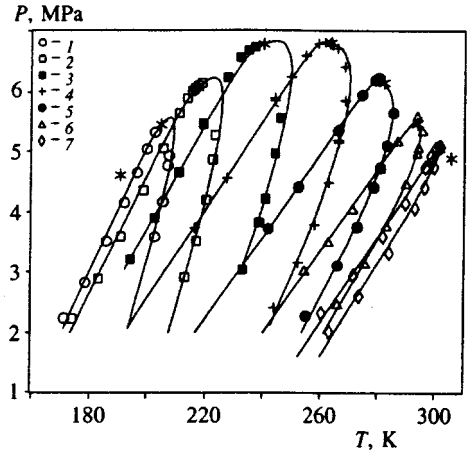

FIG. 2. Cross sections of the phase diagram of the methane–ethane mixture at different concentrations x (mole fraction of ethane). Solid lines show calculations by Eq. (13). The values of fitting parameters B_1 and D at corresponding concentrations are given in braces. (*1*) $x=0.075\{3.25,-0.77\}$; (*2*) $x=0.15\{1.99,-1.22\}$; (*3*) $x=0.30\{1.01,-1.95\}$; (*4*) $x=0.50\{0.47,-2.31\}$; (*5*) $x=0.70\{0.02,-2.09\}$; (*6*) $x=0.85\{0.16,-1.60\}$; (*7*) $x=0.95\{0.51,-1.15\}$. The measurements[8] are plotted with different symbols. The critical points of mixtures and pure components are shown as asterisks.

$$A_0^{-(\mathrm{CH_4})}=5.1,\quad A_0^{-(\mathrm{C_2H_6})}=6.5.$$

In calculating the corresponding parameters of the mixture, we used the simplest mixing rules:

$$\left(\frac{\partial P}{\partial T}\right)^c_{h_1=0,\mu_c}=(1-x)\left(\frac{\partial P}{\partial T}\right)^{c(\mathrm{CH_4})}_{\rho=\rho_c}+x\left(\frac{\partial P}{\partial T}\right)^{c(\mathrm{C_2H_6})}_{\rho=\rho_c},$$

$$B_0=(1-x)B_0^{(\mathrm{CH_4})}+xB_0^{(\mathrm{C_2H_6})},$$

$$A_0^-=(1-x)A_0^{-(\mathrm{CH_4})}+xA_0^{-(\mathrm{C_2H_6})}. \tag{15}$$

The parameters D and B_1 were varied to fit the curve to experimental data and were found to be smooth functions of the concentration. As expected, the factor D tends to zero for pure components. The values of B_1 and D are given in the caption to Fig. 2. One can see in Fig. 2 that Eqs. (12) and (13) satisfactorily describe the available experimental data on this mixture.

For many technical applications it is sufficient to know the maximum pressure $P_{\max}$ and temperature $T_{\max}$ at which the two-phase equilibrium is possible. In the lowest-order approximation, the distance between these singular points of the boundary curve and the critical point in Eq. (13) is estimated by retaining only terms linear in ΔT and ΔP, and also the term proportional to $|\tau(\mu)|^\beta$. In this case the values $\Delta P_{\max}=P_{\max}-P_c(x)$ and $\Delta T_{\max}=T_{\max}-T_c(x)$ can be calculated analytically:

$$\Delta P_{\max}=\frac{1-\beta}{\beta}\,T_c(x)\left[\left(\frac{\partial P}{\partial T}\right)^c_{h_1=0,\mu_c}-\frac{D}{T_c}\frac{dP_c}{dx}\right]^{-\beta/(1-\beta)}$$

$$\times\left[\frac{\beta B_0x(1-x)}{T_c^2}\,\frac{K_0}{\rho_cR}\,\frac{dT_c}{dx}\,\frac{dP_c}{dx}\right]^{1/(1-\beta)}, \tag{16}$$

$$\Delta T_{\max}=T_c(x)\,\frac{1-\beta}{\beta}\left(1-\frac{D}{T_c}\,\frac{dT_c}{dx}\right)^{-\beta/(1-\beta)}$$
$$\times\left[\beta B_0 x(1-x)\,\frac{K_0}{\rho_c R}\left(\frac{1}{T_c}\,\frac{dT_c}{dx}\right)^2\right]^{1/(1-\beta)}. \quad (17)$$

The value $\Delta T_{\max}$ determines the width of the temperature interval in which retrograde condensation is possible.[5] It follows from Eq. (17) that the width of this region is largely determined by the combination $(K_0/\rho_c R)(T_c^{-1}dT_c/dx)^2$. For example, when there is no azeotropic point, the parameter $K_0/\rho_c R$ is usually of order unity, and the width of the retrograde condensation region is largely controlled by the derivative dT_c/dx: the larger the derivative, the wider the region.

The number of fitting parameters can be reduced if the values $\Delta T^*=T(P_c)-T_c(x)$ and $\Delta P^*=P_c(x)-P(T_c)$ are measured. The first of them determines the ''width'' of the boundary curve on the critical isobar, and the second on the critical isotherm.[1)] Thus by substituting into Eq. (13) $\Delta P=0$ and then $\Delta T=0$ we obtain two equations from which the factors B_1 and D can be derived in terms of other parameters and experimental results. Hence, the number of fitting parameters can be reduced to three.

In conclusion, note that Eq. (13) coincides in the lowest-order approximation with that derived earlier by Rainwater[12] using the Leung–Griffiths model.[13] The relationship between the more general approach used in this work and the Leung–Griffiths model was discussed previously.[3]

This work was supported by the Russian Fund for Fundamental Research (Grant No. 96-02-18235). One of the authors (M.A.A.) acknowledges support by the U.S. Department of Energy (Grant No. DE FG02-95ER-14509).

*)e-mail: gorod@fluid.msk.ru

1)These parameters make sense if the critical point does not coincide with singular points on the boundary curve.

[1] M. A. Anisimov, E. E. Gorodetskiĭ, V. D. Kulikov, and J. V. Sengers, Pis'ma Zh. Éksp. Teor. Fiz. **60**, 522 (1994).
[2] M. A. Anisimov, E. E. Gorodetskiĭ, V. D. Kulikov, and J. V. Sengers, Phys. Rev. E **51**, 1199 (1995).
[3] M. A. Anisimov, E. E. Gorodetskiĭ, V. D. Kulikov *et al.*, Physica A **220**, 277 (1995); **223**, 272 (1996).
[4] A. Z. Patashinskiĭ and V. L. Pokrovskiĭ, *Fluctuation Theory of Phase Transitions* [in Russian], Nauka, Moscow (1982).
[5] J. S. Rowlinson and F. L. Swinton, *Liquids and Liquid Mixtures*, Butterworth, London (1982).
[6] J. V. Sengers and J. M. H. Levelt Sengers, Ann. Rev. Phys. Chem. **37**, 189 (1986).
[7] H. Cheng, M. A. Anisimov, and J. V. Sengers, submitted to Fluid Phase Equil. (1996).
[8] O. T. Bloomer, D. C. Gami, and J. D. Parent, Institute of Gas Technology Research Bulletin **22**, 42 (1953).
[9] A. A. Povodyrev, S. B. Kiselev, and M. A. Anisimov, Int. J. Thermophys. **14**, 1187 (1993).
[10] A. A. Povodyrev, G. X. Gin, S. B. Kiselev, and J. V. Sengers, submitted to Int. J. Thermophys. (1996).
[11] S. B. Kiselev and J. V. Sengers, Int. J. Thermophys. **14**, 1 (1993).
[12] J. C. Rainwater, Int. J. Thermophys. **10**, 357 (1989).
[13] S. S. Leung and R. B. Griffiths, Phys. Rev. A **8**, 2670 (1973).

Translation was provided by the Russian Editorial office.

Effect of a random crystalline field on the Curie temperature of an anisotropic crystalline ferromagnet

M. V. Medvedev

Institute of Electrophysics, Ural Branch of the Russian Academy of Sciences, 620049 Ekaterinburg, Russia

E. V. Rozenfel'd

Institute of the Physics of Metals, Ural Branch of the Russian Academy of Sciences, 620219 Ekaterinburg, Russia

(Submitted 17 November 1995)
Zh. Éksp. Teor. Fiz. **111**, 127–143 (January 1997)

We examine how substitution of nonmagnetic atoms of one species by another that leads to the emergence of a random crystalline field affects the Curie temperature T_C of an anisotropic crystalline ferromagnet. We study the case of low concentrations, in which individual substitutional impurities create isolated clusters of perturbed magnetic ions with additional easy- or hard-magnetization axes. Finally, we analyze the various sign relations among the parameters D and d of regular and impurity second-order anisotropies with Kramers ($J = 1$) and non-Kramers ($J = 3/2$) angular momenta, and show that usually the effects of a random crystalline field lower the Curie temperature as the concentration of the nonmagnetic impurity atoms increases.
 [S1063-7761(97)00901-3]

1. INTRODUCTION

Magnetic compounds of the RNi_5 type, where R stands of rare-earth ions, and the Ni atoms have no localized magnetic moments, are convenient objects for studying magnetic anisotropy effects, since in such substances the energy of magnetocrystalline anisotropy is at least comparable to the exchange-interaction energy.[1] Recently a number of solid $RNi_{5-x}Cu_x$ solutions (R=Pr, Nd, Tb, and Er) have been studied. The research established that in such substances, with the exception of the special case of $PrNi_{5-x}Cu_x$, gradual substitution of Cu ions for Ni ions lowers spontaneous magnetization and, at the same time, elevates the Curie temperature T_C as the concentration of copper increases (with T_C passing through its maximum at a certain concentration).

There can be two reasons why the Curie temperature increases as one type of nonmagnetic ion is replaced by another. First, the effect can be explained by the assumption that the number of conduction electrons and, accordingly, the Fermi wave vector k_F, which enters into the expression for the Ruderman–Kittel indirect-exchange integral, change. Obviously, under certain conditions the change in k_F can lead to an increase in the ferromagnetic exchange interaction. Second, the increase in the Curie temperature T_C can be attributed to symmetry breaking in the local crystal neighbors and the appearance of additional random sources of crystalline field acting on the nearest magnetic atoms. For some of the magnetic atoms, which are already characterized by regular directions of easy or hard magnetization, extra anisotropy directions emerge that additionally restrict the mobility of magnetic ions caused by thermal fluctuations and in this way elevate the Curie temperature.

Since much remains to be done in studying the simultaneous effect of regular and random magnetic anisotropies on the concentration dependence of the Curie temperature of crystalline ferromagnets, in the present paper we attempt to establish the nature of the variation in T_C due to a random crystalline field. Here, to initially estimate the tendencies in the concentration behavior of the Curie point, we limit our discussion to low concentrations of the impurity sources of the random crystalline field. This makes it possible to assume that the regions in which the random crystalline field acts on magnetic atoms do not overlap, and that each atom from such a region experiences the action of only one impurity electric charge.

2. THE HAMILTONIAN OF IMPURITY SINGLE-ION ANISOTROPY

We assume that the magnetic atoms in an anisotropic ferromagnet form a single magnetic sublattice, and that the crystalline field at the magnetic ions is generated by the Coulomb potential of the nonmagnetic ions at the interstitial sites of the magnetic sublattice. Let the impurity nonmagnetic atoms substitute for the host nonmagnetic atoms, and let their charge $eZ_{\rm imp}^{\rm eff}$ differ from the effective charge of the host atoms, $eZ_{\rm host}^{\rm eff}$. Then the appearance of a nonmagnetic substitutional impurity in the vicinity of a magnetic ion can be modeled by the appearance of an additional charge q at the position of the nonmagnetic ion,

$$q=e(Z_{\rm imp}^{\rm eff}-Z_{\rm host}^{\rm eff}), \tag{1}$$

against the background of the existing symmetric distribution of charges $eZ_{\rm host}^{\rm eff}$ responsible for the single-ion anisotropy of the initial regular crystal.

For the origin we select the point occupied by the magnetic ion with an additional charge q in its vicinity. Then, if the radius vector $\mathbf{R}=(R\sin\theta\cos\psi,\ R\sin\theta\sin\psi,\ R\cos\theta)$ specifies the position of charge q in the laboratory system of coordinates (X,Y,Z) and $\mathbf{r}_i$ is the radius vector of the ith electron in the unfilled shell of the magnetic ion, the electric potential $V(\mathbf{r}_i)$ for a point charge q can be expanded in a power series in r_i/R (see Ref. 4):

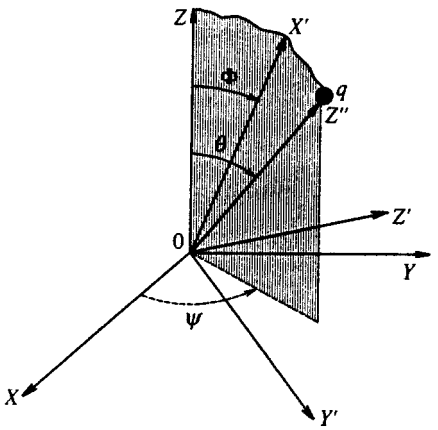

FIG. 1. The local system of coordinates $X'Y'Z'$ used in diagonalizing the single-ion anisotropy Hamiltonian.

$$V(\mathbf{r}_i)=\frac{q}{|\mathbf{r}_i-\mathbf{R}|}=\frac{q}{\sqrt{R^2+r_i^2-2(\mathbf{r}_i\cdot\mathbf{R})}}$$
$$\simeq\frac{q}{R}+\frac{q(\mathbf{r}_i\cdot\mathbf{R})}{R^2}+\frac{q}{2}\left[\frac{3(\mathbf{r}_i\cdot\mathbf{R})^2}{R^5}-\frac{r_i^2}{R^3}\right]+\ldots . \quad (2)$$

Summing the action of this potential on all the electrons in the unfilled shell and going over to the equivalent Steevens Hamiltonian,[4] we find that the emergence of an additional charge q leads to the appearance in the neighboring magnetic ions of additional contributions to the single-ion anisotropy Hamiltonian, of the form

$$\Delta H_0^{(2)}=\text{const}-dJ_{Z''}^2=\text{const}-d\left[\frac{1}{2}(3\cos^2\theta-1)J_Z^2\right.$$
$$+\frac{1}{4}\sin 2\theta(\{J_+,J_Z\}e^{-i\psi}+\{J_-,J_Z\}e^{i\psi})$$
$$\left.+\frac{1}{4}\sin^2\theta(J_+^2e^{-i2\psi}+J_-^2e^{i2\psi})\right]. \quad (3)$$

Here $\text{const}=(1/6)(3\cos^2\theta-1)J(J+1)d$, and in the model of a point charge acting on the shells of the f-ions, the parameter d of impurity single-ion anisotropy is given by

$$d=\frac{3|e|q\alpha_{2J}\langle r_f^2\rangle}{4R^3}. \quad (4)$$

Since α_{2J} is positive for Sm, Er, Tm, and Yb, and negative for Pr, Nd, Tb, Dy, and Ho,[5] the parameter d can be either positive or negative, depending on the magnetic-ion species and the sign of the additional charge q.

The expression for $\Delta H_0^{(2)}$ is written both in terms of the projections of the total angular momentum J on the X, Y, Z axes of the laboratory system of coordinates, and in terms of the projections on the Z'' axis of the local system of coordinates, in which this axis is directed from the magnetic ion to the additional charge q (Fig. 1). Moreover, since the additional charge q acts not on a single magnetic ion but on a whole cluster of magnetic ions surrounding the interstitial site with a nonmagnetic impurity, for each magnetic ion of this cluster we must introduce the appropriate coordinate angles θ and ψ in the Hamiltonian (3). Finally, note that (3) does not contain the higher-order terms in powers of the ratio $\langle r_f\rangle/R$. Such terms lead to fourth- and sixth-order invariants in the projections J_α of the angular momentum operator, with $\alpha=X,Y,Z$.

3. THE RANDOM-MOLECULAR-FIELD APPROXIMATION

We assume that additional charges q lead only to the appearance of additional terms (3) in the single-ion anisotropy of some of the magnetic ions in the crystal, and do not appreciably change the exchange interaction between the magnetic moments. We also assume that the crystal symmetry of the initial compound allows for the coexistence of regular single-ion second-order anisotropy, which we choose to be of the simplest possible form $-DJ_Z^2$, with D either positive or negative. We introduce the random-molecular-field approximation for such a system.

First we note that although formally the localized magnetic moments at all magnetic sites correspond to the same angular momentum operator J, the thermodynamic averages of the projections of angular momentum J_α may differ considerably for the sites surrounding a nonmagnetic impurity site (we call such sites cluster sites) and for the sites that are not the nearest neighbors of the additional impurity charge q (we call such sites matrix sites). This difference can be related primarily to the dramatic difference in the crystalline fields for ensembles of the sites of the corresponding type, while the difference resulting from variations in the random magnetic fields can be considered less significant.

The single-site Hamiltonian of the molecular field for an arbitrary matrix site m is then

$$H_h(m)=H_{h,ex}(m)+H_{h,0}(m)$$
$$=-\mathbf{J}(m)\mathbf{h}_h(m)-DJ_Z^2(m), \quad (5)$$

and for a cluster site n it is

$$H_{cl}(n)=H_{cl,ex}(n)+H_{cl,0}(n)$$
$$=-\mathbf{J}(n)\mathbf{h}_{cl}(n)-DJ_Z^2(n)-dJ_{Z''}^2(n). \quad (6)$$

By writing the exchange contribution as a scalar product, we allow for the fact that after additional local anisotropy axes have appeared, the equilibrium orientations of the magnetic moments at different sites can lose their collinearity.

Furthermore, if for the sake of simplicity we use the nearest-neighbor approximation for the exchange interaction, then in writing the molecular fields for the matrix and cluster sites, $\mathbf{h}_h(m)$ and $\mathbf{h}_{cl}(n)$, we must allow for the principal difference between our system and disordered magnetic alloys: whereas for matrix sites the nearest magnetic neighbors are of a random nature (there is a certain probability that the nearest magnetic neighbors are either matrix sites or cluster sites), the nearest magnetic neighbors of a cluster site consist of a fixed number of matrix and cluster sites.

For instance, Fig. 2 is a rough sketch of a crystal lattice in which the magnetic ions form a simple orthorhombic crys-

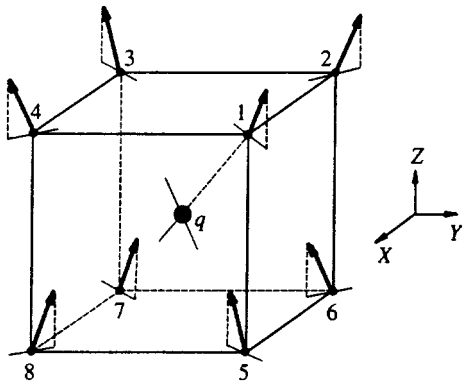

FIG. 2. Equilibrium orientations of the magnetic moments of cluster sites on a pseudocubic lattice for $D>0$ (a ferromagnet of the easy-axis type with magnetization along the Z axis) and $d>0$ (additional easy-magnetization axes along the principal diagonals of the cube).

tal sublattice, in which the difference between the crystal-lattice parameters $a\neq b\neq c$ is so small that the lattice is essentially cubic. If an impurity charge q is placed at one of the interstitial sites of the magnetic sublattice, its nearest magnetic neighbors form a cluster of eight magnetic atoms occupying the vertices of a pseudocube. Here each cluster site always has three cluster sites and three matrix sites as its nearest magnetic neighbors.

Taking all this into account, we can write the following expression for the molecular field of a matrix site m:

$$\mathbf{h}_h(m)=I\sum_{\delta=1}^{z}\{[1-p_{cl}(m+\delta)]\langle\mathbf{J}_h(m+\delta)\rangle + p_{cl}(m+\delta)\langle\mathbf{J}_{cl}(m+\delta)\rangle\}. \tag{7}$$

Here I is the exchange integral involving the nearest neighbors, the sum over δ runs through the nearest z magnetic neighbors, the projection operator $p_{cl}(m+\delta)$ can be written

$$p_{cl}(m+\delta)=\begin{cases}1 & \text{if site } m+\delta \text{ is a cluster site,}\\ 0 & \text{if site } m+\delta \text{ is a matrix site,}\end{cases} \tag{8}$$

and the labels h and cl are introduced to distinguish between the thermodynamic averages $\langle\cdots\rangle$ at matrix and cluster sites, respectively.

Let c_{cl} be the probability that the site $m+\delta$ is a cluster site, provided that m is a matrix site. Then averaging the projection operators over concentrations yields

$$\overline{p_{cl}(m+\delta)}=c_{cl}. \tag{9}$$

For a specific type of lattice we can always establish a relationship between the conditional probability c_{cl} and the overall concentration of magnetic atoms of the cluster type, c, and the concentration of nonmagnetic impurity atoms x. For instance, in the pseudocubic-lattice model (Fig. 2), the overall concentration of atoms of the cluster type is $c=z_1x$, since each nonmagnetic atom is surrounded by z_1 magnetic atoms. Since near each magnetic site there are in turn $z_1=8$ interstitial sites and the probability of occupying each interstitial site is x, we obtain

$$\overline{p_{cl}(m+\delta)}\equiv c_{cl}=\frac{1}{2}\,z_1x=\frac{1}{2}\,c. \tag{10}$$

The factor 1/2 allows for the fact that only half of the z_1 interstitial sites near the site $m+\delta$ can be filled by nonmagnetic impurities, while the other half of the interstitial sites are common sites for the m and $m+\delta$ sites and their filling by impurity atoms transforms site m also into a cluster site (instead of a matrix site).

For the molecular field of a cluster site n we can write

$$\mathbf{h}_{cl}(m)=I\left[\sum_{\Delta_{cl}=1}^{z_{cl}}\langle\mathbf{J}_{cl}(n+\delta_{cl})\rangle+\sum_{\Delta_h=1}^{z_h}\langle\mathbf{J}_h(n+\delta_h)\rangle\right], \tag{11}$$

where z_{cl} and z_h are the number of nearest neighbors of the cluster and matrix type, respectively, with

$$z_{cl}+z_h=z. \tag{12}$$

To study the concentration behavior of the temperature of the transition from a magnetically ordered state to a paramagnetic state, we use Eqs. (5) and (6) to obtain self-consistent linear equations for $\langle\mathbf{J}_{cl}(n)\rangle$ and $\langle\mathbf{J}_h(m)\rangle$. To this end we interpret the molecular exchange terms in (5) and (6) as a perturbation in relation to the single-ion anisotropy Hamiltonians. Then, using thermodynamic perturbation theory techniques, we arrive at the following expression for $\langle J_\alpha(g)\rangle$ (here $\alpha=X,Y,Z$, and the labels cl and h are dropped for the time being) at site g:

$$\langle J_\alpha(g)\rangle=\sum_\gamma\chi^0_{\alpha\gamma}(g)h_\gamma(g), \tag{13}$$

where the components of the tensor of local magnetic susceptibility at site g are (see, e.g., Ref. 5)

$$\chi^0_{\alpha\gamma}(g)=Q^{-1}\Bigg\{\beta_c\sum_i\langle i|J_\alpha(g)|i\rangle\langle i|J_\gamma(g)|i\rangle \times\exp[-\beta_cE_i^{(0)}(g)] +\sum_{i\neq l}\frac{\langle i|J_\alpha(g)|l\rangle\langle l|J_\gamma(g)|i\rangle}{E_i^{(0)}(g)-E_l^{(0)}(g)} \times(\exp[-\beta_cE_l^{(0)}(g)]-\exp[-\beta_cE_i^{(0)}(g)])\Bigg\}, \tag{14}$$

$$Q=\sum_i\exp[-\beta_cE_i^{(0)}(g)],\quad \beta_c=\frac{1}{T_C} \tag{15}$$

(our definition of the magnetic susceptibility tensor differs from the standard one in that our tensor does not contain the factor $(g_J\mu_B)^2$).

Calculating (14) requires knowing the eigenvalues $E_i^{(0)}(g)$ and eigenfunctions $|i\rangle\equiv|\Psi_i\rangle$ of the unperturbed single-ion anisotropy Hamiltonians,

$$H_0(g)|\Psi_i\rangle=E_i^{(0)}(g)|\Psi_i\rangle,\quad |\Psi_i\rangle\equiv|i\rangle, \tag{16}$$

which are different for matrix and cluster sites. It turns out that for matrix sites the best way to diagonalize the single-ion anisotropy Hamiltonian is to use the angular-momentum basis functions in the laboratory system of coordinates, while

for cluster sites it is more convenient to introduce a new local system of coordinates X',Y',Z', which makes it possible to easily diagonalize the single-ion anisotropy Hamiltonian and calculate the components of the magnetic susceptibility tensor $\chi^0_{\lambda\nu}(n)$ $(\lambda,\nu=X',Y',Z')$. In the final step, one must go back to the components of the tensor in the laboratory system of coordinates.

4. DIAGONALIZING THE SINGLE-ION ANISOTROPY HAMILTONIAN IN THE CASE OF TWO SECOND-ORDER AXES

Let us examine the single-ion anisotropy Hamiltonian for a cluster site,

$$H_0=-DJ_Z^2-dJ_{Z''}^2, \tag{17}$$

with the direction of the Z'' axis in relation to the laboratory system of coordinates specified by a polar angle θ and an azimuthal angle ψ. We introduce a new system of (primed) coordinates in such a way that the Z' axis is perpendicular to the plane containing the Z and Z'' axes (see Fig. 1). Then the new X' and Y' axes also lie in this plane, with Φ the angle between the Z and X' axes.

We express J_Z and $J_{Z''}$ in terms of the projections of the operator J in the new system of coordinates:

$$J_Z=J_{X'}\cos\Phi-J_{Y'}\sin\Phi,$$

$$J_{Z''}=J_{X'}\cos(\theta-\Phi)+J_{Y'}\sin(\theta-\Phi). \tag{18}$$

After plugging (18) into (17) and going over to the circular projections $J_{\pm'}=J_{X'}\pm J_{Y'}$, we arrive at the following expression for the single-ion anisotropy Hamiltonian:

$$H_0=-\frac{D+d}{2}J(J+1)+\frac{D+d}{2}J_{Z'}^2$$

$$-\frac{1}{4}e^{2i\Phi}[D+de^{-2i\theta}]\,J_+^2,$$

$$-\frac{1}{4}e^{-2i\Phi}[D+de^{2i\theta}]J_{-'}^2. \tag{19}$$

Introducing the new variables

$$\epsilon=\frac{D+d}{2},\quad \Delta=\frac{1}{4}\sqrt{D^2+d^2+2Dd\cos 2\theta} \tag{20}$$

and the auxiliary angle φ,

$$\cos\varphi=\frac{D+d\cos 2\theta}{4\Delta},\quad \sin\varphi=\frac{d\sin 2\theta}{4\Delta}, \tag{21}$$

and dropping the unimportant constant term $-1/2(D+d)J(J+1)$, instead of (19) we get

$$H_0=\epsilon J_{Z'}^2-\Delta[e^{i(2\Phi-\varphi)}J_{+'}^2+e^{-i(2\Phi-\varphi)}J_{-'}^2]. \tag{22}$$

We see that it is convenient to impose a constraint on the angle Φ,

$$\Phi=\frac{\varphi}{2}, \tag{23}$$

since it reduces (22) to the simple form

$$H_0=\epsilon J_{Z'}^2-\Delta[J_{+'}^2+J_{-'}^2]. \tag{24}$$

The Hamiltonian (24) can easily be diagonalized analytically for $J=1$, 3/2, 2 if for the basis functions we take the angular-momentum functions $|J,J_{Z'}\rangle\equiv|J_{Z'}\rangle$ with projections of angular momentum on the local Z' axis.

4.1. The case $J=1$

For $J=1$, the eigenvalue spectrum $E_i^{(0)}$ and the eigenvectors $|\Psi_i\rangle$ have the form

$$E_1^{(0)}=0,\quad |\Psi_1\rangle=|0\rangle,$$

$$E_2^{(0)}=\epsilon+2\Delta,\quad |\Psi_2\rangle=(|1\rangle-|-1\rangle)/\sqrt{2},$$

$$E_3^{(0)}=\epsilon-2\Delta,\quad |\Psi_3\rangle=(|1\rangle+|-1\rangle)/\sqrt{2}. \tag{25}$$

Thus, the appearance of a second anisotropy axis splits the doublet level that exists at $J=1$ in the case of uniaxial anisotropy.

The tensor of zero magnetic susceptibility has only diagonal elements (the upper signs refer to the $X'X'$ component and the lower signs to the $Y'Y'$ component):

$$\chi^0_{X'X',Y'Y'}=\frac{2\{1-\exp[-\beta_c(\epsilon\mp 2\Delta)]\}}{(\epsilon\mp 2\Delta)[1+2\exp(-\beta_c\epsilon)\cosh(2\beta_c\Delta)]},$$

$$\chi^0_{Z'Z'}=\frac{\exp(-\beta_c\epsilon)\sinh(2\beta_c\Delta)}{\Delta[1+2\exp(-\beta_c\epsilon)\cosh(2\beta_c\Delta)]}. \tag{26}$$

In the limit $d\to 0$ (for which Φ is either zero or $1/2\pi$, depending on the sign of D), after appropriately relabeling the coordinates axes, we obtain an expression for the susceptibility tensor for matrix sites in the laboratory system of coordinates:

$$\chi^0_{XX}-\chi^0_{YY}=\frac{2[1-\exp(-\beta_cD)]}{D[2+\exp(-\beta_cD)]},$$

$$\chi^0_{ZZ}=\frac{2\beta_c}{2+\exp(-\beta_cD)}. \tag{27}$$

In the limit $d\to\infty$, for which $\Phi=1/2\varphi=\theta$ and the X' axis points to the impurity charge q, Eqs. (26) yield

$$\chi^0_{X'X'}(d\to\infty)=2\tanh\left(\frac{\beta_cD}{2}\sin^2\theta\right)(D\sin^2\theta)^{-1}$$

$$\simeq\begin{cases}\beta_c, & \beta_c|D|\sin^2\theta\ll 1,\\ 2/|D|\sin^2\theta=2\beta_c/\beta_c|D|\sin^2\theta\ll\beta_c, & \beta_c|D|\sin^2\theta\gg 1,\end{cases}$$

$$\chi^0_{Y'Y'}(d\to\infty)=\chi^0_{Z'Z'}(d\to\infty)=0, \tag{28}$$

while for $d\to-\infty$ we have

$$\chi^0_{X'X'}(d\to-\infty)=\chi^0_{Y'Y'}(d\to-\infty)=\chi^0_{Z'Z'}(d\to-\infty)=0. \tag{29}$$

4.2. The case $J=3/2$

For $J=3/2$, the appearance of a second anisotropy axis does not lift the degeneracy of doublet levels:

$$E^{(0)}_{1,2}=\frac{5}{4}\,\epsilon-\sqrt{\epsilon^2+12\Delta^2},\quad E^{(0)}_{3,4}=\frac{5}{4}\,\epsilon+\sqrt{\epsilon^2+12\Delta^2}. \tag{30}$$

The corresponding eigenfunctions can be written as

$$|\Psi_1\rangle=a\left|\frac{3}{2}\right\rangle+b\left|-\frac{1}{2}\right\rangle,\quad |\Psi_2\rangle=b\left|\frac{1}{2}\right\rangle+a\left|-\frac{3}{2}\right\rangle,$$
$$|\Psi_3\rangle=b\left|\frac{3}{2}\right\rangle-a\left|-\frac{1}{2}\right\rangle,\quad |\Psi_4\rangle=-a\left|\frac{1}{2}\right\rangle+b\left|-\frac{3}{2}\right\rangle, \tag{31}$$

where the coefficients a and b are

$$\left\{\begin{matrix}a\\ b\end{matrix}\right\}=\sqrt{\frac{1}{2}\left[1\mp\frac{\epsilon}{\sqrt{\epsilon^2+12\Delta^2}}\right]}. \tag{32}$$

The components of the magnetic susceptibility tensor in the local coordinate system are

$$\chi^0_{X'X',Y'Y'}=\beta_c\,\frac{\epsilon^2\pm6\epsilon\Delta+24\Delta^2}{2(\epsilon^2+12\Delta^2)}+\left[\beta_c\,\frac{\epsilon\pm6\Delta}{2\sqrt{\epsilon^2+12\Delta^2}}+\frac{3(\epsilon\mp2\Delta)^2}{4\sqrt{(\epsilon^2+12\Delta^2)^3}}\right]\tanh(\beta_c\sqrt{\epsilon^2+12\Delta^2}),$$
$$\chi^0_{Z'Z'}=\beta_c\,\frac{5\epsilon^2+12\Delta^2}{4(\epsilon^2+12\Delta^2)}+\frac{12\Delta^2-\beta_c\epsilon(\epsilon^2+12\Delta^2)}{\sqrt{(\epsilon^2+12\Delta^2)^3}}\tanh(\beta_c\sqrt{\epsilon^2+12\Delta^2}), \tag{33}$$

and for matrix sites of the crystal, after passing to the limit $d\to0$ and transforming the coordinate axes into the laboratory axes, we get

$$\chi^0_{XX}=\chi^0_{YY}=\frac{1}{2}\,\beta_c+\frac{1}{2}\left(\frac{3}{2D}-\beta_c\right)\tanh(\beta_cD),$$
$$\chi^0_{ZZ}=\frac{5}{4}\,\beta_c+\beta_c\,\tanh(\beta_cD). \tag{34}$$

In the limit $d\to\infty$ we have

$$\chi^0_{X'X'}(d\to\infty)=\frac{9}{4}\,\beta_c,$$
$$\chi^0_{Y'Y'}(d\to\infty)=\chi^0_{Z'Z'}(d\to\infty)=0, \tag{35}$$

and in the limit $d\to-\infty$,

$$\chi^0_{X'X'}(d\to-\infty)=\chi^0_{Z'Z'}(d\to-\infty)=\beta_c,$$
$$\chi^0_{Y'Y'}(d\to-\infty)=\frac{1}{4}\,\beta_c. \tag{36}$$

For $J=2$ the Hamiltonian (24) can be diagonalized in a similar manner.

The matrix elements of susceptibility obtained in this way in the local systems of coordinates of the cluster sites must by transformed into the matrix elements in the laboratory system of coordinates via the following relations:

$$\chi^0_{XX}=\cos^2\psi\left(\chi^0_{X'X'}\sin^2\frac{\varphi}{2}+\chi^0_{Y'Y'}\cos^2\frac{\varphi}{2}\right)+\chi^0_{Z'Z'}\sin^2\psi,$$
$$\chi^0_{YY}=\sin^2\psi\left(\chi^0_{X'X'}\sin^2\frac{\varphi}{2}+\chi^0_{Y'Y'}\cos^2\frac{\varphi}{2}\right)+\chi^0_{Z'Z'}\cos^2\psi,$$
$$\chi^0_{ZZ}=\chi^0_{X'X'}\cos^2\frac{\varphi}{2}+\chi^0_{Y'Y'}\sin^2\frac{\varphi}{2},$$
$$\chi^0_{XY}=\chi^0_{YX}=\sin\psi\cos\psi\times\left[\chi^0_{X'X'}\sin^2\frac{\varphi}{2}+\chi^0_{Y'Y'}\cos^2\frac{\varphi}{2}-\chi^0_{Z'Z'}\right],$$
$$\chi^0_{XZ}=\chi^0_{ZX}=\frac{1}{2}\cos\psi\sin\varphi(\chi^0_{X'X'}-\chi^0_{Y'Y'}),$$
$$\chi^0_{YZ}=\chi^0_{ZY}=\frac{1}{2}\sin\psi\sin\varphi(\chi^0_{X'X'}-\chi^0_{Y'Y'}). \tag{37}$$

For each magnetic ion in a cluster of z_1 ions surrounding the additional charge q, one must use the proper angles ψ and φ, but with the lattice symmetry specified, relations between the angles can be established, which means one can find the symmetry relations that link the matrix elements $\chi^0_{\alpha\gamma}$ of different cluster sites.

5. THE EQUATION FOR T_C IN THE MODEL OF AN ANISOTROPIC FERROMAGNET WITH A PSEUDOCUBIC LATTICE

Deriving an equation for the Curie temperature requires averaging the infinite system of linear equations (13) over the concentration disorder, with allowance, first, for the difference between matrix and cluster sites and, second, for the difference in the orientations of the magnetic moments at different sites of a magnetic cluster. To do this we must specify the shape of the crystal lattice of the initial regular crystal and the signs of the parameters of regular and impurity anisotropies, D and d.

As an example we take the above-mentioned pseudocubic lattice of magnetic ions, in which small concentrations of substitutional impurities occupying the positions of nonmagnetic atoms create only one type of magnetic cluster. We

start with the case in which both D and d are positive, i.e., in which there is anisotropy of the easy-axis type and an additional easy-magnetization axis for each cluster site. Since in a regular crystal and, accordingly, far from a perturbing charge, the magnetic moments are aligned along the Z axis, the magnetic moments of the cluster sites tend to align in equilibrium directions between the Z axis and the principal diagonals of the cube (see Fig. 2).

Averaging (13) over the ensemble of all matrix sites, we get

$$\sigma_Z=\chi^0_{ZZ}\overline{h_{Z,h}}=\chi^0_{ZZ}(A)Iz \times\left[(1-c_{cl})\sigma_Z+c_{cl}\frac{1}{z_1}\sum_{c=1}^{8}\tau_Z(i)\right], \tag{38}$$

where the bar stands for averaging over configurational disorder. Here $\sigma_Z\equiv\overline{\langle J_{Z,h}(m)\rangle}$, and we have allowed for the fact that the magnetic susceptibility tensor $\chi^0_{\alpha\gamma}(A)$ is diagonal in the laboratory system of coordinates (by A we denote sites of the matrix type and by B sites of the cluster type). Furthermore, in averaging the molecular field at a matrix site, $\overline{h_{Z,h}(m)}$, one must bear in mind that if the nearest neighbor of the matrix site is a cluster site (with probability c_{cl}), then the magnetic moment of an arbitrary cluster site will be oriented as at site 1 in Fig. 2 (with probability c_{cl}/z_1) or as at site 2, etc. In view of this one must distinguish between the average values $\tau_\alpha(i)\equiv\overline{\langle J_{\alpha,cl}(i)\rangle}$ of the projections of the magnetic moments at the different sites ($i=1,...,8$) of the magnetic cluster.

Averaging (13) for all sites of type 1 in the magnetic clusters, we can write the following equation:

$$\tau_\alpha(1)\equiv\overline{\langle J_{\alpha,cl}(1)\rangle}=\sum_{\gamma=X,Y,Z}\chi^0_{\alpha\gamma}(B)\overline{h_{\gamma,cl}(1)}, \tag{39}$$

where we have allowed for the fact that the magnetic susceptibility tensor $\chi^0_{\alpha\gamma}(B)$ of cluster sites is nondiagonal in the laboratory system of coordinates. Here the averaging of the projection of the molecular field at cluster sites of type 1 yields

$$\overline{h_{\gamma,cl}(1)}=I[\tau_\gamma(2)+\tau_\gamma(4)+\tau_\gamma(5)],\quad \gamma=X,\ Y, \tag{40}$$

$$\overline{h_{Z,cl}(1)}=I[\tau_Z(2)+\tau_Z(4)+\tau_Z(5)+3\sigma_Z]. \tag{41}$$

Note that according to (11), all the projections of the random magnetic field $h_{\gamma,cl}(i)$ for the cluster sites $i=1,...,8$ contain magnetizing contributions from the magnetic moments $\langle J_{\gamma,h}(i+\delta_h)\rangle$ of the nearest magnetic sites, since near a noncollinear magnetic cluster there emerges a certain noncollinearity in the magnetic structure of the matrix due to the exchange interaction between cluster and matrix.

However, it becomes immediately apparent that the cluster magnetic moments and the magnetic moments of the magnetic sites nearest to the cluster are subject to quite different physical conditions. If, for instance, we take the case of a strong impurity easy-axis anisotropy $d\gg D\gg Iz$, where the magnetic moments of the cluster are essentially aligned along the impurity easy-magnetization axes and the noncollinearity of the magnetic structure of the cluster is at its maximum, then on each magnetic moment in the cluster there act (a) the extremely strong impurity crystalline field $\sim d$ directed at an angle to the crystal's magnetization, and (b) the exchange field generated by the z nearest magnetic moments, where $z/2$ of these moments are of the cluster type and strongly disoriented in relation to the direction long-range ferromagnetic order. At the same time, even on the matrix magnetic moment nearest to the cluster there act (i) the regular crystalline field $\sim D$ aligned with the direction of long-range ferromagnetic order, and (ii) the exchange field generated by the nearest neighbors, of which only one (in our model) is a neighbor of the cluster type, and for that reason is sure to be strongly disoriented. Obviously, the noncollinearity of the magnetic moments of even the nearest magnetic neighbors in the matrix is much weaker than the noncollinearity of the magnetic moments of the cluster (all the more so for second matrix neighbors). Hence for the simplest approximation we take the one in which the following conditions hold for finding the $\overline{h_{\gamma,cl}(i)}$:

$$\overline{\langle J_{Z,h}(i+\delta_h)\rangle}=\sigma_Z, \tag{42}$$

$$\overline{\langle J_{X,h}(i+\delta_h)\rangle}=\overline{\langle J_{Y,h}(i+\delta_h)\rangle}=0. \tag{43}$$

This means that we ignore the contributions of the noncollinearity of the nearest matrix sites, which has the form of a falloff in short-range order, but fully allow for the noncollinearity of the magnetic moments of a cluster.

Of course, with a more accurate approximation one can attempt to build linearized equations for the projections of the magnetic moments at the nearest neighbors of the matrix (with respect to the cluster) and allow for the fact that the average X- and Y-projections of the magnetic moments on these atoms are nonzero, but at the same ignore the noncollinearity of the magnetic moments at second neighbors, etc. Such an approach, however, leads to a sharp increase in the number of parameters in the problem and the number of coupled equations. We will leave this problem for a future paper.

So as not to build similar equations for $\tau_\alpha(i)=\overline{\langle J_{\alpha,cl}(i)\rangle}$ for the other cluster sites $i=2,...,8$, we bring into the picture the symmetry of the orientation of the magnetic moments in the cluster of the given type (see Fig. 2). Clearly, this approach yields the following relations between the projections of the average magnetic moments of the different sites in the cluster:

$$\begin{aligned}
&\tau_Z=\tau_Z(i),\quad i=1,\ldots,8,\\
&\tau_X\equiv\tau_X(1)=-\tau_X(2)=-\tau_X(3)=\tau_X(4)=-\tau_X(5)\\
&\quad=\tau_X(6)=\tau_X(7)=-\tau_X(8),\\
&\tau_Y\equiv\tau_Y(1)=\tau_Y(2)=-\tau_Y(3)=-\tau_Y(4)=-\tau_Y(5)\\
&\quad=-\tau_Y(6)=\tau_Y(7)=\tau_Y(8),\\
&\tau_X=\tau_Y.
\end{aligned} \tag{44}$$

If we also bear in mind that in the lattice considered here the azimuthal angle for site 1 is $\psi_1=5\pi/4$ and $\sin\psi_1=\cos\psi_1$, Eqs. (37) yield

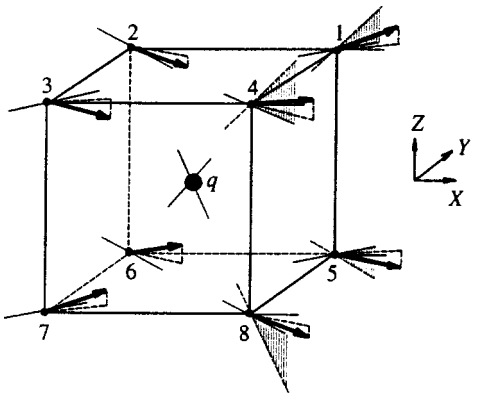

FIG. 3. Equilibrium orientations of the magnetic moments for $D<0$ (a ferromagnet of the easy-plane type with the direction of spontaneous magnetization along the X axis) and $d>0$. For clarity, the planes that pass through the principal diagonals of the cube and the diagonals of the upper and lower faces are hatched near sites *1, 2, 5*, and *6*.

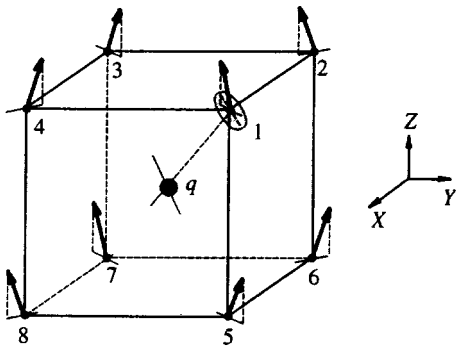

FIG. 4. Equilibrium orientations of the magnetic moments of cluster sites for $D>0$ (an easy-axis ferromagnet) and $d<0$ (additional easy-magnetization planes perpendicular to the principal diagonals of the cube). For clarity, the easy-magnetization plane near site 1 is depicted by an oval.

$$\chi^0_{ZX}(B;1)=\chi^0_{ZY}(B;1)\equiv\chi^0_{ZX}(B),$$
$$\chi^0_{XX}(B;1)=\chi^0_{YY}(B;1)\equiv\chi^0_{XX}(B). \tag{45}$$

Therefore, instead of Eqs. (38)–(41) we can finally write

$$[1-Iz(1-c_{cl})\chi^0_{ZZ}(A)]\sigma_Z-Izc_{cl}\chi^0_{ZZ}(A)\tau_Z=0,$$
$$-3I\chi^0_{ZZ}(B)\sigma_Z+[1-3I\chi^0_{ZZ}(B)]\tau_Z+2I\chi^0_{ZX}(B)\tau_X=0,$$
$$-3I\chi^0_{XZ}(B)\sigma_Z-3I\chi^0_{XZ}(B)\tau_Z$$
$$+\{1+I[\chi^0_{XX}(B)+\chi^0_{XY}(B)]\}\tau_X=0. \tag{46}$$

The next case is $D<0$ and $d>0$. The regular crystal exhibits ferromagnetism of the easy-plane type, and the long-range order in the matrix is described by an order parameter $\sigma_X=\overline{J_{X,h}(m)}\neq 0$. The magnetic moments of a separate cluster tend to align (see Fig. 3) along equilibrium directions between the X axis (the direction of magnetization of the matrix) and the principal diagonals of the pseudocube (the directions of the additional local-anisotropy axes). Then for the average values of the projections of the angular momentum operator of different sites in the cluster we have the following symmetry relations:

$$\tau_X\equiv\tau_X(i),\quad i=1,\ldots,8,$$
$$\tau_Y\equiv\tau_Y(1)=-\tau_Y(2)=\tau_Y(3)=-\tau_Y(4)=\tau_Y(5)$$
$$=-\tau_Y(6)=\tau_Y(7)=-\tau_Y(8),$$
$$\tau_Z\equiv\tau_Z(1)=-\tau_Z(2)=-\tau_Z(3)=\tau_Z(4)=-\tau_Z(5)$$
$$=\tau_Z(6)=\tau(7)=-\tau_Z(8),$$
$$\tau_Y\neq\tau_Z, \tag{47}$$

i.e., describing the magnetization of clusters involves using three order parameters.

With allowance for (45), this yields four coupled equations for T_C:

$$[1-Iz(1-c_{cl})\chi^0_{XX}(A)]\sigma_X-Izc_{cl}\chi^0_{XX}(A)\tau_X=0,$$
$$-3I\chi^0_{XX}(B)\sigma_X+[1-3I\chi^0_{XX}(B)]\tau_X+I\chi^0_{XY}(B)\tau_Y$$
$$+I\chi^0_{XZ}(B)\tau_Z=0,$$
$$-3I\chi^0_{XY}(B)\sigma_X-3I\chi^0_{XY}(B)\tau_X+[1+I\chi^0_{XX}(B)]\tau_Y$$
$$+I\chi^0_{XZ}(B)\tau_Z=0,$$
$$-3I\chi^0_{XZ}(B)\sigma_X-3I\chi^0_{XZ}(B)\tau_X+I\chi^0_{XZ}(B)\tau_Y$$
$$+[1+I\chi^0_{ZZ}(B)]\tau_Z=0. \tag{48}$$

Now we turn to the case in which $D>0$ and $d<0$ (the regular crystal exhibits ferromagnetism of the easy-axis type, and additional hard-magnetization axes emerge at the cluster sites). Equilibrium orientation of the magnetic moments of the cluster emerges because of a compromise between the tendency of the moments to align with the direction of the crystal's magnetization along the Z axis and the tendency to lie in planes perpendicular to the principal diagonals of the cube. This yields the symmetry relations (Fig. 4)

$$\tau_Z=\tau_Z(i),\quad i=1,\ldots,8,$$
$$\tau_X\equiv-\tau_X(1)=\tau_X(2)=\tau_X(3)=-\tau_X(4)=\tau_X(5)=-\tau_X(6)$$
$$=-\tau_X(7)=\tau_X(8),$$
$$\tau_Y\equiv-\tau_Y(1)=-\tau_Y(2)=\tau_Y(3)=\tau_Y(4)=\tau_Y(5)=\tau_Y(6)$$
$$=-\tau_Y(7)=-\tau_Y(8),$$
$$\tau_X=\tau_Y \tag{49}$$

and an equation for finding T_C:

$$[1-Iz(1-c_{cl})\chi^0_{ZZ}(A)]\sigma_Z-Izc_{cl}\chi^0_{ZZ}(A)\tau_Z=0,$$
$$-3I\chi^0_{ZZ}(B)\sigma_Z+[1-3I\chi^0_{ZZ}(B)]\tau_Z-2I\chi^0_{ZZ}(B)\tau_X=0,$$
$$3I\chi^0_{XZ}(B)\sigma_Z+3I\chi^0_{XZ}(B)\tau_Z$$
$$+[1+I(\chi^0_{XX}(B)+\chi^0_{XY}(B))]\tau_X=0. \tag{50}$$

Finally, we consider the case in which $D<0$ and $d<0$ (the existence of two directions of hard magnetization for the cluster sites and, at the same time, alignment of the sponta-

neous magnetization of the matrix along the X axis). We have four coupled equations for determining T_C:

$$[1-Iz(1-c_{cl})\chi^0_{XX}(A)]\sigma_X - Izc_{cl}\chi^0_{XX}(A)\tau_X = 0,$$
$$-3I\chi^0_{XX}(B)\sigma_X + [1-3I\chi^0_{XX}(B)]\tau_X - I\chi^0_{XY}(B)\tau_Y - I\chi^0_{XZ}(B)\tau_Z = 0,$$
$$3I\chi^0_{XY}(B)\sigma_X + 3I\chi^0_{XY}(B)\tau_X + [1+I\chi^0_{XX}(B)]\tau_Y + I\chi^0_{XZ}(B)\tau_Z = 0,$$
$$3I\chi^0_{XZ}(B)\sigma_X + 3I\chi^0_{XZ}(B)\tau_X + I\chi^0_{XZ}(B)\tau_Y + [1+I\chi^0_{ZZ}(B)]\tau_Z = 0. \quad (51)$$

6. CURIE TEMPERATURE T_C IN THE LIMIT OF INFINITELY STRONG IMPURITY ANISOTROPY

The systems of equations (46), (48), (50), and (51) in T_C can be solved for different numerical ratios of the parameters D and d. It is obvious, however, that magnetic clusters have the greatest effect on T_C when the parameter $|d|$ of the impurity crystalline field is at its maximum in relation to $|D|$. Therefore, to grasp the effect that clusters have on the temperature of magnetic ordering, we examine the limiting cases in which $d\to\infty$ and $d\to-\infty$ at cluster sites.

For $J=1$ and $d\to-\infty$ and allowing for (29), we have

$$1-Iz(1-c_{cl})\chi^0_{\alpha\alpha}(A)=0, \quad (52)$$

where $\alpha=Z$ for $D>0$ and $\alpha=X$ for $D<0$. Hence in the limit $d\to-\infty$, the cluster ions act as a nonmagnetic diluent of the regular ferromagnetic matrix, since they effectively weaken the exchange interaction, $Iz\to Iz(1-c_{cl})$, and this can only lower T_C.

For $J=1$ and $d\to\infty$, allowing for (28) and the fact that $\sin^2\theta=2/3$, in the laboratory system of coordinates we have

$$\chi^0_{\alpha\gamma}(B)=\frac{1}{3}\chi^0_{X'X'}(B,d\to\infty)=\frac{1}{D}\tanh\left(\frac{\beta_c D}{3}\right)\equiv\chi_0(B) \quad (53)$$

for all α, $\gamma=X$, Y, Z. As a result, from (46) and (48) we obtain

$$1-Iz\left[1-c_{cl}+c_{cl}\frac{3I\chi_0(B)}{1-I\chi_0(B)}\right]\chi^0_{\alpha\alpha}(A)=0, \quad (54)$$

where $\alpha=Z$ for $D>0$ and $\alpha=X$ for $D<0$.

For a ferromagnet of the easy-axis type ($D>0$), in the case of weak anisotropy of the matrix, $D/Iz\sim D\beta_c\ll 1$, Eq. (54) can be solved analytically:

$$T_C\approx 4I\left(1-\frac{8}{11}c_{cl}\right)+\frac{D}{3}. \quad (55)$$

Thus, even under the most favorable conditions, when a highly-anisotropic has the greatest effect on the transition temperature, only a decrease in T_C is observed. We believe the physical reason for this is that in the cluster model considered here, the greatest role is played by the geometrical factor, i.e., the large polar angle θ between the easy-magnetization axis Z and a principal diagonal of the cube. This leads to a situation in which even in the limit $d\to\infty$ and $D\to 0$, the susceptibility of the cluster sites along the laboratory Z axis, $\chi^0_{ZZ}(B)=(1/3)\beta_c$, proves to be lower than the susceptibility of the matrix sites ($\chi^0_{ZZ}(A)=(2/3)\beta_c$ in the limit $D\to 0$), with the result that cluster sites only reduce the contribution of exchange interaction to the stiffness of the magnetic system in the direction of spontaneous magnetization.

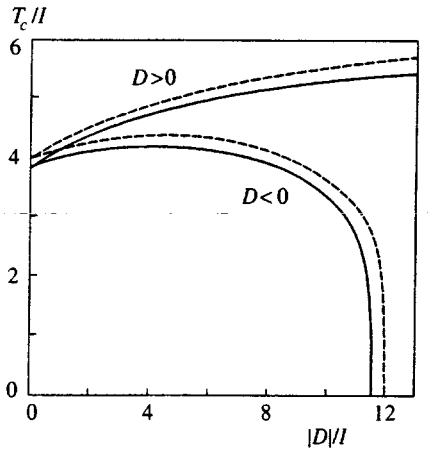

FIG. 5. The dependence of the Curie temperature (in dimensionless units of T_C/I) of an easy-axis ($D>0$) and an easy-plane ($D<0$) ferromagnet on the regular anisotropy parameter $|D|/I$ in the initial crystals (dashed curves) and in crystals with a finite concentration of cluster sites ($c_{cl}=0.05$) for $d\to\infty$. The conditional probability $c_{cl}=0.05$ for a pseudocubic lattice corresponds to a cluster-site concentration $c=0.10$ or a nonmagnetic-impurity concentration $x=0.0125$.

A more interesting case is ferromagnetism of the easy-plane type in the host matrix, since with the anisotropy being fairly strong, $|D|>0$, compared to the exchange coupling parameter I, the Curie temperature T_C in the matrix experiences a sharp drop and there can be even a transition to the nonmagnetic state (at $J=1$ this happens at $|D|/I=12$). One should therefore expect that near the threshold of the transition to the singlet state, clusters drive T_C up.

However, Eqs. (28) show that an increase in $|D|/I$ is accompanied by a decrease in the susceptibility of the cluster magnetic moments, $\chi^0_{X'X'}(d\to\infty)$, and, accordingly, by a decrease in $\chi_0(B)$, with the behavior of the magnetic moment departing from the Ising behavior in an ever more pronounced way. As a result, T_C only decreases in comparison to the Curie point of the initial crystal. This outcome is corroborated by numerical calculations of Eq. (54), whose results are depicted in Fig. 5. Clearly, for all ratios $|D|/I$, both in the case of an easy-plane ferromagnet ($D<0$) and an easy-axis ferromagnet ($D>0$) with a fixed concentration of cluster sites, the value of T_C of the impurity crystal is below that of the initial regular anisotropic ferromagnet.

The lack of a rise in T_C for $J=1$ is due to the splitting of the ground-state doublet $|\pm 1\rangle$ that results from the regular anisotropy of the crystal (the parameter D). It is obvious that for moments with $J>1$, where for $d\to\infty$ the doublet $|\pm J\rangle$ is the principal doublet, second-order regular anisotropy is unable to split the doublet. Then in the limit $d\to\infty$, we have $\chi^0_{X'X'}(d\to\infty)=J^2\beta_c$, and for integer angular momenta $J=2$, 4,..., the susceptibility of the cluster sites can become

larger than that of the matrix sites near the threshold of the transition to the singlet state. This allows for the possibility of T_C rising because of the appearance of clusters with strong impurity anisotropy, but detailed analysis of such a near-threshold situation requires a more detailed approach than that of the molecular-field approximation, since the accuracy of the latter is of order z^{-1}.

For a Kramers ion with $J=3/2$, the maximum possible impurity anisotropy of cluster sites is

$$\chi^0_{\alpha\beta}(B,d\to\infty)=\frac{3}{4}\,\beta_c \quad \text{for } \alpha,\beta=X,Y,Z \tag{56}$$

for $d\to\infty$, and

$$\chi^0_{XX}(B,d\to-\infty)=\chi^0_{YY}(B,d\to-\infty)=\chi^0_{ZZ}(B,d\to-\infty)=\frac{3}{4}\,\beta_c,$$

$$\chi^0_{XY}(B,d\to-\infty)=\chi^0_{YZ}(B,d\to-\infty)=\chi^0_{XZ}(B,d\to-\infty)=-\frac{1}{4}\,\beta_c \tag{57}$$

for $d\to-\infty$. This leads to the following equations for the transition temperature:

$$1-Iz\left(1-c_{cl}+\frac{9I\beta_c}{4-3I\beta_c}\,c_{cl}\right)\chi^0_{\alpha\alpha}(A)=0 \tag{58}$$

for $d\to\infty$, and

$$1-Iz\left[1-c_{cl}+\frac{3I\beta_c(3+I\beta_c)}{4-7I\beta_c-3(I\beta_c)^2}\,c_{cl}\right]\chi^0_{\alpha\alpha}(A)=0 \tag{59}$$

for $d\to-\infty$, where $\alpha=Z$ for an easy-axis ferromagnet ($D>0$), and $\alpha=X$ for an easy-plane ferromagnet ($D<0$).

When $c_{cl}\ll 1$, Eqs. (58) and (59) can easily be solved analytically in the limits of weak ($|D|/I\ll 1$) and strong ($|D|/I\gg 1$) anisotropies, and for all four relations between the signs of the parameters D and d, these equations yield a decrease in T_C as c_{cl} grows. For instance, for $D<0$ and $d\to\infty$ we have

$$T_C=\begin{cases}\dfrac{15}{2}\,I\left(1-\dfrac{2}{3}\,c_{cl}\right)+\dfrac{2}{5}\,|D|, & \dfrac{|D|}{I}\ll 1,\\[2ex] 6I\left(1-\dfrac{4}{7}\,c_{cl}\right)+27\,\dfrac{I^2}{|D|}, & \dfrac{|D|}{I}\gg 1.\end{cases} \tag{60}$$

The reason is obvious: even in the limit $D\to-\infty$ with $J=3/2$, the susceptibility of matrix sites does not drop below $\chi^0_{XX}(A)=\beta_c$, while, for instance, the susceptibility of cluster sites $\chi^0_{\alpha\beta}(B)$ does not exceed $(3/4)\beta_c$.

Furthermore, since for $d\to-\infty$ and $J=3/2$ cluster sites do not become nonmagnetic, although their susceptibility does decrease, the decrease in T_C with concentration in the entire sample occurs more slowly than when the ferromagnetic matrix is simply diluted with diamagnetic atoms. For instance, for $D<0$ and $d\to-\infty$ we have

$$T_C=\begin{cases}\dfrac{15}{2}\,I\left(1-\dfrac{66}{113}\,c_{cl}\right)+\dfrac{2}{5}\,|D|, & \dfrac{|D|}{I}\ll 1,\\[2ex] 6I\left(1-\dfrac{14}{33}\,c_{cl}\right)+27\,\dfrac{I^2}{|D|}, & \dfrac{|D|}{I}\gg 1,\end{cases} \tag{61}$$

i.e., the concentration factor has the form $1-Ac_{cl}$, instead of the factor $1-c_{cl}$ corresponding to simple diamagnetic dilution.

7. CONCLUSION

In the above calculations we employed a regular crystal lattice in which the angle θ between the regular anisotropy axis Z and the random anisotropy axis Z'' is quite large ($\sim 55°$). Since even the maximum possible impurity anisotropy of the easy-axis type ($d\to\infty$) drives the susceptibility of the cluster sites (in the local system of coordinates) up only to a certain limit, when we go over to the laboratory system of coordinates the large-angle geometrical factor comes into play, and this lowers the susceptibility of the cluster magnetic ions in comparison to that of the host ions. Hence the temperature T_C, corresponding to the onset of spontaneous magnetization along one of the laboratory axes of coordinates, drops.

Thus, we can probably expect a rise in the Curie temperature T_C due to the emergence of additional anisotropy axes, with the local symmetry being broken only when additional impurity charges produce new directions of easy magnetization at moderate angles to the direction of easy magnetization of the initial crystal.

In the latter case, the rise in T_C due to additional impurity easy-axis contributions becomes similar to the effect of the crystalline field on the magnetic ordering temperature T_C in regular ferromagnets. Regular single-ion second-order anisotropy of the easy-axis type is known to lead to a rise in T_C, in comparison to the T_C of an isotropic ferromagnet. For a magnetic moment with $J=1$, this result has been obtained both in various modifications of the method of two-time temperature Green's functions (see, e.g., Refs. 6 and 7) and in the diagrammatic technique,[8,9] while for magnetic moments with J from 1 to 7/2, it has been obtained in the so-called molecular-field correlation theory[10] (a detailed review of this problem for regular ferromagnets can be found in the monograph by Zvezdin *et al.*[5]).

The situation described in this paper differs from that of a regular ferromagnet in only one respect: crystalline-field impurity sources of the easy-axis type in our case increase the local magnetic susceptibility (in the laboratory system of coordinates) only at Nc cluster sites of the magnetic lattice, with the result that the increase in the Curie temperature, ΔT_C, is proportional to the concentration c of cluster sites.

Two concluding remarks are in order. First, the appearance of additional local anisotropy axes and the disorientation of magnetic moments near the impurity sources of a

crystalline field also lead to a drop in spontaneous magnetization. This drop is sudden, even at low concentrations x of the nonmagnetic atoms, since it involves approximately $z_1 x$ magnetic ions. Second, at higher concentrations x of the nonmagnetic atoms, random configurations of two, three, etc. impurity charges can form near each magnetic ion, while the finite clusters of perturbed magnetic ions overlap and form an infinite cluster. The situation resembles the model of an amorphous magnetic material with random anisotropy, but in our case the additional random-anisotropy axes have a denumerable number of directions, and random anisotropy effects emerge against the background of the regular anisotropy of the crystals.

The authors are grateful to A. S. Ermolenko and A. G. Kuchin for the experimental data and for discussing the results. The present work was made possible by financial support from the Russian Fund for Fundamental Research (Project No. 95-02-03664) and the International Science Foundation (Grant RG 7300).

[1] W. E. Wallace, *Rare Earth Intermetallics*, Academic Press, New York (1973).
[2] A. G. Kuchin, A. S. Ermolenko, V. I. Khrabrov, and G. M. Makarova, Fiz. Met. Metalloved. **79**, No. 3, 48 (1995) [Phys. of Metals and Metallography **79**, 266 (1995)].
[3] A. G. Kuchin, A. S. Ermolenko, V. I. Khrabrov, G. M. Makarova, E. V. Belozerov, Fiz. Met. Metalloved. **81**, No. 2, 54 (1996) [Phys. of Metals and Metallography **81**, 156 (1996)].
[4] M. T. Hutchings, in *Solid State Physics: Advances in Research and Applications*, H. Ehrenreich, F. Seitz, and D. Turnbull (Eds.), Vol. 16, Academic Press, New York (1964).
[5] A. K. Zvezdin, V. M. Matveev, A. A. Mukhin, and A. I. Popov, *Rare Earth Ions in Magnetically Ordered Crystals* [in Russian], Nauka, Moscow (1985).
[6] J. F. Devlin, Phys. Rev. B **4**, 136 (1971).
[7] M. Tanaka and Y. Kondo, Progr. Theor. Phys. **48**, 1815 (1972).
[8] D. H. Yang and Y. L. Wang, Phys. Rev. B **10**, 4714 (1974).
[9] D. H. Yang and Y. L. Wang, Phys. Rev. B **12**, 1057 (1975).
[10] M. E. Lines, Phys. Rev. B **12**, 3766 (1975).

Translated by Eugene Yankovsky

Unified picture of the distribution of electric field gradients at Cu, O, and Tm sites in $ReBa_2Cu_3O_{7-\delta}$

M. V. Eremin and O. V. Lavizina

Kazan State University, 420008 Kazan, Russia
(Submitted 27 March 1996)
Zh. Éksp. Teor. Fiz. **111**, 144–157 (January 1997)

An abundant set of published experimental NMR/NQR data on electric field gradients in $ReBa_2Cu_3O_{7-\delta}$ high temperature conductors, where Re=Y and Tm, is used as a test for the singlet-correlated band theory. Because of the unusual spectral weight (''capacity'') of this band, it has been possible to match the number of holes per lattice site to photoemission data on the energy spectrum and the location of the Fermi level. In the framework of a unified picture of the distribution of holes (charges) it has been possible for the first time to explain satisfactorily the observed electric field gradients at the Cu(1), Cu(2), O(1), O(2), O(3), and O(4) sites, as well as NMR and inelastic neutron scattering data on the crystal electric field at the Tm ions.
 [S1063-7761(97)01001-9]

1. INTRODUCTION

There are quite a few papers devoted to studies of the internal electric field gradients at different sites of the $YReBa_2Cu_3O_{7-\delta}$.[1–5] Recently, Yureva *et al.*[6] have published a review article on the hyperfine fields at ^{63}Cu nuclei. Two different approaches are used to analyze the nature of the electric field gradients. One of them is based on numerical calculations (*ab initio*) of the multielectron band structure,[7–9] as for ordinary metals, while the other proceeds from a picture of almost localized electron shells, as for dielectrics.[10–12] The first approach has an obvious defect, as it cannot describe the dielectric–metal transition that takes place in the $YBa_2Cu_3O_{6+\delta}$ system when the doping index δ is raised, or explain photoemission data on the energy spectrum of the cuprates. As noted previously in a review,[13] the unsoundness of the ordinary band structure calculations is a direct consequence of an improper description of the strong electron correlations intrinsic to the cuprates. Here it is not surprising that the calculated electric field gradients[7,8] at the Cu nuclei are roughly half the experimentally measured values, and this indicates that the model is unable to provide a correct description of the state of the copper. This defect of the model[7–9] and of the entire approach as a whole is fundamental in nature, since the copper states play an important role in the formation of a band near the Fermi surface.

On the other hand, the picture of almost completely localized electronic shells[10–12] accounts well for the correlation among the copper electrons, but does not provide any systematic procedure for calculating the dispersion relation of the quasiparticles for metal samples of $YBa_2Cu_3O_{7-\delta}$ and the effective charges at the copper and oxygen sites for different doping levels. The purpose of our paper is to construct a more general model that retains the best aspects of the above approaches. Here we show that a proposed model[14,15] of singlet-correlated bands with hole tunnelling between the CuO_2 planes offers an entirely suitable basis for doing this. It has been shown[15] that this model provides a good description of the photoemission data on the energy spectrum of bilayer cuprates. It has been found[16] that it also gives a good description of the dielectric–metal phase transition phenomenon and of the change in spectral weight (''capacity'' of the band) with doping of the CuO_2 planes.

We briefly describe a picture of charge carrier motion in the CuO_2 plane in an improved (over Refs. 15 and 16) decoupling variant of the equations of motion.[17–19] As shown previously,[18] the new decoupling variant is better than ''Hubbard I'' and duplicates the Hubbard model dispersion relation obtained by numerical cluster calculations on modern supercomputers.[20] This band picture ensures a proper description of the dielectric–metal transition and gives a systematic procedure for calculating the effective charges at the copper and oxygen sites. Sections 3, 4, and 5 are devoted to an analysis of the different contributions to the electric field gradients at the Cu(1), Cu(2), O(1), O(2), O(3), and O(4) sites for $YBa_2Cu_3O_7$. Furthermore, we have included inelastic neutron scattering data for the crystal field potential at the unfilled $4f$-shell of the Tm ion and nuclear magnetic resonance data[21,22] in our analysis.

2. BAND STRUCTURE AND CALCULATION OF THE EFFECTIVE CHARGES OF Cu AND O

The effective charges at the Cu(2) and the O(2) and O(3) sites in the dielectric $YBa_2Cu_3O_6$ are roughly $+2|e|$ and $-2|e|$, respectively. We are interested now in how these magnitudes will change when the crystal is doped with holes, as a result of which it becomes a conductor ($YBa_2Cu_3O_7$).

The Hamiltonian for a single CuO_2 plane has the form[14,16]

$$\mathscr{H}=\mathscr{H}_0+\mathscr{H}_1, \tag{1}$$

where

$$\mathscr{H}_0=\varepsilon_d\sum_{i\sigma}\Psi_i^{\sigma_d,\sigma_d}+V_{pd}\sum_{i\sigma}\Psi_i^{pd,pd} \tag{2}$$

is the Hamiltonian for a single site. Here $\Psi_i^{\sigma_d,\sigma_d}$ and $\Psi_i^{pd,pd}$ are Hubbard operators, and ε_d and V_{pd} are the energies of the copper and oxygen singlet-correlated holes, respectively. The second term in Eq. (1) describes intraplanar jumps and can be written in the form[16]

TABLE I. Jump intervals (in meV).

Number of neighboring site	1	2	3	4	5	6
$t_{ij}^{(1)}$	59.83	2.33	7.33	2.04	0.79	3.00
$t_{ij}^{(2)}$	51.84	4.38	5.30	2.13	0.89	2.33
$t_{ij}^{(12)}$	−56.99	−3.79	−6.28	−2.19	−0.89	−2.68

$$\mathscr{H}_1=\sum_{i\neq j} t_{ij}^{(1)}\Psi_i^{pd,\overline{\sigma_d}}\Psi_j^{\overline{\sigma_d},pd}+\sum_{i\neq j} t_{ij}^{(2)}\Psi_i^{\sigma_d,0}\Psi_j^{0,\sigma_d}$$
$$+\sum_{i\neq j} t_{ij}^{(12)}(-1)^{1/2-\sigma_d}(\Psi_i^{pd,\overline{\sigma_d}}\Psi_j^{0,\sigma_d}$$
$$+\Psi_i^{\sigma_d,0}\Psi_j^{\overline{\sigma_d},pd}). \tag{3}$$

Here $t_{ij}^{(1)}$, $t_{ij}^{(2)}$, and $t_{ij}^{(12)}$ are the jump integrals for holes between copper sites in the plane. The relative magnitudes of the jump integrals between the first, second, third, etc. neighbors are determined by the Wannier construction and are given in Ref. 16. Their absolute values were found by fitting the calculated dispersion curves to published photoemission data[23] and are listed in Table I.

Since $YBa_2Cu_3O_7$ has two CuO_2 planes, as before[15] we have assumed an interplanar coupling effect. The complete Hamiltonian of a bilayer of planes a and b has the form[15]

$$\mathscr{H}_{ab}=\mathscr{H}_a+\mathscr{H}_b+\mathscr{H}_{tun}, \tag{4}$$

where $\mathscr{H}_{tun}$ describes jumps of singlet-correlated oxygen holes between planes a and b. In the Hubbard operator representation it looks like

$$\mathscr{H}_{tun}=\sum_{i\neq j} t_{ij}^{(ab)}(\Psi_{ai}^{pd,\sigma_d}\Psi_{bj}^{\sigma_d,pd}+\Psi_{bi}^{pd,\sigma_d}\Psi_{aj}^{\sigma_d,pd}). \tag{5}$$

The $t_{ij}^{(ab)}$ were estimated from photoemission data and the equations of Ref. 16 to be

$$t_0^{(ab)}=40 \text{ meV}, \quad t_1^{(ab)}=16.48 \text{ meV},$$
$$t_2^{(ab)}=-7.39 \text{ meV}, \quad t_3^{(ab)}=3.93 \text{ meV},$$
$$t_4^{(ab)}=-0.97 \text{ meV}.$$

We now introduce even and odd combinations of the operators with respect to the reflection plane between neighboring planes in a unit cell of $YBa_2Cu_3O_7$:

$$\Psi_{0i}^{pd,\sigma_d}=\frac{1}{\sqrt{2}}(\Psi_{ai}^{pd,\sigma_d}-\Psi_{bi}^{pd,\sigma_d}),$$
$$\Psi_{0i}^{\sigma_d,0}=\frac{1}{\sqrt{2}}(\Psi_{ai}^{\sigma_d,0}-\Psi_{bi}^{\sigma_d,0}), \tag{6}$$
$$\Psi_{ei}^{pd,\sigma_d}=\frac{1}{\sqrt{2}}(\Psi_{ai}^{pd,\sigma_d}+\Psi_{bi}^{pd,\sigma_d}),$$
$$\Psi_{ei}^{\sigma_d,0}=\frac{1}{\sqrt{2}}(\Psi_{ai}^{\sigma_d,0}+\Psi_{bi}^{\sigma_d,0}). \tag{7}$$

Then the Hamiltonian (4) can be represented in the form

$$\mathscr{H}_{ab}=\sum_{i\neq j}(t_{ij}^{(1)}+t_{ij}^{(ab)})\Psi_{ei}^{pd,\overline{\sigma_d}}\Psi_{ej}^{\overline{\sigma_d},pd}$$
$$+\sum_{i\neq j} t_{ij}^{(2)}\Psi_{ei}^{\sigma_d,0}\Psi_{ej}^{0,\sigma_d}$$
$$+\sum_{i\neq j} t_{iJ}^{(12)}(-1)^{1/2-\sigma_d}(\Psi_{ei}^{pd,\overline{\sigma_d}}\Psi_{ej}^{0,\sigma_d}$$
$$+\Psi_{ei}^{\sigma_d,0}\Psi_{ej}^{\overline{\sigma_d},pd})+\sum_{i\neq j}(t_{ij}^{(1)}-t_{ij}^{(ab)})\Psi_{0i}^{pd,\overline{\sigma_d}}\Psi_{0j}^{\overline{\sigma_d},pd}$$
$$+\sum_{i\neq j} t_{ij}^{(2)}\Psi_{0i}^{\sigma_d,0}\Psi_{0j}^{0,\sigma_d}$$
$$+\sum_{i\neq j} t_{ij}^{(12)}(-1)^{1/2-\sigma_d}(\Psi_{0i}^{pd,\overline{\sigma_d}}\Psi_{0j}^{0,\sigma_d}$$
$$+\Psi_{0i}^{\sigma_d,0}\Psi_{0j}^{\overline{\sigma_d},pd}) \tag{8}$$

and can easily be diagonalized. Clearly, we obtain four quasiparticle bands: two ''odd,''

$$\varepsilon_{1k}^o=\frac{1}{2}(O_k^{pp}+O_k^{dd})+\frac{1}{2}[(O_k^{pp}-O_k^{dd})^2+4O_k^{pd}O_k^{dp}]^{1/2},$$
$$\varepsilon_{2k}^o=\frac{1}{2}(O_k^{pp}+O_k^{dd})-\frac{1}{2}[(O_k^{pp}-O_k^{dd})^2+4O_k^{pd}O_k^{dp}]^{1/2} \tag{9}$$

and two ''even,''

$$\varepsilon_{1k}^e=\frac{1}{2}(E_k^{pp}+E_k^{dd})+\frac{1}{2}[(E_k^{pp}-E_k^{dd})^2+4E_k^{pd}E_k^{dp}]^{1/2},$$
$$\varepsilon_{2k}^e=\frac{1}{2}(E_k^{pp}+E_k^{dd})-\frac{1}{2}[(E_k^{pp}-E_k^{dd})^2+4E_k^{pd}E_k^{dp}]^{1/2}. \tag{10}$$

When using the procedure to decouple the equations for the Green functions, as in Refs. 17–19, the quantities in Eq. (10) are defined by the expressions

$$E_k^{dd}=\varepsilon_d+\sum_{ij}\left(\frac{1-\delta_e}{2}+\frac{2}{1-\delta_e}\langle S_iS_j\rangle\right)t_{ij}^{(2)}$$
$$\times\exp\{i\mathbf{k}\cdot(\mathbf{R}_i-\mathbf{R}_j)\},$$
$$E_k^{pp}=V_{pd}^e-\varepsilon_d+\sum_{ij}\left(\frac{1+\delta_e}{2}+\frac{2}{1+\delta_e}\langle S_iS_j\rangle\right)$$
$$\times(t_{ij}^{(1)}+t_{ij}^{(ab)})\exp\{i\mathbf{k}\cdot(\mathbf{R}_i-\mathbf{R}_j)\},$$
$$E_k^{dp}=\sum_{ij}\left(\frac{1+\delta_e}{2}+\frac{2}{1+\delta_e}\langle S_iS_j\rangle\right)t_{ij}^{(12)}$$
$$\times\exp\{i\mathbf{k}\cdot(\mathbf{R}_i-\mathbf{R}_j)\}, \tag{11}$$

and

$$E_k^{pd}=\sum_{ij}\left(\frac{1-\delta_e}{2}+\frac{2}{1-\delta_e}\langle S_iS_j\rangle\right)t_{ij}^{(12)}$$
$$\times\exp\{i\mathbf{k}\cdot(\mathbf{R}_i-\mathbf{R}_j)\},$$

$$O_k^{pp}=V_{pd}^o-\varepsilon_d+\sum_{ij}\left(\frac{1+\delta_e}{2}+\frac{2}{1+\delta_e}\langle S_iS_j\rangle\right)\times(t_{ij}^{(1)}-t_{ij}^{(ab)})\exp\{i\mathbf{k}\cdot(\mathbf{R}_i-\mathbf{R}_j)\}. \quad (12)$$

The formulas for O_k^{dd}, O_k^{dp}, and O_k^{pd} are analogous. The spin–spin correlation functions[19] $\langle S_iS_j\rangle$ were taken to be to -0.047, 0.028, and 0.031 for the first, second, and third neighbors, respectively.

The chemical potential is a function of temperature and doping. It can be calculated self-consistently using the equations

$$2+\delta_e+\delta_o=\frac{1}{N}\sum_k(\langle\Psi_o^{pd,\sigma_d}\Psi_o^{\sigma_d,pd}\rangle_k+\langle\Psi_o^{\sigma_d,0}\Psi_o^{0,\sigma_d}\rangle_k)+\frac{1}{N}\sum_k(\langle\Psi_e^{pd,\sigma_d}\Psi_e^{\sigma_d,pd}\rangle_k+\langle\Psi_e^{\sigma_d,0}\Psi_e^{0,\sigma_d}\rangle_k), \quad (13)$$

where $\delta=\delta_e+\delta_o$ connotes the number of holes per two copper sites Cu(2). The thermodynamic averages are

$$\langle\Psi_o^{pd,\sigma_d}\Psi_o^{\sigma_d,pd}\rangle_k=\frac{1+\delta_o}{2}\left[\frac{\varepsilon_{1k}^o-O_k^{dd}}{\varepsilon_{1k}^o-\varepsilon_{2k}^o}f(\varepsilon_{1k}^o)-\frac{\varepsilon_{2k}^o-O_k^{dd}}{\varepsilon_{1k}^o-\varepsilon_{2k}^o}f(\varepsilon_{2k}^o)\right],$$

$$\langle\Psi_o^{\sigma_d,0}\Psi_o^{0,\sigma_d}\rangle_k=\frac{1-\delta_o}{2}\left[\frac{\varepsilon_{1k}^o-O_k^{pp}}{\varepsilon_{1k}^o-\varepsilon_{2k}^o}f(\varepsilon_{1k}^o)-\frac{\varepsilon_{2k}^o-O_k^{pp}}{\varepsilon_{1k}^o-\varepsilon_{2k}^o}f(\varepsilon_{2k}^o)\right],$$

$$\langle\Psi_e^{pd,\sigma_d}\Psi_e^{\sigma_d,pd}\rangle_k=\frac{1+\delta_e}{2}\left[\frac{\varepsilon_{1k}^e-E_k^{dd}}{\varepsilon_{1k}^e-\varepsilon_{2k}^e}f(\varepsilon_{1k}^e)-\frac{\varepsilon_{2k}^e-E_k^{dd}}{\varepsilon_{1k}^e-\varepsilon_{2k}^e}f(\varepsilon_{2k}^e)\right],$$

$$\langle\Psi_e^{\sigma_d,0}\Psi_e^{0,\sigma_d}\rangle_k=\frac{1-\delta_e}{2}\left[\frac{\varepsilon_{1k}^e-E_k^{pp}}{\varepsilon_{1k}^e-\varepsilon_{2k}^e}f(\varepsilon_{1k}^e)-\frac{\varepsilon_{2k}^e-E_k^{pp}}{\varepsilon_{1k}^e-\varepsilon_{2k}^e}f(\varepsilon_{2k}^e)\right], \quad (14)$$

where the Fermi functions $f(\varepsilon_{1k}^o)$ and $f(\varepsilon_{1k}^e)$ for the ''even'' and ''odd'' bands have the standard form:

$$f(\varepsilon_{1k}^o)=\left[1+\exp\left(\frac{\varepsilon_{1k}^o-\mu}{kT}\right)\right]^{-1},$$

$$f(\varepsilon_{1k}^e)=\left[1+\exp\left(\frac{\varepsilon_{1k}^e-\mu}{kT}\right)\right]^{-1}. \quad (15)$$

Here μ is the chemical potential, which we have shifted by 10 meV below the saddle point of the singular peak (see Fig. 1) in accordance with the photoemission data.[23] Obviously, the expressions

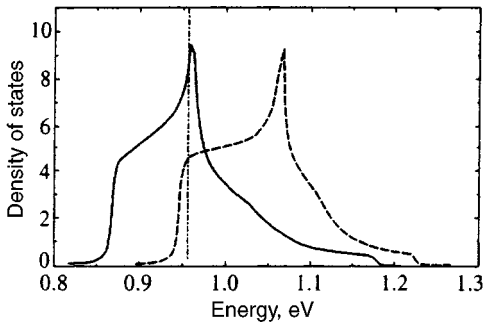

FIG. 1. Density of states of the ''even'' (smooth curve) and ''odd'' (dashed) bands. The vertical line denotes the chemical potential.

$$\frac{1}{N}\sum_{k,\sigma_d}\langle\Psi_{o,e}^{pd,\sigma_d}\Psi_{o,\varepsilon}^{\sigma_d,pd}\rangle_k,\quad\frac{1}{N}\sum_{k,\sigma_d}\langle\Psi_{o,e}^{\sigma_d,0}\Psi_{o,e}^{0,\sigma_d}\rangle_k \quad (16)$$

yield the number of copper and singlet-correlated oxygen holes per CuO_2 site. Their variation during doping leads to a shift in the values of the effective charges at the copper and oxygen sites. The equation for the chemical potential and the number of holes was solved self-consistently. As a result, we obtained $\delta_e=0.0223$ and $\delta_o=0.3277$. The effective charges at Cu(2) and O(2), O(3) calculated in this way for the compound $YBa_2Cu_3O_7$ are shown in Table II. Then, knowing the effective charges at the O(2) and O(3) sites, we can find the effective charges for O(1) and O(4) from the photoemission data,[24] where the relative numbers of oxygen holes at different oxygen sites were determined from polarized electron loss spectra. The available experimental data on the dispersion relation[23] and the curves we have calculated are shown in Fig. 2.

As noted previously,[25] in contrast to a two-dimensional band, the lower band ε_d of a chain is partially filled. As a consequence, we have a lower effective charge in a Cu(1) than in a Cu(2) site. Finally, we estimate the effective charge of Ba as $+2.13|e|$ from the electrical neutrality condition for a unit cell, in agreement with photoemission data.[26]

Lattice atoms occupying sites without an inversion center can be polarized. Effective dipole moments are induced at these positions by the total electric field from point charges ($\mathbf{E}_j^{ch}$), point dipoles ($\mathbf{E}_j^{dip}$), and quadrupoles ($\mathbf{E}_j^{qd}$). The magnitudes of the point dipole moments at the lattice sites were calculated from the following system of self-consistent equations:

TABLE II. Calculated values of the effective point charges (in units of $|e|$) and dipole moments (in units of $|e|$Å).

Site in unit cell	Effective charge	Dipole moment in $YBa_2Cu_3O_7$	Dipole moment in $TmBa_2Cu_3O_7$
Cu(2)	1.9994	0.0211	0.0289
O(2)	−1.9122	−0.1423	−0.1342
O(3)	−1.9122	−0.1768	−0.1654
Cu(1)	1.7000	0	0
O(1)	−1.7016	0	0
O(4)	−1.8042	−0.0685	−0.0828
Ba	2.1300	−0.0241	−0.0321
Re(Y,Tm)	3.0000	0	0

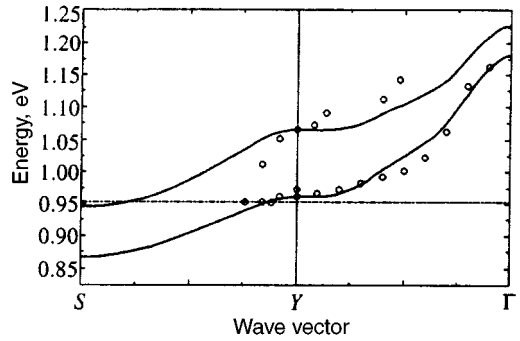

FIG. 2. Calculated dispersion (smooth curve) and photoemission data[23] (points). The horizontal line denotes the chemical potential.

$$\mathbf{d}_j=\alpha_j(\mathbf{E}_j^{ch}+\mathbf{E}_j^{dip}+\mathbf{E}_j^{qd}), \tag{17}$$

where the α_j are the polarizability parameters of the ions, which have been taken from published data: $\alpha(Cu^{2+})=0.65$,[27] $\alpha(O^{2-})=1.717$, and $\alpha(Ba^{2+})=2.24$.[28] The required lattice sums for formulating Eq. (17) were calculated using the Ewald method. The dipole moments calculated in this way are listed in Table II.

3. ELECTRIC FIELD GRADIENTS AT THE OXYGEN NUCLEI IN $YBa_2Cu_3O_7$

The following sources contribute to the electric field gradient at the oxygen sites:

(1) effective point charges, dipoles, and quadrupoles of the lattice sites;

(2) exchange charges, proportional to the overlap integrals of the oxygen $2p$-shell with the surrounding Cu, Ba, and Y shells;

(3) covalent charges resulting from the virtual transport of electrons from oxygen $2p$-shells to unfilled copper $3d$-shells; and

(4) dipole holes that appear in the $2p_\sigma$-states of oxygen owing to doping.

The gradients of the electric fields from point charges (q_j), dipoles ($\mathbf{d}_j$), and quadrupoles (Q_j) were calculated using the customary formula:

$$V_{\alpha\beta}^{(1)}=(1-\gamma_\infty)\sum_j \frac{\partial^2}{\partial x_{j\alpha}\partial x_{j\beta}}\left(\frac{q_j}{R_j}+\frac{\mathbf{d}_j\cdot\mathbf{R}_j}{R_j^3}+\frac{1}{6}\,Q_j^{lm}\,\frac{3x_{j\alpha}x_{j\beta}-R_j^2}{R_j^5}\right). \tag{18}$$

Here and in the following j is the index of a lattice site and $x_{j\alpha}$ and $x_{j\beta}$ (where $\alpha,\beta=x,y,z$) are the components of the radius vector $\mathbf{R}_j$. The Steinhamer antishielding factor $1-\gamma_\infty=12.287$ was taken from Schmidt *et al.*[29]

The effects owing to overlap of the $2p$-orbitals of oxygen with surrounding shells were taken into account using the formula

$$V_{\alpha\beta}^{(2)}=\frac{2}{5}\,|e|\left\langle\frac{1}{r^3}\right\rangle_{2p}\sum_j\left(N_{j\sigma}S^2_{n_jl_j,2p\sigma}-\frac{1}{2}\,N_{j\pi_x}S^2_{n_jl_j,2p\pi_x}-\frac{1}{2}\,N_{j\pi_y}S^2_{n_jl_j,2p\pi_y}\right)\frac{3x_{j\alpha}x_{j\beta}-R_j^2\delta_{\alpha\beta}}{R_j^2}. \tag{19}$$

Here $S_{n_j,l_j,2p\sigma}$, $S_{n_j,l_j,2p\pi_x}$, and $S_{n_j,l_j,2p\pi_y}$ are the overlap integrals of the p_z, p_x, and p_y orbitals with the n_jl_j-shells of neighboring ions (barium, copper, yttrium) in a local coordinate system with its z axis directed along $\mathbf{R}_j$. The N_j denote the occupation numbers of the orbitals. $N_j=2$ for a filled orbital. The radial wave functions of the $2p$-shell of O^{2-} were taken from Clementi and McLean,[30] while those of the $3s$-, $3p$-, and $3d$-shells of copper, the $4s$- and $4p$-shells of yttrium, and the $4s$-, $4p$-, $4d$-, and $5p$-shells of barium were taken from tables.[31,32] The calculated value of $\langle 1/r^3\rangle_{2p}$ was 3.272 a.u.

The effects of the covalent copper–oxygen bonds were taken into account by perturbation theory. The corresponding effective Hamiltonian for the quadrupole interaction in the second quantization representation can be written in the following way:

$$\mathscr{H}=-\frac{1}{2}\sum_{\eta\eta'}(\gamma_{\eta k}+2S_{\eta k})\langle k|h_Q|k'\rangle\gamma_{\eta' k'}a_{\eta'}a_\eta^+ +\text{H.c.}, \tag{20}$$

where h_Q is the operator for the interaction of the quadrupole moment of the nucleus with the copper electrons, $\gamma_{\eta k}$ is the electron jump amplitude, and k,k' and η,η' denote the quantum numbers of the $2p$-electrons of oxygen and the $3d$-electrons of copper, respectively.

The operator (20) yields the following expression for the electric field gradient at oxygen:

$$V_{\alpha\beta}^{(3)}=\frac{2}{5}\,|e|\left\langle\frac{1}{r^3}\right\rangle_{2p}\sum_j(2-N_{j\sigma})\gamma_{n_jl_j,2p\sigma}[\gamma_{n_jl_j,2p\sigma}+2S_{n_jl_j,2p\sigma}]\,\frac{3x_{j\alpha}x_{j\beta}-R_j^2\delta_{\alpha\beta}}{R_j^2}. \tag{21}$$

The ground state of Cu(2) is $|x^2-y^2\rangle$, so that $N_j=1$. The wave function of the ground state of Cu(1) can be represented by the combination

$$C_1|3z^2-r^2\rangle+C_2|x^2-y^2\rangle.$$

Because of the difference in the Cu(1)–O(4) and Cu(1)–O(1) distances, we have chosen the following coefficients: $C_1=0.9068$ and $C_2=0.4216$. N_j also equals unity, as does Cu(2). The covalence parameter $\gamma_{3d,2p\sigma}$ was taken in accordance with double electron–nuclear resonance data for $MgO:Ni^{2+}$, where $(\gamma_{3d,2p\sigma}+S_{3d,2p\sigma})^2=0.085$.[33]

In this analysis, the holes, which are distributed over the oxygen sites, only occupy σ-orbitals. In particular, the electric field gradient owing to these holes is calculated as follows for chain oxygen O(1):

$$V_{xx}^{(4)}=\frac{4}{5}\,|e|\left\langle\frac{1}{r^3}\right\rangle_{2p}n_x,\quad V_{yy}^{(4)}=V_{zz}^{(4)}=-\frac{1}{2}\,V_{xx}^{(4)}, \tag{22}$$

where n_x is the number of holes at one oxygen site. The results of the calculations together with the available experimental data are listed in Table III.

TABLE III. Electric field gradients at oxygen sites (10^{21} V/m^2).

Site in unit cell	$V_{\alpha\beta}$	$V^{(1)}_{\alpha\beta}$	$V^{(2)}_{\alpha\beta}$	$V^{(3)}_{\alpha\beta}$	$V^{(4)}_{\alpha\beta}$	$\Sigma V_{\alpha\beta}$	Experimental data[4]
	V_{xx}	−2.615	0.949	−1.560	−3.796	−7.022	−5.1
O(1)	V_{yy}	9.373	−2.375	3.120	7.592	17.710	17.2
	V_{zz}	−6.758	1.426	−1.560	−3.796	−10.688	12.1
	V_{xx}	−1.821	1.915	−1.032	−2.491	−3.429	−4.0
O(4)	V_{yy}	−4.918	1.297	−1.032	−2.491	−7.144	−7.6
	V_{zz}	6.739	−3.212	2.064	4.982	10.573	11.6
	V_{xx}	8.804	−2.041	3.036	2.234	12.033	10.5
O(2)	V_{yy}	−3.859	1.579	−1.557	−1.117	−4.954	−6.3
	V_{zz}	−4.945	0.462	−1.479	−1.117	−7.079	−4.2
	V_{xx}	−2.774	1.557	−1.562	−1.117	−3.896	−6.3
O(3)	V_{yy}	6.994	−2.155	3.039	2.234	10.112	10.2
	V_{zz}	−4.220	0.598	−1.477	−1.117	−6.216	−3.9

4. ELECTRIC FIELD GRADIENTS AT THE Cu(1) AND Cu(2) SITES

The expressions for the electric field gradients at the copper sites have almost the same form as those for the oxygen sites. Some differences arise because the $3d$-shells of copper are not completely filled and the matrix elements of the quadrupole electron–nuclear interaction are different.

The contribution from overlap of the inner $3d$-shell of copper and the $2p$-shell of oxygen in the Cu(1) site is given by an expression of the form

$$V^{(2)}_{zz}=\frac{8}{5}\,|e|\left\langle\frac{1}{r^3}\right\rangle_{3p}[(S1^2_\sigma-S1^2_\pi)-2(S4^2_\sigma-S4^2_\pi)],$$

$$V^{(2)}_{xx}-V^{(2)}_{yy}=-\frac{24}{5}\,|e|\left\langle\frac{1}{r^3}\right\rangle_{3p}(S1^2_\sigma-S1^2_\pi), \tag{23}$$

where $S1_\sigma$ and $S1_\pi$ are the overlap integrals of the $S_{3p,2p\sigma}$ and $S_{3p,2p\pi}$ states of Cu(1) and O(1), while $S4_\sigma$ and $S4_\pi$ are those for Cu(1) and O(4), respectively. For the Cu(2) sites the corresponding expressions have the form

$$V^{(2)}_{zz}=\frac{8}{5}\,|e|\left\langle\frac{1}{r^3}\right\rangle_{3p}[(S2^2_\sigma-S2^2_\pi)+(S3^2_\sigma-S3^2_\pi)],$$

$$V^{(2)}_{xx}-V^{(2)}_{yy}=\frac{24}{5}\,|e|\left\langle\frac{1}{r^3}\right\rangle_{3p}[(S2^2_\sigma-S2^2_\pi)-(S3^2_\sigma-S3^2_\pi)]. \tag{24}$$

Here $S2_{\sigma,\pi}$ and $S3_{\sigma,\pi}$ are the overlap integrals of Cu(2) with O(2) and O(3).

The contribution owing to overlap of the $3d$-shell with the $2p$-shell of oxygen and transfer of an electron from the $2p$- to the $3d$-shell for a Cu(2) site is given by

$$V^{(3)}_{zz}=-\frac{2}{7}\,|e|\left\langle\frac{1}{r^3}\right\rangle_{3d}\{[(S2^2_\sigma+4S2^2_\pi)+(S3^2_\sigma+4S3^2_\pi)]$$
$$+3[\gamma3_\sigma(\gamma3_\sigma+2S3_\sigma)+\gamma3_\sigma(\gamma3_\sigma+2S3_\sigma)]\},$$

$$V^{(2)}_{xx}-V^{(2)}_{yy}=\frac{24}{7}\,|e|\left\langle\frac{1}{r^3}\right\rangle_{3d}(S2^2_\sigma-S2^2_\pi). \tag{25}$$

Here $\gamma2_\sigma$ and $\gamma3_\sigma$ are the electron jump amplitudes for Cu(2)–O(2) and Cu(2)–O(3) pairs, respectively. Since the ground state of Cu(1) is the combination $C_1|3z^2-r^2\rangle+C_2|x^2-y^2\rangle$, the expressions for this contribution change slightly to

$$V^{(3)}_{zz}=\frac{2}{7}\,|e|\left\langle\frac{1}{r^3}\right\rangle_{3d}\{[(\widetilde{S}1^2_\sigma-4S1^2_\pi)+4(\widetilde{S}4^2_\sigma+2S4^2_\pi)]$$
$$-(C_1^2-C_2^2)[(C_1+\sqrt{3}C_2)^2\gamma1_\sigma(\gamma1_\sigma+2S1_\sigma)$$
$$+4C_1^2\gamma4_\sigma(\gamma4_\sigma+2S4_\sigma)]\},$$

$$V^{(3)}_{xx}-V^{(3)}_{yy}=-\frac{4\sqrt{3}}{7}\,|e|\left\langle\frac{1}{r^3}\right\rangle_{3d}C_1C_2\{[\widetilde{S}4^2_\sigma+(C_1$$
$$+\sqrt{3}C_2)^2\gamma1_\sigma(\gamma1_\sigma+2S1_\sigma)]-4[\widetilde{S}1^2_\sigma$$
$$+C_1^2\gamma4_\sigma(\gamma4_\sigma+2S4_\sigma)]\}, \tag{26}$$

where

$$\widetilde{S}4^2_\sigma=(C_1^2-2C_2^2)S4^2_\sigma,\quad \widetilde{S}1^2_\sigma=[(C_1+\sqrt{3}C_2)^2-2(C_1$$
$$-\sqrt{3}C_2)^2]S1^2_\sigma.$$

The valence contribution for the Cu(2) site is calculated using the customary formula

$$V^{(4)}_{zz}=\frac{4}{7}\,|e|\left\langle\frac{1}{r^3}\right\rangle_{3d}(1-R_Q)n_x,$$

$$V^{(4)}_{yy}=V^{(4)}_{zz}=-\frac{1}{2}\,V^{(4)}_{xx}, \tag{27}$$

and that for Cu(1), using

$$V^{(4)}_{zz}=-\frac{4}{7}\,(C_1^2-C_2^2)|e|\left\langle\frac{1}{r^3}\right\rangle_{3d}(1-R_Q)n_x,$$

$$V^{(4)}_{xx}-V^{(4)}_{yy}=\frac{8\sqrt{3}}{7}\,C_1C_2|e|\left\langle\frac{1}{r^3}\right\rangle_{3d}(1-R_Q)n_x, \tag{28}$$

where R_Q is the antishielding factor. $\langle1/r^3\rangle_{3p}=82.725$ a.u. and $\langle1/r^3\rangle_{3d}=8.265$ a.u. were calculated on the basis of the

TABLE IV. Electric field gradients at copper sites (10^{21} V/m^2).

Site in unit cell	$V_{\alpha\beta}$	$V^{(1)}_{\alpha\beta}$	$V^{(2)}_{\alpha\beta}$	$V^{(3)}_{\alpha\beta}$	$V^{(4)}_{\alpha\beta}$	$\Sigma V_{\alpha\beta}$	Experimental data[5]
Cu(1)	V_{xx}	13.698	−1.488	9.413	−29.249	−7.626	−7.4
	V_{yy}	−4.287	5.084	−3.270	10.099	7.626	7.5
	V_{zz}	−9.411	−3.596	−6.143	19.150	0.000	−0.1
Cu(2)	V_{xx}	−6.393	−1.754	−4.431	19.046	6.468	6.2
	V_{yy}	−4.774	−2.663	−4.431	19.046	7.112	6.2
	V_{zz}	11.167	4.416	8.928	−38.092	−13.580	−12.4

Hartree–Fock wave functions for Cu^{2+}.[30] The electric field gradients calculated with $1-\gamma_\infty=12.34$ and $R_Q=0.17$ are listed in Table IV. Experimental NQR data are also shown there in the last column.

5. CRYSTAL ELECTRIC FIELD AT THE RARE EARTH ION

The crystal electric field at the Re ion can be written in the following standard form:

$$\mathscr{H}_{CEF}=\sum_{k,q} B^q_k\langle \mathbf{J}\|\Theta_k\|\mathbf{J}\rangle O^q_k, \tag{29}$$

where $\mathbf{J}$ is the total momentum of the ground state, $\langle \mathbf{J}\|\Theta_k\|\mathbf{J}\rangle$ are the Stevens factors, O^q_k are the equivalent operators, and B^q_k are the so-called crystal electric field parameters. For HTSC materials they can be determined from NMR and inelastic neutron scattering measurements. Thus, we have an additional possibility of verifying our picture of the distribution of charges and dipoles in ReBaCuO.

The crystal electric field parameters were calculated as the sum of several contributions. Since the computational procedure has been described elsewhere,[34,35] we omit the details here and only present the results in Table V. In this table B^q_k(I), B^q_k(II), and B^q_k(III) denote the contributions from point charges, dipoles, and quadrupoles, respectively, B^q_k(IV), the contribution from overlap of the $4f$-shell of thulium with the $2p$-shells of oxygen, B^q_k(V), the contribution arising from the effects of exchange overlap and virtual transport of an electron from the $2p$-shell of O into the $4f$-shell of Tm, and B^q_k(VI), the contribution owing to transport of an electron from the $2p$-shell of O into the unfilled $5d$-shell of Tm.

The NMR spectrum of the Tm ion, with a singlet ground state, can be described using a spin Hamiltonian of the type

$$\mathscr{H}_I=\hbar\sum_i \gamma_i \mathbf{H}_i\cdot\mathbf{I}_i, \tag{30}$$

where $i=x,y,z$. Here the $\gamma_i=\gamma_I(1+\alpha_i)$ are the experimentally measured effective gyromagnetic ratios for Tm nuclei in the crystal and γ_I is the gyromagnetic ratio for a ''free'' nucleus. For the van Vleck paramagnetic material $TmBa_2Cu_3O_7$, the parameter α_i in the singlet ground state can be calculated as follows:

$$\alpha_i=\frac{2g_J\mu_B A_J}{\gamma_I\hbar}\sum_\nu \frac{|\langle g|\mathbf{J}_i|\nu\rangle|^2}{E_\nu-E_g}. \tag{31}$$

The energies E_ν can be found by diagonalizing the Hmiltonian (29). Here E_ν and $|\nu\rangle$ are the energies and wave functions of the excited states of the Tm ion. The symbol g denotes the singlet ground state, g_J the Lande factor, μ_B the Bohr magneton, and A_J the hyperfine interaction constant for the free Tm ion. The γ_i and the energy intervals are known from experimental NMR[22] and inelastic neutron scattering data.[21] The results of our calculations of the crystal electric field parameters, the γ_i, and the Stark splitting energies are listed in Table VI. As can be seen from the table, the calculated values are in good agreement with the available experimental data.

6. CONCLUSION

It can be seen from Tables III and IV that our proposed picture of the electronic structure of $YBa_2Cu_3O_7$ explains the available experimental data on the electric field gradients at the Cu(1), Cu(2), O(1), O(2), O(3), and O(4) sites just as well as the nuclear magnetic resonance data and data on the inelastic scattering of neutrons on Tm ions in $TmBa_2Cu_3O_7$. This supports the band structure model used here. The basis for the success in simultaneously explaining the entire set of NMR/NQR and photoemission data is the unusual behavior of the spectral weight (''capacity'') of the singlet band. As can be seen from Fig. 1, in our model, the bonding band is roughly half full by the time there are 0.175

TABLE V. Parameters of crystal electric field in $TmBa_2Cu_3O_7$ (cm^{-1}).

Parameter	B^k_q(I)	B^k_q(II)	B^k_q(III)	B^k_q(IV)	B^k_q(V)	B^k_q(VI)	ΣB^k_q
B^2_0	208.69	−192.29	−6.00	−11.41	37.91	22.32	59.22
B^2_2	110.84	59.15	1.97	−36.97	23.44	−0.83	157.62
B^4_0	−87.82	−4.26	-	20.40	−171.20	−2.23	−245.12
B^4_2	26.90	1.67	-	−11.38	22.21	0.02	39.42
B^4_4	477.38	155.94	-	−93.70	786.53	10.32	1284.10
B^6_0	2.85	1.43	-	−2.29	30.09	-	32.07
B^6_2	−3.11	−8.64	-	3.11	−7.90	-	−16.54
B^6_4	104.22	15.21	-	−57.06	747.73	-	810.10
B^6_6	1.42	1.15	-	−2.32	6.04	-	6.31

TABLE VI. $\gamma_i/2\pi$ (in kHz/Oe) and Stark splitting energies (in cm^{-1}).

Parameter	Calculated values	Experimental data[21,22]
	0	0
	115	106
	127	127
	198	-
	213	208
	280	-
E_ν	638	-
	678	-
	701	-
	708	-
	728	-
	729	-
	767	-
$\gamma_x/2\pi$	5.115	5.254
$\gamma_y/2\pi$	6.136	6.593
$\gamma_z/2\pi$	2.409	2.254

holes per copper site. It is precisely because of this that it was possible to match the distribution of charges and dipoles, needed to explain the NMR/NQR data, with the photoemission data.

The principal features of the proposed band structure are the following: in the dielectric $YBa_2Cu_3O_6$ the formal valence of the copper ions is 2 for Cu(2) and 1 for Cu(1). From the standpoint of the band structure, the lower Hubbard copper band ε_d in a chain is empty, while the band ε_d in a plane is completely filled. With doping, because of the strong exchange interaction between copper and oxygen holes in the plane, a new singlet band $\varepsilon_{pd}=V_{pd}-\varepsilon_d$ develops in the plane which is also filled with extra holes. At the same time, some of the extra holes begin to fill the ε_d band in the chain. As a result, the effective charge at a Cu(1) position begins to rise, but does not reach 2.

This picture of the band structure answers our question regarding the symmetry of the extra holes. In fact, why do the oxygen holes in the copper planes have a σ-character? This is hard to understand from the conventional standpoint, since their Coulomb repulsion from neighboring copper holes is much stronger than from π-holes. Nevertheless, photoemission[24] and NMR data[5] showed that the holes are mainly in σ-orbitals. And only in this case can we describe the electric field gradient at the oxygen sites. Our comment on this is the following: among the oxygen ε_p-states the π-orbitals actually lie below the σ-orbitals, as has been noted elsewhere.[36] But, as opposed to the earlier discussion,[36] in our case the ordinary oxygen band is empty, while extra holes fill the newly created ε_{pd} band, which lies below the oxygen band. This band appears because of strong electron correlations.

Finally, we wish to mention the importance of interplanar tunnelling. If we neglect it, then the number of holes arriving at a single site of the unit cell increases by roughly a factor of two, since in this case there are two degenerate bands from two planes, each of which must be filled to the saddle point of the singular peak in the density of states. However, the distribution of charges and dipoles obtained for this distribution of holes cannot produce reasonable agreement between the electric field gradients and the experimental data discussed above.

We thank Prof. M. A. Teplov and Dr. R. Markendorf for useful comments. This work was carried out with the partial support of the Russian Scientific-Technical Program in High Temperature Superconductivity (Project 94029) and with the financial support of St. Petersburg, Grant 95-0-7.1-35.

[1] M. Mali, D. Brinkmann, L. Pauli *et al.*, Phys. Lett. A **124**, 112 (1987).
[2] Y. Kitaoka, S. Hiramatsu, T. Kondo, and K. Asayama, J. Phys. Soc. Japan **57**, 30 (1980).
[3] T. Shimizu, H. Yasuoka, T. Imai *et al.*, J. Phys. Soc. Japan **57**, 2494 (1988).
[4] C. H. Pennington, D. J. Durand, D. B. Zax *et al.*, Phys. Rev. B **37**, 7944 (1988).
[5] M. Takigawa, P. C. Hammel, R. H. Heffner *et al.*, Phys. Rev. Lett. **63**, 1865 (1989).
[6] E. I. Yureva, V. P. Zhukov, N. I. Medvedeva, and V. A. Gubanov, Phys. Stat. Sol. A **146**, 557 (1994).
[7] C. Ambrosch-Draxl, P. Blaha, and K. Schwarz, J. Phys. Cond. Matter **1**, 4491 (1989).
[8] P. Blaha, D. J. Singh, P. I. Sorantin, and K. Schwarz, Phys. Rev. B **46**, 1321 (1992).
[9] J. Yu, A. J. Freeman, R. Podloucky *et al.*, Phys. Rev. B **43**, 532 (1991).
[10] A. Yu. Zavidonov, M. V. Eremin, O. N. Bakharev *et al.*, SFKhT **3**, 1597 (1990).
[11] T. Shimizu, J. Phys. Soc. Japan **62**, 772 (1993).
[12] K. Hanzawa, J. Phys. Soc. Japan **62**, 3302 (1993).
[13] W. Brenig, Phys. Reports **251**, 153 (1995).
[14] M. V. Eremin, R. Markendorf, and S. V. Varlamov, Solid State Commun. **88**, 15 (1993).
[15] M. V. Eremin, S. G. Solov'yanov, S. V. Varlamov *et al.*, JETP Lett. **60**, 125 (1994).
[16] M. V. Eremin, S. G. Solovjanov, and S. V. Varlamov, J. Phys. Chem. Sol. **56**, 1713 (1995).
[17] L. M. Roth, Phys. Rev. **184**, 451 (1969).
[18] J. Beenen and D. M. Edwards, Phys. Rev. B **52**, 13636 (1995).
[19] N. M. Plakida, R. Hayn, and J.-L. Richard, Phys. Rev. B **51**, 16599 (1995).
[20] N. Bulut, D. J. Scalapino, and S. R. White, Phys. Rev. B **50**, 7215 (1994); Phys. Rev. Lett. **73**, 748 (1994).
[21] P. Allenspach, U. Staub, J. Mesot *et al.*, Progress Report, LNS 154, Labor für Neutronenstreuung, ETH Zürich (Januar-Dezember 1990), pp. 22, 23.
[22] A. V. Egorov, H. Luetgemeier, U. Poppe, and R. Hojczyk, in *Ext. Abstr. of the XXVIIth Amp. Cong.*, Kazan, Aug. 21–28, 1994, p. 953.
[23] K. Gofron, J. C. Campuzano, H. Ding *et al.*, J. Phys. Chem. Sol. **154**, 1193 (1993).
[24] N. Nucker, E. Pellegrin, P. Schweiss *et al.*, Phys. Rev. B **51**, 8529 (1995).
[25] M. V. Eremin, R. Markendorf, and S. G. Solovjanov, Z. Naturforsch. a **49**, 379 (1994).
[26] V. V. Nemoshkalenko, V. Kh. Kasiyanenko, L. I. Nikolaev *et al.*, SVKhT **3**, 851 (1990).
[27] P. C. Schmidt, A. Weiss, and T. P. Das, Phys. Rev. B **19**, 5525 (1979).
[28] G. D. Mahan, Solid State Commun. **33**, 797 (1980).
[29] P. C. Schmidt, K. D. Sen, T. P. Das, and A. Weiss, Phys. Rev. B **22**, 4167 (1980).
[30] E. Clementi and A. D. McLean, Phys. Rev. **133**, 419 (1964).
[31] E. Clementi and C. Roetti, Atomic Data and Nuclear Data Tables **14**, 177 (1974).
[32] A. D. McLean and R. S. McLean, Atomic Data and Nuclear Data Tables **26**, 197 (1981).
[33] P. Freund, J. Phys. C **7**, L33 (1974).
[34] M. V. Eremin, Opt. Spektrosk. **68**, 860 (1990). [Opt. Spectrosc. (USSR) **68**, 502 (1990)].
[35] O. V. Lavizina, Fiz. Tverd. Tela **37**, 2247 (1995) [Phys. Sol. State **37**, 1228 (1995)].
[36] J. B. Goodenough, Supercond. Sci. Technol. **3**, 26 (1990).

Translated by D. H. McNeill

Theory of retardation of magnetic domain walls in rhombic magnetic materials

E. G. Galkina, B. A. Ivanov, and K. A. Safaryan

Institute of Magnetism, Ukrainian National Academy of Sciences, 252680 Kiev, Ukraine
(Submitted 17 April 1996)
Zh. Éksp. Teor. Fiz. **111**, 158–173 (January 1997)

We calculate the retardation of a magnetic soliton describing a magnetic domain wall by using the generalized phenomenological theory of relaxation. We show that in this theory, based on the real dynamical symmetry of magnetic materials, the dissipation function has a different structure for high and low wall velocities. Finally, we calculate the viscous force of the wall in the Walker model and show that certain features, not discussed in the literature, emerge even when the generalized theory is applied to this simple model. In particular, the dependence of the viscous friction force on the wall velocity may be highly nonlinear and regions of unstable motion may appear. © *1997 American Institute of Physics.*
[S1063-7761(97)01101-3]

1. The problem of the dynamics of topological solitons that describe magnetic domain walls occupies an important place among the nonlinear problems of the physics of magnetism (see the reviews in Refs. 1–4). An important parameter in describing the dynamics of solitons is the viscous friction force **f** that is exerted on a soliton moving with a velocity **v**, i.e., $\mathbf{f}=-\eta(v)\mathbf{v}$. Calculations of the viscous friction coefficient $\eta(v)$ for a magnetic domain wall based on the Landau–Lifshitz equation with the usual relaxation term of the Hilbert type lead to contradictions with the experimental data (see a discussion of this aspect in Refs. 2 and 3). Bar'yakhtar[5,6] suggested a generalized phenomenological theory of relaxation in ferromagnets based on allowing for the real dynamical symmetry of magnetic materials. He introduced relaxation terms of different origin (exchange and relativistic), which resulted in correct expressions for the dependence of the magnon damping constant on the wave vector and made it possible to describe several experiments in the dynamics of magnetic inhomogeneities. Bokov *et al.*[7] noted that this theory allows for a quantitative description of the results of their measurements of the dependence of the viscosity coefficient of a magnetic domain wall on the strength of a magnetic field perpendicular to the easy axis (a specific calculation can be found in Ref. 8). Exchange relaxation, considered in Ref. 9, made it possible to explain the results of the experiments[10] on retardation of a Bloch point. These facts suggest that the generalized theory can provide a quantitative description of nontrivial relaxation phenomena.

We calculate the viscous force of a magnetic domain wall in the Walker model and show that certain features, not discussed in the literature, emerge even when the generalized theory[5,6] is applied to this simple model. In particular, we find that the dependence of the viscous friction force of the wall velocity may be highly nonlinear and regions of unstable motion may appear.

2. In accordance with Bar'yakhtar's results,[5,6] we write the Landau–Lifshitz equation for the magnetization vector **M** of a ferromagnet as

$$\frac{\partial \mathbf{M}}{\partial t}=-g[\mathbf{M}\times\mathbf{F}]+gM_0[\mathbf{\Lambda}\times\mathbf{F}]-\lambda_e a^2 gM_0\nabla^2\mathbf{F}. \qquad (1)$$

Here g is the gyromagnetic ratio, the vector **F** represents the effective field of the ferromagnet ($\mathbf{F}=-\delta W/\delta\mathbf{M}$, with $W=W\{\mathbf{M}\}$ the ferromagnet's energy written as a functional of the magnetization vector), λ_e is the exchange relaxation constant, and $\mathbf{\Lambda}$ is the tensor of relativistic relaxation constants (see below and Ref. 6). We base our reasoning on expressions of the type

$$W\{\mathbf{M}\}=\int d\mathbf{r}\left\{f(M^2)+\frac{\alpha}{2}(\nabla\cdot\mathbf{M})^2+w_a(\mathbf{M})\right\}, \qquad (2)$$

where α is the inhomogeneous exchange constant, $f(M^2)$ describes the isotropic exchange interaction determining the absolute value of magnetization, and $w_a(\mathbf{M})$ is the energy of relativistic interactions, which incorporates the anisotropy energy and the energy of the demagnetizing field. With allowance for (2), we arrive at the following expression for the effective field **F**:

$$\mathbf{F}=-\frac{df}{dM}\mathbf{m}+\alpha\nabla^2\mathbf{M}-\frac{\partial w_a}{\partial\mathbf{M}}, \qquad (3)$$

where $\mathbf{m}=\mathbf{M}/M$. Clearly, **F** has a longitudinal part and a transverse part:

$$\mathbf{F}=F_{\parallel}\mathbf{m}+\mathbf{F}_{\perp}, \quad (\mathbf{m}\cdot\mathbf{F}_{\perp})=0. \qquad (4)$$

The expression for $F_{\parallel}$ can be reduced to

$$F_{\parallel}=-\frac{df}{dM}+\alpha\nabla^2 M-\alpha(\nabla\cdot\mathbf{m})^2 M-\left(\mathbf{m}\frac{\partial w_a}{\partial\mathbf{M}}\right)=-\frac{df}{dM}+\alpha\nabla^2 M-\frac{\partial w}{\partial M}, \qquad (5)$$

where we have introduced the quantity

$$w=\frac{\alpha}{2}M^2(\nabla\cdot\mathbf{m})^2+w_a(\mathbf{M}). \qquad (6)$$

This is an expression for the energy of a ferromagnet and is important when one writes the Landau–Lifshitz equation without allowing for variations in the length of the magnetization vector.

Let us discuss the structure of the relativistic relaxation term. Since here we consider ferromagnets whose symmetry is no lower than rhombic, the tensor $\mathbf{\Lambda}$ can be chosen in diagonal form, $\mathbf{\Lambda}=\mathrm{diag}(\lambda_x,\lambda_y,\lambda_z)$, with the x,y,z axes directed pointing along the principal axes of the ferromagnet. For a uniaxial ferromagnet $\lambda_x=\lambda_y=\lambda$ and, if we allow only for intrinsic relaxation processes, $\lambda_z=0$, in view of conservation of the z-projection of the total magnetization.[6] But if impurity relaxation (say, on rare-earth ions for which the nearest-neighbor symmetry is lower than the uniaxial but the different nonequivalent ion positions are distributed with equal probability) is taken into account, the properties of $\mathbf{\Lambda}$ are different. For instances, the symmetry of the tensor $\mathbf{\Lambda}$ for ferrite garnets is cubic, i.e., $\lambda_x=\lambda_y=\lambda_z$ (see Ref. 11). For this reason we select the tensor $\mathbf{\Lambda}$ in the form

$$\mathbf{\Lambda}=\lambda\ \mathrm{diag}(1,1,\varepsilon), \tag{7}$$

with the value of the constant ε specified later. Equation (1) makes it possible to write the dissipation function of a ferromagnet as a functional of the effective field $\mathbf{F}$:

$$Q=\frac{1}{2}\,gM\int d\mathbf{r}\{\lambda_{ik}F_iF_k+\lambda_e a^2(\nabla\cdot\mathbf{F})^2\}. \tag{8}$$

Equation (8) is not very suitable for analyzing the retardation of a magnetic domain wall since the dissipation function Q is defined in terms of the effective field $\mathbf{F}$ rather than in terms of the time derivative of magnetization. To calculate the rate of dissipation of the domain-wall energy, $dE/dt=-2Q$, we must express $\mathbf{F}$ in terms of $\mathbf{m}$ and its derivatives. In view of (4), $\mathbf{F}$ can be written as the sum of two terms corresponding to the transverse and longitudinal magnetizations. Calculating the transverse component in the principal approximation in the relaxation constant only requires using the nondissipative variant of (1), with the result that[5,6]

$$\mathbf{F}_\perp=\frac{1}{g}\left[\mathbf{m}\times\frac{\partial\mathbf{m}}{\partial t}\right]. \tag{9}$$

The longitudinal component of $\mathbf{F}$ is related to variations in the length of the magnetization vector $\mathbf{M}$, so that the Landau—Lifshitz equation without dissipation is of no help. The point is that while in the nondissipative approximation Eq. (1) has the integral of motion $\mathbf{M}^2=M_0^2=\mathrm{const}$ and can be written as an equation for the unit vector $\mathbf{m}$, with a dissipation term of general form one must also allow for variations in $|\mathbf{M}|$. As noted in Refs. 8, 9, 12–14 and as demonstrated below, the calculation of $F_\parallel$ constitutes the main problem in analyzing the dissipation of solitons within the generalized phenomenological approach.

3. The equation for $F_\parallel$ can be obtained by multiplying $\mathbf{m}$ into Eq. (1) and using the explicit form of $\mathbf{F}_\perp$. The result is

$$-\lambda_e a^2\nabla^2F_\parallel+[\lambda(\mathbf{m})+\lambda_e a^2(\nabla\cdot\mathbf{m})^2]F_\parallel=-\frac{1}{gM_0}\frac{\partial M}{\partial t}+\frac{1}{g}\left(\mathbf{m}\cdot\mathbf{\Lambda}\left[\mathbf{m}\times\frac{\partial\mathbf{m}}{\partial t}\right]\right)-\lambda_e\frac{a^2}{g}\left(\mathbf{m}\cdot\nabla^2\left[\mathbf{m}\times\frac{\partial\mathbf{m}}{\partial t}\right]\right), \tag{10}$$

where $\lambda(\mathbf{m})=(\mathbf{m}\cdot\mathbf{\Lambda}\mathbf{m})$. For the case where $\lambda_{ik}=\delta_{ik}$ the contribution of relativistic relaxation to the right-hand side of Eq. (10) is nil.

Note that no approximations have been introduced with the exception of formula (9) for $\mathbf{F}_\perp$. The only requirements are $\lambda\ll1$ and $\lambda_e(a/\Delta)^2\ll1$ (where Δ is the characteristic inhomogeneity scale), which are met by almost all magnetic materials.

If only these inequalities are taken into account, $F_\parallel$ is found by solving an inhomogeneous linear differential equation whose right-hand side is determined not only by the nature of the solution for the unit vector $\mathbf{m}$, but also by the variation in the length of the magnetization vector. For the majority of solitons without singularities there is an additional small parameter, the variation of magnetization in magnitude, $\mu=M-M_0\ll M_0$ (actually the small parameter is the longitudinal susceptibility χ). Taking all this into account, we can write $\partial M/\partial t$ in general form in terms of the function w introduced by Eq. (6). To simply matters, we write the energy of homogeneous exchange interaction as

$$f(M)-f(M_0)=\frac{1}{2}\frac{d^2f(M_0)}{d^2M_0}(M-M_0)^2=\frac{1}{2\chi}(M-M_0)^2, \tag{11}$$

where we have allowed for the fact that $df/dM=0$ at $M=M_0$ and introduced the longitudinal susceptibility of χ a ferromagnet under homogeneous magnetization.

Using Eq. (5) and assuming that $\chi\gg1$ and $\alpha\nabla^2\mu\ll\mu/\chi$, we can write $F_\parallel$ in terms of μ and $\partial w/\partial M$ as follows:

$$F_\parallel=-\frac{\mu}{\chi}-\frac{\partial w}{\partial M}. \tag{12}$$

Substituting (12) into Eq. (10) yields the desired equation for finding $F_\parallel$ at $M\approx M_0$:

$$-\frac{\chi}{gM_0}\frac{\partial F_\parallel}{\partial t}-\lambda_e a^2\nabla^2F_\parallel+[\lambda(\mathbf{m})+\lambda_e a^2(\nabla\cdot\mathbf{m})^2]F_\parallel=\frac{\chi}{gM_0}\frac{\partial}{\partial t}\left[\frac{\partial w}{\partial M_0}\right]+\frac{1}{g}\left(\mathbf{m}\cdot\mathbf{\Lambda}\left[\mathbf{m}\times\frac{\partial\mathbf{m}}{\partial t}\right]\right)-\frac{\lambda_e a^2}{g}\left(\mathbf{m}\cdot\nabla^2\left[\frac{\partial\mathbf{m}}{\partial t}\right]\right). \tag{13}$$

Here we can set $M=M_0$ in all the parts of the equation. Thus, solving the equation for $F_\parallel$ and calculating the contribution of $F_\parallel$ to the dissipation function is equivalent to allowing for the variations in $|\mathbf{M}|$.

The same equation for the case in which $w_a=\beta M_z^2$ and $\lambda_x=\lambda_y=\lambda_z$ has been derived in Refs. 14 and 15. Generally, when

$$w=\frac{\alpha}{2}M^2(\nabla\cdot\mathbf{m})^2+\sum_n w_n(\mathbf{M}) \tag{14}$$

($w_n(\mathbf{M})$ is the nth-order anisotropy, with $w_n(\mathbf{M})\propto M^n$), we have

$$\frac{\partial w}{\partial M}=\alpha M(\nabla\cdot\mathbf{m})^2+\frac{1}{M}\sum_n nw_n(M\mathbf{m}). \tag{15}$$

Let us now examine Eq. (13), which is central to the subsequent discussion. As we proceeded from Eq. (1) for **M** to Eq. (13), the problem acquired not only spatial dispersion but also temporal dispersion. Indeed, as we show below, $F_\parallel$ changes dramatically as we go from low soliton velocities, $v<v_c$, to high velocities, $v>v_c$, with v_c the characteristic value of the velocity defined by the relationship

$$\frac{v_c}{gM_0}\frac{\partial \mathbf{F}_\parallel}{\partial \xi}\approx \max\{\lambda(\mathbf{m})F_\parallel,\ \lambda_e a^2(\nabla\cdot\mathbf{m})^2F_\parallel,$$
$$\lambda_e a^2\nabla^2 F_\parallel\}.$$

The value of v_c for a magnetic domain wall in a ferromagnet will be specified later.

Bearing in mind the equation for $F_\parallel$, we can now formulate a complete approach to describing the dynamics and relaxation of magnetization perturbations to first order in the small parameters λ and χ. The approach is based on writing the equation for the unit magnetization vector **m**, which in view of Eq. (1) has the form

$$\frac{\partial \mathbf{m}}{\partial t}=-g[\mathbf{m}\times\mathbf{F}]+gM_0\{\mathbf{\Lambda F}-\mathbf{m}(\mathbf{m}\cdot\mathbf{\Lambda F})\}$$
$$+gM_0\lambda_e a^2\{\mathbf{m}(\mathbf{m}\cdot\nabla^2\mathbf{F})-\nabla^2\mathbf{F}\}, \tag{16}$$

where in the dissipation terms

$$\mathbf{F}=\frac{1}{g}\left[\mathbf{m}\times\frac{\partial \mathbf{m}}{\partial t}\right]+\mathbf{m}F_\parallel,$$

and $F_\parallel$ is determined by Eq. (13). Actually, the system of equations (13) and (16) contains three independent equations for three quantities, for which we can select $F_\parallel$ and **m** or, more precisely, $F_\parallel$ and the angular variables of vector **m**, the angles θ and φ:

$$m_z=\cos\,\theta,\quad m_x=\sin\,\theta\,\cos\,\varphi,\quad m_y=\sin\,\theta\,\sin\,\varphi. \tag{17}$$

Using this system of equations, we can analyze the dissipation of arbitrary nonlinear magnetization waves. Bar'yakhtar *et al.*[14] examined two-parameter solitons of the bion type and non-one-dimensional solitons, including topological solitons. But since we are interested only in simple traveling-wave solutions $\mathbf{M}=\mathbf{M}(\mathbf{r}-\mathbf{v}t)$, where $\mathbf{v}=$const is the wave velocity, calculating the friction force requires only writing the formula for the dissipation function. The quantity Q determines the energy dissipation rate, and for simple traveling-wave solitons the friction force is

$$\mathbf{f}=-\eta(v)\mathbf{v},\quad \eta(v)=\frac{2Q}{v^2}. \tag{18}$$

Employing (9), we can write the formula for the dissipation function in terms of $F_\parallel$, **m**, and $\partial\mathbf{m}/\partial t$ as

$$Q=\frac{gM_0}{2}\int q\,d\mathbf{r},$$

where the dissipation function density q is given by a rather cumbersome formula:

$$q=\lambda(\mathbf{m})F_\parallel^2+\frac{1}{g^2}\left(\left[\mathbf{m}\times\frac{\partial \mathbf{m}}{\partial t}\right],\mathbf{\Lambda}\left[\mathbf{m}\times\frac{\partial \mathbf{m}}{\partial t}\right]\right)$$
$$+\frac{2F_\parallel}{g}\left\{\left(\mathbf{m}\cdot\mathbf{\Lambda}\left[\mathbf{m}\times\frac{\partial \mathbf{m}}{\partial t}\right]\right)\right.$$
$$\left.-\lambda_e a^2\left(\mathbf{m}\cdot\nabla^2\left[\mathbf{m}\times\frac{\partial \mathbf{m}}{\partial t}\right]\right)\right\}$$
$$+\lambda_e a^2\left\{(\nabla F_\parallel)^2+F_\parallel^2(\nabla\cdot\mathbf{m})^2+\frac{1}{g^2}\right.$$
$$\left.\times\left(\nabla\cdot\left[\mathbf{m}\times\frac{\partial \mathbf{m}}{\partial t}\right]\right)^2\right\}. \tag{19}$$

The dissipation function density q contains terms quadratic in $F_\parallel$ or $\partial\mathbf{m}/\partial t$ and terms bilinear in $F_\parallel$ and $\partial\mathbf{m}/\partial t$.

To analyze the relaxation of an arbitrary soliton of the simple-wave type by using Eqs. (13) and (16), we must first establish its structure $\mathbf{m}=\mathbf{m}_0(\boldsymbol{\xi})$, with $\boldsymbol{\xi}=\mathbf{r}-\mathbf{v}t$, as a solution of the Landau–Lifshitz equation (16) for the unit vector **m** at $\mathbf{\Lambda}=0$ and $\lambda_e=0$. Then, using the explicit form of $\mathbf{m}_0(\boldsymbol{\xi})$, we must build Eq. (13) for $F_\parallel$. Solving this equation, we can write the explicit form of the dissipation function solely in terms of $\mathbf{m}_0(\boldsymbol{\xi})$ and $d\mathbf{m}_0(\boldsymbol{\xi})/d\xi$. After this we can use the formula $\mathbf{f}=-(2Q/v^2)\mathbf{v}$ to calculate the friction force acting on the wall.

Equation (13) is a linear partial differential equation with a right-hand side, and its solution can always be written as the sum of the general solution of the corresponding homogeneous equation and a particular solution of the inhomogeneous equation. Clearly, the general solution of the homogeneous equation contributes nothing to the dissipation function, so that any particular solution of Eq. (13) will do. But finding such a solution in the general case is a difficult problem. Various approximate solutions of this problem have been discussed in Refs. 8, 9, 12–14. The problem simplifies considerably if the exchange relaxation constant is small in a certain sense, i.e.,

$$\lambda_e a^2(\nabla\cdot\mathbf{m})^2,\quad \lambda_e a^2(\nabla F_\parallel)^2/F_\parallel^2\ll\lambda. \tag{20}$$

Such an approximation reflects the actual situation for various ferromagnets: weakly anisotropic yttrium iron garnets, and epitaxial films of ferrite garnets in magnetic-bubble devices. The physical reasons for the smallness are different for these cases: for yttrium iron garnets it is the smallness of the magnetization gradients in the magnetic domain wall, and for materials with magnetic bubbles it is the large value of the constant λ (see Refs. 8, 12, and 13).

If the conditions (20) are met, Eq. (13) for $F_\parallel$ simplifies and becomes first order in time:

$$\frac{\chi}{gM_0}\frac{\partial F_\parallel}{\partial t}+\lambda(\mathbf{m})F_\parallel=\frac{\chi}{gM_0}\frac{\partial}{\partial t}\left[\frac{\partial w}{\partial M_0}\right]+\frac{1}{g}\left\{\left(\mathbf{m}\cdot\mathbf{\Lambda}\left[\mathbf{m}\times\frac{\partial \mathbf{m}}{\partial t}\right]\right)-\lambda_e a^2\left(\mathbf{m}\cdot\nabla^2\left[\mathbf{m}\times\frac{\partial \mathbf{m}}{\partial t}\right]\right)\right\}. \tag{21}$$

If the soliton's velocity is low, $v<v_c$, and the characteristic value of v_c is given by the formula

$$v_c=\frac{gM\lambda\Delta}{\chi}, \tag{22}$$

where Δ is the characteristic soliton width, we can drop the term with $\partial F_\parallel/\partial t$ are write the solution explicitly:

$$F_\parallel=-\frac{1}{\lambda_{ik}m_im_k}\left\{\frac{\chi}{gM_0}\frac{\partial}{\partial t}\left[\frac{\partial w}{\partial M_0}\right]+m_i\lambda_{ik}\left[\mathbf{m}\times\frac{\partial\mathbf{m}}{\partial t}\right]_k\right.$$
$$\left.-\lambda_e a^2\left(\mathbf{m}\cdot\nabla^2\left[\mathbf{m}\times\frac{\partial\mathbf{m}}{\partial t}\right]\right)\right\}. \tag{23}$$

Then the formula for the dissipation function in the case of slow variations of the magnetization (say, when the domain wall velocity v is lower than v_c) can be written in terms of only $\mathbf{m}$ and its derivatives, without $F_\parallel$. Plugging $F_\parallel$ in the form (23) into the expression for the dissipation function density and performing straightforward but cumbersome transformations, we get

$$Q=\frac{M_0}{2g}\int d\mathbf{r}\left\{\lambda_{ik}\left[\mathbf{m}\times\frac{\partial\mathbf{m}}{\partial t}\right]_i\cdot\left[\mathbf{m}\times\frac{\partial\mathbf{m}}{\partial t}\right]_k\right.$$
$$-\frac{1}{\lambda_{ik}m_im_k}\left(\lambda_{ik}m_i\left[\mathbf{m}\times\frac{\partial\mathbf{m}}{\partial t}\right]_k\right)^2$$
$$+\frac{1}{\lambda_{ik}m_im_k}\left(\frac{\chi}{M_0}\frac{\partial}{\partial t}\left[\frac{\partial w}{\partial M_0}\right]\right)^2$$
$$\left.+\lambda_e a^2\left(\mathbf{m}\cdot\nabla^2\left[\mathbf{m}\times\frac{\partial\mathbf{m}}{\partial t}\right]\right)\right\}. \tag{24}$$

Here we have kept only the direct contribution of the exchange relaxation, i.e., we have ignored terms that are small due to (20). Thus, when magnetization varies slowly, the dissipation function consists of three terms:

$$Q=Q_r+Q_e+Q_\chi, \tag{25}$$

each of which allows for a simple physical interpretation. The quantity Q_r is determined by the first two terms on the right-hand side of Eq. (24), is proportional to the first power of the relativistic constant λ, and can be interpreted as the direct contribution of relativistic relaxation. Note, however, that Q_r is not equal to $\lambda_{ik}F_{\perp i}F_{\perp k}$ (the first term in (24)) and contains contributions from $F_\parallel$ (the second term in (24)). If we express the magnetization vector in terms of angular variables and select the tensor $\mathbf{\Lambda}$ in the form diag$(\lambda,\lambda,\lambda_z)$, then Q_r can be reduced to

$$Q_r=\frac{M_0}{2g}\int d\mathbf{r}\left\{\lambda\left(\frac{\partial\theta}{\partial t}\right)^2\right.$$
$$\left.+\frac{\lambda\lambda_z\sin^2\theta}{\lambda\sin^2\theta+\lambda_z\cos^2\theta}\left(\frac{\partial\varphi}{\partial t}\right)^2\right\}. \tag{26}$$

At $\lambda=\lambda_z$, when $\lambda_{ik}=\lambda\delta_{ik}$, the expression in braces is $\lambda\{(\partial\theta/\partial t)^2+\sin^2\theta(\partial\varphi/\partial t)^2\}$, and this expression can be reduced to the dissipation function in Hilbert form. But if $\lambda_z=0$, Q_r contains no term with $(\partial\varphi/\partial t)^2$ for all values of θ. Note that this result, which is important for describing relaxation of spin waves in ferromagnets with continuous degeneracy (ferromagnets of the easy-plane type), can only be obtained if $F_\parallel$ is consistently taken into account. If we use the formula $\lambda_{ik}[\mathbf{m}\times(\partial\mathbf{m}/\partial t)]_i\cdot[\mathbf{m}\times(\partial\mathbf{m}/\partial t)]_k$, the term with $(\partial\varphi/\partial t)^2$ is present in Q_r, for instance, in the cone phase of an easy-plane ferromagnet,[6] which leads to incorrect results for the spin-wave damping constant.

The exchange dissipation function Q_e written in terms of angular variables can be found in Ref. 14, and we do not write it here. We merely note that in the limit of weakly excited states of an easy-plane ferromagnet (when $\theta\to\pi/2$ and $\nabla\theta\to0$),

$$Q_e\to\frac{M_0}{2g}\int d\mathbf{r}\left(\nabla\left[\frac{\partial\varphi}{\partial t}\right]\right)^2,$$

i.e., Q_e has the same structure as the dissipation function Q_{el} in elasticity theory,

$$Q_{el}\propto\int d\mathbf{r}\left(\nabla\left[\frac{\partial\mathbf{u}}{\partial t}\right]\right)^2,$$

with $\mathbf{u}$ being the medium's displacement vector.[16] Halperin and Hohenberg[17] selected this form of dissipation function for a hydrodynamic description of spin waves in easy-plane magnetic materials.

Finally, if we allow for (23), the third term in Q can be written as

$$Q_\chi=\frac{M_0}{2g}\int d\mathbf{r}\left\{\frac{\chi^2}{\lambda\sin^2\theta+\lambda_z\cos^2\theta}\right\}\left\{\frac{d}{dt}\left[\alpha(\nabla\theta)^2\right.\right.$$
$$\left.\left.+\alpha\sin^2\theta(\nabla\varphi)^2+\left(\frac{1}{M_0^2}\right)\sum_n nw_n(\theta,\varphi)\right]\right\}^2, \tag{27}$$

where $w_n(\theta,\varphi)$ describes nth-order anisotropy. This term determines the contribution of variations in the length of the magnetization vector to the soliton dissipation. Bar'yakhtar *et al.*[13] were the first to examine this contribution, which is nonzero only if the longitudinal susceptibility χ of the ferromagnet is finite. In this term χ^2/λ acts as the ''effective relaxation constant.''

Note that the same combination emerges in the description of longitudinal or slow relaxation in magnetic materials with rare-earth ions both for linear excitations, or magnons,[18] and for mobile magnetic domain walls.[11]

With all the difference in the physical processes in these problems, there is a lot in common. In both cases relaxation occurs because the dynamical variable (the normalized magnetization $\mathbf{m}$ in our case and the iron-sublattice magnetization $M_{\rm Fe}$ in Ref. 11) takes the variable with pure relaxation dynamics (the length M of the magnetization vector and the rare-earth-sublattice magnetization $\mathbf{M}_R$) out of equilibrium. Here the contribution to dissipation increases both with the corresponding susceptibility χ and with a decrease in the value of the relaxation constant λ. The effective relaxation constant in Q_χ is proportional to the square of the small parameter χ, but it also contains the small parameter λ in the

denominator. Hence this contribution to the retardation of the magnetic domain wall in ferromagnets with low dissipation can become significant.

4. Now let us calculate the friction force acting on a moving topological soliton, the magnetic domain wall in a ferromagnet. In the simplest model of a ferromagnet, which allows for an exact solution in the nondissipative approximation, we examine the relaxation of the magnetic domain wall at low and high velocities and show the effect of temporal dispersion on the soliton relaxation in the process.

Studying the dynamics of a magnetic domain wall that is moving with a considerable velocity is a fairly complicated problem for an arbitrary model of a ferromagnet, and the general solution to this problem is unknown. The only model for which there is a known exact solution describing a magnetic domain wall that moves with any velocity lower than what is known as the limit velocity is described by an anisotropy energy w_a that is a quadratic form in the magnetization components.[1,4] We use the expression characteristic of a rhombic ferromagnet:

$$w_a=\frac{1}{2}\,(\beta M_x^2+\beta' M_y^2)=\frac{M_0^2}{2}\beta\,\sin^2\,\theta(1+\rho\,\sin^2\,\varphi). \tag{28}$$

Let us send the z axis along the easy-magnetization axis and the y axis along the hard-magnetization axis, so that $\beta'>\beta>0$. The angular variables are chosen in the ordinary manner (see Eq. (17)). In writing formula (28) for w_a in angular variables we have $\rho=(\beta'-\beta)/\beta$. Note that (28) is also used for uniaxial ferromagnets if the energy of the demagnetizing fields is taken into account in the local (Winter) approximation, in which case $\rho=4\pi/\beta=1/q$, where q is the quality factor introduced for materials with magnetic bubbles (see, e.g., Refs. 2 and 4).

As shown by Walker (see the reviews in Refs. 1–4), with the energy given by (28) the Landau–Lifshitz equation has an exact solution of the form $\varphi=\varphi_0=\text{const}$ and $\theta=\theta(\xi)$, with $\xi=x-vt$, where

$$\cos\,\theta=\pm\tanh\frac{\xi}{\Delta(\varphi_0)},\quad \Delta(\varphi_0)=\frac{\Delta}{\sqrt{1+\rho\,\sin^2\,\varphi_0}},$$
$$\Delta=\sqrt{\frac{\alpha}{\beta}}\,. \tag{29}$$

The value of φ_0 is determined by the velocity v:

$$\frac{v}{gM_0\sqrt{\alpha\beta}}=\frac{\rho\,\sin\,\varphi\,\cos\,\varphi}{\sqrt{1+\rho\,\sin^2\,\varphi}}. \tag{30}$$

Equation (30) has a solution only if $v<v_W$, where v_W is the Walker limit value (the Walker limit), which vanishes in the limit $\rho\to 0$ (i.e., for a purely uniaxial ferromagnet) and reaches its maximum (which coincides with the minimum phase velocity of magnons) when $\rho\gg 1$:

$$v_W=gM_0\sqrt{\alpha\beta}(\sqrt{1+\rho}-1)$$
$$=gM_0\begin{cases}(\beta'/2\beta)\sqrt{\alpha\beta}, & \beta'\ll\beta,\\ \sqrt{\alpha\beta'}, & \beta\ll\beta'.\end{cases} \tag{31}$$

With $\rho\to 0$ we can ignore the variations in the thickness of the magnetic domain wall during the wall's motion and assume that $\Delta=\sqrt{\alpha/\beta}$. But if $\rho\gg 1$, under a change in the wall velocity the wall thickness changes considerably, from $\Delta=\sqrt{\alpha/\beta}$ at $v=0$ to $\Delta_W=\sqrt{\alpha/\beta'}=\Delta/\sqrt{\rho}\ll\Delta$ at $v=v_W$.

Let us calculate the friction force acting on a magnetic domain wall of type (29) when $v<v_c$, i.e., when we can use the dissipation function in the form (24)–(27). The contribution of relativistic relaxation for this solution is completely independent of the relationship between the parameters λ and λ_z in the tensor of dissipation constants, since at $\varphi=\text{const}$ Q_r is given by the same expression as in the standard theory with the relaxation term in the Landau–Lifshitz or Hilbert form:

$$\eta_r(v)=\frac{2\lambda_r M_0}{g\Delta(v)}. \tag{32}$$

Here and in what follows we use the notation $\Delta(v)=\Delta[\varphi_0(v)]$, where $\varphi_0(v)$ is defined in Eq. (30). For exchange relaxation the same result can be obtained by using Eqs. (41) and (43) of Bar'yakhtar's paper,[5] in which case the thickness Δ of the magnetic domain wall must be replaced by $\Delta(v)$:

$$\eta_e(v)=\frac{2\lambda_e a^2 M_0}{3g\Delta^3(v)}. \tag{33}$$

The term Q_χ given by (27) can be written in the form

$$f_\chi=\eta_\chi(v)v,\quad \eta_\chi(v)=\frac{64M_0}{15g\Delta(v)}\,\frac{\chi^2\beta^2}{\langle\lambda\rangle},$$
$$\langle\lambda\rangle=\frac{\int_0^\pi d\theta\,\sin^3\,\theta\,\cos^2\,\theta}{\int_0^\pi d\theta[\sin^3\,\theta\,\cos^2\,\theta][\lambda\,\sin^2\,\theta+\lambda_z\,\cos^2\,\theta]^{-1}}, \tag{34}$$

with $\langle\lambda\rangle=\lambda$ at $\lambda=\lambda_z$ and $\langle\lambda\rangle=12\lambda/5$ at $\lambda_z=0$.

The quantities $\eta_r(v)$, $\eta_e(v)$, and $\eta_z(v)$ can be interpreted as the nonlinear viscous-friction coefficients for the magnetic domain wall. For $\rho\ll 1$, a condition characteristic of standard materials with magnetic bubbles, the Δ vs. v dependence is weak, and in the principal approximation in ρ both $\eta_r(v)$ and $\eta_e(v)$ are independent of v.

But if we examine the case in which $\rho\gg 1$ (which corresponds to an easy-plane ferromagnet with a weakly anisotropic plane of soft magnetization and can by used to describe yttrium iron garnets), $\eta_r(v)$, $\eta_\chi(v)$, and especially $\eta_e(v)$ are velocity-dependent due to the Δ vs. v dependence, and the values of η_r and η_e at $v=v_W$ are much higher than at $v=0$:

$$\frac{\eta_{r,\chi}(v_W)}{\eta_{r,\chi}(0)}=\rho^{1/2},\quad \frac{\eta_e(v_W)}{\eta_e(0)}=\rho^{3/2}.$$

For the velocity v of forced motion of a magnetic domain wall in a driving field H parallel to the z axis we can write

$$v\,\eta(v)=2M_0H_z\,.$$

By solving this equation we can easily build the desired dependence $v=v(H)$ for various relationships among the constants ρ, λ, and $\lambda_e(a/\Delta)^2$. Clearly, for $\rho\ll 1$ the v vs. (H_z)

dependence is essentially linear, and the contributions of the exchange and relativistic relaxations are indistinguishable. But when $\rho \gg 1$, the v vs. H_z dependences, with one of the contributions (exchange or relativistic) being dominant, differ considerably (Fig. 1). Note that for this nonlinearity to affect Eqs. (32)–(34), which were obtained for $v \ll v_c$, the following inequalities must be satisfied simultaneously:

$$\rho \gg 1 \quad \text{and} \quad v_W \ll v_c.$$

5. Now let us examine the case in which the velocities are not low, $v \geqslant v_c$. Here the expression (23) for $F_\parallel$ and Eqs. (25)–(27) for the dissipation function are inapplicable, and one is forced to solve Eq. (21) and calculate the dissipation function by using the general expression (19). As noted earlier, in this case the dissipation function cannot even be represented by a sum of three terms like Q_r, Q_χ, and Q_e, since the dissipation function density (19) contains terms quadratic in $F_\parallel$ or $\partial \mathbf{m}/\partial t$ and terms bilinear in $F_\parallel$ and $\partial \mathbf{m}/\partial t$.

If we use the Walker solution $\varphi = \text{const}$ and $d\varphi/d\xi = 0$ and select the tensor of relativistic dissipation constants in the form $\mathbf{\Lambda} = \lambda\, \text{diag}(1,1,\varepsilon)$, all terms in (19) that are bilinear in $F_\parallel$ and $\partial \mathbf{m}/\partial t$ vanish. Indeed,

$$\left(\mathbf{m} \cdot \mathbf{\Lambda} \left[\mathbf{m} \times \frac{\partial \mathbf{m}}{\partial t} \right] \right) = \frac{\partial \varphi}{\partial t} (\lambda - \lambda_z) \cos\,\theta \sin^2\,\theta. \tag{35}$$

The fact that the term corresponding to exchange relaxation, $(\mathbf{m} \cdot \nabla^2[\mathbf{m} \times (\partial \mathbf{m}/\partial t)])$, vanishes for the Walker solution has been noted in Ref. 15. The same is true of Eq. (13): all terms on the right-hand side vanish except $(\partial/\partial t)[\partial w/\partial M]$. With allowance for these simplifications, we can again write the dissipation function as the sum of three terms of the type (25), $Q = Q_r + Q_e + Q_\chi$. Furthermore, Q_r and Q_e have the same form as when $v \ll v_c$.

Note that the above is true only for a specific Walker solution, since the coefficient of $(\partial\varphi/\partial t)^2$ in Q_r can be shown to have different forms for high and low velocities.

The expressions for Q_χ at $v \ll v_c$ and $v \geqslant v_c$ differ considerably. Allowing for the specific form of the Walker solution, we can write Eq. (21) for F as follows:

$$-\frac{v\chi}{gM_0} F' + \lambda(\theta) F = \frac{v\chi}{gM_0} [2\beta M_0 \sin^2\,\theta]', \tag{36}$$

where $\lambda(\theta) = \lambda(\sin\theta + \varepsilon \cos^2\theta)$, and the prime stands for the first derivative with respect to ξ.

If we assume here that $v \to 0$, we can use the simple formula (23). However, the Walker solution makes it possible to do a thorough analysis of the problem for all velocities $v < v_W$. Indeed, if we proceed from differentiation with respect to ξ to differentiation with respect to θ via the formula $\Delta(d\theta/d\xi) = \sin\theta$, we can write the above equation as:

$$\frac{dF_\parallel}{d\theta} - \frac{\kappa(\theta)}{\sin\,\theta} F = -4\beta M_0 \sin\,\theta \cos\,\theta,$$

where $\kappa(\theta) = gM_0\lambda(\theta)\Delta/v\chi$.

This provides us with the explicit dependence of F on θ in the form of integrals. The solution of Eq. (36) has the form

$$F(\theta) = -\int_0^\theta 4\pi\beta M_0 \sin\,\zeta \cos\,\zeta \times \left\{ \exp\left[\int_\zeta^\theta \frac{d\psi \kappa(\psi)}{\sin\,\psi} \right] \right\} d\zeta.$$

This solution can be shown to satisfy the conditions $F_\parallel(0) = 0$ and $F_\parallel(\pi) = 0$, i.e., $F_\parallel$ vanishes far from the domain wall. However, the asymptotic behavior of $F_\parallel(\xi)$ as $\xi \to \infty$ is not the same as that of $\xi \to -\infty$. This is obvious, since Eq. (36) and its solution possess a certain symmetry under the substitution of $-\xi$ for ξ only in two limiting cases: $F_\parallel(\xi) = -F_\parallel(-\xi)$ for $v = 0$, $\lambda \neq 0$, and $1/\kappa = 0$; and $F_\parallel(\xi) = F_\parallel(-\xi)$ for $v \neq 0$, $\lambda = 0$, and $\kappa = 0$. Using the formula for $F(\theta)$, we can calculate Q as a function of the domain wall velocity over the entire velocity range from $v = 0$ to $v = v_W$. It is impossible, however, to express the result by a single analytic formula, so we limit our discussion to analyzing the asymptotic behavior in velocity.

Clearly, what is important here is the value of the parameter $\kappa = gM_0\lambda\Delta/v\chi$, which can be represented by the ratio of the domain wall velocity v to a certain characteristic velocity v_c (derived above from qualitative estimates):

$$\kappa = \frac{v_c}{v}, \quad v_c = \frac{gM_0\lambda\Delta}{\chi}. \tag{37}$$

If $v \ll v_c$, we can write the solution as a series expansion in powers of v/v_c. In the linear approximation we easily find that

$$F_\parallel = \frac{v\chi}{gM_0\Delta(v)\lambda(\theta)} 4M_0\beta \sin^2\,\theta \cos\,\theta,$$

which coincides with the result that follows from (23). Plugging this expression into the formula for Q_χ, we find that the friction force f_χ is proportional to the domain wall velocity v and can be written in the form (34).

When $v \gg v_c$, there is another way of simplifying Eq. (36). If we drop the small factor $\kappa F_\parallel$, we can write $F_\parallel(\theta) = -2\beta M_0 \sin^2\theta$, from which we find that the dissipation function Q_χ is given by

$$Q_\chi = \frac{g}{2} \int_0^\pi \lambda(\theta) 4\beta^2 M_0 \Delta(v) \sin^3\,\theta\, d\theta.$$

In this case Q_χ is velocity-independent, except for the dependence originating from $\Delta(v)$. Hence the friction force f_χ for $v \gg v_c$ is proportional to $1/v$:

$$f_\chi = \eta_\chi^* \frac{v_c^2}{v}, \quad \eta_\chi^* = \frac{16\beta^2\chi^2 M_0 \Delta(v)}{15g\Delta^2} (4\lambda + \lambda_z). \tag{38}$$

At $v \approx v_c$ the values specified by (34) and (38) coincide in order of magnitude. Thus, if the limiting domain-wall velocity $v_W \gg v_c$, the contribution to the force of friction of the domain wall due to variations in the length of the magnetization vector exhibits an anomalous (by comparison with f_r and f_e) dependence on the domain wall velocity. This dependence cannot be reduced to replacing $\Delta(v)$ by Δ in the formulas obtained for $v \to 0$ and is determined by different formulas for $v \gg v_c$ and for $v \ll v_c$:

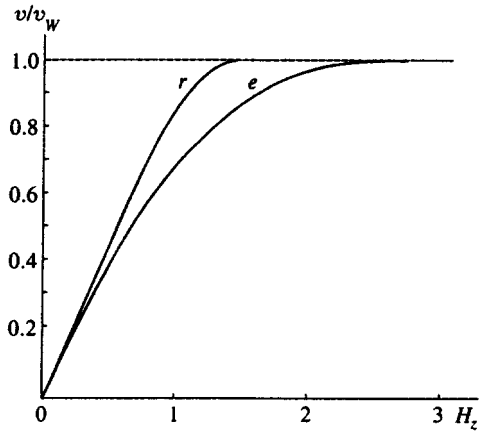

FIG. 1. Domain wall velocity as a function of the driving field H_z (in relative units) when either relativistic or exchange relaxation is dominant (the labels r and e) for $\rho=3$.

$$f_\chi=\begin{cases} v\,\eta_\chi, & v\ll v_c, \\ v_c^2\eta_\chi^*/v, & v\gg v_c. \end{cases} \tag{39}$$

Such retardation behavior of the domain wall for $v\gg v_c$ can be described as ''turning off'' the corresponding contribution (Fig. 2), and is a manifestation of temporal dispersion. The effect emerges because two fundamentally different modes of motion can be distinguished in the motion of the magnetization $\mathbf{M}=M\mathbf{m}$: the weakly dissipative dynamics of $\mathbf{m}$, and the diffusion of $\mu=M-M_0$. In studying a nonlinear wave of a domain-wall type with obvious localization of magnetization over distances $\Delta x\approx\sqrt{\alpha/\beta}$, two characteristic times are clearly distinguishable: the ''dynamical'' time $\tau_{\rm dyn}=\Delta x/v$, and the characteristic diffusion time of perturbation variation, $\tau_{\rm diff}=\chi/gM_0\lambda$. Clearly, a comparison of these times leads to the estimate of v_c described above. The nonlinearity in the f_χ vs. v dependence affects the dependence of the velocity of forced motion of the wall on the field H_z (Fig. 3).

6. Let us now summarize the results of calculating the retardation of a magnetic domain wall in the Walker model. For $v_W<v_c$ the full friction force can be written as

$$f=v\left\{\eta_r^{(0)}\left[\frac{\Delta}{\Delta(v)}\right]+\eta_e^{(0)}\left[\frac{\Delta}{\Delta(v)}\right]^3+\eta_\chi^{(0)}\left[\frac{\Delta}{\Delta(v)}\right]\right\}, \tag{40}$$

with $\eta_\alpha^{(0)}$ the viscosity coefficients at $v=0$, and its velocity dependence is described only by the Δ vs. v dependence. This dependence is important when $\rho\gg1$ (see Eqs. (29) and (30)), but it is negligible when $\rho\ll1$. In the latter case (magnetic-bubble materials) we can write $\Delta(v)=\Delta_0=\sqrt{\alpha/\beta}$.

But when $v_W\gg v_c$ (in real magnetic materials both inequalities may hold), for $v<v_c$ the f vs. v dependence is described by the same expressions, in which we put $\Delta(v)=\sqrt{\alpha/\beta}$. Thus, when $v_W\gg v_c$ and $v\ll v_c$, the f vs. v dependence is linear:

$$f=v[\eta_r^{(0)}+\eta_e^{(0)}+\eta_\chi^{(0)}]. \tag{41}$$

For $v_W>v\gg v_c$, however, η_χ is ''turned off'' and

$$f=v(\eta_r+\eta_e)+\frac{v_c^2\eta_\chi^*}{v}. \tag{42}$$

Thus, when $v_W\gg v_c$, we have two linear sections in the f vs. v dependence, $v\ll v_c$ and $v_c<v\ll v_W$, which are characterized by different slopes.

These effects lead to special features in the dependence of the velocity of forced motion of the domain wall on an external driving field H_z. If we assume that the driving field is directed along the z axis, the velocity of the wall's stable motion is determined by the equality of the external force (the magnetic pressure $2MH_z$) and the friction force $f(v)=f_e+f_r+f_\chi$. The v vs. H_z dependence is determined by the ratio of the characteristic velocities v_W and v_c.

For $v_W<v_c$ the v vs H_z dependence is always monotonic, and for $\rho\ll1$ it is close to linear. But if $\rho\gg1$, there appear nonlinearities in this dependence associated with the $=\Delta$ vs. v dependence, and as $v\to u_W$ the most rapid increase is observed in the contribution of exchange relaxation (see Fig. 1).

For $v_W\gg v_c$ the nonlinearity makes itself felt differently. For $v\ll v_c$ and $v_W>v\gg v_c$ the v vs. (H_z) dependence is linear, of the $v=\mu_* H_z$ type, but the mobility μ_* is different for high and for low velocities v: for $v\gg v_c$ the value of $\mu_*=dv/dH_z$ is greater than that for $v\ll v_c$ (see Fig. 3). With the difference in mobilities for $v\ll v_c$ and for $v\gg v_c$ being large, in the intermediate range $v\sim v_c$ negative differential mobility $\mu_*=dv/dH_z$ must be apparent, and because of this the steady motion of a flat domain wall becomes unstable.[3]

7. Our analysis has thus shown that in contrast to the standard dissipation theory, based on the Hilbert term, the generalized phenomenological theory predicts complex behavior of the friction force exerted on a domain wall as a function of the driving field. What behavior is actually realized depends on the relationship between the characteristic parameters, primarily v_W and v_c, and the relaxation constants λ, λ_e, and χ^2/λ. The values of these parameters are usually unknown and can vary significantly from crystal to crystal. Here experiments play a decisive role. Let us now discuss the possibilities of observing these effects.

Weak ferromagnets of the orthoferrite type serve as excellent objects for dynamical experiments. Exhaustive data on domain-wall dynamics at velocities up to the limiting value (about 20 km s^{-1}) in these materials have been obtained by the Chetkin group (see the review in Ref. 3). Effects of the type described above were observed in weak ferromagnets at velocities much lower than the limit velocity (the ''turning off'' of a relaxation mechanism at velocities of order 200 m s^{-1} and 500 m s^{-1} in yttrium orthoferrite $YFeO_3$ and iron borate $FeBO_3$, respectively[19]). However, our theory cannot be applied directly to weak ferromagnets. Furthermore, preliminary calculations show that a contribution of type χ^2/λ to the retardation of a domain wall is much smaller for orthoferrites than for ferromagnets. A detailed analysis[3] indicates that for weak ferromagnets of the orthoferrite type the entire body of the data on the dynamics of a domain wall moving with velocities from 1 km s^{-1} to the limiting velocity can be described by a simple relaxation term with a single relaxation constant. For this reason we turn to ferromagnets.

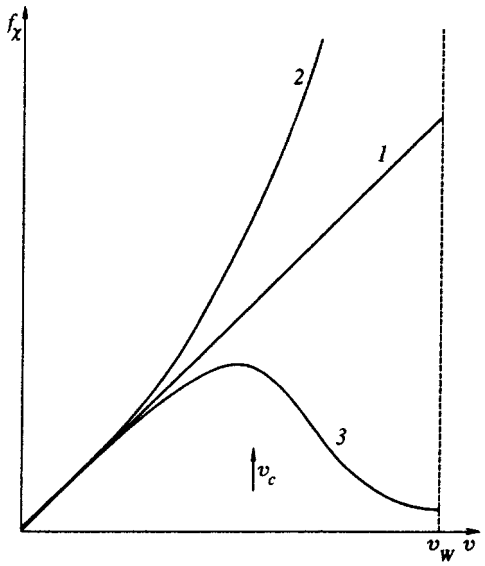

FIG. 2. The friction force f_χ as a function of the domain wall velocity v (schematically) for various limiting cases: curve *1*, $\rho \ll 1$ and $v_W \ll v_c$ (linear dependence); curve *2*, $\rho \gg 1$ and $v_W \ll v_c$ (nonlinear growth due to the factor $1/\Delta(v)$ is the same as for f_r); and curve *3*, $v_W \gg v_c$ (contribution of f_χ is ''turned off'' for $v \geqslant v_c$).

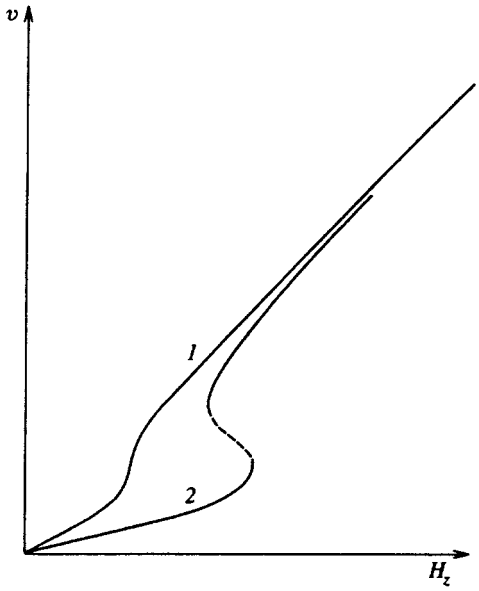

FIG. 3. Domain wall velocity as a function of the driving field H_z (schematically) at $\rho \ll 1$ and $v_W \gg v_c$ for weak (curve *1*) and strong (curve *2*) nonlinearities in the f vs. v dependence, which corresponds to a small or large contribution of $f_\chi(v)$ in comparison to that of f_r or f_e, respectively. The section in curve *2* corresponding to unstable motion is depicted by a dashed line.

The Walker model is convenient because an exact solution exists that describes a domain wall moving at considerable velocity. The problem in describing experiments on the basis of this model is that most such experiments have been conducted for thin films of magnetic-bubble materials (in which twisted domain walls are realized), i.e., even at rest the domain wall is not one-dimensional.[2] In this case the considerations leading up to the limiting velocity differ quite significantly from those in the Walker solution, with the limiting velocity being much lower than v_W. Hence the objects to which our theory might be applied are primarily magnetic materials in which the domain walls are one-dimensional, and to which the Walker solution is applicable (for instance, the maximum velocity of a domain wall should coincide with v_W).

For the described effects to show up, one more criterion must be satisfied. Relaxation must be determined primarily by intrinsic processes rather than by impurity processes, for which the $f(v)$ and $v(H_z)$ functions are different.[11] This criterion corresponds to the smallness of the effective relaxation constant λ. It is difficult to specify the exact criterion. We merely note that a film with $\lambda = 0.38$ exhibited[23] a typical Walker dependence of v on H_z characteristic of the simplest relaxation model, while for epitaxial films of a magnetic-bubble ferromagnet with $\lambda = 0.01$ and $\lambda = 0.004$ the contribution of the term with χ^2/λ reached, respectively, 90% (Ref. 7) and 40% (Ref. 21), with a fairly small exchange contribution. Let us discuss the feasibility of meeting these criteria.

There should probably be no twisting of domain walls in materials consisting of yttrium iron garnet wafers, where one-dimensional domain walls can be prepared by special methods.[20] According to Refs. 12 and 13, for yttrium iron garnets the contribution of non-Hilbert terms to domain-wall relaxation reached 90%, and the nonlinearity effect in the v vs. H_z dependence described above should play an important role. Unfortunately, the experiment described in Ref. 20 was done only for the linear mode of motion of the domain wall.

There are also two classes of epitaxial films of ferromagnets with magnetic bubbles in which the maximum velocity of the domain wall is close to v_W. These are films with strong anisotropy in the basis plane and films with a large gyromagnetic ratio ($g > 6$), i.e., close to the compensation point (see Ref. 2, p. 177, and the original work by Loginov *et al.*[22]). But usually in such materials the damping is dominated by impurity process.

A highly promising approach to building a one-dimensional domain wall is to use an external magnetic field $H_\parallel$ directed at right angles to the easy-magnetization axis of the ferromagnet. The value $H_\parallel^*$ at which twisting is suppressed can be determined from the termination of the sharp nonlinear increase in the domain-wall mobility $\mu(H_\parallel)$; for $H_\parallel > H_\parallel^*$ this dependence is linear and the rate with which mobility grows is smaller. Usually $H_\parallel^*$ is close to $4\pi M_0$ (see Refs. 7, 21, and 24). For values of $H_\parallel$ that are not small, the solution describing a domain wall moving at moderate velocity is not known, and a detailed discussion of this case lies outside the scope of the present work (see Refs. 8 and 25). We note, however, that if the field $H_\parallel^*$ is weaker than the anisotropy field in the basis plane, H_p, then for $H_\parallel^* < H_\parallel \ll H_p$ one can use the Walker solution to describe the structure of the domain wall, with the result that here our theory is valid. Logunov *et al.*[24] studied the nonlinear dynamics of a domain wall with a field in the plane and observed a nonlinear dependence of v on H_z for both low and high values of $H_\parallel$.

It will not be easy to observe the predicted effects. We do not know of any observations of the above-mentioned

type of dependence for ferromagnets with strong uniaxial anisotropy to which the Walker solution could be applied, but we believe that our theoretical investigation will stimulate further experimental studies of the relaxation of largely nonlinear magnetization waves describing a magnetic domain wall.

The authors are grateful to V. G. Bar'yakhtar, Yu. I. Gorobets, and A. L. Sukstanskiĭ for fruitful discussions. The present work was made possible by a grant from the Ukrainian Ministry of Education. One of the authors (B.A.I.) is grateful for the help from the Soros International Program for the Support of Education in the Exact Sciences (Revival Fund), Grant SPU 042025.

[1] V. G. Bar'yakhtar and B. A. Ivanov, in *Soviet Scientific Reviews, Section A, Physics*, I. M. Khalatnikov (Ed.), Vol. 16, No. 3 (1993).
[2] A. P. Malozemoff and J. C. Slonczewski, *Magnetic Domain Walls in Bubble Materials*, Applied Solid State Science, Supplement I, Academic Press, New York (1979).
[3] V. G. Bar'yakhtar, M. V. Chetkin, B. A. Ivanov, and S. N. Gadetskiĭ, *Dynamics of Topological Magnetic Solitons. Experiment and Theory*, Springer, Berlin (1994).
[4] A. M. Kosevich, B. A. Ivanov, and A. S. Kovalev, Phys. Rep. **194**, 117 (1990).
[5] V. G. Bar'yakhtar, Zh. Éksp. Teor. Fiz. **87**, 1501 (1984) [Sov. Phys. JETP **60**, 863 (1984)].
[6] V. G. Bar'yakhtar, Fiz. Tverd. Tela (Leningrad) **29**, 1317 (1987) [Sov. Phys. Solid State **29**, 754 (1987)].
[7] V. A. Bokov, V. V. Volkov, N. L. Petrichenko, and M. Maryshko, Pis'ma Zh. Tekh. Fiz. **19**, No. 11, 89 (1993) [Tech. Phys. Lett. **19**, 734 (1993)].
[8] B. A. Ivanov and K. A. Safaryan, Fiz. Tverd. Tela (Leningrad) **32**, 3507 (1990) [Sov. Phys. Solid State **32**, 2034 (1990)]; Fiz. Nizk. Temp. **18**, 722 (1992) [Sov. J. Low Temp. Phys. **18**, 511 (1992)].
[9] E. G. Galkina and B. A. Ivanov, Fiz. Tverd. Tela (Leningrad) **33**, 1277 (1991) [Sov. Phys. Solid State **33**, 723 (1991)]; E. G. Galkina, B. A. Ivanov, and V. A. Stefanovich, J. Magn. Magn. Mater. **118**, 373 (1993).
[10] Yu. P. Kabanov, L. M. Dedukh, and V. I. Nikitenko, JETP Lett. **49**, 637 (1989).
[11] B. A. Ivanov and S. N. Lyakhimets, Zh. Éksp. Teor. Fiz. **100**, 901 (1991) [Sov. Phys. JETP **73**, 497 (1991)].
[12] V. G. Bar'yakhtar, V. A. Brodovoĭ, B. A. Ivanov, I. V. Krutsenko, and K. A. Safaryan, Fiz. Tverd. Tela (Leningrad) **32**, 852 (1990) [Sov. Phys. Solid State **32**, 502 (1990)].
[13] V. G. Bar'yakhtar, B. A. Ivanov, and K. A. Safaryan, Solid State Commun. **72**, 1117 (1989).
[14] V. G. Bar'yakhtar, B. A. Ivanov, and A. L. Sukstanskiĭ, Phys. Lett. A **119**, 191 (1986); V. G. Bar'yakhtar, B. A. Ivanov, T. K. Soboleva, and A. L. Sukstanskiĭ, Zh. Éksp. Teor. Fiz. **91**, 1454 (1986) [Sov. Phys. JETP **64**, 857 (1986)].
[15] V. G. Bar'yakhtar and B. A. Ivanov, *Dynamics and Relaxation of Magnetization of Magnetically Ordered Crystals* [in Russian], Preprint ITF-86-64P, Institute of Theoretical Physics, Ukrainian Academy of Sciences, Kiev (1986).
[16] L. D. Landau and E. M. Lifshitz, *Theory of Elasticity*, 3rd ed., Pergamon Press, Oxford (1986).
[17] B. J. Halperin and P. C. Hohenberg, Phys. Rev. **188**, 898 (1969).
[18] A. G. Gurevich, *Magnetic Resonance in Ferrites and Antiferromagnets* [in Russian], Nauka, Moscow (1973).
[19] P. D. Kim and D. Ch. Khvan, Fiz. Tverd. Tela (Leningrad) **24**, 2300 (1982) [Sov. Phys. Solid State **24**, 1306 (1982)].
[20] V. S. Gornakov, L. M. Dedukh, V. I. Nikitenko, and V. T. Synogach, Zh. Éksp. Teor. Fiz. **90**, 2090 (1986) [Sov. Phys. JETP **63**, 1225 (1986)].
[21] B. A. Ivanov, A. Stankiewich, A. Maziewski, N. L. Petrichenko, and K. A. Safaryan, ''Magnetic domain mobility investigation in in-plane field,'' in *Ferrites* (Proc. of Internat. Conf. on Ferrites), Tokyo (1989).
[22] N. A. Loginov, M. V. Logunov, and V. V. Randoshkin, Fiz. Tverd. Tela (Leningrad) **31**, No. 10, 58 (1989) [Sov. Phys. Solid State **31**, 1684 (1989)]; M. V. Logunov, V. V. Randoshkin, and Yu. N. Sazhin, Fiz. Tverd. Tela (Leningrad) **32**, 1456 (1990) [Sov. Phys. Solid State **32**, 849 (1990)].
[23] M. V. Chetkin, V. B. Smirnov, A. F. Novikov, I. V. Parygina, A. K. Zvezdin, and S. V. Gomonov, Zh. Éksp. Teor. Fiz. **94**, No. 11, 164 (1988) [Sov. Phys. JETP **67**, 2269 (1988)].
[24] M. V. Logunov, V. V. Randoshkin, and A. Ya. Chervonenkis, Pis'ma Zh. Tekh, Fiz. **15**, No. 5, 64 (1989) [Sov. Tech. Phys. Lett. **15**, 358 (1989)].
[25] B. A. Ivanov, N. E. Kulagin, and K. A. Safaryan, Physica B **202**, 193 (1994).

Translated by Eugene Yankovsky

Nonlinear laser-induced regime of surface-electromagnetic-wave generation and submicron periodic relief during liquid-phase photochemical etching of *n*-III–V semiconductors

V. N. Seminogov, V. Ya. Panchenko, and A. I. Khudobenko

Scientific Research Center for Technological Lasers, Russian Academy of Sciences, 142092 Troitsk, Moscow Region, Russia
(Submitted 7 May 1996)
Zh. Éksp. Teor. Fiz. **111**, 174–198 (January 1997)

This paper is devoted to an experimental study of the physical processes underlying the phenomenon of laser-induced generation of periodic relief on the surface of *n*-III–V semiconductors during liquid-phase photochemical or photoelectrochemical etching accompanying the resonance interaction of surface electromagnetic waves (SEWs). The increments of the exponentially increasing amplitudes of the dominant Fourier harmonics of the relief have been measured at the initial (linear) stage of the time evolution of the surface profile. It is proven by comparing the theoretical and experimental results that the mechanism for forming periodic structures that we have proposed is adequate. Ways of monochromatizing the generated relief and controlling the line shape of the surface grating are studied. It is experimentally detected for the first time that the nonlinear stage of the time evolution of the relief is characterized, in accordance with the predictions of the theory developed by the authors, by amplitude and phase oscillations of the first and second Fourier harmonics of the surface profile. It is shown to be possible to generate relief that suppresses specular reflection from the surface. A new nonmasked laser method is developed for forming high-quality submicron relief diffraction gratings, combining a holographic method and a method involving laser-induced relief generation during resonance excitation of SEWs. Diffraction gratings with a period of $d=0.24-0.54$ μm and a depth of $h=0.1-0.2$ μm over an area of 0.5×1 cm have been created on an *n*-InP surface. © *1997 American Institute of Physics.* [S1063-7761(97)01201-8]

1. INTRODUCTION

Relief diffraction gratings are widely used in scientific research, integrated optics, and fiberoptic communications. Diffraction gratings have been used as a basis for systems for injecting and extracting radiation from planar and fiber optical waveguides,[1–6] semiconductor and fiber lasers with distributed feedback and with distributed Bragg reflectors,[1,7–11] optical filters,[1,12,13] couplers and equipower laser-beam splitters, including those for synchronizing the radiation of multichannel lasers,[14,15] high-efficiency polarization converters of laser radiation for technological complexes for the laser cutting of metals,[16,17] selective detectors and photodiodes,[18–21] etc. There are currently several methods for fabricating relief diffraction gratings on semiconductor surfaces: electron-beam and ion-beam lithography, a photographic method, etc. These methods assume the use of a mask and are therefore complex and have many steps. Unlike this conventional method for fabricating gratings. the laser holographic etching of semiconductors is a maskless method. Periodic relief is formed on a semiconductor surface by direct spatially inhomogeneous photochemical and photoelectrochemical etching (see Sec. 2) caused by the interference intensity distribution created by having two laser beams converge on the substrate surface. One of the main drawbacks of the method is that it is highly sensitive to vibration of the optical elements.

Besides the holographic method, there is another method for the maskless formation of surface periodic relief under the action of one laser beam. A periodically inhomogeneous intensity distribution appears on the sample surface because of laser-induced generation of surface electromagnetic waves (LIG-SEW) and because these waves interfere with the incident wave. The phenomenon whereby periodic structures form during LIG-SEW has a fairly universal character. It has been observed during laser-stimulated pyrolytic etching and deposition of films (see Panchenko *et al.*'s review[22] and the citations therein), during the laser generation of acoustic waves on solid surfaces, and during the laser melting and vaporization of metals, semiconductors, and insulators (see Ref. 23 and the citations therein). It has been theoretically and experimentally shown[22,24–27] that the generation of relief gratings accompanying LIG-SEW can be induced during the liquid-phase etching of *n*-III–V semiconductors. [The reviews listed as Refs. 22 and 23 mainly reflect studies concerning the linear (initial) stage of relief formation. Reference 26 gives an exhaustive list of works concerning the nonlinear stage, which is characterized by the interaction of the generated harmonics with each other.] It should be pointed out that the LIG-SEW method is insensitive to vibrations. Nevertheless, we know of no work in which this method could have been used to fabricate diffraction gratings comparable in quality with gratings formed by the holographic method.

This paper is devoted to an experimental study of the physical processes underlying a new maskless method that we have proposed for the laser-stimulated formation of high-

quality submicron relief diffraction gratings on the surface of the semiconductors n-InP and n-GaAs during liquid-phase photochemical or photoelectrochemical etching. This method (the modified LIG-SEW method) is a combination of the holographic method and the LIG-SEW method and combines the advantages of both methods. To provide a basis for the method, we have studied both the linear and the nonlinear stage of the time evolution of the relief during LIG-SEW.

Section 2 explains the photochemical etching mechanism of n-III–V semiconductors. Section 3 discusses features of the formation of relief gratings on the surface of n-InP and n-GaAs by the holographic method. The influence of laser-beam polarization on the depth of high-quality gratings is studied. The main advantages and disadvantages of the holographic method are formulated.

Section 4 is devoted to an experimental study of the time evolution of the surface periodic relief formed under the action of one laser beam by the LIG-SEW method. Sections 4.1–4.3 present the physical mechanism for the appearance of positive feedback of LIG-SEW during photochemical etching and the main theoretical results of Refs. 22, 25 and 26 for the linear and nonlinear regimes of the time evolution of the surface relief. Section 4.4 for the first time presents the results of our measurements of the gain factors of the exponentially increasing Fourier amplitudes of the dominant gratings at the linear (initial) stage. By comparing the experimental and calculated increments, it is proven that the theory developed in Refs. 22 and 25 is valid. The possibilities for monochromatizing the relief are studied. An experimental estimate of the quality of the diffraction gratings is given, and the advantages and disadvantages of the LIG-SEW method are explained.

Section 5 describes the main ideas of a modified LIG-SEW method that results in a substantial monochromatization of the generated relief. The temporal dynamics of relief formation accompanying LIG-SEW at the nonlinear stage are experimentally studied for the first time. It is shown that, in accordance with theoretical predictions (see Ref. 26 and the citations therein), the temporal evolution of the Fourier amplitudes of the surface relief has an oscillatory character and is accompanied by the laser-stimulated suppression of specular reflection. The possibilities of controlling the shape of the surface profile of the generated relief are studied. In particular, it is shown that the modified LIG-SEW method can be used to shape high-quality diffraction gratings not only with a symmetric line profile, as in the case of holographic etching, but also with an asymmetric line profile.

2. THE PHYSICAL MECHANISM OF LASER-INDUCED VARIATION OF THE LIQUID-PHASE ETCHING RATE OF n-III–V SEMICONDUCTORS

It is well known that the etching of n-type III–V semiconductors is initiated by the formation of III^{3+} and V^{3+} ions in accordance with[28,29]

$$\text{III–V}+6h(+)=\text{III}^{3+}+\text{V}^{3+}, \tag{1}$$

where the symbol $h(+)$ denotes a hole. The subsequent chemical reaction of the positively charged ions of the semiconductor with negatively charged electrolyte ions results in the oxidation and subsequent etching of the surface. During dark etching with no external electrical potential applied to the sample, each surface point of the semiconductor is alternately the cathode and the anode of the electrochemical reaction. This means that oxidation of the material and reduction of the etchant components occur simultaneously at any surface point.

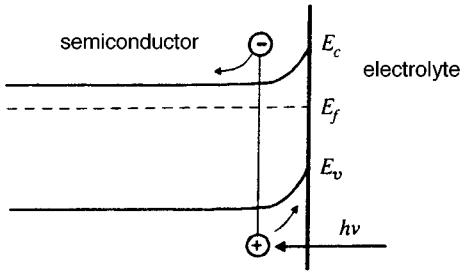

FIG. 1. Diagram illustrating the bending of the valence band and the conduction band close to an n-type semiconductor–etchant interface, where E_f is the Fermi level. The arrows show the separation of photogenerated electron–hole pairs.

Now let laser radiation whose photon energy is greater than the band gap of this material be incident on the surface of the semiconductor immersed in the etchant. If the semiconductor is n type, the band boundaries at the surface are bent upward, as shown in Fig. 1. Because of this, the laser-induced holes are attracted to the surface, while the photoinduced electrons are repelled from the surface of the semiconductor. As a result, an illuminated region becomes positively charged with respect to unilluminated surface points. According to Eq. (1), the etching rate in the illuminated region increases in this case. We can thus write

$$\nu_0=\nu_L-\nu_D=\beta n(x)=\alpha I_L(x), \tag{2}$$

where ν_L and ν_D are the etching rates at illuminated and unilluminated surface points, respectively, ν_0 is the laser-induced change in the etching rate, $I_L(x)$ and $n(x)$ are the light-intensity distribution and the hole concentration on the surface, and α and β are constants.

It follows from Eq. (2) that photochemical etching can be used to produce relief with a given profile on a semiconductor surface if the corresponding spatially inhomogeneous intensity distribution is created on the surface by some means or other.

3. FEATURES OF THE FORMATION OF RELIEF DIFFRACTION GRATINGS ON THE SURFACE OF n-InP BY A HOLOGRAPHIC METHOD

The conventional maskless method of forming periodic relief is a holographic method in which two laser beams interfere to create a periodic intensity distribution on the sample surface. We carried out experiments on the laser formation of diffraction gratings on n-InP samples ($n\approx 5\times 10^{18}$ cm^{-3}), using an $\text{HCl:HNO}_3\text{:H}_2\text{O}=4\text{:}1\text{:}70$ etchant. The experimental layout is shown in Fig. 2. All the equipment was mounted on a holographic table. To eliminate the effect of vibrations of the etchant surface on the quality of the resulting gratings, quartz window *3* was put in contact

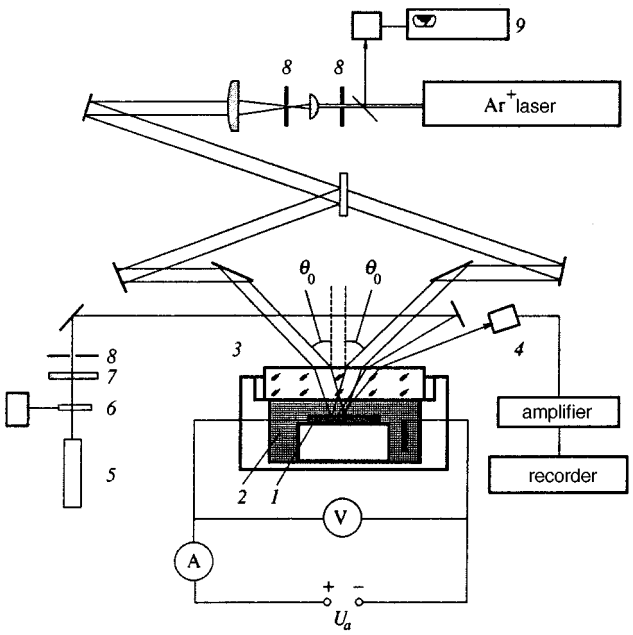

FIG. 2. Layout of experimental apparatus for forming relief diffraction gratings on semiconductor surfaces by the holographic method during photoelectrochemical etching: *1*—sample, *2*—etchant, *3*—entrance window, *4*—detector, *5*—He–Ne laser, *6*—mechanical modulator, *7*—optical filter, *8*—stops, *9*—power meter.

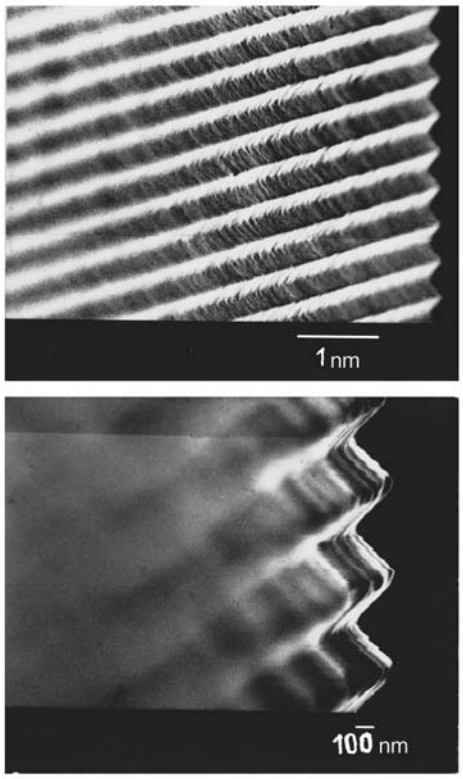

FIG. 3. SEM micrographs of a diffraction grating with a period of 480 nm and a depth of 180 nm, fabricated on an *n*-InP surface by the holographic method. The grating lines are oriented parallel to the $(01\bar{1})$ axis of the crystal; $U_a = 1.38$ V, $t = 3$ min, Ar^+ laser power $P = 25$ mW, *p*-polarized laser beams.

with the etchant. The radiation of an Ar^+ laser with a wavelength of $\lambda = 488$ nm and a power of 100 mW was used to record the gratings. The laser beam was split by a beamsplitter into two *s*- or *p*-polarized beams 1.4 cm in diameter, which then converged at an angle θ_0 onto the sample surface. The time evolution of the grating amplitude $\xi(t)$ was monitored from the diffraction intensity $I_{-1}(t) \sim \xi^2(t)$ of the probe radiation of a He–Ne laser in the minus-first order. To prevent the probe radiation from affecting the etching process, the intensity of the He–Ne laser was a factor of 1000 less than that of the Ar^+ laser. The $I_{-1}(t)$ signal was fed to a recorder. The InP semiconductor is fairly stable with respect to etching by the material. Therefore, to etch the InP, it is necessary to apply to the sample an external potential of $U_a = 0.8–1.5$ V, positive with respect to the electrolyte.

In accordance with the etching mechanism explained in Sec. 2, the spatially inhomogeneous intensity distribution along the sample surface, caused by the interference of the two laser beams, creates a spatially inhomogeneous concentration of electron–hole pairs and causes spatially inhomogeneous etching of the sample. As a result, we can expect periodic relief with reciprocal lattice vector **g** to be formed,

$$\mathbf{g} \| \mathbf{k}_t, \quad g = 2k_t = 2k_0 \sin\theta_0, \quad d = \lambda/2 \sin\theta_0, \tag{3}$$

where $d = 2\pi/g$ is the grating period, $k_0 = \omega/c = 2\pi/\lambda$, c and ω are the speed of light in vacuum and the frequency of the incident laser radiation, and the $\mathbf{k}_t$ are the projections of the wave vectors $\mathbf{k}_0$ of the incident beams onto the sample surface. In this case, according to Eq. (2), the time evolution of the Fourier amplitude of the grating of Eqs. (3) is described by

$$\xi(t) = \alpha I t, \tag{4}$$

where I is the intensity of the laser beams, and t is the exposure time.

Using the holographic method, we formed high-quality diffraction gratings with periods of $d = 0.24–0.54$ μm on an area of about 1 cm^2. To form gratings with periods of $d = 0.24$ μm, we used a prism instead of input window *3*. The periods of these gratings and the initial stage of the time evolution are well described by Eqs. (3) and (4).

Let us point out some features of the generation of relief by the holographic method.

(a) Figures 3 and 4 show micrographs of two gratings formed under virtually identical conditions but with different orientations of the crystallographic axes of the semiconductor substrate relative to the grating lines. It can be seen that the grating in Fig. 3 has a symmetric triangular surface profile, while the grating in Fig. 4 has a symmetric U-shaped profile. Gratings formed by holographic recording always have symmetric relief, but the specific form of the surface profile strongly depends on the crystal orientation.

(b) It has been found experimentally that, besides the crystallographic orientation of the substrate, the polarization of the recording laser beams strongly affects the shape and depth of the surface relief. It should be pointed out that when highly doped *n*-InP is etched photoelectrochemically, the effective hole-diffusion length is very small, and the effect of the blurring of the photoinduced charge carriers on the depth and shape of the grating profile can therefore be neglected in

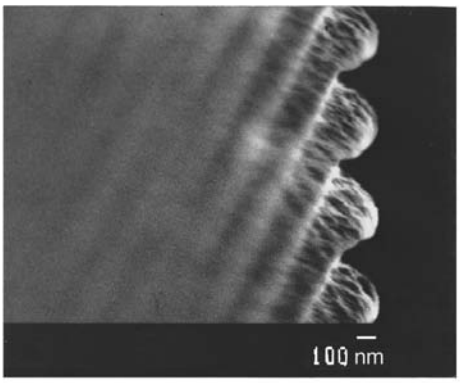

FIG. 4. SEM micrograph of a diffraction grating with a period of 480 nm and a depth of 200 nm, fabricated on an n-InP surface by the holographic method. The grating lines are oriented parallel to the (011) axis of the crystal; $U_a = 1.1$ V, $t = 3$ min, Ar^+ laser power $P = 25$ mW, p-polarized laser beams.

our experiments. Therefore, to achieve the maximum depth for the grating of Eqs. (3), it would seem necessary, according to Eq. (4), to provide a long exposure time t. However, as shown by experiment, when time t is greater than some limiting exposure time t_l, the Fourier amplitude of the grating of Eqs. (3) decreases, and the generation of stray Fourier harmonics of the surface relief becomes appreciable. Figures 5a and 5b show micrographs of two gratings obtained under identical experimental conditions except for the polarization state of the laser beams. It can be seen from Fig. 5b that a grating with the parameters of Eqs. (3) is made ''noisy'' by a perpendicularly oriented quasi-periodic structure. With p polarization of the laser beams, as seen from Fig. 5a, the relief was formed with no loss of quality of the grating. This means that time t_l, or, what is the same thing, the limiting depth of ''quieted'' gratings depends on the polarization of the incident laser beams. It was noted experimentally for the first time that, to attain the limiting depths of good-quality gratings, it is best to use p-polarized laser beams at small angles θ_0 and s-polarized laser beams at large angles θ_0. In particular, we formed good-quality gratings with a period of $d = 0.24$ μm and a depth of $h = 0.1$ μm when we used s-polarized laser radiation. With p polarization of the laser beams, the quality of gratings with such a period is substantially worse. We assume that the stray gratings are formed by a competing process of laser-induced relief generation, caused by resonance excitation of SEWs (see Section 4.2).

In concluding this section, we enumerate the main advantages and disadvantages of the holographic method of recording gratings. The advantages are that the resulting gratings are highly monochromatic and that they are homogeneous in amplitude and phase within the limits of the laser beam. The disadvantages are that the shape of the surface profile depends on the crystallographic orientation of the substrate and that the method is highly sensitive to vibrations of the optical elements.

4. LASER-INDUCED GENERATION OF SURFACE ELECTROMAGNETIC WAVES AND OF PERIODIC SURFACE RELIEF UNDER THE ACTION OF ONE LASER BEAM—THE LIG-SEW METHOD

In this section, the main results of the theory that we developed for the linear[22,25] and nonlinear[26] regimes of the induced generation of SEWs and of periodic relief during the liquid-phase etching of semiconductors are formulated. It is experimentally proven that the theory of Refs. 22 and 25 is valid. The theoretically predicted possibilities of monochromatizing the generated relief are studied, and the advantages and disadvantages of the LIG-SEW method are discussed.

4.1. The physical mechanism[22,25] of the induced generation of SEWs and of periodic surface relief during the liquid-phase photochemical etching of semiconductors

Let the surface of an n-type semiconductor placed in a liquid-phase etchant (see Fig. 6) be illuminated by laser radiation with a photon energy greater than the band gap of the semiconductor ($\lambda = 514$ nm). Because of diffraction of the incident plane electromagnetic wave by the ever-present roughness of the surface, resonance SEWs are excited. The interference of these SEWs and the Fresnel wave refracted into the medium results in a spatially inhomogeneous intensity distribution of the electromagnetic field along the semiconductor surface, which provides spatially inhomogeneous electron–hole-pair generation. Since the photochemical etching rate depends on the hole concentration close to the semi-

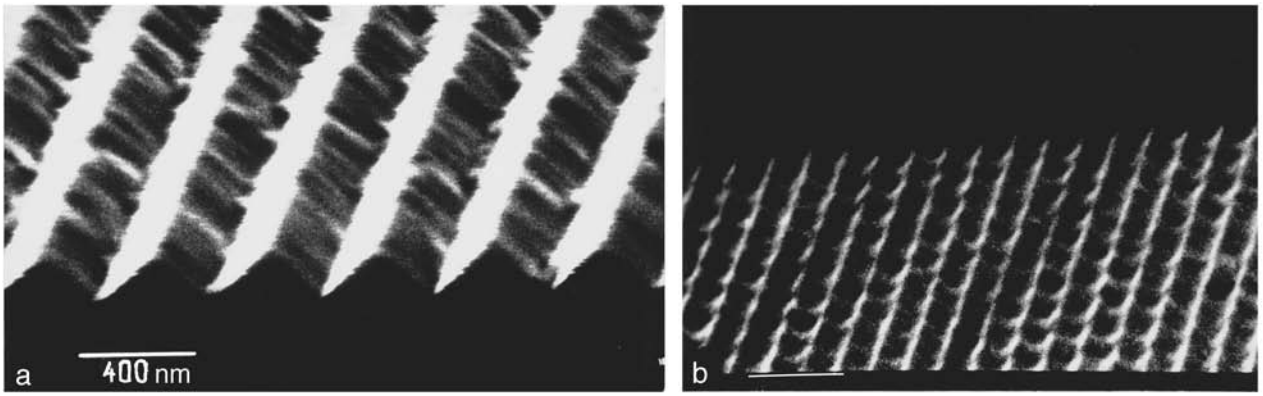

FIG. 5. SEM micrograph of two diffraction gratings with a period of 400 nm, fabricated on an n-InP surface by the holographic method with (a) p-polarized laser beams, (b) s-polarized laser beams, grating depth 60 nm.

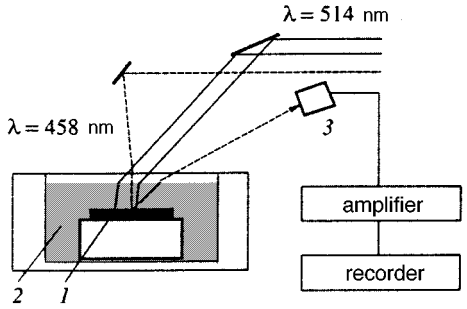

FIG. 6. Layout of the experimental apparatus: *1*—*n*-GaAs sample, *2*—etchant, *3*—device to record the time dependence of diffraction intensity $I_{-1}(t)$ of the probe radiation ($\lambda = 458$ nm) in the minus-first order.

conductor surface [see Eq. (2)], spatially inhomogeneous surface etching occurs, and the Fourier amplitudes of the initial trigger roughness are altered. This in turn results in the time evolution (strengthening) of the diffraction of the light and causes feedback, as a consequence of which the Fourier amplitudes ξ_g of the surface relief exponentially increase (or are damped) at the linear (initial) stage [compare with Eq. (4)]:

$$\xi_g = \xi_g^{(0)} \exp(\gamma_g t), \tag{5}$$

where $\xi_g^{(0)}$ is the amplitude of the Fourier harmonic of the trigger roughness with reciprocal lattice vector **g**. The relief becomes periodic because of the dominant grating, which possesses the maximum growth factor γ_g.

4.2. Theoretical results for the linear stage of the generation of periodic surface relief

According to the theory developed in Refs. 22 and 25, when laser radiation acts on the (x,y) surface of a semiconductor immersed in an etchant, a class of resonance gratings is generated (with vector **g**) for which the ends of the wave vectors $\mathbf{k}_g = \mathbf{k}_t - \mathbf{g}$ of the SEWs lie on a circle of radius $k_0 n^+$ (see Fig. 7a). In this case, if the incident radiation is p-polarized ($\mathbf{E}_{it} \| \mathbf{k}_t$), the two gratings whose periods and orientations are described by (compare Fig. 7b)

$$\mathbf{g} \| \mathbf{E}_{it}, \quad \mathbf{k}_g = \mathbf{k}_t - \mathbf{g}, \quad |\mathbf{k}_g| = k_0 n^+, \quad \cos\varphi_s = \pm 1,$$
$$d = \lambda/(n^+ \mp \varepsilon_0^{1/2} \sin\theta),$$
$$n^{+2} = \varepsilon_0[1 + \varepsilon_0(n+m)^2/(n^2+m^2)^2] \tag{6}$$

are dominant in the class of resonance structures, where $|\mathbf{g}| = 2\pi/d$; $k_0 = 2\pi/\lambda$; λ is the wavelength of the light in vacuum; θ is the angle of incidence of the exciting wave at the etchant–semiconductor interface; ε_0 and $\varepsilon = (n+im)^2$ are the permittivities of the etchant and the semiconductor, respectively; φ_s is the angle between the propagation direction of the SEW and $\mathbf{k}_t$; and $\mathbf{E}_{it}$ and $\mathbf{k}_t$ are the projections of the electric vector and the wave vector of the incident wave onto the (x,y) plane, with vector $\mathbf{k}_t$ ($|\mathbf{k}_t| = k_0 \varepsilon_0^{1/2} \sin\theta$) being parallel to the y axis. The increments of these two dominant gratings ($\cos\varphi_s = \pm 1$) are given by

$$\gamma_g^{(\mp)} = \nu_0 k_0 \frac{n^2+m^2}{2n\varepsilon_0}(n^+ \mp \varepsilon_0^{1/2} \sin\theta),$$
$$\nu_0 = \nu_L - \nu_D = \alpha I_i, \tag{7}$$

where I_i is the intensity of the incident radiation, and the exact expression for the constant α is given in Refs. 22 and 25. It was assumed in deriving Eq. (7) that $gL \ll 1$, where L is the effective hole diffusion length close to the semiconductor surface.

If the incident radiation is s-polarized ($\mathbf{E}_i = \mathbf{E}_{it} \perp \mathbf{k}_t$), when $\theta \leqslant 45°$, the grating (see Fig. 7c, $\cos\varphi_s = \varepsilon_0^{1/2} \sin\theta/n^+$) with parameters

$$\mathbf{g} \| \mathbf{E}_{it}, \quad d = \lambda/[n^{+2} - \varepsilon_0 \sin^2\theta]^{1/2}, \quad \theta \leqslant 45° \tag{8}$$

is dominant in the class of resonance structures, whereas when $\theta \geqslant 45°$, the two lattices (for which $\cos\varphi_s = 0$ in Fig. 7a) with periods

$$d = \lambda/[n^{+2} + \varepsilon_0 \sin^2\theta]^{1/2}, \quad \theta \geqslant 45° \tag{9}$$

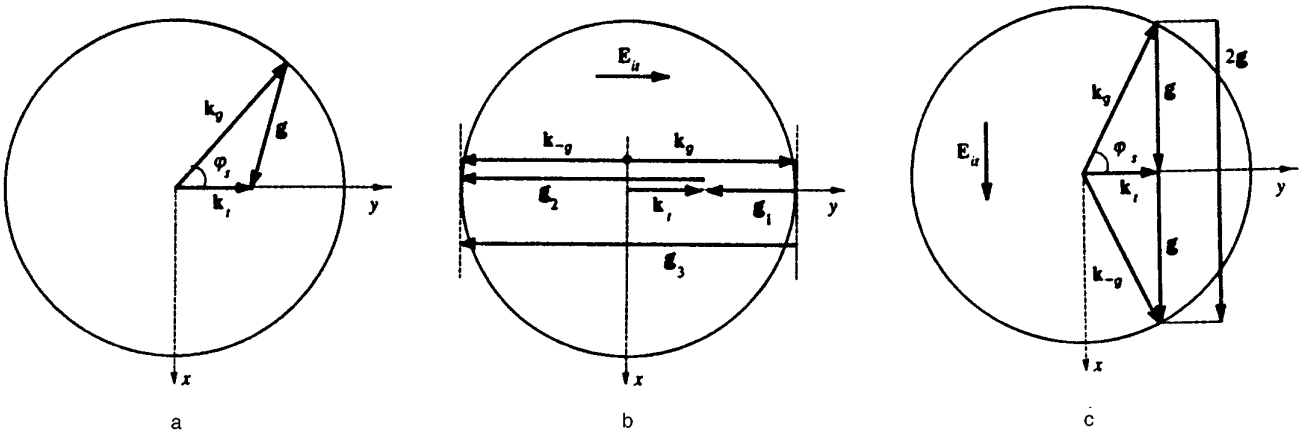

FIG. 7. (a) Class of resonance gratings **g** and resonance SEWs for which $|\mathbf{k}_g| \simeq k_0 n^+$. (b) At the linear stage, the interference of a p-polarized incident wave $\mathbf{k}_t$ with the resonance SEWs $\mathbf{k}_g$ and $\mathbf{k}_{-g}$ causes the induced generation of two dominant resonance gratings with $\mathbf{g} = \mathbf{g}_1$ and $\mathbf{g} = \mathbf{g}_2$. (c) At the linear stage, the interference of an s-polarized incident wave $\mathbf{k}_t$ with the resonance SEWs $\mathbf{k}_g$ and $\mathbf{k}_{-g}$ causes the stimulated generation of the dominant resonance grating **g**.

have the greatest increment, where n^+ is defined in Eqs. (6). The expression for the increment of the grating of Eqs. (8) when $Lg \ll 1$ has the form

$$\gamma_g = \nu_0 k_0 \frac{n^2+m^2}{nn^{+2}} [n^{+2} - \varepsilon_0 \sin^2 \theta]^{1/2},$$

$$\nu_0 = \nu_L - \nu_D = \alpha I_i . \tag{10}$$

It should be pointed out that when Eqs. (5), (7), and (10) are used for calculations, it is possible to obtain somewhat overestimated values for the increments by comparison with the experimental values. There are two reasons for this. First, when the inequality $Lg \ll 1$ breaks down, charge-carrier diffusion becomes substantial, and this reduces γ_g. Second, Eqs. (5), (7), and (10) are valid for nonpolishing etchants. If polishing electrolytes are used, the substitution $\gamma_g \to \gamma_g - \alpha_g$ must be made in Eq. (5), where $\alpha_g > 0$ characterizes the roughness-polishing rate when $I_i = 0$.

Let us discuss the experimental results described in paragraph (b) of section III from the viewpoint of the mechanism considered here for laser-induced surface instability. When two *s*-polarized beams act on the surface, the holographic grating of Eqs. (3) and (4) is formed. However, under the action of each of these laser beams, a continuum of resonance gratings should increase exponentially [see Eq. (5)], dominated by the grating of Eqs. (8), the lines of which are oriented perpendicular to the lines of the holographic grating (see Fig. 5b). Actually, the experimentally measured periods of the perpendicularly oriented structures in Fig. 5b are in good agreement with the theoretical estimates from Eqs. (3) and (8). Likewise, if the laser beams are *p*-polarized, a superposition of the holographic grating of Eqs. (3) and the resonance gratings of Eqs. (6) should be generated. The experimental fact that an optimal polarization exists for holographic recording of deep gratings for small and large angles θ_0 [see Sec. 3, Paragraph (b)] can be interpreted theoretically on the basis of a comparison of the values of the increments given by Eqs. (7) and (10). It follows from what has been said that the competing process of LIG-SEW imposes a fundamental limitation on the limiting depth of the holographic gratings of Eqs. (3).

4.3. The oscillatory regime of the generation of spatial Fourier harmonics at the nonlinear stage of the laser-induced formation of relief. Theory

The linear stage of the stimulated generation of relief, characterized by a rise in the Fourier amplitudes of the resonance gratings that is exponential in time, Eq. (5), occurs only for small ξ_g, when the amplitudes of the resonance SEWs are $E(\mathbf{k}_g) \ll E_i$. In this case, according to perturbation theory, $E(\mathbf{k}_g) \sim \xi_g$; i.e., the generation of a continuum of resonance gratings is accompanied by exponentially increasing amplitudes of the resonance SEWs. As the exposure time increases, the dependence of the amplitudes of the resonance SEWs on ξ_g becomes nonlinear, while the amplitudes can become comparable to that of the incident field E_i $[E(\mathbf{k}_g) \approx E_i]$ and can even significantly exceed it $[E(\mathbf{k}_g) \gg E_i]$.[30] It is clear in this case that the dynamics of the relief formation will be determined not only by the interference of the incident wave with the laser-induced continuum of SEWs but also by the interference of the different SEWs with each other. If one restricts oneself in the theoretical analysis to considering only the dominant gratings and the resonance SEWs corresponding to them (the discrete-mode model), it is easy to see from Fig. 7c that when the incident radiation is *s*-polarized, along with grating **g** of Eqs. (8), a grating with twice the spatial frequency 2**g** should be generated at the linear stage; this grating is caused by the interference of the dominant resonance SEWs, which have wave vectors $\mathbf{k}_g$ and $\mathbf{k}_{-g}$, with each other. Likewise, if the incident radiation is *p*-polarized, one should expect interconnected generation of gratings $\mathbf{g}_1$ and $\mathbf{g}_2$ of Eqs. (6) and gratings with a total spatial frequency of $\mathbf{g}_3 = \mathbf{g}_1 + \mathbf{g}_2$ (see Fig. 7b). The time evolution of the relief in the case of *s*-polarized laser radiation, calculated in terms of the discrete-mode model on the basis of the analytical theory of Ref. 26, is shown in Fig. 8, where

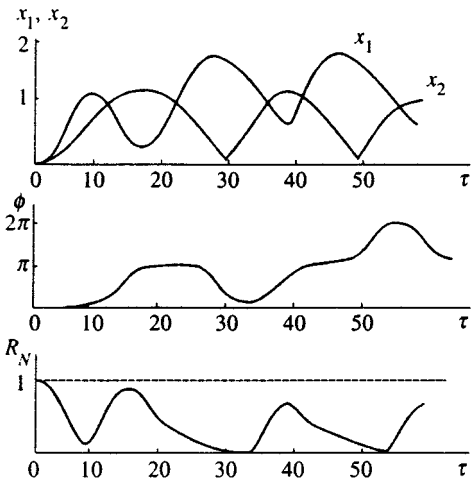

FIG. 8. Time evolution of the normalized amplitudes of the first (x_1) and second (x_2) spatial Fourier harmonics of the surface relief, the relative phase ϕ, and the normalized specular reflectance R_N during photochemical etching of an *n*-GaAs surface, stimulated by one *s*-polarized laser beam; $\lambda = 530$ nm, $n = 4.2$, $m = 0.33$, and $\varepsilon_0^{1/2} = 1.35$.

$$\tau = 2\gamma_g t, \quad \xi_{pg} = |\xi_{pg}| \exp(-i\varphi_p), \quad \phi = 2\varphi_1 - \varphi_2,$$

$$p = 1, 2,$$

$$x_1 = g|\xi_g|/\beta_n, \quad x_2 = 2g^2|\xi_{2g}|/(\beta_n k_0 \varepsilon_0^{1/2}),$$

$$R_N = R_s/R_f .$$

Here R_s and R_f are the specular reflectances, respectively, from the corrugated and the flat surface, $\beta_n = \varepsilon_0^{1/2} n/(n^2+m^2) \ll 1$, the increment γ_g is determined from Eq. (10), and φ_1 and φ_2 are the phases of the first (**g**) and the second (2**g**) harmonics of the surface relief. It can be seen from Fig. 8 that the process of relief generation has the character of out-of-phase oscillations of the moduli of the amplitudes of the first and second harmonics of the surface profile and is accompanied by the temporal variation of the phase difference $(\varphi_1 - \varphi_2)$. It also follows from Fig. 8 that when $R_N = 0$, such a profile of the surface relief is formed that the specularly reflected radiation from the laser-induced

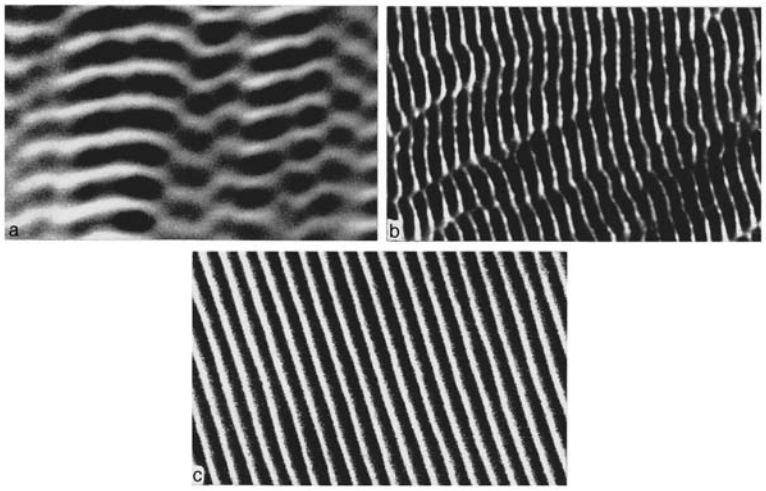

FIG. 9. SEM micrographs of diffraction gratings formed on n-GaAs samples by the LIG-SEW method. In all cases, the grating lines are oriented perpendicular to the electric field vector $\mathbf{E}_{it}$; (a) p-polarized laser beam, $\theta=38°$, $I_i=100$ mW/cm^2, etchant HF:H_2O_2:H_2O=1:2:30; (b) $\theta=0$, $I_i=50$ mW/cm^2, etchant HF:H_2O_2:H_2O=1:2:60; (c) s-polarized laser beam, $\theta=38°$, $I_i=50$ mW/cm^2, etchant HF:H_2O_2:H_2O=1:2:60, grating depth $h=50$ nm.

surface is completely suppressed. An oscillatory regime of generation of the harmonics of $\mathbf{g}_1$, $\mathbf{g}_2$, and $\mathbf{g}_3$ (see Fig. 7b) in the process of laser evaporation of the material is also predicted in the case of p-polarized laser radiation.[31] Reference 32 showed that it is possible for an oscillatory regime to appear when light is normally incident, on the basis of a solution of the diffraction problem by a numerical method that does not use the Rayleigh hypothesis. However, we know of no work in which the existence of an oscillatory regime of the time evolution has been confirmed experimentally.

4.4. Experimental study of the process of forming periodic relief on the surface of *n*-GaAs by the LIG-SEW method

The layout of the experimental apparatus is shown in Fig. 6. We studied the laser-induced generation of relief gratings on n-GaAs substrates ($n\approx 2\times 10^{18}$ cm^{-3}) under the action of s- and p-polarized radiation from an Ar^+ laser with a wavelength of $\lambda=514$ nm, an intensity of 5–100 mW/cm^2, and a cross-sectional diameter of the laser beam at the sample surface of 0.4 cm. The time evolution of the Fourier amplitude of the surface relief $\xi_g(t)$ was monitored by measuring the intensity $I_{-1}(t)$ [$I_{-1}\sim\xi_g^2(t)$] of the probe beam ($\lambda=458$ nm) in the minus-first order of diffraction. The degree of nonmonochromaticity of the generated relief was estimated by measuring the divergence of the diffracted probe beam.

According to the theory developed in Refs. 22 and 25, to reduce the nonmonochromaticity of gratings generated by the LIG-SEW method, an s-polarized laser beam must be used at angles of incidence of $0\ll\theta<45°$. This fact has been confirmed experimentally. Figures 9a, 9b, and 9c show SEM micrographs of gratings obtained with p and s polarization of the generating radiation and with normal incidence of the beam on the sample surface. The monochromaticity of the grating shown in Fig. 9c is significantly greater than for the gratings shown in Figs. 9a and 9b. The measured periods and orientations of the gratings are in good agreement with the theoretical values computed from Eqs. (6) and (8), where $n=4.3$, $m=0.36$, and $\varepsilon_0^{1/2}=1.35$ for $\lambda=514$ nm.[33] The crystallographic orientation of the substrate had no substantial effect on the parameters of the resulting gratings.

Figure 10a shows the characteristic time dependence of the probe-beam intensity $I_{-1}\sim\xi_g^2$ in minus-first order of diffraction, obtained during the growth of the grating of Eqs. (8) under the action of an s-polarized laser beam. An increase in the signal is initially observed, then saturation, and, after reaching a maximum at time $t=t_m$, a drop to a virtually zero value of I_{-1}. In this case, despite the disappearance of the resonance grating of Eqs. (8), the GaAs sample surface is

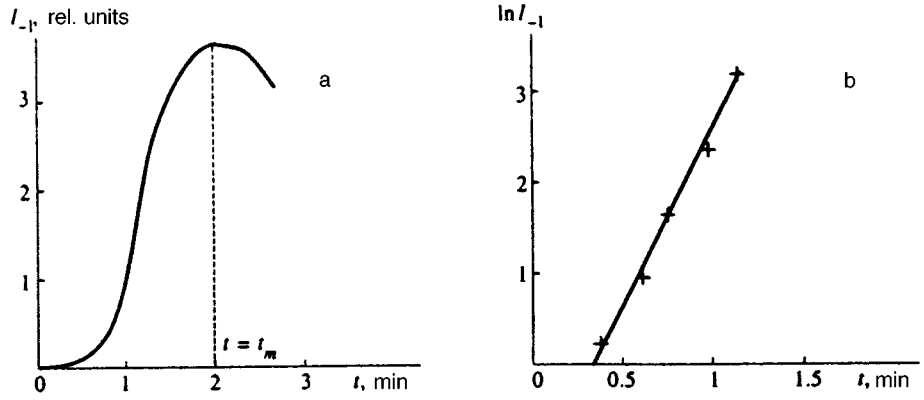

FIG. 10. Probe-signal intensity in the minus-first order of diffraction vs. exposure time t. The periodic relief [Eqs. (8)] was generated by an s-polarized beam incident at an angle of $\theta=18°$ in an etchant of HF:H_2O_2:H_2O=10:1:30; (a) $I_i=50$ mW/cm^2, $\gamma_g-\alpha_g=2.25$ min^{-1}; (b) $I_i=30$ mW/cm^2, $\gamma_g-\alpha_g=1.5$ min^{-1}.

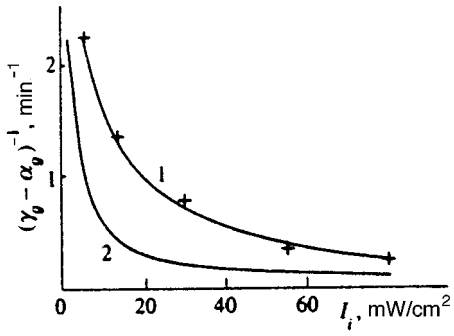

FIG. 11. Growth increment of the diffraction grating of Eqs. (8) vs. intensity of *s*-polarized radiation incident at an angle of $\theta = 18°$ (etchant HF: H_2O_2:H_2O=10:1:30): *1*—experimental curve of $1/(\gamma_g - \alpha_g)$; 2—theoretical curve of $1/\gamma_g$, constructed from Eq. (10).

strongly undulating. Oscillations of $I_{-1}(t)$ corresponding to Fig. 8 were not observed in any of the experiments. Figure 10b gives an experimental graph of $\ln(I_{-1})$ vs t for a time interval $t \ll t_m$. The linear form of this dependence is evidence of the validity of the theoretical prediction [see Eq. (5)] that the growth of the resonance grating of Eqs. (8) has an exponential character at the initial stage of relief formation by the LIG-SEW method. The slope of the straight line in Fig. 10b determines the increment $2(\gamma_g - \alpha_g)$.

Figure 11 shows the theoretical (γ_g) and experimental $(\gamma_g - \alpha_g)$ dependences of the increments on the intensity I_i of incident *s*-polarized laser radiation with $\lambda = 514$ nm. The theoretical γ_g values were calculated from Eq. (10). The values of the homogeneous etching rate ν_0 needed for this were found by experimentally measuring (using a Talystep profilometer) the dependence of the depth of an etched pit on the etching time for given values of I_i and θ. It was found, in agreement with theory, that the dependence of ν_0 on I_i is linear. In particular, when the etchant HF:H_2O_2:H_2O=10:1:30 is used, $\theta = 0$, and $I_i = 100$ mW/cm^2, the measured etching rate is $\nu_0 = 0.5$ μm/min. It can be seen from Fig. 11 that the measured $(\gamma_g - \alpha_g)$ values are about a factor of 4 less than the calculated γ_g values. Nevertheless, the agreement between the theoretical and experimental values of the increments can be considered good, taking into account the remarks made in the text after Eq. (10).

Thus, the comparison of the theoretical and experimental results carried out in Sec. 4.4 is evidence that the mechanism that we have proposed (see Sec. 4.1) suffices to explain the laser-induced surface instability, and that the theory developed in Refs. 22 and 25 for the linear stage of the relief formation accompanying LIG-SEW is valid (see Sec. 4.2).

Let us consider the quality of the gratings formed by the LIG-SEW method. The grating shown in Fig. 9c is only a small segment of the relief structure that has been formed. An examination of larger areas of the surface by means of optical and electron microscopes showed that the laser-stimulated relief structure is a set of islands within which the gratings have the quality shown in Fig. 9c. The boundaries between the islands are characterized by an interruption of the phase of the gratings—breaks and bends of the grating lines. The degree of nonmonochromaticity Δg of gratings formed on a large area was estimated from the divergence $\Delta\theta''_{\text{probe}}$ of the probe radiation ($\lambda = 488$ nm) diffracted in the minus-first order:

$$k_0 \sin \theta'_{\text{probe}} + g = k_0 \sin \theta''_{\text{probe}},$$

$$\Delta g = k_0 \cos \theta''_{\text{probe}} (\Delta\theta''_{\text{probe}}),$$

where θ'_{probe} is the angle of incidence of the probe radiation at the air–etchant interface, and θ''_{probe} is the angle of reflection into the air of the probe laser beam diffracted in minus-first order. For the highest-quality gratings that we fabricated by the LIG-SEW method, the measured divergence is $\Delta\theta''_{\text{probe}} = 3°$, and consequently, the experimental nonmonochromaticity is $(\Delta g)_{\text{exp}} = 6.3 \times 10^3$ cm^{-1}. This means that the mean linear size Δx of the islands ($\Delta g \Delta x \simeq 2\pi$) is $\Delta x \simeq 10$ μm. This estimate shows that the gratings formed by the LIG-SEW have rather low quality.

The physical nature of the nonmonochromaticity of the generated relief consists of the following: the SEW-excitation resonance width Δk_g is finite, with $\Delta k_g = k_0(2nm + n^2)/(m^2 + n^2)^2$.[18] This means that because of the LIG-SEW mechanism, not only will a continuum of resonance gratings for which $\mathbf{k}_t - \mathbf{g} = \mathbf{k}_g$, $|\mathbf{k}_g| = k_0 n^+$ (see Fig. 7) be generated, but also a continuum of quasi-resonance gratings with a spectral width of $\Delta g \simeq \Delta k_g$, for which the discrimination of the increments γ_g for different g increases as Δk_g decreases. The resulting surface relief at the linear stage of the formation can be written, according to Eq. (5), as

$$z(t) = \int\int \xi_g^{(0)} \exp(\gamma_g t - i\mathbf{g}\cdot\mathbf{r}) d\mathbf{g}. \tag{11}$$

When the spectrum of the trigger roughnesses $\xi_g^{(0)}$ is wide (statistical roughness), the shape of the relief is determined only by the discrimination of the increments, i.e., by the resonance width Δk_g of the SEWs. The Q of the SEW resonance in the case of GaAs and $\lambda = 514$ nm is small ($k_0/\Delta k_g = 16$, whereas $k_0/\Delta k_g = 100$–140 for metals); consequently, the degree of nonmonochromaticity of the relief given by Eq. (11) is high.

We assume that this is why no oscillatory regime of the laser-induced relief generation (see Section 4.3) appears in our experiments, since the condition of discreteness of the modes assumed in the theory is not fulfilled.

Thus, the main drawback of the LIG-SEW method is the high degree of nonmonochromaticity of the relief formed on the semiconductor surface. The advantages of the method include (a) weak dependence of the grating parameters on the crystallographic orientation of the substrate, and (b) insensitivity of the method to vibrations. The reason for the latter is that the phase difference of the incident laser wave and the excited SEW is constant as the sample is vibrationally displaced in space.

The experimental studies described in this section apparently confirm the opinion that currently exists that the formation of periodic relief by LIG-SEW is of interest only from a scientific viewpoint as a dramatic example of the nonlinear optics of a surface, but that it is impossible to

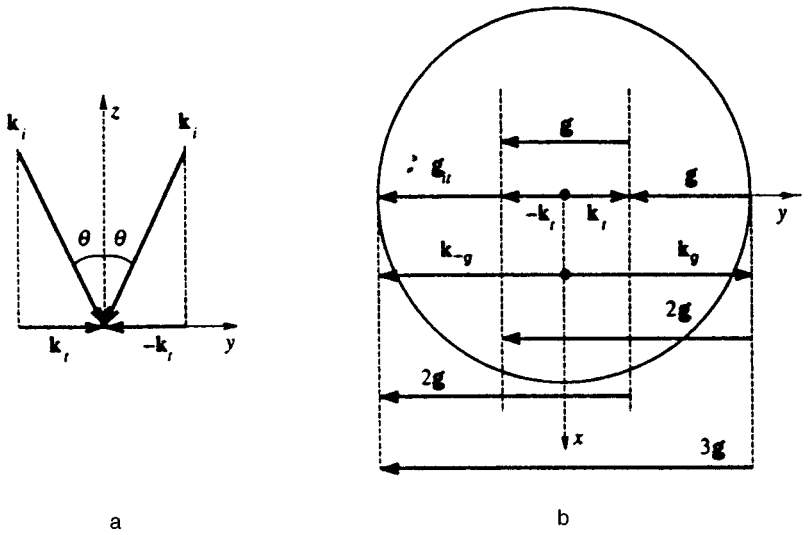

FIG. 12. First technique of the modified LIG-SEW method: (a) geometry of the laser irradiation of the etchant–semiconductor interface at $z=0$; (b) mutual orientation of the wave vectors $\mathbf{k}_t$ and $(-\mathbf{k}_t)$ of the incident waves, of the resonance SEWs $\mathbf{k}_g$ and $\mathbf{k}_{-g}$, and of the resulting gratings $\mathbf{g}$, $2\mathbf{g}$, and $3\mathbf{g}$. The radius of the circle equals $k_0 n^+$. Interference between the waves with $\mathbf{k}_t$ and $(-\mathbf{k}_t)$ results in the formation of holographic grating $\mathbf{g}$. As a result of the diffraction of the incident waves on grating $\mathbf{g}$, resonance SEWs with $\mathbf{k}_g$ and $\mathbf{k}_{-g}$ are excited. Deepening of grating $\mathbf{g}$ occurs because of the interference of wave $\mathbf{k}_t$ with $\mathbf{k}_g$ and of wave $\mathbf{k}_{-t}$ with $\mathbf{k}_{-g}$. Grating $2\mathbf{g}$ is generated by the interference of wave $\mathbf{k}_t$ with $\mathbf{k}_{-g}$ and of wave $\mathbf{k}_{-t}$ with $\mathbf{k}_g$. The formation of Fourier harmonic $3\mathbf{g}$ is caused by the interference of the resonance SEWs with $\mathbf{k}_g$ and $\mathbf{k}_{-g}$ with each other.

develop a process based on this effect for fabricating high-quality diffraction gratings. Is this so? The next section is devoted to an investigation of this question.

5. FORMING HIGH-QUALITY DIFFRACTION GRATINGS ON SEMICONDUCTOR SURFACES BY A MODIFIED LIG-SEW METHOD

5.1. The fundamental idea of the modified LIG-SEW method

We shall analyze the case [opposite to that considered in Section 4.4 when discussing Eq. (11)] in which the spectral width of the trigger relief is much less than the resonance width Δk_g of the SEWs. For clarity, we shall consider the limiting case in which there is only one trigger resonance grating $\xi_g^{(0)} \neq 0$, while the amplitudes of the other Fourier harmonics (with $g' \neq g$) are $\xi_g^{(0)}=0$. It can be seen from Eqs. (5) and (11) that the relief will remain monochromatic at the linear stage of the LIG-SEW, despite the large SEW-excitation resonance width characteristic of semiconductors.

Thus, to enhance the quality of the resulting grating, a trigger relief with large amplitude $\xi_g^{(0)}$ and a high degree of monochromaticity must first be created on the sample surface. This can be done by a holographic method, and a single-beam LIG-SEW method can be used to deepen the trigger structure. The holographic process and the LIG-SEW process in some cases can be carried out simultaneously.

It can be expected that the discrete-mode model will be implemented (see Section 4.3) under these conditions. Observation that the time evolution of the relief predicted by this model has an oscillatory character would serve as a good check of the theory that has been developed, and also as an additional confirmation that the generated relief is highly monochromatic.

There are two possible techniques for implementing the modified LIG-SEW method.

(a) Two p-polarized laser beams with tangential components $\mathbf{k}_t$ and $(-\mathbf{k}_t)$ of the wave vectors (Fig. 12) form a holographic grating with vector $\mathbf{g}=2\mathbf{k}_t$, i.e., with period $d=\lambda/2\varepsilon_0^{1/2}\sin\theta$. On the other hand, each of the incident beams generates gratings with period $d=\lambda/2\varepsilon_0^{1/2}(1\pm\sin\theta)$ as a consequence of the LIG-SEW mechanism [see Eqs. (6), where $n^+\approx\varepsilon_0^{1/2}$]. If the periods of these gratings coincide, both the holographic mechanism and the LIG-SEW mechanism participate in forming the relief. To realize this situation, it is necessary that $\theta=\theta_c=\arcsin(1/3)\approx 19.5°$. In this case, the grating period equals

$$d=3\lambda/2\varepsilon_0^{1/2}, \quad g=2k_t=(2/3)k_0\varepsilon_0^{1/2}, \quad \mathbf{g}\|\mathbf{E}_{it}\|\mathbf{y}. \qquad (12)$$

It is clear from Fig. 12 and its caption that one can expect the first ($\mathbf{g}$), second ($2\mathbf{g}$), and third ($3\mathbf{g}$) harmonics of the surface relief to be generated simultaneously, with vectors $2\mathbf{k}_t$, $4\mathbf{k}_t$, and $6\mathbf{k}_t$.

The technique considered above possesses a substantial drawback: to vary the grating period, the wavelength λ of the incident laser beams must be varied. The second technique for a modified LIG-SEW method is free from this drawback.

(b) A trigger grating with period $d=\lambda/2\varepsilon_0^{1/2}\sin\theta$ is formed by two s- or p-polarized laser beams $\mathbf{k}_t$ and $(-\mathbf{k}_t)$ by the holographic method (see Fig. 13). Under the action of a third s-polarized laser beam $\mathbf{k}_{3t}$ incident at angle θ_3, the grating of Eqs. (8), with a period $d=\lambda/\varepsilon_0^{1/2}\cos\theta_3$, is generated by the LIG-SEW mechanism. When the periods of these gratings coincide, i.e., when

$$d=\lambda/\varepsilon_0^{1/2}\cos\theta_3, \quad \cos\theta_3=2\sin\theta \quad (\theta<30°),$$

$$\mathbf{g}\|\mathbf{E}_{3t}\|\mathbf{x}, \qquad (13)$$

both the holographic mechanism and the LIG-SEW mechanism are involved in the process of creating the grating of Eqs. (13). It can be seen from Fig. 13 and its caption that one can expect relief to be formed that is a superposition of the first ($\mathbf{g}$) and second ($2\mathbf{g}$) Fourier harmonics. The period of Eqs. (13) can be varied in this case by varying the angles of incidence θ and θ_3 according to the equation $\cos\theta_3=2\sin\theta$.

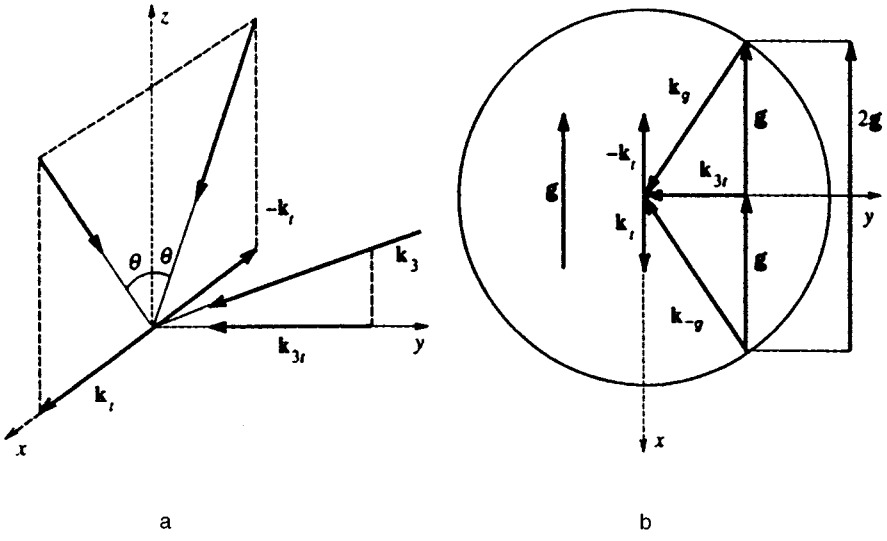

FIG. 13. Second technique of the modified method: (a) geometry of the laser irradiation of the etchant–semiconductor interface at $z=0$; (b) the radius of the circle equals $k_0 n^+$. Interference of the laser beams with $\mathbf{k}_t$ and $(-\mathbf{k}_t)$ results in the formation of holographic grating **g**. The diffraction of the third incident laser beam $\mathbf{k}_{3t}$ on grating **g** results in the excitation of two resonance SEWs $\mathbf{k}_g$ and $\mathbf{k}_{-g}$. Deepening of grating **g** occurs because of the interference of wave $\mathbf{k}_g$ with $\mathbf{k}_{3t}$ and of wave $\mathbf{k}_{-g}$ with $\mathbf{k}_{3t}$. The second Fourier harmonic $2\mathbf{g}$ is generated by the interference of the resonance SEWs with wave vectors $\mathbf{k}_g$ and $\mathbf{k}_{-g}$ with each other.

5.2. The time evolution of the depth and shape of the periodic relief formed by the modified LIG-SEW method. Experiment

The experimental setup for studying the time evolution of the relief formed using the first technique of the modified LIG-SEW method is shown in Fig. 2. To implement the second technique for this method, the apparatus was modified according to the geometry shown in Fig. 13a. The radiation of an Ar^+ laser (power 30 mW, beam diameter 1.4 cm) with a wavelength of $\lambda=514$ nm was used in the experiments to record gratings according to the first technique, and radiation with $\lambda=488$ nm was used to form relief on the basis of the second technique of the modified LIG-SEW method. Photoelectrochemical etching was done on *n*-InP samples ($n=5\times10^{18}$ cm^{-3}) using $U_a\approx1.1$ V and an electrolyte of HNO_3:HCl:H_2O=1:4:70. As before, the temporal dynamics of the amplitude of the first Fourier harmonic of the relief were monitored from the intensity $I_{-1}(t)$ of the diffraction of the probe radiation in minus-first order.

Figure 14 shows the characteristic dependence of I_{-1} on the time of formation of the relief in the geometry shown in Fig. 12. It follows from Fig. 14 that the temporal dynamics of the first Fourier harmonic of the relief of Eqs. (12) has an oscillatory character, which is in complete agreement with the predictions of the theory based on the discrete-mode model (see Sec. 4.3). According to this theory, surface profiles of the relief with different ratios of the amplitudes and phases of the first, second, and third Fourier harmonics are generated at different instants t_1 and t_2 (Fig. 14). This fact is actually confirmed by the SEM micrographs of the gratings in Fig. 15. It can be seen from Fig. 15b that, unlike the holographic method, the modified LIG-SEW method makes it possible to form gratings not only with a symmetric profile but also with an asymmetric profile. Similar results were obtained for laser-induced photochemical etching ($U_a=0$) of *n*-GaAs samples.

Figure 16 shows the dependence of I_{-1} on time *t* when relief was formed on the surface of *n*-InP using the second technique of the modified LIG-SEW method, see Fig. 13. In the experiment, the trigger grating of Eqs. (13), with a depth of 20 nm, was formed in a time of 20 sec by the holographic method by two *p*-polarized laser beams ($\mathbf{k}_t$) and ($-\mathbf{k}_t$) of equal intensity ($I_1=I_2\neq0$). In this case, the intensity of the third beam is $I_3=0$. Further evolution of the grating of Eqs. (13) was accomplished under the action of only one *s*-polarized beam $\mathbf{k}_{3t}$, i.e., with $I_3\neq0$, $I_1=I_2=0$, by the LIG-SEW mechanism. We should point out that the experimental conditions correspond to the prerequisites imposed when constructing the theory of Ref. 26, see Sec. 4.3 and Fig. 8. It can be seen from Fig. 16 that the amplitude of the first Fourier harmonic, given by Eqs. (13), oscillates in time during formation of the relief, as follows from the theory of Ref. 26 (see Fig. 8a). Unfortunately, we were not able during the experiment to obtain the curve (analogous to that shown in Fig. 16) that characterizes the time evolution of the amplitude of the second Fourier harmonic ξ_{2g}, since a shorter-wavelength source of probe radiation is needed for the radia-

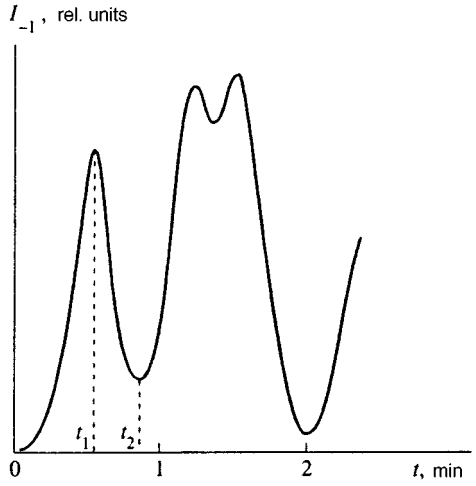

FIG. 14. Intensity of the probe radiation diffracted in minus-first order vs time when relief is formed using the first technique of the modified LIG-SEW method.

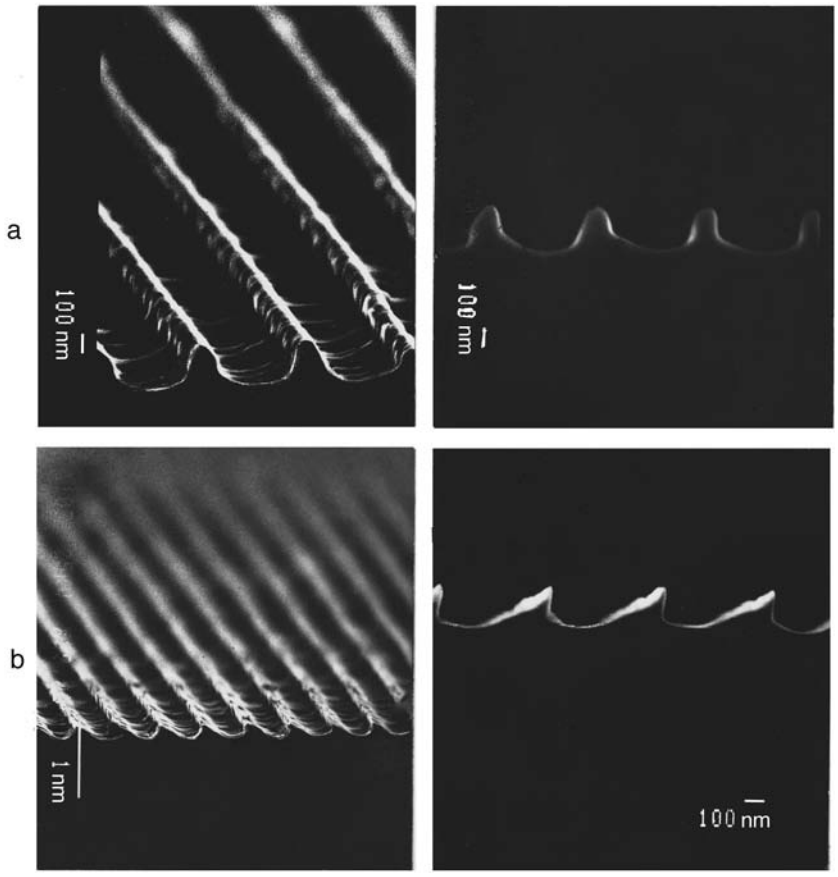

FIG. 15. SEM micrographs of diffraction gratings with period $d=540$ nm, formed on n-InP substrates. The relief-formation process was halted at time t_1 (micrograph a) and at time t_2 (micrograph b), see Fig. 14. The different slope of the lines in micrographs b corresponds to micrographs of the transverse cleavage of two halves of the same sample.

tive first or minus-first orders of diffraction to appear in this harmonic. However, certain conclusions concerning the time evolution of the amplitude ξ_{2g} can be drawn on the basis of the SEM micrographs (see Fig. 17) of the resulting gratings.

Figure 17 shows SEM micrographs of the gratings fabricated when the etching process is halted at times $t_a, t_b, \ldots, t_f$, shown in Fig. 16 by points. It can be seen from these micrographs that a significant change in the depth and shape of the surface profile occurs in the time interval $t_a - t_f$. On the other hand, it follows from Fig. 16 that the intensity of the probe signal I_{-1} is virtually constant over this time interval. This is evidence that there is little change in the amplitude ξ_g of the first Fourier harmonic of the relief given by Eqs. (13). From an analysis of the shape of the surface profile of the gratings shown in Fig. 17, we have determined the following: first, the second harmonic $2\mathbf{g}$ is present in the Fourier spectrum of these gratings; second, a significant change of the amplitude ξ_{2g} occurs over the time interval $t_a - t_f$. Next, the virtually symmetric shape of the relief on micrographs $a-e$ is evidence that the phase difference of the first and second Fourier harmonics changes little over the time interval $t_a - t_e$. A barely noticeable shape asymmetry appears only at time $t=t_f$: the left-hand slope of the line is steeper than the right-hand slope. It is easy to see that the experimental results enumerated above are in good agreement with the theoretical results shown in the upper and middle graphs of Fig. 8 if it is noted that the time interval $t_a - t_f$ in Fig. 16 corresponds to the normalized time interval $\tau = 8-12$ in Fig. 8.

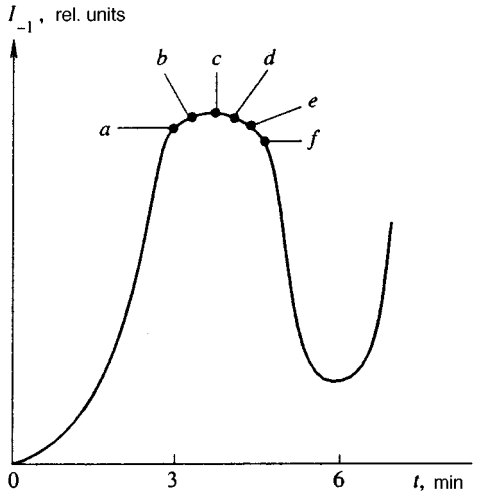

FIG. 16. Diffraction probe signal I_{-1} vs. time when relief is formed using the second technique of the modified LIG-SEW method.

The surface profile of the fabricated gratings was also studied by means of a scanning tunnelling microscope. As an example, Fig. 18 shows an image made with a scanning tunnelling microscope of the diffraction grating shown in the SEM micrograph in Fig. 17d.

In experiments to study the time evolution of the surface relief, we also visually traced the intensity of the specularly reflected beam $I_s(t) = R_s(t) I_3$, where I_3 is the intensity of a laser beam with wave vector $\mathbf{k}_3$ (see Fig. 13), and $R_s(t)$ is

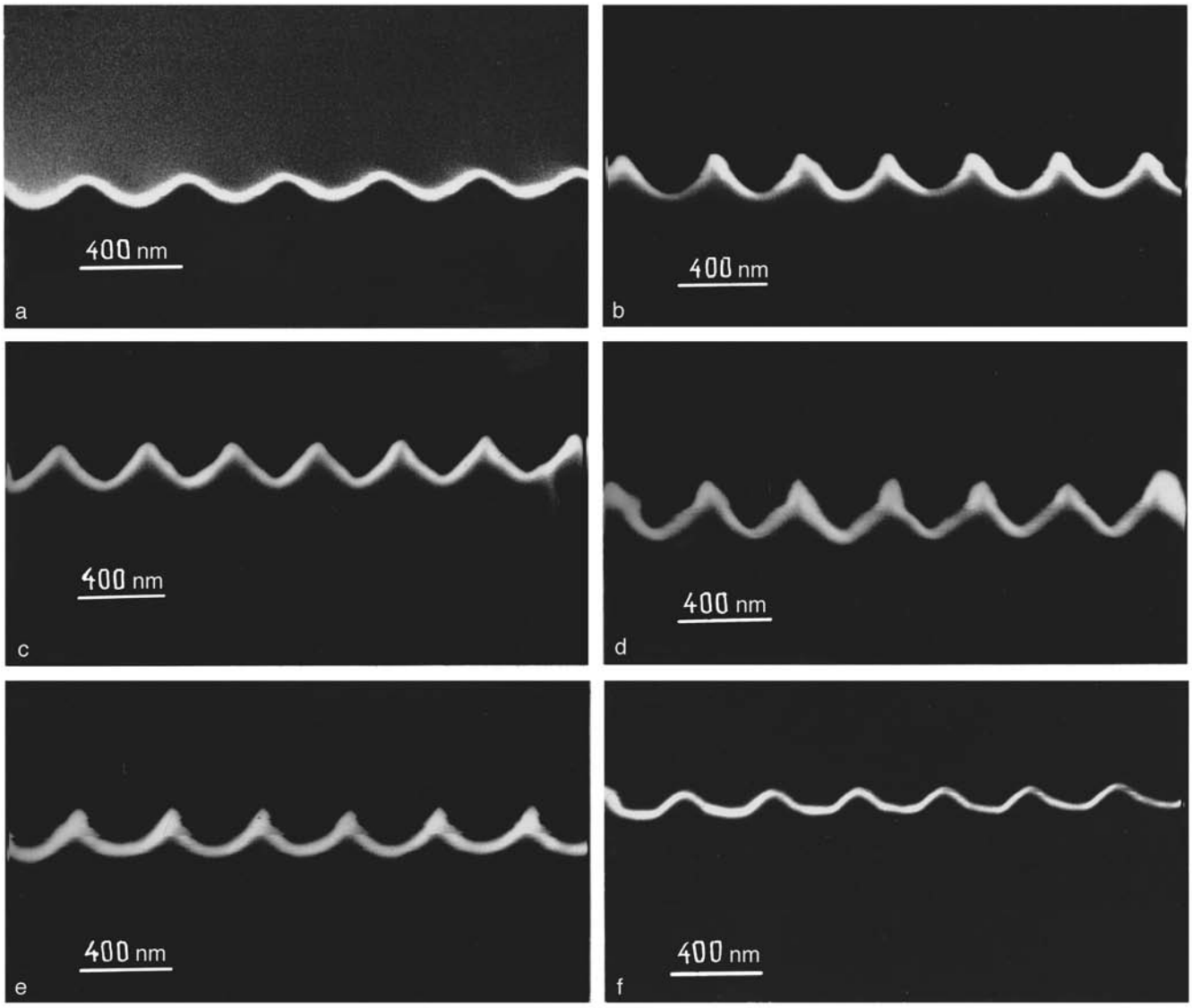

FIG. 17. SEM micrographs of cleaved diffraction gratings. The formation process was halted at times t_a, t_b, t_c, t_d, t_e, and t_f, shown in Fig. 16.

the specular reflectance from the grating at time t. During the time evolution of the first Fourier harmonic, shown in Fig. 16, the intensity $I_s(t)$ decreased significantly, reached a minimum at $t=t_e$, and then substantially increased; i.e., the effect of laser-induced suppression of specular reflection[30,34] during LIG-SEW was observed. This result also agrees with the theoretical predictions (see the bottom graph of Fig. 8).

Thus, we have experimentally shown that the time evolution of the amplitudes and phases of the first and second Fourier harmonics of the surface profile during the formation of gratings based on the first and second techniques of the modified LIG-SEW method has an oscillatory character. The patterns of the time evolution shown in Figs. 14 and 16 are reproducible in this case. This means that the modified LIG-SEW method makes it possible to fabricate diffraction gratings with controllable line shape, where the profile can be varied by varying the grating-formation time. In particular, this method makes it possible to fabricate gratings not only with a symmetric surface (as in the case of the holographic method) but also with asymmetric surface relief.

We estimated the degree of monochromaticity of the diffraction gratings formed by the modified LIG-SEW method on an area of 0.5×1 cm by measuring the divergence of the probe radiation in the minus-first order of diffraction. These measurements showed that the quality of the gratings thus fabricated is no worse than that of gratings formed by the holographic method. From this fact and the remarks above, it can be concluded that the modified LIG-SEW method combines the advantages of the holographic method (see Sec. 3) and the LIG-SEW method (see Sec. 4.4).

6. CONCLUSION

In this paper, a new maskless modified LIG-SEW method has been developed for forming submicron relief diffraction gratings in the process of liquid-phase photochemical or photoelectrochemical etching of the semiconductors *n*-GaAs and *n*-InP. The modified LIG-SEW method is a combination of the holographic method and the LIG-SEW

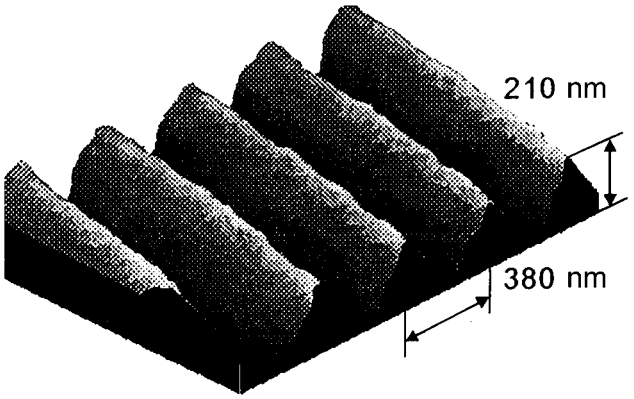

FIG. 18. Image of the grating shown in Fig. 17d, made with a scanning tunneling microscope.

method and combines the advantages of these methods: high quality of the resulting gratings, enhanced stability against vibrations, and the possibility of controlling the shape of the periodic relief. Unlike the holographic method, this method makes it possible to form diffraction gratings not only with symmetric but also with asymmetric line profiles.

The physical processes underlying the method developed here have been studied experimentally. The increments of the exponentially increasing amplitudes of the dominant Fourier harmonics have been measured at the linear stage of formation of the relief. By comparing them with the theoretical values, it has been proven that the mechanism of laser-induced generation of diffraction gratings that we have proposed is adequate. Ways of monochromatizing the generated relief have been studied.

It has been experimentally shown for the first time that the time evolution of the laser-induced relief at the nonlinear stage has the character of out-of-phase amplitude and phase oscillations of the first and second Fourier harmonics of the surface profile. It has been proven that relief can be formed by laser-induced generation of surface structures in such a way that significant suppression of specular reflection from the surface occurs. Good agreement has been demonstrated between the theoretical and experimental results.

Using the modified LIG-SEW method and the holographic method, high-quality relief diffraction gratings have been formed with periods of $d=0.38-0.54$ μm and $d=0.24-0.54$ μm, respectively, with a depth of $h=0.1-0.2$ μm on an area of 0.5×1 cm.

The authors are grateful to V. I. Panov, in whose laboratory the images of the grating surfaces were produced, using a scanning tunneling microscope.

Our research was supported by the Russian Fund for Fundamental Research (Projects No. 95-02-05825, 96-02-18532), the Russian State Scientific–Technical ''Scientific Technologies'' Program, and International Program INTAS-94-902.

[1] T. Tamir (ed.), *Beam and Waveguide Couplers*, Vol. 7 of *Integrated Optics*, T. Tamir (ed.) (Mir, Moscow, 1978; Springer-Verlag, Berlin, 1979).
[2] V. A. Kiselev, Kvant. Elektron. (Moscow) **1**, 1578 (1974) [Sov. J. Quantum Electron. **4**, 872 (1974)].
[3] T. Aoyagi, Y. Aoyagi, and S. Namba, Appl. Phys. Lett. **29**, 303 (1976).
[4] M. T. Wolodarczyk and S. R. Seshadri, J. Appl. Phys. **58**, 69 (1985).
[5] R. L. Roncone, L. Li, A. K. Bates *et al.*, Appl. Opt. **32**, 4522 (1993).
[6] J. Sarathy, R. A. Mayer, K. Jung *et al.*, Opt. Lett. **19**, 798 (1994).
[7] K. Utaka, S. Akiba, K. Sakai, and Y. Matsushima, IEEE J. Quantum Electron. **QE-22**, 1042 (1986).
[8] M. Okai, T. Tsuchiya, K. Uomi *et al.*, IEEE J. Quantum Electron. **27**, 1761 (1991).
[9] V. Mizzahi, D. J. DiGiovanni, R. M. Atkins *et al.*, J. Lightwave Technol. **11**, 2021 (1993).
[10] H. Hillmer, H. L. Zhu, A. Grabmaier *et al.*, Appl. Phys. Lett. **65**, 2130 (1994).
[11] V. N. Seminogov, A. I. Khudobenko, V. Ya. Panchenko, and V. I. Sokolov, Proc. SPIE **2382**, 224 (1995).
[12] L. D. Hutchenson, (ed.), *Integrated Optical Circuits and Components* (Marcel Dekker, New York, 1987).
[13] J. Martin and F. Ouellette, Electron. Lett. **30**, 811 (1994).
[14] H. Haidner, P. Kipfer, J. T. Sheridan *et al.*, Opt. Eng. **32**, 1860 (1993).
[15] J. R. Leger, G. J. Swanson, and W. B. Veldkamp, Appl. Opt. **26**, 4391 (1987).
[16] N. N. Golovatyuk, V. N. Okorkov, V. Ya. Panchenko *et al.*, Izv. Akad. Nauk Ser. Fiz. **57**, No. 12, 39 (1993).
[17] V. N. Okorkov, V. Ya. Panchenko, B. V. Russkikh *et al.*, Opt. Eng. **33**, 3145 (1994).
[18] L. V. Belyakov, D. N. Goryachev, and O. M. Sreseli, Pis'ma Zh. Tekh. Fiz. **11**, 1162 (1985) [Sov. Tech. Phys. Lett. **11**, 481 (1985)].
[19] K. Berthold, W. Beinstingl, and E. Gornik, Opt. Lett. **12**, 69 (1987).
[20] A. Koch, W. Beinstingl, K. Berthold, and E. Gornik, Appl. Phys. Lett. **52**, 1164 (1988).
[21] V. I. Konov, P. I. Nikitin, D. G. Satjukov, and S. A. Uglor, J. Sensors and Actuators A **22**, 498 (1989).
[22] V. Ya. Panchenko, V. N. Seminogov, and V. I. Sokolov, *Summary of Science and Engineering. Physical Principles of Laser and Beam Technology*, N. I. Koroteev and V. Ya. Panchenko (eds.) (VINITI, Moscow, 1989), Vol. 3, p. 92.
[23] S. A. Akhmanov, V. I. Emel'yanov, N. I. Koroteev, and V. N. Seminogov, Usp. Fiz. Nauk **147**, 675 (1985) [Sov. Phys. Usp. **28**, 1084 (1985)]; V. I. Emel'yanov and V. N. Seminogov, *Summary of Science and Engineering. Physical Principles of Laser and Beam Technology*, N. I. Koroteev and V. Ya. Panchenko (eds.) (VINITI, Moscow), Vol. 1, p. 118 (1988); Vol. 3, p. 57 (1989).
[24] G. A. Golubenko, A. M. Prokhorov, V. A. Sychugov, and T. V. Tulaĭkova, Poverkhnost Fiz. Khim. Tekh. No. 1, 88 (1985).
[25] V. Ya. Panchenko, V. N. Seminogov, and A. I. Khudobenko, Kvant. Elektron. (Moscow) **16**, 1226 (1989) [Sov. J. Quantum Electron. **19**, 794 (1989)].
[26] V. N. Seminogov and A. I. Khudobenko, Zh. Éksp. Teor. Fiz. **96**, 504 (1989) [Sov. Phys. JETP **69**, 284 (1989)].
[27] V. Ya. Panchenko, V. K. Popov, V. N. Seminogov, and A. I. Khudobenko, Izv. Ross. Akad. Nauk Ser. Fiz. **56**, No. 4, 91 (1992).
[28] G. C. Tisone and A. W. Jonson, Appl. Phys. Lett. **42**, 530 (1983).
[29] R. M. Osgood, A. Sanchez-Rubio, D. J. Ehrlich, and V. Daneu, Appl. Phys. Lett. **40**, 391 (1982).
[30] S. A. Akhmanov, V. N. Seminogov, and V. I. Sokolov, Zh. Éksp. Teor. Fiz. **93**, 1654 (1987) [Sov. Phys. JETP **66**, 945 (1987)].
[31] L. A. Bol'shov, A. V. Moskovchenko, and M. I. Persiantsev, Zh. Éksp. Teor. Fiz. **94**, No. 4, 62 (1988) [Sov. Phys. JETP **67**, 683 (1988)].
[32] V. V. Kapaev, Poverkhnost' Fiz. Khim. Tekh. No. 4, 110 (1991).
[33] R. K. Willardson and A. C. Beer (eds.), *Semiconductors and Semimetals*, Vol. 3 of *Optical Properties of III–V Compounds* (Academic Press, New York, 1967; Mir. Moscow, 1970).
[34] V. I. Emel'yanov, V. N. Seminogov, and V. I. Sokolov, Kvant. Elektron. (Moscow) **14**, 33 (1987) [Sov. J. Quantum Electron. **17**, 17 (1987)]; V. I. Emel'yanov and V. N. Semenov, Kvant. Elektron. (Moscow) **14**, 47 (1987) [Sov. J. Quantum Electron. **17**, 26 (1987)].

Translated by W. J. Manthey